Defect tolerant lifing of airframe components and the influence of corrosion damage.

Morgans, Christopher

Defect Tolerant Lifing of Airframe Components and the Influence of Corrosion Damage

Christopher Morgans

Ph.D Thesis 2007

ProQuest LLC.
789 East Eisenhower Parkway
P.O. Box 1346
Ann Arbor, MI 48106 – 1346

ABSTRACT

The present thesis describes a programme of research into corrosion pitting in the airframe aluminium alloy AA 7010-T7651 and its subsequent influence on fatigue performance. The alloy is employed extensively in airframe structures, most commonly as wing spars and skins of the BAE SYSTEMS Hawk Mk127 lead-in fighter aircraft. The research programme followed from the major international project SICAS (Structural Integrity assessment of pitting Corrosion in Aircraft Structures), which was instigated as an attempt to minimise the costs associated with in-service corrosion damage. Existing corrosion management techniques are time consuming and expensive, typically involving grinding and mechanical blending of corrosion damaged areas. However, by adopting damage tolerant fatigue lifing procedures in partnership with corrosion detection, a reduction in the cost of corrosion management and safe extensions to aircraft operation lives may be achievable.

Flat plate specimens were subjected to pitting damage via a laboratory based corrosion protocol. Secondly, a centre hole plate specimen was employed, in this case incorporating end grain corrosion within the root of central hole. Detailed characterisation of the pits demonstrated the critical role of microstructure on pit geometry. Both forms of pre-corroded specimen were subjected to a comprehensive matrix of constant amplitude load controlled fatigue testing under controlled humidity and room temperature. Multiple repeat tests were performed at specific stress levels to produce data sets corresponding to fatigue lives of approximately $1x10^4$, $7x10^4$ and $3x10^5$ cycles.

Post testing, LEFM based modelling was performed to describe test specimen performance. This proved successful for the relatively large scale corrosion pitting under consideration.

ACKNOWLEDGEMENTS

I would like to take this opportunity to give thanks to the people that have helped me through my higher education, in particular the staff at Swansea University, who helped me gain my M.Res and B.Eng honours degree in Materials Science and Engineering. I would also like to take the opportunity to thank my Academic Supervisor for this PhD thesis, Professor Martin Bache, for all his time, effort and support over the research period. I would also like to thank my Industrial Supervisor from BAE SYSTEMS, Dr Stuart Spence, for providing the necessary material to complete the programme, and for his support during the project. I would like also to thank EPSRC and BAE SYSTEMS for their financial support of the project.

It is also worth mentioning the assistance I received from the technical staff based at Swansea University, their input in terms of specimen design and manufacture was invaluable. A mention also has to be given to Mr Peter Davies for his expertise and advice in using the Electron microscopes. The support was much appreciated.

TABLE OF CONTENTS

1.0 INTRODUCTION

Aluminium in its purest form is a soft conductive material with many useful properties. Low density coupled with light weight characteristics alongside good machineability and formability make it an attractive material for weight critical components. Additionally, pure aluminium has a good resistance to corrosion, hence its numerous industrial applications. Aluminium's ability to be alloyed with many elements allows taylored properties for specific applications. The main alloying elements are copper (Cu), magnesium (Mg), lithium (Li), zinc (Zn), manganese (Mn) and silicon (Si), with other various elements used as minor additions. These alloying elements make up the aluminium alloy series, ranging from 1000 to 9000 respectively.

The 7000 series alloys were primarily designed for plate and forgings to improve upon such properties as: -

- Strength,
- Fracture toughness,
- Stress corrosion cracking resistance.

Zinc (Zn) is the main alloying element, although small amounts of magnesium (Mg) and copper (Cu) are added for optimised mechanical and corrosion properties. Choices of other elements are also added to customise the alloy to specific applications. The minor addition of Zn, Mg and Cu to the parent aluminium material forms precipitates along grain boundaries within the matrix.

The particular AA 7010 alloy was developed in the late 1970's for strength critical aerospace applications by HDA forgings and Alcan International, under the sponsorship of the UK Ministry of Defence. The over-aged temper condition T-7651, produces Al_7Cu_2Fe and Mg_2Si precipitates in the matrix which appear irregular and round in shape respectively, and lay mainly in recrystallised areas, figure 1.1. The alloy 7010 consists of recrystallised and unrecrystallised grains, the ratios of which are controlled solely by the processing procedures. Subsequent heat treatments determines precipitate size, shape and density, factors which

significantly control the overall mechanical properties of the material. A micrograph of the materials grain structure can be seen in figure 1.2, which illustrates the grain orientation in the three principal planes.

The material is employed for numerous applications within the aerospace industry, with the most common use being airframe structures such as wing spars and skins, figure 1.3. The alloy was a breakthrough for the aerospace industry providing an alternative to the frequently used 7075 and 7079 alloys and is used extensively in the airframe of the BAE SYSTEMS Hawk Mk 127, selected as the Royal Australian Air Force (RAAF) Lead-in-Fighter as figure 1.4 shows. The material exhibits ideal mechanical properties for airframe structures, although is susceptible to in-service environmental damage, particularly through the development of various types of corrosion, including :-

- Pitting Corrosion
- Intergranular Corrosion
- Stress Corrosion Cracking
- Crevice Corrosion

Important transformations in the usage patterns and maintenance practices for military and civil aircraft have occurred over the last thirty years. The most important changes being the use of damage tolerant design in component lifing and the extension of service lives of aircraft beyond their designed lives. The extentended lives of aircraft may appear advantageous in manys ways, however prolonged use beyond defined periods create further corrosion and lifing problems. Operation and ownership of ageing fleets therefore become financially unfavourable since corrosion damage management tools are uncommon and under utilised. Currently, corrosion control on aircraft is based on the "find it, fix it" basis, whereby corrosion damage is removed upon human or Non-Destructive (NDT) detection. Figure 1.5 illustrates examples of corrosion pitting found on an aluminium airframe in service. Removal is carried out via a mechanical grinding and blending process until all damage is seemingly eradicated, which can be time consuming and costly to the fleet. Equally, corrosion may exist in areas of resricted access and possibly will go undetected. Under such circumstances, the possibilty of fatigue crack initiation and growth may be considered through defect tolerant lifing procedures.

Following the removal process, components are strength verified under static and fatigue loading. Failure to meet required standards involves component replacement or modification to restore acceptable strength levels. If this solution is not appropriate, then the aircraft is removed from service This procedure is presently employed as there is no quantitative means of evaluating the severity of corrosion damge with regard to structural integrity. The lack of corrosion damage tools indicate that corrosion may be removed from areas that pose no considerable threat to structural integrity of aircraft. Hence, the advancement of a corrosion management system would greatly reduce maintenance costs and improve aircraft availability and service life.

One solution to manage corrosion damage within aircraft components is the Equivalent Initial Flaw Size (EIFS) approach to LEFM lifing, which considers corrosion pitting damage as fatigue cracks of an equivalent semi-circular size. Data from this approach is considered valuable as it may be directly fed into well documented fatige damage tools. The EIFS approach was comprehensively evaluated in the Structural Inegrity of pitting Corrosion in Aircraft Structure (SICAS) programme, which was launched in September 1999 by BAE Systems in conjunction with CSIRO, DSTO and Swansea University, to assess and minimise the cost of corrosion pitting damage in aluminium alloys and to optimise the corrosion and fatigue management process.

The comprehensive SICAS programme evaluated the AA 7010 alloy in a chromic acid anodising condition under three loading conditions, -0.3, 0.1 and 0.5, using a sigmoidal waveform. This programme considered the very early onset of pitting corrosion for face grain orientation under a fixed environment. A large matrix of repeat testing at planned specific loading conditions, allowed a thorough statistical analysis of the results, which enabled the assesment of the EIFS approach and the distribution within the results. In addition, the repeat testing maximised the confidence amongst the statistical analysis of the EIFS. Since the EIFS technique is extremely sensitive to the form and size of defects, further research was required to evaluate an EIFS associated with pitting that represented a wider range of potential in-service conditions (i.e. larger pits).

The current research work is essentially a direct follow on from the SICAS programme. Once again the model AA 7010 alloy with chromic acid anodising will be employed since a comprehensive database was generated by SICAS. The basic corrosion protocol developed for SICAS is carried forward, however, numerous crucial paramaters will be changed in order to develop the required larger scale pits (corrosion pit depth greater than 200 μm). A change to smaller test coupon geometry will be necessary to reduce costs and allow an extensive assesment of the material in different orientations relative to the rolling direction, including a novel study of "end grain" effects. Whilst fatigue crack growth data has been produced during SICAS, it will be essential to produce a limited amount of additional data to provide confidence in LEFM modelling of the different orientations.

The present programme will require a comprehensive matrix of load control constant amplitude fatigue testing at a single load ratio of 0.1 at ambient temperature and constant environmental conditions. The control of the test environment is essential in order to negate cross continent humidity variation and seasonal effects. Therefore all tests will be carried out at an approximate humidity of 95% Room Humidity (RH), using a specifically designed environmental chamber to accommodate the new specimen design. In support of the fatigue matrix, tensile tests representative of the loading axis of the fatigue specimens will be completed to evaluate basic mechanical properties.

In addition to mechanical testing, the programme will also support fatigue life prediction tools via LEFM techniques. Software packages such as the freely available AFGROW will be implemented to predict constant amplitude fatigue lives subject to pre defined inputs, such as; peak stress conditions, loading ratios, starter defect sizes and specimen dimensions. The predicted lives will be compared to actually generated lives and any variance discussed.

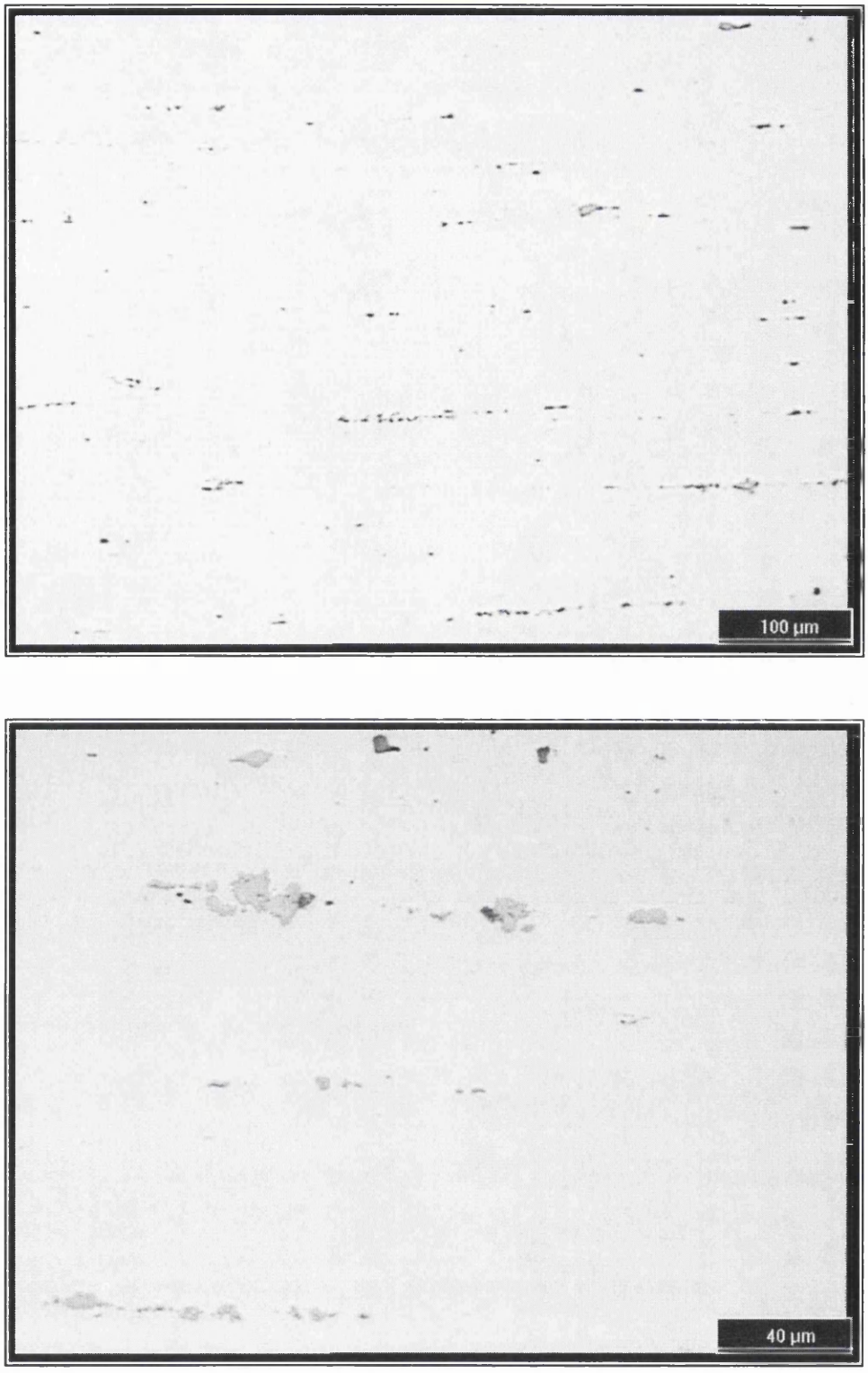

Figure 1.1 Optical micrographs illustrating the intermetallic phases present within the heat treated material. The dark phases represent the Mg_2Si particles, while the lighter phases represent the Al_7Cu_2Fe particles

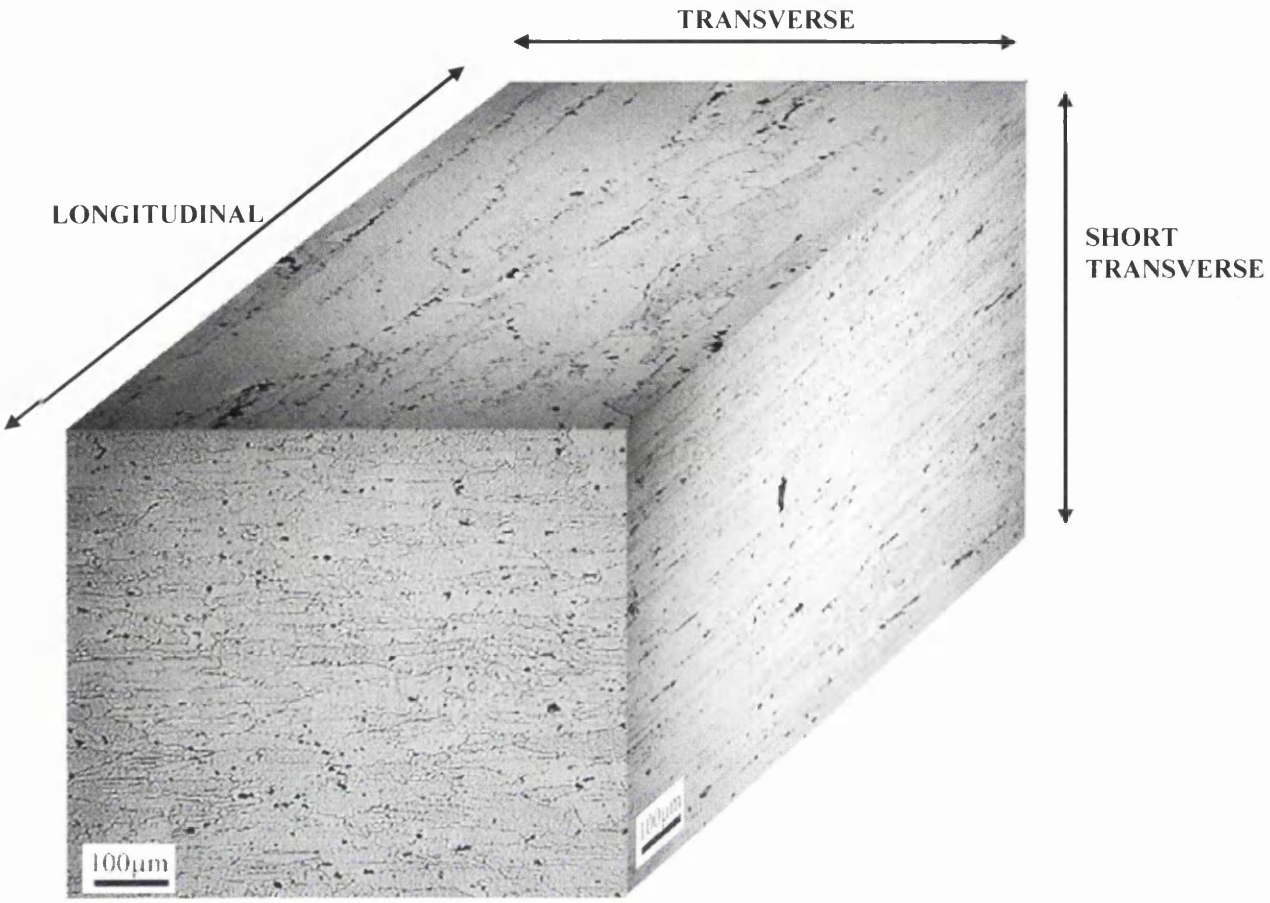

Figure 1.2 AA7010-T7651 grain structure in the three principal planes.

Figure 1.3 BAE SYSTEMS Hawk Mk 127, Lead in Fighter.

Figure 1.4 Illustrations of wing spars and skin. (a),(b) Examples of aluminium wing spars, (c) and skins.

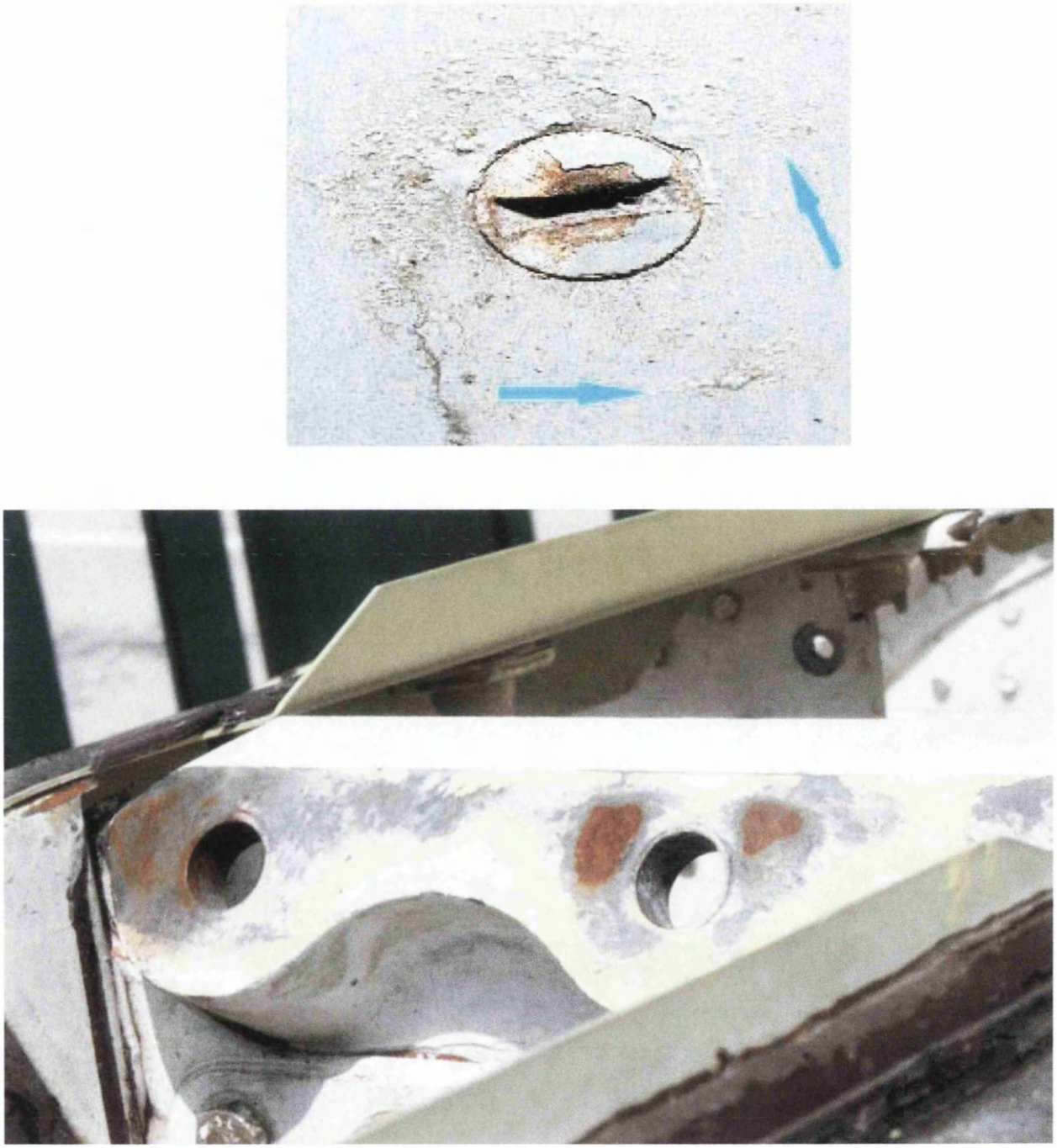

Figure 1.5 Example of in-service corrosion on a fastener hole and surrounding area.

2.0 LITERATURE REVIEW.

This is a review of the scientific literature in the fields of corrosion mechanisms and subsequent mechanical properties of the Aluminium alloy 7010. The material is under a programme of research aimed at the management of corrosion damage in aircraft structures.

2.1 ALUMINIUM AND ITS ALLOYS.

Aluminium is the third most abundant element after oxygen and silicon, and is the most common metal found on earth. The metal ore is mined as bauxite, which contains aluminium oxide, together with oxides of silicon, iron and other metals, which forms eight per cent of the earth's crust. All commercial production of aluminium is based on the Hall-Heroult smelting process whereby the aluminium and oxygen in the alumina are separated by a process known as electrolysis. An electric current is passed through a molten solution of alumina and cryolite which is contained in reduction cells or pots, which are lined at the bottom with carbon (the cathode). Carbon anodes are then inserted through the top of the cell and are partially immersed in the molten solution, thus setting up an electrical circuit. This causes the oxygen from the alumina to combine with the carbon of the anode forming carbon dioxide gas. The remaining molten metallic aluminium collects at the cathode site at the base of the reduction cell. The molten aluminium is then periodically siphoned and cast into large ingots.

Since its maiden extraction in 1886, aluminium has become one of the world's most popular engineering materials, due to its low density and superior corrosion resistance; although alloying has been necessary to improve its mechanical properties, figure 2.1. Major engineering aluminium alloys of the twenty-first century are represented by a series, ranging from 1000 through to 8000. Each series has its specific mechanical and chemical properties, engineered to suit specific applications. A brief overview explains the major alloying elements, applications and attributes:-

- The 1xxx series alloys are detrimentally pure alloys, with applications mainly in the food and beverage packaging industry. Products such as aluminium foil, food containers and beverage cans are good examples of this series type. They are primarily utilised for wrapping and containing foods because of their good corrosion resistance and barrier properties against UV light, moisture and odour. Their strength may be increased by strain hardening, while iron and silicon are considered the major impurities. The 1xxx series have recently been employed in overhead high voltage power lines due to their good electrical conductivity, comparable to that of copper, but somewhat less dense.

- The 2xxx series alloys require solution heat treatment to achieve their optimum properties. After this treatment, mechanical properties are similar to, and sometimes exceed those of low-carbon steel. In some instances, precipitation heat treatment also known as ageing can be employed to further increase mechanical properties. This treatment increases yield strength, with minimal loss in elongation, while the effect on tensile strength is not as good. Corrosion resistance of these alloys are not as good as most other aluminium alloys and under certain conditions they are vulnerable to intergranular corrosion.

- The 3xxx Series. These alloys generally are non-heat treatable but have approximately 20% more strength than the 1xxx series alloys. Because only a limited percentage of manganese (up to ~1.5%) can be effectively added to aluminium, it is used as a major element in only a few alloys.

- 4xxx Series. The major alloying element in 4xxx series alloys is silicon, which can be added in sufficient quantities (up to 12%) to cause substantial lowering of the melting range. For this reason, aluminium-silicon alloys are used in welding wire and as brazing alloys for joining aluminium, where a lower melting range than that of the base metal is required. The

alloys containing appreciable amounts of silicon become dark grey to charcoal when anodic oxide finishes are applied and hence are in demand for architectural applications.

- The major alloying element of the 5xxx series is magnesium or manganese; the result is a moderate-to-high-strength work-hardenable alloy. Magnesium is considerably more effective than manganese as a hardener (approximately 0.8% Mg being equal to 1.25% Mn) and it can be added in considerably higher quantities. Alloys in this series possess good welding characteristics and relatively good resistance to corrosion in marine atmospheres. However, limitations should be placed on the amount of cold working and the operating temperatures, as to avoid susceptibility to stress-corrosion cracking.

- Alloys in the 6xxx series contain silicon and magnesium in the proportions required for formation of magnesium silicide (Mg_2Si), thus making them heat treatable. Although not as strong as most 2xxx and 7xxx alloys, 6xxx series alloys have good formability, weldability, machinability, and relatively good corrosion resistance, combined with medium strength.

- Zinc (1 to 8%) is the major alloying element in 7xxx series alloys, and when coupled with a smaller percentage of magnesium results in heat-treatable alloys of moderate to very high strength. Copper and chromium, are also added in small quantities. 7xxx series alloys are used in airframe structures, mobile equipment, and other highly stressed components. Higher strength 7xxx alloys exhibit a reduced resistance to stress corrosion cracking and are often utilized in a slightly over-aged temper in order to provide better combinations of strength, corrosion resistance, and fracture toughness.

- Alloys in the 8xxx series contain lithium as the major alloying element (up to 2.5%). They are considered novel and specialist alloys because of their commanding mechanical properties. The 8xxx series alloys are deemed high strength alloys combining good conductivity with a unique blend of low density and good specific hardness. The alloys are heat treatable and are excellent bearing materials. They are ideally suited to aerospace applications because an increase in stiffness combined with high strength reduces component weight. Representative alloys include 8090, 8017 and 8081.

General mechanical properties of all the aluminium alloy series can be seen in figure 2.2.

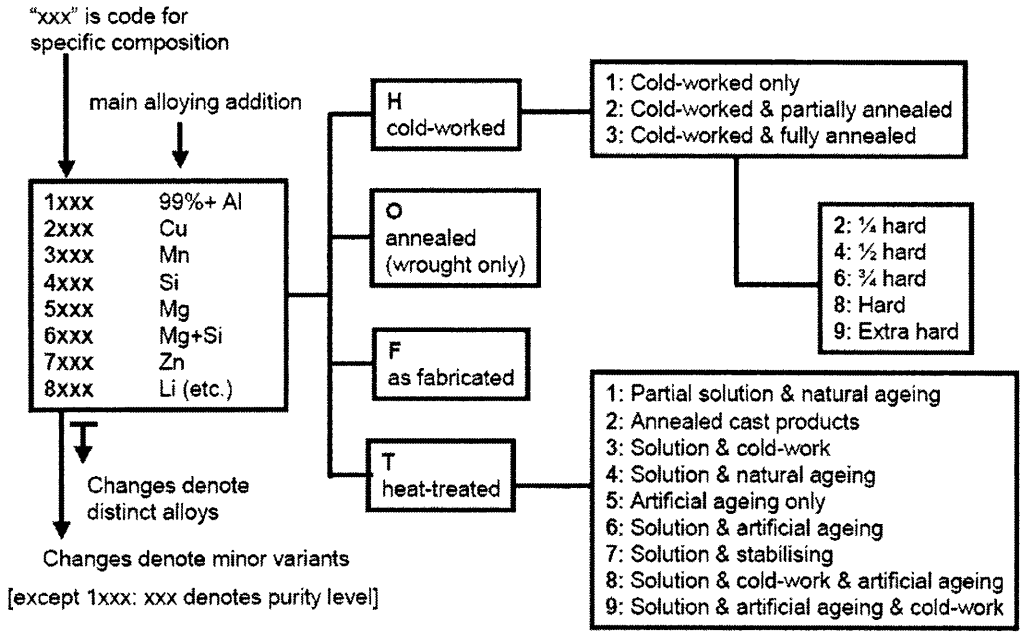

Figure 2.1 Aluminium alloys and treatment classification table.

Alloy series	Composition	σ_y (MPa)	UTS (MPa)	ε_F (%)	Notes
1000	"pure" Al.	30 - 100	100 - 135	up to 50	Foil, decoration, electrical conductors
2000	~4.5%Cu (+Mn,Si,Mg) age-hardened	up to 480	up to 520	5 – 20	General purpose forgings and extrusions, esp. airframes.
3000	~1%Mn, Mg. cold-worked	up to 215	up to 290	5	Ductile sheet for cladding trucks, trailers. Food containers. Drink cans.
4000	12%Si, (+ Mg,Ni,Cu) forgeable, age-hardened	~295	~325	0.5	IC engine pistons. (aka LM13, A332)
5000	~5%Mg (+Cr. Mn). cold-worked	up to 350	up to 415	15	Good formability & weldability. Excellent corrosion resistance. Structural applications, esp. marine.
6000	up to 1%Mg-Si. age-hardened	~275	~310	12	Hot extrusions. Window frames, etc.
7000	up to 8%Zn (+Mg,Cu,Cr). age-hardened	500	575	11	Highest strength alloys. Aircraft structures.
8000	"Other", e.g. up to 2.5%Li				Novel and specialist alloys
Cast	near Al-13%Si eutectic + 0.01%Na	up to 200	up to 300	2 - 5	Automotive castings. Can age-harden if Cu and Mg added.

Figure 2.2 Table detailing basic mechanical properties and notes concerning the aluminium alloy series.

2.2 INTRODUCTION TO THE ALUMINIUM ALLOY 7010.

In the 7000 series Aluminium alloys, zinc (Zn) is the main alloying element, although small amounts of magnesium (Mg) and copper (Cu) are added for optimised mechanical and corrosion properties. Choices of other elements are also added to customise the alloy to specific applications. The 7000 series alloys are heat treatable, therefore are considered extremely high strength alloys.

2.2.1 Review of the Published Articles on Aluminium Alloy 7010.

The particular alloy 7010 was developed in the late 1970's for strength critical aerospace structural applications by HDA forgings and Alcan International, under the sponsorship of the UK Ministry of Defence. The alloy was primarily designed for plate and forging alloy to improve upon such properties as: - strength, fracture toughness and stress corrosion cracking resistance, properties which are predominantly seen in 7075-T651 and 7079-T6 alloys. The 7010 alloy varies from other alloys in the series since the combined iron (Fe) and silicon (Si) content is kept below 0.27% and zirconium (Zr) is used as a grain modifier as opposed to chromium (Cr). The minor addition of Zn, Mg and Cu to the parent aluminium material forms precipitates along grain boundaries within the matrix. Microstructurally the alloy 7010 consists of recrystallised and unrecrystallised grains, the ratios of which are controlled solely by the processing procedures. Subsequent heat treatment to the alloy determines precipitate size, shape and density, factors which significantly control the overall mechanical properties of the material.

The over-aged temper condition T-7651, produces (temper condition used for current research programme) Al_7Cu_2Fe and Mg_2Si precipitates in the matrix which appear irregular and round in shape respectively, and lay mainly in recrystallised areas. Particle sizes reach approximately 20μm for the Al_7Cu_2Fe and 5 μm for Mg_2Si. The over ageing condition when

applied to 7010 alloy increases the thickness of the passive layer (oxide layer) and in some instances increases the layers hardness. Hydrogen entrapment is also noticed with this temper condition, caused primarily by the large precipitates, effectively decreasing the materials susceptibility to stress corrosion cracking.

Strength is a crucial requirement of any alloy playing a load-bearing role in aerospace applications. However, the potential tensile ductility and toughness of 7xxx series alloys is reduced by the presence of the coarse secondary phase particles. Intermetallic phases of concern in the 7010 alloy are the previously described Al_7Cu_2Fe and Mg_2Si. The volume fractions of Al_7Cu_2Fe and Mg_2Si are essentially fixed by alloy chemistry and so can be lowered by altering composition. In terms of mechanical properties, yield and tensile strength for the slightly over-aged 7010-T7651 alloy reach approximate values of 470 and 535 MPa, respectively, while ductility reaches a maximum value of 12% (see table 2.1).

Patton et al studied the fatigue damage in aluminium alloy 7010-T7651, the alloy used in the current research project. The chemical composition of the alloy can be seen in table 2.2 and the applied heat treatment programme seen in table 2.3. The study describes the experimental investigations performed to identify the various damage mechanisms and their relative importance in the nucleation, propagation and final failure steps within the material. An optical micrograph of the 7010-T7651 alloy used in the study can be seen in figure 2.3. The material is partly recrystallised yielding two types of grains, recrystallised and unrecrystallised, with sub grains evident in the later grain structure. The recrystallised volume fraction of the studied grain structure is reported to be around 10%. Table 2.4 quotes the grain sizes of 7010-T7651 as measured by Patton.

Constant amplitude fatigue testing was undertaken on the alloy, utilising a positive stress ratio of 0.1 and a cyclic frequency of 10Hz. Testing was carried out at room temperature, hence neutralising the effect of frequency. Fatigue crack initiation in the 7010 material was predominantly found to be at the intermetallic particles and always took place in the vicinity of the free surface of the specimens (Figure 2.4). Cracks were also noted to initiate between the Mg_2Si intermetallic phase and the matrix interface decohesions or grain boundary decohesions.

With the aid of electron backscattered diffraction techniques, crystallographic orientations of the cracked grains were clearly identified and therefore were called "twisted cube texture". This grain orientation corresponds to the two highest Schmid factors that are comparable and relatively large. Grains exhibiting this crystallographic orientation with respect to the tensile axis were found to initiate cracks by means of intermetallic rupture.

Crack propagation within the material was found to be variable, with numerous routes available for cracking to follow. This is clearly illustrated by figure 2.5. Here, the crack path is primarily inter-subgranular with very few intra-grains. The study also identified and found the final fracture events to be either by multiple crack coalescence (found at very high maximal stresses) or by a single crack unstable propagation (at low and intermediate peak stresses). The study, after concluding the mechanisms involved during damage accumulation of the aluminium alloy, attempts to model the crack growth rate and predict the number of cycles to failure of the AA7010 material, a topic which is reviewed later on in the literature [1].

The author **Forsyth** also studied the alloy 7010, but in the T7361 condition. The composition of this alloy is seen in table 2.2. The work looked at influence of tensile stress on the distribution of etch figures that are formed by corrosion on metallographically polished surfaces of an aluminium alloy. The material used for the corrosion work was extracted from several forgings and immersed in acidified seawater at a temperature exceeding 40°C. Active etch pitting was noticed on the polished material, but not exclusively in the dendritic regions of the microstructure. Tensile stresses were applied to these polished specimens at the same time as being exposed to the active etch in acidified seawater. The results showed that pits tended to align in the direction parallel to the applied stress axis, as a direct consequence of the presence of a sufficiently high elastic stress. No definite explanation of this phenomenon is presented within the study; possible reasons include stress relief or blunting of the lateral pit corners. The study undertaken by Forsyth concluded that:-

- Corrosion of metallographically polished surfaces of 7010-T736, under the action of seawater + 1%HCl at temperatures above 40°C, was almost totally concentrated in the

interdendrite regions of the microstructure, and the attack was noticed to be of a cubic etch form.

- The presence of a tensile stress during corrosion aligned the etch pits in the direction of the stress. These pits were noticed to grow until they formed furrows on the specimen surface, although this directional attack was noticed to fade as depth increased [2].

The engineering property comparison of three 7xxx series aluminium alloy plate material was completed by **Schra** and **Hart** for the National Aerospace Laboratory. The alloys under investigation were 7010 and 7050, which are similar alloys in many respects, although 7050 has a higher copper content. The chemical compositions of the evaluated 7010 alloys can be seen in table 2.1. Two temper conditions were applied to the alloys, these being; T7651 and T73651. The paper investigates several engineering properties including strength, fracture toughness, fatigue crack propagation resistance under flight simulation loading and stress corrosion cracking (SCC), which is specifically reviewed in section 2.3.

The mechanical properties of the 7010 and 7050 alloys were evaluated using tensile testing, from which yield stress and ultimate tensile stress were measured. Elongation was determined post fracture using a 50mm gauge length. The results can be seen in figure 2.6. The testing considered the possibility of specimen strength variance i.e. specimens taken from different areas of the stock plate, but this was shown to vary only slightly. Grain orientation of the specimens was also studied (Longitudinal and Long Transverse); again the strength results were very similar. Elongation seemingly was more affected by the location of the specimen in the plate than strength. A clear trend was noted in the longitudinal direction, whereby the elongation decreases from the surface to the core. The effect was less pronounced in the long transverse direction. In terms of alloy specifics, the strength properties of 7050-T73651 are closer to 7010-T7651 than those of 7010-T73651. Yield and ultimate strength of 7050-T73651 is slightly less than 7010-T7651, but higher than 7010-T73651. In terms of elongation, 7010-T73651 is considered highest closely followed by 7010-T7651 and 7050-T73651.

Fracture toughness testing was executed on 20mm thick compact tension specimens, pre-cracked using a 20kn Amsler vibrophore. 7050 during the pre-cracking phase had a tendency to crack branch, leading to optimistic fracture toughness values due to lower k_t factors at the crack tip areas. This effect was avoided by stopping the pre-cracking while only unbranched crack tips were visible. This showed that 7050 was more susceptible to crack branching than 7010. Figure 2.7 illustrates the results. 7010-T73651 evidently showed the greater fracture toughness of the alloys tested, with 7050 lying in between both heat treatment conditions of 7010. The effect of specimen orientation on fracture toughness is also visible in figure 2.7; k_{IC} was highest for the L-T orientation, with the T-L orientation some 10% lower. The S-T and S-L orientations are fairly similar, although they are ~20% lower than the L-T orientation.

Fatigue crack propagation testing on the material was conducted using a flight simulation loading sequence known as TWIST (Transport WIng Standard), established by the NLR and the Laboratorium für Betriebsfestighkeit (Darmstadt). The simulation programme may be considered representative for the load history of the wing root of a transport aircraft. Specimen thickness was investigated in the study, where it was found to have an effect on fatigue life. It was discovered that as the plate thickness increased, fatigue life decreased, a common phenomenon with all materials. From the alloys tested, it was found that the performance of the T73651 temper alloys were equivalent, while the higher strength T7651 alloy exhibited inferior fatigue properties, as depicted by figure 2.8 and 2.9.

Conclusions drawn from the paper illustrate that both 7050 and 7010 are deep hardenable alloys with good fracture toughness properties. Engineering properties between the two alloys vary slightly, although 7050 is considered superior under gust spectrum flight simulation loading (resistance to fatigue crack propagation, possibly due to its crack branching properties), however to all intents and purposes it may be concluded that the alloys are essentially equivalent for engineering usage [3].

Table 2.1 Mechanical properties of the 7010 aluminium alloy reported by various authors. (L = Longitudinal, LT = Long Transverse).

Author	Temper	Yield Stess	Tenile Strength	Relative Elongation	Fracture Energy
		σ_e 0.2 (Mpa)	σ_r (Mpa)	ε_r (%)	W (MJm^{-3})
Forsyth (1999)	T-736	Min.500	n/a	n/a	n/a
Patton et al (1998)	T-7651	n/a	535	n/a	n/a
Puiggali et al (1998)	T-351	381	555	9.5	44.1
	T-651	470	545	5.4	24.2
	T-7451	410	484	7	30.2
Robinson (2000)	T-6	545	583	7.3	n/a
	T-7	500	551	10	n/a
Schra and Hart (1983)	T-7651	(L) ~470	~530	~11.0	n/a
		(L-T) ~471	~540	~12.0	
	T-73651	(L) ~420	~500	~10.25	n/a
		(L-T) ~421	~510	~10.75	

Table 2.2 Comparison of the 7010 aluminium alloy investigated by various authors (% weight). Remainder aluminium.

Author		Elements (% weight)								
		Zn	**Mg**	**Cu**	**Zr**	**Fe**	**Si**	**Ti**	**Mn**	**Cr**
Patton et al (1998)		6.07	2.43	1.60	0.103	0.098	0.079	0.028	n/a	n/a
Deshais & Newcombe (2000)		6.15	2.34	1.59	n/a	n/a	n/a	n/a	n/a	n/a
Forsyth (1999)	**Max.**	6.70	2.60	2.00	0.16	0.15	0.12	0.06	0.10	n/a
	Min.	5.70	2.10	1.60	0.10	-	-	-	-	n/a
Schra & Hart (1983)	**Max.**	6.70	2.70	2.00	0.17	0.18	0.10	0.05	0.30	0.05
	Min.	5.70	2.20	1.50	0.11	n/a	n/a	n/a	n/a	n/a
Robinson (2000)	**Max.**	6.70	2.60	2.00	0.16	0.15	0.12	0.06	0.10	0.05
	Min.	5.70	2.20	1.50	0.11	n/a	n/a	n/a	n/a	n/a
Puiggali et al (1998)		6.12	2.33	1.60	0.113	0.093	0.054	0.031	0.016	0.010

Table 2.3 Aluminium alloy 7010 with the applied heat treatments.

Author	Temper Name	Heat Treatment				
Patton et al (1998)	**T-7651** Over-Aged	24 Hours at 120°C		Followed by 8 Hours at 170°C		
Puiggali et al (1998)	**T-351** Under-Aged	Heat Solution at 477°C for 8 Hours 05 min		Water Quench	Straining for 2.30%	RT Ageing
	T-651 Peak-Aged	As for T-7351	Followed by ageing at 155°C for 9 Hours			
	T-7451 Over-Aged	As for T-7351	Followed by ageing at 155°C for 6 Hours	Followed by ageing at 172°C for 10 Hours		
Deshais and Newcomb (2000)	**T-7451 Over-Aged**	Not Specified				
	T-651 Under-Aged	Boiling Water Quench				
	T-651 Peak-Aged	Cold Water Quench				
	T-351 Under-Aged	Boiling Water Quench				
	T-351 Peak-Aged	Cold Water Quench				
Robinson (2000)	**W-52**	Solution heat treatment 6 Hours at 475°C		Water Quenched (<40°C)	Cold compressed 2.25±0.5	
	T-7 Over-aged	Same as W-52		8 Hours at 100°C	10 Hours at 175°C	
	RRA200	Same as W-52	24 Hours at 120°C.T-6	Retrogressed for 40 mins at 200°C in a potassium and sodium nitrate salt bath		

Table 2.4 Grain sizes (μm) of aluminium alloy 7010-T7651 as reported by Patton et al.

Grain Type	Longitudinal Direction	Transverse Direction	Normal Direction
Unrecrystallised grains	350	150	60
Equiaxed grains	2 - 5	-	-
Recrystallised	80	60	40

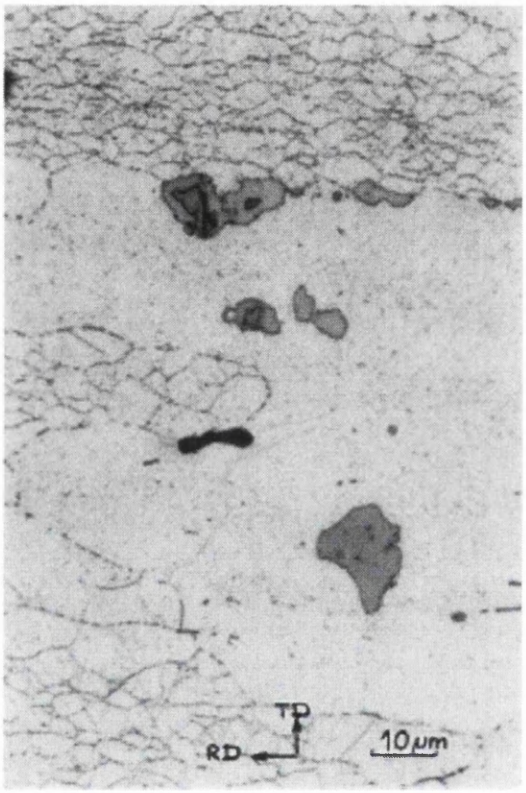

Figure 2.3 Optical micrograph of 7010-T7651 aluminium alloy. Evident are grains and subgrain boundaries, along with the intermetallic phases Al_7Cu_2Fe and Mg_2Si, which appear grey and black respectively.

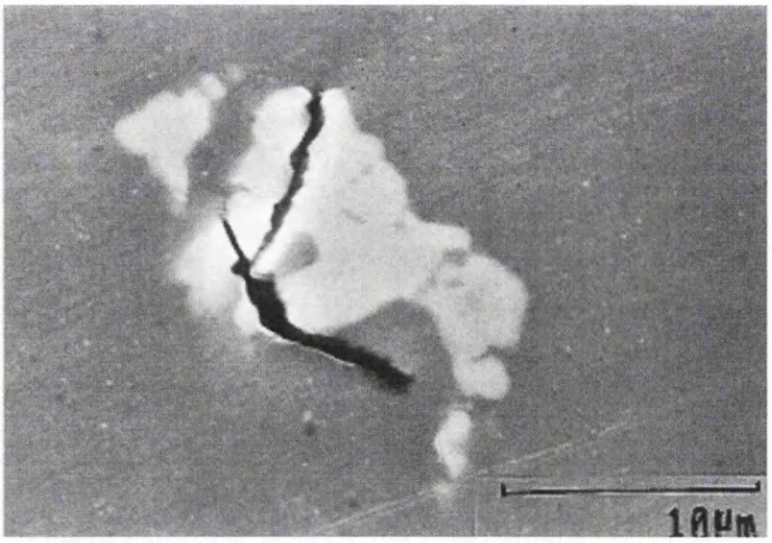

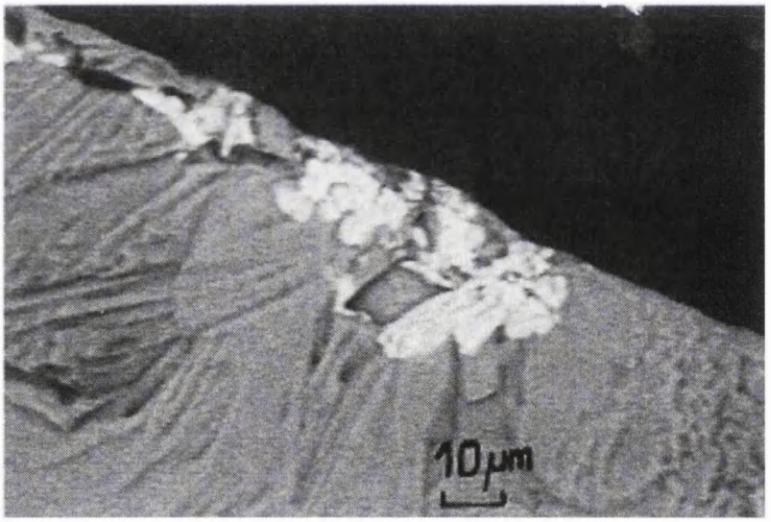

Figure 2.4 (Above) Fatigue crack initiation site: fracture of Al_7Cu_2Fe intermetallic, (Below) Initiation site at an Al_7Cu_2Fe intermetallic cluster at the vicinity of the free surface of the specimen.

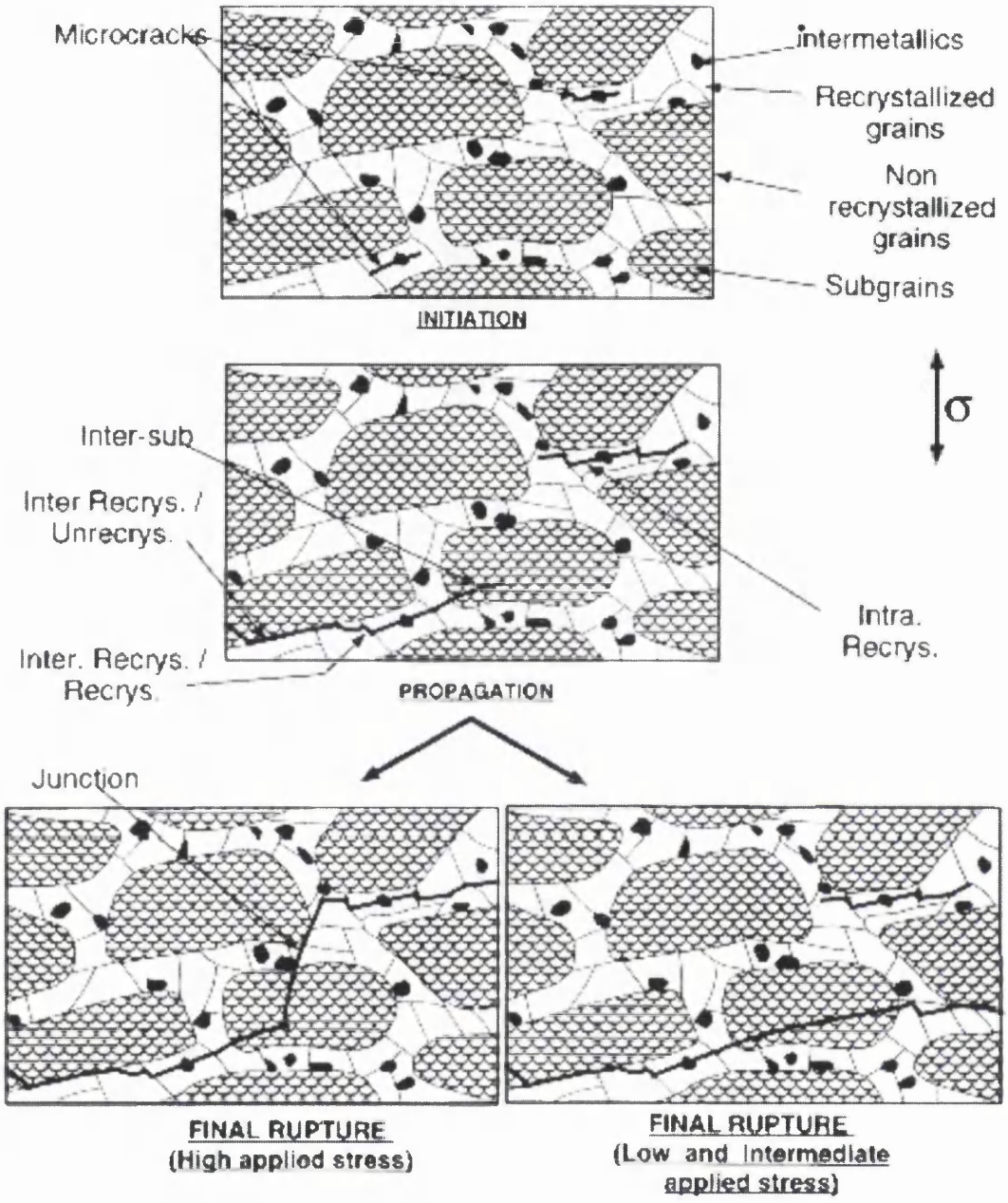

Figure 2.5 Schematic description of fatigue damage accumulation in 7010-T7651 aluminium alloy.

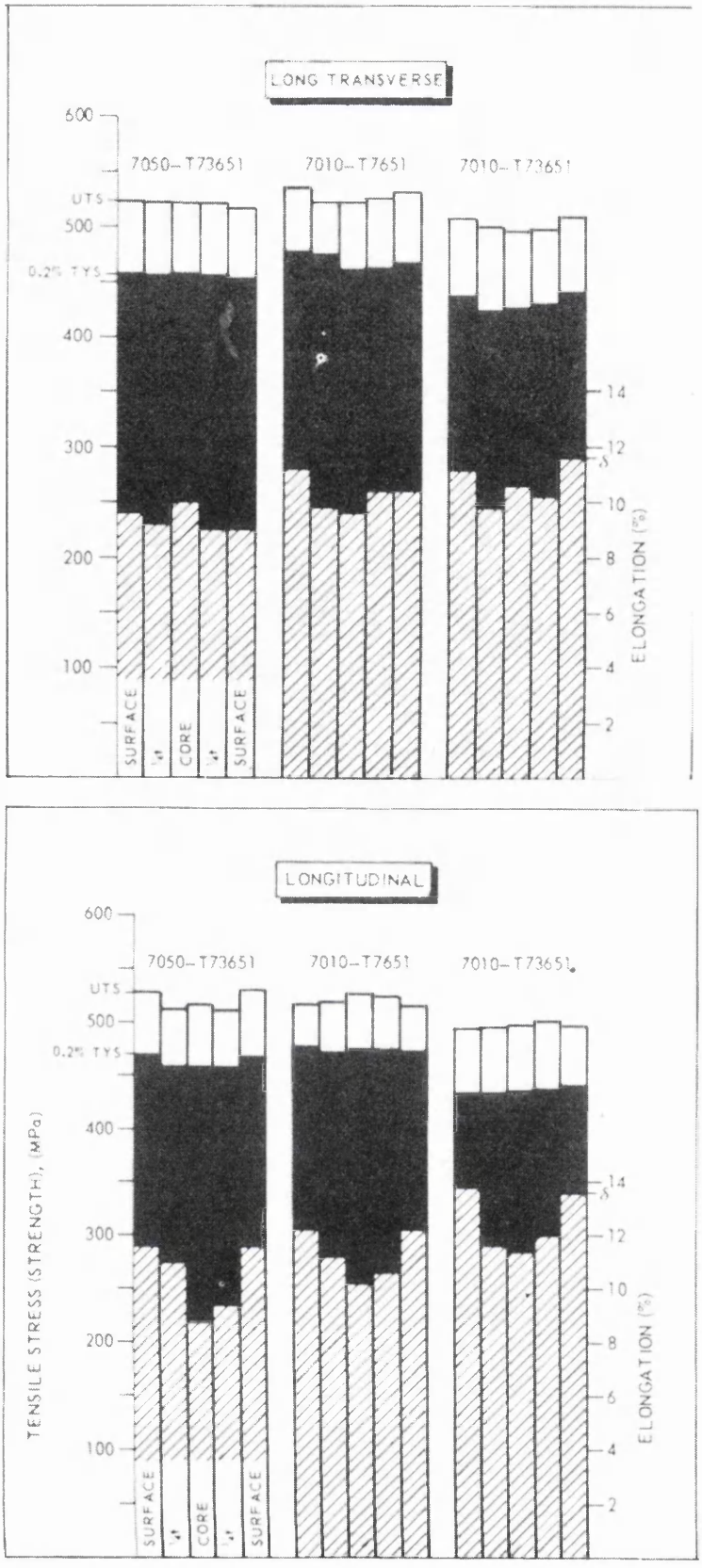

Figure 2.6 Comparison of mechanical properties of the tested 7010 and 7050 aluminium alloys. Each vertical bar represents one test.

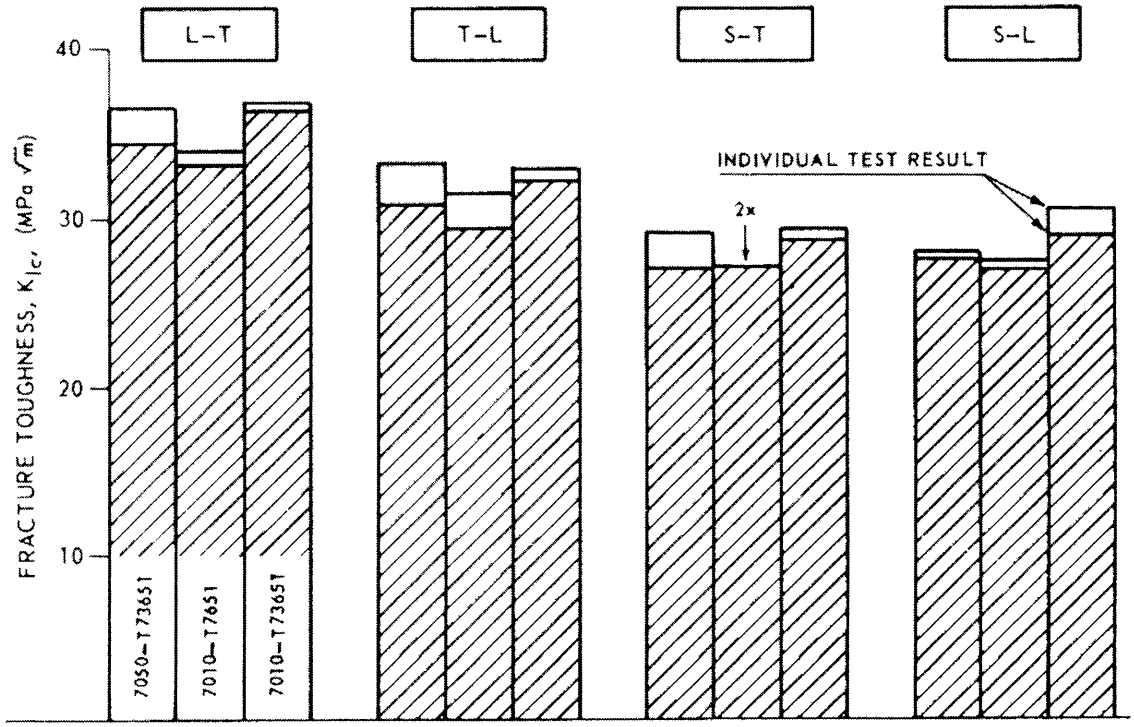

Figure 2.7 Fracture toughness (K_{1C}) properties for various test orientations.

(a)

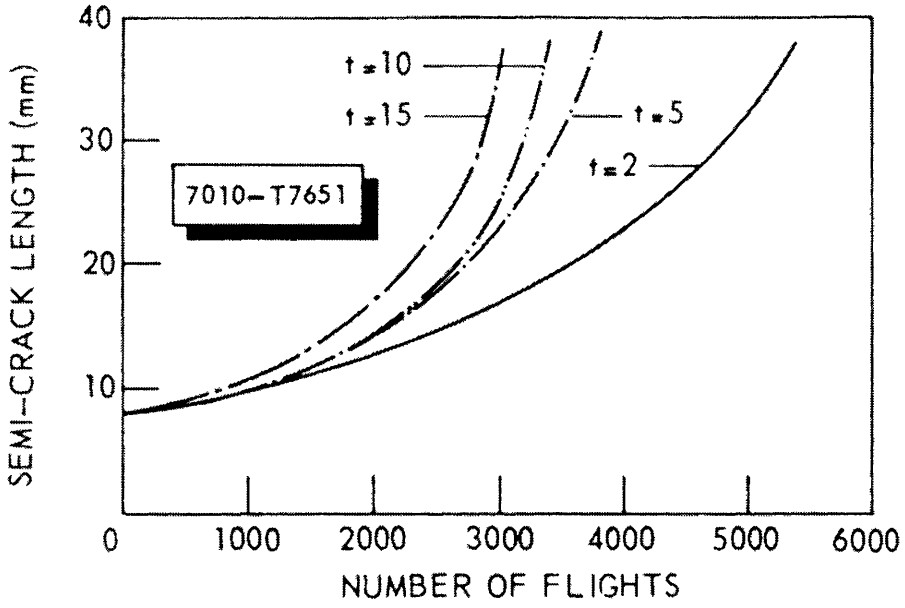
SEMI–CRACK LENGTH (mm)
40
30
20
10
0
1000
2000
3000
4000
5000
6000
NUMBER OF FLIGHTS
t=10
t=15
t=5
t=2
7010–T7651

(b)

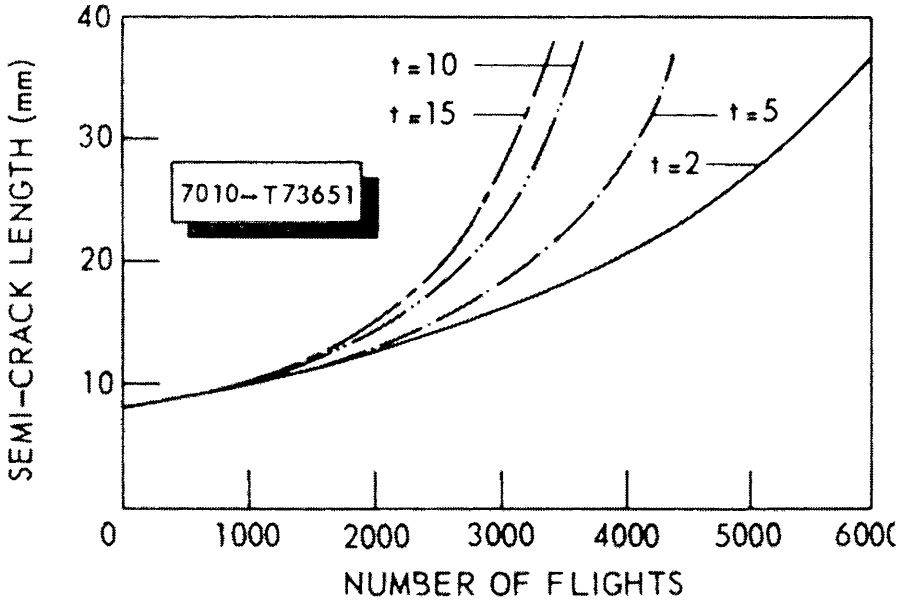
SEMI–CRACK LENGTH (mm)
40
30
20
10
0
1000
2000
3000
4000
5000
NUMBER OF FLIGHTS
t=10
t=15
t=5
t=2
7010–T73651

(c)

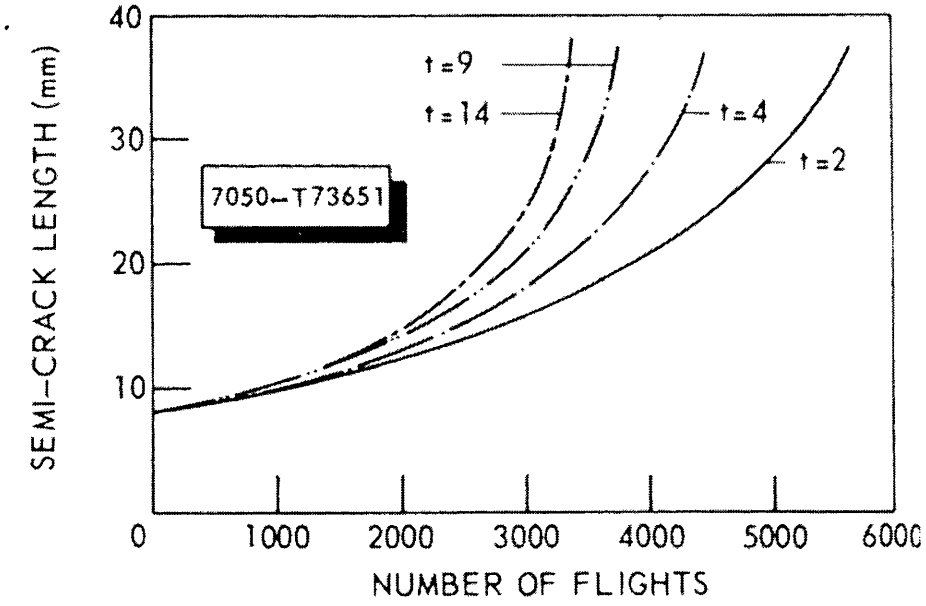

(d)

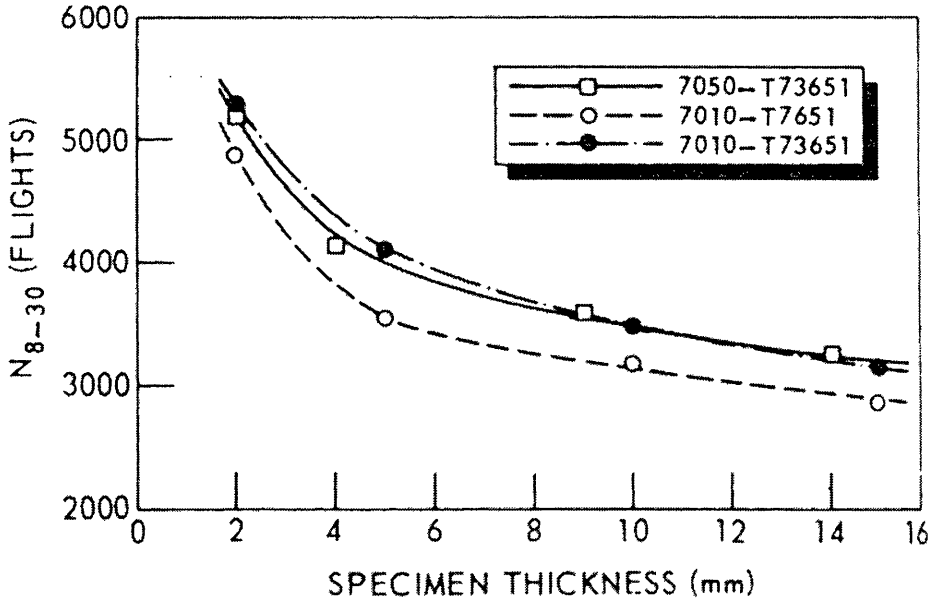

Figure 2.8 The effect of plate thickness on fatigue crack propagation life. (a)-(c) Plots of semi-crack length versus number of flights, (d) Number of flights to grow a crack from 8 – 30 mm (N_{8-30}).

(a)

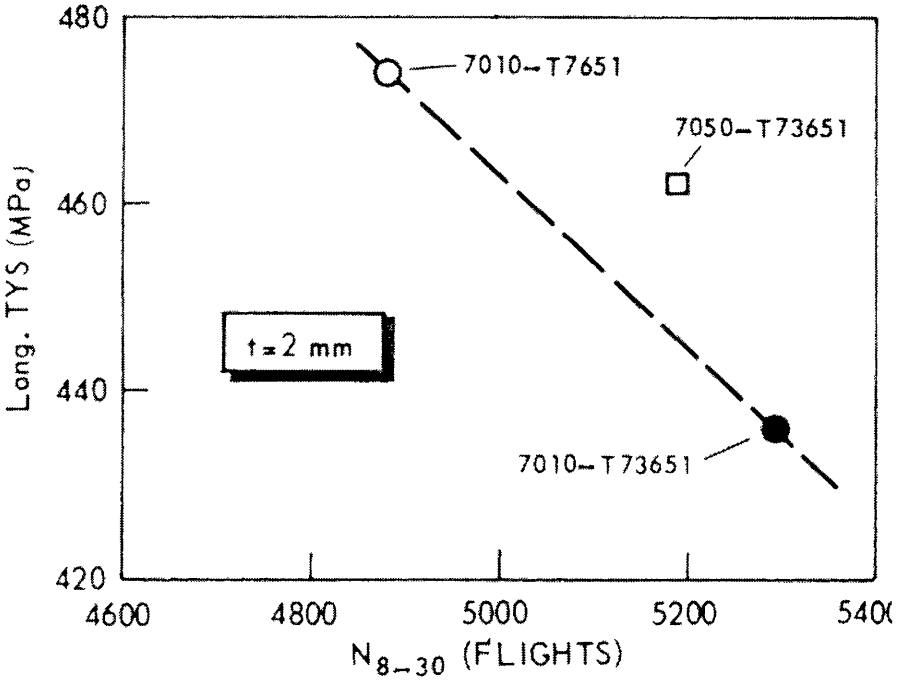
480
460
440
420
Long. TYS (MPa)
7010–T7651
7050–T73651
t = 2 mm
7010–T73651
4600
4800
5000
5200
540
N_{8-30} (FLIGHTS)

(b)

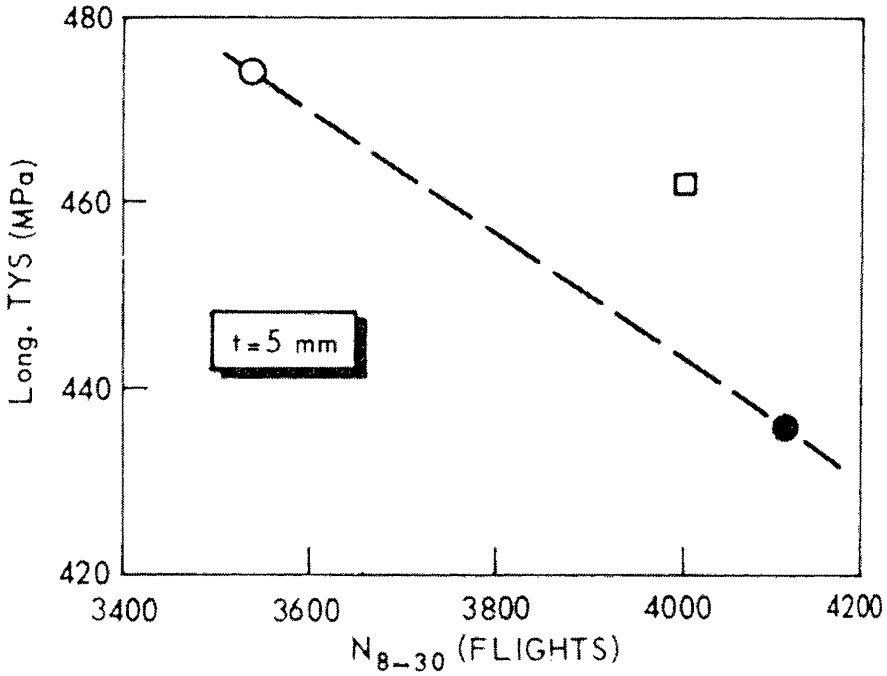
480
460
440
420
Long. TYS (MPa)
t = 5 mm
3400
3600
3800
4000
4200
N_{8-30} (FLIGHTS)

(c)

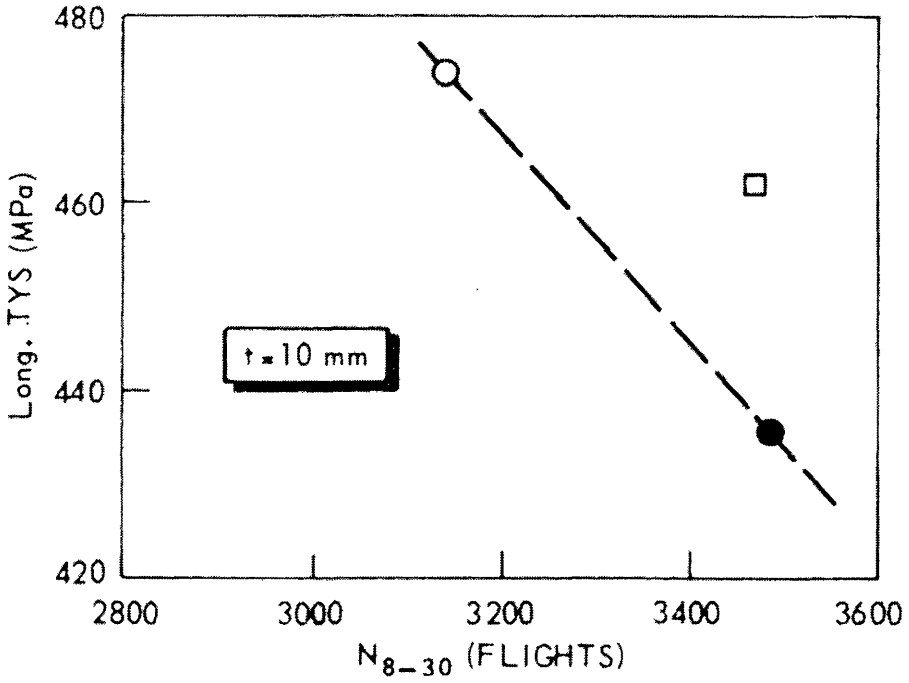

(d)

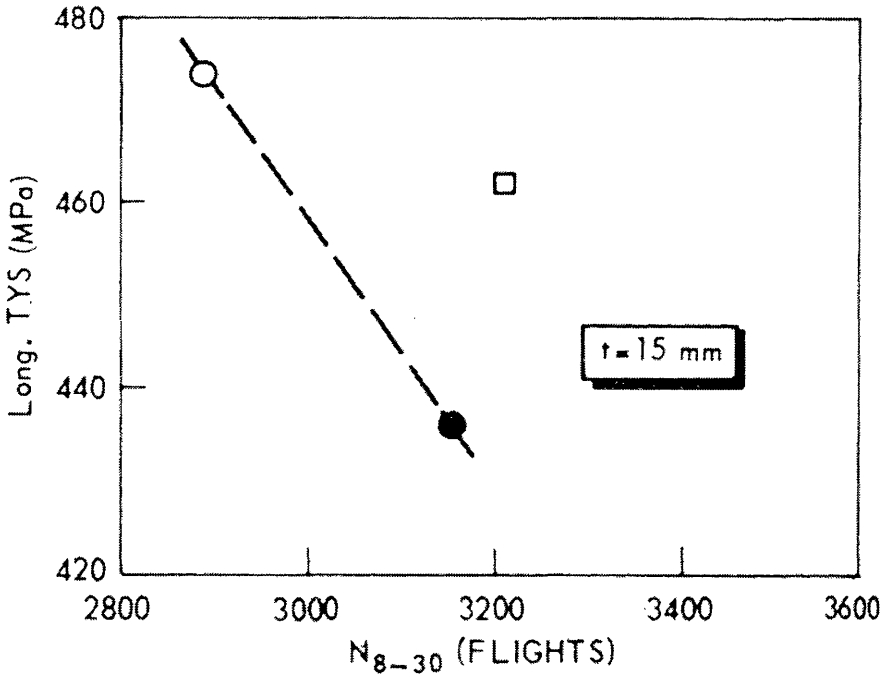

Figure 2.9 (a) – (d) Comparison of the fatigue crack propagation performance of 7050 and 7010.

2.3 AEROSPACE CORROSION PROBLEMS.

Many authors have reviewed various corrosion problems and possible protection systems for aluminium alloy structures in military and civil aerospace applications [4 - 9]. Anodic and cathodic treatments have favourably been employed as surface protection, in addition to organic treatments and the use of cladding. Effective corrosion prevention used in the 80's included chromic primers, organic inhibitors along with phosphoric acid anodisers and the barrier protection technique (e.g. Painting of components) applied prior to component assembly. Effective alloying techniques have also been used to tackle corrosion prevention. Modern day aluminium alloys even now are still as susceptible to corrosion problems as they were some years ago, with no real advancements in material properties. The corrosive environments that a modern-day aircraft encounters can potentially cause extreme physical damage to alloys that have been primarily chosen for their excellent mechanical properties instead of their corrosion resistance properties. Certain authors (***Cordier et al*** [10], ***Waller et a l*** [11]) have reviewed this problem and have ultimately found that a compromise is reached between mechanical properties and corrosion resistance. Generally it can be presumed that an alloy will be chosen for a specific application with corrosion limitation in mind rather than prevention, hence corrosion in some form will occur within the material. Therefore knowledge of the different types of corrosive behaviour of aluminium alloys is a continued requirement. Aluminium alloys are therefore susceptible to a wide range of corrosion mechanisms, including:-

- Intergranular Corrosion
- Pitting Corrosion
- Exfoliating Corrosion
- Crevice Corrosion
- Layer Corrosion
- Stress Crack Corrosion
- Contact Corrosion
- Filiform Corrosion
- Galvanic Corrosion
- Fretting Corrosion
- Corrosion Fatigue
- Surface Corrosion

Detecting the corrosion once it has initiated on an aircraft structure is deemed difficult, therefore a series of Non-Destructive Tests (NDT) are carried out to pinpoint the exact location, these include (details of the techniques mentioned below can be seen in chapter 2.3.4):-

- Visual Examination
- Eddy Current Examination
- Ultrasonic Examination
- X-Radiography
- Neutron Radiography
- Acoustic Emission Techniques

Due to the frequent changes in aircraft design over time, coupled with the development of alloys with improved corrosion resistance, each aircraft will invariably behave differently in service. Therefore it becomes necessary to classify the type of corrosion damage according to the type of aircraft. ***Doruk et al*** [6] investigated the various corrosion problems and their location, encountered in several fighter aircraft. It was noted that exfoliation, galvanic, pitting and stress corrosion cracking were the common forms of damage frequently detected in critical areas in fighter aircraft, such as; the inside of air inlet ducts, vertical stabilisers and the Main Landing Gear (MLG) up-lock support rib. ***Warnhill et al*** [12] states in his studies that selected areas on a fighter aircraft are more susceptible to certain types of corrosion, than others. Observation has showed that general corrosion is unlikely to occur at joints which provide stress concentrations or faying surface contacts, crevices or moisture entrapment areas, regions of galvanic coupling (i.e. fastener holes). ***McLoughlin et al*** [9] demonstrated in a review of corrosion control measures for military aircraft that aluminium alloys are classified according to their susceptibility to exfoliation corrosion. The Alloy 7010 in the T76 and T736 conditions in McLoughlin's study are classed as immune or highly resistant to exfoliation corrosion, although surprisingly a similar alloy 7075-T6 was found to be highly susceptible to exfoliation corrosion.

Mitchell et al [13] reviewed corrosion problems from a commercial airline point of view and found very similar corrosion problems to those in military aircraft, but with the added problem of liquid spillage within pedestrianised areas (i.e. galleys, toilets, etc). Indeed, there are a number of factors that are cause for concern for commercial aircraft as apposed to military. Such concerns include: - spillage during maintenance, spillage and waste products in galley areas, condensation from passengers and livestock and potential corrosive freight. In terms of examination, military aircraft are routinely serviced for corrosion damage after 300 to 400 flying hours, with no attention to cost, in addition to a water and detergent wash every 100 flying hours and prior to major and minor service intervals. In contrast

civilian aircraft are examined for corrosion after several thousand flying hours, with the downtime costing the airlines dearly.

2.3.1 Stress Corrosion Cracking (SCC) of Aluminium Alloys.

Stress Corrosion or SCC (Stress Corrosion Cracking) as it is known, is the conjoint action of stress (normally a tensile stress above a critical value) and a corrosive environment (for Al alloys - moist air, sea water, chloride, bromide and iodide solutions) which leads to the formation of a crack which would not have developed by the action of the stress or environment alone. The magnitude of this combined effect is a measure of the susceptibility of the material to stress corrosion. Stress corrosion causes microcracking along intergranular paths within the material. With the continuation of the constant load, the microcracks tend to form larger cracks, reaching a critical value and finally causing material failure. The condition gives normal ductile materials the appearance of brittleness. Common features of SCC include:-

- Brittle failures or no gross ductility.
- Localised corrosion with little or no general attack.
- Failure is deemed premature based on mechanical considerations.
- Specificity of the alloy environment system.

A number of authors have reviewed stress corrosion cracking; ***Sprowls and Brown*** [14] looked at the general theory behind stress corrosion in aluminium alloys. The authors signified a sequence of events that lead to material failure, involving:-

- Corrosion along localised paths (grain boundary areas),
- The production of Fissures,
- Tensile stress normal to the path that creates a stress concentration at the base of the localised fissures.

The deeper the attack of the corrosion at the grain boundary areas, and the smaller the radius at the base of the fissure, the greater is the stress concentration. At a critical stress

concentration, the fissures are further forced open, exposing fresh unpassivated material, which is more anodic. An increase in current flow from the crack tip would be expected, for this reason corrosion rate increases until repassavition of the fresh metal area. Continued corrosion results in further separation of the metal, and a s a result, an increased rate of penetration occurs because of the mutually accelerating effects of tensile stress and corrosion.

A detailed study of the effect of heat treatment on the resistance to stress corrosion using 7075 in the T6 and T73 temper conditions was carried out. Most instances in the T6 condition revealed that the margin along the grain boundary was preferentially corroded instead of the grain boundary constituents. For the T73 condition, the margin area appeared depleted in copper when compared to the grain boundary, due to the heat treatment applied which reduces the copper in the grain and grain margin to a low value, hence minimising the anodic electrochemical effect and increasing the stress corrosion resistance.

Deshais and Newcomb [15] investigated the influence of microstructure on the formation of stress corrosion cracks in the 7xxx series aluminium alloys, aged to several different tempers. The study well documents the fact that stress corrosion cracking can greatly shorten the life of structural components such as the significant 7010 alloy, used extensively in the aeronautical industry. The compositions and the various applied heat treatments of the alloy used to conduct the study are seen in table 2.2 and 2.3 respectively. Cold and boiling water quenching was employed to compare differences in peak and over-ageing conditions. The study was performed using a Double Cantilever Beam (DCM) type specimen, exposed to a sodium chloride solution (57g/l NaCl in distilled water), whereby the tests were stopped before complete failure. Thin foil Transmission Electron Microscope (TEM) specimens from the crack tip region were cut from the test pieces for observation. Analysis from the TEM was used to determine the influence of Al-Cu-Fe(-Si) intermetallics on stress corrosion cracking.

Results from the investigation illustrated that if constituent particles were aligned along the intergranular stress corrosion path, then they would have a detrimental effect on crack propagation. The roles played by the second phase constituent particles in the SCC of the alloy can be seen in figure 2.10. Figure 2.10a shows the Al-Cu-Fe (-Si) particles nucleating voids under the influence of external stresses, while figure 2.10b illustrates the fact that the applied stress was large enough to cause decohesion at the particle and grain

boundary. Compositional profiles were made at grain boundaries with and without precipitates. Figure 2.11a shows a composition profile of a grain boundary located away from any grain boundary precipitates. Local peaking in the Zn, Mg and Cu concentrations are clearly visible, while the adjacent precipitate free zones are depleted in the identical concentrations. For a grain boundary containing precipitates as that illustrated in figure 2.11b, the profile (figure 2.12a) shows the diffusion of solute elements along the grain boundary, leaving the boundary depleted in solute. The study showed that the grain boundaries which contained precipitates could lead to deviations in grain boundary composition of 7010. It was also shown that there was clear evidence for segregation along grain boundaries to be retained in over aged tempers.

Conclusions drawn from the Deshais and Newcomb study included:-

- The influences of second phase constituent particles have little effect on the propagation of stress corrosion cracking because of the low stresses observed under SCC.
- Grain boundary segregation of Zn, Mg and Cu is retained even in over-aged material, although diffusion along grain boundaries to form precipitates can take place.

- Cold water quenching specimens as apposed to boiling water quenching was found to be more susceptible to SCC because of the slower re-passivation in the boiling water quenching.

Another study concerning stress corrosion cracking was undertaken on a French 7010 alloy, carried out by ***Puiggali et al*** [16]. The study looked at the effect of microstructure on stress corrosion cracking of an Al-Zn-Mg-Cu alloy. The composition of the alloy evaluated is displayed in table 2.2; while the heat treatments applied can be seem in table 2.3. Each heat treatment process produced various individual ageing conditions (i.e. Under, Peak and Over-aged). The mechanical properties of these unique temper conditions are displayed in table 2.1. Testing was carried out utilising artificial sea water (pH = 8.2) and dry air (humidity below 6%) by slow strain rate testing at rates varying between 10^{-5} and 10^{-7} s^{-1}.

Optical microscopy of the material structure showed that precipitates of the same composition, size and shape were found for all tempers in the matrix and grain boundaries.

These precipitates compared well to those studied and measured by Patton et al. Corrosion and pitting potential values in electrochemical measurements of potentiostatic curves (figure 2.13 and table 2.5) were found to increase with ageing time. An examination of the loss in fracture energy during stress corrosion testing was suggested to be due to electrochemical corrosion and stress corrosion for under-aged and peak-aged alloys, and almost entirely to electrochemical corrosion for the over-aged alloy. Prolonged ageing was found to increase the thickness and/or hardness of the passive layer (i.e. the oxide layer that forms on the surface of the aluminium material). Stabilisation of this layer is achieved by increasing its thickness, hence providing greater resistance to pit formation and crack initiation. The electrochemical testing showed that the various temper conditions altered the materials susceptibility to corrosion pitting as well as the range of electrochemical potential within which the passive layer was unstable. The pitting potential value found in potentiostatic tests, E_p, characterises the value above which first pits may appear and pitting may develop. It was noticed that this value was most negative for the T351 temper, and most positive for the T7451 temper (table 2.5). The investigation established that the effect of prolonged ageing on the susceptibility to stress corrosion cracking may be attributed to the change in volume and distribution of $MgZn_2$ phase precipitates with the under-aged alloy containing the smallest particles and the over-aged alloy having the largest. The over-ageing procedure is thought of as beneficial in terms of stress corrosion cracking, as it allows the precipitates to trap large amounts of hydrogen, hence decreasing the lattice concentration to below a critical value which reduces the susceptibility for stress corrosion cracking. The peak and under aged alloys in contrast have a hydrogen content that is high enough to initiate local failure.

The conclusions drawn from the investigation by Puigali et al include: -

- The prolonged ageing time results in a decrease in the susceptibility to stress corrosion cracking.

- The effect of prolonged ageing on susceptibility to stress corrosion cracking may be attributed to the change in volume and distribution of $MgZn_2$ phase precipitates.

- Prolonged ageing has a positive effect on the growth and stability of the passive layer, which increases the inhibition for pitting and intergranular corrosion and crack initiation

Schra and Hart [17] reviewed the engineering property comparisons of three 7xxx series aluminium alloy plates. AA7010 and 7050 were evaluated, with two tempers assessed in the 7010 alloy, these being T7651 (important to the current research) and T73651, the properties and chemical compositions of which can be seen in table 2.2. The difference between the two alloys is the lower copper content of the 7010, making it easier to cast, however, at the expense of stress corrosion resistance. Material properties investigated in the study included the relative strength, corrosion resistance, fracture toughness and fatigue crack propagation resistance under flight simulation loading as previously reviewed in chapter 2.2. Stress corrosion cracking in terms of initiation and propagation is also discussed in some depth. The mechanical properties of the alloys as defined by Schra et al are visible in table 2.1. Two testing methods were used to investigate stress corrosion cracking; alternate immersion in aqueous 3.5%NaCl and periodic moistening, utilising the same aqueous solution.

The SCC testing was undertaken using double cantilever beam specimens. It was discovered that the alternate immersion testing appeared to be somewhat more aggressive than the periodic moistening, although after 1457 hours (2 months), no cracking was obvious. However, specimens were seen to be heavily pitted, with the 7050 alloy showing a slightly higher pitting density when compared to the 7010 alloy. Mean crack growth rates of approximately 10^{-10} m/s were recorded for both alloys for initial K_I values of 22MPa$\sqrt{m}$. The results indicate that both alloys have a high resistance to stress corrosion crack growth, but the mean crack growth rate for 7010-T7651 was noticed to be 2-3 times higher, (For initial K_I value of 18 MPa$\sqrt{m}$). Both alloys i.e. 7050 and 7010 showed similar fracture toughness values of between 28 and 36 MPa$\sqrt{m}$, with grain orientation providing the highest variation in the test results with respect to the plate rolling orientation (up to 20%).

Similarly to the other authors documented, ***Forsyth*** [18] looked at the effects of stress corrosion on metallographically polished aluminium alloy 7010-T736, under the influence of a tensile stress. Material compositions and properties are seen in table 2.1 and 2.2. Polished surfaces were immersed in acidified seawater at temperatures greater than 40°C, yielding active etch pits in the interdendrite regions of the microstructure (figure 2.14). It was discovered during the investigation that if a tensile stress was also utilised during the active etch pitting, then the pits would align on the polished surface in the direction of the applied tensile stress, consequently producing troughs or grooves in the material surface (figure

2.15). Applying the tensile stress in other directions eliminated microstructural features as the cause of the grooving, hence suggesting that the formation of aligned pits is due to the presence of a suitably high elastic stress. A thorough explanation of this effect is not offered within the study, possibilities suggested by the author include stress relief or perhaps blunting of the lateral pit corners.

Material precipitates were shown to be preferential sites for stress corrosion attack from the study completed on a precipitate free aluminium alloy by ***Tanguy et al*** [19]. The study looked at the stress corrosion cracking mechanics of a precipitate free aluminium alloy, immersed in 30 g/l of NaCl solution. The susceptibility of Al–5Mg based alloys to intergranular stress corrosion cracking (IGSCC) was classically related to intergranular dissolution. Long ageing times within such alloys can form precipitates at grain boundaries. These precipitates become anodic with respect to the matrix, therefore provide preferential dissolution paths along grain boundaries. As dissolution is more easily activated when the sample is stressed, fast intergranular stress corrosion cracking is expected, especially in an oxidising environment.

In the absence of precipitates, it was found that a critical surface defect had to be formed in order to promote single cracking and solution confinement. Crack propagation in precipitate free material was caused by grain boundary rupture caused as a result of local dissolution and hydrogen reduction.

In an attempt to control or resist stress corrosion cracking, artificial ageing treatments, such as retrogression and re-ageing (RRA) were studied by the author ***Robinson*** [20]. RRA treatments are used to achieve the SCC resistance exhibited by over-aged alloys while maintaining peak aged strengths. These thermal treatments consist of a retrogression or reversion stage in which the near peak-aged material is heated for a short time at 200-280°C, followed by re-ageing at lower temperatures. During retrogression, strength falls rapidly to a minimum, partially recovers and finally decreases. Re-ageing after short retrogression stages restores strength to that of the peak aged material, but extended re-ageing ultimately results in a loss of strength. The RRA treatments are well suited to high strength aluminium alloys, especially the 7xxx series, giving aircraft manufacturers improved combinations of strength and stress corrosion / exfoliation corrosion resistance.

Robinsons' study looked at how RRA can enhance SCC resistance in 7010 aluminium alloy. The alloy is widely known to respond well to RRA thermal treatments. The chemical composition and heat treatments applied to the material are given in table 2.2 and 2.3 respectively. Many microstructural investigations have been conducted aimed at determining the reason for the enhanced SCC resistance in RRA treated 7xxx series alloys. Two theories have been promoted, the first and most widely quoted, states that RRA encourages coarse precipitation of the equilibrium phase η ($MgZn_2$) in the grain and subgrain boundaries while maintaining a fine distribution of η' in the grain interiors. The precipitates then act as hydrogen trapping sites, reducing the atomic hydrogen concentration locally in the matrix and at the grain boundary.

The other theory put forward suggests that dislocations introduced from the quenching stage, anneal out during the RRA treatment, therefore reducing the susceptibility to hydrogen embrittlement at the grain boundaries. The open die forged material used for the investigation was undertaken by HDA Forgings, the co-producers of the 7010 alloy. The forging was noticed to be similar to part of the wing spar assembly in the Airbus A330/A340 airliner. The material was solution heat treated at 475°C for 6 hours, water quenched at 40°C followed by cold compression at 2¼±½% (W52 condition). The microstructure produced was typical of a forged product, yielding 'pancake' shaped partially recrystallised grains. Second phase particles of the order of 20μm and 1-5mm were noticed in the matrix, comparable to the findings by Patton et al [1] and Puigali et al [16]. Figure 2.16 illustrates the constituent particles in the 7010-W52 alloy. Subsequent heat treatments followed to allow RRA to be investigated. The investigation mainly compared the results between smooth bar constant load and constant crack opening displacement double cantilever beam (DCB) type tests. A low resistance to stress corrosion cracking was discovered for the T7 and RRA200 smooth bar specimens, with the latter showing prominent evidence of pitting corrosion. However, DCB testing of T6 and RRA200 showed effectively no signs of SCC, although evidence of slight surface pitting was noticed. The pitting present in the DCB specimen would have raised the local stress, but the rapid rate of failure suggested an alternate mechanism in the smooth bar.

2.3.2 Pitting Corrosion of Aluminium Alloys.

Pitting is the most common form of aluminium corrosion, and is highly localised in the presence of aggressive chloride ions. Pitting within aluminium alloys is initiated at the so-called 'weak' sites in the oxide film, by chloride attack [21] [22]. Pits propagate according to the reactions stated below: -

$$Al = Al^{3+} + 3e^- \quad (1)$$

$$Al^{3+} + 3H_2O = Al(OH)_3 + 3H^+ \quad (2)$$

Hydrogen evolution and oxygen reduction are the important reduction processes at the intermetallic cathodes, as illustrated by figure 2.17:

$$2H^+ + 2e^- = H_2 \quad (3)$$

$$O_2 + 2H_2O + 4e^- = 4OH^- \quad (4)$$

As the pit propagates, the environment inside the pit (anode) changes. According to reaction 2 the pH will decrease. To balance the positive charge produced by reaction 1 and 2, chloride ions will migrate into the pit. The resulting HCl formation inside the pit causes accelerated pit propagation. The reduction reaction will cause local alkalinisation around cathodic particles. As previously mentioned aluminium oxide is not stable in such environment, and aluminium around the particles will dissolve (alkaline pits). The active aluminium component of the particles will also dissolve selectively, thereby enriching the particle surface with Fe and increasing its cathodic activity. Etching of the aluminium matrix around the particles may detach the particles from the surface, which may repassivate the alkaline pits. This may also reduce the driving force for the acidic pits causing repassivation of some in the long run. Figure 2.18a, b shows corrosion pitting on an aluminium alloy [23]. The resistance of aluminium to pitting depends significantly on its purity, due mainly to localised corrosion. Hence, the 1xxx pure aluminium grades are most resistant to pitting followed by these alloys in decreasing order of resistance: 5xxx, 3xxx, 6xxx, 7xxx and 2xxx.

Pitting is considered to be more dangerous than uniform corrosion damage due to the extreme difficulty in detecting, predicting and designing against the problem. Corrosion products can often cover the pits, a small narrow pit with minimal overall metal loss can lead to the failure of an entire engineering system. Pitting corrosion, with its localised attack, may assume various forms. Pit morphology is greatly influenced by the material the microstructure, grain orientation, surface features and the corroding environment [23]. Figure 2.19 a - f illustrates the various pit morphologies identified within aluminium alloys.

Pitting corrosion in aluminium alloys has recently been comprehensively reviewed in the publication by ***Szklararska-Smialowska*** [24], which details the experiments performed during the last few decades. The review endeavours to enhance the knowledge of pitting in aluminium alloys. The paper primarily discusses metastable and stable pits, pit chemistry, inhibitors and the effects of intermetallics on pitting. The majority of the paper reviews aspects of passivity and pitting of aluminium and its alloys. The document provides invaluable information regarding the formation and growth of pits. Initially, the main stages of corrosion pitting are defined, these being:-

1. Processes occurring on the passive film, at the boundary of the passive film and the solution.
2. Processes occurring within the passive film, when no visible microscopic changes occur in a film.
3. Formation of so-called metastable pits which initiate and grow for a short period of time below the critical pitting potential and then repassivate (intermediate step in pitting).
4. Stable pit growth, above a certain potential termed the critical pitting potential.

Little is known of the first two stages seen above. These stages are the processes which lead to the breakdown of the protective film, hence the interaction of Cl^- with the oxide film. These stages are dependant upon the composition and structure of the oxide film. The structural characteristics of the oxide film on the other hand is dependant on the material composition, the presence and distribution of micro and macro defects, crystal structure and the degree of non-crystallinity of the oxide film. Electrolyte composition, potential and temperature are also considered important factors. The author then states that varying external conditions i.e. air temperature, anodic film solutions (sulphuric acid, phosphoric

acid, borate and tartaric acid) have a dramatic affect on the type and structure of oxide produced on the surface of the aluminium, hence resulting in different chemical and physical properties.

The author goes on to review analytical techniques that were used to measure the adsorption of chlorine ions on the passive films of aluminium. Techniques reviewed included: - Autoradiography, SIMS and X-ray photoelectron spectroscopy. It was concluded that a corroding aluminium surface has a variety of adsorption sites with different adsorption properties, where only a minority of these sites are active for pitting corrosion, whereby there is no threshold for the chloride concentration below which pitting will not occur. Similarly, the presence of an inhibitor will delay but not prevent the onset of pitting. From the X-ray photoelectron spectroscopy technique, Augustynski et al [25] recognised that at higher temperatures, adsorption of Cl- increased at the oxide solution interface, due to the increased porosity of the passive layer.

It is known scientifically that only a few metals dissolve in aluminium above a few atomic percent, those that do dissolve are Mg, Zn and Li. Copper, one of the most important alloying elements in aluminium has an equilibrium solubility 5.7 at% in aluminium and when in solid solution inhibits the formation of pitting corrosion. Current commercial alloys have poor resistance to localised corrosion, hence, efforts have been carried out to develop a 'stainless' aluminium alloy, with a high resistance to localised corrosion in a chloride solution. Here elements with good resistance to pitting were added to chemically and physically homogenise supersaturated aluminium alloys, alongside having an influence on the electronic structure of the passive film. These alloys, termed 'Metastable' were produced in the form of thin films, to provide fundamental information on the effect of alloying elements on pitting. The pitting potential of aluminium can be increased substantially by adding elements such as W, Ta, Mo, and Cr.

The author discusses the role of intermetallic particles in the pitting corrosion of aluminium and its alloys. The behaviour of the intermetallics depends upon the potential difference (PD) between the particle and the matrix in solution. The phases which are electrochemically more Noble than the matrix become the cathodic sites, while to the inclusions matrix undergoes anodic dissolution. Reviews of anodic dissolution of some 1xxx, 2xxx, 3xxx and 6xxx series alloys by the author show that corrosion potential is different

between the particle and the matrix in solution. Subsequently, preferential corrosion occurs leading to pitting with variations in local pH values in and around the pit, with pit geometry playing a detrimental role in affecting pitting behaviour in aluminium alloys.

In a review of metastable and stable pit formation, Sklarska-Smialowska discovered that metastable pits are able to form hundreds of millivolts below the pitting potential. Here, pit frequency is seen to increase, the closer the voltage approaches the pitting potential. Metastable pits as described by the author are pits which are small in size and grow and repassivate in less than a few seconds. The important issues concerning metastable pits are the processes leading to their formation and the electrochemical factors that influence the transition of metastable to stable pits. When metastable pits first occur, the current increases as pit nucleation and growth takes place, however, the current is seen to decrease after a short space of time. It is necessary for the ratio of current in the pit to the pit radius to be above a certain value for stable pits to form, otherwise only metastable pits would do so, as depicted by figure 2.20.

It is obvious that a pit will develop when the conditions within the pit are such that the pits are in the active state. The investigations performed by Galvele et al [26] some time ago suggest that if a critical value of the pit current density times pit depth is exceeded, then continuous growth of the stable pit would occur. Galvele developed this theory taking into consideration the acidification of the pit solution. Pitting can be said to only occur (with certain exceptions) in halogen solutions. Hence, both acidification and chloride ions are needed for pit development. The magnitude of the pH is coupled with the concentration of chloride ions in the pit solution. (The pH is lower when the concentration of chloride is higher until a solid metal salt is formed.) For stable pit growth to occur, the presence of a salt film at the pit bottom is necessary. The existence of a salt film is as a result of a high dissolution rate within the pit and the resultant acidification. These chloride salt films are only stable in a high acidic solution.

Corrosion pit growth also is discussed somewhat in the literature. A review by the author of the work undertaken by Godard et al [27] (study into kinetics of pit growth) states that pit depth is proportional to $t^{1/3}$ (t = time). However, the work carried out by Hunkeler and Boehni [28] show that pit growth is ohmically controlled due to its relationship with the conductivity of the bulk electrolyte, hence pit depth d is given as a function of time as ($d \sim t^{0.5}$)

as was pit density, I ($i \sim t^{-1/2}$). The author suggests that the discrepancy between Godard et al and Hunkeler and Boehni might have been caused as a result of varying experimental conditions, although their results were found to fit in well with the theories of diffusion controlled and an ohmic controlled pit growth rate, respectively.

In addition pitting chemistry is also reviewed. Within this section the author states that it is well documented that Al pits contain salt layers, if not during pit nucleation and first stage pit growth, then during a later period of pit growth. Vijh [29] noted that on metals that suffer pitting (Mg, Zn, Al, Fe, Ni and Zr) the dissolution product $MeCl_x$ forms a solid salt in pits. This salt film is said to unanimously stable the pit. However, the composition of the salt layer is not known. Hagyar and Williams [30] suggest the following sequence of reactions occur; ionization of the bare surface of Al takes place rapidly and Al^{3+} undergoes hydrolysis very rapidly. Hydrolysis is a chemical reaction in which the action of water or its ions breaks down a substance into smaller molecules. Hydrolysis occurs in certain inorganic salts in solution, in nearly all non-metallic chlorides, in esters, and in other organic substances.

$$Al^{3+} + H_2O \Leftrightarrow H + Al(OH)^{2+} \qquad 5$$

Aluminium hydroxide reacts with chloride:

$$Al(OH)^{2+} + Cl^- \Rightarrow Al(OH)Cl^+ \qquad 6$$

And then with water producing acidic conditions:

$$Al(OH)Cl^+ + H_2O \Leftrightarrow Al(OH)_2Cl + H^+ \qquad 7$$

The author reviewed several papers that tried to quantify the pH value within pits and crevices. The pH of the solution measured in pure Al pits was found to be between 3 and 4 by using a freezing method when the pH of the bulk solution was 11, although other authors measured pH values of between 1 and 3.

Effects of corrosion inhibition were also evaluated in the paper, with special reference towards chromate inhibitors. The author's review of work by Pride, Scully and Hudson

showed that chromate also has an effect on metastable pits. The metastable pit nucleation decreases at a given potential and Cl^- concentration. Experimentation results imply that after immersion of the Al in neural chromate solutions, two definite trends occur; adsorption of chromate and its partial reduction. Possible actions of chromates include:-

1. Chromates can adsorb in defective spots, decreasing the active area of the surface and therefore increasing the passive properties of a film.
2. It is possible for chromates to incorporate into the defective sites of the film, and can be reduced into chromium oxides increasing the protectiveness of the film against the chloride attack.
3. Chromates and/or chromium oxides can change electronic properties of the passive film.

The conclusions drawn by the author regarding chromates as inhibitors of pitting corrosion are that they can act in several different ways, as described above. Chromate anions can increase the pH in neutral solutions thereby increasing the cathodic polarization reaction and decreasing the corrosion potential. Secondly, they can increase the pitting potential as a result of an increasing pH in neutral solutions; they can improve the film against pitting by a restriction of adsorption of chloride anions on the surface or by restriction of the entrance of chloride to the passive film and they can change the electronic structure of the passive film.

The development of chromate on the growth of corrosion pitting is yet not known, although it is clear that only a high concentration of chromate will decrease pit growth.

In accordance with Sklarska-Smialowska, the author ***Lajain*** [31] discovered that pitting was only incurred on materials capable of being passivated and consisted of local corrosion in a surface that, for alternative materials, remains passive. In a study entitled corrosion protection schemes for aircraft structure: some examples for the corrosion behaviour of aluminium alloys, it was uncovered that corrosion pitting in particular required the presence of halogen ions in the attacking electrolyte, to cause the passive film to collapse at weakened points, hence making these points active.

Other authors have also reviewed pitting corrosion in aluminium alloys. ***Blanc*** and ***Mankowski*** [32] studied the susceptibility to pitting corrosion of AA 6056-T6 compared to AA 2024-T351. The study was undertaken to determine whether the 6056 alloy could replace 2024 alloy in conditions where pits can appear. Both alloys have a similar composition although 2024 has a higher copper content. The two alloys were potentiostatically polarised with an aggressive type of chloride ions, to induce the formation of corrosion pits. The variation in pitting rate with potential for the two alloys is seen in figure 2.21. The plot also compares the pit germination rate with potential of pure aluminium. For the pure aluminium, the logarithm of chloride concentration varies linearly with the potential at low potentials and then becomes stable. This behaviour showed the competition between two trends; the activation of the pitting corrosion with increasing potential and the thickening of the passive film, in other words, the increasing of the resistance to pitting of the passive film with increasing potential. The high copper content of the 2024, incidentally concentrated in the intermetallic phases, were preferential sites for corrosion pitting at low pitting potentials. At this low pitting potential, the particles containing Al, Mg and Cu dissolves, depositing copper around the particles, incidentally altering the properties of the passive film on the 2024 alloy. From figure 2.21, it is clear that the 2024 alloy shows a peak of susceptibility to pitting, caused by the addition of chloride ions, which formed a synergy with the sulphate ions to produce the most aggressive environment. The study also showed that the passive layer on the 2024 alloy thickened at higher pitting potentials, essentially behaving similarly to pure aluminium.

In contrast to the 2024 alloy, the copper in the 6056 alloy distributed between the matrix and the precipitates, without the precipitates being enriched with copper. Pits were found to initiate in the matrix or in the vicinity of the coarse particles for the 6056 alloy, instead of preferentially initiating corrosion pitting at the site of the coarse particles. It was therefore deduced in the investigation that the performance of 6056 was similar to that of pure aluminium. For low chloride ion concentrations, the 6056 alloy was less resistant to pitting than the 2024 alloy, but was more resistant for the high concentrations. Conclusions therefore showed that the 6056 alloy was better suited than the 2024 alloy and adapted better in conditions where pits can appear.

In an attempt to quantify pit proportions in three dimensions, ***Frantziskonis et al*** [33] investigated multiscale characterisation of pitting corrosion in an aluminium alloy. Although

the investigation was carried out on a 2xxx series alloy, much of the techniques and analysis used are supportive of the current research programme. This work in particular attempted to characterise corrosion pitting damage through multiscale analysis and identify:-

a) Properties that allow complete characterisation from two-dimensional images of pitting, which are easily acquired in practice;
b) The morphology of the pits, described in a multiscale fashion, important for crack initiation and propagation under fatigue loading.

The research paper applies 'Wavelet analysis' to quantify pit dimensions. Wavelet transforms can be seen as a possible mathematical microscope; when increasing the magnification, insights into complicated structures of patterns can be observed. Wavelets are basically a means to mathematically represent functions space and scale wise, with a few parameters. The research clearly showed that achieving 3-D information from 2-D images is possible, as illustrated by figure 2.22. Additionally, the process is rather independent of the magnification the 2-D pitting images are captured in; within a range of magnifications, of course, as far as the perimeter of the pits is captured in enough detail. The work is amenable to examining a large number of corroded surfaces, corroded under various conditions, by obtaining both 3-D and 2-D images at a range of magnifications.

Similarly to Frantziskonis et al, ***Balázs and Gouyet*** [34] studied two-dimensional pitting corrosion of aluminium thin layers. The authors examined the influence of Cl^- and Fe^{3+} ions on the morphology of pits grown in aluminium thin films. Corrosion pit growth kinetics were compared to fractal pattern behaviour in an attempt to overcome the assumption, of many authors, that hemispherical pits are always etched into the metal surface. The study revealed that above a certain threshold of electrolyte composition, pits nucleate spontaneously on the metal surface. The probability of multiple pit formation on the same specimen increases with Cl^- concentration. Pit evolution was regarded as a 'spreading' phenomenon producing the fractal-like patterns, as illustrated by figure 2.23. The results showed that spontaneous occurrence of active sites on a previously inactive surface are not allowed. Dissolution takes place with constant current density. The active metal surface will be locally passivated once the aggressiveness of the electrolyte above the actual surface drops below a critical value. Various models were produced with some success, to simulate pit growth behaviour based on the concept of fractal patterns.

The study of pitting corrosion of AA2024-T3 by scanning microreference electrode technique was performed by ***Shao et al*** [35]. Micro-pitting was investigated within the 2024 alloy utilising the scanning microreference electrode technique combined with scanning electron microscopy and X-ray energy dispersive spectroscopy.

It is known that AA2024-T3 is widely used in the aerospace industry due to its extremely high strength. Heterogeneous microstructures within the material make it susceptible to pitting corrosion in media containing chloride ions. Pitting corrosion in this type of aluminium alloy, initiates on or around copper rich intermetallic particles. Micro flaws on the oxide film near these particles causes the localised corrosion attack that leads to eventual pitting.

This study used a microcomputer-aided measuring system with a scanning microreference electrode (SMRE) to probe pit initiation at the initial stage. The technique utilised the lateral resolution of the attached micrometer to measure the depth of the imposed corrosion pitting. The SEM was used to characterise and evaluate the second phase particles (Cu_2FeAl_2, Al_2CuMg) present within the material, and to correlate the surface inhomogeneity with the localised corrosion activity for the 2024-T3 alloy.

The material for the investigation was supplied by Xiamen Airline Company. Cylindrical specimens 8 mm in diameter and 3 mm in length, were machined from the original block, polished and sealed in a polymethyl methacrylate holder with epoxy resin. A glass tube was connected to the specimens and filled with 1 M KCl solution; wax was used to seal the cell. Potential imaging measurements of the specimens were taken every 10 minutes. The morphology of the second phase particles were examined using an SEM combined with a Energy Dispersive Spectroscopy (EDS). Potential imaging of the surface of the 2024 material at various immersion times revealed a variety of plots, as illustrated by figure 2.24. The height of the potential peak represents a tendency towards localised corrosion. The higher the potential peak, the more damaging the corrosion.

Conclusions from the study revealed that the early stages of pitting within the 2024 can be detected using the SMRE technique. Measurements using the technique revealed that pitting corrosion occurred on the surface of the material immediately after the exposure to NaCl solution. Detailed microscopy work identified the second phase particles within the

material as the sites for the localised corrosion pitting areas. Pitting corrosion seemingly developed and reached its maximum value after two hours of immersion time.

2.3.3 Corrosion Fatigue of Aluminium Alloys.

Corrosion-fatigue can be defined as the combined action of an alternating stress and a corrosive environment. The fatigue process is thought to cause rupture of the protective passive film on the aluminium, upon which corrosion is accelerated. The introduction of a corrosive environment often eliminates the normal "fatigue" limit of a ferrous alloy, thereby creating a finite life regardless of stress level.

The corrosive environment can cause the fatigue crack to grow at a faster rate. Even relatively mild corrosive atmospheres can reduce the fatigue strength of aluminium structures considerably. Control of corrosion fatigue can be accomplished by either lowering the cyclic stresses or by corrosion control.

The researchers ***Hart, Tennant*** and ***Hooper*** [36] reviewed solution chemistry modifications that occur within corrosion fatigue cracks. The authors state that the electrolyte within the corrosion fatigue crack becomes modified in relation to the bulk solution. Fatigue crack growth rate is dependent upon electrolyte chemistry near the crack tip; therefore it is important that recognition is given towards influential variables. The study analysed how fatigue variables can influence mixing between the crack and bulk solutions (figure 2.25). The basis for the research looked at how the mixing is governed primarily by net momentum of the periodically exhausted and ingested electrolyte.

Crack opening angle, cyclic frequency and cube of crack length were shown to be proportional to momentum of the electrolyte. Decreasing mean stress was also seen to increase momentum, with further increases seen for stress functions that result in crack closure, during a period of each cycle. Temperature, stress wave form, specimen geometry, test method and applied current density were factors which also had an effect.

From a general point of view, ***Scott*** [37] studied the general chemistry effects in corrosion fatigue, while ***Bamford*** [38] reviewed the variables effecting general corrosion

fatigue in metals and alloys, in a study entitled Implementing Corrosion-Fatigue Crack Growth Rate Data for Engineering Applications.

Several authors have reviewed corrosion fatigue, their effects and consequences. ***Duquette*** [39] studied the mechanisms of corrosion fatigue in aluminium alloys. The review examines various fatigue characteristics of high strength aluminium alloys in gaseous and aqueous environments and explains that the specific mechanisms of corrosion fatigue can be attributed to Strain Enhanced Dissolution (SEN), Surface Energy Reductions (SER) and Hydrogen Assisted Cracking (HAC).

High strength aluminium alloys are known to be highly susceptible to environmental degradation in the presence of halide ions. Pitting corrosion along with crevice corrosion or exfoliation corrosion are good examples of material degradation in the unstressed state. However, under conditions of applied or residual stresses, SCC may take place, or if cyclic loads are present, alloys may suffer corrosion fatigue. As mentioned previously, there are three specific mechanisms of corrosion fatigue as explained by Duquette. The mechanisms reduce fatigue lives in aluminium alloys that are exposed to aggressive environments. The mechanism theories are:-

- *Strain Enhanced Dissolution.*

Older versions of this mechanism suggested that strained atomic bonds are more likely to lead to atomic dissolution (corrosion) than unstrained bonds. Another version of this mechanism is the film rupture theory. Mechanical rupture of a protective film (passive layer), leads to rapid localized corrosion at the film rupture sites, which leads to crack initiation in emerging slip bands and subsequently to corrosion assisted crack growth due to the high stress concentrations associated with crack tips.

- *Surface Energy Reductions*

Specific species which are strongly adsorbed at surfaces serve to lower the local bond energy and lead to increases in crack propagation rates. A reduction in the surface energy

may enhance plasticity and cause early crack initiation and propagation, has also been suggested by certain authors.

- *Hydrogen Assisted Cracking*

All aluminium alloys which contain hydrogen are consequently embrittled; therefore interactions between dislocations and hydrogen are prominent.

In summary, the investigation managed to create a model for corrosion fatigue of high strength Al alloys. The model is dependant upon surface film integrity, which if damaged by chemical or mechanical means, would allow exposure of hydrogen to emerging dislocations (slip planes), which effectively pump hydrogen to crack processing zones. It is also thought that the hydrogen gathers at the precipitate and matrix interface, causing separation within these areas. The author infers that corrosion fatigue is an extension of stress corrosion cracking, except that the cyclic nature of the dislocation motion creates a preferentially high diffusion path into the process zone rather than into the normal high diffusity zone of grain boundaries.

2.3.3.1 Corrosion Fatigue Crack Propagation.

Aliaga and ***Budillon*** [40] dealt with the evaluation of corrosion fatigue strength of aluminium alloys used in the aeronautical industry. More importantly, crack propagation was evaluated in various environments such as dry argon, wet air and sea water. Frequency, specimen thickness and load ratio effects were investigated, with the effects of these various environments on the endurance limit at 10^7 cycles studied.

The authors argue that laboratory tests are not always indicative of service conditions, in particular, environmental effects, which sometimes can be considerable. The environments chosen for the study was suggestive of the least and most aggressive conditions aircraft encounter during flight and also whilst on the ground. The study mainly looked at the corrosion fatigue crack initiation and propagation with a particular emphasis drawn towards service conditions. Various aluminium alloys were used to conduct the investigation, with specific emphasis on comparing the 2xxx and 7xxx series alloys. The alloys 2618 A and 7175 were evaluated with three varying surface treatments; as machined, chromic acid anodising

and aircraft specific protection. Two test specimen designs were used to carry out the evaluation, compact tension and centre crack tension specimen. Crack initiation was determined using the "Moore" type specimens using a rotating-bending machine.

It was established in all cases that the salt water environment was the most aggressive, with the dry argon proving to be the least. Specimen thickness and ΔK under certain conditions of R ratio and environment appeared to have an effect on crack growth rates. Test frequency was found to have a negligible effect on crack growth rates. In terms of alloy specifics, the 7xxx series demonstrated considerable sensitivity towards the environment, unlike the 2xxx series. Graphical representation of the 2xxx series results can be seen in figure 2.26. The authors state that the alochrome plus a paint coat (aircraft specific protection) seemed to be the most effective.

Santner and ***Kumar*** [41] also studied crack propagation of corrosion fatigue in commercial 7xxx aluminium alloys. The review compared the crack growth rates of two differently produced aluminium alloys; P/M X7091 a powder metallurgy alloy and I/M 7075-T651, an ingot metallurgy alloy. It was revealed during the investigation that crack growth rates for the ingot metallurgy produced alloy were ten times faster than the powder metallurgy alloy over the range of stress intensities evaluated. This statement holds true for the S-T and T-L orientations. Fractographic analysis of the fracture surfaces revealed large amounts of surface debris, which corresponded to the area where crack closure occurred most. This suggested that the presence of corrosion debris between the fracture surfaces increases the closure effects, and invertedly improves fatigue resistance.

A in depth review of corrosion fatigue crack propagation in metals was carried out by ***Gangloff*** [42]. The paper compiled and evaluated experimental data and mechanistic models from various sources for corrosion fatigue crack propagation in structural alloys exposed to ambient temperatures, gases and electrolytes. The effect of alloy copper content on corrosion fatigue crack propagation of aluminium alloys, heat treated to either the peak strength or over-aged condition, was examined. It was shown during the investigation that normalised corrosion fatigue growth rate decreased with increasing copper content, predominantly for the peak aged condition and intermediate ΔK. These results were explained based on the damaging interaction between absorbed hydrogen and localised planar slip with crack tip cyclic plastic zone. Planar slip is eliminated by increasing the copper content and over-

ageing, factors that in turn, reduce precipitate coherency and increase precipitate looping by dislocations to homogenise plastic deformation. This work provides a hypothesis for the superior corrosion fatigue resistance of copper bearing 2xxx alloys compared to the 7xxx series materials. It is documented elsewhere in the literature that as resistance to corrosion fatigue is increased by the addition of more copper content, the authors Sprowls and Brown and Blanc and Mankowski showed, respectively, that stress corrosion and pitting corrosion resistance are decreased.

2.3.4 Corrosion Detection Techniques in Aircraft Structures.

Corrosion detection techniques within aircraft structures have become a major component in the aerospace industry, alongside novel approaches of corrosion inhibition. Currently, the most successful detection method employed to identify corrosion and similar defects is Non-Destructive Testing (NDT). Modern NDT is used by manufacturers and in particular the aerospace industry to ensure: product integrity and reliability; failure prevention, cost effective techniques to ensure safety and component integrity within service conditions; control manufacturing process; lower manufacturing costs; maintain uniform quality level and certify operational readiness. Common NDT methods used include:-

- Thermography
- Acoustic Emission
- Potential - drop
- Holography
- Visual Methods
- Magnetic Particle Inspection
- Ultrasonic
- Eddy Current
- Radiography
- Dye Penetrant

Localised corrosion is recognized as one of the degradation mechanisms that affect the structural integrity of aging aircraft structures. Several non-destructive testing systems have been used to obtain the images of damaged regions. There is a growing demand for improving existing NDT techniques to achieve maximum confidence and reliable results with minimum damage components. There is always a constant outlook for methods that identify the damaged regions on the image and also that gives a quick estimate of the extent of the damage [43]. Common NDT methods used for aircraft inspection include;

- ***Eddy Current***

The eddy current technique has been very prominent in the detection of cracking in metal structures alongside corrosion detection. Eddy current is particularly successful over areas of thin or single plate material or components. They technique has also been used for the detection of pitting and intergranular corrosion within aircraft structures such as skins and wing spars. The detection of cracks growing from fastener holes is a common use of this technique, although certain limitations have been noticed.

In standard eddy current testing, a circular coil carrying an AC current is placed in close proximity to an electrically conductive specimen. The alternating current in the coil generates a changing magnetic field, which interacts with the test object and induces eddy currents. Variations in the phase and magnitude of these eddy currents can be monitored using a second 'search' coil, or by measuring changes to the current flowing in the primary 'excitation' coil. Variations in the electrical conductivity or magnetic permeability of the test object, or the presence of any flaws, will cause a change in eddy current flow and a corresponding change in the phase and amplitude of the measured current. This is the basis of standard (flat coil) eddy current inspection, the most widely used eddy current technique.

The penetration depth of eddy currents is indicated by a parameter known as the 'skin depth'. This is dependent upon operating frequency (lower frequencies give deeper penetration) and specimen conductivity and permeability, and is typically between 5 μm and 1 mm or more. For most inspection applications, eddy current probe frequencies in the range 1 kHz to 3MHz are used.

To help simplify the often complex eddy current response, changes in amplitude and phase are displayed on an impedance plane diagram (a plot of system inductance against resistance). In this way, changes in operator variability, such as the distance between the probe and the test piece (lift-off) will cause a horizontal shift in the spot forming the trace, while the presence of any flaws causes the spot to shift vertically [44].

- ***X-Radiography***

X-radiography is the most straightforward approach to corrosion detection within aircraft structures. X-ray beams are weakened by their passage through aluminium; therefore any loss of material can be detected as an area of higher intensity in the radiograph. Detection of localised material loss is simple and instantly recognisable to the user. X-radiography is unaffected by the presence of a number of layers, as some NDT methods are. The limitations of the system however are for example, in a layered structure such as a lap joint, where the metal may corrode at an interior surface causing loss of strength. The corrosion products will, however, remain trapped within the joint, causing a reduction in the X-ray, consequently proving difficult to locate [45].

- ***Neutron Radiography(NR)***

Neutron radiography is considered a complementary nondestructive testing technique to conventional radiography. In X- and gamma radiography, attenuation increases uniformly with mass number and density, whereas, with neutrons, attenuation is random with a tendency for certain light elements such as hydrogen to absorb and scatter neutrons rather well. Thus, neutron radiography is especially well suited to detecting corrosion and moisture entrapment, especially in aircraft structures [45].

Neutron radiography was used to examine and detect corrosion in aircraft aluminium alloys in a study performed by ***Crispim et al*** [46]. The work illustrates the application of an aqueous solution of gadolinium nitrate as a contrast agent in samples of AA7075 for neutron radiography detection of pitting and exfoliation corrosion.

With aircrafts being exposed to corrosive environments such as exhaust gases, moisture, waste water and spillages at constant/regular intervals, it is necessary for airline companies to monitor the corrosion contaminant. Neutron radiographic images are often advantageous in this situation due to the high neutron sensitivity caused as a result of the hydrogen contained in the corrosion products. The relatively high slow-neutron attenuation by hydrogen, coupled with the relative neutron transparency of many metals, leads to the prospect for early detection of hidden corrosion in structures. The early detection of several types of corrosion in aluminium structures by means of NR has consequently resulted in many

useful applications, mainly as a tool in commercial and military aircraft maintenance. The inspection of in-service aircraft requires the use of a contrast agent usually in a liquid or powder form, to readily improve the image contrast. These hydrogenous agents can be water, oil, paraffin or neutron absorbing metals, although the most effective contrast agent is often gadolinium compounds. This compound improves the detection of porous areas and microscopic flaws due to its high scattering or high thermal neutron absorption cross section.

The conclusions drawn from the study include:-

- NR can detect corrosion in shielded AA7075 to depths of 19.9mm.
- Contrast agents dramatically improve image sharpness.
- NR can resolve images of hidden pits with dimensions of the order of 30μm in diameter and larger.

- ***Thermography***

Thermography has considerable potential and has been used by airlines for the early detection of the presence of water within structures. The technique is suitable for use on composites, metals, and ceramics on a number of applications such as delaminations, impact damage, disbonds, corrosion and water ingress. The technique uses infra-red technology to map airframe components, yielding a temperature plot of the various areas examined, (figure 2.27).

Table 2.5 Electrochemical measurements of the alloy 7010 in various temper conditions.

Temper	Corrosion Potential mV	Pitting Potentials (Potentiostatic tests)	Instability Region mV
T351	-775	-800	70
T651	-755	-770	35
T7451	-740	-740	15

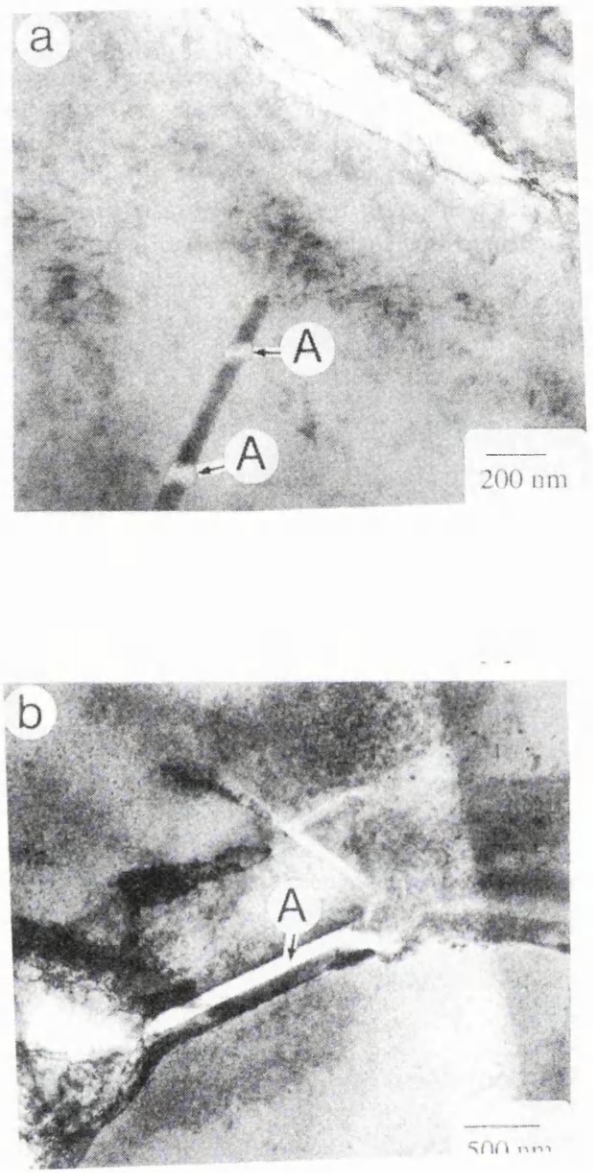

Figure 2.10 TEM micrographs of cracks formed in 7010 showing a) void formation at an intermetallic situated close to a crack and b) decohesion at an intermetallic/ alloy grain boundary interface.

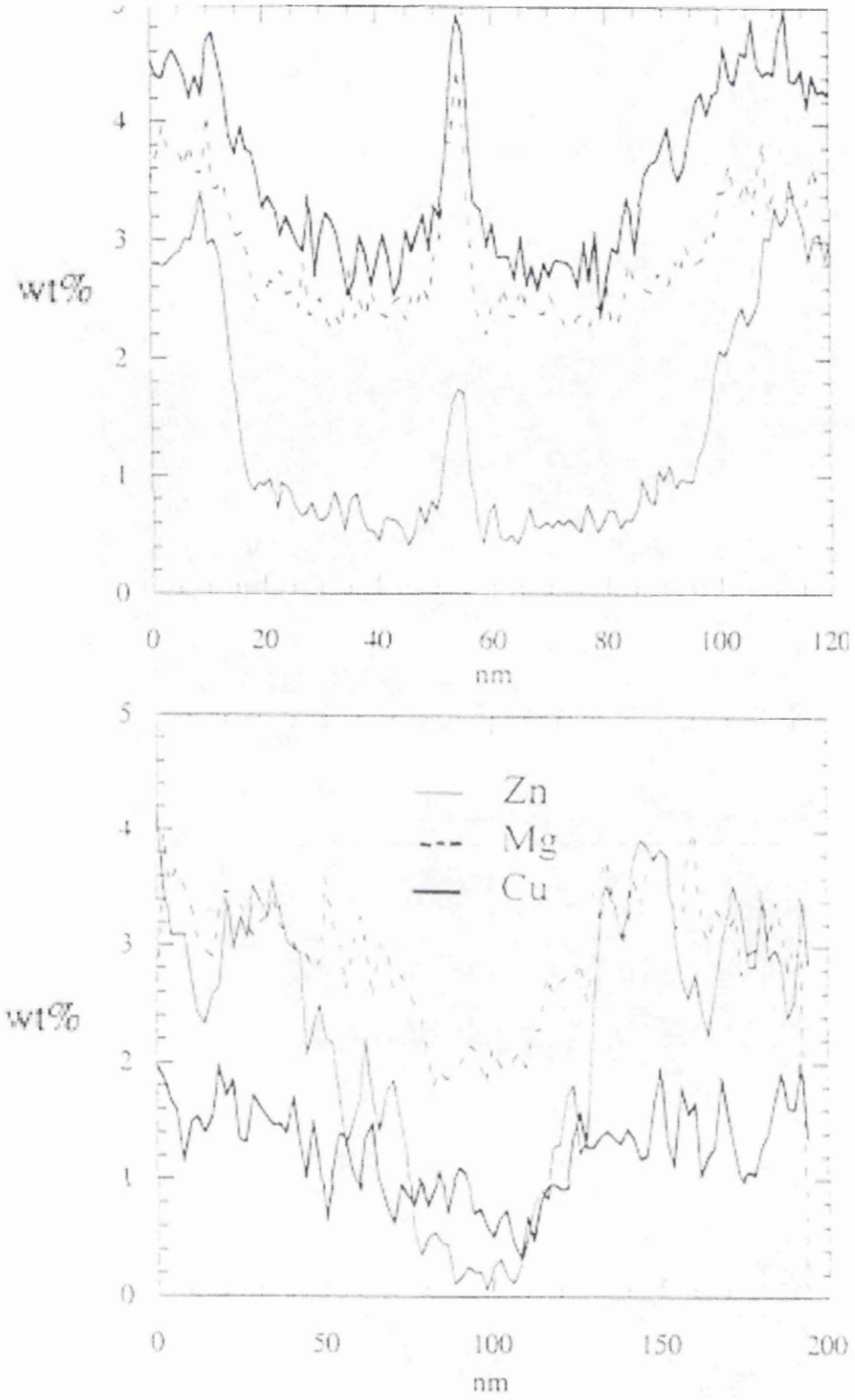

Figure 2.11 (a) and (b) Compositional profiles of the grain boundaries formed in the 7010 alloy.

(a)

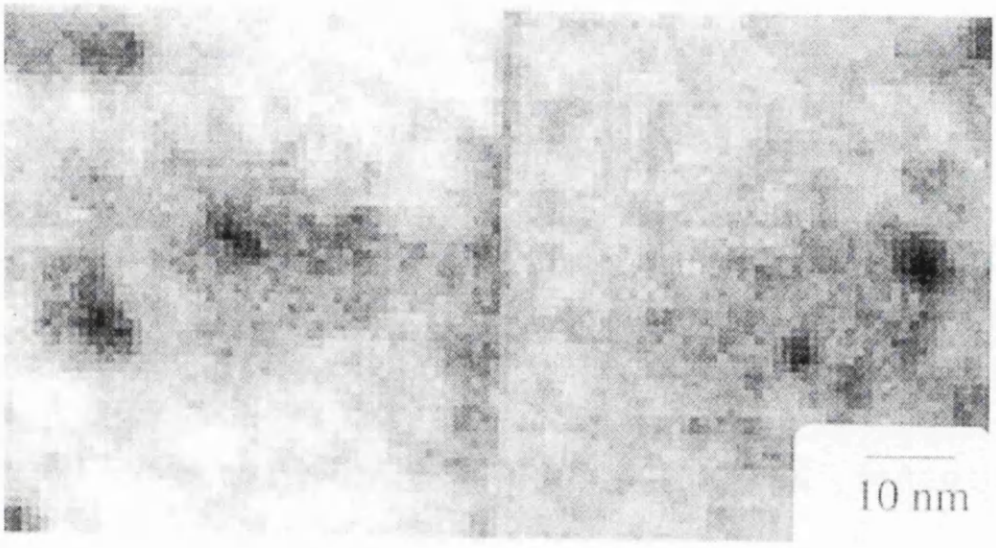

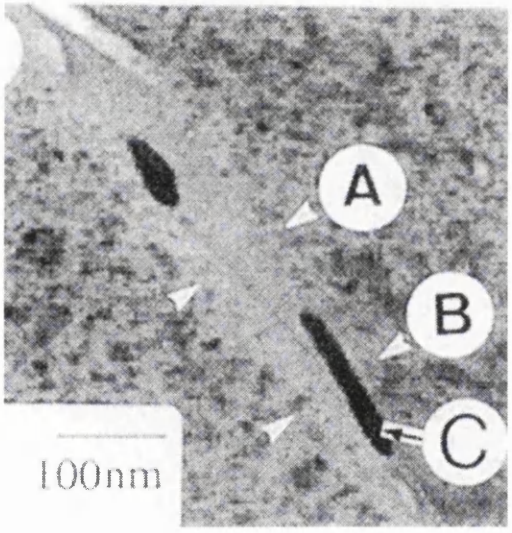

(b)

Figure 2.12 (a) and (b) STEM images for the boundaries illustrated in figure 2.11.

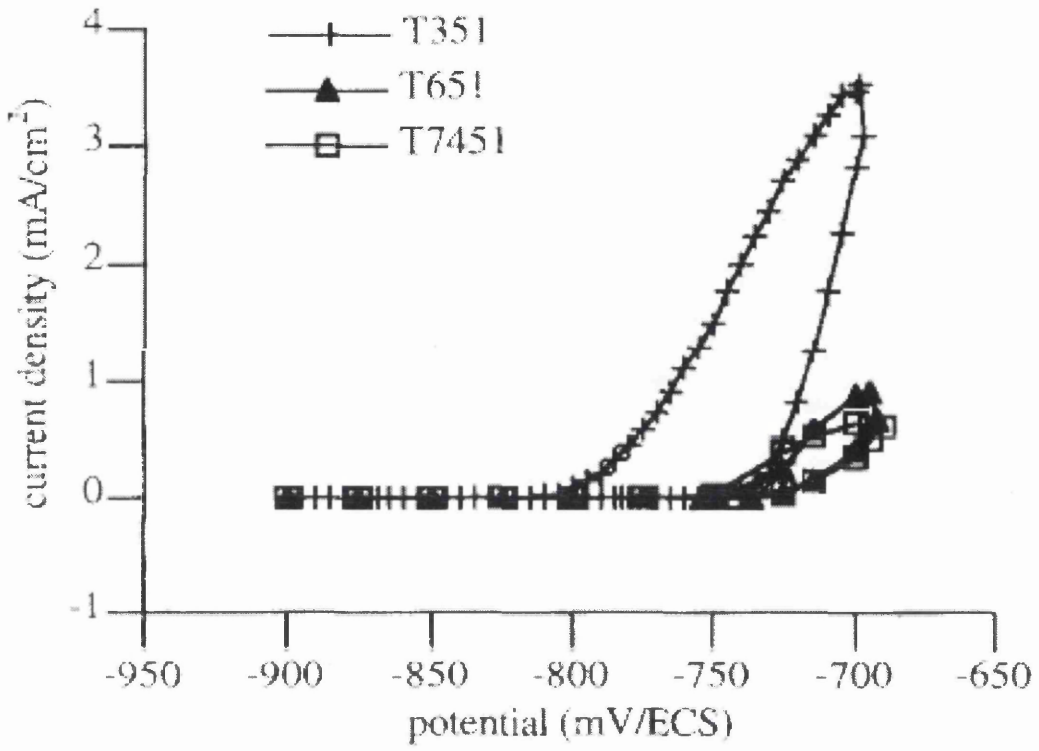

Figure 2.13 Potentiokinetic polarisation curves.

(a)

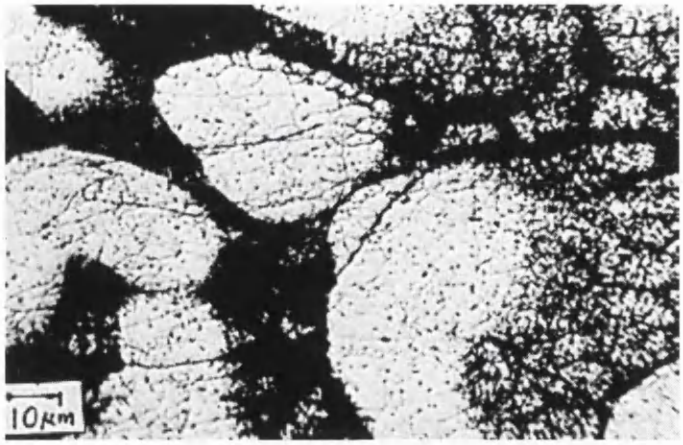

(b)

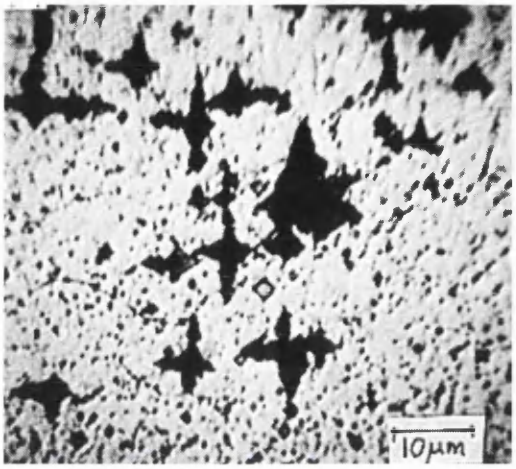

(c)

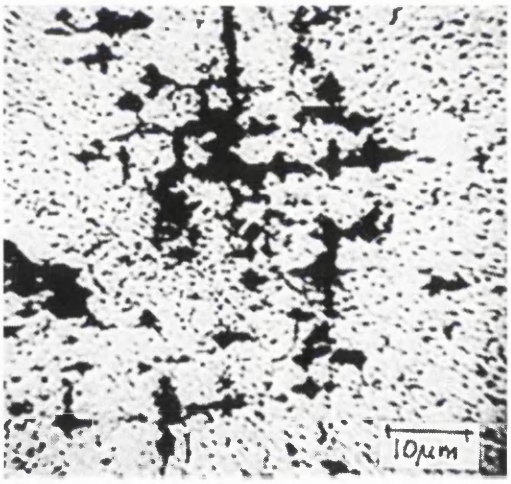

Figure 2.14 7010-T736, unstressed, etched for 2 minutes in seawater and 1 % HCl at 90°C. (b), (c) 7010-T736, unstressed, etched for 25 minutes in same corrodent at 40°C.

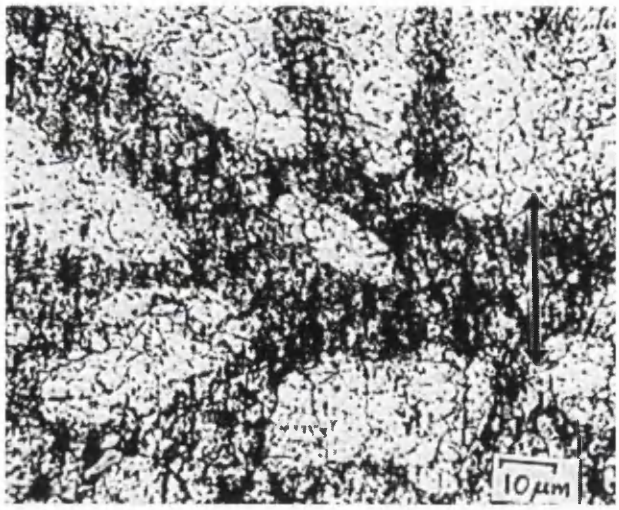

(a)

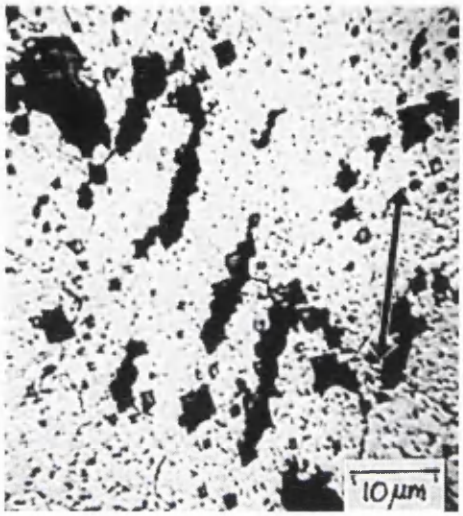

(b)

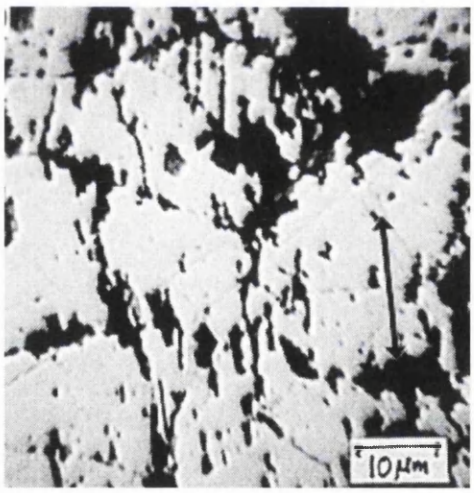

(c)

Figure 2.15 (a) 7010-T736, etched under a tensile stress applied in the direction indicated by the arrows, 2 minutes in seawater + 1 % HCl at 90°C. (b), (c) 7010-T736, stressed as above, while being etched for 45 minutes at 40°C.

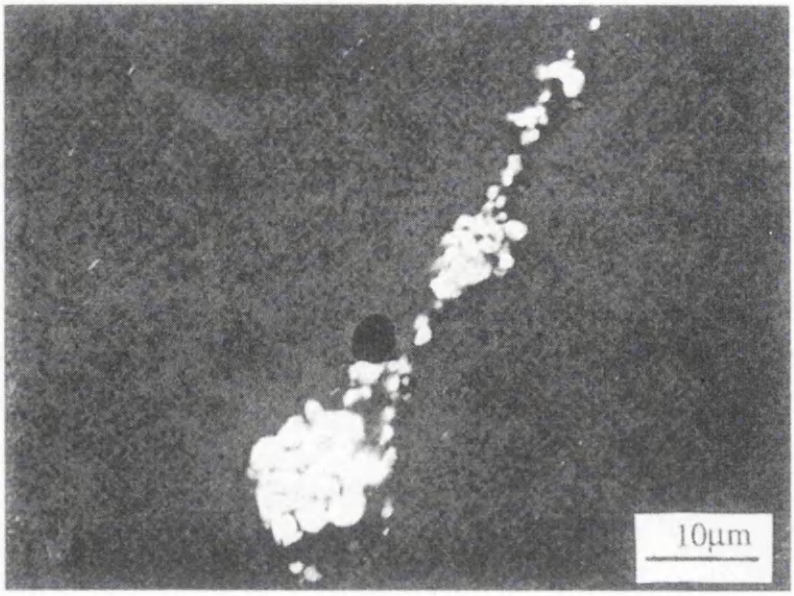

Figure 2.16 Constituent particles in 7010-W52.

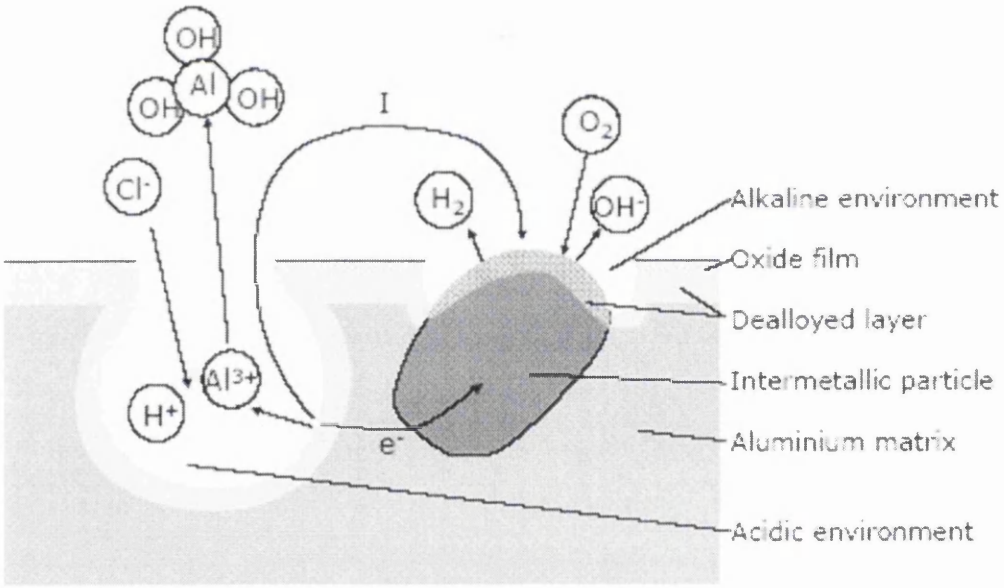

Figure 2.17 Pitting corrosion process on aluminium alloys.

(a)

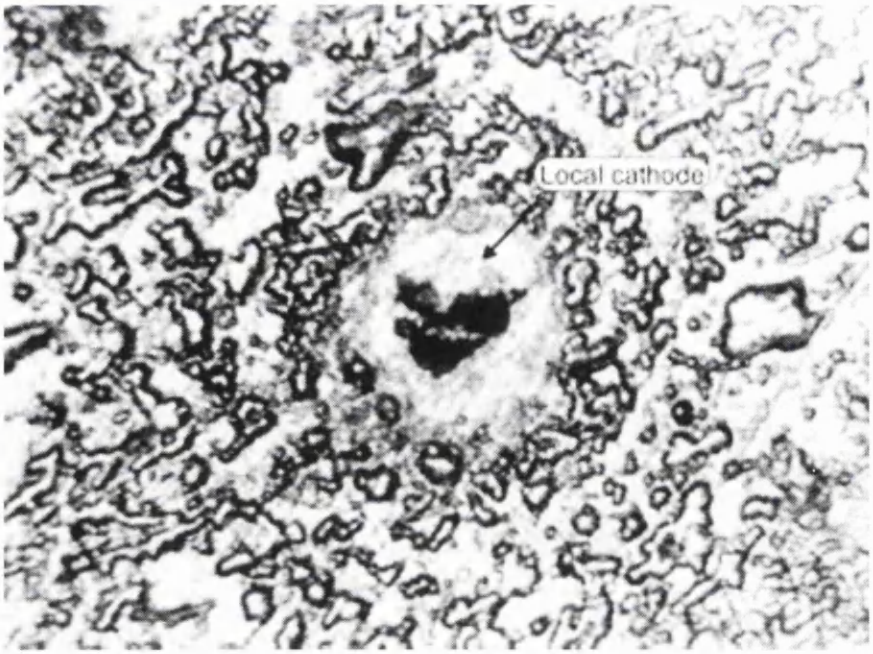

(b)

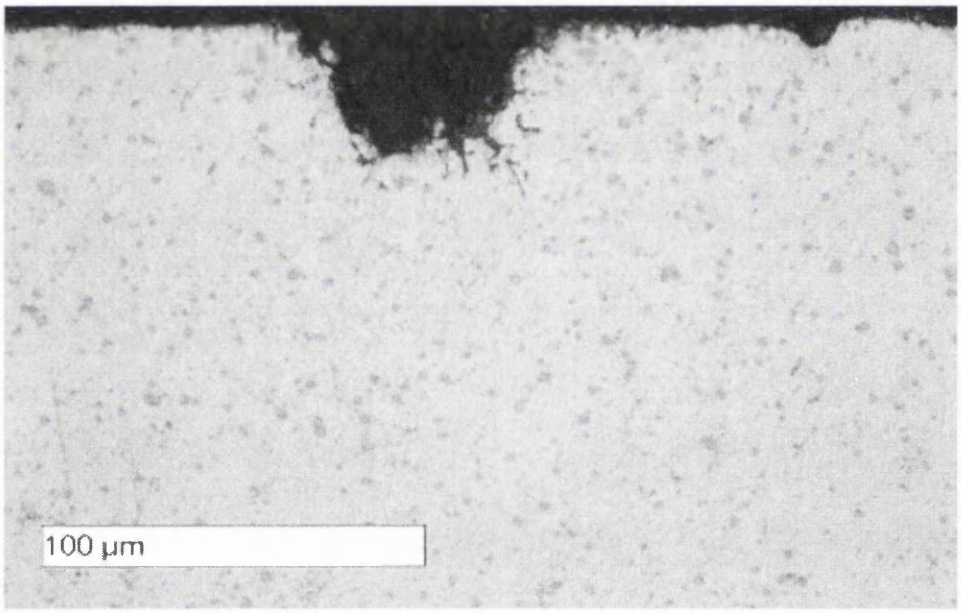

Figure 2.18 (a) Image of a corrosion pit taken from above, (b) Profile view of a corrosion pit propagated within an aluminium alloy.

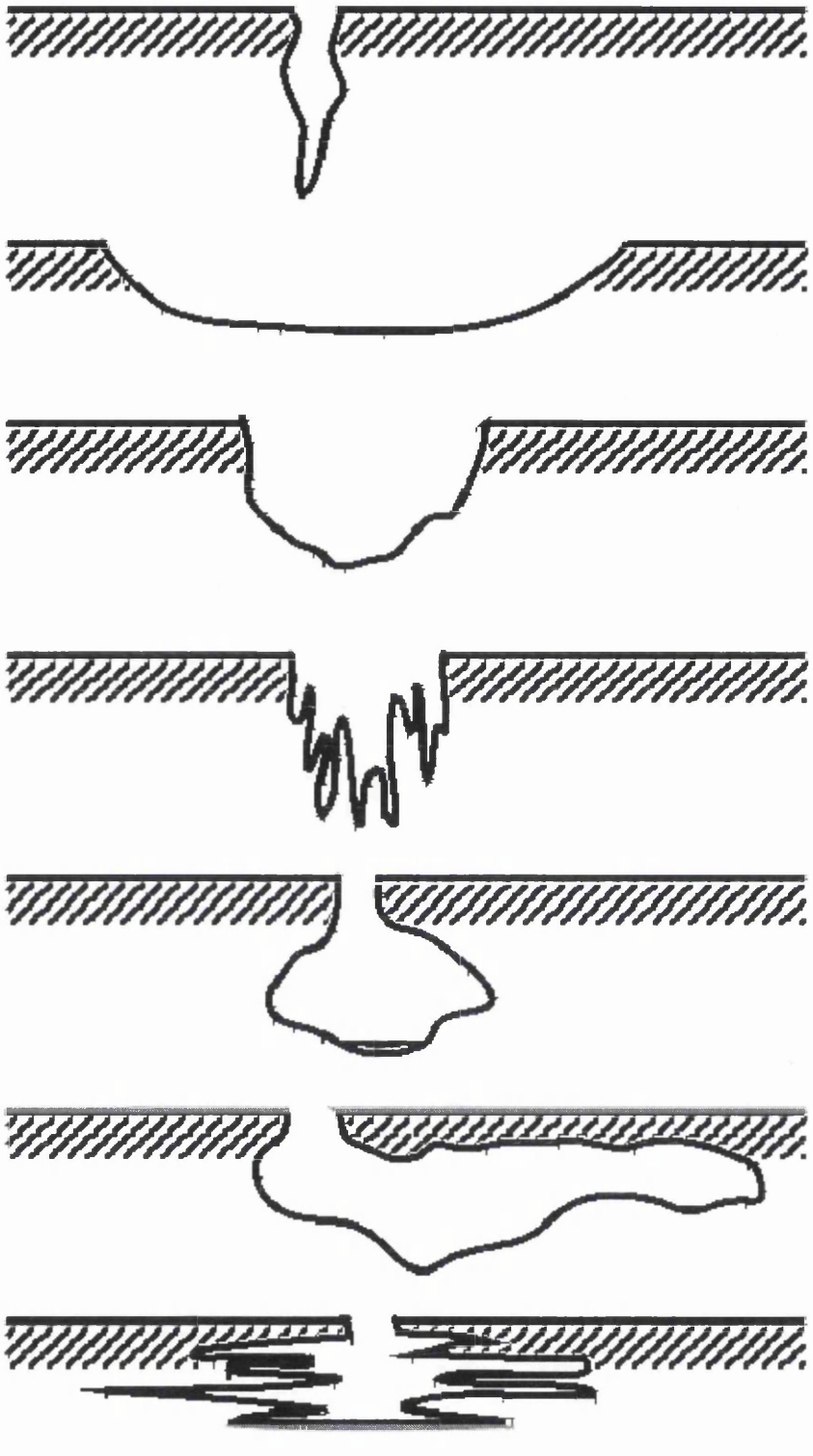

Figure 2.19 Various forms of corrosion pit morphology. (a) Narrow and deep (b) Shallow and wide (c) Elliptical (d) Vertical grain attack (e) Subsurface (f) Undercutting (g)Horizontal grain attack.

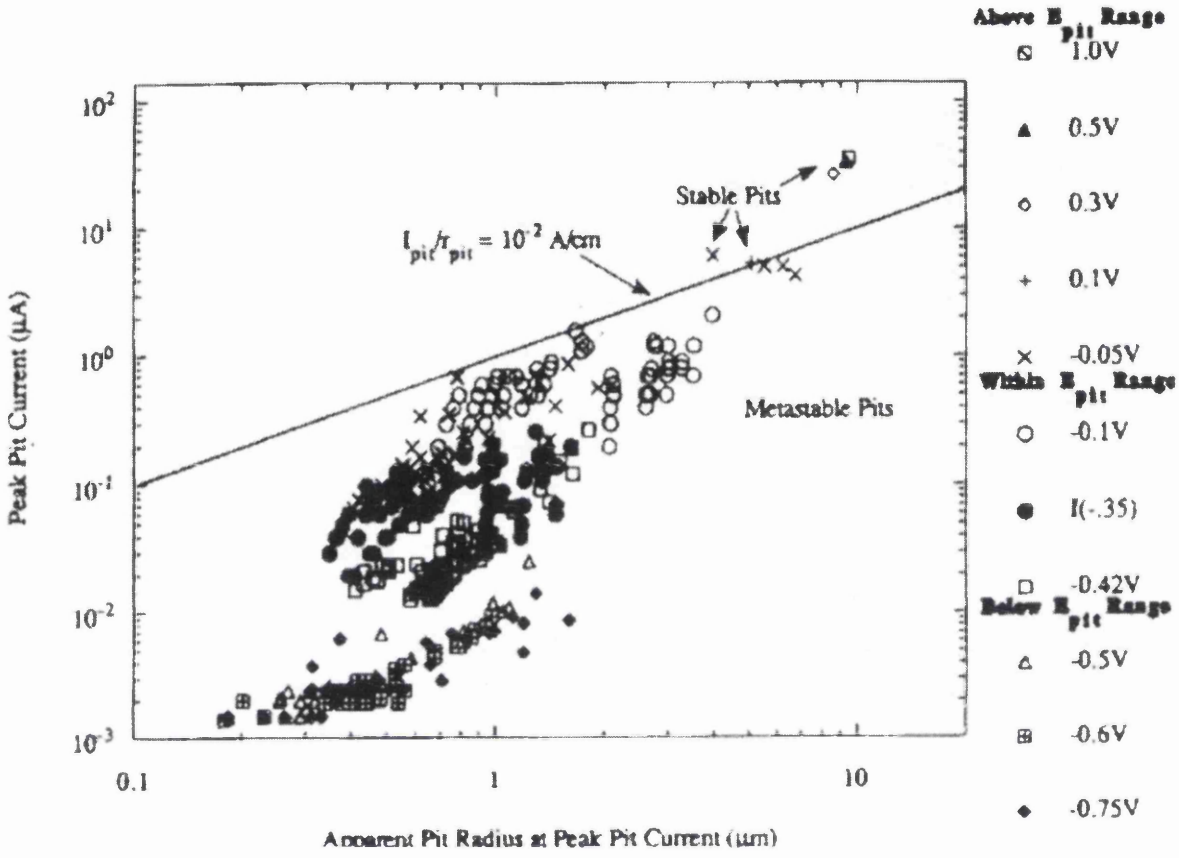

Figure 2.20 Relationship between peak pit currents and apparent pit radii at peak pit current for a large population of metastable and stable pitting current spikes

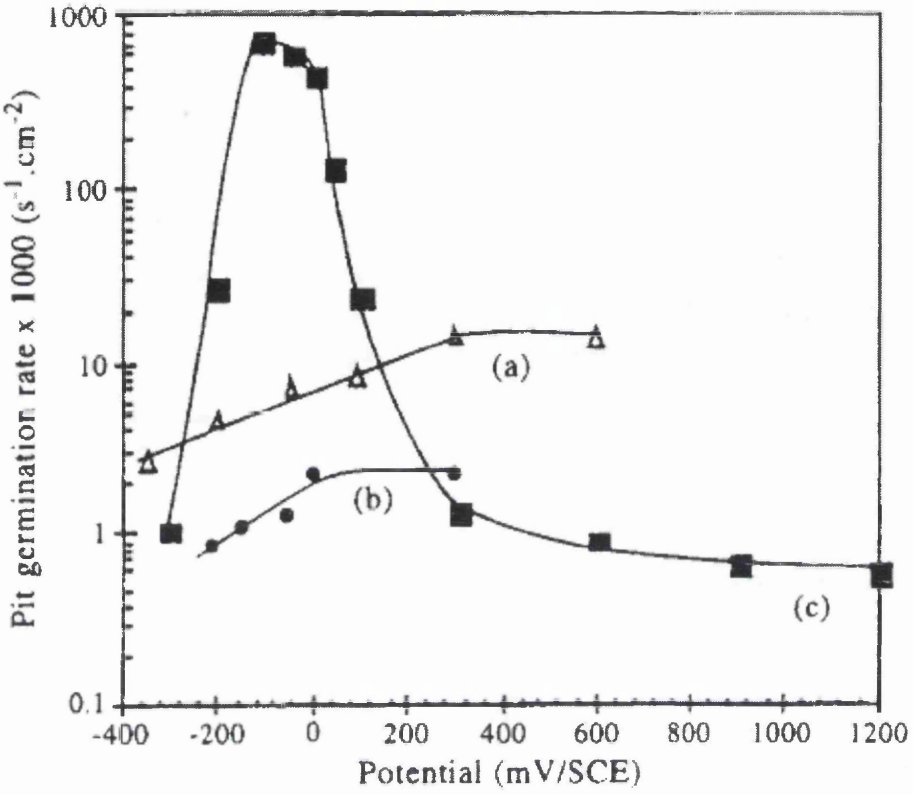

Figure 2.21 Variation of the pit germination rate with the potential. (a) Al 99.99%, 0.05 M Cl^-. (b) 6056, 0.004 M Cl^-. (c) 25 mm 2024, 0.004 M Cl^-.

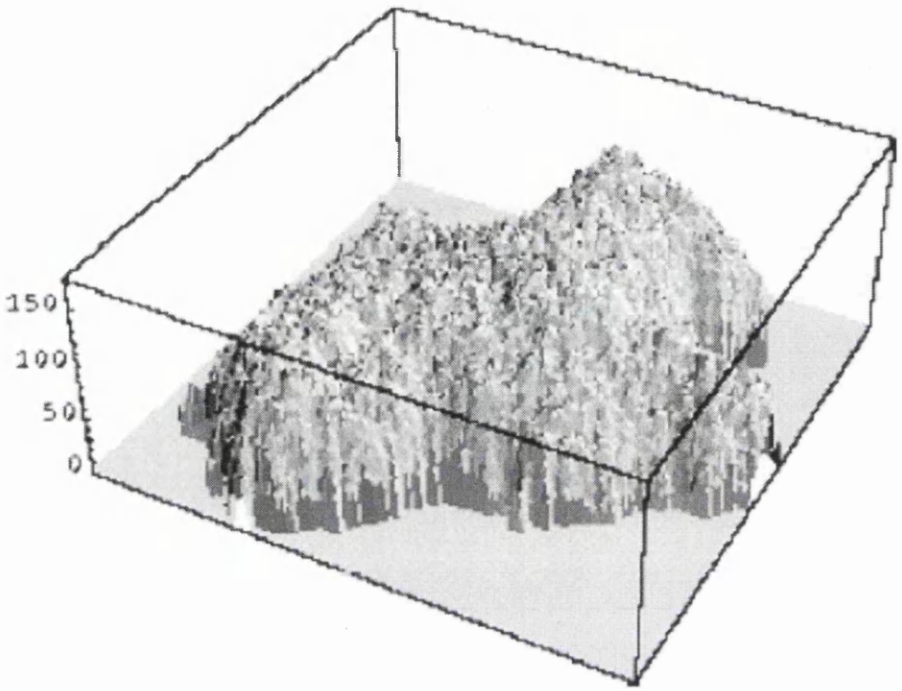

Figure 2.22 A 3-D image of a pit constructed from a 2-D SEM image.

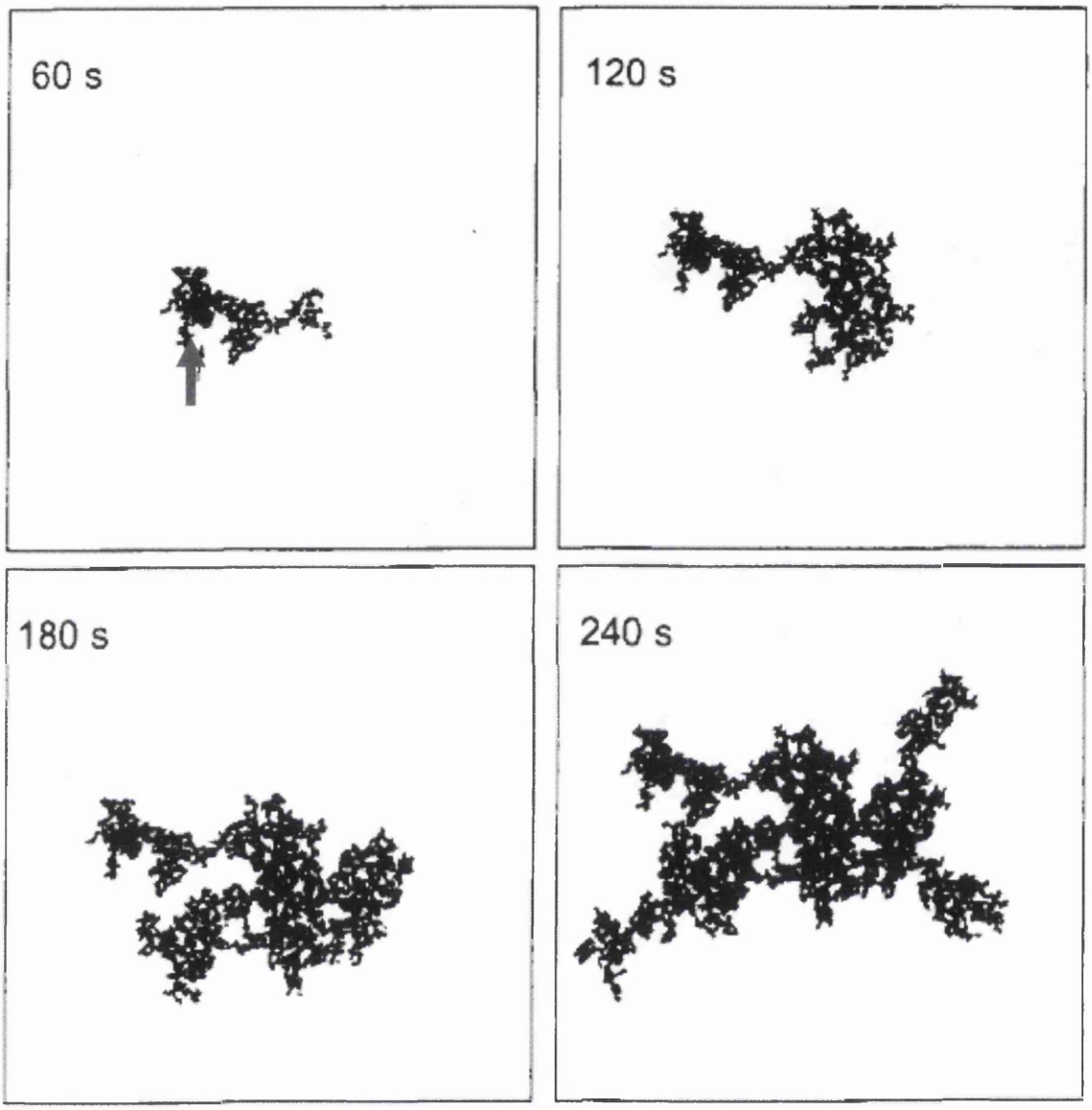

Figure 2.23 Digitised images taken from a fractal-like pit propagating in 10 mM Cl-, 0.2 mM Fe3+ solution at time from 1 – 4 minutes after pit nucleation. Pit growth started by forming a dense spot indicated by the red arrow.

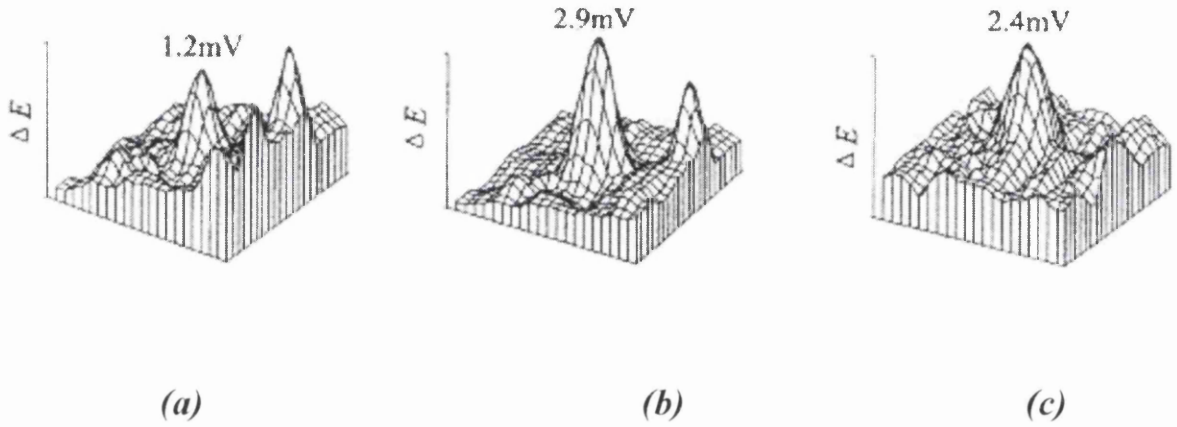

Figure 2.24 SMRE imaging of Al 2024-T3 in 0.01 M NaCl at OCP after immersion for (a) 0 h, (b) 2 h and (c) 2.5 h, scanning area: 2 x 2 mm^2.

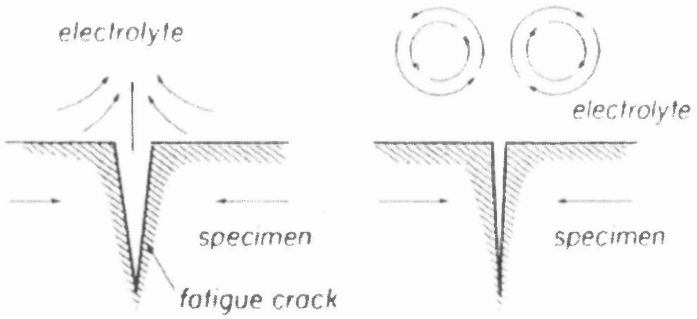

(a)

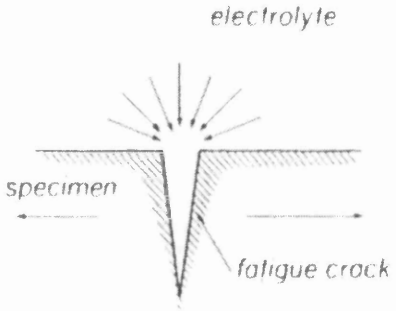

(b)

Figure 2.25 Schematic representation of crack and bulk solution flow during (a) closing portion of the stress cycle for cases where net exit momentum is large and (b) opening portion of the stress cycle.

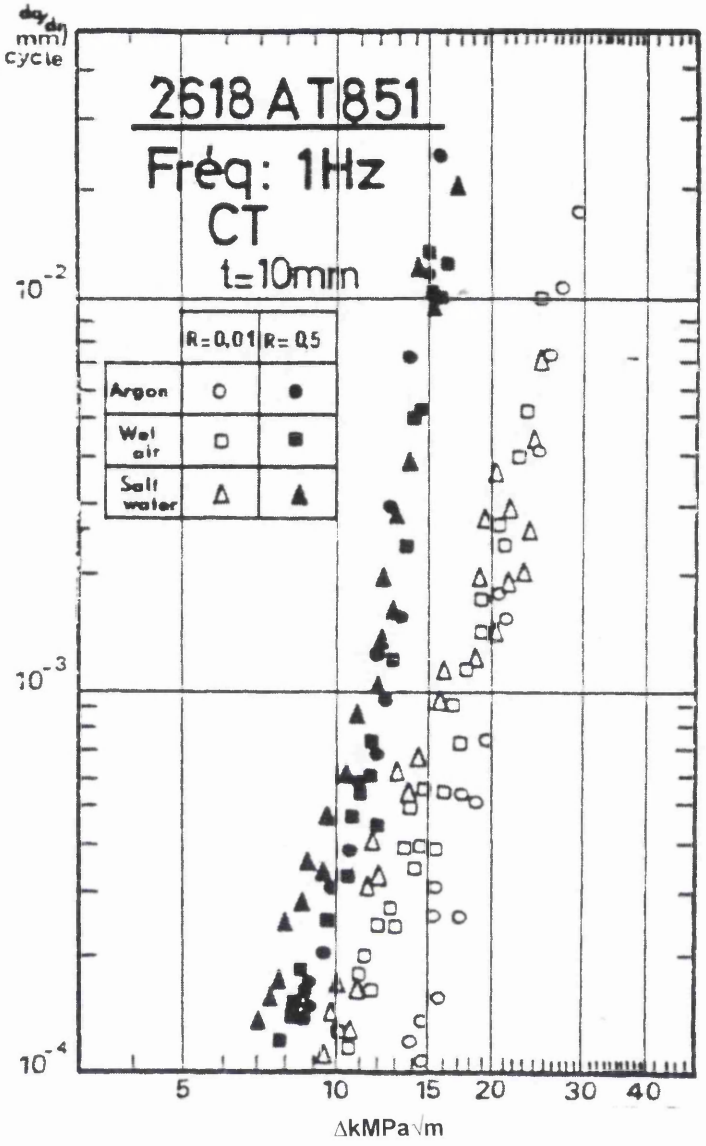

Figure 2.26 The effect of R-ratio and environment on AA 2618 AT851.

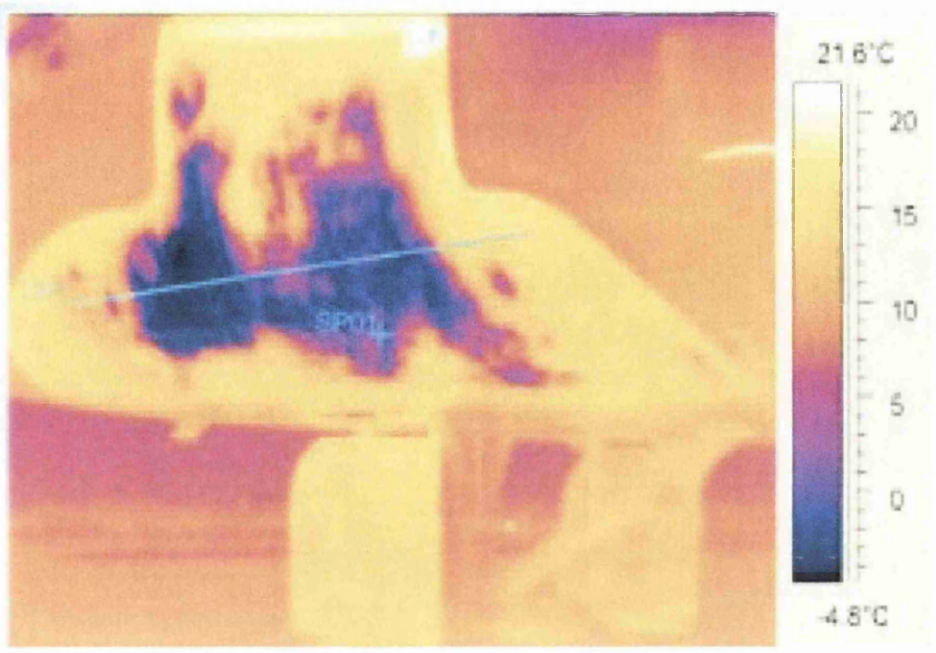

Figure 2.27 Thermal map of an aircraft component created by the NDT technique – thermography.

2.4 FATIGUE OF ALUMINIUM

Fatigue is commonly defined as the property change in a metallic or non metallic material caused as a result of a repeated application of stresses or strains.

2.4.1 Fatigue Crack Initiation in Aluminium

The fatigue life of aluminium alloys is governed primarily by crack initiation, which is accelerated by the presence of microstructural and physical features within the alloy structure. In terms of microstructure, there are various features that can cause fatigue crack initiation in aluminium and its subsequent alloys;

- **Casting Defects:**

Common casting defects in aluminium are microporosity, shrinkage porosity, hydrogen adsorption and oxide inclusions. Casting defects have a detrimental effect on fatigue life by shortening not only fatigue crack propagation but also the initiation period; with an order of magnitude lower for fatigue life compared to defect-free materials. Porosity is deemed most detrimental to fatigue life. The decrease in fatigue life can be directly correlated to the increase in defect size. There exists a critical defect size for fatigue crack initiation, below which fatigue crack initiates from other competing initiators such as slip planes and other microstructural features.

- **Intermetallic Particles:**

The precipitates present in aluminium alloys improve the materials mechanical strength, but on the other hand deteriorate their fatigue properties by localising the plastic deformation, hence reducing the materials ductility. In terms of the 7010-T7651 alloy under investigation for the current research study, these intermetallic phases (Al_7Cu_2Fe and Mg_2Si) on the materials surface are fatigue crack initiators since they are more brittle than the surrounding matrix, causing microcracking under cyclic conditions and particle and matrix delamination. The

intermetallic phases are also preferential sites for corrosive attack, allowing large corrosion pits to be formed which have a significant effect on the materials fatigue life.

Other metallurgical aspects in aluminium that can cause fatigue crack initiation include; solidification rate, eutectic particles and applied heat treatments. The physical features that can cause fatigue crack initiation in aluminium consist of;

- **Machining Defects:**

Machining defects present on material surfaces induce local stress concentrations within the material, hence acting as ideal sites for fatigue cracks to initiate. With this theory in mind stress critical components within structures such as aircraft have a minimum amount of machining as possible so as to decrease the risk of component failure from machining defects. Typical machining defects include coarse surface finishes, grooving caused as a result of blunt tooling equipment and residual stresses imposed as a result of the machining procedure.

2.4.1.1 Fatigue Crack Initiation and Growth at Corrosion Pits: 7xxx Aluminium Alloys.

Corrosion pitting as previously covered in chapter 2.3.2 is a major problem in some aluminium alloys used for aerospace applications. Corrosion pitting can adversely affect aircraft structural integrity since fatigue cracking can nucleate from corrosion pitted areas and grow in a corrosive environment, causing catastrophic failures in stress critical components. Corrosion and particularly pitting, is also an economic inconvenience, given that maintenance and repair operations carried out to remove corrosion damage is often over conservative due to the lack of a reliable methodology to predict future corrosion effects.

A quantitative evaluation technique is therefore needed to permit the continued safe and economical operations of aircraft. A recent review (2001) of the effects of pitting corrosion on the fatigue behaviour of 7075-T6 was carried out by ***Sankaran*** et al [47]. The research was

undertaken as a first step towards developing an integrated experimental and modelling approach to quantitatively account for the effects of prior corrosion on the fatigue behaviour of structural aluminium alloys. The effects of pre-existing localised surface pitting corrosion on the fatigue lives of the 7075-T6 alloy was measured and compared with the predicted lives using measures of corrosion (metrics) obtained from characterisation of the corrosion damage. The study exposed the 7075-T6 to a dilute electrolyte cyclic fog-dry spray test procedure. The dilute nature of the prohesion electrolyte coupled with the alternating spray-dry exposure cycle results in the test providing a more realistic simulation of corrosion attack of systems in-service.

The material utilised for the study consisted of a mixture of recrystallised and un-recrystallised grains, which are typical of wrought high strength aluminium alloys. Second phase particle exist within the material and generally have a size of 20 – 30μm. Rectangular panels of the material were exposed in the prohesion chamber for 24, 48, 96, 192, 384, 768 and 1536 h respectively, fig 2.28 illustrates pits exposed for 24, 96 and 384 hours. Clearly from the images, pits form an irregular shape, with preferential pit growth in the rolling direction of the material. Figure 2.29a details the pit dimensions, figure 2.29b histograms of the pit depths and figure 2.29c the variation of the average pit depth with exposure time. It was shown during the study that the rate of growth of the average pit depth for the material obeyed a power law, with a time exponent close to 1/3 (figure 2.29).

Pit depths of the corroded specimens were recorded and analysed using a metallurgical microscope with a fine focusing wheel, calibrated to 1μm. Depths were measured by firstly focusing on the specimen surface, noting the fine focus wheel position, then focusing on the deepest visible area of the pit and again noting the focus wheel position. Pit depth would then be calculated from the difference in the fine focusing wheel from the two positions.

Fatigue lives for the 7075-T6 alloy were predicted for various depths using AFGROW, a US Air Force computer based lifing package derived from linear elastic fracture mechanics. The software utilises stress intensity factor calculated from particular crack geometry, dimensions and stress condition. The crack growth rate (da/dN) is obtained from the da/dN vs. ΔK curve. The crack growth increment is added to the original crack length and the critical crack size

determined by AFGROW. The modelling of the crack growth behaviour from corrosion pits within this material will be discussed in some depth at a later stage of this literature survey.

Corsetti and ***Duquette*** [48] examined the effect of mean stress and environment on corrosion fatigue behaviour also of 7075-T6 aluminium. Axial fatigue tests were performed in air and in a corrosive 0.5 N NaCl solution.

The authors state that HCF crack propagation in dry air for high strength precipitation hardened aluminium alloys show a significant amount of stage I cracking along (111) crystallographic planes, with the fracture surface resembling "quasi-cleavage". Within an aqueous environment, fatigue life is significantly reduced, with a change in crack propagation plane to on or near (100). Fractography also detailed the occurrence of striations in the fracture surface noticed at high applied stresses and low cyclic frequencies to failure. The striations were either "brittle" in corrosive environments or "ductile" in dry air. Cleavage type cracking along (100) planes were promoted by applying anodic potentials and currents to the material. Cathodic currents reduced crack propagation rates and reverted to a more ductile type of failure. Mechanisms of corrosion fatigue in aqueous environments have been proposed within the study, and include either preferential dissolution of deformation induced anodic sites in active slip bands or adsorption of a damaging species, possibly the cl^- ion at a growing crack tip.

The studies revealed that:-

- Large positive mean stresses reduce fatigue life for constant cyclic stress range, whilst mean stress has no noticeable effects in terms of the number of cycles to crack initiation.
- Smooth surfaced specimens initiated fatigue cracks from pits formed from electropolished sites.
- Stage I mode cracking dominates fracture, with the production of typical river line patterns, a key feature of high strength precipitation hardened aluminium alloys.
- Aqueous NaCl solution decreases fatigue life by the production of severe corrosion pits within the vicinity of the intermetallic particles.
- Hydrogen embrittlement accelerates corrosion fatigue cracking in high strength precipitation hardened aluminium alloys.

Fatigue crack growth from corrosion damage in 7075-T6511 aluminium alloy under aircraft loading conditions was investigated by ***DuQuesnay et al*** [49]. The paper investigates the growth behaviour of fatigue cracks initiated at corrosion pits in laboratory coupons of 7075-T6511 aluminium alloy subjected to a transport aircraft loading spectrum. Corrosion pitting was artificially induced into the flat dogbone specimens by exposing the coupons to EXCO (exfoliation corrosion solution, prepared according to ASTM G34-Standard test method) solution for a period of 6 hours up to 21 days, to produce corrosion damage varying from mild to extremely severe (Pre-test corrosion apparatus and specimen dimensions seen in figure 2.30a,b).

Fatigue testing was carried out on corroded and as-machined coupons, to give a direct comparison on fatigue life knock down of the corroded specimens. Examples of the severity of the corrosion produced via the EXCO solution can be seen in figure 2.31. Testing was performed in laboratory air at room temperature using a closed loop servohydraulic testing machine with computer control at cyclic frequencies of approximately 25 Hz. The loading spectrum was derived from several CC-130 *Hercules* transport aircraft and representing a medium duty usage incorporating a variety of flying missions. The spectrum, measured on the primary structure in the wings of the airframes contains 33,948 cycles representing 125 simulated flying hours (SFH). Testing stresses were scaled linearly to represent those experienced in-service at the root of a rivet hole, or a similar notch with a stress concentration (k_t) of approximately 2.9.

In order to provide data on the knock down effect on fatigue life from corrosion pitting, uncorroded specimens were tested at the exact same conditions. Figure 2.32 details the recorded fatigue lives in SFH hours for corroded and uncorroded specimens. Corrosion pits were measured using an optical microscope at 50x magnification. Pit depths were recorded for all pits within the corroded area, while detailed measurements of the pit initiating the crucial fatigue crack was also undertaken. The technique for measuring pit dimensions is seen in figure 2.33a, b, whilst pit sizes can be seen in figure 2.32.

In conclusion:-

- Fractographic examinations post testing revealed one critical crack in each coupon, although several other cracks were noted on planes adjacent to the plane of final fracture.

Fatigue cracking was also found to initiate on pits that weren't necessarily the largest within the corroded area. These observations are also consistent with other investigators who too viewed similar results with fatigue cracking from artificially controlled pitting corrosion.

- Artificially produced pitting corrosion can give a severe reduction in fatigue life of laboratory prepared specimens, when subjected to transport aircraft spectrum loading in laboratory air.
- Corrosion pit *depth* is considered the important factor affecting the fatigue life of aluminium alloys (Figure 2.34).

The modelling aspect of the paper which precedes the fatigue testing will be reviewed in some depth further on within the literature.

In a similar manner to ***DuQuesnay et al***, ***Medved et al*** [50] studied the corrosion pit size distribution and fatigue lives of Alclad 7475 aluminium alloy. The investigation looked into the distribution of pit depths in a 3.18mm radius edge notch, subjected to natural and artificial corroding environments. The study also evaluated the Equivalent Initial Flaw Size Distributions (EIFSD) from the fatigue life data generated.

The material selected for the investigation was Alclad 7475-T761 aluminium alloy. The Alclad layer consists of a 100μm thick layer of aluminium on one surface of the sheet. Single Edge Notch (SEN) specimens were machined from the sheet, with the long axis of the sample parallel to the rolling direction, hence cracking would occur in the transverse direction, perpendicular to the rolling direction. The specimens were coated in varnish, exposing the semi-circular notch area for corrosion. Samples were corroded via ASTM 94-G85 in acidified salt spray and according to ASTM G50-76 in a natural coastal environment. Figure 2.35 details the corrosion and fatigue test matrix. The salt spray used consisted of 5% NaCl solution acidified to a pH of 3 using glacial acetic acid. Exposure times varied from 8 days up to 91 days.

Variable and constant amplitude fatigue testes were carried out as shown by figure 2.35. The Fighter Aircraft Loading Standard For Fatigue (FALSTAFF) spectrum was used to conduct the variable amplitude testing. Each pass through the spectrum consists of 1.8 x 104 cycles

corresponding to 200 flights or one year's service for a fighter aircraft. Maximum remote stresses of 262 MPa were set in FALSTAFF. Pit morphologies and sizes were determined using high powered Scanning Electron Microscopy. Crack length measurements under constant amplitude loading were performed using the replica technique for short cracks and the DC potential drop method for longer cracks. The secant method was utilised to calculate crack growth rates using the replicas technique, while the incremental polynomial method (7 point) was implemented for the DCPD data. Cracks were assumed to have either a semi-elliptical form for growth from pits from within the notch bore, or a quarter elliptical form for cracks initiating at the corners of the notched area.

In terms of corrosion pit development, all specimens were seen to loose material from the exterior layer due to pitting corrosion, although it was identified that specimens subjected to the salt spray environment suffered significantly greater material loss. In all cases, material was not removed from the underlying 7475-T671 aluminium, even in the areas of severe degradation, pitting did not penetrate the primary material. Pitting was noticed to reach the interface area between the clad layer and the parent material, but was found to spread laterally across the clad layer at depths of 100μm, as depicted by figure 2.36. This occurrence often led to the large scale removal of the clad layer, and incidentally had a minor role in the fatigue failure process. Pits which initiated failure cracks were generally noted to be in the notched area of the specimens, and were generally circular or elliptical in their form, with a sharp apex. They were often discovered in clusters which regularly coalesced (Figure 2.37 a, b).

Fractography undertaken using SEM investigative techniques revealed that crack initiating pits had an irregular and complex morphology. They can be described as needle like pits with large depth to width aspect ratios, as illustrated by figure 2.38 a, b. Pits as small as 20 – 30 μm were noticed to initiate fatigue cracking up to maximum values of 300μm. Similarities therefore can be deduced from these results and the results produced by DuQuesnay et al, which are; that the largest pit within the sample does not necessarily initiate fatigue cracking, pit location therefore has a more dominant emphasis on fatigue life. Flat bottomed pits as discussed earlier, did not initiate fatigue cracking as a result of their 'bluntness', instead smaller pits located in the regions of high stress concentration seemed to initiate the majority of fatigue cracks.

In conclusion:-

- Exposure of the material to 6-8 days of salt spray produced a wide distribution of pit sizes, up to maximum value of 300μm deep on sample edges. The exposure period was equivalent in pit size to 91 days coastal exposure. Pits were noticed to be deeper rather than wider, with aspect ratios of up to 4.
- Post corrosion fatigue lives were reduced by 40 – 50% from those of pristine samples. Fatigue cracks always initiated from corrosion and pits; in many cases the largest pits were not the most potent crack initiators.
- Fatigue crack growth rates of micro and macro cracks were identical to those measured in uncorroded samples. Progress of the fatigue cracks was complicated by means of multiple crack initiation and crack linkage.

In a recent study by ***Wang et al*** [51], the effect of pre existing corrosion pits on the fatigue behaviour of 7075-T6 aluminium alloy was investigated. Piezoelectric accelerated fatigue testing at a frequency of 19.5 kHz and load ratio of R= -1 was carried out to explore very long life range and near threshold regime. Most of the fatigue data produced to date on aluminium alloys is limited to lives of up to 10^7 cycles. Many industries such as aerospace, automotive, railway and offshore structures require design lifetimes of components exceeding 10^9 cycles, therefore this study aimed to provide high cycle fatigue data for aluminium alloys.

The corrosion pitting was produced by prior immersion in 3.5 wt% NaCl solution for 1, 4 and 7 days. Specimens containing single edge notches of radius 0.5 mm and k_t factor of 3.05 were designed to resonate longitudinally at 19.5 kHz. Specimens were mechanically polished to leave a pristine finish. Pits grown on the surface of the material after various exposure times can be seen in figure 2.39. From figure 2.39, it is clear that as exposure time increases, pit size generally increases. Maximum depths attained after 1, 4 and 7 days exposure are approximately 30, 50 and 60 μm respectively.

Figures 2.40 a, b are SEM images of fatigue crack growth fracture surfaces of a 7 day exposed specimen. A clear dissimilarity is seen between the fracture mode near threshold and

fracture mode at high crack growth rates. Figure 2.40 c are optical micrographs of crack growth near threshold conditions.

Conclusions drawn from the investigation revealed that fatigue properties are significantly affected by pre-existing corrosion pits, especially crack initiation in the very long life range. Exposure time also had an effect on fatigue properties, as pit size increased; fatigue life was seen to decrease. Fatigue crack growth rates were also affected by pre-existing corrosion pits. Crack growth rates increased with increasing surface corrosion pitting due to the corrosion pits acting as stress concentrators.

In a paper by NASA, ***Smith et al*** [52] looked at the simulation of fatigue crack initiation at corrosion pits with EDM notches. Uniaxial fatigue tests were conducted to compare the fatigue life of laboratory produced corrosion pits, similar to those observed in the Orbiter (shuttle vehicle) Main Landing Gear (MLG) wheel bolt-hole, and an Electro-Discharged Machined (EDM) flaw.

Visual inspection of the forged aluminium alloy (AA 7050) used for the MLG of an Orbiter during routine maintenance, revealed small regions of localised corrosion pitting in the tie-bolt holes, as shown by figure 2.41 a, b. Pitting within the component in question revealed pits of average depth of 0.5 mm, although certain pits achieved depths of 1.0 mm. In-service removal of corrosion in the aerospace industry is conducted by grinding, however, if corrosion damage is still present after the assembly process then localised stress at pits increases, hence resulting in possible reduction of fatigue strength of the component.

To establish the overall effect of pitting on shuttle wheel (stress critical component) fatigue life, a series of dynamometer fatigue tests were undertaken. MLG wheels with the "worst case" corrosion damage from service were very difficult to obtain, therefore flaws similar to those seen in-service were produced within test MLG wheels. Corrosion pit configuration within aluminium alloys is associated with several microstructural features; constituent particles, grain boundaries and precipitates. Corrosion pit location and morphology are also difficult to control, hence the wide range of pitting found within components in-service and under laboratory

conditions. Consequently, pitting for the fatigue testing evaluation were manufactured using EDM notches that simulated the local stress states produced by corrosion pitting. However the approach raises the question to whether the fatigue behaviour of MLG wheels containing EDM notches corresponds to that of in-service corrosion, therefore this investigation was commissioned to answer this problem.

Test specimens containing an EDM notch or corrosion pits were examined under fatigue loading at stress levels representative of the bolt-hole region in-service, to determine the fatigue life. Specimens were machined in two grain orientations (figure 2.42) to simulate all possible pit morphologies and sizes. The specimens were produced so that the loading axis was parallel to the rolling direction of the material. The defect (EDM, corrosion) was positioned in the centre of the gage section of the specimen. Due to the grain structure in rolled aluminium plate, corrosion pitting produced in different orientations, namely L-S and L-T, range widely in size and shape. The L-S orientation exposes fewer grain boundaries, yielding wide but shallow pits that are virtually hemispherical in shape (low stress concentration factor). On the other hand, the L-T orientation exposes more grain boundaries and constituent intermetallic particles, leading to irregular and elongated pit morphologies (high stress concentration factor).

Corrosion pitting was produced in the selective area by immersion in an aqueous solution containing 3-g/L of NaCl and 0.11 N nitric acid (HNO_3). An anodic current was applied to corrode the specimens, to produce pit depths in the range 0.5 mm to 1.5 mm, over exposure times of 24 – 96 hours. The EDM notches used were of a semi-circular in form, with a height of 0.254 mm, a depth (a) and a surface width (2c), as illustrated by figure 2.43. Specimens were fatigue tested using a closed loop servo-hydraulic test machine at a load ratio of R = 0.05. Maximum remote stress of 310 MPa (~70% of yield stress) was used to simulate in-service stress conditions of the MLG wheel bolt-hole. Testing was undertaken at room temperature laboratory air and at a cyclic frequency of 4 Hz. Fatigue tests were periodically interrupted and held at mean load conditions, while the visual surface crack length (2c) was measured.

The data received is plotted in various forms. Figure 2.44 a, b represents surface crack length (2c) versus load cycle (N) for the two tested orientations. Large variations in the number of cycles to initiate a visually detectable surface fatigue crack N_i were found, as illustrated by

tables 2.6 and 2.7. Failure was caused predominantly by pre-introduced flaws (EDM notch, pitting) initiating fatigue cracking. Post fracture examples of EDM notches can be seen in figure 2.45. Clearly illustrated by the SEM images is the initiation of fatigue cracking at the EDM notch. Corrosion pits shown in figures 2.46 and 2.47, represent those found in the L-S and L-T orientations, respectively.

Pits within the L-S orientation were hemispherical in shape, while pitting in the L-T orientation were deeper but narrower. Multiple pit coalescence also occurred within the L-T orientation yielding a greater aspect ratio (depth/width ratio) than pits in the L-S orientation. The pit morphology within the L-T orientation is a result of the greater number of grain boundaries available for pitting. Fatigue cracking occurred in both orientations by multiple initiations along the boundaries of corrosion pits. Plotting initial flaw depth (a_i) versus cycles to failure (N_f) for both orientations revealed that the fatigue life obtained from EDM notches and pitting were similar (figure 2.48). The plot also indicates that at high local stress conditions, fatigue behaviour is in principal insensitive to significant differences in flaw morphology. At the maximum applied remote stress (310 MPa), local stress at the flaw resulted in yielding at the root, hence minimising the initiation stage of crack growth. Therefore any geometric differences between the EDM notches and corrosion pits were declared a second order effect.

Another paper produced by NASA, written by ***Newman et al*** [53], looked at the failure analysis of a U.S Coast Guard HH-60 "Jayhawk" helicopter external fuel-tank pylon. Although not as relative as the previous paper, the failure investigation examined the effect of corrosion pitting as fatigue crack initiation sites within a fastener hole in an external helicopter fuel-tank pylon. Fastener holes can create a crevice-like environment that entraps water resulting in a corrosive environment where pitting is possible. Pitting damage therefore can be very difficult to detect in areas such as fastener holes, the damage is very localised and only initially affects a small amount of material.

An eight inch (0.2 m) crack was discovered within the fuel-tank pylon. The external tanks are mainly used to extend the range of operation times of U.S Coast Guard (USCG) helicopters

and are fastened to pylons, which are attached to the helicopter fuselage, as shown by figure 2.49. The fuel tanks are manufactured from 7075 aluminium alloy forgings. Helicopter components are known to experience fatigue loading alongside corrosive marine environments or a combination of both, leading to brittle crack growth. Following the crack detection, destructive examinations were conducted to determine the cause of the cracking. A photograph of the cracked pylon can be seen in figure 2.50. The loads applied to the pylon were in the vertical downward direction, thus creating high bending stresses in the corner area as illustrated by the red circle in figure 2.4-23. Cracking initiated at fastener holes in the in the upper flange (regions of high stress) and propagated vertically downward. The crack finally arrested as it grew towards a vertical stiffener, a feature of the component designed to introduce extra stiffness and stability alongside crack arresting properties. Figure 2.51 a, b and c illustrates the cracking emanating from one fastener hole (4.8 mm diameter) and bisecting another.

To perform detailed examination of the crack surface, the pylon was carefully broken by applying a load to its end, preserving the incurred pre-cracking for examination purposes. The fractured pylon and its surface can be seen in figure 2.52. Dark coloured regions found on the fracture surface of the pylon, near the fastener holes where the crack appeared to initiate were corrosion products (most likely oxide debris), produced as a result of fatigue crack growth in an aggressive environment. In order to examine the fracture surface in detail, the pylon was sectioned and chemically cleaned using 50% nitric acid (HNO_3). SEM examination of the fracture surface identified failure as a result of fatigue loading. No deformation markings were noticed along the crack path, although some were present near the initiation area (fastener hole). Detailed images of the crack initiation sites can be viewed in figure 2.53a - d and 2.54a - c. The striations seen in figure 2.55d are equally spaced and are typical examples of fatigue loading. Assuming each striation is created by a single load cycle, by utilising laboratory generated data on aluminium 7075; values of ΔK for the material correspond to 15 MPa$\sqrt{m}$ and 20 MPa$\sqrt{m}$.

Conclusions from the failure analysis by Newman et al have an influential bearing on the current research programme. Fastener hole testing has been outlined for the PhD programme; hence, the paper reviewed gives a worthwhile insight into fracture mechanisms and corrosion pitting understanding.

- A fastener hole within the pylon fuel-tank structure of a USCG helicopter provided a crevice like environment where entrapped water formed a highly corrosive environment, leading to the formation of corrosion pitting.
- Large localised bending stresses within the fastener hole region coupled with the presence of corrosion pitting, initiated fatigue cracking within the fastener hole.
- Striations on the fracture surface indicated that the failure mode was attributed to fatigue loading. Corrosion products and debris scattered near the initiation area suggested that the fatigue crack grew within a corrosive environment. The combination of both fatigue loading and a corrosive environment intensifies cracking.
- Cracks contained within 7000 series aluminium alloys under conditions of high humidity (90%) will continue to grow under low applied loads.
- Vertical stiffener within the component diverted the fatigue crack, effectively blunting and lowering the crack tip driving force, and arresting the crack at 80% of the component width.

2.4.1.2 Fatigue Crack Initiation and Growth at Corrosion Pits: 2xxx Aluminium Alloys.

Several authors have reviewed the effects of pitting corrosion on the fatigue life of other common aluminium aerospace alloys such as 2024-T3 (susceptibility of this 2xxx series alloy to pitting has been discussed in section 2.3). Various fatigue testing techniques of pitted specimens are discussed below.

Chen et al [54] investigated the nucleation of fatigue cracking from corrosion pits at room temperature. The investigation entitled Transition from pitting to fatigue crack growth-modelling of corrosion fatigue crack nucleation detailed the fatigue response of 2024-T3, tested in 0.5M NaCl solution at various frequencies (0.1 – 20Hz) at a load ratio of R = 0.1. A pre corroded specimen was also evaluated for comparison purposes. Pit growth within the specimen hole

evolved with the occurrence of pit coalescence of individual, particle nucleated, pits, a development also observed by Sankaran et al in the 7075-T6 alloy.

The study showed that cracks typically nucleated from the larger pits within the specimens, and occurred near the areas of maximum stress. The size of the pit that nucleated the fatigue crack was also found to be a function of stress level and the load frequency. The authors in their results and discussion suggest a concept whereby a transition period occurs from pitting into fatigue cracking. This arises as the fatigue crack growth rates exceed that of the pit growth rate. To quantify pitting induced corrosion fatigue, two models were proposed to characterise the corrosion fatigue crack nucleation process, a critical pit size model and a pitting/cracking competition model, the details of which will be discussed in chapter 2.5.

The specific effect of pitting corrosion on fatigue crack initiation and life was examined in some detail by ***Rokhlin et al*** [55]. Artificial pits of varying depths were used to study their influence on fatigue crack initiation and growth again in Al 2024-T3. Simple models were developed to analyze the results received. The modelling discussed within the study will be reviewed in a specifically titled chapter on modelling further on in this literature review. The study was carried out to examine the effect of reduced fatigue life on an aircrafts total flying hours. This reduced life is attributed mainly to pitting corrosion. Pitting corrosion is extensively quoted as being one of the major mechanisms initiating widespread fatigue cracking and eventual component failure. Pitting corrosion within hidden structures/components of aircraft can be considered extremely critical as NDT methods are the only means of detection.

The 2024-T3 aluminium alloy was chosen for the study as a model material system. Dogbone test specimens were machined parallel to the rolling direction of the original plate material. Artificial pits were placed in the centre of the specimens using a spark erosion technique, which produced pit depths ranging from 30μm up to through thickness (1.6mm). Pit metrics were measured using optical and scanning microscope techniques. Fatigue testing was undertaken at room temperature at frequencies of 15 Hz and 50 Hz at a load ratio of 0.2 (selected to avoid compressive stresses). Crack initiation and propagation tests were completed using

erosion spark pits of 240μm diameter and 170μm depth. Results achieved by the authors are discussed in some depth within the modelling chapter of the literature review.

A baseline S-N curve was plotted to determine the fatigue endurance limit and to examine possible frequency effects. The curve outlined no discrepancies between tests at 15 and 50 Hz (at the load ratio of 0.2). The stress range $\Delta\sigma$ was determined to be 206 MPa with $\sigma_{max} = 0.47\sigma_{UTS}$, which corresponds to the number of cycles to failure being higher than 1×10^6 for unpitted samples. 15 Hz was chosen as the pitting testing frequency.

Test results revealed that cracking is initiated from the largest pits on the specimens, assuming homogenous stress distribution in an unpitted sample. SEM fractographs of the fatigue samples containing artificial pits are shown clearly in figure 2.56. Pit morphology is seen to dominate the fatigue crack initiation area. Cracks tended to initiate at corners or edges of corrosion pits, where the stress concentration factor is greater, often forming two corner cracks. These corner cracks grow independently of each other at both sides of the pit, with a quarter elliptical form, until their depth reaches that of the pit, as illustrated by figure 2.4-29a. Crack growth continues beyond pit size and forms a semi-elliptical crack whose initial aspect ratio (a/2c) is dependant on the ratio of depth to diameter of the initiating pit. This phase of crack growth is commonly known as first stage of fatigue life, with the remaining period being the second stage. For the deep pit (d>2R) the initial crack of the second stage is almost semicircular (a/2c = 0.5). For the shallow pit (d<2R) the initial crack has a long elliptical shape whose aspect ratio is much smaller than 0.5. First it grows to a semicircular shape as illustrated in figure 2.4-29b and c. The entire fatigue life therefore can be divided into two main stages, each stage with its particular geometry. Modelling of fatigue crack growth was also conducted in the study, in the first and second stage of growth, applying corner crack and equivalent through thickness crack models. This is detailed in chapter 2.5.

The effect of pitting corrosion on fatigue life of 2024-T3 has been reviewed in some depth by ***Dolley et al*** [56]. Similarly to the current research programme, holed and semi circular edge notched specimens were utilised to determine fatigue lives for pre-corroded material.

Specimens were masked exposing only the required area and pre-corroded using 0.5 M NaCl solution for periods ranging from 48h – 384h. It was found that fatigue lives were reduced by an order of magnitude for the 384h specimens as compared to pristine, corrosion free specimens. Pit sizes of crack initiators were found to vary from 20μm up to 70μm.

In terms of pit metrics, the study revealed that pit depths significantly varied for the same exposure time, contradicting the general tendency of pit metrics to increase with exposure time, therefore an accurate estimation of fatigue life based on exposure time is not appropriate. To best correlate the data received, pit depth was plotted against fatigue life (figure 2.57). Fatigue life reduced by an order of magnitude as a result of nucleating pit depths of 1μm to one of 30 – 50μm. Figure 2.58 clearly illustrates morphology and metrics of a fatigue crack nucleating pit. The image also details the pit dimensions used for modelling. The authors also showed that there was a relationship between test frequency and corrosion pit size that indirectly affected fatigue life as depicted by figure 2.59.

Analysis illustrated that the reduction in fatigue life depended upon the pre-corrosion time and in turn the initial pit size. Additionally, increasing cyclic load frequency, increased the fatigue life at a given stress level during concurrent corrosion and fatigue because of early nucleation from smaller sized pits (as crack nucleation predominantly occurs from the high number of cycles rather than from the effect of pre-corrosion). It was concluded, as longer pre-corrosion times led to deeper initial pits, that the fatigue life was reduced significantly as compared to the fatigue life of the uncorroded material. Fatigue lives from initial pit sizes for the material were estimated using AFGROW, similarly to the study conducted by Sankaran et al.

2.4.2 Effect of Environment on Fatigue Crack Growth.

Fatigue cracks growing in environments other than laboratory air can vary in growth rate due to the aggressive environments in which they are growing. Environmental fatigue plays a major role in the degradation and failure of components operating within violent environments. Saline environments are seen to be extremely hostile and can pose major problems in lifing aircraft components. High humidity conditions are also seen to cause increases in fatigue crack

growth rates, and predominantly cause premature component failure. The review of the available literature below details the work undertaken by ***Ruiz et al*** [57]. The author is one of the major researchers in the field of environmental fatigue, with a series of papers representing their work.

In a study entitled Environmental Fatigue in a 7000 Series Aluminium Alloy, the effect of water vapour pressure on fatigue crack growth in 7017-T651 was analysed. Fatigue tests were performed in gaseous environments under various water vapour concentrations to produce results which could be correlated with morphology of the fracture surfaces. Thorough examinations of the fatigue fracture surface under environmental conditions were made to distinguish possible variability. A hydrogen embrittlement hypothesis model was established to explain the crack growth response at the lower water vapour pressures (between 1 – 5 Pa). Figure 2.60 shows crack growth rates under various water pressures.

In conclusion, the study revealed that the water vapour contained in the aggressive environment was responsible for the embrittlement of the aluminium alloy. Crack growth rates increased with increasing water vapour pressure and fracture surfaces revealed correlation with macroscopic fatigue crack growth rates.

Table 2.6 Summary of flaw characteristics and fatigue data for L-S specimens.

specimen	flaw type	a_i (mm)	$2c_i$ (mm)	N_f	N_i
LS-N-1	EDM notch	1.02	2.37	10,327	1,848
LS-N-2	EDM notch	0.84	2.32	11,349	2,011
LS-N-3	EDM notch	0.89	2.32	10,502	3,509
LS-N-4	EDM notch	0.52	1.43	16,946	5,014
LS-N-5	EDM notch	0.68	1.49	13,835	3,390
LS-N-6	EDM notch	1.47	3.17	7,881	1,005
LS-P-1	Corrosion pit	0.85	2.63	19,698	10,010
LS-P-2	Corrosion pit	1.24	2.39	10,852	3,504
LS-P-3	Corrosion pit	0.68	2.64	18,761	6,206
LS-P-4	Corrosion pit	0.29	1.29	30,472	20,009
LS-P-5	Corrosion pit	0.91	2.59	10,383	2,009

Table 2.7 Summary of flaw characteristics and fatigue data for L-T specimens.

specimen	flaw type	a_i (mm)	$2c_i$ (mm)	N_f	N_i
LT-N-1	EDM notch	0.51	1.15	17,627	6,005
LT-N-2	EDM notch	0.79	1.72	12,853	4,523
LT-N-3	EDM notch	0.83	1.71	12,343	2,513
LT-N-4	EDM notch	0.96	1.95	12,021	2,516
LT-N-5	EDM notch	1.09	2.31	11,366	3,513
LT-N-6	EDM notch	1.31	2.87	9,352	2,011
LT-N-7	EDM notch	1.59	3.40	7,192	1,524
LT-P-1	Corrosion pit	0.51	1.14	30,861	24,024
LT-P-2	Corrosion pit	0.49	0.76	16,425	5,002
LT-P-3	Corrosion pit	0.21	1.27	32,490	19,024
LT-P-4	Corrosion pit	0.44	1.62	24,282	18,017
LT-P-5	Corrosion pit	1.51	2.29	10,984	7,812

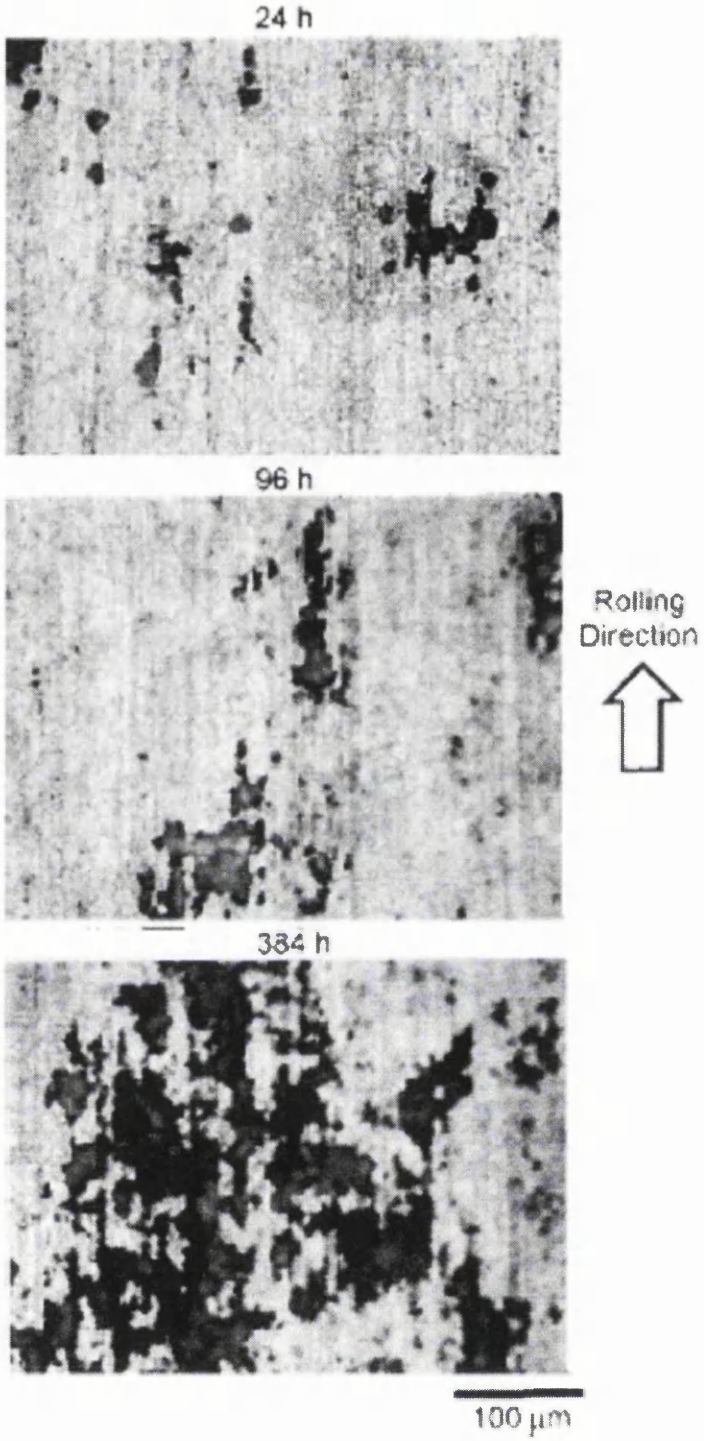

Figure 2.28 Typical pit appearance on the surface of 7075-T6 exposed to a prohesion spray.

xposure time (h)	Maximum length	Maximum width	Maximum depth	Average length	Average width	Average depth
4	240	160	36	36.2	19.1	9.3
8	500	200	35	115.0	61.4	12.1
6	300	200	29	107.0	64.3	13.9
92	400	300	35	150.0	91.1	18.5
84	1300	1400	55	238.0	187.0	25.4
68	600	600	37	163.0	140.3	23.5
536	1300	1000	83	426.0	399.0	50.5

(a)

(b)

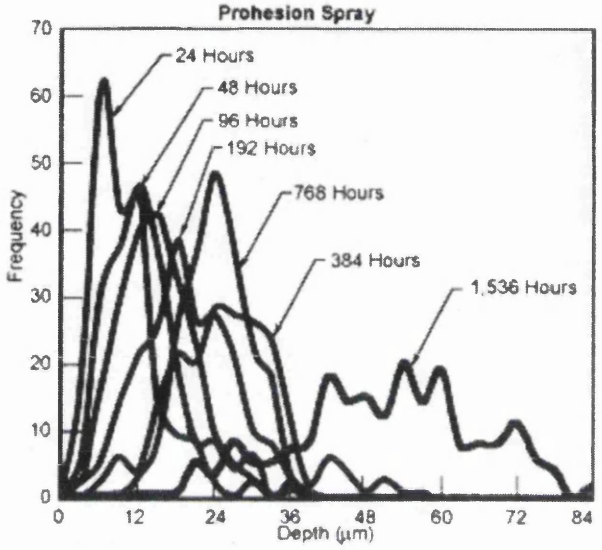

(c)

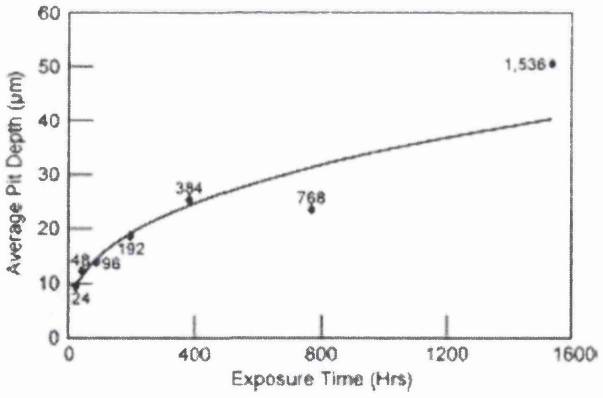

Figure 2.29 (a) Pit dimensions (μm) of 7075-T6 sheet exposed to prohesion spray, (b) Histograms of pit depth for 7075-T6 resulting from exposure to prohesion spray, (c) Effect of prohesion exposure time on average pit depth.

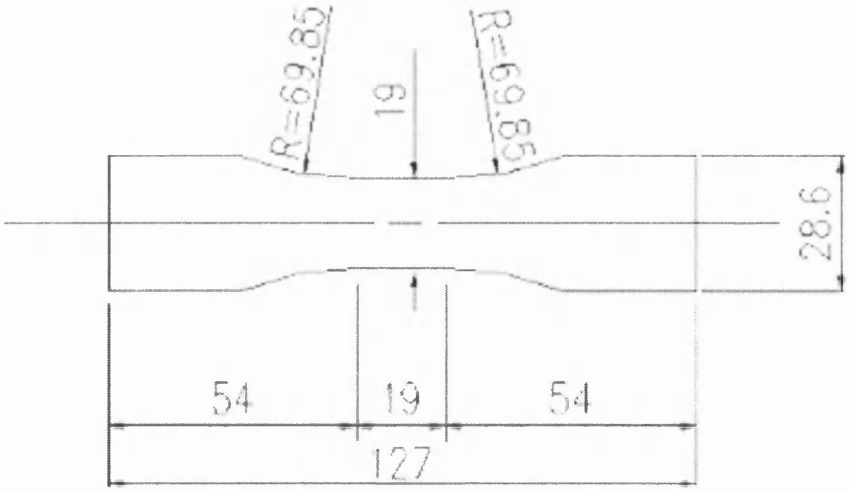

(a)

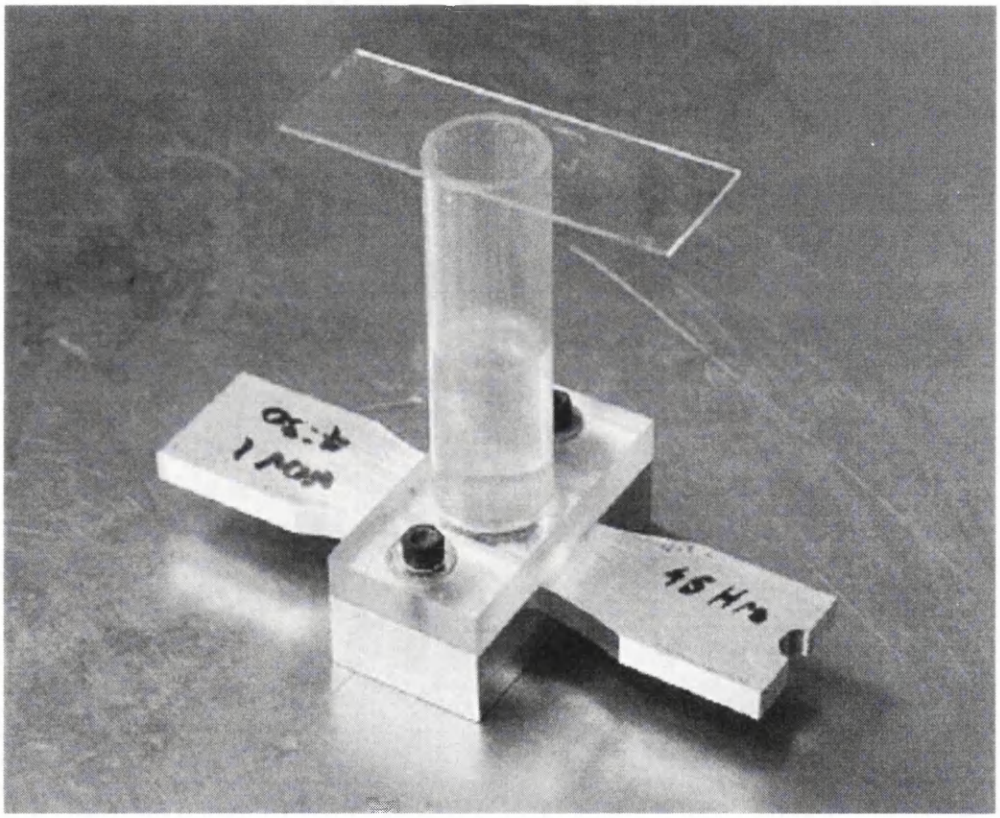

(b)

Figure 2.30 (a) Fatigue specimen details and (b) Apparatus for producing artificial corrosion damage in the test coupons.

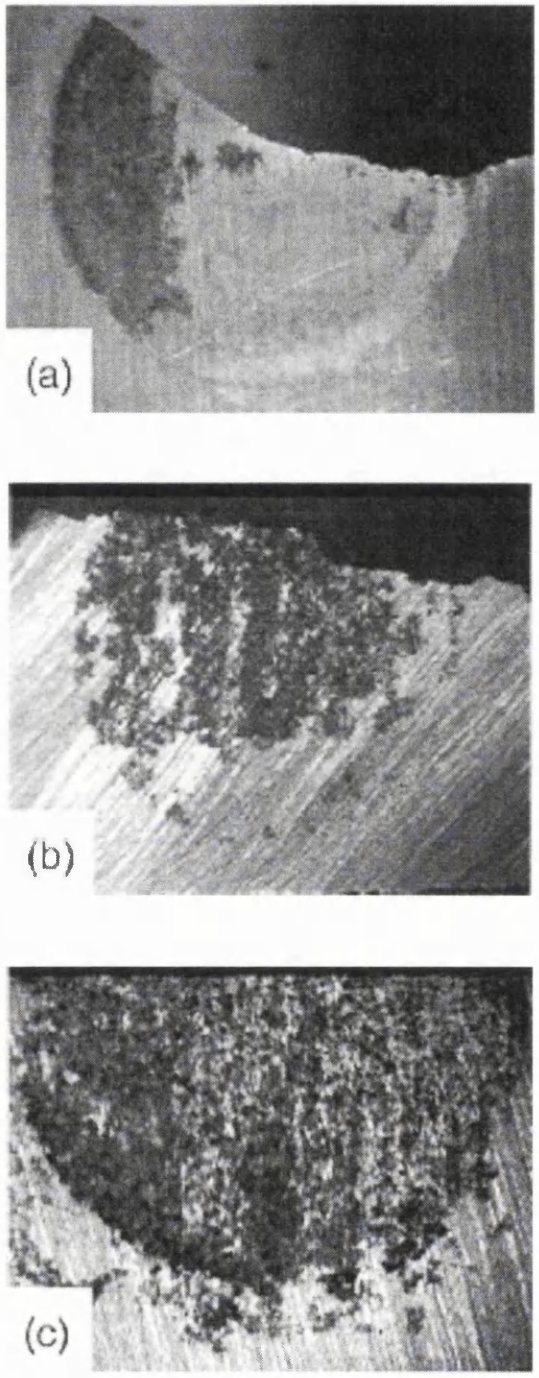

Figure 2.31 Corrosion damage in fatigue coupons using EXCO solution after (a) 12 hours (mild), (b) 6 days (medium) and, (c) 12 days exposure (severe).

EXCO exposure time	Initiating pit depth[a], a (mm)	Initiating pit width, $2c$ (mm)	Maximum pit depth (mm)	Fatigue life SFH (h)
Uncorroded	–	–	–	75,000 (unbroken)
6 h	0.115 ± 0.007	1.206	0.202	21,698
7 h	0.155 ± 0.017	1.290	0.200	20,580
12 h	0.146 ± 0.002	1.044	0.158	22,461
23 h	0.275 ± 0.015	2.579	0.275	10,198
24 h	0.206 ± 0.022	1.246	0.240	14,080
33 h	0.304 ± 0.014	2.190	0.304	11,955
2 days	0.185 ± 0.014	1.488	0.185	20,955
2 days[b]	0.238 ± 0.032	1.880	0.238	18,450
3 days	0.295 ± 0.017	1.706	0.295	10,152
4 days	0.339 ± 0.014	3.571	0.427	8705
5 days	0.186 ± 0.015	0.972	0.268	13,955
6 days	0.397 ± 0.021	3.175	0.397	8938
10 days	0.225 ± 0.049	2.429	0.225	13,868
11 days	0.204 ± 0.024	0.837	0.245	17,185
21 days	0.737 ± 0.017	3.960	0.737	5580

[a] Average ±1 standard deviation for 3–4 measurements.
[b] Surface crack length monitored with replicas.

Figure 2.32 Corrosion pit size and fatigue life measurement for the range of corrosion periods.

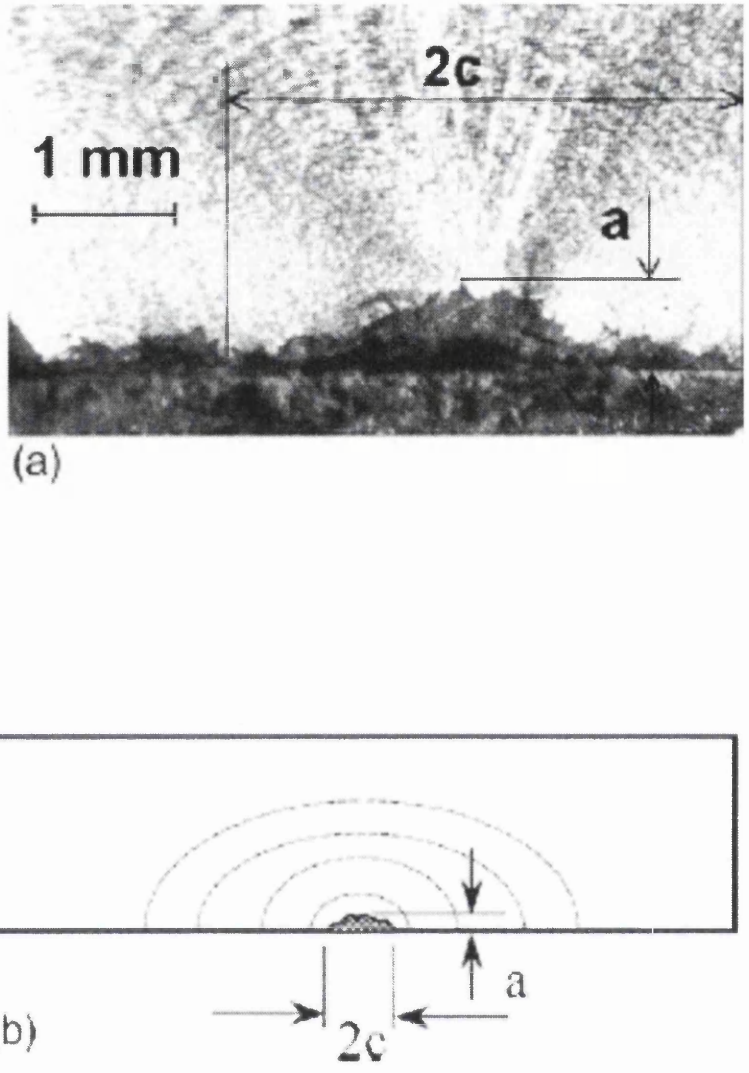

Figure 2.33 Typical fracture surface of a pre-corroded coupon (a) fractograph illustrating the fatigue crack initiating pit and typical fatigue crack growth marking, (b) a schematic representation of pit size and crack front development.

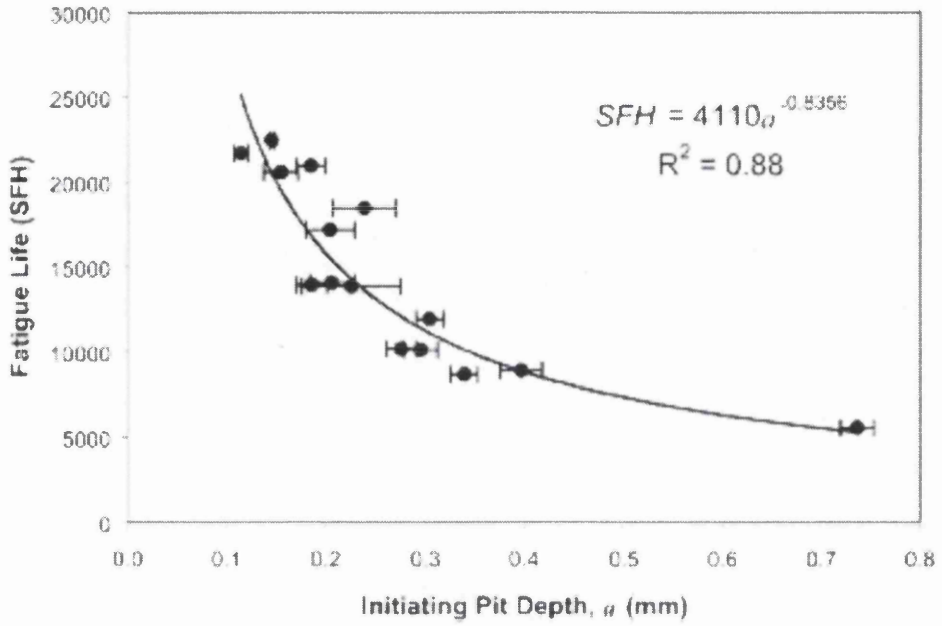

Figure 2.34 Effect of corrosion pit depth on the observed fatigue life in SFH.

Specimen preparation	Number of tests	Load spectrum, σ_{max}(MPa), R, f (Hz)
8 d, ASTM 94-G85	20	Constant amplitude, peak global stress 100 MPa, R = 0.1 at 10 Hz
6 d, ASTM 94-G85	10	Variable amplitude (FALSTAFF), peak stress 262 MPa at 15Hz
91 d ASTM G50-76	10	Variable amplitude (FALSTAFF), peak global stress 262 MPa at 15 Hz
Uncorroded	2	Constant amplitude global peak stress 100 MPa
Uncorroded	2	Variable amplitude (FALSTAFF) peak global stress 262 MPa

Figure 2.35 Fatigue and corrosion test matrix.

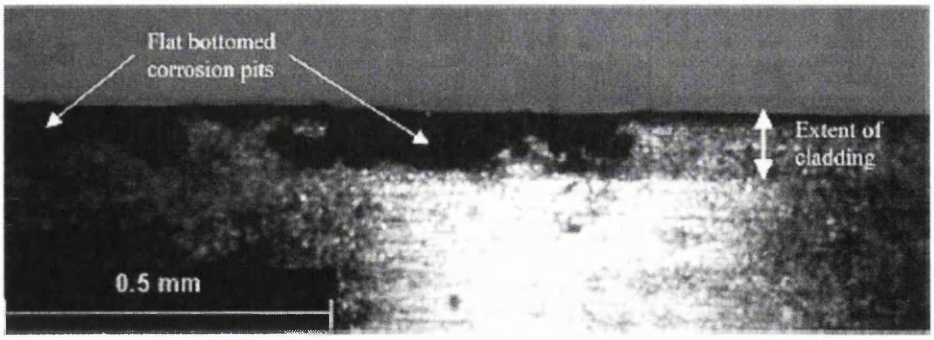

Figure 2.36 Pitting damage evident in the clad layer of 7475-T671 sheet material after 6 days salt spray showing flat bottomed pit development.

(a)

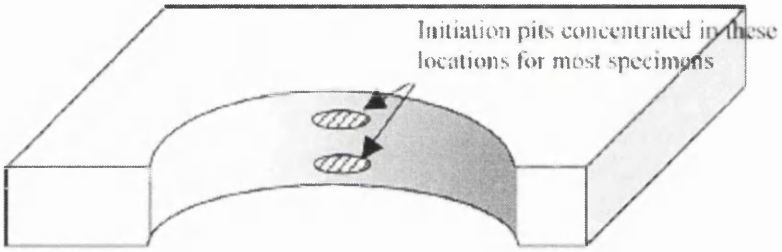

(b)

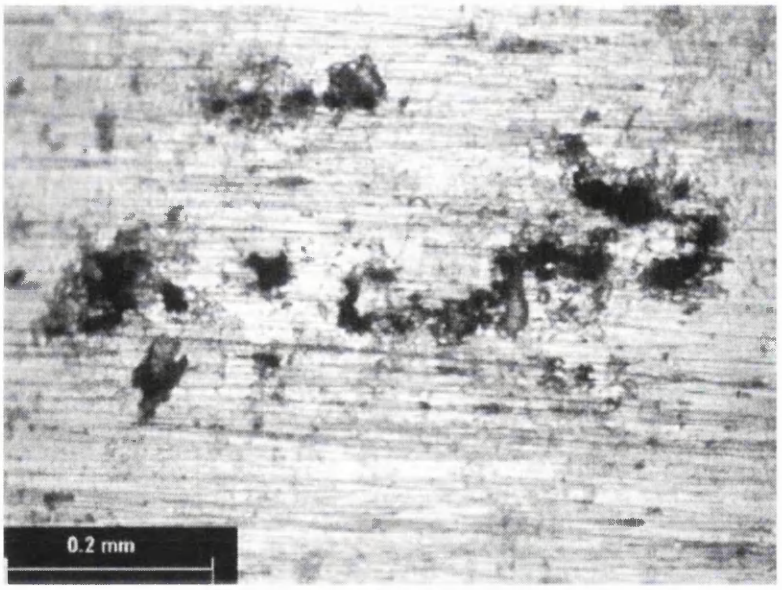

Figure 2.37 (a) Schematic illustration of the location of the pitting and pitting clusters within the notched area, and (b) Surface of notched area showing pit clustering after 6 days salt spray.

(a)

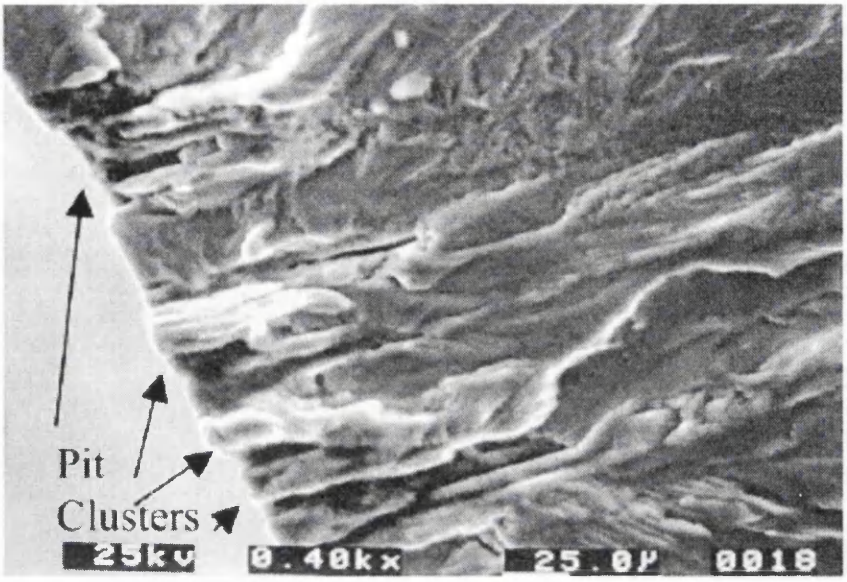

(b)

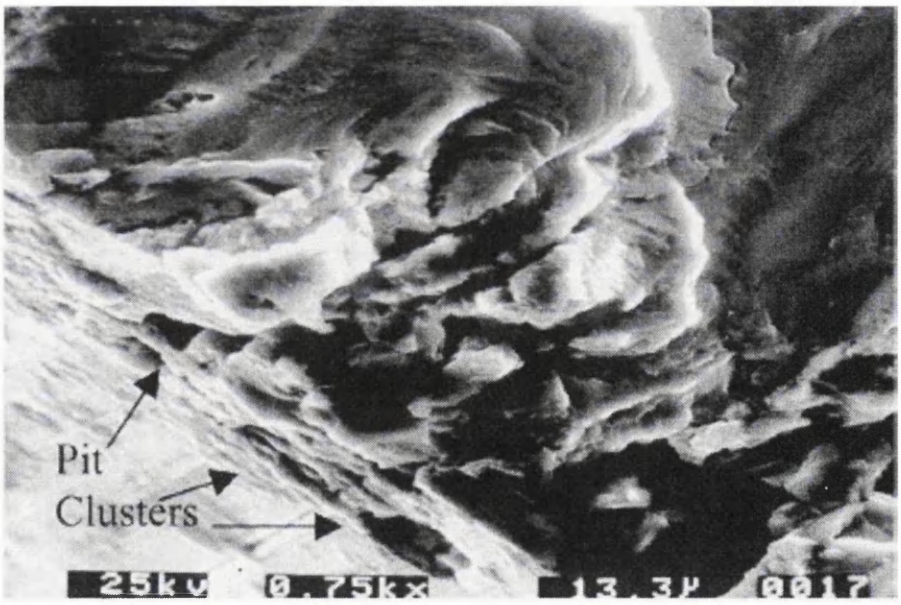

Figure 2.38 SEM images of pitting clusters which caused fatigue crack initiations (a) 6 days salt spray specimen and (b) pitting produced as a result of 91 days coastal exposure.

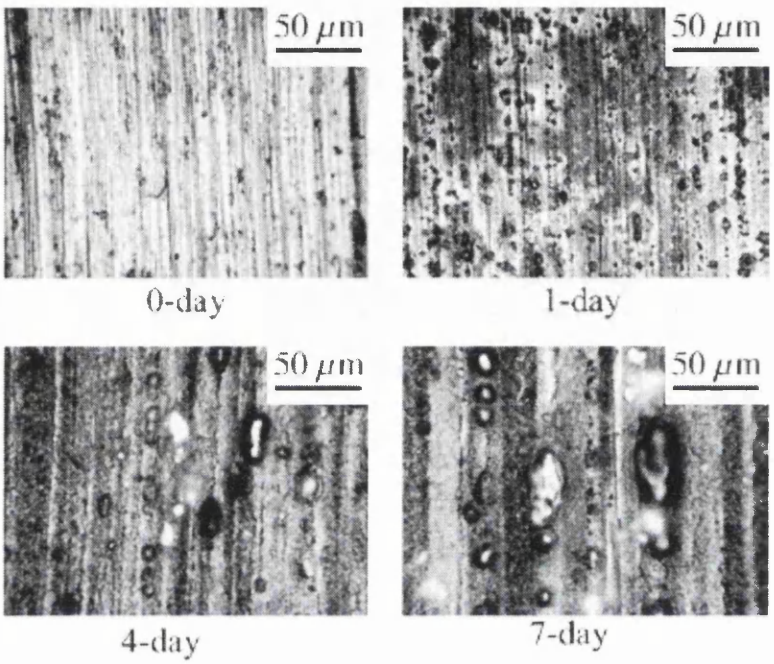

Figure 2.39 Typical appearance of the pits produced on the polished material after exposure to salt solution for 1, 4 and 7 days.

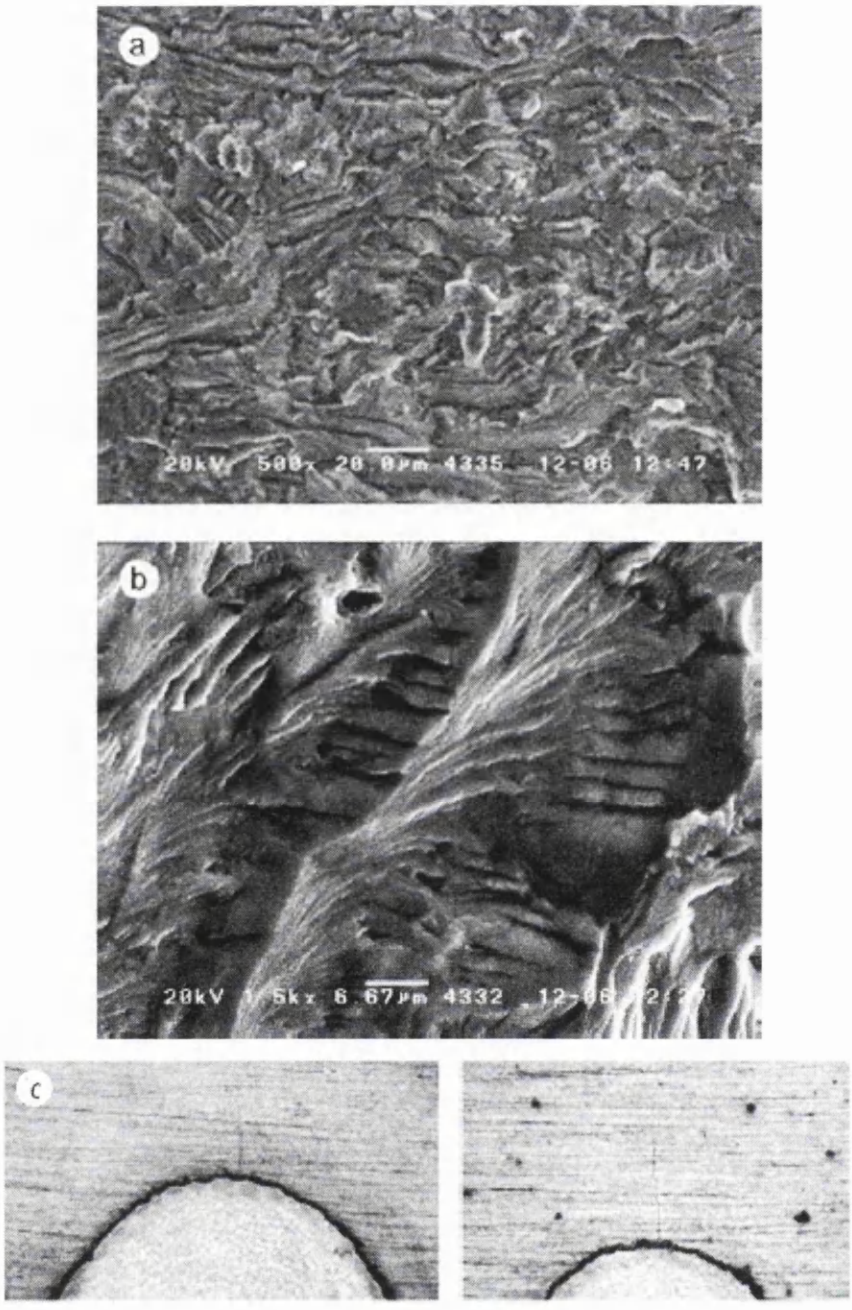

Figure 2.40 SEM micrographs showing various fracture modes (a) Quasi-cleavage fracture mode in near threshold crack growth, (b) ductile fracture surface at high crack growth rates, and (c) optical micrographs of small cracks in near threshold fatigue crack growth.

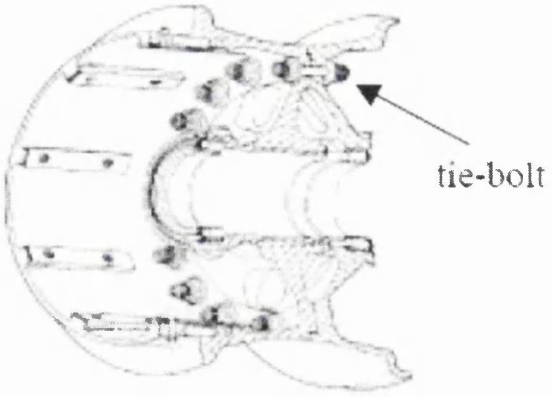

(a)

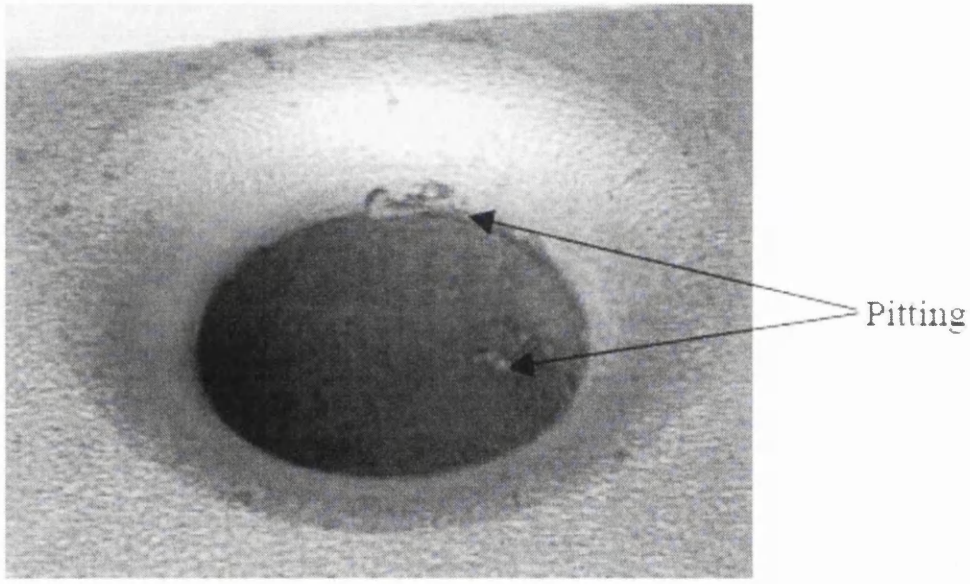

(b)

Figure 2.41 (a) Schematic of MLG wheel outer half, (b) Typical MLG wheel tie-bolt pitting.

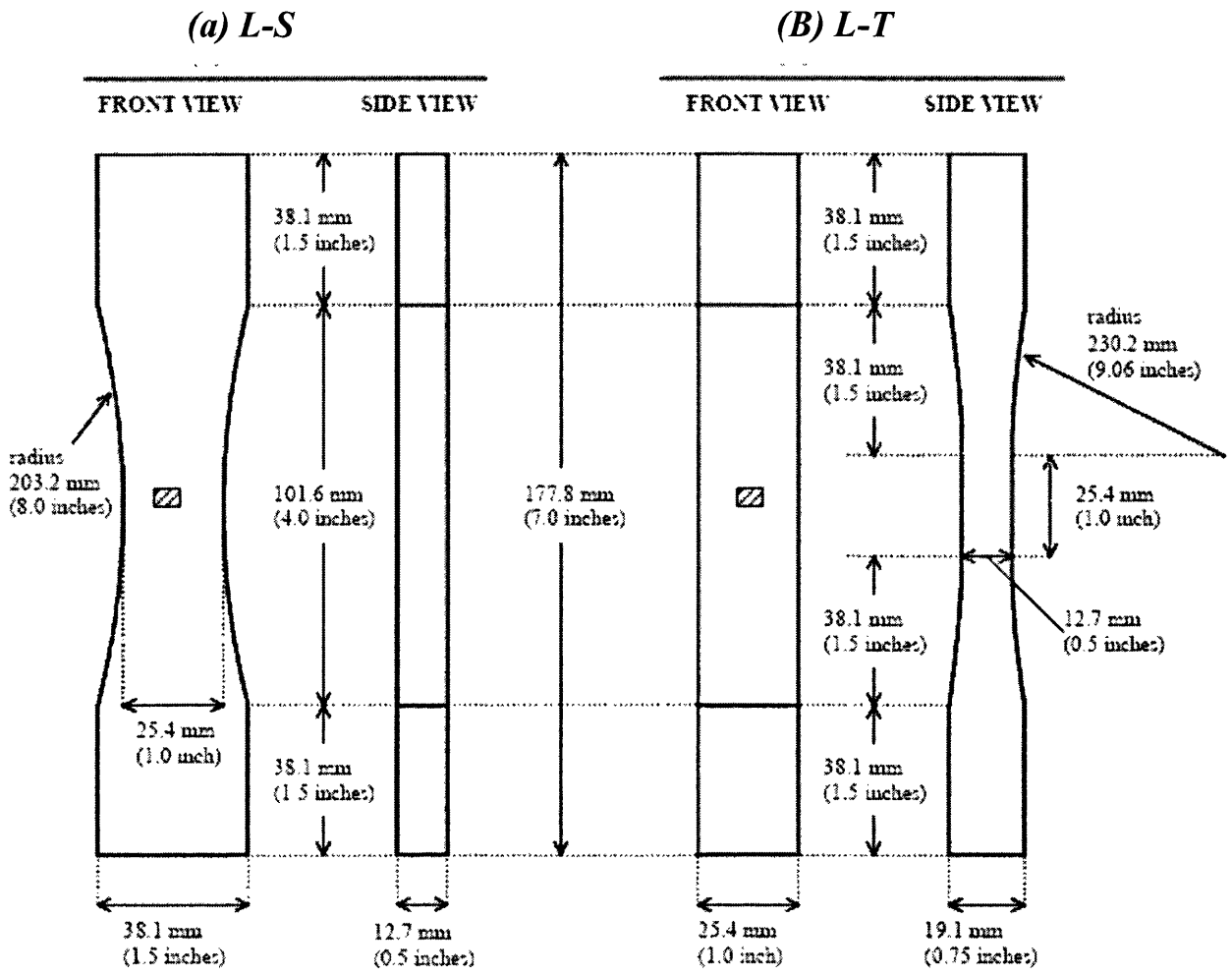

Figure 2.42 Fatigue specimen configurations for: (a) L-S specimen and (b) L-T specimen. The hatched region in the centre of the gauge section represents the location of the corrosion pit or EDM notch.

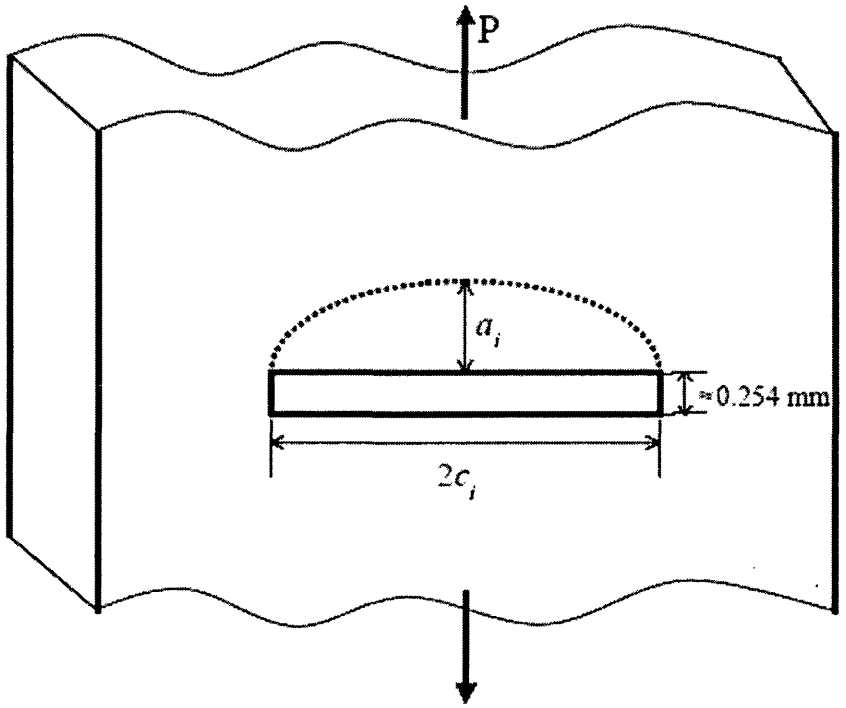

Figure 2.43 The EDM notch configuration.

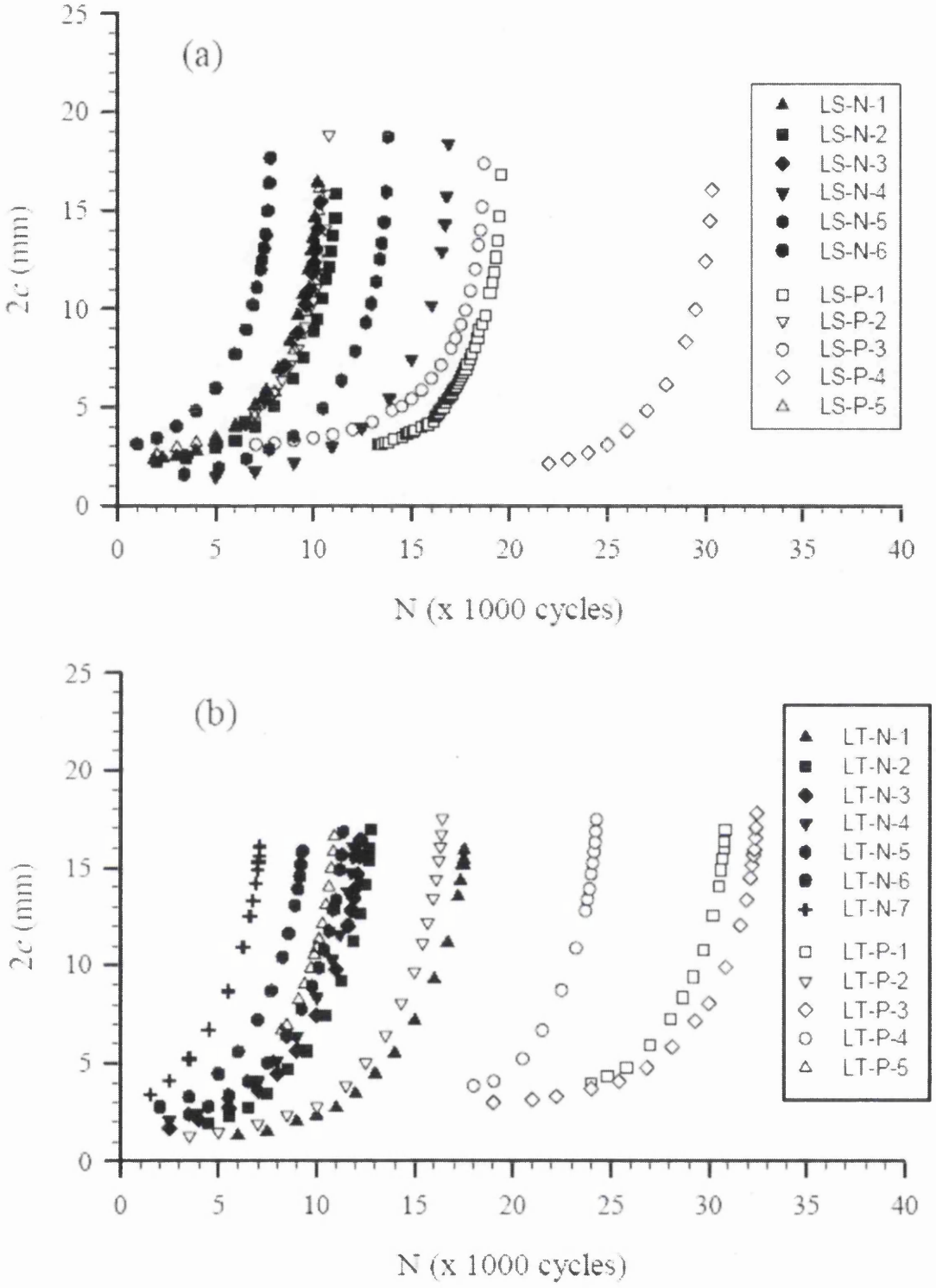

Figure 2.44 Surface crack length (2c) plotted versus cycle count (N) for: (a) L-S specimens, (L-T) specimens. Open and solid symbols represent pitted and EDM notch specimens, respectively.

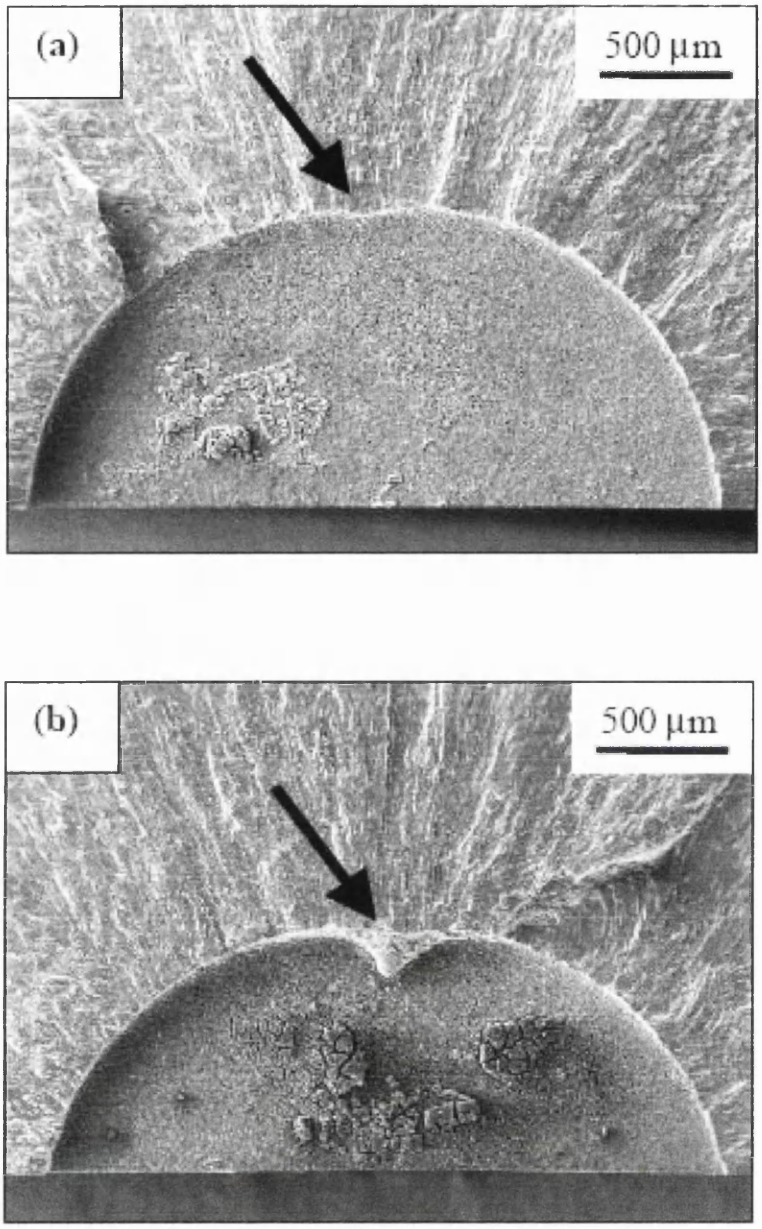

Figure 2.45 Typical fracture surface containing examples of EDM notches in the L-S orientation (a) LS-N-1 and (b) LS-N-2. Small irregularities can be seen at the base of the EDM notches.

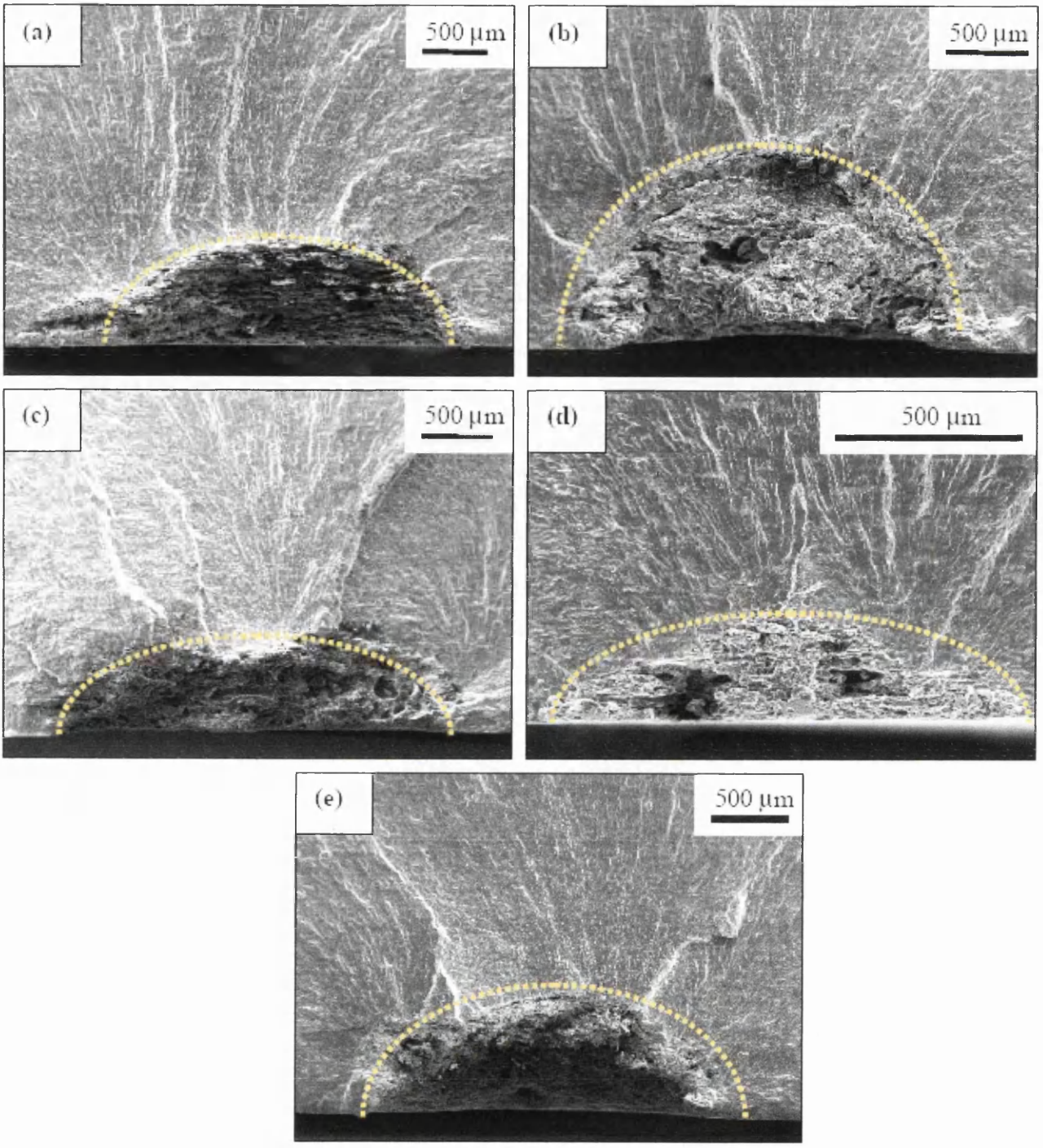

Figure 2.46 Fracture surfaces of corrosion pitted specimens in the L-S orientation. Dashed yellow lines indicate estimations of pit sizes, characterized by values of a_i and $2c_i$, listed in tables 2.6 and 2.7.

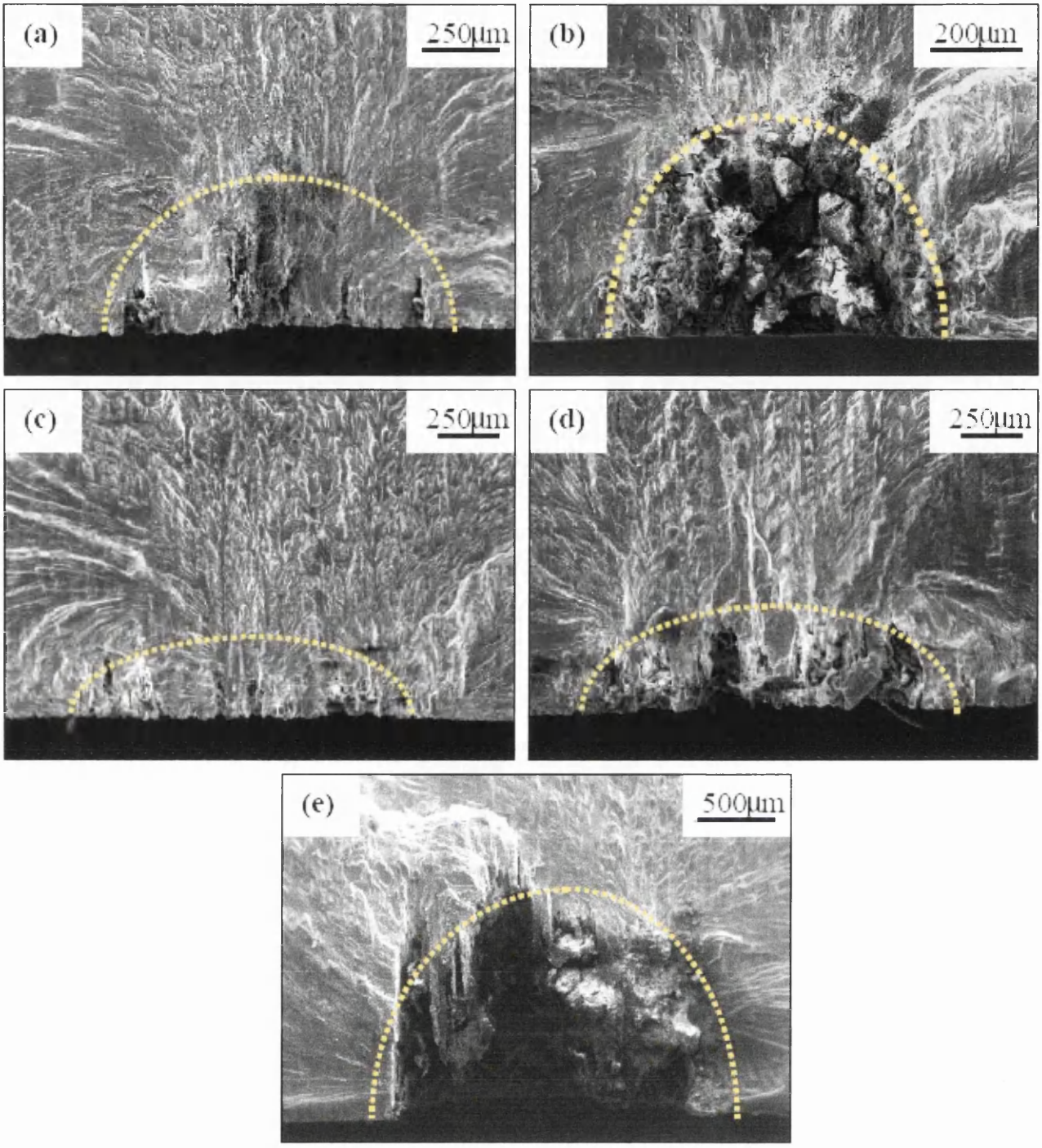

Figure 2.47 Fracture surfaces of corrosion pitted specimens in the L-T orientation. Clearly noticeable is the difference in pit morphology between the two orientations.

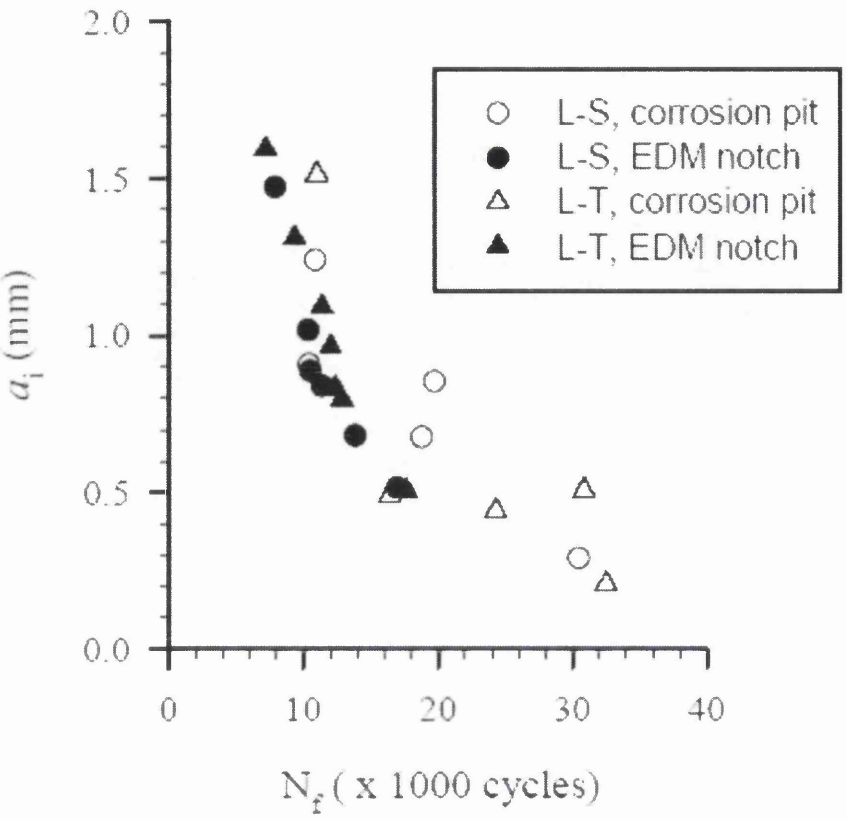

Figure 2.48 Initial flaw size (a_i) versus cycles to failure (N_f) for L-S and L-T orientations. Open symbols denote corrosion pits, while solid symbols denote EDM notches.

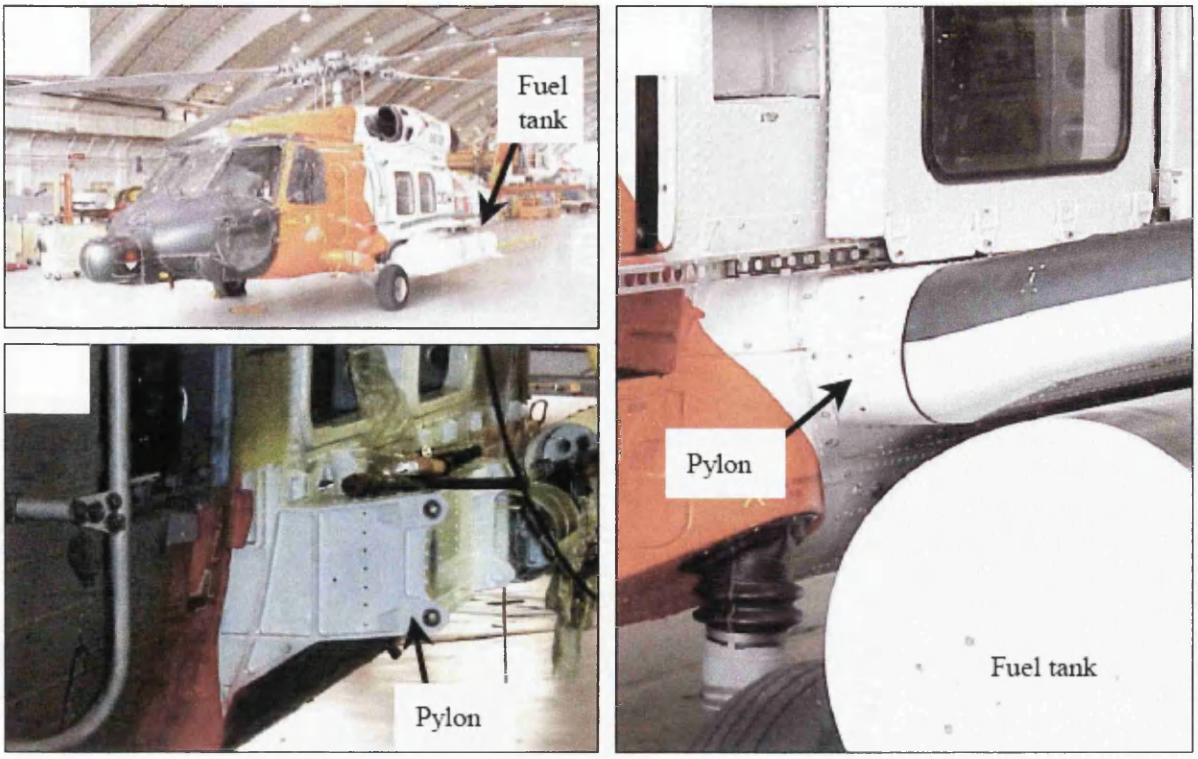

Figure 2.49 Photographs illustrating the location of the corrosion pitting within the external pylon-mounted fuel-tank.

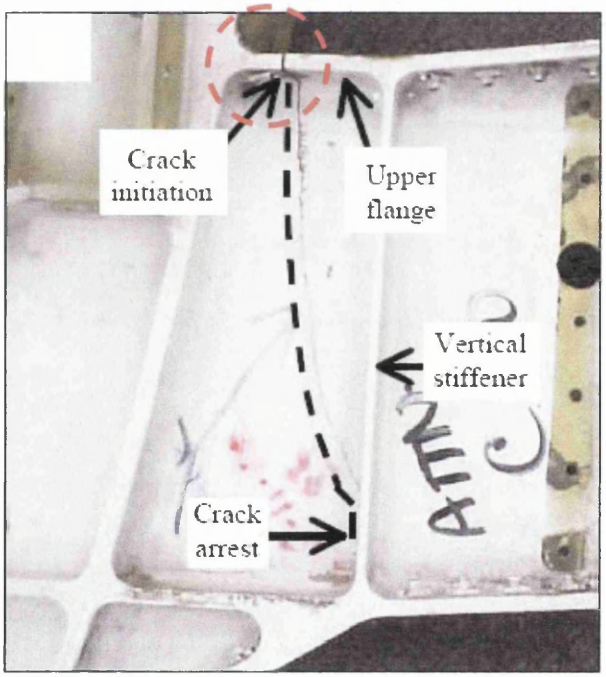

Figure 2.50 Photograph of the cracked pylon.

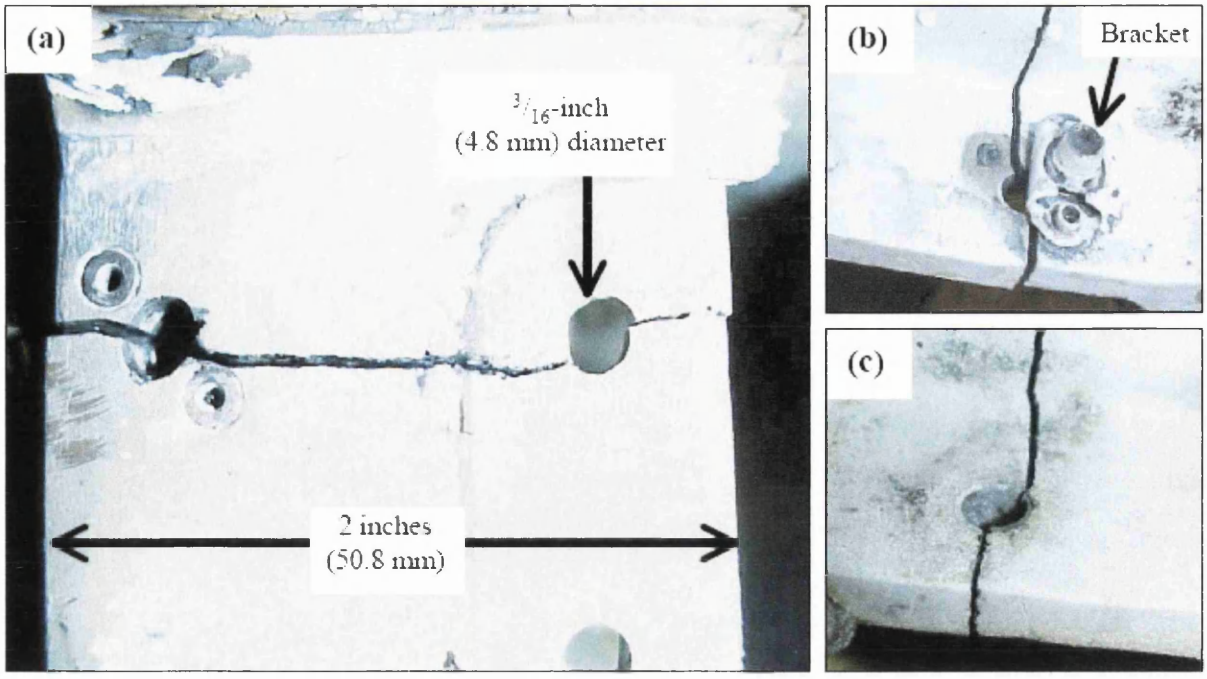

Figure 2.51 Crack initiation area (a) Crack dissecting two fastener holes in the upper flange region, (b) Closer image of the fastener hole on the left hand side of photograph *a* and (c) Closer image of the fastener hole on the right hand side of photograph *a*.

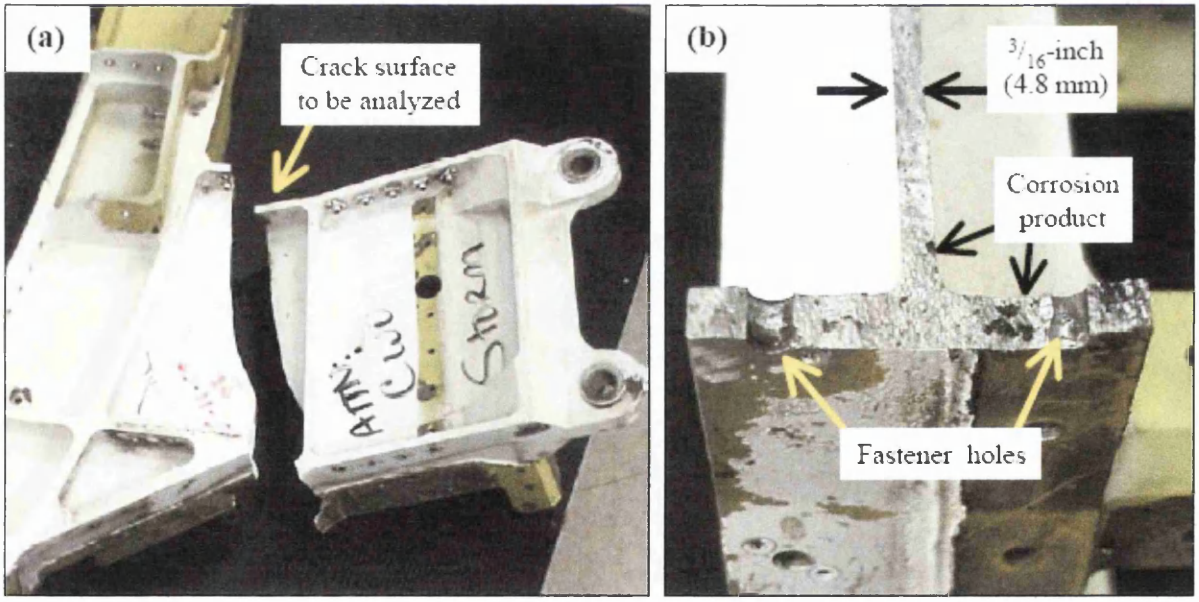

Figure 2.52 (a) Broken pylon. (b) Fracture surface of the pylon, illustrating corrosion product near the fastener holes.

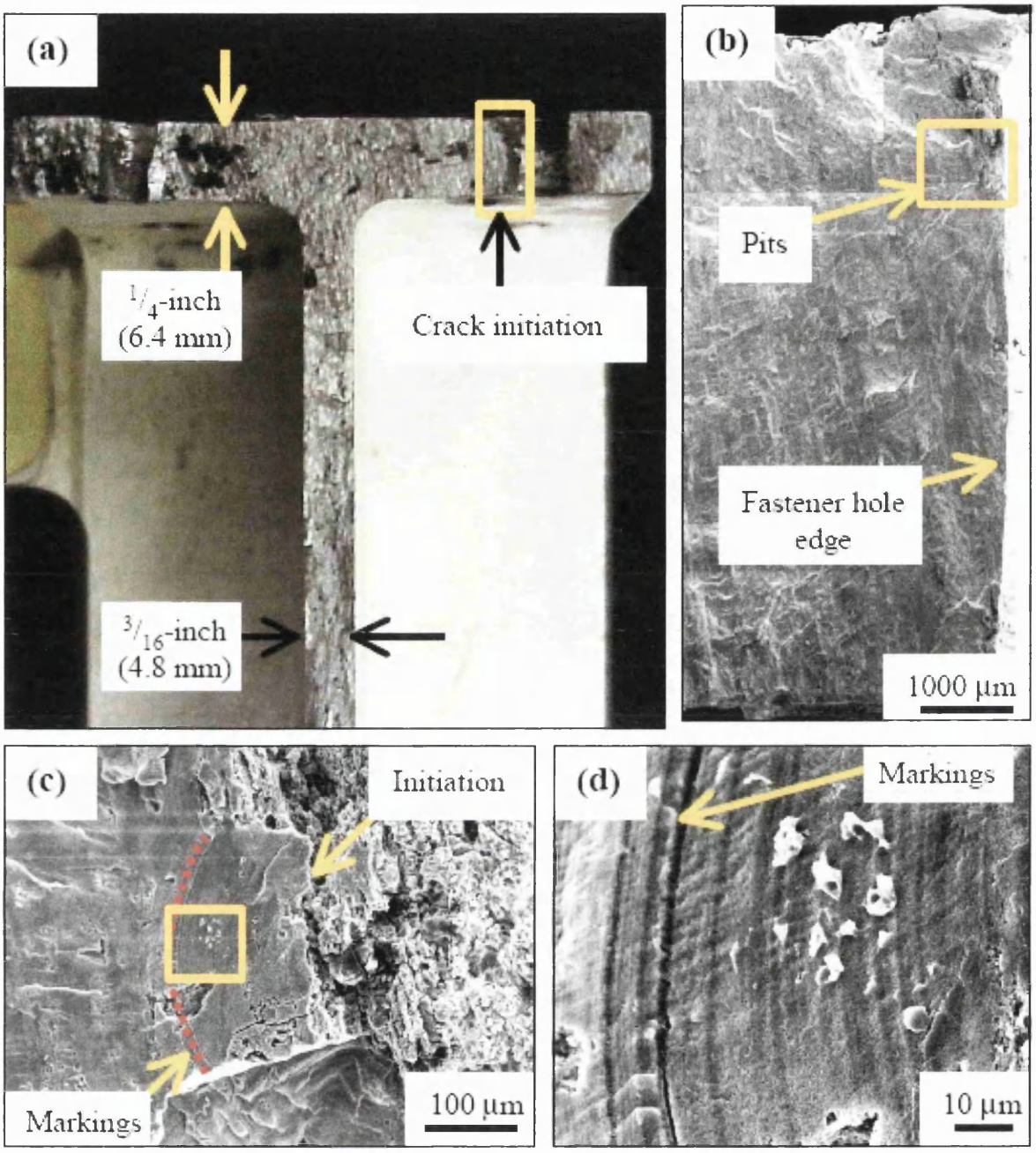

Figure 2.53 (a) Crack Initiation in the upper flange area, (b) Crack surface at edge of fastener hole, (c) Crack initiating from corrosion pit and (d) Crack surface markings in initiation area.

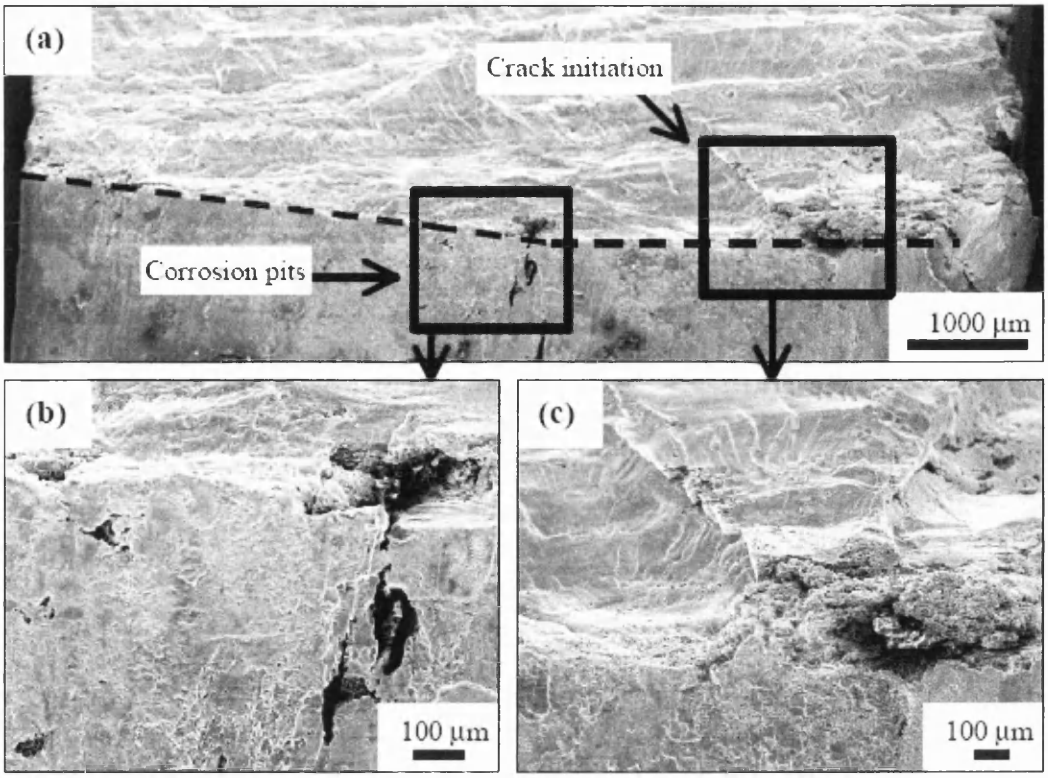

Figure 2.54 Images of the initiation area at a 45° angle.

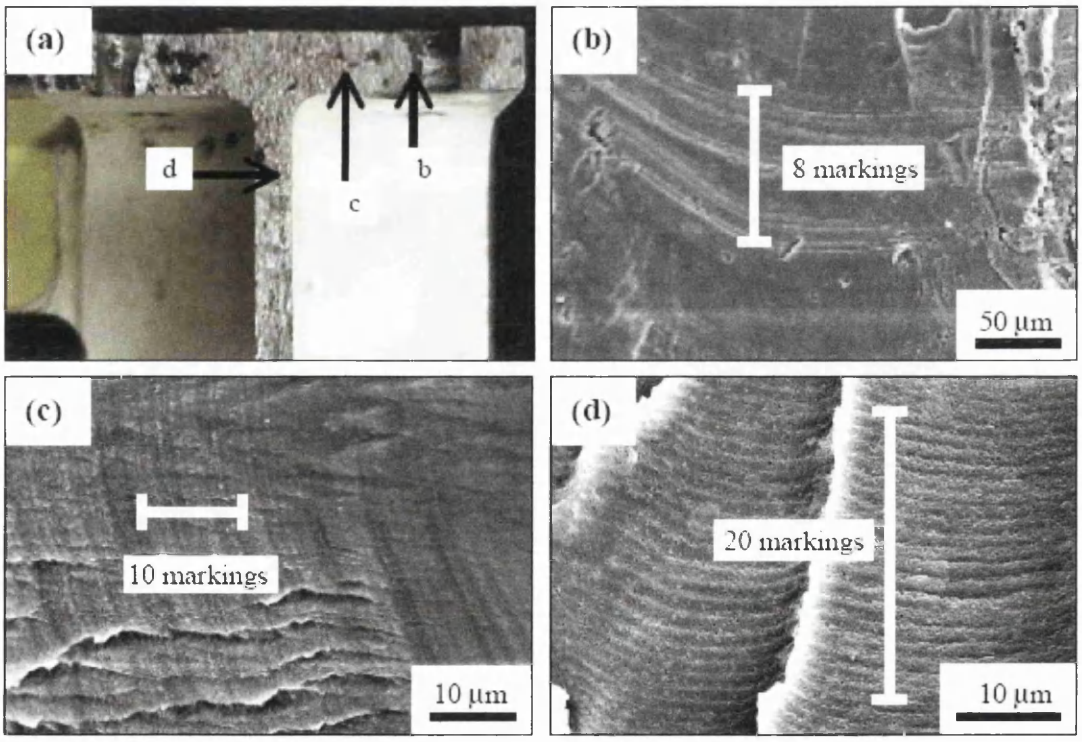

Figure 2.55 Micrographs illustrating cyclic loading and the formation of striations.

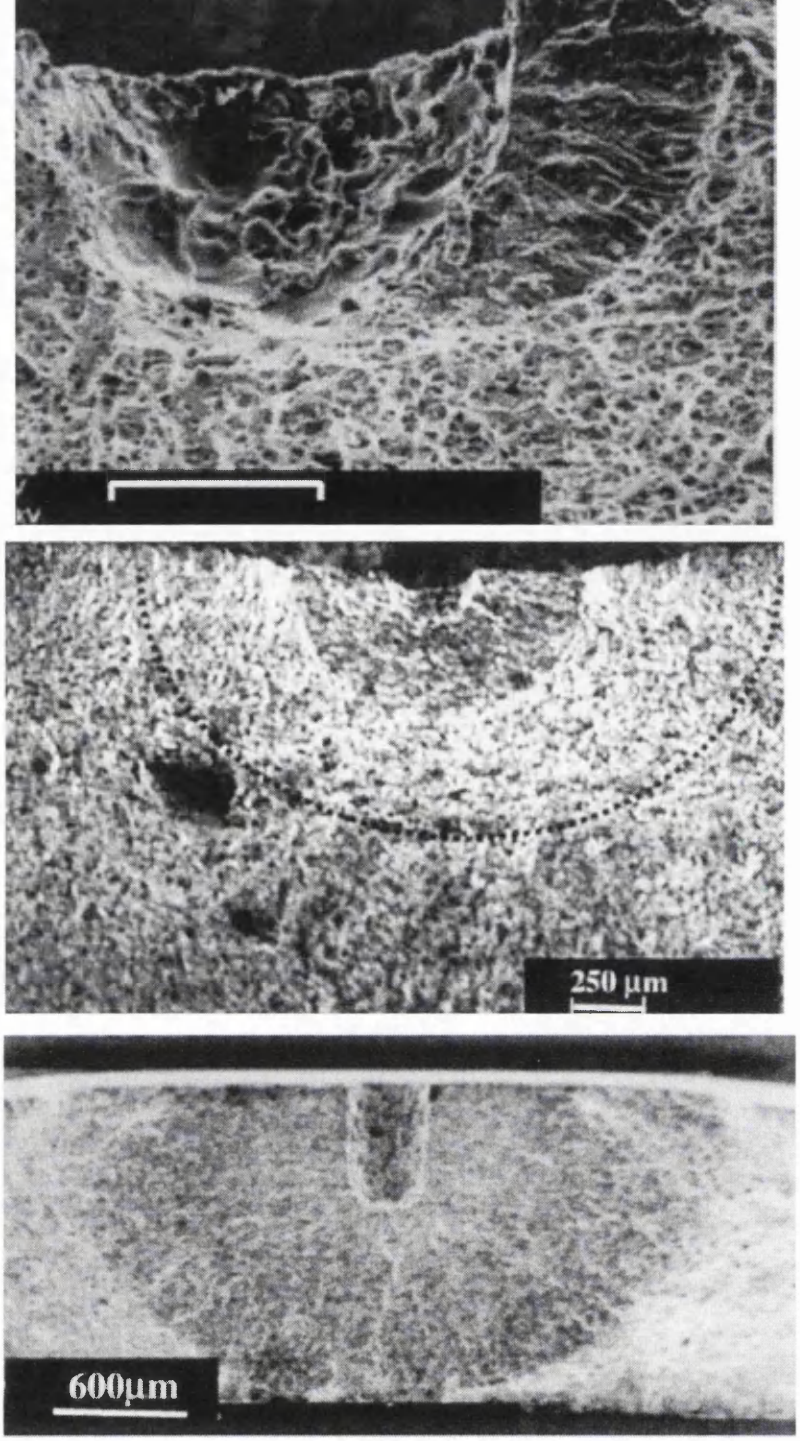

Figure 2.56 SEM fractographs of fatigued samples containing artificial pits. (a) Pit depth of 170 µm after 3 x 10^4 cycles. Crack depth: 170 µm. (b) Pit depth of 170 µm after 2.2 x 10^5 cycles. Crack depth: 850 µm. (a) and (b) failed under tensile load after fatigue. (c) Pit depth of 570 µm after 1.4 x 10^5 cycles. Sample failed under fatigue with crack depth slightly under through thickness (Crack depth: 1445 µm).

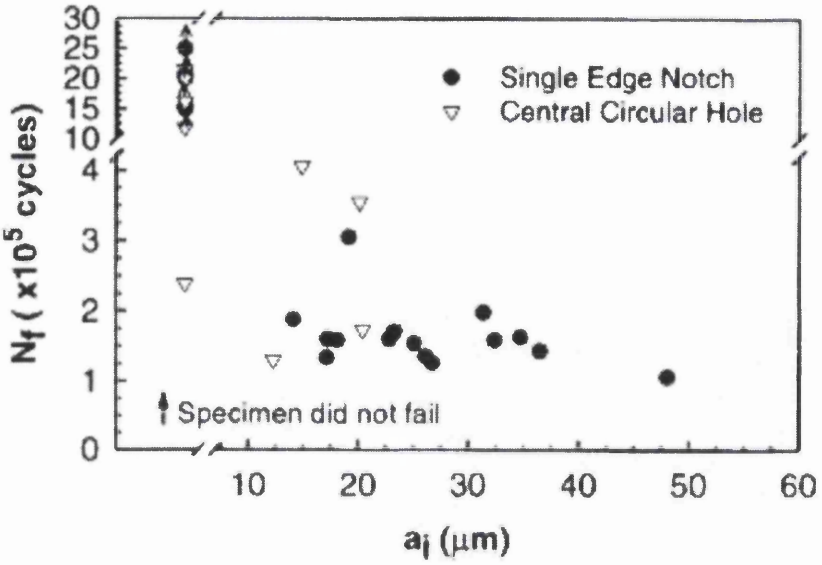

Figure 2.57 Reduction in fatigue life (N_f) of 2024-T3 as a function of initial pit size (a_i).

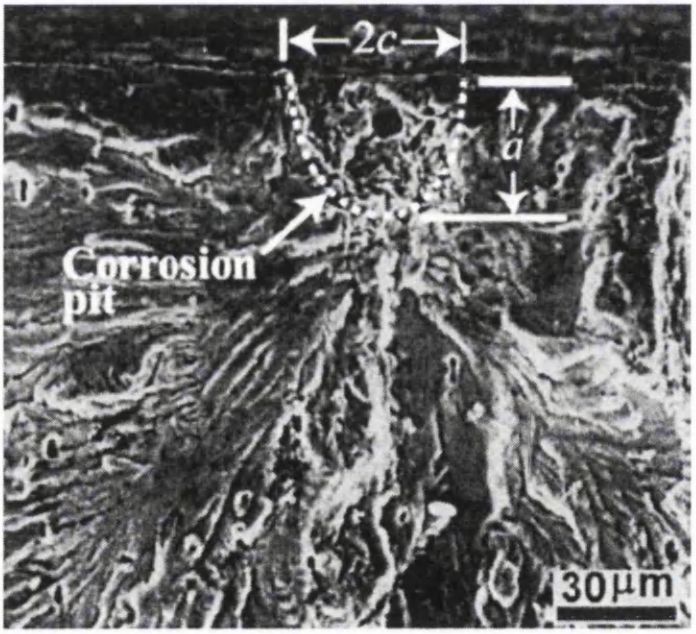

Figure 2.58 A fractograph detailing the morphology of the crack nucleating corrosion pit in 2024-T3 after 384h pre-corrosion. (Pit metrics are highlighted).

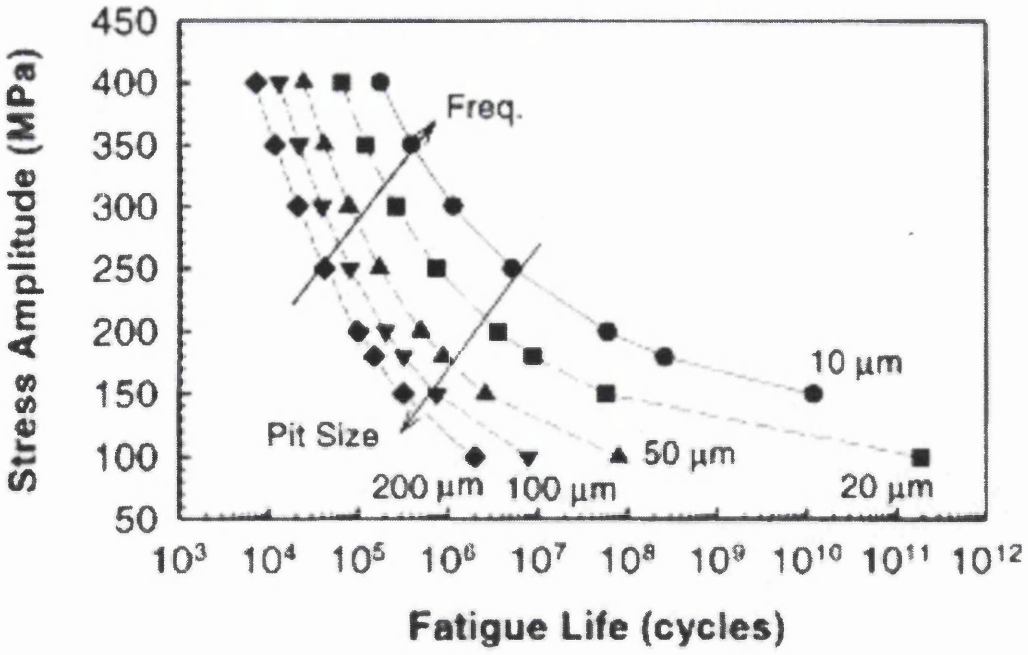

Figure 2.59 The estimated reduction in fatigue life given an increase in initiating pit size for the 2024-T3 aluminium alloy using a fracture mechanics approach.

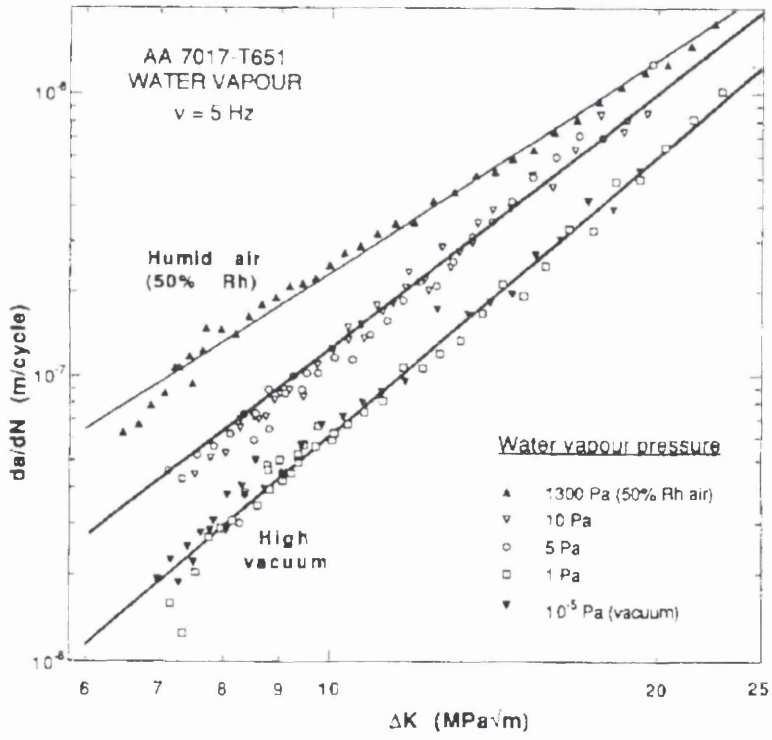

Figure 2.60 da/dN vs. ΔK data for 7017-T651 aluminium alloy tested in different water vapour pressures.

2.5 MODELLING OF CORROSION FATIGUE MECHANISMS

Fatigue crack growth data are critical inputs for damage tolerant designs, which acknowledge initial flaws in materials subject to cyclic loading. Fatigue crack growth data are also used for life predictions, and in addition, provide understanding of the microstructural effects on crack propagation at various stages during service life of components. Linear Elastic Fracture Mechanics (LEFM) methods have been employed to illustrate how microstructure and heat treatments can be selected and optimised for given design requirements. Life predictions based on LEFM calculations along with other methodologies can be performed using freely available software packages such as AFGROW and other simulation and modelling software [58]. The following literature, reviews the suitable modelling techniques available for corrosion pitting and fatigue crack growth.

2.5.1 AFGROW Based Corrosion Fatigue Modelling.

The author ***James A. Harter***[59] compared the contemporary fatigue crack growth life prediction tools. The paper summarised the closure based load interaction models used in two popular crack growth life prediction programs called FASTRAN and AFGROW, used extensively by government, industry and academia. Crack closure models have become widely accepted as the most accurate means of determining analytical crack growth lives under spectrum loading conditions.

- *FASTRAN*

The FASTRAN program is written and maintained by Newman at NASA/Langley Research Centre. Newman developed the crack closure model used within FASTRAN. The model assumes that crack growth rate data for all stress ratios may be reduced to a single curve using constraint parameters, known as alpha values. The single curve is based upon the concept of an effective change in stress intensity factor for a given load cycle (ΔK_{eff}). A

number of alpha values (for various crack growth rates) are used to collapse the crack growth rate data to a single curve. The effective stress intensity range is the difference between the maximum stress intensity for a given load cycle and the minimum stress intensity factor required to open the crack tip. This assumes that the crack tip is fully closed when unloaded and a certain amount of tensile load must be applied to open the crack and overcome the effect of the plastic zone behind the crack tip.

- *AFGROW*

AFGROW was developed by James A. Harter and Analytical Services and Materials at the US Air Force Research Laboratory. There exists major difference between the closure models used in AFGROW and FASTRAN. The model in AFGROW does not assume that all of the crack growth rate data can be reduced to a single curve. Opening stress is determined using the relationship between stress ratio (R) and a closure factor (Cf) as illustrated by figure 2.61. The closure factor is represented in AFGROW by the equation –

$$Cf = 1.0 - [(1-Cf_0)(1 = 0.6R)(1 - R)] \qquad 8$$

Cf_0 is known as the value of Cf at R = 0 and is used to adjust the curve for a given material. The Cf value in AFGROW is defined as the ratio of the stress intensity value required to 'open' the crack to the maximum stress intensity factor for a given cycle.

Major assumptions in the AFGROW closure model include :-

- Overload defined when the current yield zone grows beyond the previous overload zone.
- Irwin yield zone model is used (yield Zone size = $(k_{max}/\text{Yield stress})^2 / (\pi \times PSX)$, where PSX = 2 for plane stress and 6 for plane strain or any intermediate value.
- Opening stress changes linearly with crack length and reaches the overload state when the crack has grown ¼ of the distance into the current overload yield zone.

- Compressive stresses will cause an instant change in the opening stress if the opening stress for R = σ(compression)/σ(overload) is less than the current opening stress.
- The effective ΔK (when R is greater than or equal to zero or k_{max} (when R is less than zero) is converted back to apparent ΔK using the value of Cf for the current load cycle (to use existing apparent da/dN vs. ΔK data).

$$\Delta K = \Delta Keff\,(1 - R)/(1 - Cf) \qquad 9$$

and

$$K_{max} = \Delta K_{eff}/\,(1 - Cf) \qquad 10$$

To compare the two life prediction tools a testing program was outlined. Test specimens made from 7075-T651 aluminium were subjected to a loading sequence obtained from the Mirage fighter (see figure 2.62). Each spectrum was edited based on a maximum 'g' level. Testing was conducted at 8.5, 7.5 and 5.0G, using CCT (centre cracked tension) type specimens. A comparison of the predictions made by AFGROW and FASTRAN for the Mirage spectrum tests can be seen in figure 2.63a-c.

Conclusions from the study show that AFGROW and FASTRAN both make reasonable life predictions. Crack growth rate data for a given material can differ by as much as a factor of 2 on growth rate; therefore a safety factor of 2 is commonly applied to determine inspection intervals. Both AFGROW and FASTRAN return values well within the allowed safety factor of 2. Although the results from the predictions are within the safety factor boundaries, the shapes of the curves do not reflect the data in all cases. If the shape of the life prediction curve generated does not follow the experimental data, the results would not be the same if the predictions were started at a different initial crack length, hence there appears room for improvement in crack growth retardation models. AFGROWS advantages include the ability to use a variety of crack growth rate models or actual tabular material data. The program uses these data directly and performs all conversions to an effective stress intensity range internally, whereas the FASTRAN model requires crack growth rate data to be converted to a single curve before entry and analysis

is performed. The author states that more work should be done on crack growth retardation models [59].

The authors ***Dolley, Lee and Wei***[60] also used the prediction software package AFGROW to estimate fatigue lives for two 2xxx series aluminium alloys. AFGROW was used to account for the hole or edge notch in the tests specimens and their influence on the stress intensity factor as well as variations in the aspect ratio of the nucleating pit. Estimations of fatigue life for the aluminium alloy were made by assuming a power law relationship. In order to estimate fatigue life, material properties, loading conditions, specimen and pit size, and geometry parameters are inputted into AFGROW. The stress intensity factor solution used in the program was a three-dimensional solution for a crack in a finite body. Crack size prior to fast fracture was measured from the fracture surface and was used as the final crack size. Estimated fatigue lives were seen to be in good agreement with actual measured fatigue data. The results suggested that the number of cycles required to nucleate a crack from a corrosion pit is relatively small and may be neglected. As such, the fatigue lives represent essentially the crack growth lives from nucleating pits, and can be estimated straightforwardly if the nucleating pit sizes are known.

Probabilistic analysis of the test data showed that the distribution in fatigue lives was directly related to the distribution in the size of crack nuclei; however, this distribution is also expected to reflect variations in crack growth properties through the crack growth rate coefficient. Consequently, the AFGROW software could be used to predict fatigue lives if the initial crack size, local stress and fatigue crack growth properties were know [60].

Other authors to use AFGROW were ***Sankaran et al*** [47]. The study looked at the effect of pitting corrosion on the fatigue behaviour of aluminium 7075-T6. The fatigue lives of the material containing various levels of corrosion damage were predicted using the United States Air Force (USAF), AFGROW software package. The software makes use of stress intensity factor solutions derived from linear elastic fracture mechanics (LEFM). Stress intensity factors are computed for the particular crack geometry, dimensions and stress condition. Crack growth

rates (da/dN) are obtained via the da/dN vs. ΔK curve for the specific material. For a given stress cycle, (da/dN) defines the increment in crack growth, this value is then added to the original crack length. AFGROW repeats the process until the critical crack size is reached. The critical crack size can be defined to occur when ΔK reaches the fracture toughness (k_{IC}) of the material.

Pit dimensions within the study were used as equivalent initial cracks, which were modelled as semi-elliptical surface flaws. Fatigue lives computed by AFGROW are shown as the solid lines in figure 2.64, plotted against actual fatigue data. It was assumed that corrosion pits were randomly distributed on the corroded surface of the specimen as illustrated by figure 2.65. The figure illustrates the development of a semi-elliptical surface crack at a corrosion pit. Crack growth on the surface (using pit length as twice the initial crack length) as well as through thickness (using the pit length) is calculated independently by the model. The model assumes that crack growth begins at the first applied cycle, neglecting the crack initiation stage, due to the assumption that pre-existing surface damage can initiate fatigue cracking immediately upon application of a suitable load.

Measured fatigue lives of the pitted 7075-T6 specimens can be seen in figure 2.66. The fatigue lives are compared with bare 7075-T6 fatigue data for K_t values of 1 and 2. It is interesting to note that the pitted data is bounded by the Kt values, suggesting that fatigue can be related to the effects of equivalent stress concentration factors. It was also noted that corrosion pits acting as initiating sites for fatigue crack growth could be compared with sharp pre-existing cracks by determining the apparent threshold stress-intensity value ΔK_0 associated with the corrosion pits. Pit shapes were predominantly found to be semi-elliptical, with their depths small when compared to specimen dimensions and stress intensity factor solutions, therefore, first approximations were made adopting the semi elliptical surface crack in a semi-infinite plate model. Threshold stress intensity factor associated with fatigue crack initiation at corrosion pits was not notably affected by a reduction in pit depth from 250 – 70 μm. This was true for tests with a maximum stress below yield stress. LEFM calculations were not suitable for pits lower than 40 μm in depth. A critical pit depth was calculated, although in order to encourage a reduction in the fatigue limit of pitted specimens compared to smooth specimens, this critical pit depth must be exceeded. These pits should be sufficiently deep to initiate cracking at stress levels

which do not exceed the elastic limit of the material. The critical pit depth for the material used in the study was 100 μm.

Fully reversed tests were shown to produce complications due to the difference between crack closure in pitted specimens compared to sharp cracks. Subsequently, the threshold stress intensity values calculated using the full stress range for crack initiation at pits could be well below those associated with sharp cracks. This was due to the open nature of the corrosion pits limiting crack closure during the compressive part of the cycle, so that material at the tip of the pit is exposed to a greater overall stress range than would be experienced at the tip of a sharp crack. It was therefore concluded that the threshold stress intensity for crack initiation at pits can be estimated by applying concepts from LEFM, provided that validity requirements similar to those for sharp cracks are satisfied [61].

Conclusions from the predictive fatigue life modelling include:-

- The accuracy of the fatigue life prediction model can be improved by the availability of short crack growth data and a probabilistic analysis that will help quantify the probability of initiating cracks at pits of different sizes.
- The effects of pitting corrosion on the fatigue lives of alloys such as 7075 can be related to the effects of equivalent stress concentration factors that are routinely used in structural design.

DuQuesnay[61] et al also used the commercial fatigue crack growth software, AFGROW. Various metrics were considered for characterisation of the corrosion pit geometry for crack growth based fatigue life predictions. However, pit depth was the dominant factor affecting fatigue life. The analysis assumes a single crack initiating from a corrosion pit of depth a and length $2c$. The analysis is strictly a crack growth analysis and does not include the initiation of the crack from the corrosion pit. Life expended in crack nucleation is ignored since corrosion pits are very sharp alongside the loading spectrum, which contains frequent compression and tension

'overload' cycles due to the Ground-Air-Ground loading. The fatigue process is therefore modelled from pit to fracture.

AFGROW assumes a pre-existing sharp crack and assimilates the standard da/dN vs. ΔK curve for the material between the starting crack dimensions of a and 2c and a critical crack size at fracture. Fracture occurs when ΔK equals the fracture toughness of the material, K_Q. Experimental observations revealed that this occurred in all specimens at a surface crack length 2c; of approximately 11 mm with an aspect ratio a/c of about 0.9 which was consistent with results generated using AFGROW.

Comparing the experimental and predicted fatigue lives, it is clear that the software over predicts the life for the longer life specimens (shallow pits) as illustrated clearly by figure 2.67a. Although the software over predicts somewhat, the predicted are lives are contained within a factor of two of the experimentally derived lives (figure 2.67b). The authors state that at relatively small pit depths, fatigue life is influenced greatly by short crack behaviour. This accelerates the growth as suggested by Sankaran et al [47]. Unlike the work of Sankaran, AFGROW under predicted the lives of the CC-130 spectrum test by an order of magnitude. Therefore it was deduced that due to the shape and sizes of the pits included in the study, short crack effects were neglected.

The use of total fatigue life as an indicator of the ability of any crack growth analysis to predict fatigue behaviour within the study is questioned. Figure 2.68 plots the development of a surface crack, initiated at a corrosion pit and measured using the plastic replica technique, periodically taken over the fatigue life of the specimen. From the plot it can be seen that the predicted lives conform well to the observed experimental data. The accuracy is within that observed for AFGROW predictions under aircraft spectrum loading conditions. Problems were encountered in determining the surface widths of the starting pits and vital measurements were required, especially where pits are within a close proximity to each other. Therefore a practical solution was derived and the average surface width of the corrosion pits was used to input into AFGROW. This value was approximately 2 mm. By using a power law relationship; the prediction was in good agreement with the experimental data, as demonstrated by figure 2.69.

Altering the pit surface length by ± 0.5 mm also encompasses the scatter within the data (figure 2.69).

Pit depth is identified as the appropriate metric in characterising corrosion damage and to start crack growth analysis. This may be illustrated in figure 2.70, where the data tends to lie above the AFGROW curve ($2c$ = 2 mm), indicative of a conservative prediction. Suitable safety factors would also be introduced to predicted life to determine inspection intervals and repair and removal periods.

In conclusion, the authors state that a simple two dimensional crack growth calculation using the software AFGROW, successfully predicts the fatigue lives of the pitted material, utilising pit depth and average pit surface width as the starting points for crack size analysis. The methodology of predicting fatigue life in corrosion damaged aircraft components and structures using AFGROW, therefore, has great potential [61].

Medved et al[62] also utilised the fracture mechanics model, AFGROW, to compare experimental lives with predicted ones, in a study entitled; Corrosion pit size distributions and fatigue lives – a study of the EIFS (Equivalent Initial Flaw Size) technique for fatigue design in the presence of corrosion. The NASGO growth model was used; C and n (Paris constants) were obtained experimentally. For the variable amplitude loading calculations, a closure model was applied. The single through crack model was then used to calibrate the retardation parameter (OPR = 0.3). Surface and corner crack geometries were employed to simulate measured initial pit dimensions. Figure 2.71a and b, shows the comparison between predicted and experimental lives for constant and variable amplitude loading. The lives for the constant amplitude loading show significant conservative and non conservative predictions, where as the variable amplitude predictions are predominantly conservative. Weibull cumulative and probability density functions were generated to represent the distributions in fatigue lives.

An EIFS approach was used to design against pitting. To examine the performance of the EIFS approach, an EIFSD (Equivalent Initial Flaw Size Distribution) was determined by back

extrapolating the measured fatigue lives to zero cycles using the AFGROW model. This was possible by finding the initial flaw size, which would produce the observed life under the relevant loading, crack configuration and model conditions. The EIFSD was then used as a starting flaw size distribution to calculate using AFGROW, a cumulative distribution for the number of cycles to reach a crack length of 1.27 mm. Figure 2.72 shows the comparison between the predicted distribution and that measured experimentally from crack growth data. Clearly, AFGROW produces a non-conservative prediction of the probability of a crack exceeding 1.27 mm.

In conclusion; Applying the EIFS approach highlighted the difficulties in trying to create equivalent flaw sizes to match the fatigue lives, and also emphasised the poor correlation at the extremities of the distribution. The distribution of the fatigue lives and the AFGROW generated EIFSD both showed a reasonable approximation to a Weibull distribution. It was not confirmed in the approach, that the design details had a single dominant fatigue crack that governed the durability of the structure. Also, the form of the crack length cycles-curves differed considerably from that predicted from an EIFS analysis, resulting in non-conservative crack population predictions [62].

Lados and Apelian[58] researched fatigue crack growth characteristics in cast Al-Si-Mg alloys. While the material and subject has no direct bearing on the current focus of research, life prediction using fatigue crack growth data is examined using AFGROW. The paper looked at simulations completed by AFGROW, background information and input and output parameters required by the programme.

The origins of the AFGROW program date back twenty years, when it was firstly known as ASDGRO. Several changes and performance updates have been implemented since its first release, to accommodate the advancements in fracture mechanics definitions and interpretation. Stress ratio effects at low and high crack growth rates are accounted for by the Forman crack growth rate equation (eq 9a), although data shifting as a function of stress ratio is not permitted. Parameters to adjust the R shift unfortunately don't exist within the equation, due to the fact that

the amount of shift is solely controlled by plane stress fracture toughness. AFGROW, therefore introduced an alternative formulation of the da/dN vs. ΔK relationship, similarly to the NASGRO equation, used extensively in NASA's crack growth life prediction program:

$$\frac{da}{dN} = C\left[\left(\frac{1-f}{1-R}\right)\Delta K\right]^m \frac{(1-(\Delta K_{th}/\Delta K))^p}{(1-K_{max}/K_{FT_{crit}})^q} \qquad 11$$

Various case studies were carried out within the examination. Experimentally generated fatigue crack growth data was used in AFGROW to predict fatigue life. The input data therefore needed to run a simulation in AFGROW includes:-

- **Crack growth data**: ΔK_{th}; empirical Paris law coefficient and exponent, C and m; p and q exponents needed in the NASGRO da/dN vs. ΔK (eq 9b), empirically determined as 0.5 and 1, respectively; the parameter f in (eq 9b), $f = K_{op}/K_{max}$; and K_{FTcrit} which takes into account thickness effects;
- **Material properties**: yield strength, YS, flow stress σ_{flow} = (YS + UTS)/2, Young's modulus, E, Poisson's ratio (~0.33), coefficient of thermal expansion, plane strain fracture toughness, K_{IC}, and plane stress fracture toughness, K_C;
- **Geometry and dimensions**: of the component, initial flaw geometry, size and location;
- **Loading conditions:** Maximum applied load, stress ratio, constant/variable amplitude loading, retardation/closure corrections, residual stress adjustments for known residual stresses, environmental conditions.

Case studies illustrating several design problems were constructed within the paper, to understand how different parameters influence fatigue behaviour of Al-Si-Mg cast alloys. The outcomes of the case studies are not relevant to this research programme, therefore are not discussed [58].

2.5.2 Other Corrosion Fatigue Models.

Patton et al after studying the damage mechanisms and accumulation during fatigue in 7010 aluminium alloy, attempted to model fatigue damage accumulation, crack growth and predict the number of cycles to failure. The study derives the local criteria for the fracture propagation path and includes these criteria in a global model for crack growth up to a critical length in order to predict fatigue life. In order to predict the fatigue life and model crack growth, energy balance equations were utilised to calculate crack growth in various microstructures, (e.g. intergranular or subgranular) and then estimating the probability that the crack will deviate from mode I crack growth and follow the predicted path.

Firstly the author describes a crack deviation model from an elastic approach, which enables the prediction of possible crack deviation on encountering grains or subgrain boundaries. For low applied stresses or short cracks it is shown that intergranular deviation is highly likely to take place, but on the other hand, for high applied stresses or long cracks the propagation is to remain intergranular along its current plane. Finally for intermediate fatigue stress amplitudes a fatigue lifetime model was developed to show the qualitative influence of the microstructural parameters on the fatigue behaviour of the 7010 aluminium alloy. As the effect of microstructure was known for the extreme stresses, the model was therefore used to predict the qualitative influences of the microstructure on the fatigue behaviour during intermediate stress amplitudes. The number of cycles to failure was obtained using the following equation:-

$$Nr = \frac{1}{\pi B\{(1-R)\sigma_{max}\}^2\{fr\chi_t + (1-fr)\alpha_t\}} \ln\left[\left(\frac{\sigma_r}{\sigma_{max}}\right)^2\right] + \left(\frac{\sigma_r}{\sigma_{max}}\right)^2 \qquad 12$$

R is the stress ratio (R = σmin/σmax), fr is the recrystallised volume fraction, χ_t and α_t are the fraction of the intergranular crack path in the crystallised and unrecrystallised grains, respectively. σr is the uniaxial monotonic tensile strength and B is a constant with units MPa^{-2}.

A plot of both experimental and theoretical curves generated by the model (eq 10) is shown clearly in figure 2.73. The fatigue model can be used qualitatively and quantitatively since the theoretical cycle number to rupture is found to be close to what expected, based upon identified parameters experimentally estimated. A critical parameter identified was the intergranular crack growth rate; this could be experimentally determined in order to improve the predictive capability of the present model. Also for low applied stress amplitudes, the damage initiation regime should be introduced in the modelling [1].

Similarly to Harter, ***Newman et al***[63] reviewed the capabilities of a plasticity induced crack closure model to predict fatigue lives of metallic materials using 'small-crack' theory for various materials and loading conditions. 'small crack theory' is defined as the treatment of fatigue as a crack propagation process from a micro defect (or crack) to failure. On the basis of Linear Elastic Fracture Mechanics (LEFM), studies on small cracks (10 μm – 1 mm) have shown that they grow much faster than would be predicted from large-crack data, as illustrated by figure 2.74. Here, Crack growth rate da/dN or dc/dN is plotted against stress intensity factor ΔK.

In conclusion a 'plasticity induced' crack closure model, was used to correlate large crack growth rate data on two aluminium alloys (2024-T3, 7075-T6), and a steel, under constant amplitude loading for a wide range of stress ratios. A constraint factor, which accounts for three dimensional state of stress effects, was used in determining the effective stress intensity factor range against rate relations. Comparisons between measured and predicted small crack growth rates for an aluminium alloy showed that the closure model could predict the trends that were observed in the tests, figure 2.75 is used to demonstrate the accuracy of the closure model. Using the model and microstructural features such as inclusion particle sizes, a total fatigue life prediction method was demonstrated. Calculated and predicted lives of the two aluminium alloys tested compare well with the received data under constant amplitude and spectrum loading. In a similar manner, the predicted fatigue lives of the steel alloy under investigation also compared well with the test data under constant amplitude and spectrum loading [63].

The author ***Hoeppner***[64] over the last three decades has compiled and reviewed pitting corrosion fatigue models. In a review of various pitting corrosion fatigue models, ***Hoeppner, Chandrasekaran and Taylor*** [64] determined the critical pit sizes that would initiate cracking. The study reviews various models published by many authors over the last two decades. The models reviewed include those by: - Hoeppner et al, Lindley et al, Kondo, and Kawai and Kasai. In depth reviews of these models can be seen within this chapter, as follows:-

In the study entitled Fracture Mechanics Based Modelling of the Corrosion Fatigue Process by ***Hoeppner, Mann and Weekes***[65], 'Safe-Life' and 'Damage-Tolerant; approaches to fatigue design are discussed.

The safe life concept is based mainly on idealised elasticity and plasticity concepts with '*no*' cracks or crack-like discontinuities allowed because of the simplistic assumptions. Safe life utilises S-N curves, ε-N curves and constant life fatigue diagrams to estimate life to first crack in a component or structure. Nevertheless, defects contained or created within structures before use present problems, hence fracture mechanics have been developed to aid the design of aircraft structures to tolerate the presence of either inherent discontinuities or those created in the use cycle. The damage tolerant approach is essentially the idealistic method of designing against failure. The chart in figure 2.76, summarises the various aspects of damage tolerant design. In order to make a life estimate, in service stresses and environments at the sub-critical growth stage are needed. In addition, crack growth rates for the component and the environment in which the crack is growing are also required. Inherent discontinuities within the structure can assume any of the following types:-

- Inherent material discontinuity
- Inherent manufacturing and assembly discontinuities
- Inherent geometric discontinuity

The fracture mechanics based modelling within the paper basically attempted to evaluate the corrosion pit depth using pitting theory. An estimation of depth was made by combining the pit growth rate theory with the fatigue crack growth curve fit in a corrosive environment.

Knowledge of fatigue crack growth threshold behaviour in the environment under consideration was essential in understanding the depth at which the pit converts from a pit to a mode I crack. Using a four parameter Weibull fit, fatigue crack growth threshold (ΔK_{th}) was found from corrosion fatigue experiments for the particular environment, material, frequency and load spectrum. The pit was modelled as a surface flaw in the material as illustrated by figure 2.77, although not representative of complex pit morphologies, the model is a good starting point.
The stress intensity relation for surface discontinuity was used to simulate a hemispherical pit.

$$K = 1.1\ \sigma \sqrt{\pi}\ (a/Q) \qquad 13$$

Where σ is the applied stress, a is the pit length and Q is the function of $a/2c$.

Several problems have been noticed to exist with this model type, these include :-

- The use of surface flaw equations enables simple pit geometries to be modelled, but do not accommodate complex pit morphologies.
- Several small cracks have been noticed to form within the pits and the transition stage from multiple cracking to mode I type cracking needs further investigation.
- The model requires fatigue crack growth threshold data for the material, a process which is time consuming and expensive, but mandatory as threshold of mode I crack growth is a critical parameter within the model.

This model provides a reasonable estimate for the total corrosion fatigue life with knowledge of the kinetics of pitting and fatigue crack growth. Mechanisms of crack nucleation from corrosion pits are not included within the model, which is only valid for the conditions in which LEFM concepts are applicable, as well as material dependant [65].

In a similar fashion to Hoeppner, ***Lindley et al***[66] looked at a model for determining the threshold at which fatigue cracks would grow from corrosion pits. Similarly to Hoeppner, pits were assumed to be semi-elliptical shaped sharp cracks. An estimation of the threshold stress

intensity values related to fatigue crack nucleation at corrosion pits was determined using Irwin's stress intensity solution for an elliptical crack in an infinite plate, given by :-

$$\Delta K_{th} = \frac{\Delta\sigma \sqrt{(\pi a)}\,[1.13 - 0.07\,(a/c)^{1/2}]}{[1 + 1.47\,(a/c)^{1.64}]^{1/2}} \qquad 14$$

where, $\Delta\sigma$ is the stress range, a is the minor axis, and c is the major axis of a semi-elliptical crack.

The threshold stress intensity was calculated from the observed pit geometry (a/c ratio), which led to the estimation of the critical pit depth. The proposed stress intensity relation could be used in tension – tension loading situations where stress intensity for pits and cracks are similar. Additionally, critical pit depths for crack specimens could be estimated using the existing threshold stress intensity values. However, again this model is valid only for the conditions in which LEFM concepts are applicable and is material dependant [66].

Similarly to many authors mentioned within this review, ***Chen et al*** [67] modelled corrosion fatigue crack nucleation in a 2024-T3 aluminium alloy as equivalent semi-elliptical surface crack. The investigation was conducted using open hole specimens, subjected to 0.5 M NaCl solution at room temperature and various loading frequencies.

It was suggested within the study that crack nucleation for the transition from pitting to corrosion fatigue crack growth occurs when the stress intensity factor ΔK of the equivalent crack reaches the threshold ΔK for fatigue crack growth ΔK_{th}. The ΔK of each pit therefore can be estimated using stress intensity factor solution for semi-elliptical surface cracks in which $c/a \leq 1$:

$$\Delta K = \frac{1.12 K_t \Delta\sigma\sqrt{\pi c}\,[\sin^2\phi + (c/a)^2\cos^2\phi]^{1/4}}{\Phi} \qquad 15$$

where, Φ is a shape factor determined by the c/a ratio, c, a and ϕ are defined in figure 2.78.

The results showed that by modelling pits as equivalent semi-elliptical surface cracks, pit size and stress intensity factor at crack nucleation was frequency independent at high frequencies ($f \geq 5$ Hz) but increased with decreasing frequency at $f < 5$ Hz. The phenomena were interpreted by the transition from pit growth to fatigue crack growth based on concepts of fatigue crack growth threshold and pitting/cracking rate competition. Criteria for the transition from pitting to fatigue cracking were proposed within the study as:-

- The equivalent stress intensity factor for a corrosion pit has to reach the threshold stress intensity factor (ΔK_{th}) for fatigue crack growth, and
- The time-based corrosion fatigue crack growth rate also exceeds the pit growth rate.

2.5.3 Modelling of Non Aluminium Materials.

Kondo[68] predicted fatigue crack initiation life of a low alloy steel, based upon pit growth. The corrosion fatigue life of a material could be determined by estimating the critical pit condition using stress intensity factor relations as well as pit growth rate relation. The diameter of corrosion pits were measured intermittently during various corrosion fatigue tests. Test results showed that corrosion pit growth law could be expressed as:-

$$2C \propto C_p t^{1/3} \qquad 16$$

where, 2c is the pit diameter, t is the time and C_p is an environment/material parameter. The critical pit condition (ΔK_p) in terms of stress intensity function was then proposed by assuming the pit acted as a crack:-

$$\Delta K_p = 2.24\sigma_a \sqrt{(\pi c \alpha / Q)} \qquad 17$$

where, σ_a is the stress amplitude, a is the aspect ratio, and Q is the shape factors.

The critical pit condition was determined by the relationship between the pit growth rate theory and fatigue crack growth rates:-

$$C = c_p (N/f)^{1/3} \quad 18$$

Where, N is the number of cycles, f is the frequency, and 2c is the pit diameter.

The pit growth rate dc/dN was developed using ΔK relation as:-

$$dc/dN = (1/3)C^3_p f^{-1} \alpha^2 \pi^2 Q^2 (2.24 \sigma_a)4 \Delta K^{-4} \quad 19$$

dc/dN was determined using the experimental parameter C_p.

Finally, the critical pit size $2C_{cr}$ was calculated from stress intensity factor relation:-

$$2C_{cr} = (2Q/\pi\alpha) (\Delta K_p /2.24\sigma_a)^2 \quad 20$$

This model was material and environment dependant and the aspect ratio was assumed as constant.

Conclusions derived from the investigation reveal that; corrosion pit size increased in proportion to $t^{1/3}$ where t is the time. The effect of stress level on pit growth rate was not so pronounced at low stress levels. The critical pit condition at which the transition into a crack, from a pit could be evaluated, using the stress intensity factor range. The critical pit condition was $(\Delta K)_p$ = 1.2 MPa $\sqrt{m}$ for low alloy steel in 90°C deionised water. The fatigue crack propagation from a pit occurred at ΔK below the threshold condition ΔK_{th} of a long crack [68].

Kawai and Kasai[69] proposed a model based on an estimation of allowable stresses under corrosion fatigue conditions, with an emphasis on pitting. The study entitled Considerations of

Allowable Stress of Corrosion Fatigue (Focused on the Influence of Pitting), discusses long life corrosion fatigue behaviour. The importance of quantification of corrosion pit depth as a function of service period and corrosion pit modelling is also emphasised. The study also illustrates that a corrosion pit can be treated as an elliptical crack with the same depth and surface length as a pit. A method of determining a reasonable allowable stress in corrosion fatigue is proposed. The investigation utilises an actual example in an attempt to illustrate the results.

The model used was based on experimental data generated on stainless steel. The authors studied rotating bending corrosion fatigue strength in the high cycle region of fatigue and corrosion fatigue crack growth behaviour including the threshold stress intensity factor range $\Delta K_{th,CF}$. New allowable stresses based on allowable stress intensity threshold were proposed:-

$$\Delta\sigma_{all} = \frac{\Delta K_{all}}{F\sqrt{(\pi\, h_{max})}} \qquad 21$$

where, ΔK_{all} can be determined from da/dN vs. , ΔK plot for a material, h_{max} is the maximum pit depth and f is a geometric factor.

Using this model, allowable stress in relation to corrosion fatigue threshold as a function of time could be estimated. Again, this model is only valid for the conditions in which LEFM concepts are applicable and is material dependant [69].

Müller[70]looked at Theoretical Considerations on Corrosion Fatigue Crack Initiation. The investigation was based on corrosion kinetics and fracture mechanics, and determined quantitatively the corrosion fatigue life for three different types of corrosion behaviour. The three corrosion conditions reviewed were general corrosion, passive corrosion and localised corrosion, otherwise known as pitting corrosion. Derivations of the corrosion fatigue initiation life time for

the three corrosion conditions were completed. Since the main interest of the literature review has been on corrosion pitting, which is the area reviewed herein.

During corrosion fatigue under pitting conditions, pits grow into the material. If such a pit reaches a critical depth d_{CL}, a fatigue crack can develop. The critical pit depth is a function of the applied stress range. In order to model pitting corrosion, certain assumptions were made:-

- Constant corrosion condition (i.e. pH concentration of bulk solution),
- Constant alternating load $d\Delta P/dt = 0$, and
- Constant loading frequency $dv/dt = 0$.

The critical pit depth d_{CL} depends on applied stress range $\Delta\sigma_0$, cyclic yield strength σ_{FC}, fatigue crack growth threshold ΔK_0, and the geometry of the specimen, expressed in terms of a geometrical factor G. Elastic-plastic fracture mechanics calculations based on the Dugdale model can be used to calculate the critical pit depth, d_{CL}, by the following equation:-

$$d_{CL} = \frac{\mathrm{COS}\,(\pi\Delta\sigma_n/\,4\sigma_{FC})\,\pi\Delta K_0^{\,2}}{32G^2\sigma_{FC}2\,[1-\mathrm{COS}(\pi\Delta\sigma_n/\,4\sigma_{FC})]} \qquad 22$$

Therefore the numbers of cycles to initiate a corrosion fatigue crack under pitting conditions, N_i:-

$$N_i = v\,[\,t_0 + (d_{CL}/C_2)^{\,1/\beta}] \qquad 23$$

Where v is the test frequency, t_0 is the incubation period for pit nucleation and C and β are experimental constants. The dependence of N_i on the applied stress range $\Delta\sigma_0$, calculated according to the above equation (eq 20) is schematically shown in figure 2.79. The figure shows that under pitting conditions no corrosion fatigue limit exists. For Ni $\leq v.t_0$ the influence of corrosion on the fatigue life disappears. The life time is then determined by the air fatigue behaviour. Comparing the modelled data with that of experimental results showed that there exists a good agreement, with all the data falling within an order of magnitude [70].

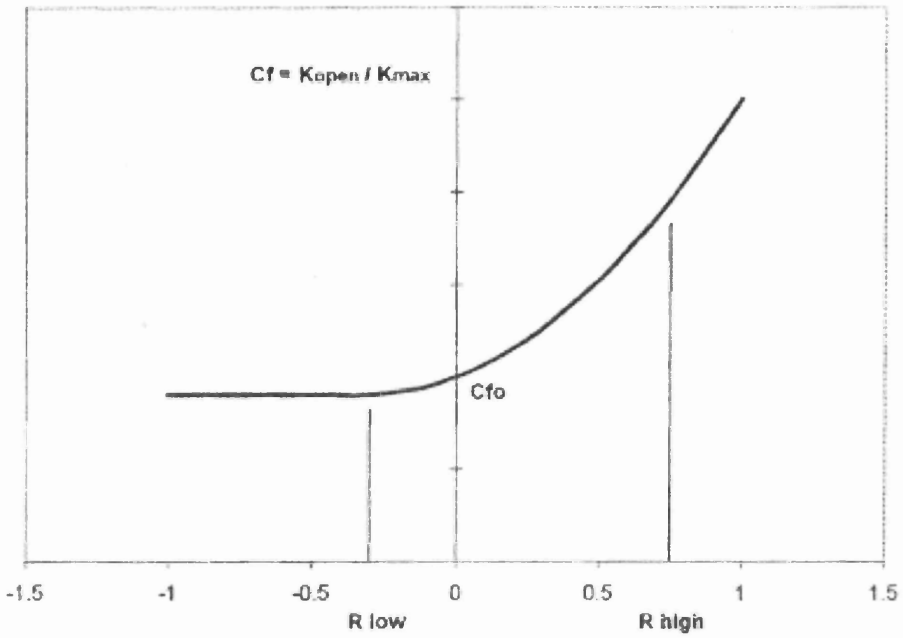

Figure 2.61 Closure factor vs. stress ratio (AFGROW)

Figure 2.62 Mirage fighter.

(a)

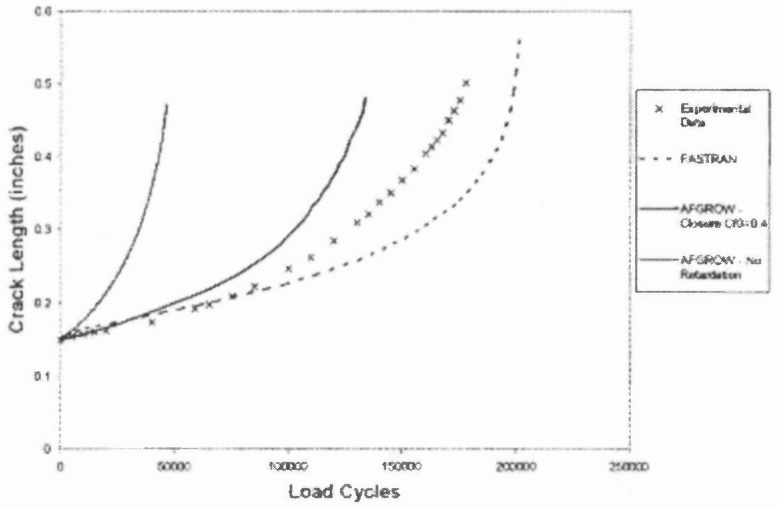

(b)

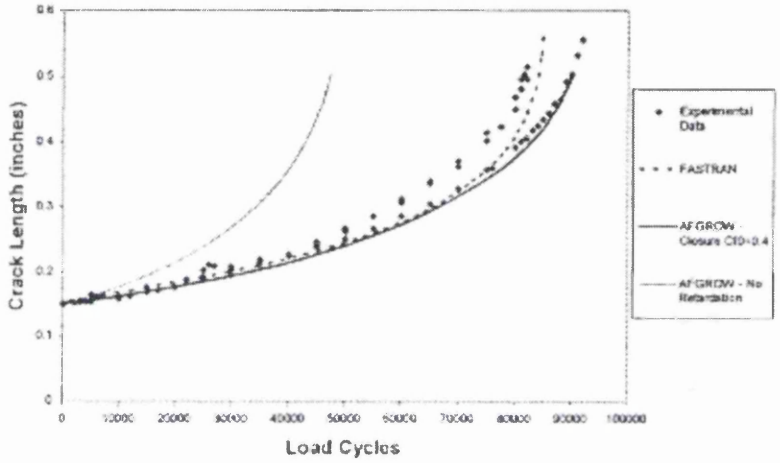

(c)

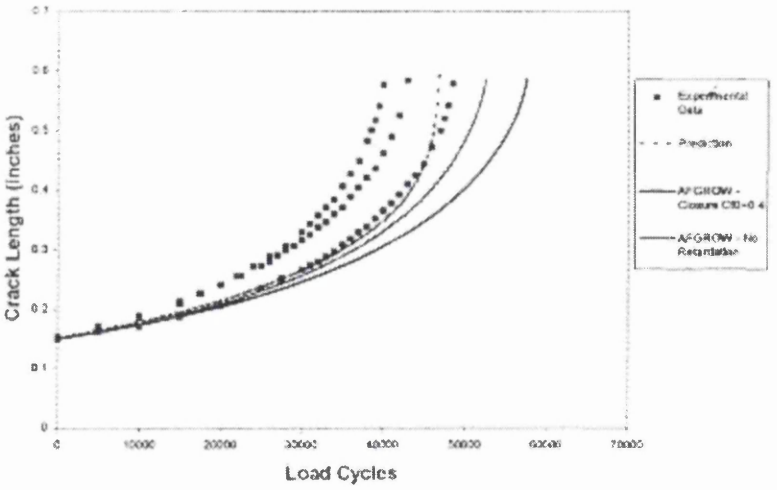

Figure 2.63 AFGROW and FASTRAN predictions for the Mirage spectrum at (a) 8.5G, (b) 7.5G and (c) 5.0G.

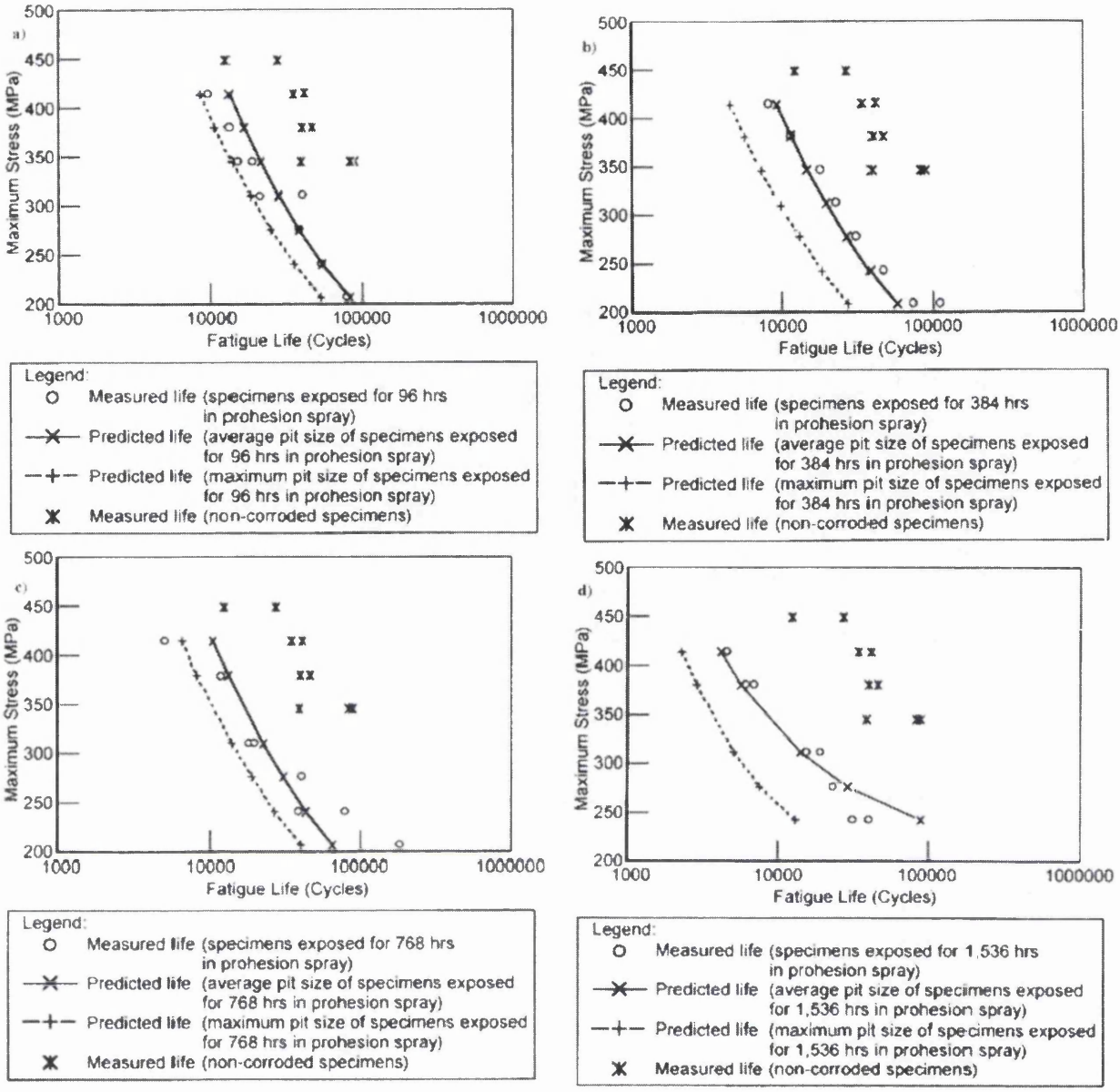

Figure 2.64 Predicted and measured lives of 7075-T6 exposed for various times in a prohesion spray.

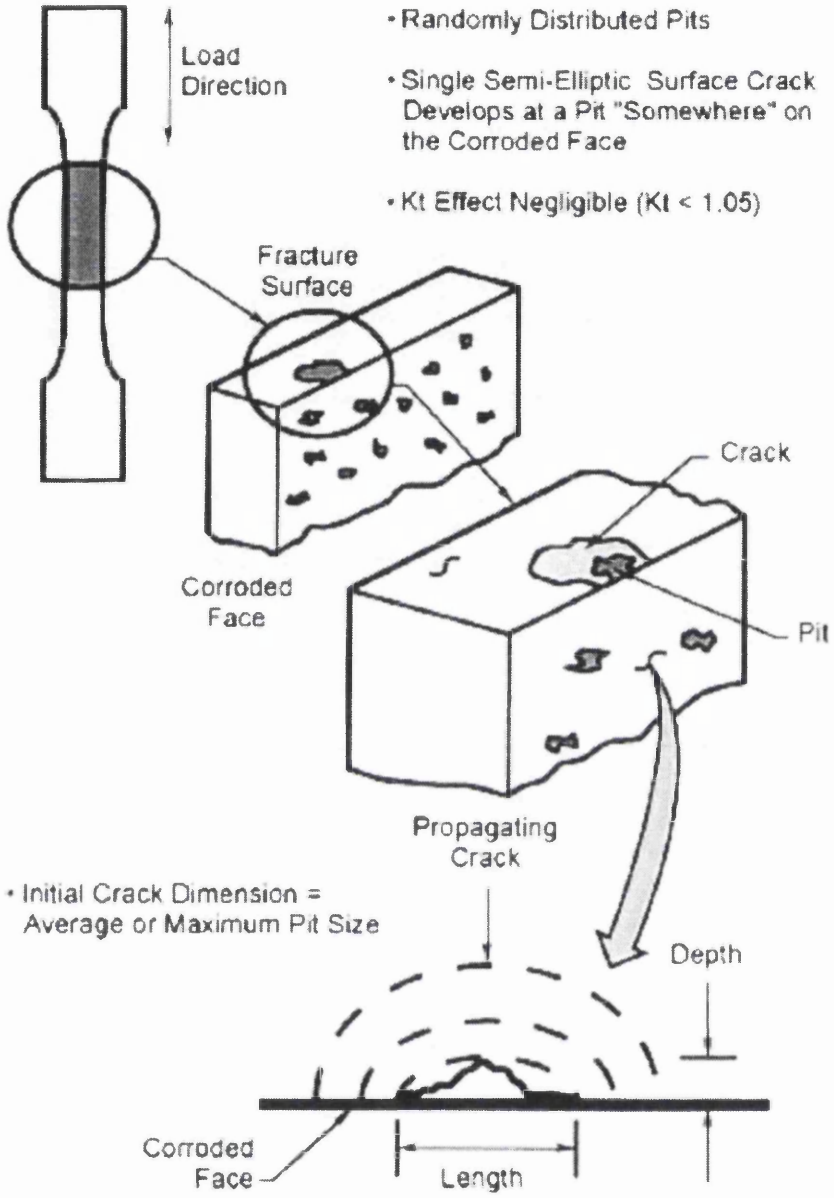

Figure 2.65 Illustration of the assumptions used in the modelling of fatigue crack growth and life prediction.

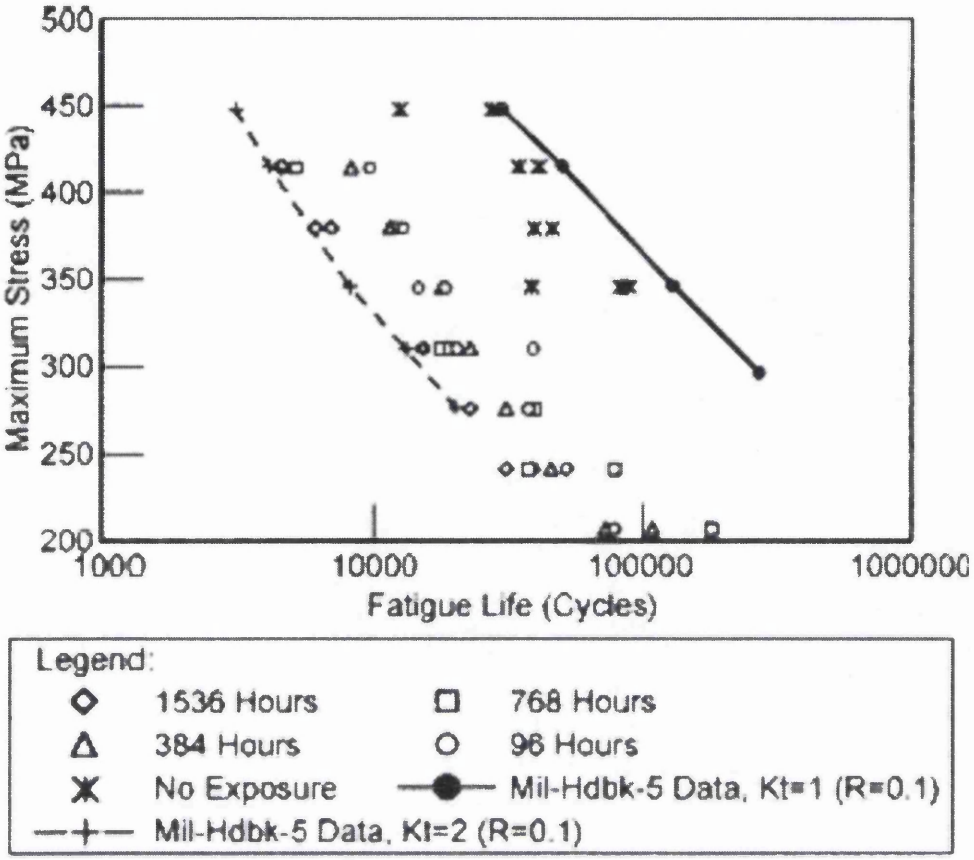

Figure 2.66 Fatigue properties of corroded, 2 mm thick 7075-T6 compared to design data.

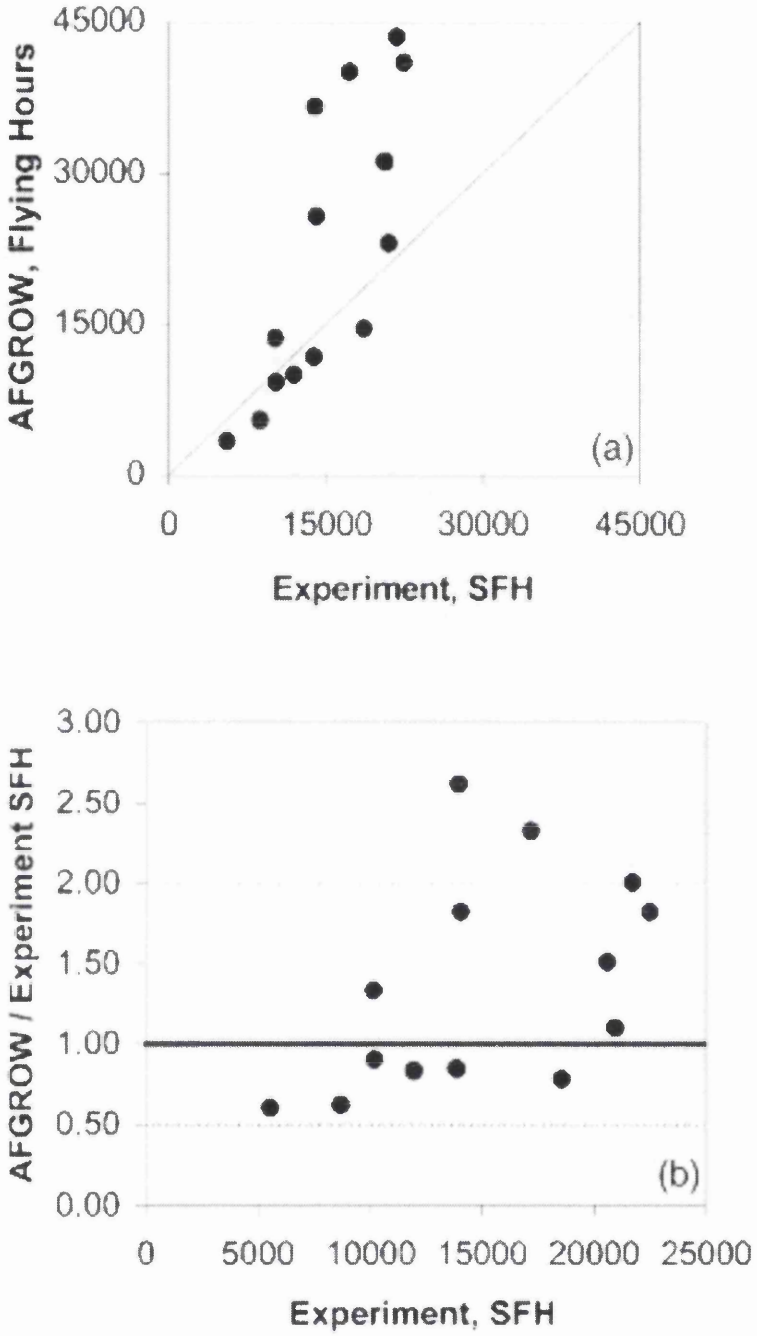

Figure 2.67 Comparison between experimental and AFGROW predicted fatigue lives (a) absolute values, and (b) relative values.

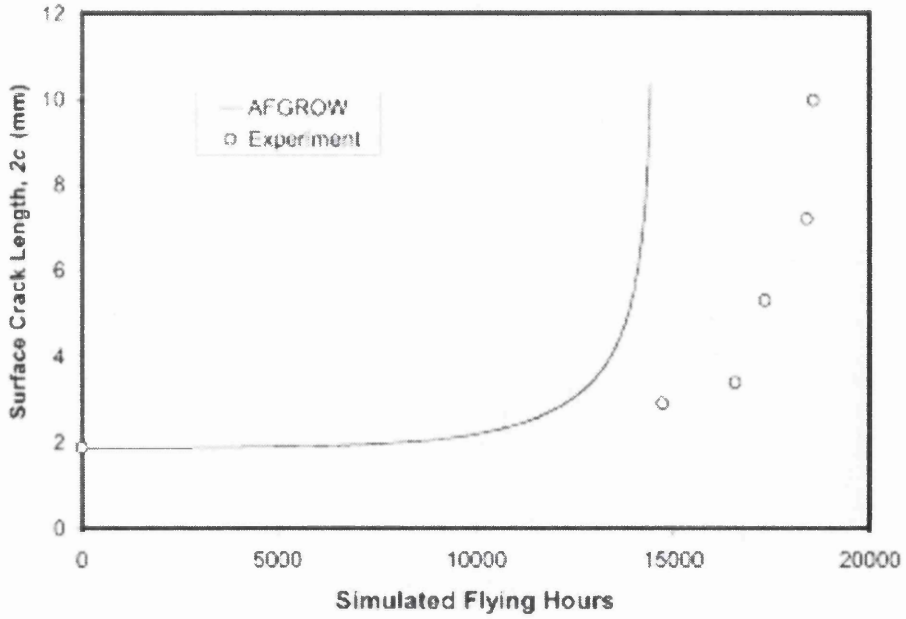

Figure 2.68 Development of a surface crack initiated at a corrosion pit. Experimental observations compared with AFGROW prediction.

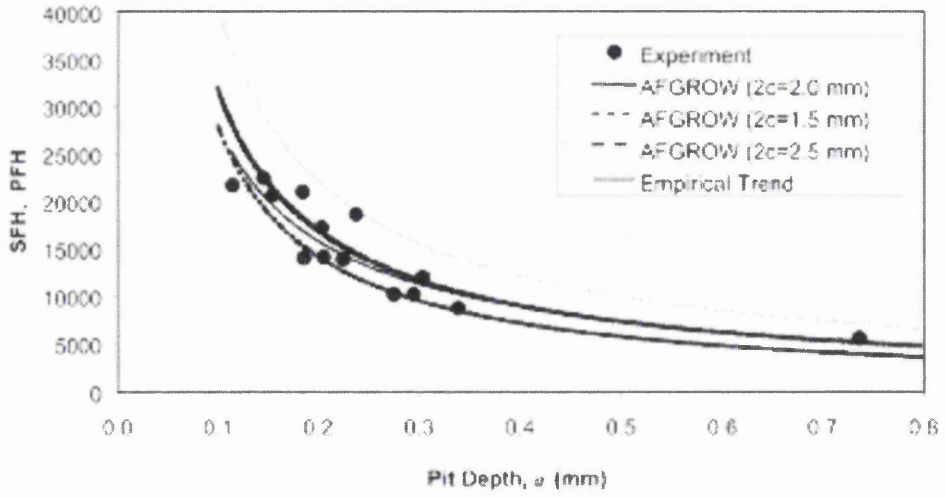

Figure 2.69 Comparison of AFGROW life predictions (predicted flying hours, PFH) with experimental data (SFH) based on average surface widths of corrosion pits.

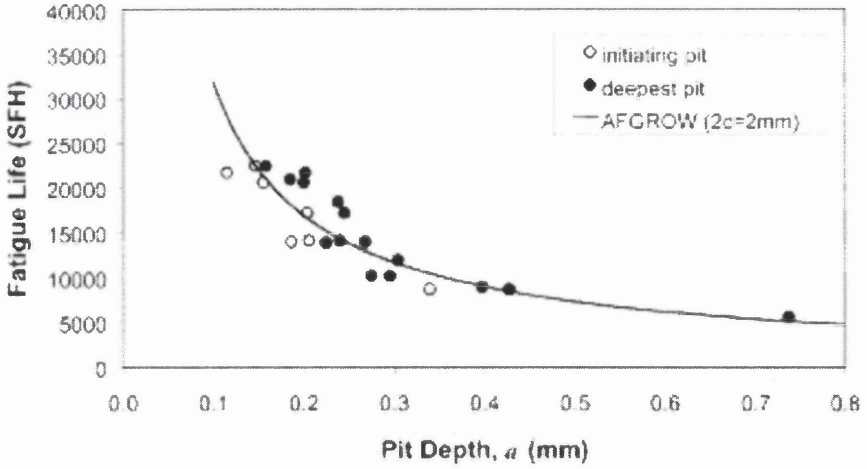

Figure 2.70 Comparison of experimental fatigue lives with AFGROW predicted lives for pitting corrosion specimens subjected to transport loading spectrum.

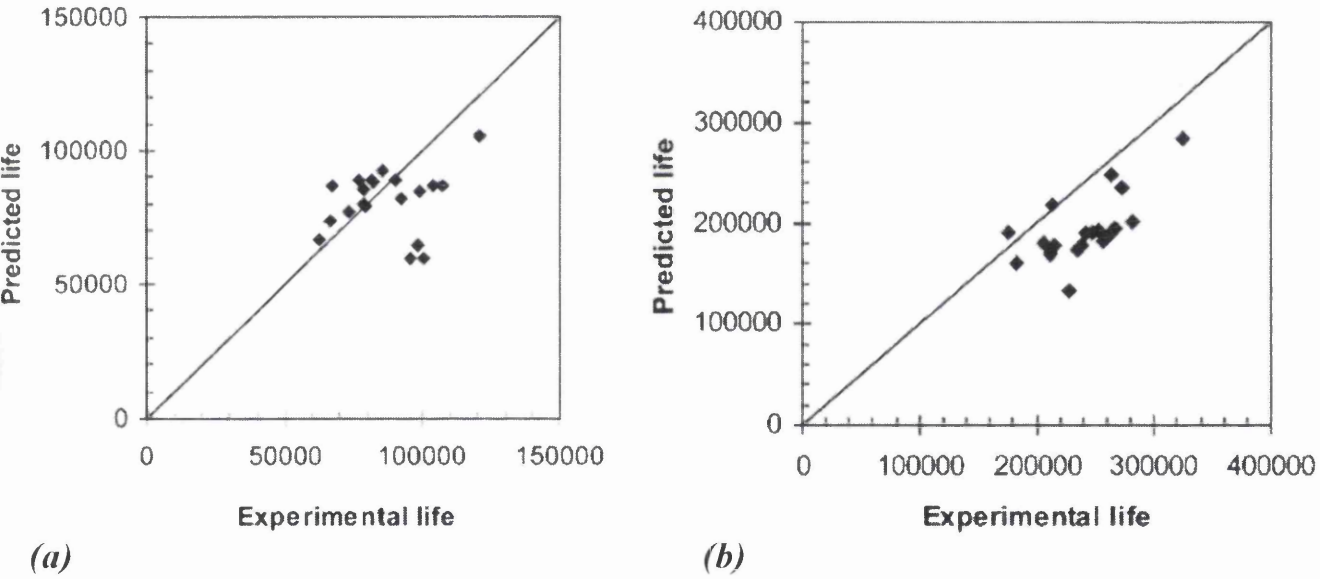

Figure 2.71 Comparison of experimental and AFGROW lives together with measured starting pit sizes. (a) Constant amplitude loading, (b) Variable amplitude loading.

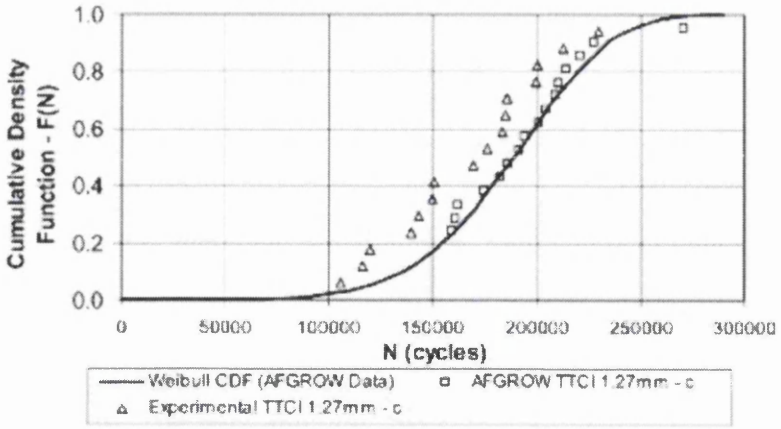

Figure 2.72 Cumulative distribution of number of cycles to achieve 1.27 mm based on AFGROW EIFSD, for constant amplitude loading results.

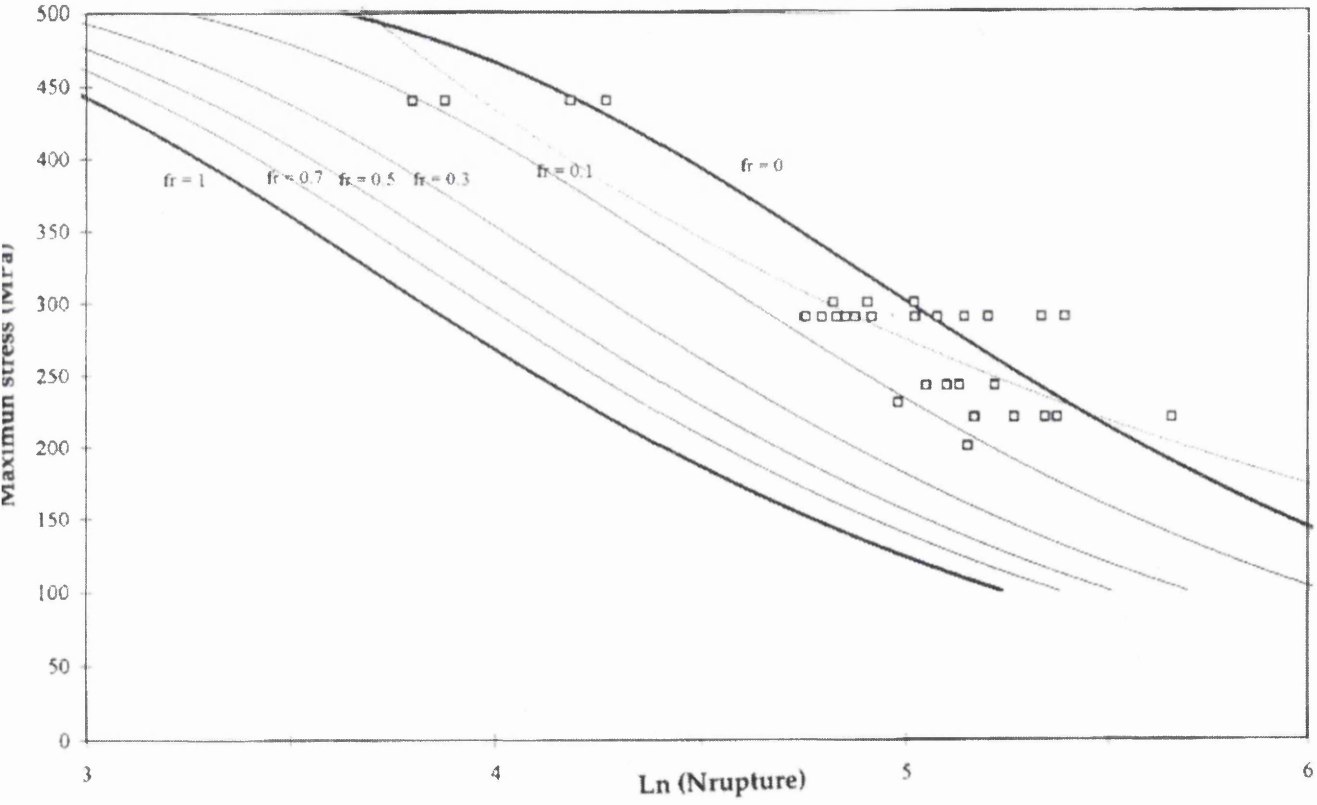

Figure 2.73 Theoretical S-N curves for different volume fractions of recrystallised grains, fr.R = 0.1 σr = 535 MPa, χt = 0.76 and αt = 0.05. Bold lines on chart correspond to volume fractions fr = 0 and fr = 1, □: experimental values..... fitted curve.

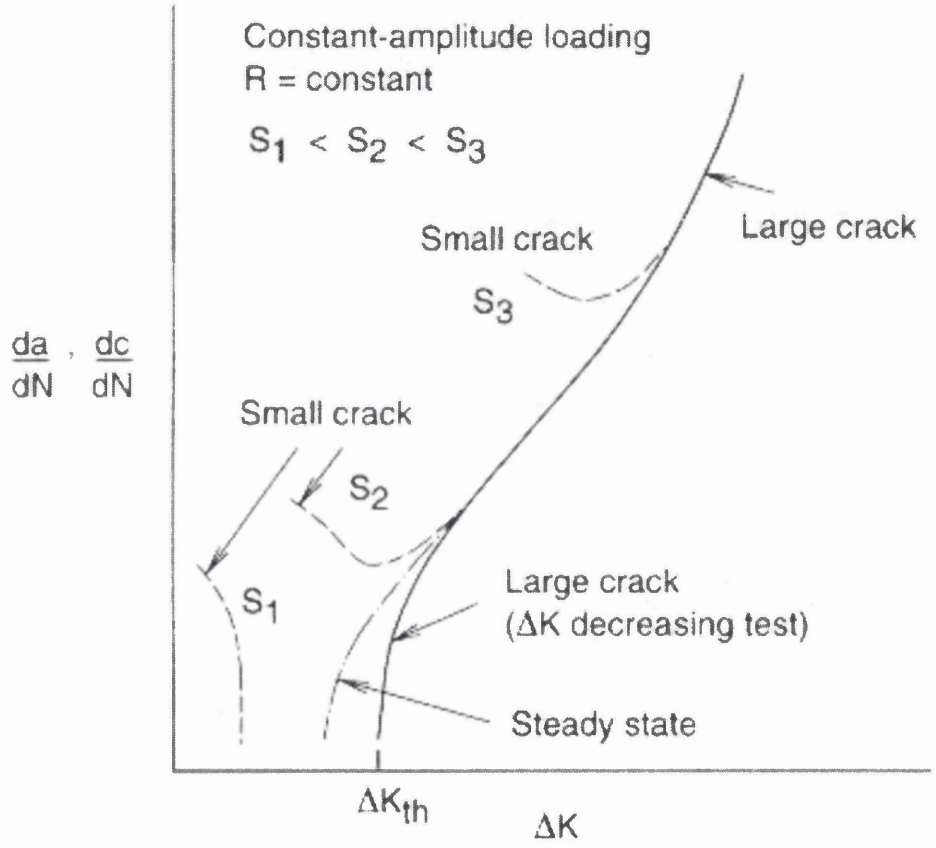

Figure 2.74 Typical fatigue crack growth behaviour for small and large cracks.

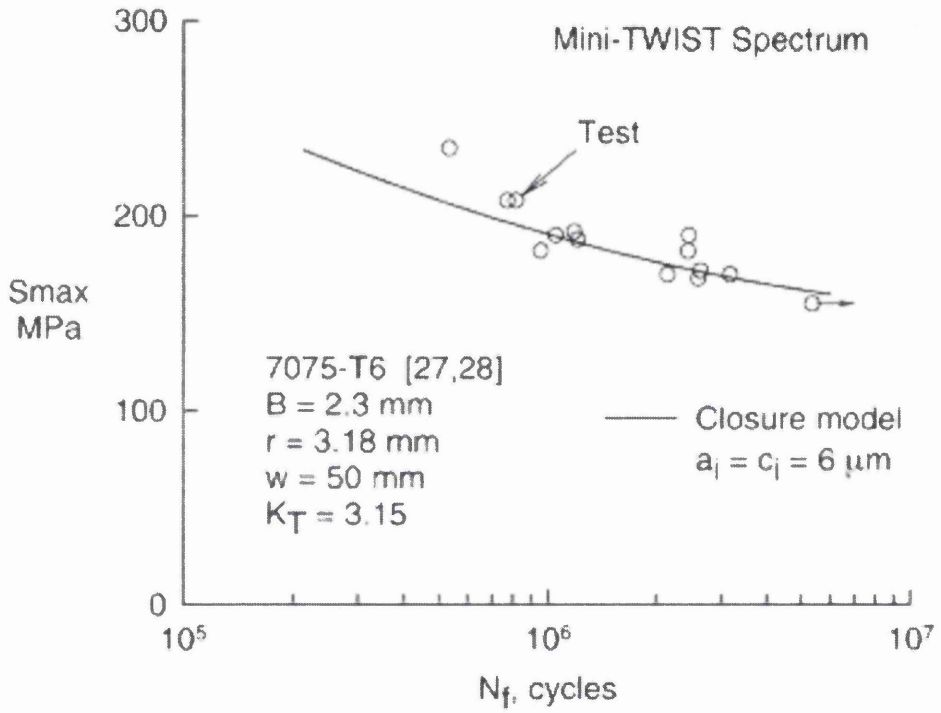

Figure 2.75 Measured and predicted fatigue lives for 7075-T6 aluminium alloy SENT (Single Edge Notch Tension) specimens under mini-TWIST spectrum loading.

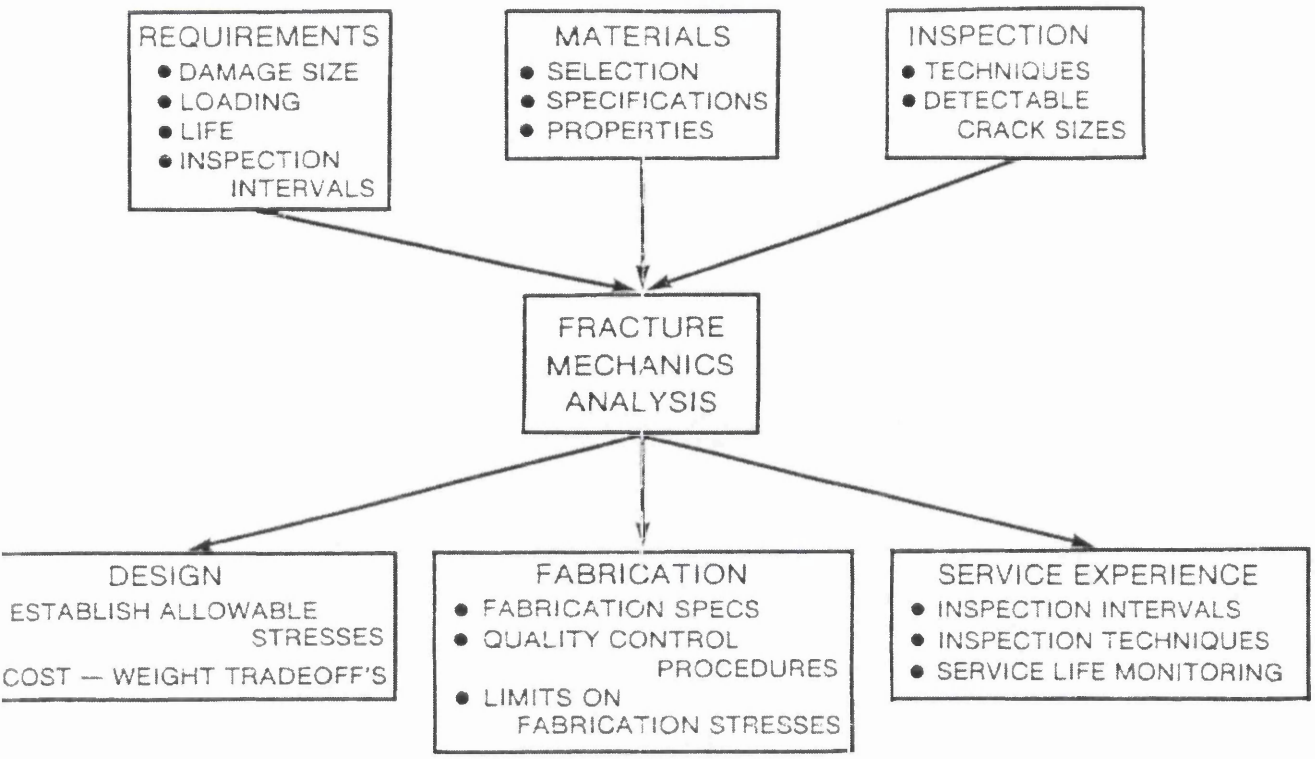

Figure 2.76 Elements of fracture mechanics based design methodology used in damage tolerant design of aircraft.

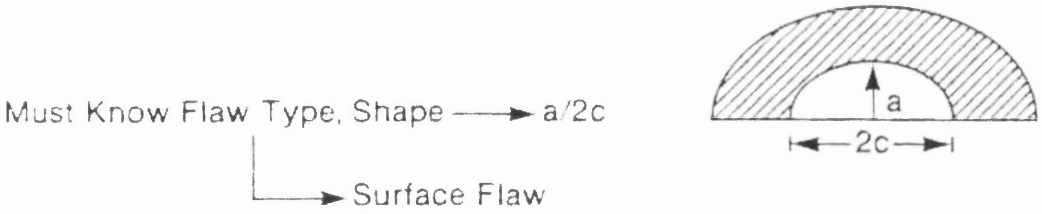

Figure 2.77 Corrosion pit within the material being modelled as a surface 'flaw'.

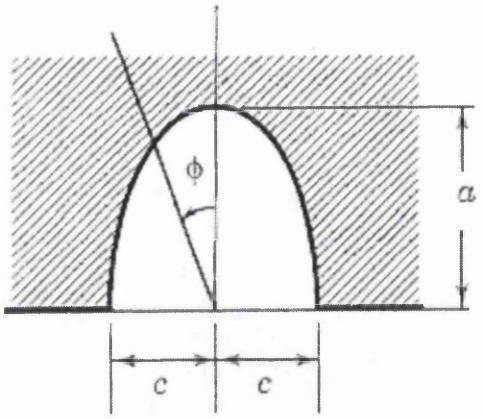

Figure 2.78 Schematic illustration of an equivalent semi-elliptical surface crack as modelled by Chen et al.

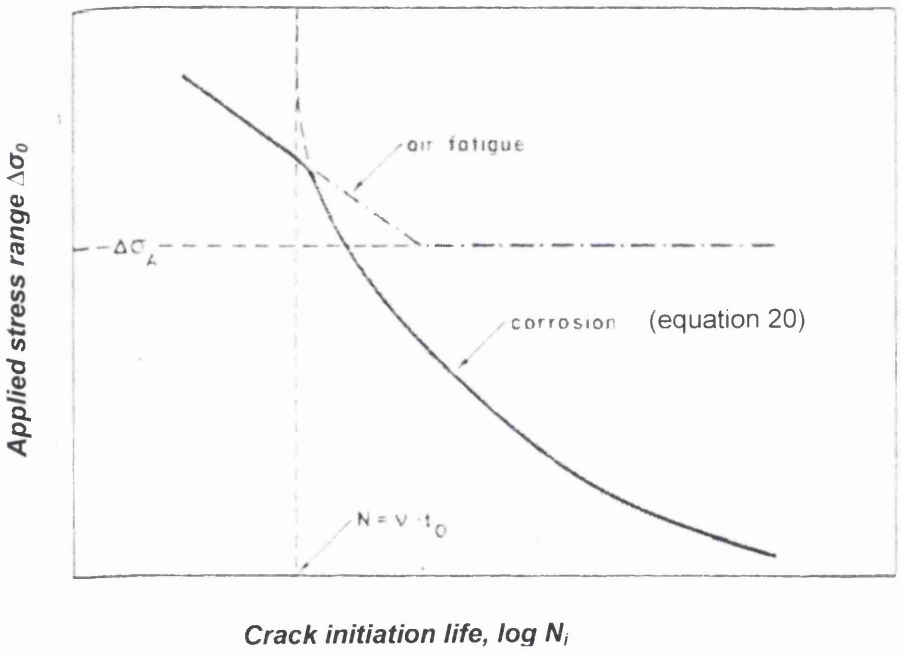

Figure 2.79 Corrosion fatigue crack initiation by pitting corrosion. Schematic representation of equation 20.

2.6 STRUCTURAL INTEGRITY OF PITTING CORROSION IN AIRCRAFT STRUCTURES (SICAS): GENERAL OVERVIEW.

The Structural Integrity Assessment of Pitting Corrosion in Aircraft Structures (SICAS) international research programme was commissioned by BAE SYSTEMS, Commonwealth Scientific and Industrial Research Organisation (CSIRO) and the Defence Science and Technology Organisation (DSTO). The following literature details the project objectives, a snapshot of the test results and some of the conclusions reached. The main focus of the programme was to manage corrosion issues in aircraft structures by developing a component lifing system that could be integrated into service. The programme was extensive and a large amount of the information unearthed is commercially in confidence.

2.6.1 Introduction.

Corrosion accounts for a major proportion of maintenance and support costs of aircraft, and the effect of corrosion on structural integrity is very poorly understood. Currently, efforts are focused towards the characterisation, prevention and repair of pitting corrosion damage on the fatigue life of components in aerostructures. A trend towards the damage tolerance design philosophy for military aircraft has enhanced the interest in the Equivalent Initial Flaw Size (EIFS) concept as a means for defining initial (at build) fatigue quality. A collaborative programme by the above partners was established to investigate the use of the Equivalent Initial Flaw Size (EIFS) concept as a metric for the inclusion of the susceptibility to pitting corrosion, into the quantification of initial fatigue quality, and in order to enhance the design process.

The Al alloy 7010-T7651 which is used extensively in the airframe of the BAE SYSTEMS Hawk Mk 127, selected as the RAAF Lead-in-Fighter, was used to conduct the study. Methods were developed to simulate service pitting corrosion, and to identify the critical characteristics of in-service pitting corrosion which control the magnitude of the EIFS and its distribution, and the viability of the approach. A large test matrix was used to gain a good understanding of the EIFS and damage characteristics and distributions and the programmes

focus was linked in with standardised 'as per aircraft build' surface treatments. The defined methodology allowed the generation of design data and significant cost savings exploited from increased effectiveness of characterising materials/coatings combinations which also reduce the costs of generating fatigue design data for future aircraft [72].

2.6.2 Objectives.

In order to undertake and validate the applicability of an Equivalent Initial Flaw Size (EIFS) concept to assess the impact of pitting corrosion on fatigue strength, certain objectives had to be determined. The objectives were as follows:-

- Identify critical characteristics of pitting corrosion which control the magnitude of the EIFS and its distribution.

- Incorporate pitting corrosion damage into aircraft structural Durability and Damage Tolerance Analyses (DADTA) by modelling the damage as an equivalent fatigue crack.

- Develop methods for simulating service pitting corrosion damage in aluminium alloys representative of aircraft in current military service.

- Evaluate methods for assessing pitting corrosion in aerospace aluminium alloys, in terms of the effects of such pitting on fatigue life.

- Minimise future testing by optimising the analytical design input.

2.6.3 Corrosion and Fatigue Results.

The main focus of the SICAS programme was to investigate the influence of corrosion pitting on fatigue through a chromic acid anodic film. Anodising is used to modify the surface of

the aluminium which significantly increases its corrosion and wear resistance. However, anodising is also thought to accelerate crack propagation at the initiation stage due to its inherently brittle structure. Anodising is an electrochemical process in which the oxide layer present on the surface of the aluminium material is artificially thickened. Artificially produced anodised layers have more complex microstructures than naturally occurring or thermal layers. Figure 2.89 illustrates the intricate structure of the anodised layer. Clearly the layer is divided into two regions. The first, known as the base layer, is adhered to the base material and provides the corrosion resistance. The second layer is columnar and consists of a large number of hexagonal pores and is generally thought to be the region which reduces fatigue endurance.

Corrosion pitting was introduced into the anodised material via a pre defined protocol. The protocol was designed to introduce pits representative of in-service examples and provided circular pitted areas, approximately 15 mm in diameter, on one face of the 'dog-bone' test pieces. An illustration of the test piece design can be seen in figure 2.90. A corroding solution consisting of 3.5% NaCl was used. Glass tubes were adhered to the test specimens using a stopoff lacquer. The corroding solution was poured into the glass tubes, sealed from the air and left to corrode for a total of eight weeks (figure 2.91). Figure 2.92 illustrates an example of the corroded surface. Maximum pit depths after eight weeks corrosion were measured at approximately 150 μm, with an average depth of 95 μm.

Subsequent to corrosion exposure, specimens were fatigue tested at constant amplitude, employing three stress ratios; -0.3, 0.1 and 0.5. Tests were conducted under a frequency of 10 Hz using a sinusoidal waveform. Complete specimen rupture was chosen as the criterion for failure. Two laboratories were chosen to complete the comprehensive matrix of fatigue testing; these were the IRC at the University of Wales, Swansea and the DSTO in Melbourne, Australia. Servo-hydraulic test facilities under closed loop computer control and utilising hydraulic wedge grips are employed within each laboratory. All testing was performed at a constant room temperature of 20°C and controlled humidity conditions in excess of 90 % Relative Humidity (RH). Humidity conditions were controlled since testing was carried out at two separate locations and it is widely documented that humidity can significantly effect fatigue lives.

Initial fatigue assessments were undertaken to scope the 'baseline' fatigue response of the material subject to three specimen conditions; as-machined, as-machined & edge peened and anodised & corroded. Peak stress levels were employed to obtain failure lives in the region of 10^3 to 10^6 at a single stress ratio of 0.1. All tests were conducted initially at 40% RH. The resulting S-N curve can be seen in figure 2.93. From this baseline response, two stress levels were subsequently chosen for a series of repeat tests providing fatigue lives in the order of 10,000 and 500,000 cycles (460 and 270 MPa respectively). The objectives of this series of tests was to ascertain the typical scatter to be expected in the measured fatigue life, determine a mean EIFS value and also allow for a comparison between data provided by the different test laboratories. To assure that semi elliptical cracks rather than edge cracks initiated and grew to failure, edge peened specimens were employed during the repeat series. The relative humidity level was set to 90% RH, and employed throughout the remaining test programme.

The main programme of testing involved anodised specimens subjected to the predefined corrosion protocol. Twenty five repeat tests were conducted at four designated peak stress conditions for each of the three stress ratios in order to characterise the EIFS distribution (EIFSD) as well as the mean EIFS. Appropriate stress levels set to meet target lives were determined from the S-N curve seen in figure 2.93. The curve also demonstrates that, relative to the baseline data, the introduction of corrosion damage clearly reduces fatigue endurance, particularly for lower stress levels where the total cyclic lives are dominated by the initiation stage under constant amplitude loading. The four peak stress condition employed to evaluate the effect of corrosion pitting on fatigue were 380 MPa, 270 MPa, 210 MPa and 160 MPa. These peak stress conditions yielded cyclic lives between 10^3 and 10^6 for the evaluated stress ratios as illustrated by the S-N plot in figure 2.94, which encompasses all the repeat test data. It can be seen from the reported data that the stress ratio of 0.5 has less of an effect on fatigue life when compared to -0.3 and 0.1, suggesting that the higher stress amplitudes noticed with -0.3 and 0.1 are more damaging.

In support of the comprehensive matrix of repeat testing on the anodised and corroded specimens, a large package of Fatigue Crack Growth (FCG) rate testing was completed. The FCG rates of the material were evaluated for the three stress ratios (-0.3, 0.1, 0.5) using a

complex Marker Banding technique for the 'dog-bone' specimens and Centre Crack Tension (CCT) specimens. The crack growth rates generated for each stress ratio was used as an input in the software program AFGROW to generate predicted lives.

The marker band spectrum used in the SICAS work derived from work conducted at the National Research Laboratory of Holland (NLR) and is designed to produce distinct marks on the fracture surface of samples while being as close as possible to constant amplitude. In addition, it produces alternating marker bands consisting of 6 lines and 4 lines on the fracture surface, which allows a degree of error correction in the collection of marker band data. If, for example, during testing two 4 line marker bands are found then a 6 line marker band can be expected to be located between them and vice versa. The marker band spectrum is as follows:

1. M cycles at σ_{max}.
2. 4 repeats of:
    a. 100 Cycles at 80% σ_{max}
    b. 10 Cycles at σ_{max}
3. M Cycles at σ_{max}
4. 6 repeats of:
    a. 100 Cycles at 80% σ_{max}
    b. 10 Cycles at σ_{max}
5. Return to beginning.

The variables σ_{max}, the maximum stress, and M, the number of cycles between marker bands, therefore define the marker band cycle. The minimum load (σ_{min}) in each cycle was the product of the load ratio (R) and σ_{max} and, therefore, remained unchanged for the entire test. Figure 2.95 illustrates the technique used to produce marker bands, while figure 2.96 shows the appearance of marker bands on the fracture surface.

The results received highlighted that the marker band data collected was not sufficient to produce a dataset that would be accepted by the United States Air Force (USAF) prediction software AFGROW. This occurred as the slope of the data collected at R = -0.3, 0.1 and 0.5

differed, as illustrated by figure 2.97. This caused the fitted curves obtained at different R values to cross, which AFGROW will not accept. This made it necessary to enforce a slope upon the fitted curves. Given that a far larger number of data points were collected at R = 0.1 versus the other series the slope of the fit to the 0.1 data was enforced on the remaining data. This produced a combined dataset that could successfully be entered into AFGROW.

The CCT test matrix comprised of fatigue crack growth rate tests undertaken at ambient temperature, at the R values of 0.1, 0.5, and -0.3, and at the relative humidities of 30%RH and 90%RH. From the received results it was shown that increased humidity has a marked effect upon the fatigue crack growth rates in the stage II steady crack growth regime across all the R ratios tested. Noticeably for R ratios of 0.1 and 0.5 at 25°C, the increase in humidity from 30 to 90% relative humidity results in an increase by 3 orders of magnitude of the Paris Coefficient, and a decrease by approximately one half of the Paris Exponent. The fatigue crack growth curves for all three R levels at 25°C and 90% RH can be seen in figure 2.98.

Fractographic examinations of the fractured specimens enabled pit sizes and morphologies to be determined along with final crack profiles. The characteristics that were measured for each primary pit were depth, width and area, defined as shown by figure 5.10 in the results chapter. Measurements were made and recorded using a Scanning Electron Microscope (SEM). A pixel counting technique was used to calculate the pit area. Examples of a corrosion pits are visible in figure 2.99. Figure 2.100 has pit area and initial flaw size of the same area super imposed onto the image, appearing red and green respectively. The fracture surfaces of the material were typical of a high strength aluminium alloy, with areas of smoothness surrounding the initiating defect and an increase in roughness noticed as the distance from the defect increased. Certain specimens showed evidence of inter-granular etching, caused as a result of the high humid conditions. Fracture surfaces were noticed to be coated with a non-conductive corrosion film, which required removal before analysis using the SEM.

Fatigue striations were present on all examined coupons, although were not visible near the crack origin, but became clearer as crack growth increased. Transverse cracking was also observed on the majority of fracture surfaces and are characterised by the presence of small

voids in the fracture surface that are elongated in the long transverse direction of the material. An example of transverse cracking (white arrows) and multiple point initiation (red arrows) can be seen in figure 2.101. A selection of specimens also contained cracks that ran parallel to the applied loading direction. These cracks ranged from millimetres up to centimetres in size and were attributed to the stresses created by the straightening of the coupon under loading. A large number of coupons tested in the SICAS programme contained significant curvature along the length of the coupon and was introduced via the heat treatment process or possibly by machining.

2.6.4 Modelling.

The Equivalent Initial Flaw Size (EIFS) modelling carried out in SICAS used the AFGROW fatigue life prediction code. AFGROW was chosen due to its reliability, free availability and relative ease of use. It also can be driven from an external program, which allowed the development of a Microsoft Excel based program to seek the required EIFS values. This program, the SICAS EIFS Estimator, was the basis of all the constant amplitude EIFS calculations made in SICAS.

The basis of the EIFS model is that for any defect that can cause fatigue failure there must exist a fatigue crack that would produce the same fatigue life if exposed to the same loading. That is, if the actual defect was somehow replaced by the equivalent crack there would be no change in fatigue life. This is illustrated in figure 2.102. The EIFS is calculated by an iterative process by which an initial estimate of life is made and then refined by comparison to the observed life. The refinement of the estimated life is made by altering the size of the equivalent defect until the required accuracy is obtained. The schematic presented in figure 2.103 explains the inputs and process flow for AFGROW based EIFS modelling. Below is a brief description of several of the inputs required by AFGROW:-

- Material Model

  Basic mechanical properties such as yield stress, plain strain fracture toughness and modulus are required along with crack propagation rates, supplied here with the CCT specimens and Marker band data.

- Loading

  This is simply the loading spectra used. AFGROW requires the spectra to be inputted via a maximum stress and R ratio.

- Retardation Model

  AFGROW allows the use of closure models, although closure is considered insignificant for constant amplitude loading.

- Coupon Geometry

  The coupon geometry input to AFGROW describes the shape and size of the coupon plus the position of the fatigue crack. This is described in terms of a K-solution. The actual shape of the coupon is not required as it is represented by the input stress. In the case of SICAS the "centre semi-elliptic surface flaw" K-solution programmed into AFGROW was used. This is based on the work of Raju and Newman (1986).

- Defect Size

  The defect size is simply the width and depth of the semi-elliptical surface flaw input to AFGROW. This semi-elliptical flaw is the equivalent defect intended to represent the corrosion pit.

All of these inputs are entered into the AFGROW program, which subsequently makes an estimate of fatigue life. This estimate is then compared to the actual measured fatigue life. If the estimated life is within the specified tolerance of the actual life then estimation ends. If, however, the difference between the actual life and predicted life is outside the required tolerance then a two-stage search for the required EIFS size is commenced. These two stages are a linear search and a binary search.

The modelling element of the SICAS programme was a large and novel to a certain extent, therefore the outcomes of which are commercially sensitive and outside the boundaries of this research.

2.6.5 Additional Research.

A portion of work undertaken as a precursor to the SICAS programme was completed by ***Sharp et al*** [73] of DSTO and Aerostructures Technologies entitled Aircraft Structural Integrity: The Impact of Corrosion. The conclusions unearthed by the investigation spawned further study into the effects of corrosion pitting on the structural integrity of aircraft and the use of an EIFS type approach. The conclusions also encouraged further investigation into corrosion management techniques in military aircraft and subsequently were a major influence on the setup of the SICAS programme.

The paper discusses the development of methods, which allow aircraft structural integrity to be maintained under conditions where an airframe is deteriorating through corrosion. The paper also explores methods of assessing corrosion damage in terms of; which are compatible with existing life management approaches. The effects of pitting corrosion on aircraft structural integrity were established by DSTO in 1997. The research aimed to provide a basis for introducing corrosion into the approaches used to manage aircraft structural integrity in the Australian Defence Force (ADF). If successful, this approach would allow the ADF to minimise cost and risk of owning and operating aircraft in which corrosion might become a threat to safety or fleet viability. The RAAF have had numerous problems with pitting corrosion in structural components initiating fatigue cracking. Airworthiness requires immediate removal of any detectable corrosion damage. This in turn incurs extensive service times while components are repaired or even replaced. In the review the authors ask the question 'Can pitting corrosion be treated and left in place to a more suitable maintenance opportunity? To answer the question, a corrosion pit is equated to a crack of identical size which yields the same fatigue life. Firstly a number of issues need to be addressed:-

- What are the shape and dimensions of the corrosion pits?
- What is the pit distribution?
- Which critical pit metric can be correlated to fatigue life?
- Which way can the information gained be used in aircraft lifing models?

Fractographic investigation can determine the shape, size and distribution of pits, while a more complex approach is needed to establish correlations between pit metrics and fatigue life. The United States Air Force (USAF) has developed an EIFS parameter which they used in relating the effects of machining marks on fatigue life. The authors describe ways in which an Equivalent Precrack Size (EPS) approach relies on identifying the crack size which gives the same fatigue life as the corroded specimen. Two important factors of this approach are; the fatigue life of the cracked configuration is determined using a fatigue life prediction model and the EPS is not real and may bear no relationship to any physical dimension.

The investigation focused on the aluminium alloy 7050-T7451, used in structural components of the F/A-18 aircraft, see figure 2.104. The plate material is prone to corrosion damage, especially pitting. Deep pits can be seen to form due to its microstructural condition. The effects of pitting on a components integrity was examined via a large test matrix. 'Dog-bone' style specimens measuring 30 mm wide and 10 mm thick containing a 6mm diameter hole in the middle were tested subject to a 3.5% NaCl solution for 24 hours, the results of which can be seen in figure 2.105. From the S-N curve it is obvious that the corrosion pitting has two major effects on fatigue; a 50% reduction in the fatigue strength limit and a general reduction in fatigue life which varies with stress. The results shown here compare well with the work of Pao et al, which also examined the same alloy but a differing specimen configuration and corrosion period (>300 hrs). Post test analysis using electron microscopy revealed large corrosion pits, as shown by figure 2.106. Corrosion pits which caused fatigue cracking were measured on the fracture surface, creating a distribution of pit depths that initiated fatigue cracks. Figure 2.107 is a histogram illustrating the observed distribution. The investigation states that it is difficult to differentiate between pits and inclusions at depths below 100 μm, while depths above 380 μm generally are areas of pit clustering, where it is not possible to distinguish individual pits. Other pit metrics evaluated include; pit aspect ratio, pit tip radius, pit area and pit opening width.

The EPS modelling work carried out in the study was completed using the USAF fatigue crack growth program, AFGROW. Several specimen geometries were examined:-

- Double corner crack
- Double surface crack
- Double through crack

Pit depth was compared to EPS depth, with the best correlation being observed for the double corner crack geometry.

The paper also studied the effects of exfoliation corrosion on fatigue life. Again 7050-T651 was analysed, and was compared to aluminium 2024-T351. A circular region of the dog-bone specimen was exfoliated using EXCO solution. Exposure times ranged from 2 – 300 hrs. Damage was seen to vary from mild pitting at short exposure times to severe flaking at time approaching 300 hrs. Specimens were fatigue tested until fracture. Figure 2.108 is an example of exfoliation corrosion damage in 7075-T651 prior to 48 hrs exposure in EXCO.

The conclusions drawn from the study highlight the importance of modelling the fatigue impact of pitting and exfoliation corrosion. The study states that the next stage of the investigation is to determine whether the models described can be applied equally as well for spectrum loading on laboratory specimens and can the approach be extended to a wider range of materials or aircraft components. At the time of publishing, real aircraft structures were being tested containing laboratory produced corrosion. The study gave an invaluable insight into corrosion problems in aircraft structures and attempted to address the management issues concerned. Since the completion of the study, further advancements have been successfully completed such as the SICAS programme, which addressed a differing alloy. Spectrum loading conditions was also evaluated and the EPS technique further developed.

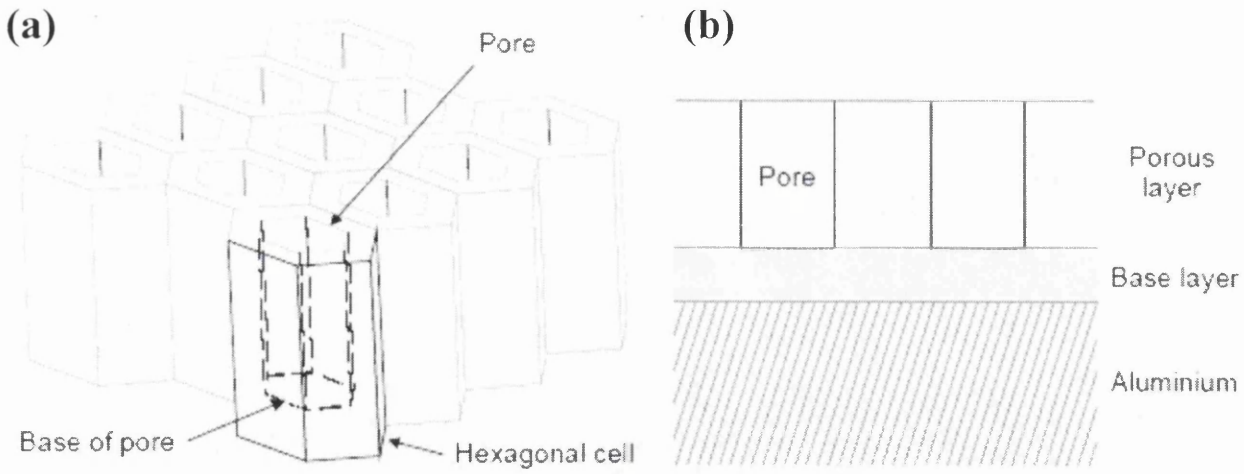

Figure 2.89 (a) Isometric view of an anodised layer showing the hexagonal cells with their central pores. (b) Cross-sectional view showing the aluminium alloy substrate, the continuous Al_2O_3 layer and the porous amorphous Al_2O_3 layer. Note that the size of the pores relative to the hexagonal cells is exaggerated for clarity.

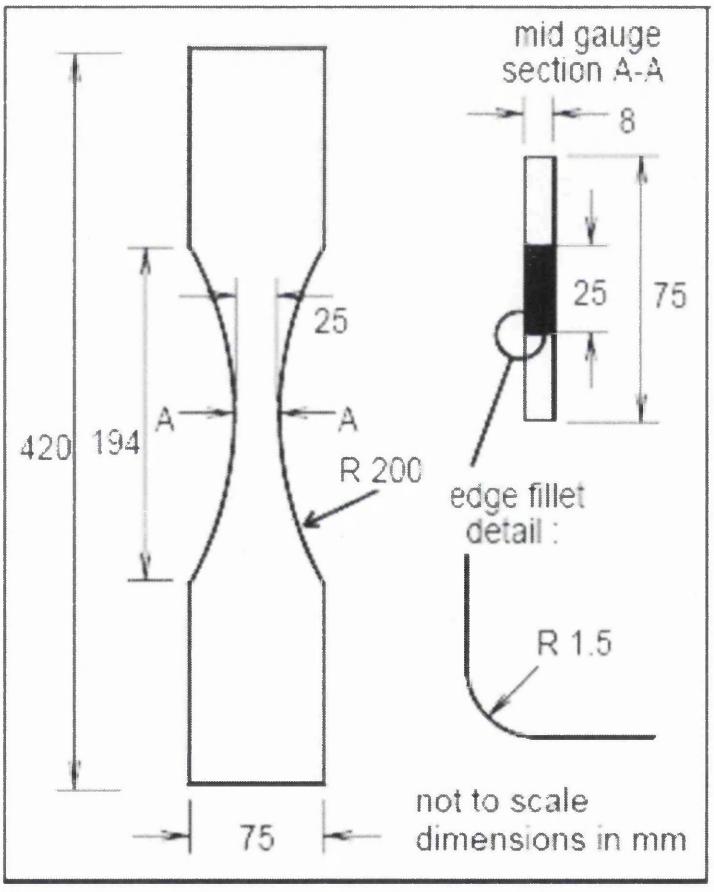

Figure 2.90 Dog-bone specimen design including dimensions.

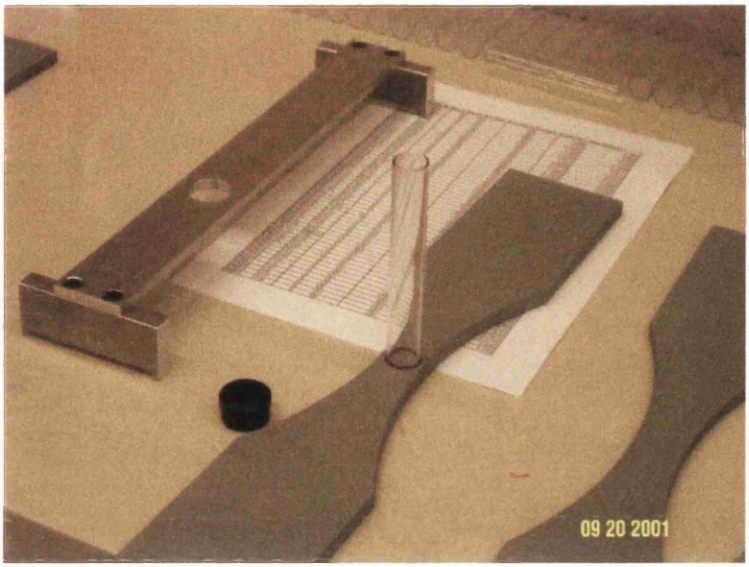

Figure 2.91 Glass tubes adhered to anodised 'Dog-bone' style specimens.

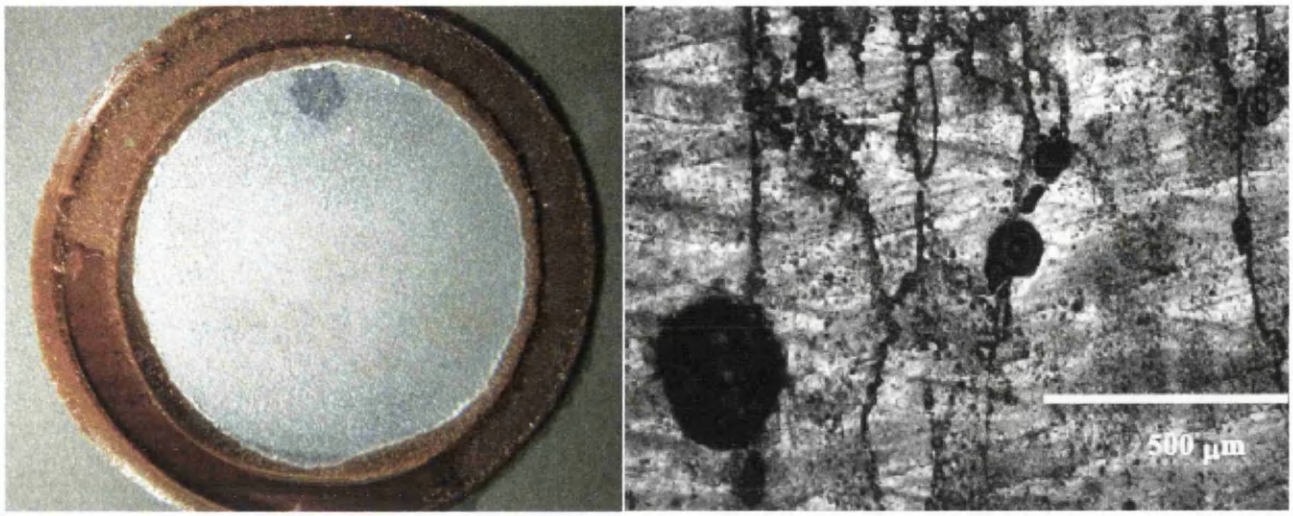

Figure 2.92 Typical corrosion surface after eight week sealed to air immersion

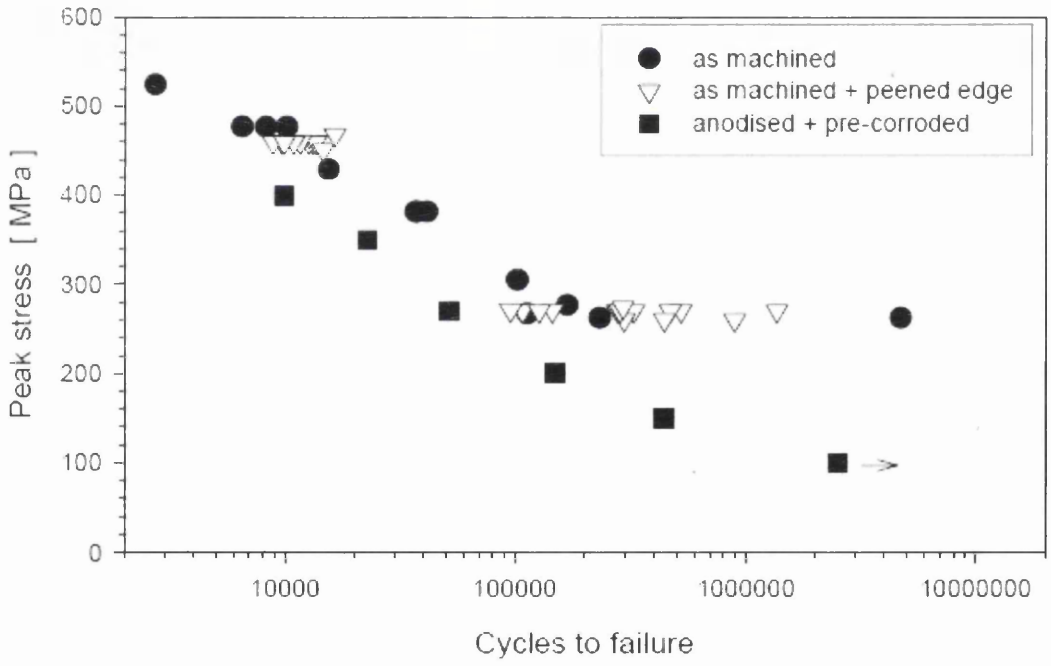

Figure 2.93 Baseline S-N curve for as-machined and anodised test coupons.

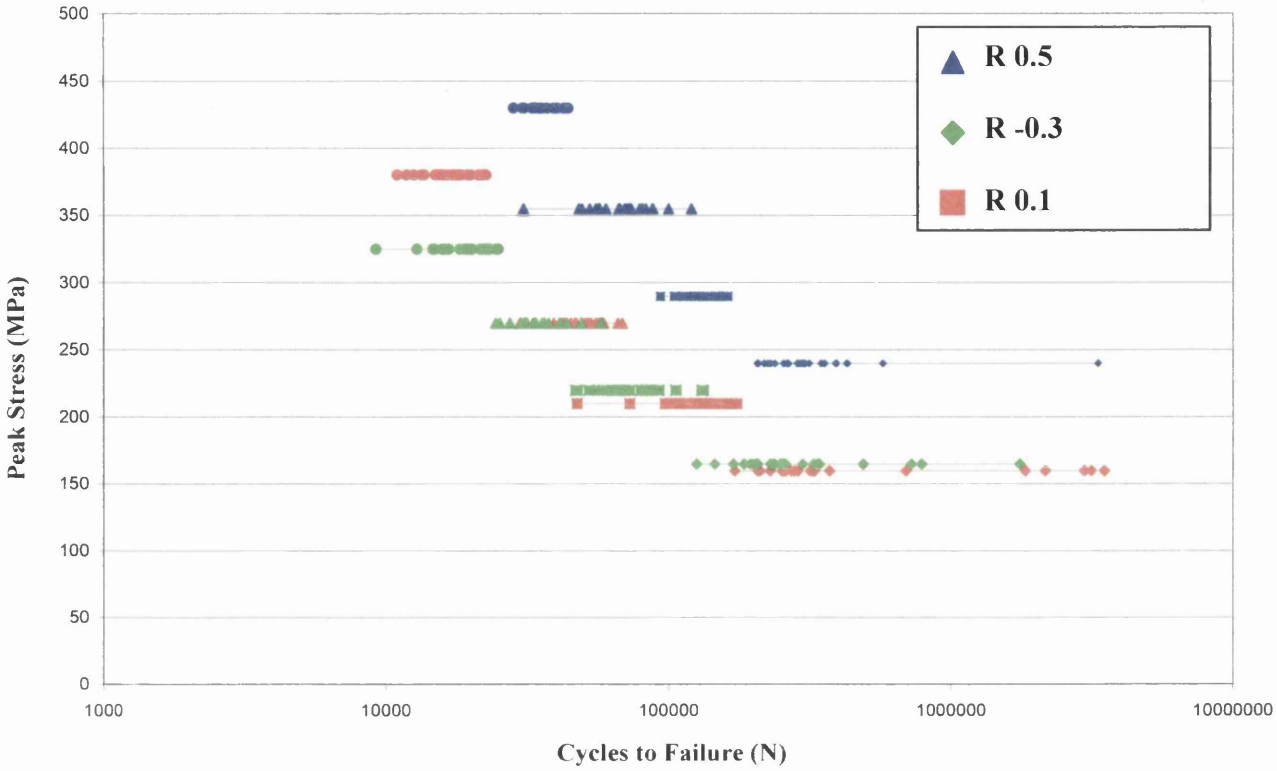

Figure 2.94 Peak stress as a function of cyclic life for the anodised and corroded 'dog-bone' specimens.

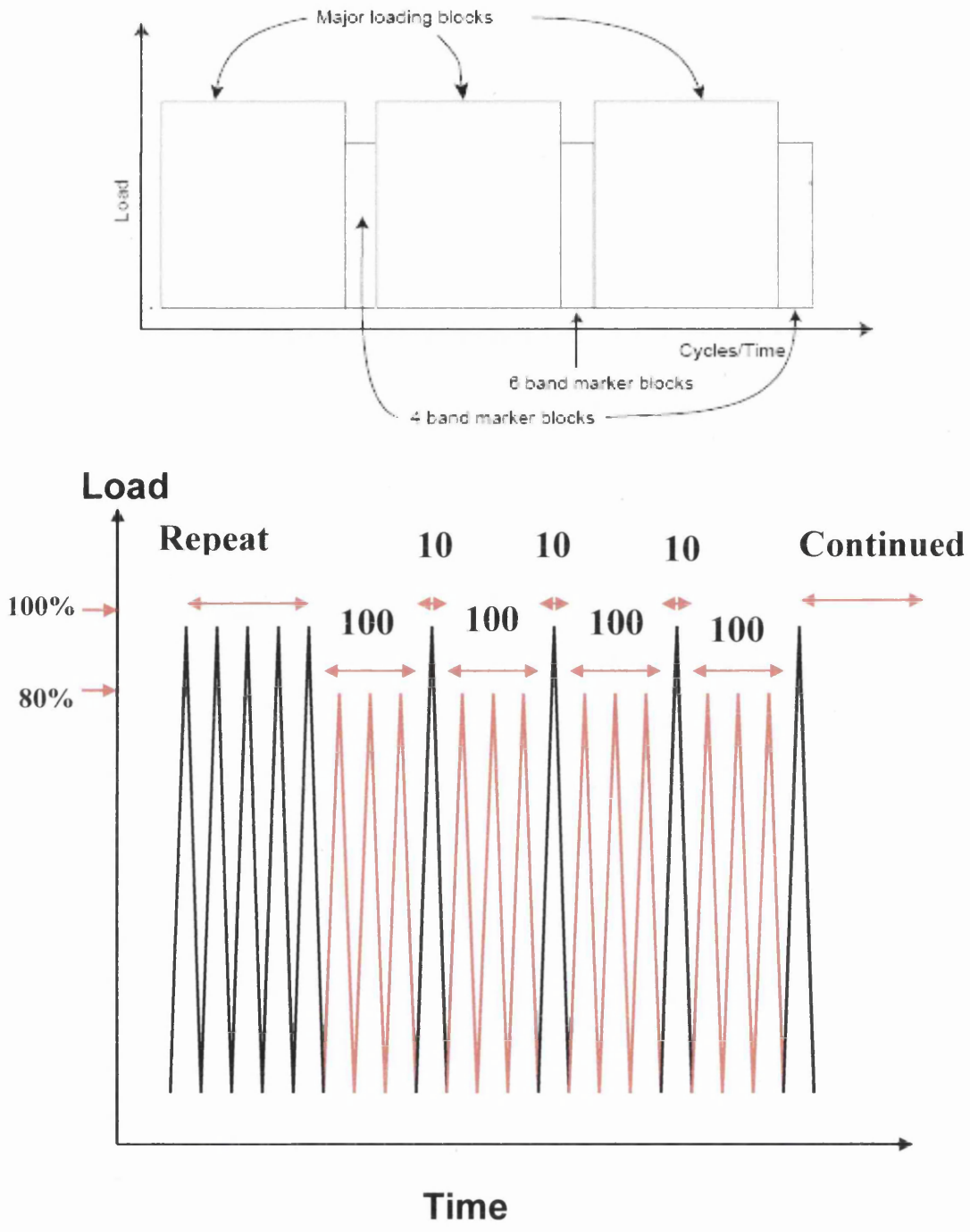

Figure 2.95 Schematic representing the marker band technique used. (a) Overview of the entire spectrum showing the major loading block and the two types of under load marking block, a 4 – band marker block and a 6 – band marker block, (b) a 4 band marker block showing 10 full loads interspersed with 100 under loads.

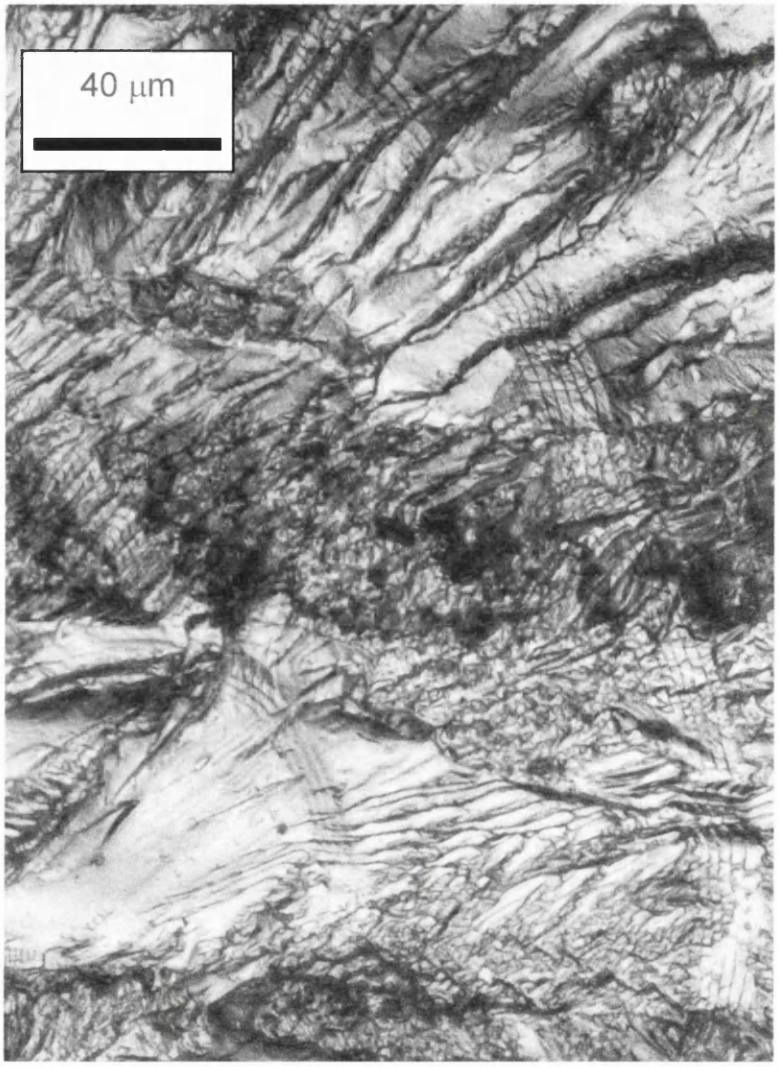

Figure 2.96 Image of a typical fracture surface containing marker banding. Here we can see a band of 4 marks followed by a band of 6 marks.

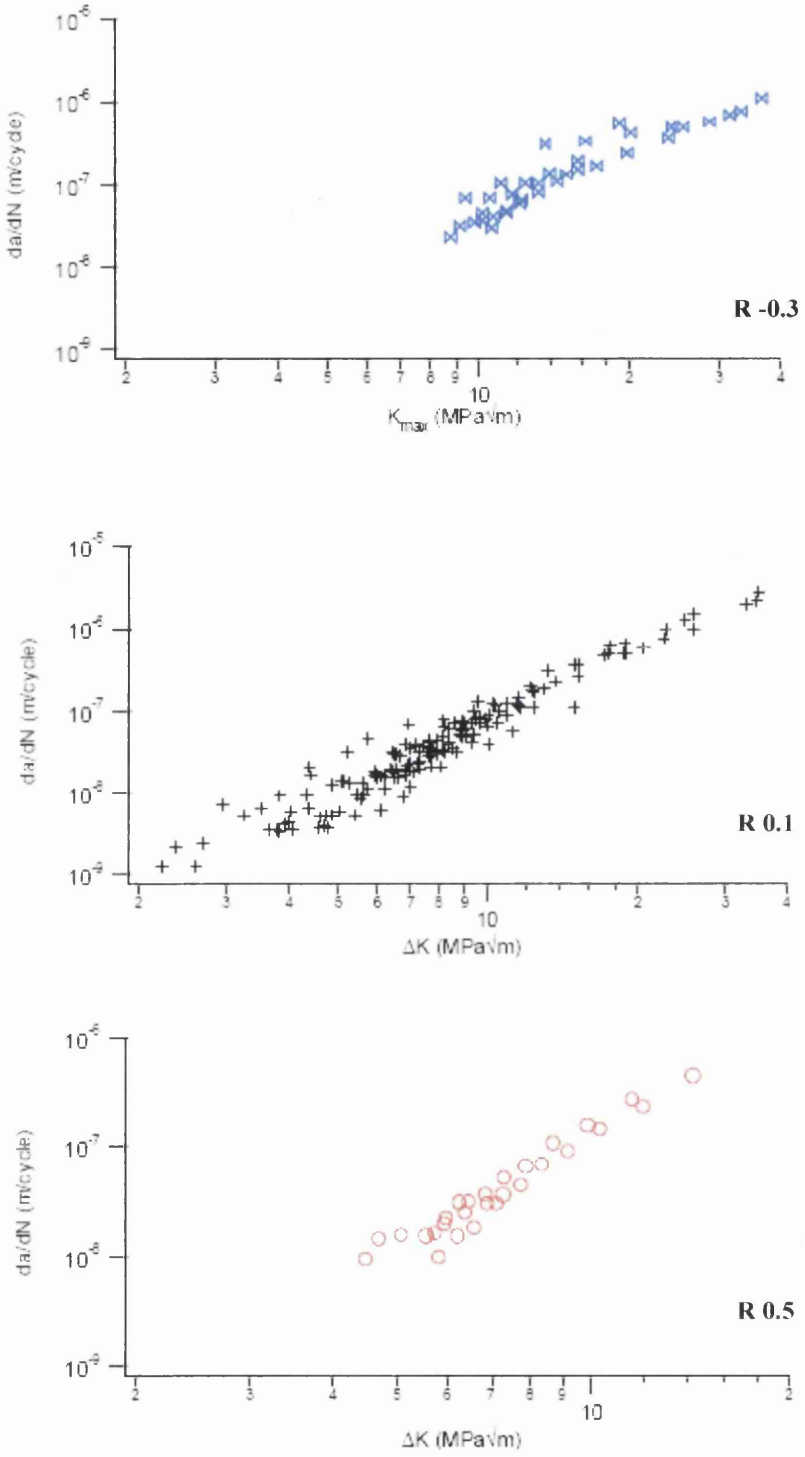

Figure 2.97 Fatigue crack growth rates produced via marker band technique using the three explore R ratios.

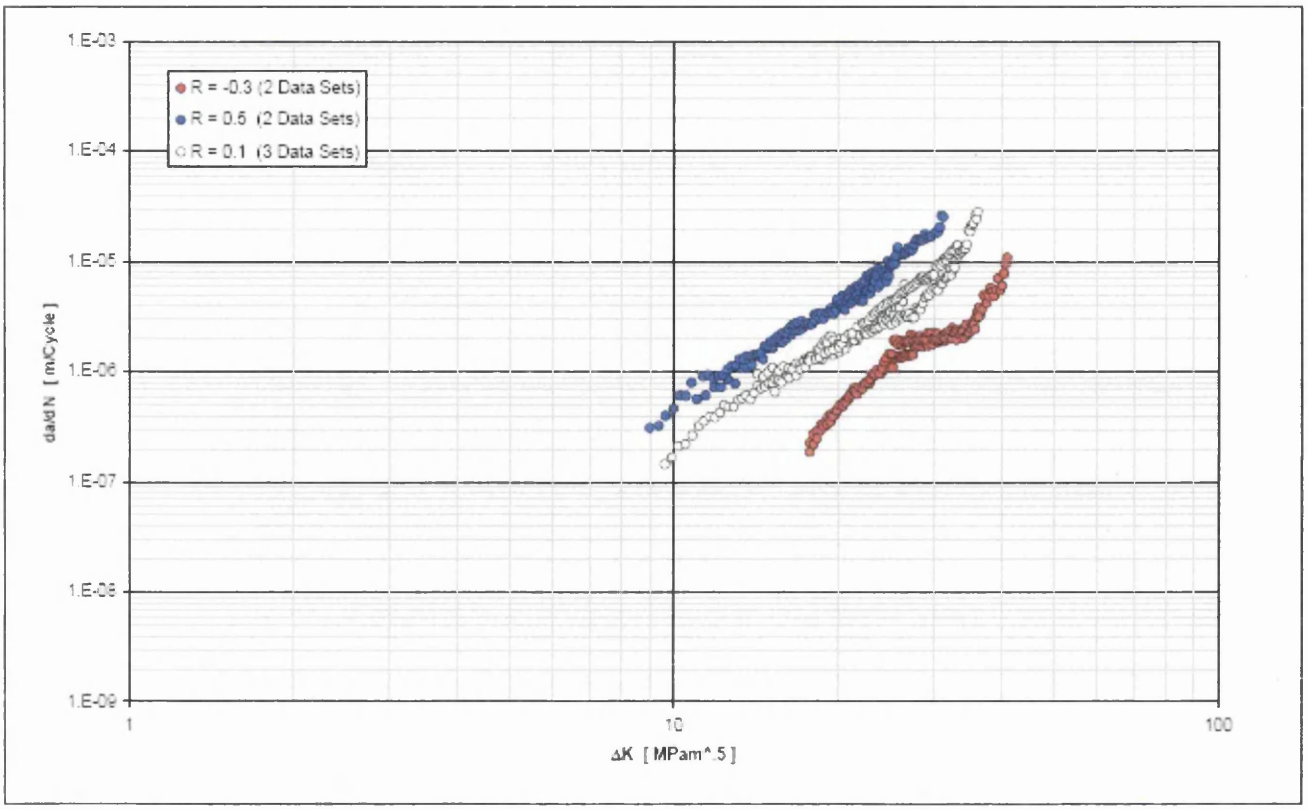

Figure 2.98 Fatigue crack growth data produced via CCT specimens at 25°C, 90% RH for all three R ratios.

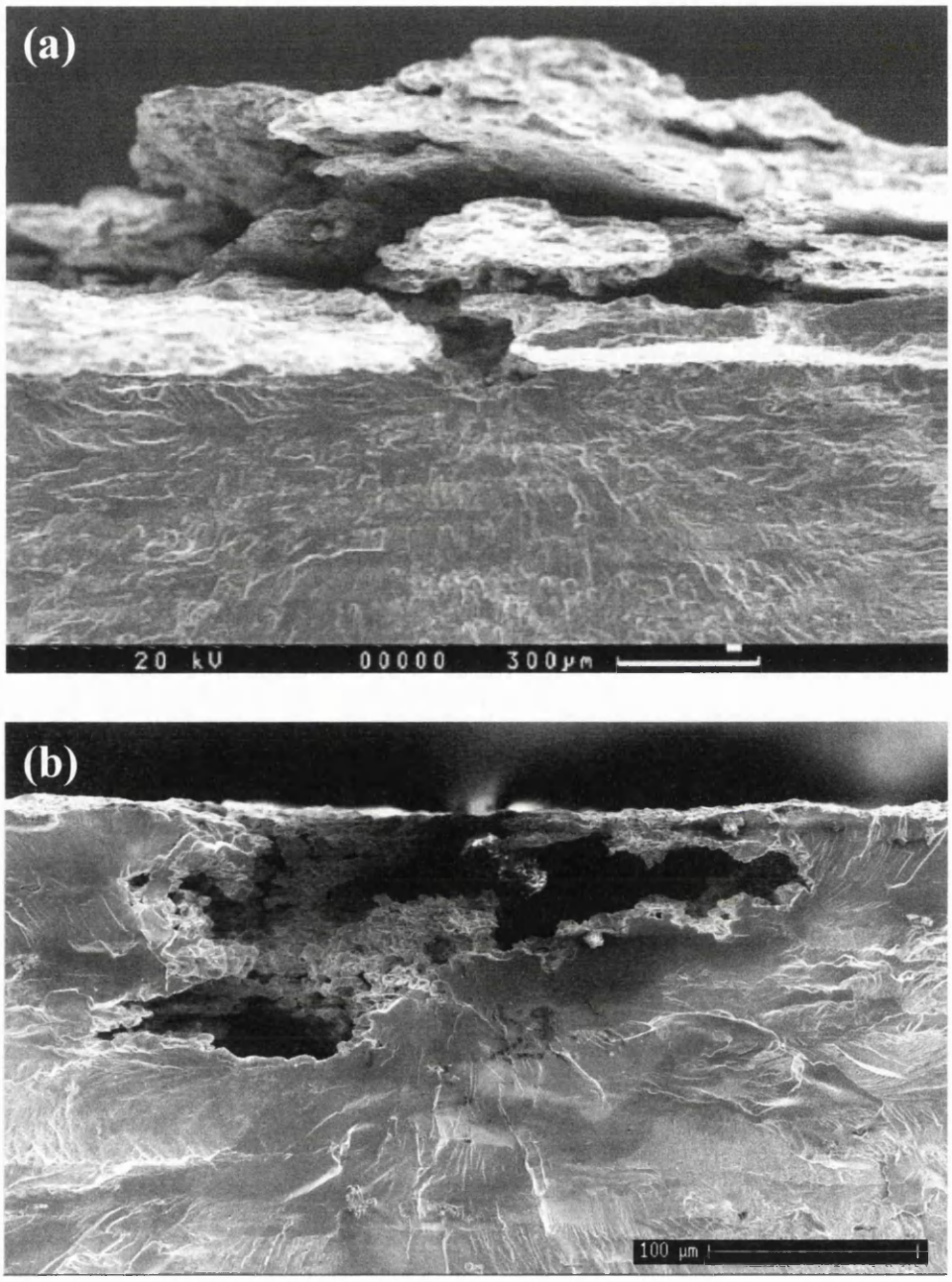

Figure 2.99 Examples of corrosion from the SICAS programme, images taken from the plane of final fracture using an SEM (a) Exfoliation corrosion (b) Pitting corrosion.

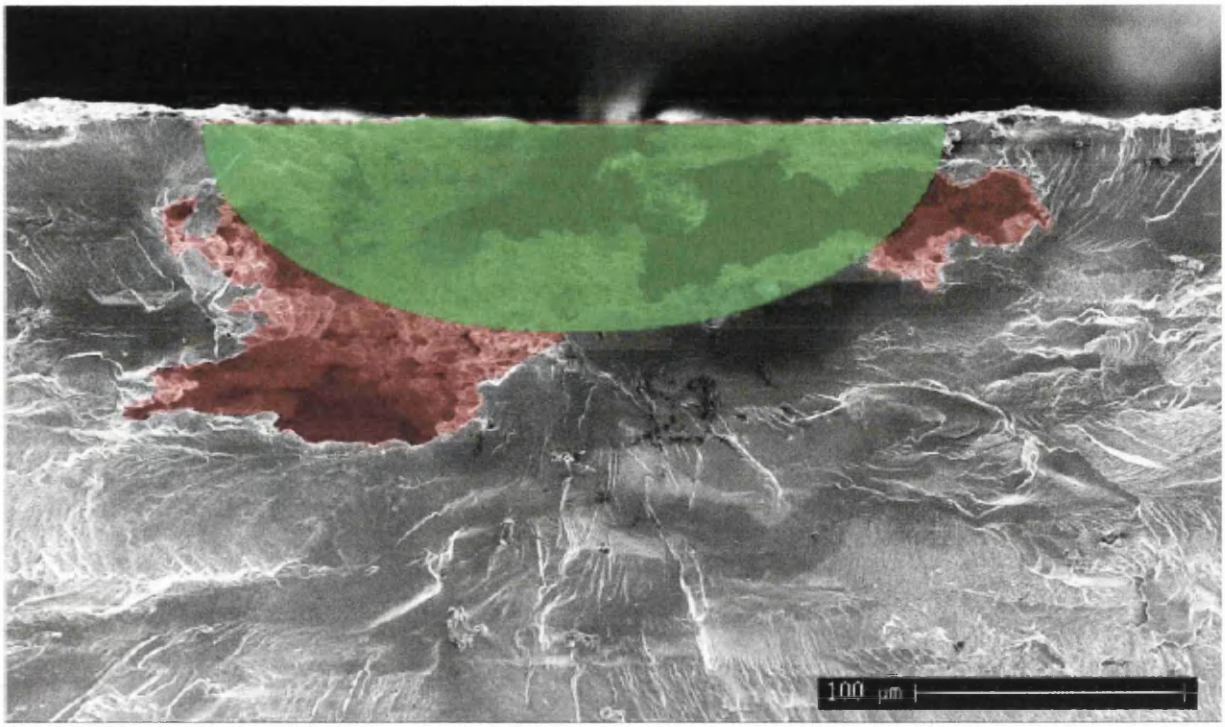

Figure 2.100 SEM image showing pit cross section on fracture surface. Pit area is indicated red, green area indicates initial flaw size of same area.

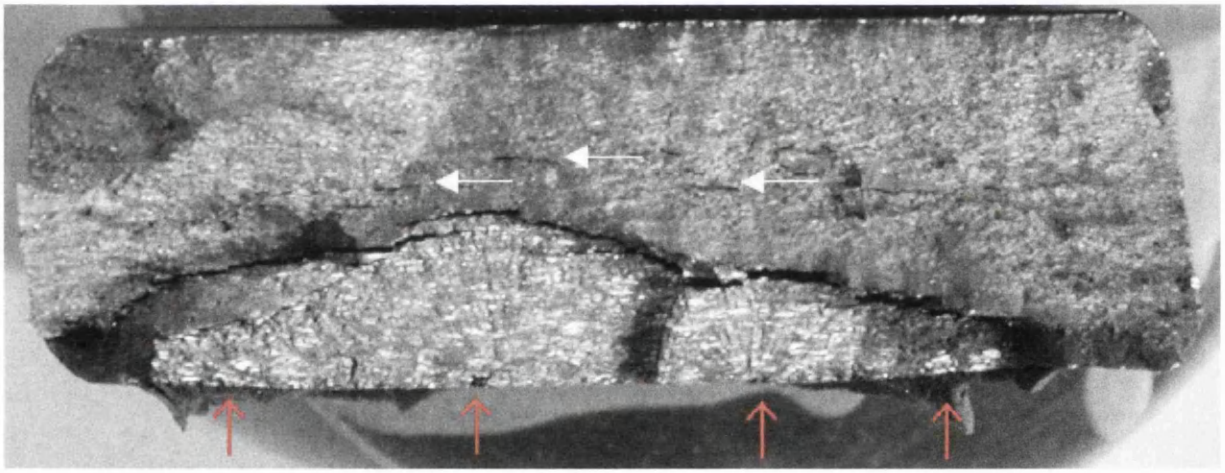

Figure 2.101 Optical micrograph illustrating multiple points of initiation (red arrows) and transverse cracking (white arrows) in an anodised and corroded specimen.

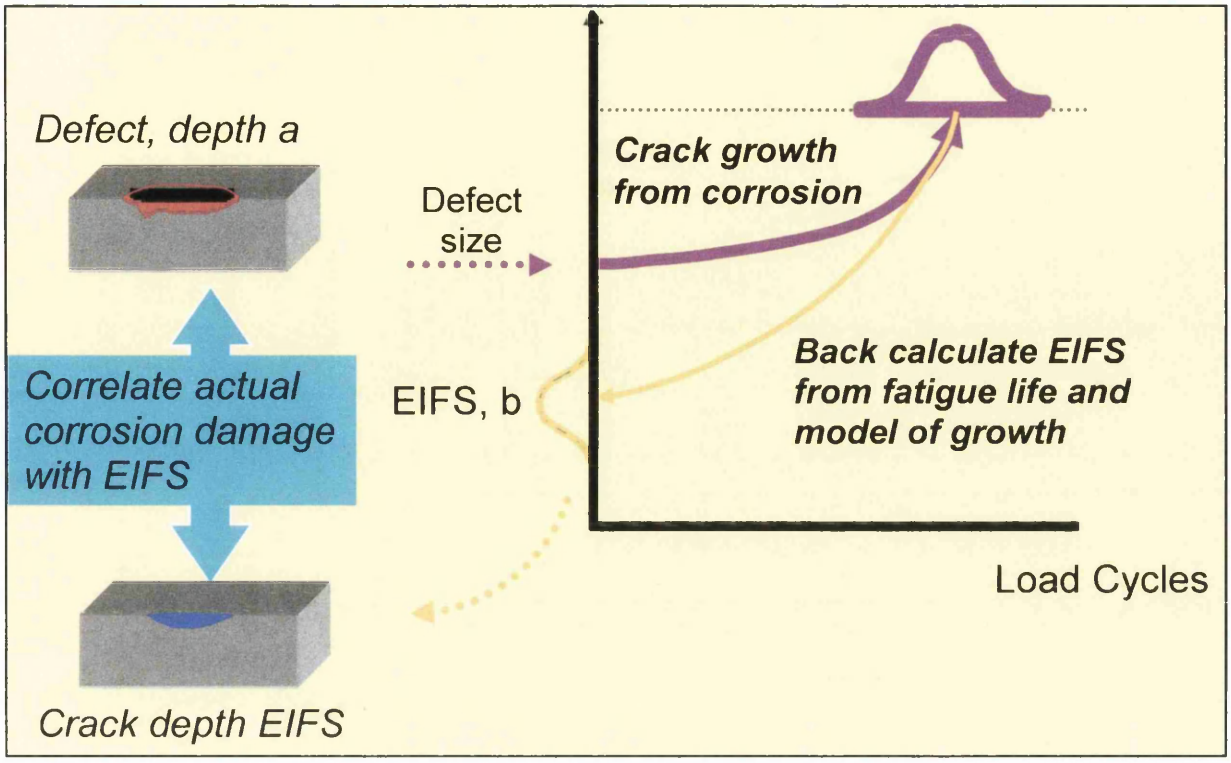

Figure 2.102 Plot illustrating the relationship between defect size and equivalent crack size.

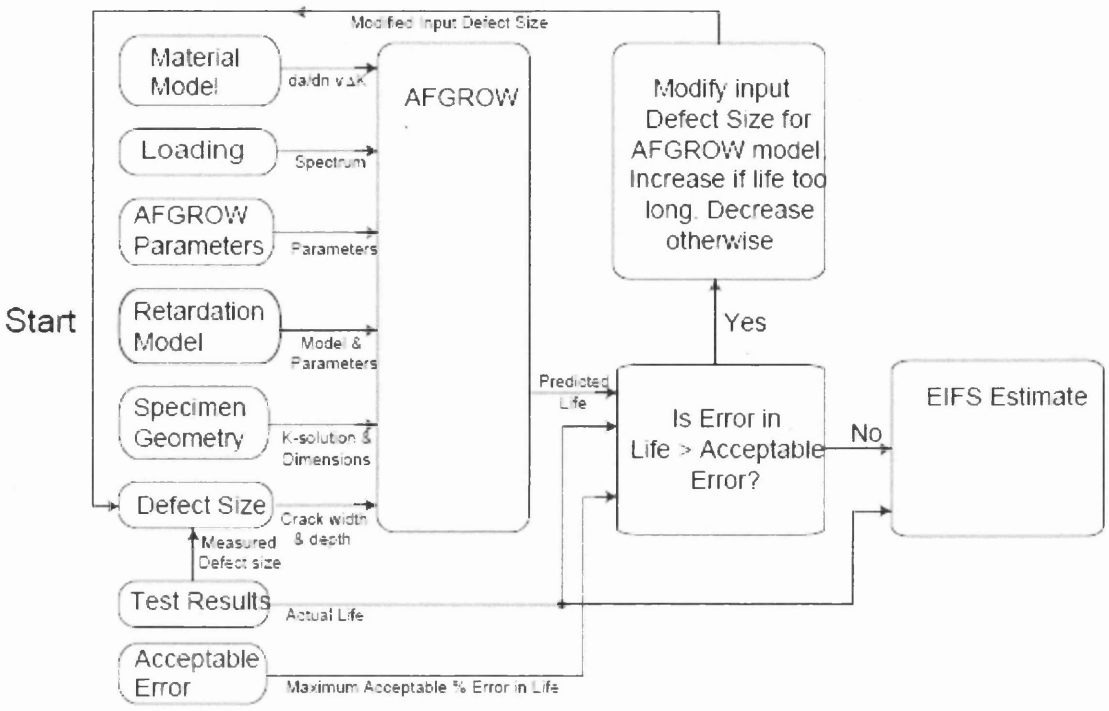

Figure 2.103 Schematic illustrating the inputs and process flow for AFGROW modelling.

Figure 2.104 Illustration of the F/A-18 military aircraft.

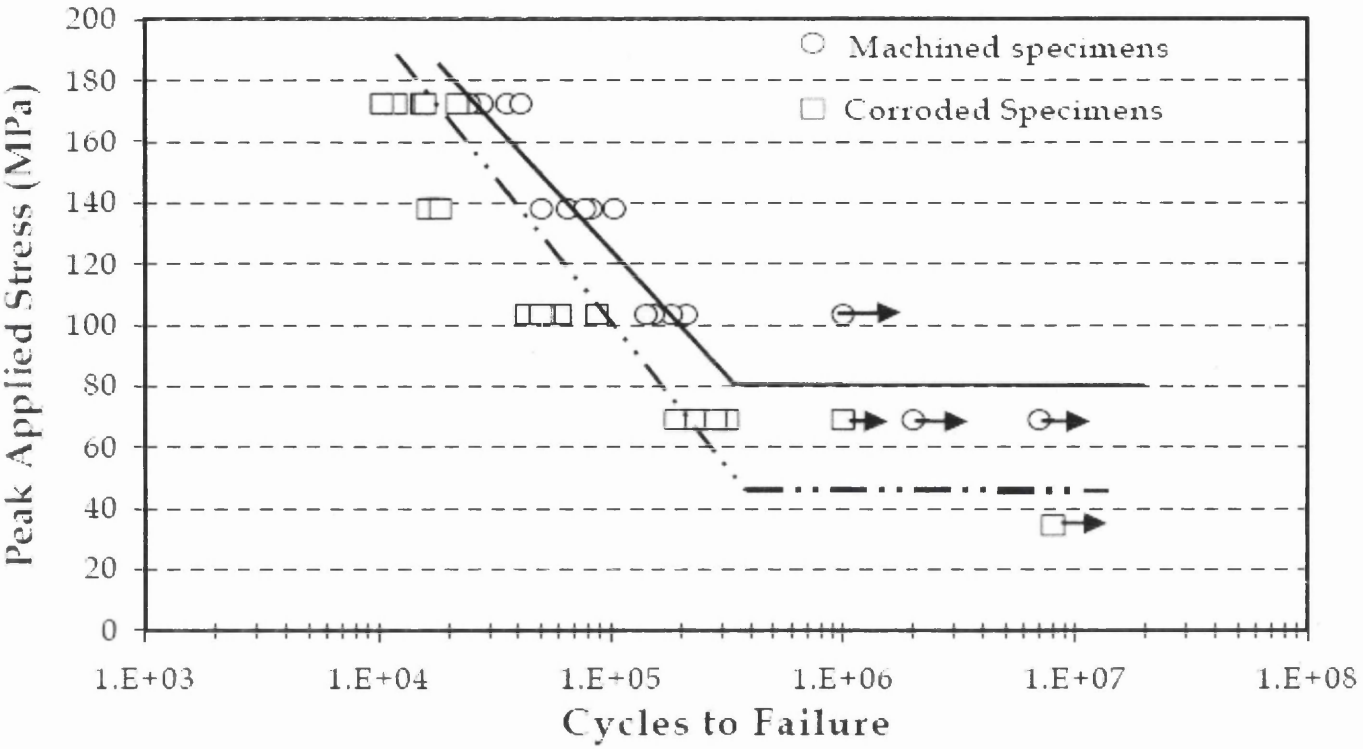

Figure 2.105 Comparison of fatigue lives of machined and corroded specimens.

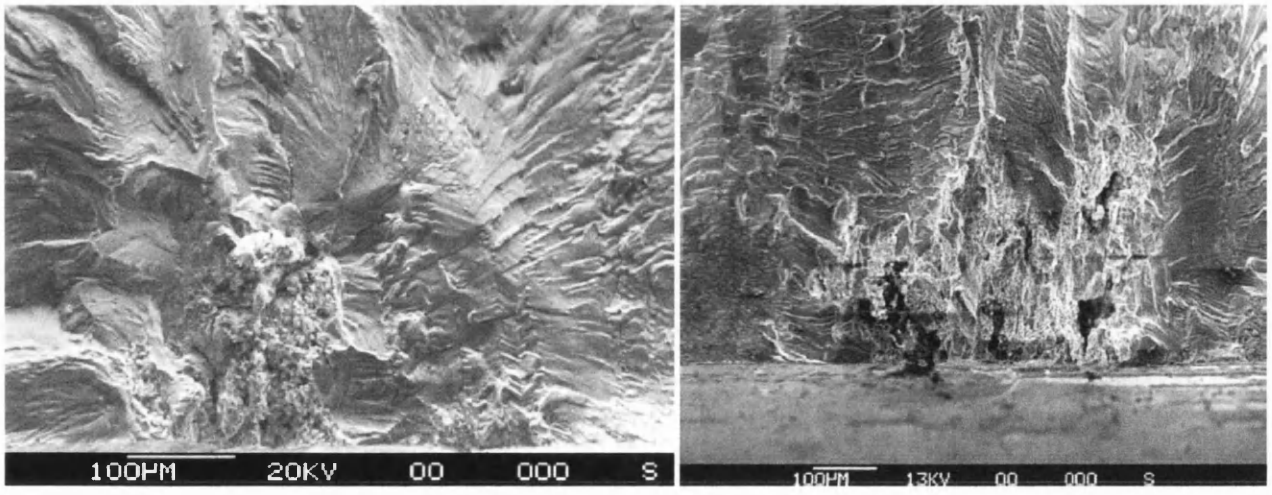

Figure 2.106 Corrosion pitting in 7050-T7451 subsequent to 24 hrs exposure at 3.5 % NaCl. Both pits clearly initiated fatigue cracking.

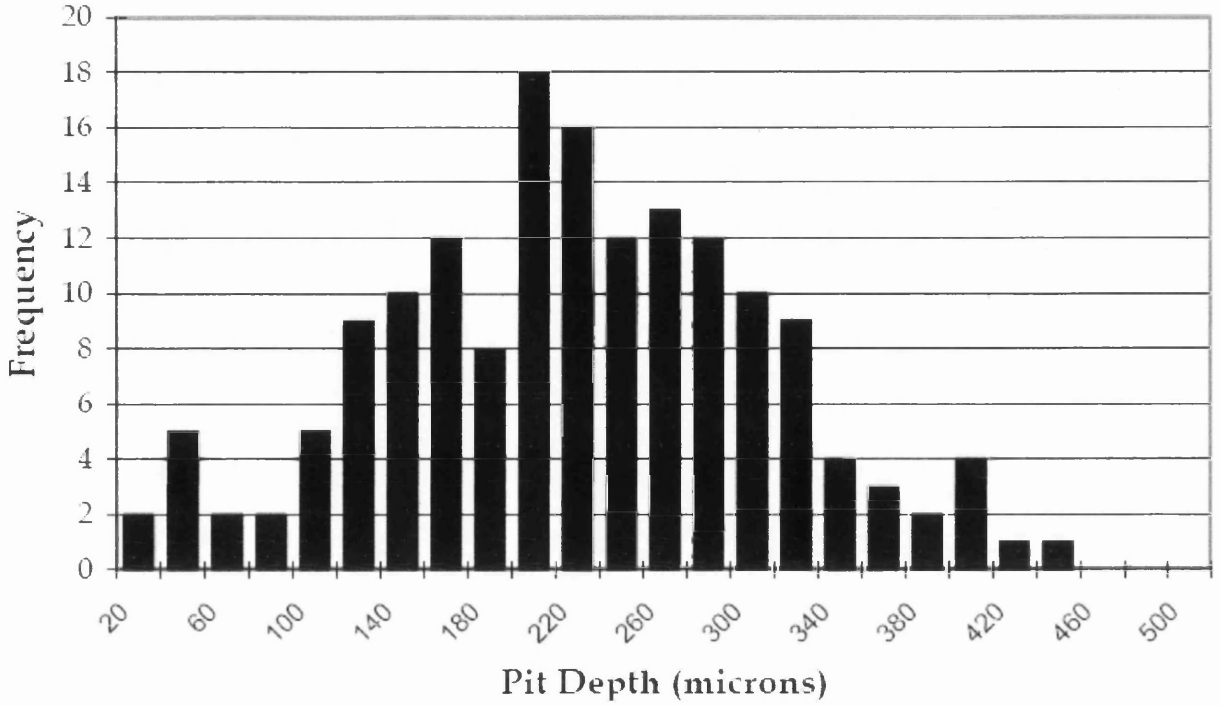

Figure 2.107 Distribution of pit depths that initiated fatigue cracking.

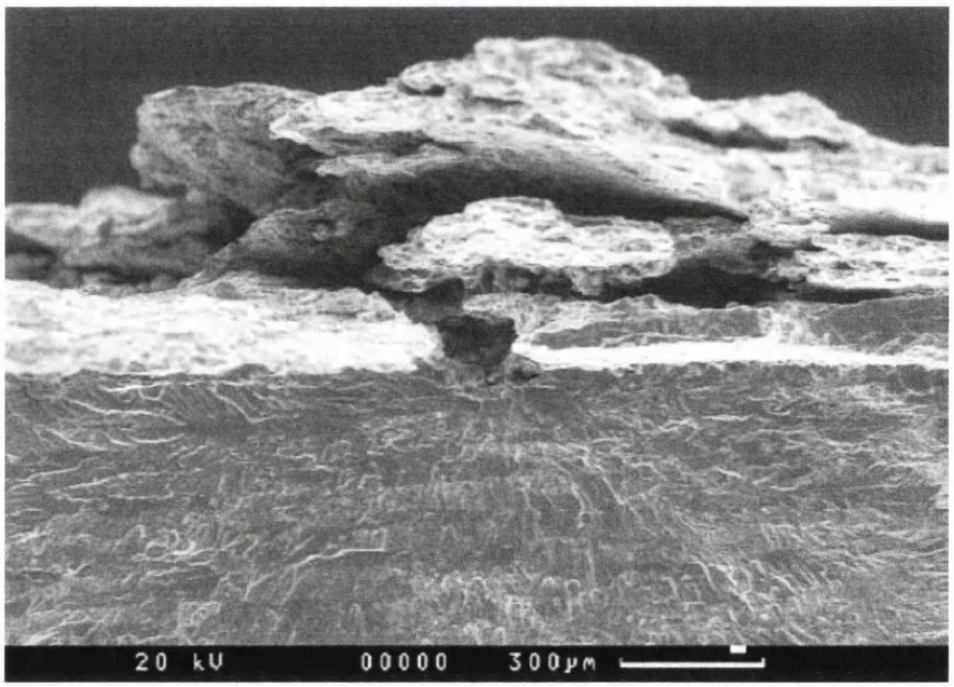

Figure 2.108 Fatigue crack initiation from exfoliated 7075-T651 grains.

2.7 CONCLUSIONS FROM THE LITERATURE REVIEW

The scientific literature has provided valuable information regarding various corrosion mechanisms and their subsequent effect on mechanical properties of a range of aluminium alloys, in particular those related to the 7xxx series. Although the compositions of several alloys reviewed differ from that of the current AA 7010-T7651, they have given an insight into the mechanical properties, and particularly the tensile and fatigue characteristics of this type of material. The literature has also presented information regarding potential material applications material processing methods, and the effects of alloying on the mechanical and physical properties.

It has been concluded that the works undertaken by the previous SICAS project and that completed in the study in 1997 by Patton et al is of most relevance to the current research programme. Both investigations focussed on the fatigue response of the current alloy, subsequent to the T7651 heat treatment. The effect of corrosion pitting on fatigue endurance was furthermore comprehensively investigated by Sharp et al at the DSTO and Aerostructures Technologies in Australia, and entitled Aircraft Structural Integrity: The Impact of Corrosion. Although focussed on the 7050-T7451 alloy, many of the mechanical properties compare favourably to the current alloy. The study discussed the development of methodologies, which allow aircraft structural integrity to be maintained under conditions where an airframe is deteriorating through corrosion. The conclusions encouraged further investigation into corrosion management techniques in military aircraft and subsequently the study was a major influence on the setting up of the Structural Integrity of pitting Corrosion in Aircraft Structures (SICAS) programme.

Similarly to Sharp et al, the work carried out earlier by H. Lajain in 1981 also highlighted the corrosion problems currently observed within military aircraft and the protection schemes available for aluminium structures. These treatment schemes involved chromate primers, organic corrosion inhibitors and physical barrier methods. In a dissimilar fashion, the SICAS programme proposed methods for defect tolerant lifing of airframe components subject to pre-defined corrosion damage. The research programme proposed a solution to manage corrosion damage

within aircraft components, by using an Equivalent Initial Flaw Size (EIFS) concept to LEFM lifing. This approach considered corrosion pitting damage as fatigue cracks of an equivalent semi-circular size. In theory the EIFS concept is considered successful, however, subsequent investigations have shown that the approach relies on more detailed post failure corrosion pit metrics such as actual maximum depth and maximum width, measurements that are virtually impossible from a service engineer's perspective. In order to quantify these metrics, components would require comprehensive NDT evaluation or possible removal or replacing. As the industry is primarily driven by cost, procedures such as these would be highly unlikely. A pronounced outcome from the SICAS programme was the lack of information regarding large scale pitting representative of the "worst case" found in service. It was decided that the size of pits produced, were not symbolic of actual pitting in airframe components.

Another study of relevant interest to the present research was that conducted by DuQuesnay et al, which examined fatigue crack growth from corrosion damage in 7075-T6511 aluminium alloy under aircraft loading conditions. Although not directly related, in terms of material and fatigue loading conditions evaluated, numerous established results were of interest. Certain conclusions also suggested some areas to examine in the current research programme.

3.0 AIMS OF THE PROJECT

The conclusions drawn from the literature review has highlighted the following aims for the current research project:-

Characterize examples of corrosion pits produced during the previous SICAS project and subsequently develop a new corrosion protocol capable of producing larger scale corrosion pitting on the same stock plate AA 7010-T7651 material.

Perform baseline mechanical property tests on the AA 7010-T7651 alloy.

Complete a comprehensive load control, constant amplitude fatigue test matrix evaluating two specimen geometries – Flat Plate and Centre Hole, exposed to various corrosion periods.

Compare corroded flat plate generated fatigue data with previous tests carried out in the SICAS programme.

Examine the potential knock down effect of "end grain" corrosion (centre hole specimen geometry) on non corroded material.

A comprehensive fractographic analysis of corrosion pitting in the alloy.

Complete a limited amount of Fatigue Crack Growth (FCG) tests to provide confidence in existing SICAS FCG data and examine any possible effects of crack orientation.

Fracture mechanics based computer software will be utilised to firstly evaluate the EIFS concept. Other various Linear Elastic Fracture Mechanics (LEFM) codes will be considered to model the fatigue lives of the alloy subject to large scale corrosion pitting.

4.0 EXPERIMENTAL PROCEDURE.

The section below details the procedures and standards undertaken to complete the current investigation. The source material, specimen manufacture, mechanical testing and methods of data analysis are reported herein.

4.1 ALUMINIUM 7010-T7651: THE MATERIAL.

The material investigated within the research project was the 7000 series aerospace aluminium alloy 7010-T7651, supplied by BAE SYSTEMS. The chemical composition of the material as determined via the Jeol 35C Scanning Electron Microscope (SEM) with an Electron Dispersive X-ray (EDX) attachment can be seen in table 4.1. Zinc, magnesium and copper are clearly the major alloying elements within the alloy and are employed to improve corrosion resistance and increase such properties as strength and ductility.

The main use for this alloy is within the aerospace industry as fuselage, wing spars and wing skin components, and is used extensively in the BAE Systems military aircraft, the Hawk Mk 127. Examples of the Hawk Mk 127 fuselage can be seen in figure 4.1 and 4.2 [75]. The stock material consisted of two rolled plates with approximate dimensions 3014 x 1304 x 60mm. The microstructural texture of the plate was of a characteristic, elongated grain structure parallel to the principal rolling direction, with stringers of intermetallic particles.

The material originated from Apollo Metals, produced from a single batch and machined by Gretones in the UK into the fatigue, fracture and other specimens for the Structural Integrity of pitting Corrosion in Aircraft Structures (SICAS) project. Due to the size of the material it was heat-treated to the 7651 specification (*24 Hours at 120°C followed by 8 Hours at 170°C*), in two sections. The heat treatment phase was followed by a chromic acid anodising stage, which is designed to increase corrosion and wear resistance of the material whilst in service. Many components in European military aircraft are chromic acid anodised, however the Americans are less enthusiastic about the treatment as they believe it reduces fatigue endurance by accelerating crack initiation and propagation.

Anodising is an electrochemical process whereby the natural oxide layer present on aluminium is artificially thickened by the following reaction:-

$$2Al + 3H_20 \,.\, Al_2O_3 + 6H^+ + 6e^- \qquad 24$$

The anodised layer has a complicated microstructure compared to the base material, as demonstrated by figure 4.3 [76]. It is divided into two layers, the first is a base layer which adheres to the parent material and provides the corrosion resistance. The second layer is a columnar region made up of a large numbers of hexagonal pores and is generally said to be responsible for the reduced fatigue endurance. In addition to this, defects in the coating can occur due to the intermetallic particles that are present on the surface of the aluminium alloy. Given that these intermetallics are not aluminium, they do not anodise and therefore produce defects in the anodised layer, causing potential sites for crack initiation and corrosion development.

4.2 SPECIMEN PREPARATION: CORROSION PROTOCOL & TRIALS.

Various corrosion trials were undertaken under SICAS to define the protocol for producing controlled amounts of corrosion damage, i.e. corrosion damage of similar nature to that found in-service. Numerous variables were considered, including: - equipment, testing method, corroding solution, corroding time. Subsequently the SICAS results indicated that the optimised constraints for producing the desired amount of corrosion (i.e. size and morphology) included a 3.5wt%NaCl solution for a total corrosion time of ten weeks in a sealed environment (i.e. no oxygen ingress). This procedure produced pits of an average depth of 100μm in anodised stock plate material.

A modified protocol has been defined for the current research to produce corrosion pitting of a larger scale than that observed in the SICAS programme. The deliberately revised protocol for the current study followed similar procedures to that of SICAS. Corrosion pitting

trials were setup to determine the most suitable method of producing large scale pitting, representative of "worst-case" in-service damage (200 μm being the deepest pits in the SICAS programme). The corroding solution of 3.5 wt% of NaCl was again employed, although various exposure techniques were tested on plain and holed samples, these included:-

- ***Open to Air; Fully Immersed,***
- ***Sealed to Air; Fully Immersed (SICAS technique),***
- ***Open to Air; Alternative Immersion (Wet/Dry).***

The following procedures were taken to produce the desired amount of corrosion pitting;

- ***Corroding Solution:***

The 3.5 wt% NaCl solution was produced by dissolving 100g of analytical grade NaCl into 2 litres of distilled water, or other ratios of that amount. Stirring was required until the NaCl was completely dissolved in the liquid at room temperature.

- ***Apparatus and Consumables:***

A silicon sealer (Silcoset 151) was used to attach glass tubes to the aluminium plate. The previous SICAS study had used epoxy resin for this purpose; however, this left a large amount of resin on the test coupon (Figure 4.4). The silicon was found to produce an integral seal with the plate material that resisted water leakage, with the advantage of being completely removed from the material prior to mechanical testing. The silicon material also removed any doubts concerning the effects of the epoxy resin on the subsequent fatigue performance.

Glass Pyrex tubes of outer diameter 16 mm (wall thickness of 1-2 mm) were employed to contain the corroding solution. Polyethylene sheets, glass slides and rubber banding were used to prevent oxygen ingress into the top of the corrosion cell for the sealed to air trials. To introduce corrosion in the bore of the centre hole specimens a glass slide was sealed on the "bottom"

surface of a specimen while the Pyrex tube was sealed to the "top" face surrounding the hole, figure 4.5.

- ***General Procedure:***

Control measures were undertaken to ensure consistency throughout the trial process. The aluminium plates were cleaned and de-greased using ethanol prior to corrosion in order to remove foreign objects that may affect the corrosion process. Sealant was applied to the base of the Pyrex tubes and bonded to the aluminium plate material. A total drying period of 24 hours was required to ensure a water tight seal. An illustration of the sealing procedure can be seen in figure 4.5. The corroding solution was poured into the tube creating an artificial corrosion cell. Various corroding times were employed, ranging from a single week up to a maximum of 52 weeks. Following the corrosion period, the solution was emptied and the glass tubes were removed. The corroded area was subsequently soaked in concentrated nitric acid for 45 minutes, to remove corrosion products that remained within the pitted areas. A further ethanol clean was necessary to remove any water that may have caused additional corrosion. The results of the corrosion trials are clearly presented in chapter 5.

4.3 SPECIMEN PREPARATION: TEST MATRIX.

The wet/dry alternation trial was found to produce corrosion pitting largely representative of pits found on the Hawk Mk127 aircraft after a period of service. Therefore, this technique was used to produce the controlled amount of corrosion damage necessary for the plain and fastener specimens. The wet/dry alternation technique involved immersing the central region of the test specimens in the corroding solution for 4 days before emptying and leaving to dry for a further 3 days. This sequence was repeated in some cases for a maximum of 52 weeks, although the matrix of repeat testing focused on a period of 8 weeks. The specimen preparation procedure detailed above in section 4.2 was again employed.

4.4 MECHANICAL TESTING: MONOTONIC TENSILE TESTING.

Tensile testing was carried out using an ESH servohydraulic test machine with a 50kN load capacity (Swansea University machine N° - SL4). The tensile testing complied with the British Standard BSEN10002 [77]. A clip gauge extensometer with a gauge length of 9.7 mm was used to measure the extension of the tensile specimens. Specimens were machined to a diameter of 4 mm and a gauge length of 15 mm. A schematic drawing of the specimen design is shown in figure 4.6. Monotonic loading was applied under position control at a rate of 1mm/min.The data produced from each test was recorded by a logging computer and converted into load and extension. Engineering stress and strain values were subsequently determined using the standard equations:-

$$Stress = Applied\ Load / Specimen\ Area \quad (25)$$

$$Strain = Specimen\ Extension / Specimen\ Original\ Length \quad (26)$$

4.5 MECHANICAL TESTING: LOAD CONTROL FATIGUE TESTING.

The constant amplitude load control fatigue testing followed guidelines set by British Standards BS3518, to ensure consistency in the testing [78]. The equipment employed to complete the fatigue testing of the pre-corroded specimens was an ESH servohydraulic testing facility (Swansea University machine N° - SL4) with a maximum load range of 50 kN. A sinusoidal waveform was externally driven and logged using a connected computer. Maximum and minimum loads were converted into voltages in order to run the waveform at an R ratio of 0.1. Tests were carried out at a frequency of 2 Hz in a humid atmosphere. High humidity conditions were produced via a novel designed environmental chamber, whereby the specimen gauge area was subjected to conditions of 90 – 95 %RH (Room Humidity). Figure 4.7 illustrates the humidity chamber surrounding the test specimen. A small amount of distilled water was poured into the base of the sealed chamber before each test to maintain a constant humidity level. The humidity was monitored using micro-sensors located inside the cell.

Fatigue specimens were extracted from anodised plate material originating from the previous SICAS project. However, a major distinction on this occasion was that the longitudinal axis of all the current specimens was perpendicular to the longitudinal rolling direction of the original plate (compared to parallel in SICAS). The specimen design and dimensions for both the plain and the holed samples can be seen in figure 4.8. As a consequence of the sectioning procedure, all the test specimens retained the original anodised surfaces on their "top and bottom" faces. Therefore, since these surfaces were anodised in preparation for the SICAS project, the anodised layers were approximately five years old. The hole through the centre hole specimens was introduced via a drill and ream process. The entrance edges to the hole were manually de-burred, but no additional finish was applied to the internal hole surface. Notably, the corrosion introduced to the centre hole specimens was, therefore, active on "as-machined" material and not an anodised surface as for the flat plate specimens. In this respect, this non-anodised hole finish would replicate service conditions, particularly fastener holes.

4.6 MECHANICAL TESTING: FATIGUE CRACK GROWTH TESTING.

Fatigue Crack Growth (FCG) experiments were completed using identical equipment to that used for the fatigue section of the project. This type of testing was necessary to provide FCG data for the material orientations under evaluation, and to provide suitable data for fatigue crack growth modelling. Although active in the same plane, the direction of crack growth in the flat plate specimen (L-ST) is different to that of the centre hole specimen (ST-L). Single Edge Notch (SEN) specimens were machined from remnant material to the specifications shown in figure 4.9. Specimens were periodically cycled under constant amplitude load control for a known amount of cycles. Suitable loads were chosen to initiate and propagate a fatigue crack at a measurable rate; with the subsequent crack growth optically measured using a Nikon digital camera attached to a travelling microscope. Crack lengths were measured in terms of metres and the subsequent data input into a stress intensity factor solution for a single edge notched plate:-

$$K_I = C\sigma\sqrt{\pi a} \qquad 27$$

Where C = 1.12 for small cracks or

$$C = 1.12 - 0.231(\tfrac{a}{W}) + 10.55(\tfrac{a}{W})^2 - 21.72(\tfrac{a}{W})^3 + 30.39(\tfrac{a}{W})^4 \qquad 28$$

Growth was restricted to within a/W = 0.6. σ is the applied stress, a is the size of the notch and W is the specimen width, which in this case, a = 2 mm and W = 25 mm. FCG data were subsequently presented as da/dN as a function of applied ΔK.

4.7 FRACTOGRAPHY: CORROSION PIT EVALUATION AND MEASUREMENT.

Subsequent to fracture, specimens were soaked in an ultrasonic bath for a period of 5 minutes in concentrated nitric acid (HNO_3) to remove corrosion product and reveal pit morphologies. This was necessary to attain true measurements of pit depth and width prior to examination. Specimens were examined and corrosion pits measured using a Philips XL30 Scanning Electron Microscope (SEM), which allowed on screen measurements. A full database of pit measurements was created for every tested specimen. A comprehensive database of images was created using SEM. Images were analysed and examined using an imaging manipulation package called Adobe Photoshop©. The software allowed corrosion pit areas to be calculated alongside providing fundamental measurements such as width, depth and surface opening width. The technique of measuring the pits, principally involved a pixel counting method. The pit boundary area was highlighted and the number of pixels within that designated area counted. The number of pixels making up the scale bar on the image was also counted in order to calibrate the number of pixels per unit of image length. A similar technique was used to measure specimen final crack profiles, as discussed below.

Digital Nikon photographic equipment was used to determine and record the fatigue crack profiles (i.e. the shape and form of the fatigue crack), and fracture surface appearance, which later would be used to measure crack lengths, using the nomenclature A1 – A5, as

illustrated by figure 4.10. These crack profile measurements were necessary for subsequent FCG modelling exercises.

4.8 MODELLING: AFGROW LIFE PREDICTION PROGRAM.

AFGROW was first developed nearly twenty years ago as a crack growth life prediction program (ASDGRO) written in BASIC for the crack growth analysis of the Sikorsky H-53 Helicopter. Over time, the program has evolved into the reliable, freely available software available today. The program is the property of the United States Air Force (USAF) and in particular James Harter who developed the programme from its early stages.

This section details the operating procedure for the AFGROW program, including the required input data and how this data is used to achieve the desired results. The programmes capabilities are substantial and many features were not required for this research. Simply, AFGROW is a component/specimen life prediction program that allows the user to define certain parameters such as specimen geometry, specimen dimensions and applied load in terms of tension and bending. The programme also allows the loading spectrum to be defined (constant or variable amplitude) and coincidentally contains a wide-ranging database of material data. Figure 2.103 in the literature review illustrates the inputs and the process flow for AFGROW modelling.

Corrosion pit metrics were measured using the image manipulation techniques discussed previously. This data was used to represent the starter defect size (crack sizes) for use within the programme. The complex morphology of the pit was ignored and a semi-elliptical starter crack shape assumed for both specimen geometries (flat plate and centre hole). Examples of typical flat plate and centre hole semi-elliptical starter defects can be seen in figure 4.11. In order to predict a fatigue life (in terms of cycles to failure N) for each specimen, a series of data were required for the program, in three specific categories:-

- ***Geometry Model Type***

Choices of three models are available within the AFGROW programme, classic, advanced and plug-in. The classic model was used in the research programme and is a database within AFGROW containing a range of crack geometries. Figure 4.12 illustrates the crack geometries of the flat plate (centre semi-elliptical) and centre hole (single surface crack at hole) specimens. Specimen dimensions and starter defect sizes in terms of 'a' and 'c' values are also entered, as shown by figure 4.13. Specimen dimensions are equivalent for both flat plate and centre hole geometries. Advanced and plug-in models are used for complex geometrical specimens or when specific requirements are required.

- ***Material Data***

The material data category consists of five options; the Forman, NASGRO and Walker equations, the Harter-T method and the tabular look-up option. The two of use to the research program were the tabular look-up, whereby material data can be manually inserted and the NASGRO equation. The tabular look up allows the user to input alloy specific data such as mechanical properties, representative crack growth rates, fracture toughness and threshold information. The NASGRO equation was developed by Forman and Newman at NASA, de Koning at NLR and Henrikson at ESA and is an attempt to use a closed form equation to model the da/dN vs. stress intensity of engineering materials. The NASGRO equation consists of a large database within the programme, containing a snapshot of most metals and alloys. The most suitable material within the NASGRO database for the research was designated AA 7010-T73651 in plate and sheet form. The properties of this alloy and AA 7010-T7651 were found to be compatible with the current research material.

The key parameters inputted into the model by the NASGRO database were:-

- Paris crack growth rate constant, $C = 1.7581 \times 10^{-10}$
- Paris exponent, $M = 3.122$
- Yield Stress, $\sigma_{YS} = 441$ MPa

- Young's Modulus, E = 69 GPa
- Threshold Stress Intensity Range at R = 0, ΔK_{TH} = 2.747 MPa$\sqrt{m}$
- Plane Strain Fracture Toughness, K_{1C} = 34 MPa$\sqrt{m}$

The crack growth data for the material 7010-T73651 alloy can be seen in figure 4.14; this curve was ultimately compared to actual 7010-T7651 crack growth data produced at Swansea.

- ***Spectrum***

The spectrum category allows the user to input the applied stress (in MPa). The spectrum also permits the user to select the required loading amplitude (i.e. constant or variable etc) or create their own spectrum file. For the current research, constant amplitude loading was used, while peak stresses varied between 90 MPa and 270 MPa for both flat plate and centre hole specimen geometries. In addition, the constant amplitude feature also requires users to input the loading ratio, which for this current research programme was 0.1.

Three various categories of life predictions were completed for both surface opening width and maximum width metrics:-

- **Predicted Life (a/c ratio varying)**

This category predicted fatigue lives subject to the a/c ratio of the starter defect size (i.e. corrosion pit size) changing throughout the growth of the fatigue crack. Each corrosion pit present on the plane of final fracture was modelled individually and used to yield a range of fatigue lives. (For example specimen PC-02 contained 3 pits on the plane of final fracture; therefore each pit's dimensions were inputted into AFGROW, resulting in 3 separate fatigue lives.

- **Predicted Life (a/c constant)**

This category was modelled very similar to the one mentioned above, although this category predicted fatigue lives subject to the a/c ratio of the starter defect size remaining constant throughout the growth of the fatigue crack.

- **Average Pit Size**

The average pit size was predicted for comparison purposes. The total surface opening widths and depths of the pits present on the plane of final fracture were averaged and modelled as an equivalent singular pit.

The programme also has a range of other features such as retardation parameters, stress state parameters and initiation parameters, however these were not considered to model the basic fatigue life (N). Additionally prediction parameters can be set within the boundaries of the software. The parameters for the current research are highlighted in figure 4.15, whereby the output intervals and propagation limits are set. Initiation conditions can also be considered within the programme, but the current research ignores initiation and assumes fatigue crack growth occurs at the first cycle. Subsequent to setting up the boundary conditions and parameters, predictions can be produced. Figure 4.16 is an example of a completed simulation. Further details of the AFGROW modelling work alongside valid results can be seen in the chapter 5.

Table 4.1 Chemical composition of AA 7010-T7651 material, as determined via EDX analysis.

Element	Zn	Mg	Cu	Zr	Fe	Cr	Si	Ti	Mn
Composition (% wt)	6.0	2.21	1.57	0.11	0.08	N/A	0.05	0.02	0.01

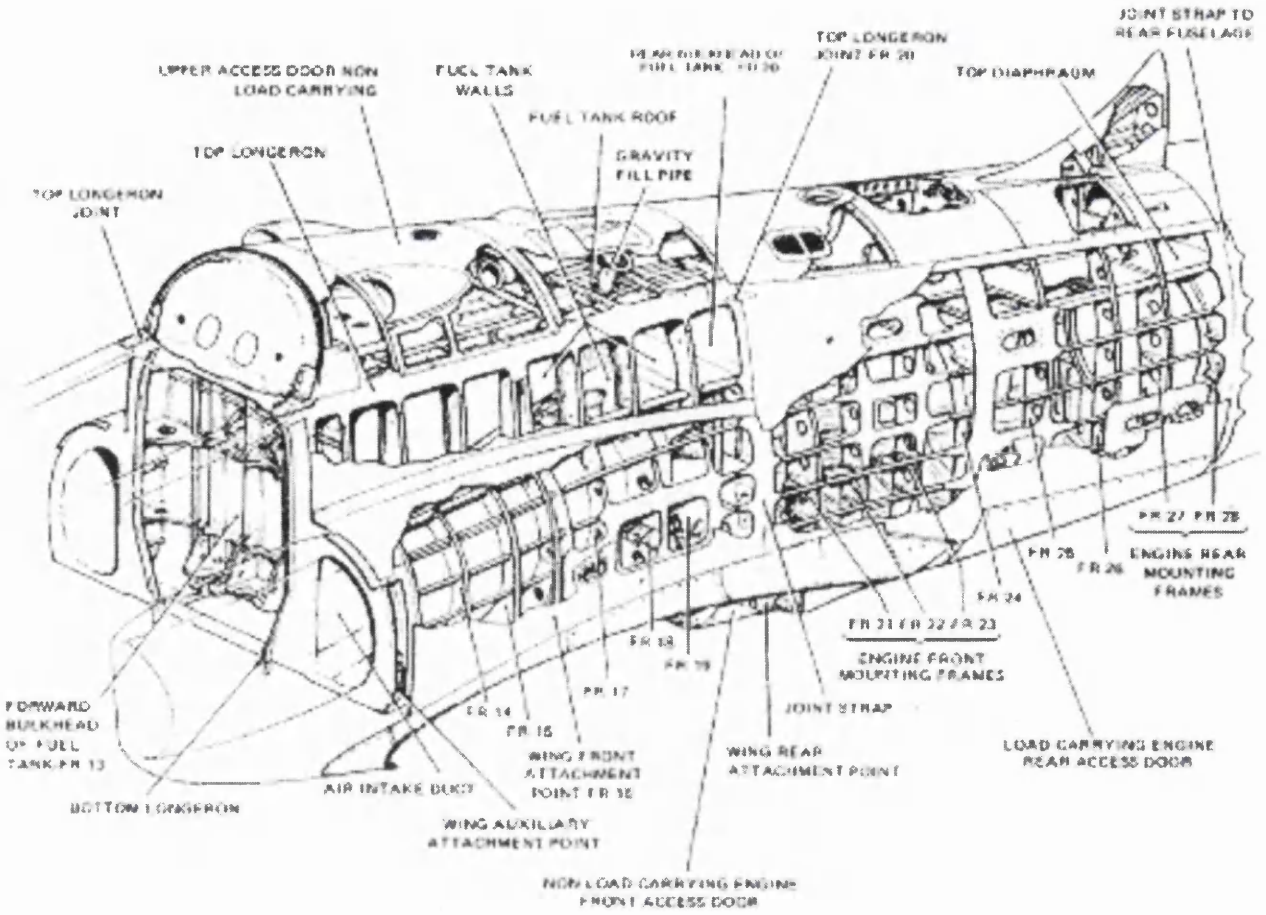

Figure 4.1 Skeletol illustration of the main fuselage of the Hawk mk 127 military aircraft [75].

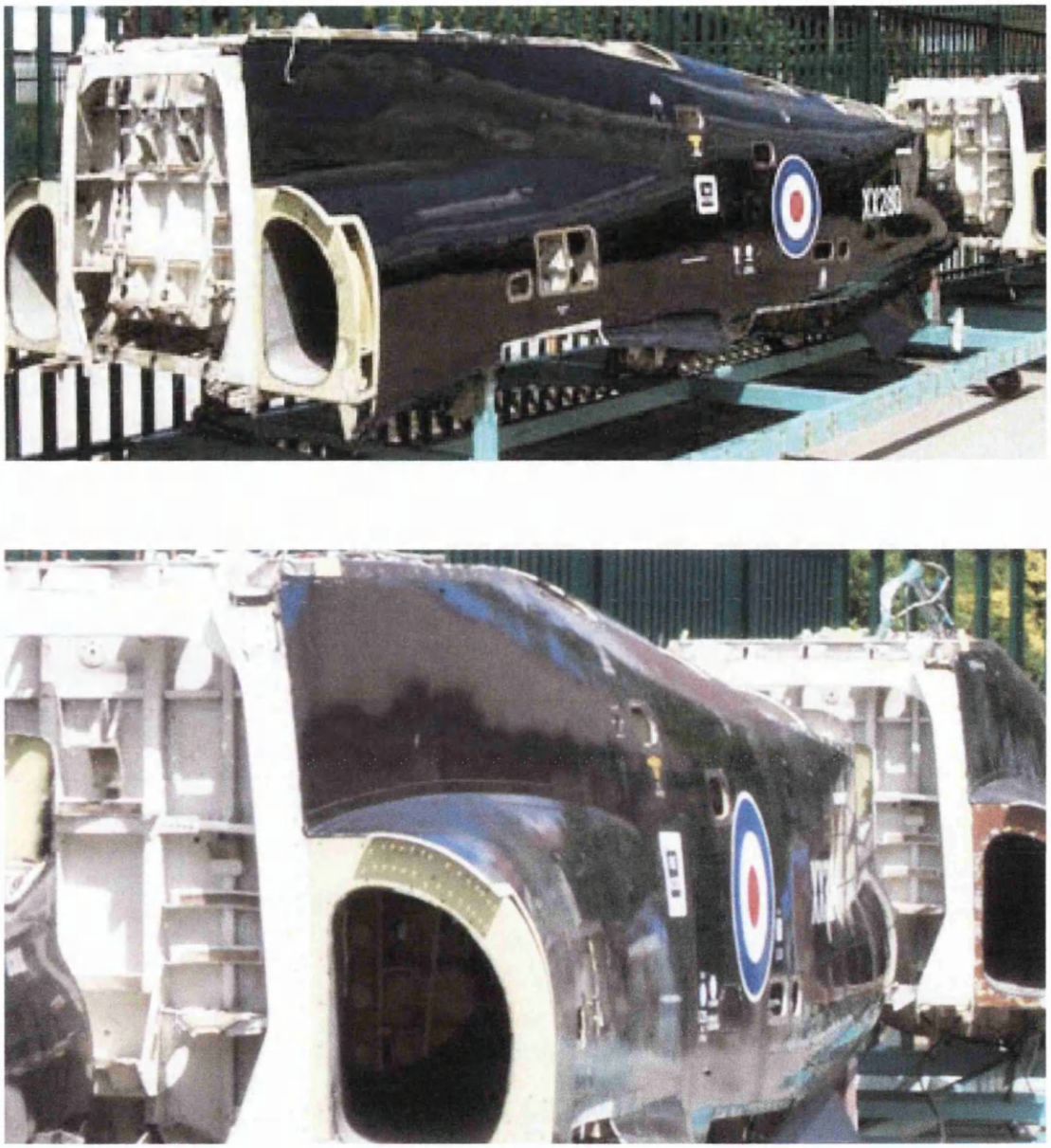

Figure 4.2 General images from a forward bulkhead Hawk fuselage [75].

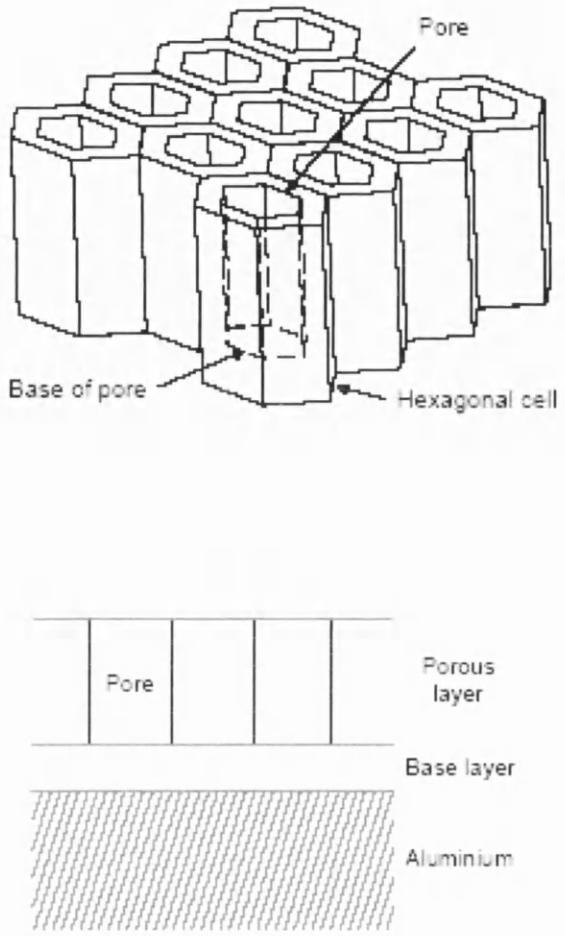

Figure 4.3 Schematic diagrams of the microstructure of the anodised layer (above) showing the hexagonal configuration of the porous layer and (below) a cross-sectional view of the aluminium substrate, base layer and porous layer [76].

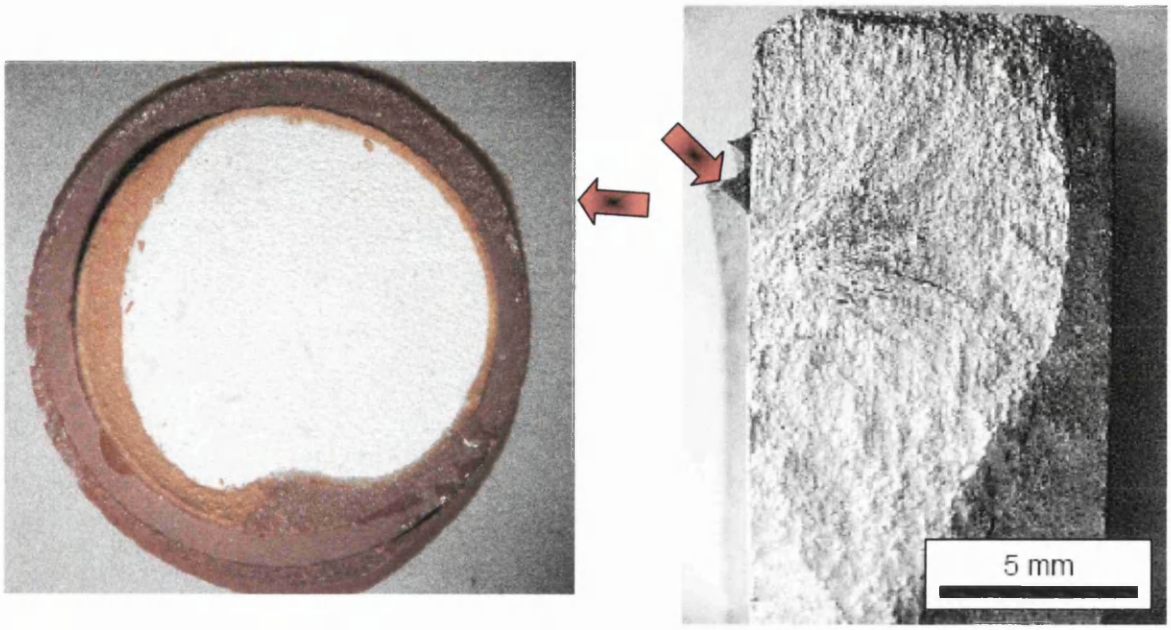

Figure 4.4 Examples of remnant epoxy resin on SICAS test specimens [76].

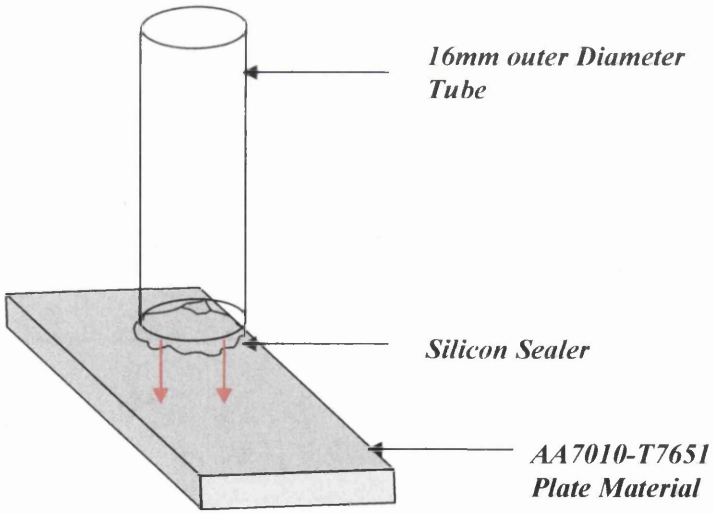

Figure 4.5 Illustration of the glass tube being adhered to the plate material

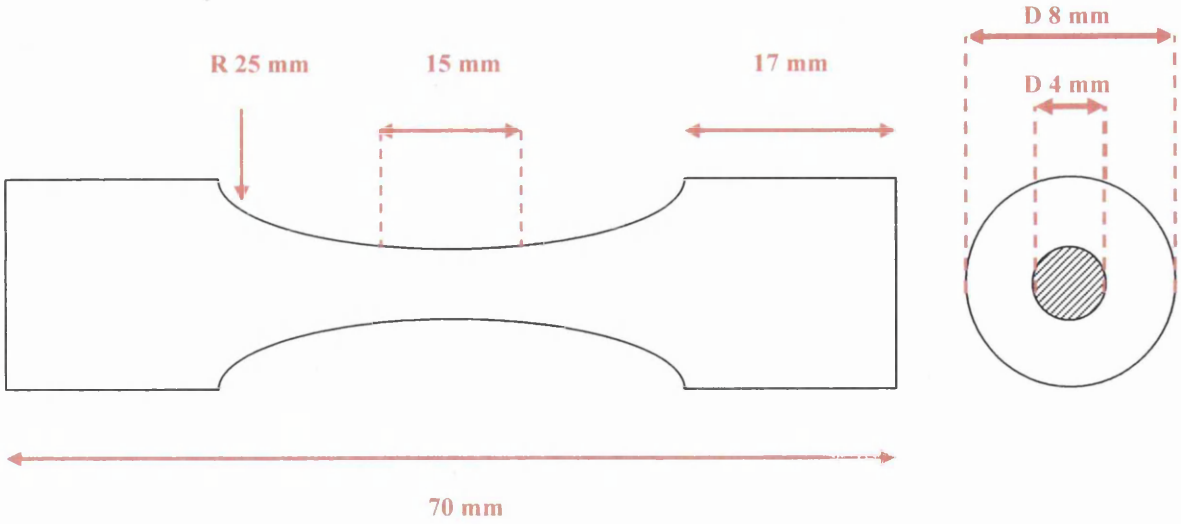

Figure 4.6 Schematic drawing of the tensile test specimen with dimensions in milimetres (Not to scale).

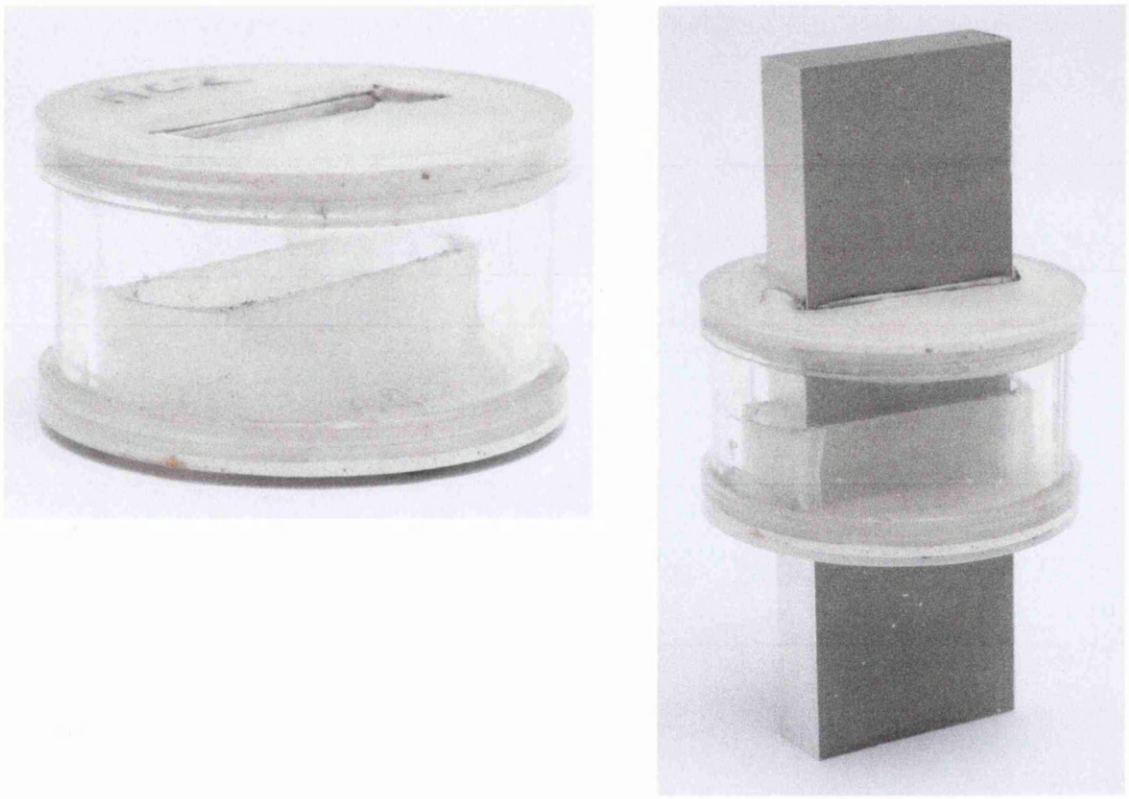

Figure 4.7 (a) Humidity chamber and (b) chamber attached to a fatigue specimen prior to testing.

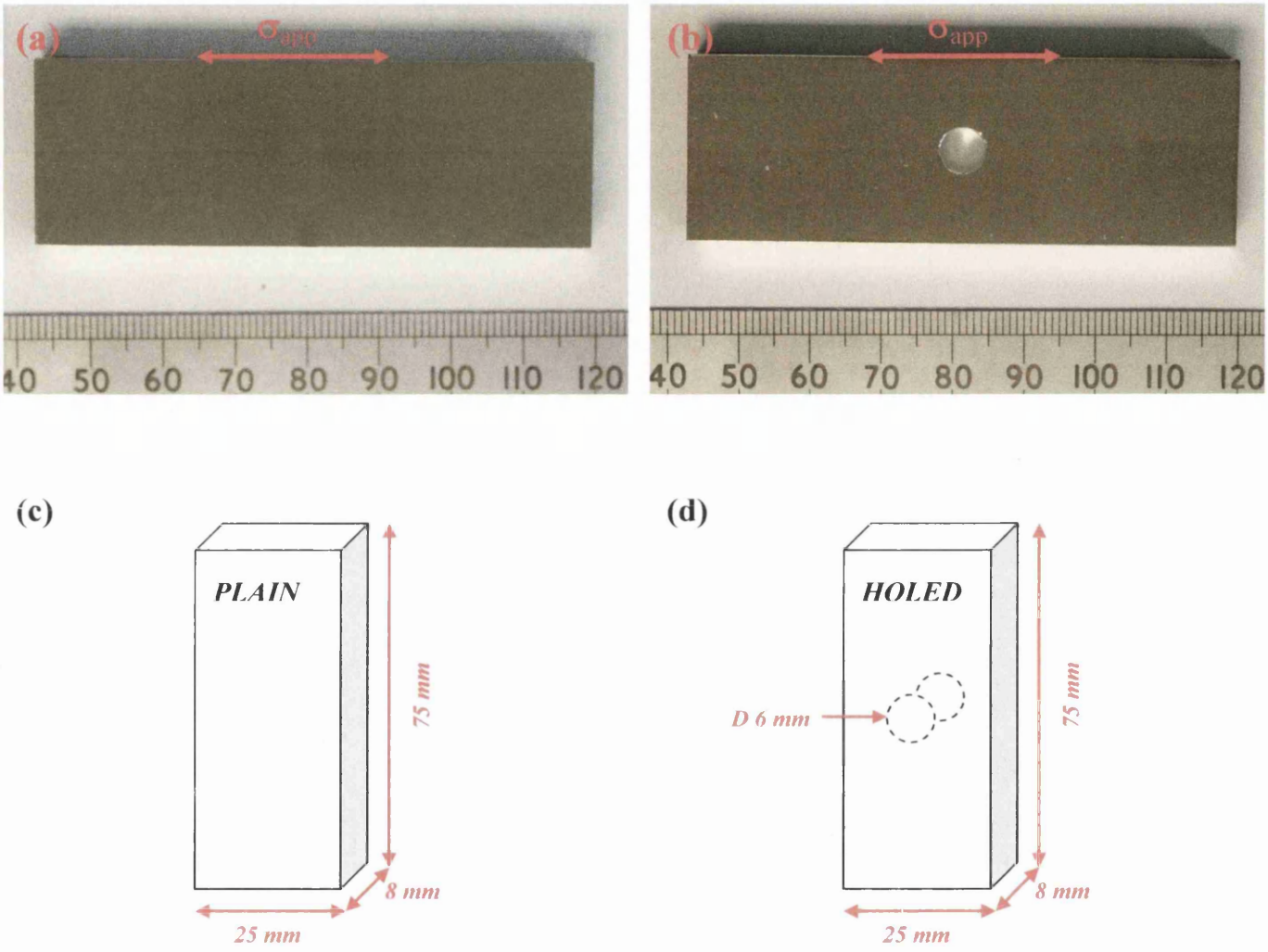

Figure 4.8 (a) plain specimen before corrosion, (b) centre hole specimen before corrosion, and (c) schematic of plain and (d) holed specimen dimensions.

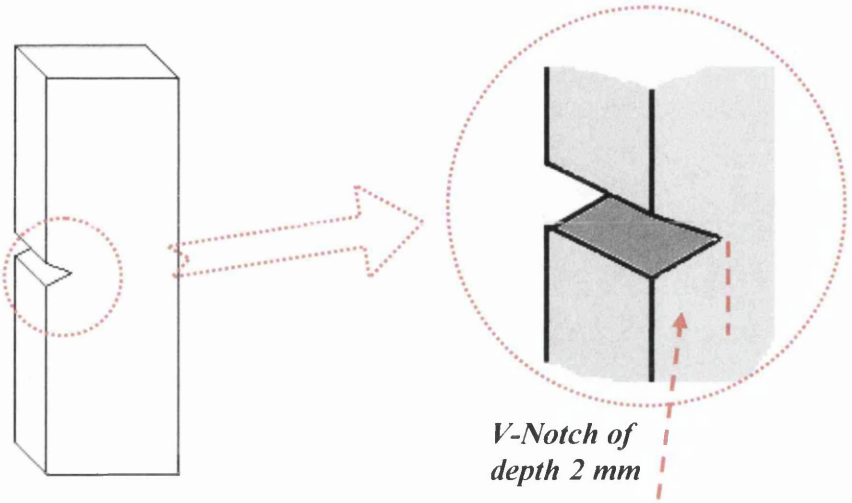

Figure 4.9 Schematic illustration of the Single Edge Notch (SEN) specimen used to determine fatigue crack growth rates.

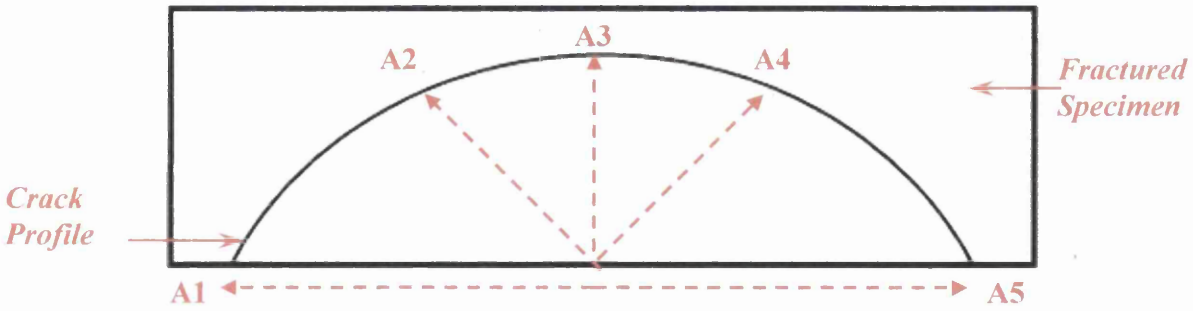

Figure 4.10 Definition of the final crack length profile measurements A1 – A5.

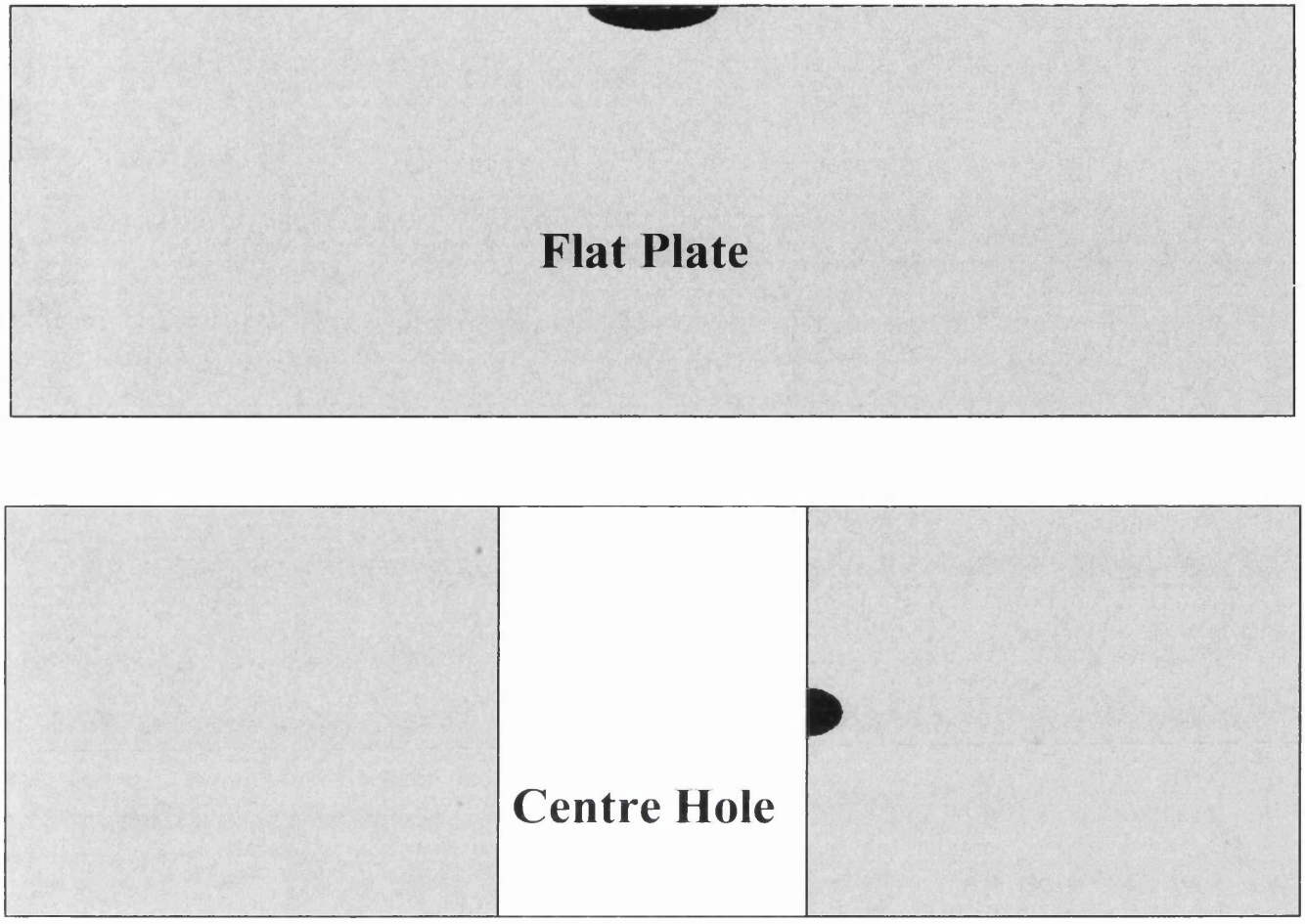

Figure 4.11 Typical cross-sectional examples of starter defects in flat plate and centre hole specimens.

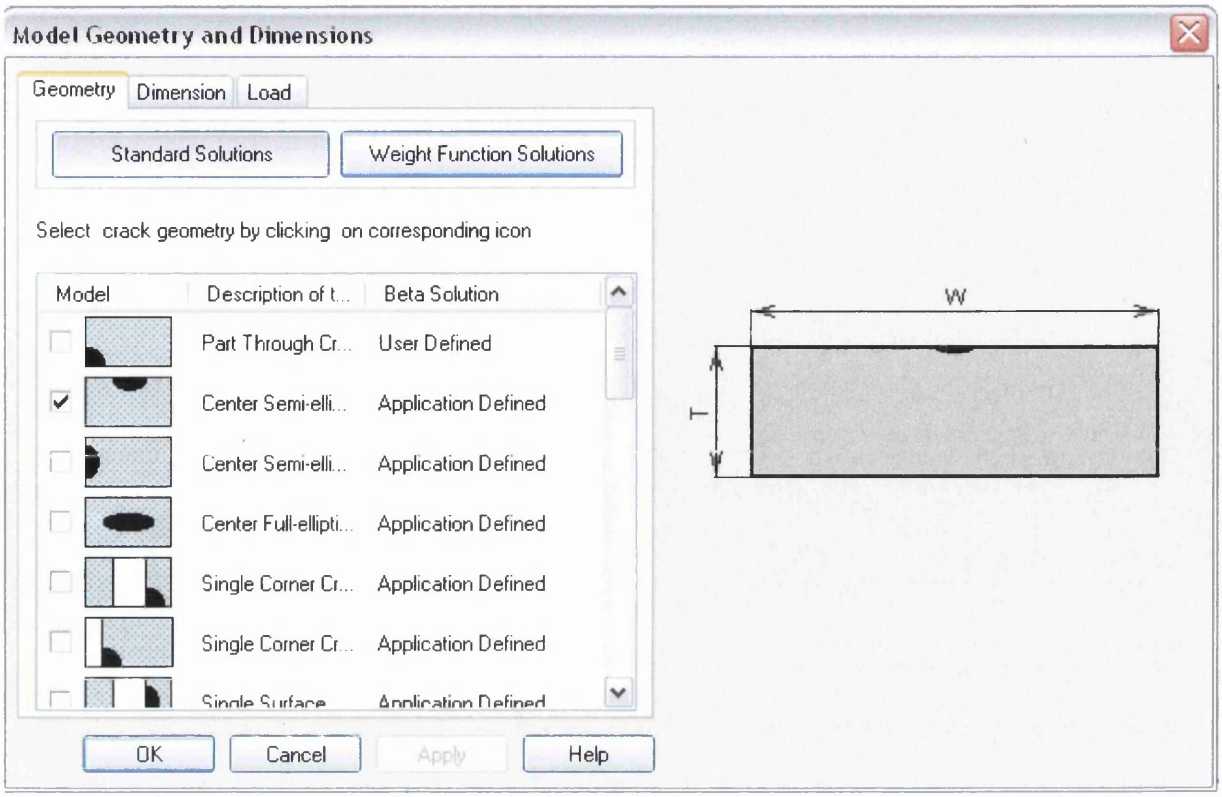

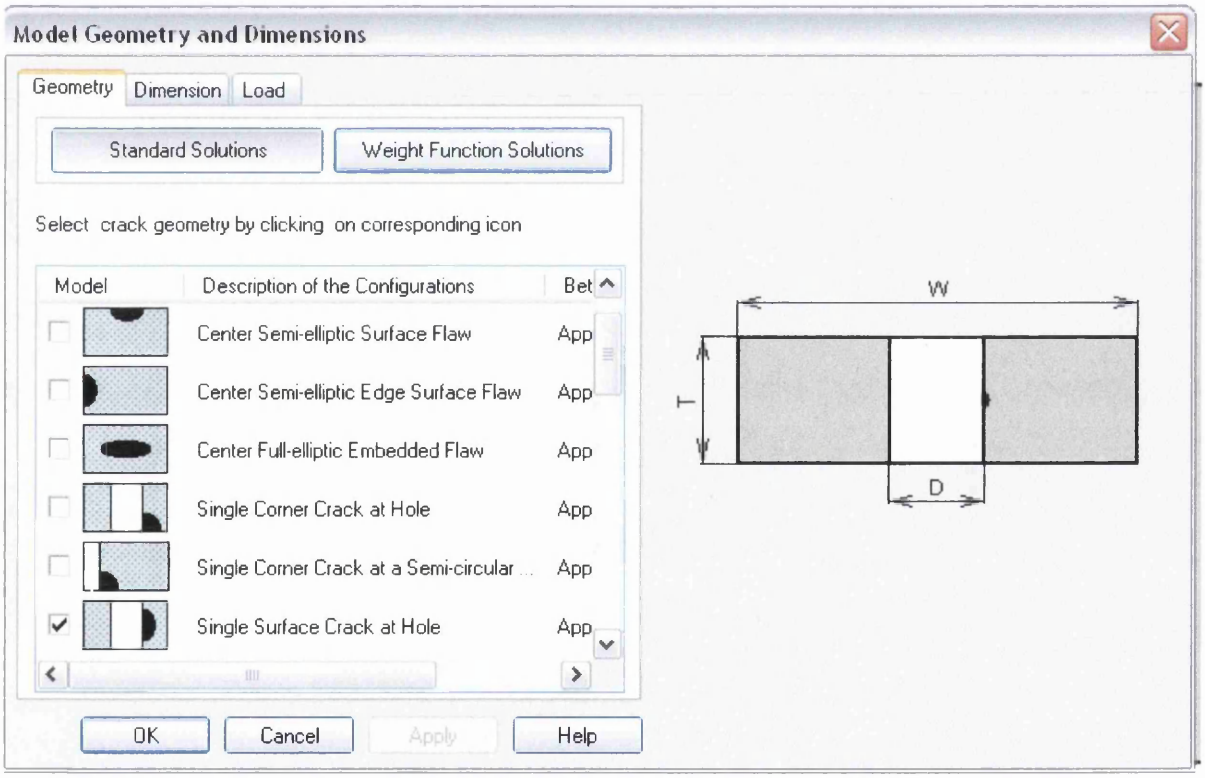

Figure 4.12 Definition of specimen models in AFGROW for flat plate and centre hole specimens.

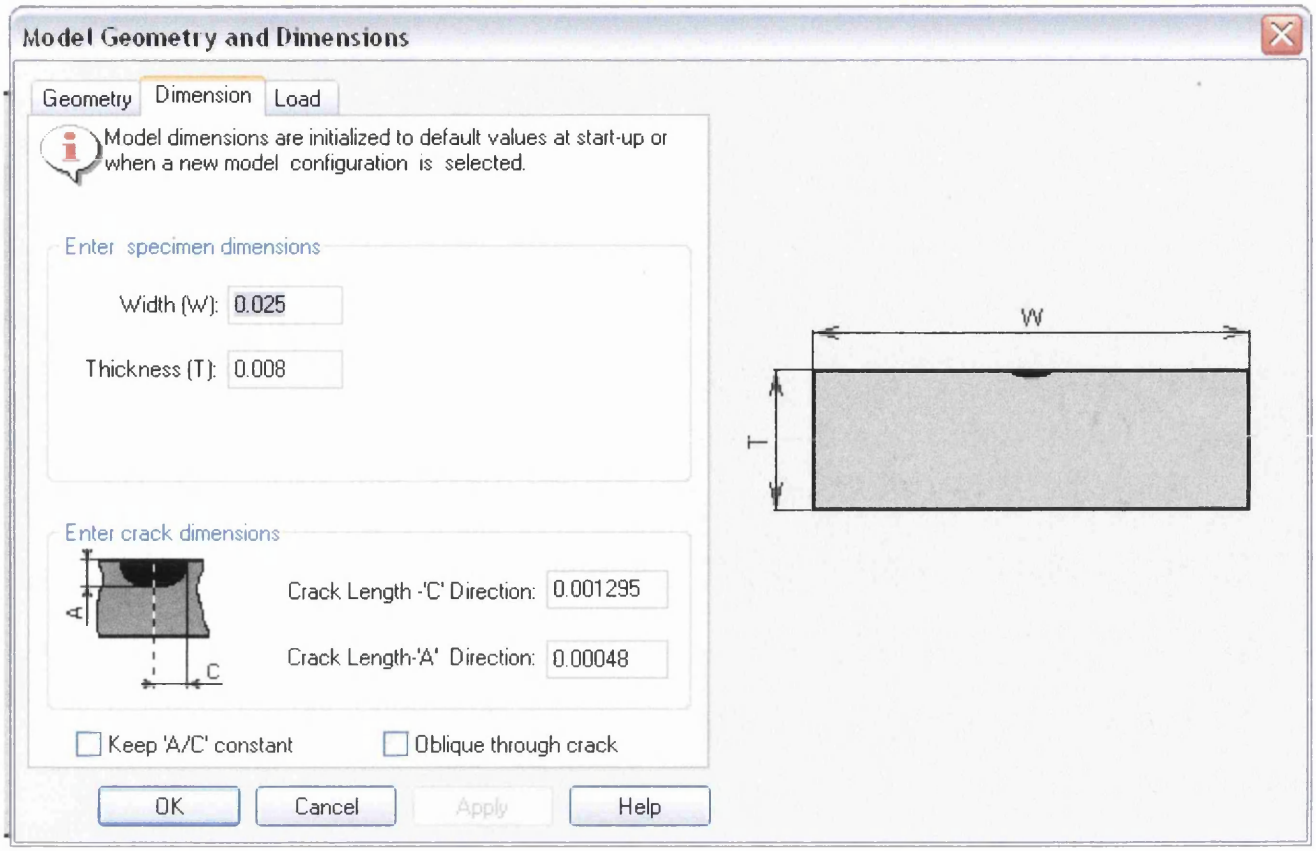

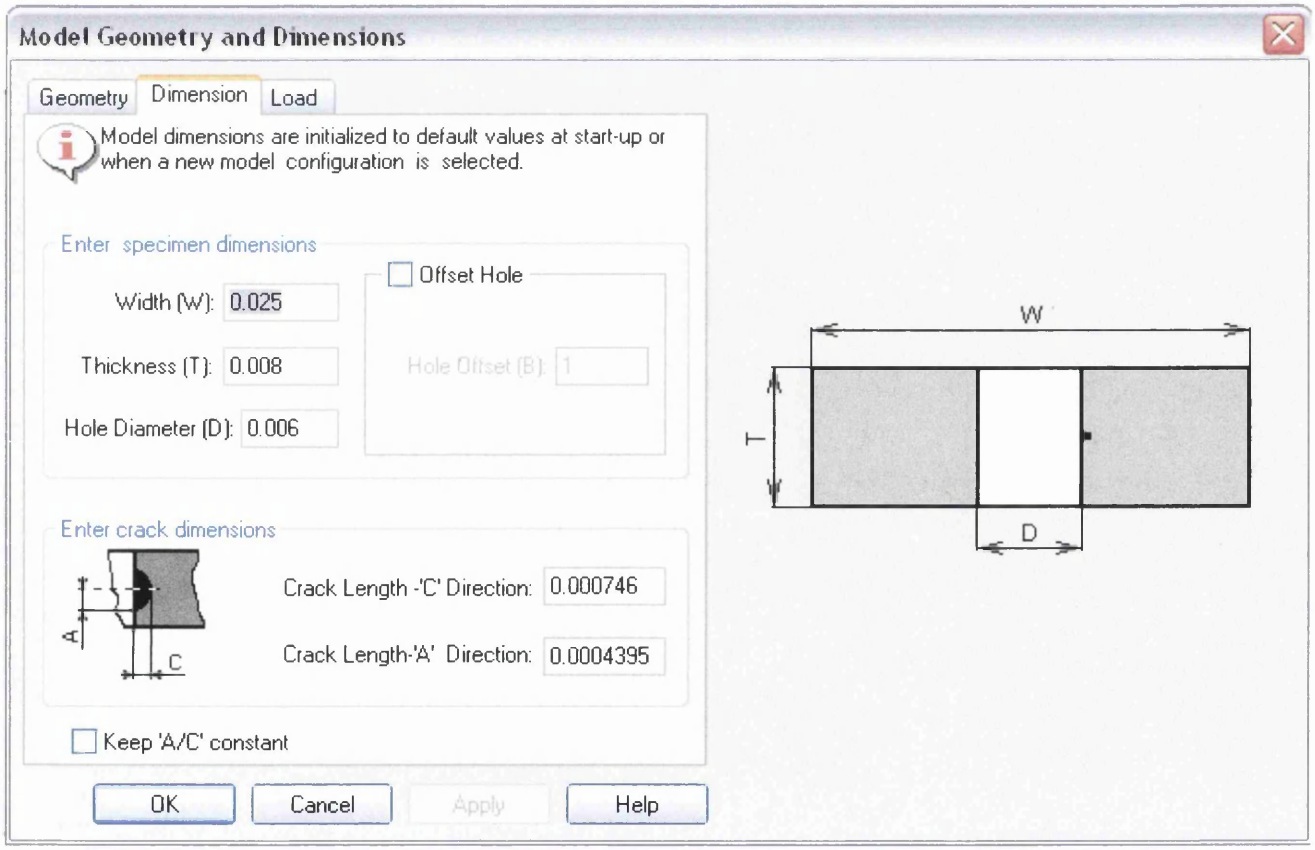

Figure 4.13 Crack dimension entries for flat plate and centre hole specimens.

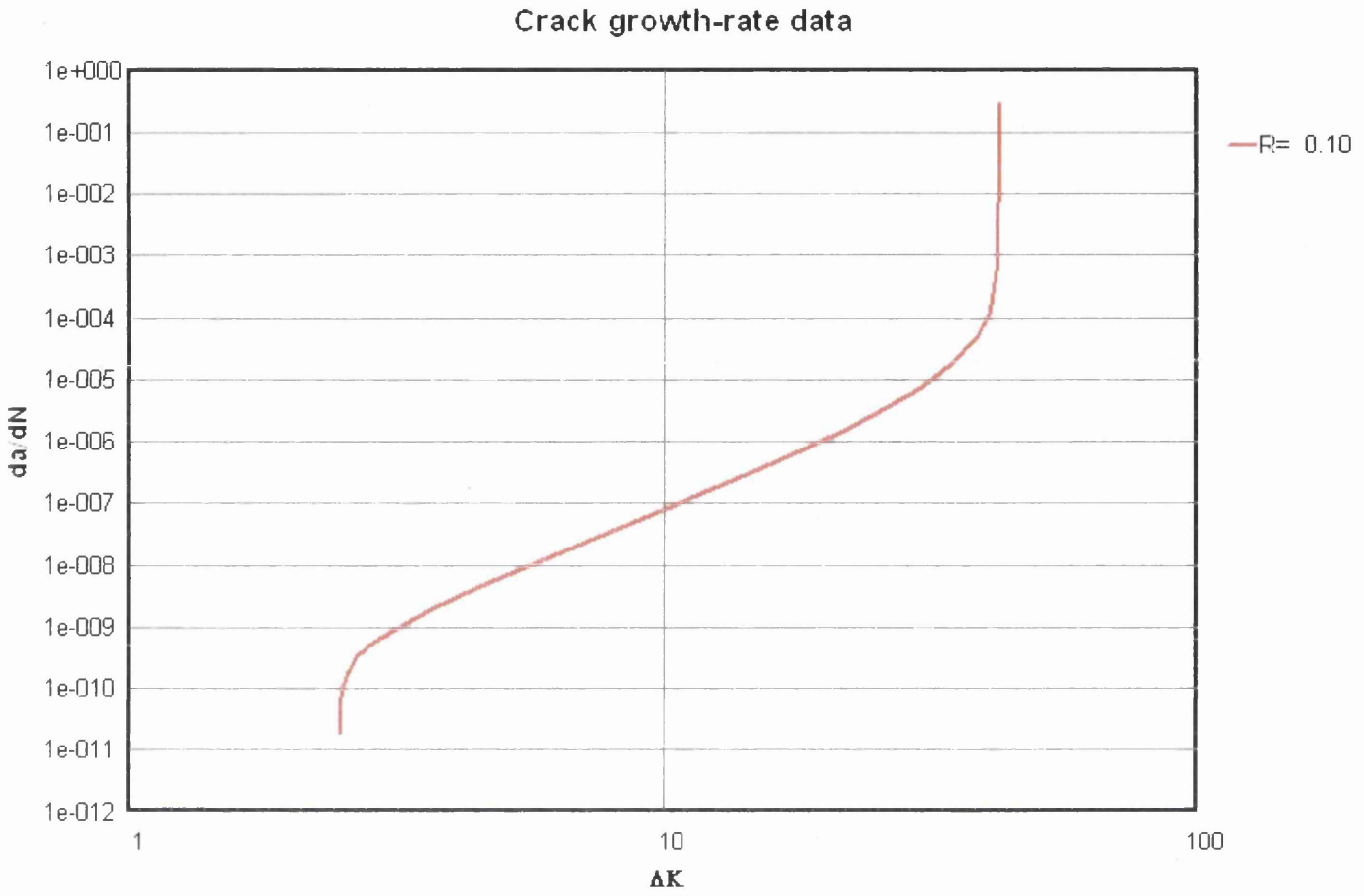

Figure 4.14 Crack growth curve for AA 7010-T73651 at R of 0.1 taken from the NASGRO database.

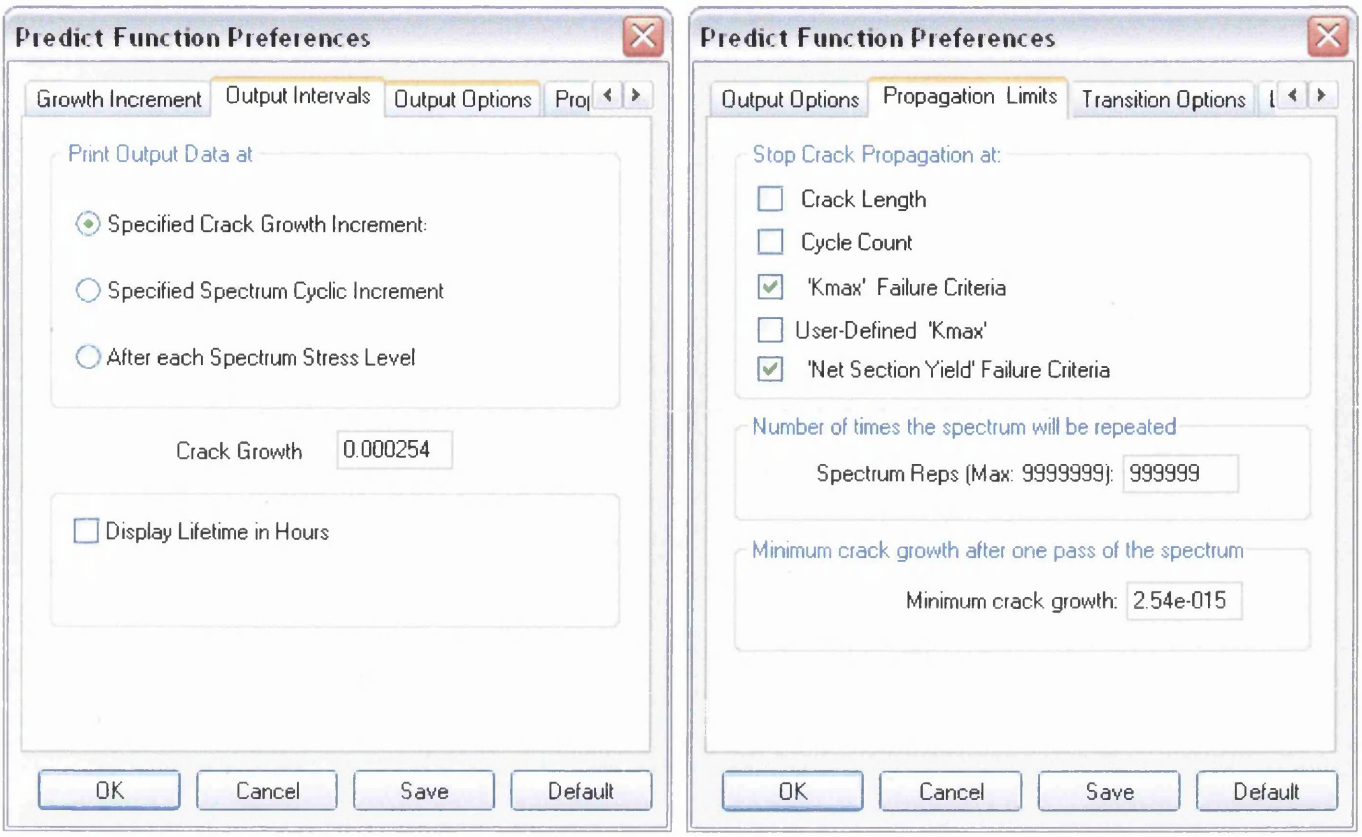

Figure 4.15 Prediction preferences setup within the AFGROW software

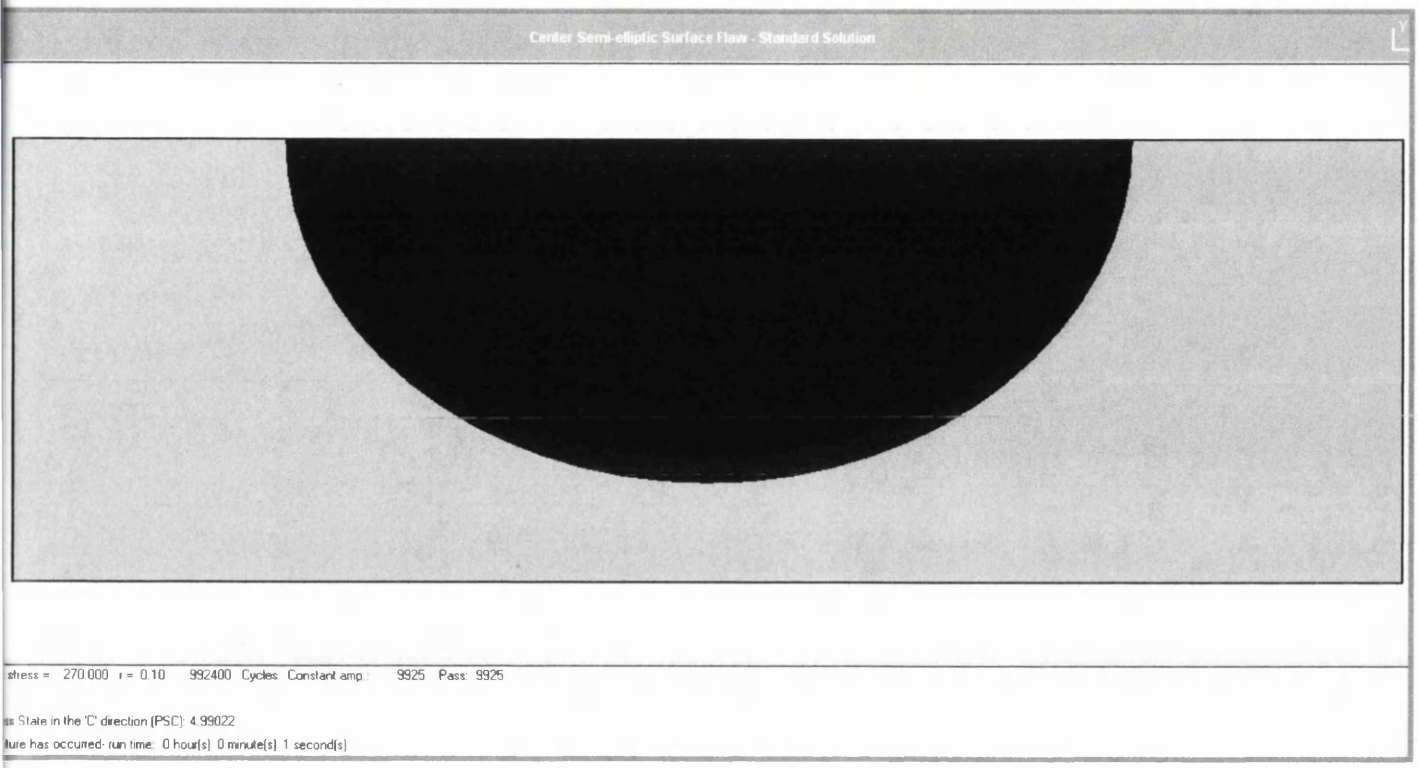

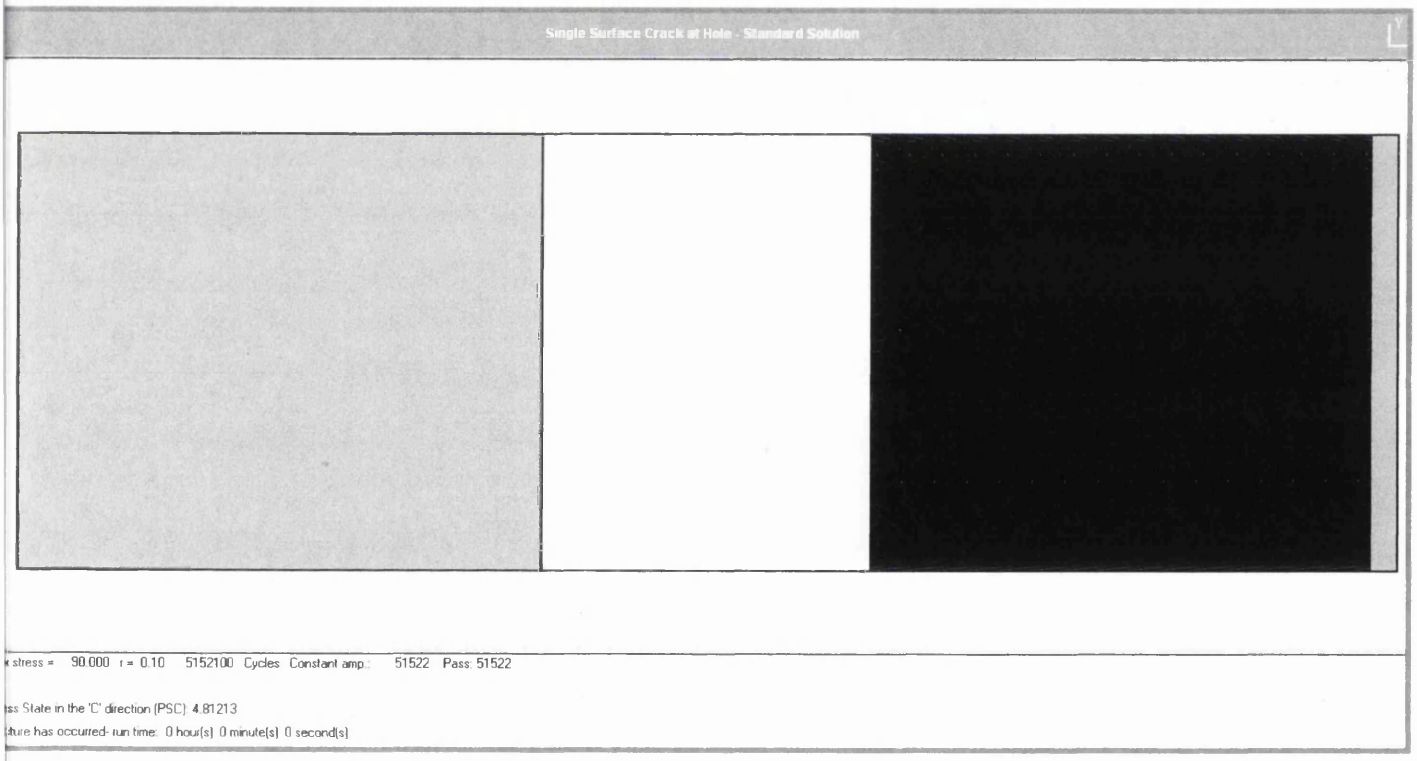

Figure 4.16 Typical examples of completed simulations for flat plate and centre hole specimens.

5.0 RESULTS

This section reports the results generated throughout the investigation period. It is emphasised that a much more extensive database has been generated and a detailed fractographic assessment completed beyond the information presented in this chapter. The entire collection of fractographic results for both specimen geometries is included as an appendix, whilst typical examples will be presented here in order to describe the measured fatigue performance and allow attempts at predicting the mechanical response.

5.1 METALLOGRAPHIC ASSESSMENT

Detailed metallographic assessment of the AA 7010-T7651 material in the three principal planes has been completed. A 3D cubic illustration of the material can be seen in figure 5.1. The microstructural texture of the plate is of a characteristic elongated grain structure parallel to the principal rolling direction, together with stringers of intermetallic particles. Figure 2.3 in the literature review also illustrates the microstructure of the material produced by Patton et al; subsequent to a chromic acid etch. The image clearly reveals the grain structure in the rolling direction. Evident are the grains and subgrains boundaries, together with the intermetallic particles; Al_7Cu_2Fe and Mg_2Si, which appear grey and black respectively.

5.2 CORROSION PROTOCOL

A new corrosion protocol capable of producing relatively large scale pitting representative of worst case in-service damage was developed. Various corrosion pit trials were undertaken to determine the most suitable method of producing large scale pitting corrosion damage. The method chosen to produce the required damage in test specimens was a wet/dry alternation method, as detailed in the experimental procedures, chapter 4. Initial trials showed good pit depths from both open and sealed to air setups, although the open to air technique produced marginally larger corrosion pits. Trials were conducted on anodised plate 7010-T7651

material and were evaluated over a 10 week period. An interesting feature noticed for both open and sealed to air environments was the peaking of pit depth at week 8. Pit depths from week 2 up to week 10 can be seen in table 5.1 and graphically represented by a histogram in figure 5.2. As a result of this investigation it was decided to corrode the fatigue specimens for a total of 8 weeks. Figure 5.3 illustrates examples of the type of pits produced subsequent to this corrosion protocol. Evidently from the pictures, the pits are large in size and have a complex geometry i.e. not spherical in shape. Figure 5.4 illustrates a single large corrosion pit. The pit appears to be larger than 1 mm in diameter in all dimensions and has a surrounding anodised area. As viewed, the actual depth of such pits was difficult to measure, however using an optical focussing technique, estimates of the order of 1 mm were obtained.

5.3. BASIC MECHANICAL PROPERTIES

Basic mechanical properties for the designated alloy were evaluated using tensile tests. Four cylindrical specimens were machined perpendicular to the longitudinal plate rolling direction i.e. parallel to the longitudinal orientation of the fatigue specimens. The specific testing conditions are reported in the experimental procedures section of this thesis. Detailed mechanical properties for the material can be seen in table 5.2 and graphically represented in figure 5.5 in the form of a stress vs. strain plot.

The stress-strain plot firstly illustrates a consistent response at room temperature. Yield stress values for all four specimens, quoted at 480 MPa, further enhance the materials consistent behaviour. Young's modulus values of 65 - 70 GPa were calculated. Ultimate Tensile Strengths (UTS) are also evidently reliable, with the four specimens producing values between 539.9 MPa and 542.8 MPa. Although the UTS and yield values are relatively similar, certain amount of scatter exists between the strain to failure values. Tensile specimen 5 produced the lowest observed strain to failure of 10.14 %, while tensile specimen 2 attained the highest failure strain of 16.06 %. Even though a 6 % difference is noticeable, the results still compare well to other published data for this material. Photographic images of tensile specimen 2 are included in figure 5.6, demonstrating that the material typically shows signs of necking. Fracture ultimately occurred at this necked region.

The current data compares favourably with published tensile information for similar and variants of the 7010 material. Table 5.3 illustrates data produced from various authors researching the 7010 alloy in a range of temper conditions, including the T7651 of current interest. Yield and UTS values compare extremely well with data produced by Schra and Hart, and Patton et al. However, current strain to failure values are marginally greater when compared to Schra and Hart.

5.4 FATIGUE RESPONSE

The fatigue behaviour of the 7010-T7651 material subsequent to corrosion pitting was examined using two specimen designs; flat plate and centre hole. These test coupons were used to provide comprehensive fatigue information in the form of stress-life (S-N) curves, hence, they are reported individually below. Various fracture analysis techniques were completed on both the flat plate and centre hole specimens using a variety of high and low magnification microscopes, together with high definition digital camera media.

5.4.1 Flat Plate Specimens

The material was assessed in an anodised condition, contàining a central area of pitting corrosion. Flat plate specimens were designed to give direct fatigue data comparisons with the international SICAS research programme. The effect of larger scale pitting was examined in terms of the reduction in cyclic lives for a given stress condition. A comprehensive matrix of constant amplitude load control fatigue tests was completed on 8 weeks wet / dry corroded specimens using a servo hydraulic testing facility under closed loop computer control. Three distinct peak stress conditions were evaluated; 270 MPa, 160 MPa and 100 MPa. Multiple repeat tests were performed at these specific conditions together with a preliminary single test at 210 MPa. Table 5.4 represents the complete flat plate test matrix. Cyclic lives, loading conditions and frequency are amongst the values reported. The test environment is also reported in terms of average humidity, temperature and dewpoint. The dewpoint can be defined as the temperature at

which a given amount of air must be cooled at constant pressure for the water vapour to condense into water, this is called dew. The test humidity was controlled in order to negate variations within the laboratory. Clearly from the table, humidity conditions were stabilised between 94.9 % and 99.6 %, while dewpoints and temperatures ranged from 20.89 °C to 27.03 °C.

An S-N curve representing the flat plate data is shown in figure 5.7. The plot illustrates the cyclic lives produced for the four peak stress conditions examined. A distribution of fatigue lives is illustrated for each selected stress condition. The data were also plotted alongside previously reported SICAS data in order to compare the effects of large scale pitting and possible second order material orientation. This stress-life information is plotted in figure 5.8. A significant difference can be observed between the two data sets, with the flat plate data illustrating shorter lives compared to the SICAS data, at any given peak stress condition. The flat plate fatigue lives effectively mirror those produced under SICAS at higher peak stress conditions, for example the SICAS lives generated at 380 MPa (10870 – 22523 cycles) correspond to the lives generated at 270 MPa (9287 – 20396 cycles) for the flat plate specimens, a feature also noticed at the other designated peak stress conditions of 160 MPa and 100 MPa.

5.4.2 Flat Plate Specimens Fracture Characteristics

Various analytical and fractographic techniques were employed on whole and fractured test specimens. These included detailed microscopial studies to identify, evaluate and measure corrosion and fatigue damage. Test specimens were imaged prior and subsequent to fatigue testing, using an array of high specification equipment including high resolution digital cameras, Scanning Electron Microscopes (SEM) and a selection of optical microscopes. This equipment allowed specific corrosion pits to be analysed and identified as fatigue crack initiators. Fractographic analysis of three specimens is reported here, representative of each of the peak stress conditions evaluated.

Figures 5.9 to 5.11 illustrate examples of corrosion pitting, crack initiation locations and final crack profiles. Figure 5.9 presents the corrosion area of test specimen PC-4, tested at the maximum peak stress condition of 270 MPa. The specimen achieved 9287 cycles, the shortest observed fatigue life for specimens examined at this peak stress condition. Figure 5.9a, illustrates the corroded area prior to testing. The image allows corrosion pits to be characterised in terms of morphology and dimension. Pitting density (i.e. the number of pits per given area) can also be determined. Pits are seen to be evenly distributed over the corroded area and appear to be large in size, in terms of the opening surface width and apparent depth defined schematically in Figure 5.10. Pit clustering is also evident within the corroded area, creating densely populated areas. A pit clustering region is highlighted within the image.

Figure 5.9b, again represents specimen PC-4, although subsequent to testing, with the two specimen halves were imaged side by side. Crack initiation can be attributed to this large pit cluster area. The fracture surfaces of specimen PC-4 reveal the complex nature of early stage fatigue crack growth on two slightly different planes in the vicinity of the corrosion pit cluster, figure 5.11. These two cracks soon merged into a single dominant semi-elliptical crack that grew on to a critical size to induce fracture by tensile overload. The final crack profile is clearly evident as defined by the measurements A1 – A5.

Figure 5.11 is an Adobe Photoshop CS© manipulated image, which includes the crack profile measurements, seen here labelled using the A1 – A5 nomenclature, as previously described by figure 4.10. The crack profile measurements for all tested flat plate specimens can be seen in table 5.5. These dimensions are recorded for every fractured specimen and may be used as valued information when relating pit and crack sizes for component lifing correlations. Cracking within specimen PC-4 is seen to advance a total of 5.90 mm (A3 direction) through the 8 mm thick plate, assuming a typical semi circular form. The large pit cluster seen in figure 5.9 was the primary cause of failure.

SEM analysis of the pitting damage present on test specimens could only be completed subsequent to fracture. Specimen PC-4 exposed three corrosion pits on the plane of final fracture. Two of these pits initiated fatigue cracking. Figure 5.12a is a good example of a corrosion pit

causing second order crack initiation. This pit measuring 815 μm wide and 206 μm deep caused a small crack to initiate and grow to approximately 500 μm in depth. The pit seen in figure 5.12b is an example of a non crack initiating pit, although it is considered relatively large in size, measuring 324 μm wide by 131 μm deep. The final image, figure 5.12c shows the largest pit on the plane of final fracture, and measures 2.873 mm wide by 345 μm deep. This pit has an elongated morphology reflecting the microstructure and orientation of the material. The deepest region of the pit can be seen to initiate a fatigue crack. Pit morphologies in this specimen type assume a shallow but wide form as a result of the rolling microstructure. Table 5.6 details pit sizes measured from the plane of final fracture for all specimens. Out of plane cracking is also present on the fracture surface. This is a feature often observed as a result of the high peak stress conditions.

Specimen PC-21 was tested at 160 MPa and achieved 59140 cycles to failure. Similar to the previously discussed specimen PC-4, failure occurred due to fatigue crack initiation from a pit cluster area. Evidence of pit clustering is highlighted in figure 5.13a, while the eventual crack initiation site can be seen in figure 5.13b. A common feature observed for higher stressed specimens is multiple crack initiation from large pits or a cluster made up of a multitude of smaller pits. This specimen is seen to contain three distinct cluster areas, with failure initiating from the largest. Analysis of the fracture surface reveals the magnitude and morphology of the corrosion pit. The location of the pit appears to be reasonably central in relation to the specimen width, which allows the crack profile to produce a near perfect semi-elliptical shape. The crack profile measurements seen in figure 5.14 illustrate a crack depth measurement of 7.08 mm.

The SEM allowed the initiating corrosion pit size to be measured, and more importantly, illustrated three distinct initiation regions along the base of the large pit. Measuring 3.22 mm in length and 410 μm in depth, figure 5.15 demonstrates the complexity and irregularity of pit morphology. This can be seen in greater detail in figure 5.16, which highlights the left hand side of the pit. Visible within the figure is the destructive nature of the pitting as corrosion matter exposes the material, firstly attacking the grain boundary area and subsequently consuming whole grain areas. SEM observations also highlighted river marking, which are features of crack coalescence, on the fracture surface of PC-21. These marks illustrate three distinct initiation

areas. Figure 5.17 also supports this fact, imaged at 45° to the stressing axis; it illustrates both the fracture and corrosion surfaces. Cracking can be seen to occur on various planes, which have coalesced and eventually grown as a single crack. This image also enhances the view of the grain structure, illustrating the short transverse orientation (see also figure 5.1). Elongated grains are clearly visible and lie horizontally in the image.

The final specimen to be presented, PC-17, was tested at the lowest peak stress condition of 100 MPa, achieving 407,564 cycles before failure. This relatively long life can be attributed to the small number of pits produced within the corroded area. The corroded area is visible in Figure 5.18a. Pit clustering again occurred in one primary location, highlighted within the figure. The cluster appears large in apparent depth and opening width, providing a large stress concentration Kt factor for crack initiation. Although large in size this area did not produce crack initiation. Figure 5.18b illustrates the initiation area and crack path and allows the initiating corrosion pit to be identified. In this case it appears small in relation to the large cluster area and is located to the extremity of the corroding area. This off-centre pit produces a crack profile that is skewed to one side. The crack profile is visible in figure 5.19 together with accurate crack dimensions. It is clear that at this relatively low peak stress condition, the crack front is close to becoming a through thickness crack at 7.70 mm in length prior to final overload. Unlike both PC-4, and PC-21, PC-17 has only one initiation area and this is illustrated in the SEM image in figure 5.20. Multiple cracks appear to have initiated around the bas of the pit.

5.4.3 Centre Hole Plate Specimens

The centre hole plate specimens contained corrosion in the bore of a drilled and reamed 6 mm hole. Corrosion pitting was initiated and grown on exposed as-machined material corresponding to the "end-grains". Specimen form and dimensions can be seen in figure 4.8 in chapter 4.

A large test matrix was completed on specimens containing centre holes. This specimen type was essentially developed to simulate fastener holes in aircraft structures/components. The stress concentration factor (K_t) of the 6 mm hole was approximated using standard stress

concentration solutions and was found to be approximately 2.2 [79]. Peak stress was calculated from the specimen net section, i.e. neglecting the area of the 6 mm hole, however, the effect of the stress concentration factor (Kt) of the hole ultimately was ignored. Corrosion periods ranged from a single week up to a maximum of 52 weeks. The humidity level was again controlled during testing. The Relative Humidity (RH) for all tests completed was greater than 95%. Table 5.7 presents the completed test data, detailing the corrosion period, peak stress, r-value, and cycles to failure. Fatigue data for specimens exposed to 8 weeks alternate wet/dry corrosion are presented in an S-N graph in figure 5.21. Ten repeat tests were performed at each of the stress levels; 90, 115 and 135 MPa. At each stress level a distribution in fatigue lives was noted. Considerable overlap was measured for the lives measured from specimens tested at 135 and 115 MPa. Consistent with the lower applied stress, specimens tested at 90 MPa tended to fail at relatively higher cyclic lives, with the longest test accumulating 266,000 cycles. Unfortunately no direct comparisons can be made between the centre hole specimen data to any SICAS generated results on a similar geometry.

In order to assess the knock down induced by corrosion, a set of baseline data were generated for centre hole specimens that were drilled but not corroded. Figure 5.22 compares data from these corrosion free specimens and the data for corroded specimens as detailed in figure 5.21 plus some additional test data relating to some other specific corrosion treatments. This demonstrates that the 8 week alternate wet/dry corrosion induces a weaker response at all stress levels and clearly reduces the fatigue endurance in particular. A corrosion period as short as one week involving intermittent wet/dry periods provided a similar knock down on performance as the 8 week continuous corrosion treatment. Extending the alternate wet/dry over 2 weeks did not appear to have any different response. However, an extended period of wet/dry exposure up to 12 months in total was assessed and specimens were tested at a single stress of 135 MPa. This promoted an even greater knick down on fatigue life at this stress condition.

A limited number of tests were conducted on centre hole specimens which had been exposed to the 8 week wet/dry corrosion procedure, but were later reamed to enlarge the centre hole and partially (or completely) remove any surface corrosion damage. Again this assessment was restricted to a single stress level at 135 MPa, figure 5.23. When compared to the data from

the various corroded data sets, reaming operation #1 clearly has no effect on the measured fatigue lives. However, applying operation reaming #2 recovered the fatigue performance of these specimens, with lives measured that were consistent with the corrosion free centre hole data.

5.4.4 Centre Hole Specimens Fracture Characteristics

Fatigue tests performed on centre hole specimens without corrosion (hole retained as-machined surface finish) tended to initiate fatigue cracking from the surface corner locations, despite the use of manual deburring of the edge location, figure 5.24. In addition, supplementary cracks were seen to initiate from surface locations along the bore of the hole, figure 5.25, which may have been related to artifacts from the machining process. Irrespective of initiation site the very early stages of crack growth generate extremely flat, featureless fracture surfaces, which later give way to radiating river markings. Although aluminium alloys are not noted for cleavage fracture, the very early stages of cracking appear to be crystallographic in nature. Generally the fractures generated in the centre hole specimens gave excellent examples of the cracking interacting with the sub surface microstructure, as in figure 5.24. This is again highlighted in figure 5.26, for cracking in the later stages of the failure process, where striations were also visible, but notably in this example restricted to within the boundaries of a single crystallographic grain.

When preparing the centre hole specimens in a corroded state, an identical corrosion protocol as used for the flat plate specimens was adopted. Inspection of the corrosion within the bore of the hole was extremely difficult prior to testing; however, inspection by eye indicated that the most severe corrosion pitting tended to correlate with the lateral locations on each side of the hole relative to the longitudinal axis of the specimen. This would appear to correlate the most severe corrosion pitting to the exposure of the microstructural end-grains within the hole geometry, as illustrated by the schematic representation of figure 5.27 (grain structure around the hole). Subsequent to fatigue testing and specimen rupture, inspections within the hole were possible.

In the following paragraphs fractures from centre hole specimens will be described adopting the nomenclature as in figure 5.28. This is necessary because in practice fatigue initiation and crack growth would usually occur from either side of the centre hole. It was not always possible from post fracture inspection to identify the actual site of the very first site of crack initiation, since multiple cracks grew from a variety of corrosion pits along the bore of the hole. Figure 5.29 is an example of this behaviour, viewing the failure locations on both sides of the sample after longitudinal sectioning. Major cracks have developed on different planes that eventually interact or intercept large pit clusters along the root of the hole were usually identified as a major site for crack initiation. The temporal relationship between fracture on the opposing side of the hole can only be estimated by the extent of the fatigue crack to the either side of the specimen immediately before final rupture. The majority of specimens produced fracture such as that illustrated in figure 5.30, where the through section fatigue crack grew to a longer length in the Y direction when compared to the X. Again it can be confirmed that the very early stages of cracking from the corrosion pit was highly crystallographic in nature.

Every tested specimen was inspected to obtain details on the size and shape of corrosion pits that initiate fracture on the eventual fracture plane, these are collated in table 5.8.

5.5 CRACK PROPAGATION TESTING

Fatigue Crack Growth (FCG) data measured using single edge notch specimens provided cracking representing the ST-L and L-ST orientations are presented in figure 5.31. These orientations correspond to cracks in the corroded centre hole and flat plate specimens respectively. No effect of crack orientation was noted. A power law line of best fit has been calculated through the data to obtain values for the Paris coefficients. This gave an m value of 2.02 and with $C = 7 \times 10^{-10}$ m/cycle. The present FCG data are then reproduced in figure 5.32, where they are compared to the best fit trend generated for the same material during the SICAS project [80] and also data extracted from the NASGRO database (R = 0.1) within the AFGROW fracture mechanics model. A difference was noted between the best fits describing the current measurements and those from SICAS, however, this difference was not great, and the SICAS

measurements were actually taken in a different orientation (L-T). The NASGRO data appears to correlate with either of these data sets over the range of ΔK between 8 and 50 MPa$\sqrt{m}$. Despite employing an optical measuring technique to define crack growth characteristics, the scatter in the current data was acceptable, given that defining the crack tip using travelling microscopes is notoriously difficult. The two optical images in figure 5.33 and 5.34 illustrate the surface fatigue cracks in two different specimens (in each case the root of the edge notch can be seen in profile at the edge of the image). These illustrate that the cracks follow a torturous path through the microstructure often branching and turning sharply, possibly affected by the presence of fine intermetallic particles.

5.6 AFGROW FATIGUE LIFE PREDICTIONS

This section details the LEFM predictions correlating to the measured fatigue performance of the corroded flat plate and centre hole specimens. Specific input parameters and the use of the NASGRO fatigue crack growth best fit data were described in detail in the experimental methods chapter.

Concentrating on the flat plate specimen the experimental data measured during the current study are replotted in figure 5.35 on an S-N basis. Each measured data point relates to the life for a single test specimen (Blue triangle). It has previously been stated that when performing a post fracture inspection, more than one corrosion pit would be exposed on the plane of fracture, therefore it was often impossible to deduce which of these pits initiated the major crack that eventually lead to fracture. Therefore, every example of pitting has been taken as a starter defect for the purpose of calculating an LEFM life to fracture at the respective level of applied stress. Each of these individual calculations generates a predicted life to failure, also plotted in figure 5.35 (red squares). Therefore, at any stress condition there will be a greater number of predicted points compared to the actual number of measured data. The data in figure 5.35 also allowed the aspect ratio of the fatigue crack to vary during the fracture model within AFGROW i.e. the two extremes of a/c will relate to the original pit dimensions and the final crack profiles immediately before overload. Irrespective of applied stress level there was always a degree of overlap

between the range of measured fatigue lives and the range of associated predicted lives. However, in general the predictions were slightly non conservative.

The same exercise was repeated but this time fixing the aspect ratio of the crack within AFGROW to that of the starter corrosion pit. The predicted lives are plotted against the measured data in figure 5.36. The act of fixing the aspect ratio clearly provides an inferior prediction of the fatigue performance. This perhaps was to be expected, knowing that in reality, the crack profiles evolve during the fracture process. In a final attempt to predict the performance of the flat plate specimens, figure 5.37 was generated. In this case the plot shows a single prediction point to correlate with each single measured datum. This was done by calculating the average surface opening width and average pit depth of any pits exposed on the eventual fracture surface. This technique appears to yield the most accurate prediction of the measured S-N curve.

Transferring attention the corroded centre hole specimens a similar modelling approach has been taken. However, in these specimens, the general fracture process was notably more complex as previously mentioned, the number of pits initiating cracks was relatively large and was often impossible to identify a single pit leading to a single dominant crack. In light of this, when viewing figure 5.38, each single test is represented by a single measured point, where as the number of predicted points is now relatively larger than in the flat plate specimen examples. Irrespective of stress level the range of measured lives straddled the measured data. By using the average surface opening width and average depth, figure 5.39, an excellent correlation is found between the measured and predicted fatigue performance.

It should be noted that to calculate the predictions of fatigue life of corroded centre hole specimens, initiation and growth has been assumed to occur solely to one side of the centre hole (i.e. within AFGROW the cracking was modelled using the single surface crack at hole geometry).

Table 5.1 Maximum apparent pit depths for open and sealed to air wet/dry corrosion pitting trials.

WEEKS	MAXIMUM PIT DEPTHS	
	OPEN	SEALED
2	240μm	135μm
4	170μm	135μm
6	250μm	189μm
8	345μm	275μm
10	210μm	180μm
Average	240 μm	183 μm

Table 5.2 Mechanical properties of the material as defined by four tensile specimens.

Specimen N°	Average Gauge Diameter (mm)	Yield Stress (Mpa)	UTS (Mpa)	Relative Elongation (%)	Youngs Modulus (Gpa)
Tens-5	4.080	480	539.9	10.14	70
Tens-4	4.064	480	542.8	13.55	66
Tens-3	4.076	480	541	15.91	65
Tens-2	4.076	480	540.3	16.06	65

Table 5.3 Mechanical property data for the 7010 alloy subjected to various heat treatments. Included is the current research data, added for comparative purposes.

Author	Temper	Yield Stess	Tenile Strength	Relative Elongation	Fracture Energy
		σ_e 0.2 (Mpa)	σ_r (Mpa)	ε_r (%)	W (MJm^{-3})
Forsyth (1999)	T-736	Min.500	n/a	n/a	n/a
Patton et al (1998)	T-7651	n/a	535	n/a	n/a
Puiggali et al (1998)	T-351	381	555	9.5	44.1
	T-651	470	545	5.4	24.2
	T-7451	410	484	7	30.2
Robinson (2000)	T-6	545	583	7.3	n/a
	T-7	500	551	10	n/a
Schra and Hart (1983)	T-7651	(L) ~470	~530	~11.0	n/a
		(L-T) ~471	~540	~12.0	
	T-73651	(L) ~420	~500	~10.25	n/a
		(L-T) ~421	~510	~10.75	
Morgans (2006)	T-7651	480	541	~13.90	n/a

Table 5.4 Constant amplitude fatigue data for the flat plate specimens.

Specimen I.D	C.S.A (mm)	Peak Load (kN)	Min Load (kN)	Max Stress (Mpa)	R-Value	Cycles to Failure	Average Relative Humidity (%RH)	Average Temperature (°C)	Average Dewpoint (°C)	Frequency
PC-1	199.76	53.94	5.39	270	0.1	**11548**	97.91	26.21	25.98	2 Hz
PC-2	199.75	53.93	5.39	270	0.1	**16648**	98.03	24.04	23.82	2 Hz
PC-3	199.82	53.95	5.40	270	0.1	**20396**	97.61	23.46	23.17	2 Hz
PC-4	199.49	53.86	5.39	270	0.1	**9287**	98.08	22.45	22.24	2 Hz
PC-5	199.30	53.81	5.38	270	0.1	**14071**	98.88	24.75	24.68	2 Hz
PC-6	199.12	53.76	5.38	270	0.1	**13437**	97.37	23.45	23.12	2 Hz
PC-7	200.03	54.01	5.40	270	0.1	**15879**	97.4	22.3	21.96	2 Hz
PC-8	199.90	53.97	5.40	270	0.1	**12217**	97.24	25.79	25.56	2 Hz
PC-9	199.33	53.82	5.38	270	0.1	**12248**	97.31	24.1	23.76	2 Hz
PC-10	199.73	53.93	5.39	270	0.1	**17031**	97.91	25.17	24.93	2 Hz
PC-11	200.70	42.15	4.21	210	0.1	**28255**	94.9	25.84	25.07	2 Hz
PC-12	199.94	19.99	2.00	100	0.1	**286088**	99.6	23.61	23.66	2 Hz
PC-13	198.02	19.80	1.98	100	0.1	**268200**	99.48	20.88	20.89	2 Hz
PC-14	198.57	19.86	1.99	100	0.1	**293225**	99.16	25.28	25.26	2 Hz
PC-15	199.95	19.99	2.00	100	0.1	**324482**	98.8	23.72	23.63	2 Hz
PC-16	200.14	20.01	2.00	100	0.1	**278408**	99.51	26.01	26.05	2 Hz
PC-17	199.08	19.91	1.99	100	0.1	**407564**	99.11	25.18	25.15	2 Hz
PC-18	199.11	19.91	1.99	100	0.1	**416137**	98.78	23.45	23.36	2 Hz
PC-19	200.56	20.06	2.01	100	0.1	**514426**	97.63	26.84	26.74	2 Hz
PC-20	199.55	19.95	2.00	100	0.1	**281552**	99.15	27.04	27.03	2 Hz
PC-21	199.11	31.86	3.19	160	0.1	**59140**	94.99	22.24	21.5	2 Hz
PC-22	199.50	31.92	3.19	160	0.1	**54489**	97.5	25.54	25.23	2 Hz
PC-23	199.33	31.89	3.19	160	0.1	**77109**	98.09	26.39	26.19	2 Hz
PC-24	198.16	31.71	3.17	160	0.1	**121437**	98.15	26.25	26.06	2 Hz
PC-25	200.34	32.05	3.21	160	0.1	**64421**	96.98	25.99	25.6	2 Hz
PC-26	199.03	31.85	3.18	160	0.1	**55393**	97.11	24.27	23.99	2 Hz
PC-27	199.42	31.91	3.19	160	0.1	**104642**	96.16	26.36	25.82	2 Hz
PC-28	198.99	31.84	3.18	160	0.1	**37027**	97.56	24.74	24.44	2 Hz
PC-29	198.53	31.76	3.18	160	0.1	**70932**	97.46	24.98	24.67	2 Hz
PC-30	199.97	31.99	3.20	160	0.1	**69500**	96.84	26.58	26.16	2 Hz

Table 5.5 Crack profile measurements for flat plate specimens.

Specimen I.D	Pit N°	Crack Profile Measurements (mm)					
		X-coord	A1	A2	A3	A4	A5
PC-01	1	14.57	8.63	6.64	5.44	6.87	6.66
PC-02	1	14.07	6.81	6.85	5.80	6.98	7.81
	2						
	3						
PC-03	1	9.20	7.67	7.54	5.90	6.61	0.00
	2	14.61	3.44	3.66	3.60	3.78	0.00
	3	18.03	1.90	2.04	1.90	1.86	1.78
PC-04	1	9.91	6.86	6.94	5.90	7.02	7.81
	2						
	3						
PC-05	1	10.87	8.67	6.38	5.70	6.60	7.61
	2						
PC-06	1	11.38	6.23	6.81	5.96	7.56	9.10
	2						
	3						
PC-07	1	11.33	5.65	6.66	5.84	7.01	8.80
	2						
	3						
	4						
	5						
PC-08	1	12.44	7.89	6.97	5.71	6.57	6.83
	2						
	3						
	4						
PC-09	1	14.84	9.36	6.35	5.80	0.00	0.00
	2						
	3						
	4	18.51	0.00	0.00	4.18	5.65	6.50
	5						
PC-10	1	6.65	5.70	5.61	4.98	4.98	4.98
	2						
	3						
	4	13.35	1.62	1.73	1.98	2.39	3.15
	5						
PC-11	1	15.58	7.96	6.81	5.43	6.68	9.47
	2						
	3						
	4						
PC-12	1	11.60	11.60	9.51	7.99	9.00	10.96
	2						
PC-13	1	12.00	12.00	10.03	8.00	9.08	10.87
PC-14	1	15.54	10.77	8.92	7.88	9.66	9.61
PC-15	1	15.54	10.73	8.98	7.96	9.64	9.57
	2						
	3						
PC-16	1	9.89	9.89	8.86	8.00	9.76	11.75
PC-17	1	8.75	8.75	9.53	7.70	8.95	10.39
PC-18	1	12.43	12.43	9.58	7.98	8.71	12.49
	2						
	3						
PC-19	1	11.90	11.90	9.71	7.91	9.43	12.13
	2						
PC-20	1	16.32	10.36	8.61	7.53	9.66	8.46
PC-21	1	11.42	11.20	8.43	7.08	8.40	10.10
PC-22	1	12.64	7.25	7.34	7.13	7.93	10.88
	2						
	3						
PC-23	1	12.31	12.31	8.71	7.14	7.95	9.73
PC-24	1	12.41	3.47	4.28	7.13	10.09	12.91
	2						
	3						
PC-25	1	13.10	8.54	7.34	6.72	8.40	10.97
PC-26	1	12.75	9.51	8.81	7.65	8.13	11.08
	2						
	3						
PC-27	1	11.38	11.38	7.89	6.64	7.91	9.13
	2						
	3						
	4						
PC-28	1	9.41	9.41	7.95	7.44	8.62	9.85
PC-29	1	9.47	8.27	7.27	6.08	0.00	0.00
	2	17.39	0.00	0.00	4.95	6.22	7.63
PC-30	1	9.72	9.72	8.97	7.33	7.74	7.79

Table 5.6 Flat Plate specimen pit metrics as measured from plane of final fracture.

Specimen I.D	Pit No	Surface Opening Width (μm)	Max Width (μm)	Max Depth (μm)	Pit Area (μm^2)
PC-01	1	889	889	193	83620
PC-02	1	476	598	183	71488
	2	593	625	135	55034
	3	2178	2590	480	661674
PC-03	1	1832	2044	324	439555
	2	400	947	232	116004
	3	1085	1376	179	138971
PC-04	1	185	324	131	22749
	2	2712	2873	345	647643
	3	526	815	206	102042
PC-05	1	2284	3240	346	629898
	2	1076	1076	165	104473
PC-06	1	424	435	104	29166
	2	3129	3278	326	569952
	3	563	593	91	27289
PC-07	1	3482	3543	391	671276
	2	599	599	120	37546
	3	473	484	131	37336
	4	750	777	182	98028
	5	481	636	155	59126
PC-08	1	410	594	148	53358
	2	1884	1957	278	358047
	3	385	385	112	28850
	4	221	251	90	14820
PC-09	1	546	546	111	35403
	2	874	1186	278	181333
	3	251	312	126	24179
	4	407	807	211	96694
	5	725	937	262	128537
PC-10	1	1124	1165	275	220111
	2	1094	1093	103	57531
	3	773	1246	203	149867
	4	423	748	131	63635
	5	850	1502	297	155332
PC-11	1	363	467	136	34624
	2	569	569	108	32413
	3	308	359	118	27060
	4	2320	2576	360	552509
PC-12	1	1859	2380	462	637467
	2	1077	1470	347	300121
PC-13	1	2200	2629	446	707892
PC-14	1	3357	3745	544	915389
PC-15	1	1841	2253	398	479693
	2	1531	1652	232	236501
	3	381	614	127	30761
PC-16	1	2212	2224	471	487042
PC-17	1	1501	1688	258	303592
PC-18	1	2331	2441	349	542444
	2	890	1268	706	288806
	3	284	684	152	56561
PC-19	1	1205	1451	189	155014
	2	1158	1283	285	207737
PC-20	1	2325	2494	470	540166
PC-21	1	2809	3219	410	870377
PC-22	1	1900	2046	365	359649
	2	207	267	134	20317
	3	473	580	138	55085
PC-23	1	1526	1599	331	371017
PC-24	1	391	458	151	45068
	2	1191	1560	301	318739
	3	679	699	144	66539
PC-25	1	1582	2184	319	458577
PC-26	1	424	545	175	61279
	2	242	352	159	31257
	3	3712	3741	465	756748
PC-27	1	807	1515	499	333547
	2	503	1025	197	112775
	3	277	292	100	17695
	4	432	475	199	60346
PC-28	1	2785	3247	628	1297471
PC-29	1	1914	2008	338	427489
	2	972	1179	246	209332
PC-30	1	1559	2310	395	523082

Table 5.7 Constant amplitude fatigue data for the Centre Hole plate specimens.

Specimen I.D	Corrosion Period (Weeks)	Hole Diameter (mm)	Max Stress (Mpa)	R-Value	Cycles to Failure	Average Relative Humidity (%RH)	Frequency
FH-NC-1	-	6.05	135	0.1	128590	Not Measured	2Hz
FH-NC-2	-	6.03	170	0.1	57324	Not Measured	2Hz
FH-NC-3	-	6.04	185	0.1	31412	Not Measured	2Hz
FH-NC-4	-	6.02	125	0.1	235014	Not Measured	2Hz
FH-NC-5	-	6.04	180	0.1	38394	Not Measured	2Hz
FH-NC-6	-	6.04	145	0.1	85708	Not Measured	2Hz
FH-NC-7	-	6.00	155	0.1	82305	Not Measured	2Hz
FH-C1-1	1	6.03	100	0.1	96333	90.7	2Hz
FH-C1-2	1	6.03	115	0.1	62968	92.1	2Hz
FH-C1-3	1	6.03	135	0.1	36971	91.2	2Hz
FH-C2-1	2	6.05	135	0.1	46536	Not Measured	2Hz
FH-C2-2	2	6.00	100	0.1	131841	Not Measured	2Hz
FH-C2-3	2	6.09	115	0.1	74317	Not Measured	2Hz
FH-C2-4	2	6.06	135	0.1	54455	90.30%	2Hz
FH-C2-5	2	6.06	100	0.1	111875	95%	2Hz
FH-C2-6	2	6.03	115	0.1	64714	96%	2Hz
FH-C8-1	8	6.00	90	0.1	265728	97.75	2 Hz
FH-C8-2	8	6.00	90	0.1	174442	Log Fail	2 Hz
FH-C8-3	8	6.03	90	0.1	160084	96.6	2 Hz
FH-C8-4	8	6.01	90	0.1	118328	96.84	2 Hz
FH-C8-5	8	5.99	90	0.1	126399	96.9	2 Hz
FH-C8-6	8	6.00	90	0.1	111646	97.32	2 Hz
FH-C8-7	8	5.99	90	0.1	162281	96.45	2 Hz
FH-C8-8	8	5.97	90	0.1	150012	97.14	2 Hz
FH-C8-9	8	6.02	90	0.1	168341	96.85	2 Hz
FH-C8-10	8	6.00	90	0.1	239120	97.68	2 Hz
FH-C8-11	8	6.03	115	0.1	74513	97.22	2 Hz
FH-C8-12	8	6.02	115	0.1	70398	96.25	2 Hz
FH-C8-13	8	6.03	115	0.1	79172	97.84	2 Hz
FH-C8-14	8	6.00	115	0.1	95542	97.38	2 Hz
FH-C8-15	8	6.02	115	0.1	94975	97.59	2 Hz
FH-C8-16	8	6.02	115	0.1	58406	97.04	2 Hz
FH-C8-17	8	6.00	115	0.1	109373	97.57	2 Hz
FH-C8-18	8	6.01	115	0.1	86704	97.61	2 Hz
FH-C8-19	8	6.02	115	0.1	74775	96.99	2 Hz
FH-C8-20	8	6.03	115	0.1	58749	97.4	2 Hz
FH-C8-21	8	6.00	135	0.1	61099	88.8	2 Hz
FH-C8-22	8	6.03	135	0.1	48273	95.97	2 Hz
FH-C8-23	8	6.01	135	0.1	53451	95.34	2 Hz
FH-C8-24	8	6.00	135	0.1	68753	95.41	2 Hz
FH-C8-25	8	6.00	135	0.1	39419	95.48	2 Hz
FH-C8-26	8	6.02	135	0.1	50369	95.82	2 Hz
FH-C8-27	8	6.02	135	0.1	49132	94.06	2 Hz
FH-C8-28	8	6.01	135	0.1	61979	95.92	2 Hz
FH-C8-29	8	6.01	135	0.1	80358	95.89	2 Hz
FH-C8-30	8	6.00	135	0.1	45329	94.66	2 Hz
FH-C8R-1	8	6.24	135	0.1	39584	Not Measured	2 Hz
FH-C8R-2	8	6.24	135	0.1	49463	Not Measured	2 Hz
FH-C8R-3	8	6.24	135	0.1	28812	Not Measured	2 Hz
FH-C8R-4	8	6.50	135	0.1	133553	Not Measured	2 Hz
FH-C8R-5	8	6.50	135	0.1	104521	Not Measured	2 Hz
FH-C8R-6	8	6.50	135	0.1	104639	Not Measured	2 Hz
FH-C12M-1	52	6.02	135	0.1	34703	Not Measured	2Hz
FH-C12M-2	52	6.03	135	0.1	21785	Not Measured	2Hz
FH-C12M-3	52	6.03	135	0.1	43596	Not Measured	2Hz
FH-C12M-4	52	6.02	135	0.1	29468	Not Measured	2Hz

Table 5.8 Corrosion pit measurements for centre hole specimens.

Specimen I.D	Pit N°	Surface Opening Width (μm)	Max Width (μm)	Max Depth (μm)	Pit Area (μm^2)
FH-C8-01	1	15	41	60	954
	2	22	36	78	1716
	3	42	54	59	1988
	4	232	263	190	32981
FH-C8-02	1	83	115	74	5670
	2	51	61	57	2228
	3	63	83	51	2506
	4	50	82	110	4583
FH-C8-3	1	118	126	273	20737
	2	374	374	98	15843
	3	71	71	30	1057
	4	212	212	81	10215
	5	66	96	264	14167
FH-C8-04	1	183	184	177	18062
	2	131	172	201	20728
	3	407	489	351	118246
	4	54	61	103	4045
	5	42	42	67	1347
	6	447	447	180	35153
	7	222	222	201	17395
	8	53	72	47	2816
FH-C8-05	1	225	225	317	31784
	2	123	171	148	14970
	3	217	245	278	25420
	4	211	246	322	54105
	5	117	132	145	12724
FH-C8-06	1	153	153	172	10602
	2	96	96	138	6003
	3	42	42	60	1041
	4	157	157	269	18103
	5	84	84	67	4220
	6	274	352	373	59526
FH-C8-07	1	123	140	209	11638
	2	128	128	28	2261
	3	834	834	341	98232
FH-C8-08	1	149	263	697	112018
	2	216	216	308	25166
	3	333	443	1074	302152
FH-C8-09	1	43	61	73	2203
	2	124	146	78	6897
	3	69	74	60	2737
	4	54	56	67	1753
	5	101	104	78	4800
	6	27	34	43	954
	7	148	148	62	5122
	8	172	172	83	5374
FH-C8-10	1	159	159	37	2959
	2	236	236	63	10711
	3	390	406	51	9322
FH-C8-11	1	168	196	113	14421
	2	22	26	51	678
	3	146	146	29	1677
	4	62	65	55	1570
	5	108	108	43	1174
	6	73	73	54	425
	7	132	132	123	657
FH-C8-12	1	145	145	60	4746
	2	147	180	31	4133
	3	270	278	71	6985
	4	80	111	40	1023
	5	129	151	102	5611
	6	141	141	119	9722
	7	55	78	86	3778

Specimen I.D	Pit N°	Surface Opening Width (μm)	Max Width (μm)	Max Depth (μm)	Pit Area (μm^2)
FH-C8-13	1	222	313	343	60452
	2	56	60	162	4979
	3	20	22	41	461
	4	22	25	76	775
	5	43	73	101	2963
	6	22	22	35	232
	7	22	22	21	277
	8	44	44	56	1147
	9	16	30	49	667
	10	25	34	33	515
	11	48	48	126	3646
	12	69	76	67	3588
FH-C8-14	1	190	190	59	4355
	2	166	166	29	2886
	3	115	115	61	2258
	4	86	86	19	1185
	5	85	85	21	1547
FH-C8-15	1	91	91	145	2325
	2	43	48	28	478
	3	20	22	40	422
	4	13	18	30	236
	5	14	14	19	217
	6	108	124	130	10852
FH-C8-16	1	457	486	693	194119
	2	113	137	273	17438
	3	53	80	158	6877
	4	149	149	127	7837
	5	21	39	42	725
	6	112	112	71	2601
	7	50	50	63	1491
	8	31	31	108	2176
	9	43	49	67	943
	10	76	90	80	4480
	11	130	130	46	3463
FH-C8-17	1	81	81	64	1173
	2	40	40	42	880
	3	16	24	54	565
FH-C8-18	1	20	30	82	1524
	2	64	120	196	11905
	3	12	12	29	63
	4	6	12	40	295
	5	32	32	96	1137
	6	28	28	18	262
	7	79	82	20	1040
	8	107	107	70	1835
	9	15	16	16	142
	10	27	28	56	784
	11	32	33	59	805
	12	33	33	60	849
	13	51	51	58	876
FH-C8-19	1	166	166	33	2412
	2	18	18	25	261
	3	21	21	35	288
	4	11	19	53	561
	5	176	176	41	3156
	6	46	49	64	1691
	7	391	417	483	136344
	8	38	43	51	1047

Specimen I.D	Pit N°	Surface Opening Width (μm)	Max Width (μm)	Max Depth (μm)	Pit Area (μm²)
FH-C8-20	1	251	259	71	6877
	2	244	298	292	47058
	3	87	99	85	5691
	4	173	177	69	6374
	5	157	157	96	10231
	6	78	98	73	1177
	7	32	35	127	1719
	8	194	255	666	103834
	9	273	360	666	129286
FH-C8-21	1	7	12	52	191
	2	90	96	93	6728
	3	116	128	61	2942
	4	285	285	78	9084
	5	107	117	107	5638
	6	85	118	57	4017
	7	48	48	16	545
FH-C8-22	1	182	216	127	19165
	2	70	75	76	3857
	3	57	56	82	3245
	4	219	219	248	24010
	5	142	161	71	4706
FH-C8-23	1	197	199	119	14513
	2	64	68	80	3078
	3	67	71	68	3659
	4	81	81	24	1277
	5	32	37	44	586
	6	52	52	43	1628
	7	78	110	128	9527
FH-C8-24	1	88	88	18	790
	2	64	64	21	875
	3	73	73	24	1115
	4	32	32	13	211
FH-C8-25	1	397	415	88	21963
	2	261	266	49	7452
	3	86	92	51	2375
	4	24	24	22	236
	5	43	43	59	1210
	6	11	22	52	546
	7	53	53	59	842
	8	314	314	463	60190
	9	59	70	109	12396
	10	93	93	187	5618
FH-C8-26	1	25	43	35	781
	2	58	58	23	617
	3	73	73	45	1160
	4	51	51	49	812
	5	59	100	104	6510
FH-C8-27	1	425	481	343	95557
	2	28	59	66	2538
	3	31	49	104	1965
	4	8	26	48	692
	5	16	17	51	441
	6	101	105	72	2400
FH-C8-28	1	92	102	44	1514
	2	755	767	55	27106
	3	46	45	45	662
	4	79	79	48	1447
	5	158	158	41	2894
	6	151	161	24	2134
	7	171	176	43	2930
	8	128	128	48	2664
FH-C8-29	1	426	426	40	10564
	2	107	107	23	927
	3	64	64	25	930
	4	107	107	40	1180
	5	97	97	30	2018
FH-C8-30	1	216	216	36	4014
	2	422	422	95	19358
	3	49	49	18	516

Table 5.9 Comparison between actual measured lives and AFGROW predicted lives for flat plate specimens using the pit surface opening width metric.

				AFGROW Predicted Lives based on Surface Opening Width Metric		
Specimen I.D	Pit No	Peak Stress (Mpa)	Actual Life	Predicted Life	PredictedLife (A/C Constant)	Average Pit Size
PC- 01	1	270	*11548*	38973	147268	38973
PC- 02	1	270	*16648*	54641	66462	30833
	2			55260	191065	
	3			15862	56666	
PC- 03	1	270	*20396*	21072	129800	31532
	2			53414	38474	
	3			36115	274800	
PC- 04	1	270	*9287*	97015	57291	31941
	2			16159	242900	
	3			49558	58482	
PC- 05	1	270	*14071*	17933	166100	24542
	2			37464	350900	
PC- 06	1	270	*13437*	72470	216200	32213
	2			15200	407600	
	3			65900	622200	
PC- 07	1	270	*15879*	12958	277700	33663
	2			57500	275600	
	3			62714	140480	
	4			43599	127846	
	5			58172	96020	
PC- 08	1	270	*12217*	64113	86689	47014
	2			22165	221800	
	3			73938	151075	
	4			106487	119737	
PC- 09	1	270	*12248*	62116	290200	48868
	2			33900	56558	
	3			86615	73250	
	4			55358	45122	
	5			38238	51097	
PC- 10	1	270	*17031*	29788	84646	39140
	2			44836	No Growth	
	3			41100	101041	
	4			66314	118674	
	5			33435	47186	
PC- 11	1	210	*28255*	183736	237132	100293
	2			158341	No Growth	
	3			215391	269591	
	4			43582	382400	
PC- 12	1	100	*286088*	738200	No Growth	984894
	2			1768094	No Growth	
PC- 13	1	100	*268200*	661900	No Growth	661900
PC- 14	1	100	*293225*	431983	No Growth	431983
PC- 15	1	100	*324482*	814871	No Growth	1693300
	2			1361775	No Growth	
	3			No Growth	No Growth	
PC- 16	1	100	*278408*	638700	No Growth	638700
PC- 17	1	100	*407564*	1290000	No Growth	1290000
PC- 18	1	100	*416137*	725400	No Growth	1272500
	2			947800	486500	
	3			No Growth	No Growth	
PC- 19	1	100	*514426*	No Growth	No Growth	2095880
	2			1772178	No Growth	
PC- 20	1	100	*281552*	103263	462500	103263
PC- 21	1	160	*59140*	97733	1075900	97733
PC- 22	1	160	*54489*	131374	694200	268471
	2			No Growth	No Growth	
	3			514638	No Growth	
PC- 23	1	160	*77109*	156493	617593	156493
PC- 24	1	160	*121437*	581236	No Growth	300394
	2			188899	525339	
	3			378261	No Growth	
PC- 25	1	160	*64421*	155736	745300	155736
PC- 26	1	160	*55393*	474314	524688	177014
	2			909316	430500	
	3			76670	1283900	
PC- 27	1	160	*104642*	182834	122897	341167
	2			390016	470150	
	3			No Growth	No Growth	
	4			429914	395463	
PC- 28	1	160	*37027*	79838	268500	79838
PC- 29	1	160	*70932*	135394	912400	171063
	2			233116	672745	
PC- 30	1	160	*69500*	142692	382138	142692

Table 5.10 Comparison between actual measured lives and AFGROW predicted lives for flat plate specimens using the maximum pit width metric.

				AFGROW Predicted Lives based on Maximum Width Metric		
Specimen I.D	**Pit No**	**Peak Stress (Mpa)**	**Actual Life**	**Predicted Life**	**PredictedLife (A/C Constant)**	**Average Pit Size**
PC- 01	1	270	*11548*	38973	147268	38973
PC- 02	1	270	*16648*	48836	88382	28237
	2			53787	210870	
	3			14200	77400	
PC- 03	1	270	*20396*	19744	162100	27091
	2			35016	99650	
	3			31773	470200	
PC- 04	1	270	*9287*	75532	85394	29274
	2			15585	276100	
	3			39758	10600	
PC- 05	1	270	*14071*	14436	359200	21265
	2			37464	350900	
PC- 06	1	270	*13437*	71537	226552	31438
	2			14764	454500	
	3			64165	717000	
PC- 07	1	270	*15879*	12814	288800	32900
	2			57500	275600	
	3			61985	145746	
	4			42813	135951	
	5			50540	147955	
PC- 08	1	270	*12217*	53285	148895	44756
	2			21688	240800	
	3			73938	151075	
	4			99971	138860	
PC- 09	1	270	*12248*	62116	290200	41971
	2			28800	90000	
	3			78160	88578	
	4			39568	98051	
	5			33500	71826	
PC- 10	1	270	*17031*	29214	89900	33358
	2			44836	No Growth	
	3			31870	248100	
	4			49585	333700	
	5			24543	114399	
PC- 11	1	210	*28255*	160098	337386	94491
	2			158341	No Growth	
	3			197421	330337	
	4			40889	479100	
PC- 12	1	100	*286088*	611100	No Growth	778000
	2			1090100	No Growth	
PC- 13	1	100	*268200*	578298	No Growth	578298
PC- 14	1	100	*293225*	398400	No Growth	398400
PC- 15	1	100	*324482*	692972	No Growth	1305600
	2			1252998	No Growth	
	3			No Growth	No Growth	
PC- 16	1	100	*278408*	636100	No Growth	636100
PC- 17	1	100	*407564*	1140300	No Growth	1140300
PC- 18	1	100	*416137*	699800	No Growth	990081
	2			742300	535000	
	3			No Growth	No Growth	
PC- 19	1	100	*514426*	No Growth	No Growth	1549675
	2			1473400	No Growth	
PC- 20	1	100	*281552*	98784	528200	98784
PC- 21	1	160	*59140*	89634	1482400	89634
PC- 22	1	160	*54489*	125597	808200	250590
	2			No Growth	No Growth	
	3			434394	No Growth	
PC- 23	1	160	*77109*	152200	675600	152200
PC- 24	1	160	*121437*	497937	No Growth	268536
	2			161135	879900	
	3			370493	No Growth	
PC- 25	1	160	*64421*	128338	1543300	128338
PC- 26	1	160	*55393*	395796	744697	171067
	2			627800	563351	
	3			76292	1307500	
PC- 27	1	160	*104642*	130134	202462	169515
	2			250200	No Growth	
	3			No Growth	No Growth	
	4			402816	431636	
PC- 28	1	160	*37027*	71997	350300	71997
PC- 29	1	160	*70932*	131534	1013600	161284
	2			207991	987900	
PC- 30	1	160	*69500*	112413	798800	112413

Figure 5.11 Comparison between actual measured lives and AFGROW predicted lives for centre hole specimens using the pit surface opening width metric.

				AFGROW Predicted Lives based on Surface Opening Width Metric		
Specimen I.D	**Pit No**	**Peak Stress (Mpa)**	**Actual Life**	**Predicted Life**	**PredictedLife (A/C Constant)**	**Average Pit Size**
FH-C8-01	1	90	265728	481583	No Growth	262049
	2			384351	No Growth	
	3			384044	No Growth	
	4			163639	803054	
FH-C8-02	1	90	174442	290156	No Growth	313954
	2			374942	No Growth	
	3			379934	No Growth	
	4			273443	No Growth	
FH-C8-3	1	90	160084	167656	No Growth	188534
	2			173847	119000	
	3			542344	485162	
	4			214243	208176	
	5			192444	No Growth	
FH-C8-04	1	90	118328	180533	No Growth	177152
	2			171052	No Growth	
	3			123252	732678	
	4			276156	No Growth	
	5			357545	No Growth	
	6			143853	162186	
	7			162358	1065529	
	8			420034	No Growth	
FH-C8-05	1	90	126399	141834	No Growth	160443
	2			202348	No Growth	
	3			148341	No Growth	
	4			142849	No Growth	
	5			205940	No Growth	
FH-C8-06	1	90	111646	183954	No Growth	186136
	2			218338	No Growth	
	3			380455	No Growth	
	4			159253	No Growth	
	5			302741	No Growth	
	6			130442	No Growth	
FH-C8-07	1	90	162281	180455	No Growth	148437
	2			362847	188000	
	3			107053	130700	
FH-C8-08	1	90	150012	126500	No Growth	113900
	2			144052	No Growth	
	3			94581	No Growth	
FH-C8-09	1	90	168341	340039	No Growth	292456
	2			252750	616487	
	3			337846	No Growth	
	4			338144	No Growth	
	5			269049	No Growth	
	6			525552	No Growth	
	7			287548	566200	
	8			225546	313400	
FH-C8-10	1	90	239120	301141	169500	228843
	2			222558	147376	
	3			199935	103380	
FH-C8-11	1	*115*	74513	82740	227651	108543
	2			170049	No Growth	
	3			124532	67630	
	4			131144	No Growth	
	5			122443	119847	
	6			126541	417891	
	7			84938	533982	
FH-C8-12	1	*115*	70398	102448	108944	97841
	2			121678	67983	
	3			82784	55936	
	4			136155	187590	
	5			89978	359951	
	6			84341	404130	

				AFGROW Predicted Lives based on Surface Opening Width Metric		
Specimen I.D	**Pit No**	**Peak Stress (Mpa)**	**Actual Life**	**Predicted Life**	**PredictedLife (A/C Constant)**	**Average Pit Size**
FH-C8-13	1	*115*	79172	57051	1905400	113341
	2			92642	No Growth	
	3			190653	No Growth	
	4			145941	No Growth	
	5			113845	No Growth	
	6			170085	No Growth	
	7			206948	250880	
	8			140944	No Growth	
	9			185553	No Growth	
	10			200942	No Growth	
	11			103383	No Growth	
	12			118849	No Growth	
FH-C8-14	1	*115*	95542	95349	72581	120285
	2			118985	62253	
	3			107983	171830	
	4			168452	90884	
	5			164284	94949	
FH-C8-15	1	*115*	94975	86752	No Growth	121651
	2			186585	471385	
	3			192752	No Growth	
	4			241783	No Growth	
	5			303343	No Growth	
	6			86741	1274000	
FH-C8-16	1	*115*	58406	41030	1348800	81247
	2			69082	No Growth	
	3			94443	No Growth	
	4			81752	404548	
	5			186650	No Growth	
	6			103783	239679	
	7			130881	No Growth	
	8			119746	No Growth	
	9			132082	No Growth	
	10			109353	573949	
	11			113454	96648	
FH-C8-17	1	*115*	109373	116079	455554	142555
	2			161884	No Growth	
	3			178483	No Growth	
FH-C8-18	1	*115*	86704	145448	No Growth	139385
	2			85155	No Growth	
	3			250153	No Growth	
	4			256584	No Growth	
	5			123548	No Growth	
	6			260052	No Growth	
	7			171348	99853	
	8			105442	260643	
	9			330353	No Growth	
	10			155348	No Growth	
	11			146850	No Growth	
	12			145885	No Growth	
	13			134453	No Growth	
FH-C8-19	1	*115*	74775	115142	63247	63541
	2			247646	No Growth	
	3			202882	No Growth	
	4			196941	No Growth	
	5			106879	64233	
	6			132484	No Growth	
	7			46779	772200	
	8			151152	No Growth	

Specimen I.D	Pit No	Peak Stress (Mpa)	Actual Life	Predicted Life	PredictedLife (A/C Constant)	Average Pit Size
				Surface Opening Width Metric		
FH-C8-20	1	115	58749	84449	60247	64545
	2			58654	828800	
	3			103944	765600	
	4			93854	96029	
	5			87655	192850	
	6			112079	739448	
	7			113049	No Growth	
	8			49348	No Growth	
	9			45849	No Growth	
FH-C8-21	1	135	61099	121437	No Growth	59496
	2			55587	437940	
	3			59589	93000	
	4			44636	31347	
	5			51388	372987	
	6			65537	165345	
	7			114437	84699	
FH-C8-22	1	135	48273	43837	131783	47386
	2			62490	571424	
	3			63939	No Growth	
	4			35136	401300	
	5			54385	78748	
FH-C8-23	1	135	53451	43888	95984	61396
	2			62683	No Growth	
	3			65394	486076	
	4			85837	58977	
	5			89885	No Growth	
	6			80799	334538	
	7			51839	No Growth	
FH-C8-24	1	135	68753	90496	48735	98689
	2			96084	71647	
	3			90896	62936	
	4			139698	128538	
FH-C8-25	1	135	39419	39889	24938	48183
	2			50669	28496	
	3			67599	130479	
	4			125800	No Growth	
	5			75692	No Growth	
	6			107589	No Growth	
	7			72285	No Growth	
	8			27636	760600	
	9			57691	No Growth	
	10			44738	No Growth	
FH-C8-26	1	135	50369	103636	No Growth	75838
	2			96338	89742	
	3			73235	151294	
	4			76939	438139	
	5			58540	No Growth	
FH-C8-27	1	135	49132	28396	137483	50937
	2			79739	No Growth	
	3			67192	No Growth	
	4			119987	No Growth	
	5			98987	No Growth	
	6			99592	No Growth	
FH-C8-28	1	135	61979	69490	89546	56389
	2			37038	20275	
	3			82389	648787	
	4			70383	141850	
	5			60892	39245	
	6			70585	36276	
	7			58938	37483	
	8			62135	57276	
FH-C8-29	1	135	80358	46292	24185	64639
	2			79496	44547	
	3			91186	83880	
	4			68586	62081	
	5			76340	55394	
FH-C8-30	1	135	45329	57438	30645	52539
	2			38599	24446	

Table 5.12 Comparison between actual measured lives and AFGROW predicted lives for centre hole specimens using the maximum pit width metric.

				AFGROW Predicted Lives based on Maximum Width Metric		
Specimen I.D	**Pit No**	**Peak Stress (Mpa)**	**Actual Life**	**Predicted Life**	**PredictedLife (A/C Constant)**	**Average Pit Size**
FH-C8-01	1	90	265728	382250	No Growth	237552
	2			342240	No Growth	
	3			362540	No Growth	
	4			159438	564200	
FH-C8-02	1	90	174442	263552	692688	289752
	2			359051	No Growth	
	3			345837	No Growth	
	4			245952	No Growth	
FH-C8-3	1	90	160084	165457	No Growth	186650
	2			173847	119000	
	3			542344	485162	
	4			214243	208176	
	5			176734	No Growth	
FH-C8-04	1	90	118328	175350	1418765	173655
	2			171052	No Growth	
	3			119031	441379	
	4			269052	No Growth	
	5			357545	No Growth	
	6			143853	162186	
	7			162358	1065529	
	8			381555	No Growth	
FH-C8-05	1	90	126399	141834	No Growth	156355
	2			188255	1090752	
	3			144935	1995071	
	4			138835	No Growth	
	5			200745	No Growth	
FH-C8-06	1	90	111646	183954	No Growth	182544
	2			218338	No Growth	
	3			380455	No Growth	
	4			159253	No Growth	
	5			302741	No Growth	
	6			124537	1361229	
FH-C8-07	1	90	162281	175950	No Growth	147738
	2			362847	188000	
	3			107053	130700	
FH-C8-08	1	90	150012	110800	No Growth	107400
	2			144052	No Growth	
	3			88400	No Growth	
FH-C8-09	1	90	168341	314649	No Growth	285739
	2			241048	403891	
	3			331049	No Growth	
	4			335248	No Growth	
	5			266658	No Growth	
	6			500137	No Growth	
	7			287548	566200	
	8			225546	313400	
FH-C8-10	1	90	239120	301141	169500	227252
	2			222558	147376	
	3			197354	102000	
FH-C8-11	1	*115*	74513	79946	158748	107148
	2			164041	No Growth	
	3			124532	67630	
	4			129540	653829	
	5			122443	119847	
	6			126541	417891	
	7			84938	533982	
FH-C8-12	1	*115*	70398	102448	108944	95048
	2			113953	59830	
	3			82148	54437	
	4			123749	106238	
	5			86944	238830	
	6			84341	404130	

				AFGROW Predicted Lives based on Maximum Width Metric		
Specimen I.D	**Pit No**	**Peak Stress (Mpa)**	**Actual Life**	**Predicted Life**	**PredictedLife (A/C Constant)**	**Average Pit Size**
FH-C8-13	1	*115*	79172	53643	594641	108042
	2			91251	No Growth	
	3			186842	No Growth	
	4			141654	No Growth	
	5			101978	No Growth	
	6			170085	No Growth	
	7			206948	250880	
	8			140944	No Growth	
	9			161754	No Growth	
	10			186941	No Growth	
	11			103383	No Growth	
	12			116078	632488	
FH-C8-14	1	*115*	95542	95349	72581	120285
	2			118985	62253	
	3			107983	171830	
	4			168452	90884	
	5			164284	94949	
FH-C8-15	1	*115*	94975	86752	No Growth	114678
	2			180148	334738	
	3			188884	No Growth	
	4			225844	No Growth	
	5			303343	No Growth	
	6			84283	750936	
FH-C8-16	1	*115*	58406	40533	1089700	79752
	2			66550	No Growth	
	3			86679	No Growth	
	4			81752	404548	
	5			162942	No Growth	
	6			103783	239679	
	7			130881	No Growth	
	8			119746	No Growth	
	9			128445	No Growth	
	10			105182	573949	
	11			113454	96648	
FH-C8-17	1	*115*	109373	116079	455554	140584
	2			161884	No Growth	
	3			163041	No Growth	
FH-C8-18	1	*115*	86704	132348	No Growth	135185
	2			75049	No Growth	
	3			250153	No Growth	
	4			215750	No Growth	
	5			123548	No Growth	
	6			260052	No Growth	
	7			168944	96343	
	8			105442	260643	
	9			325184	No Growth	
	10			155348	No Growth	
	11			146850	No Growth	
	12			145885	No Growth	
	13			134453	No Growth	
FH-C8-19	1	*115*	74775	115142	63247	62854
	2			247646	No Growth	
	3			202882	No Growth	
	4			172855	No Growth	
	5			106879	64233	
	6			130654	No Growth	
	7			46246	629500	
	8			147044	No Growth	

				AFGROW Predicted Lives based on Maximum Width Metric		
Specimen I.D	**Pit No**	**Peak Stress (Mpa)**	**Actual Life**	**Predicted Life**	**PredictedLife (A/C Constant)**	**Average Pit Size**
FH-C8-20	1	*115*	58749	83746	58292	62685
	2			56554	447894	
	3			100950	497437	
	4			93343	92653	
	5			87655	192850	
	6			106247	357936	
	7			110654	No Growth	
	8			46539	No Growth	
	9			43435	2922100	
FH-C8-21	1	*135*	61099	105284	No Growth	58298
	2			54836	360045	
	3			58184	76748	
	4			44636	31347	
	5			50438	287545	
	6			60492	81089	
	7			114437	84699	
FH-C8-22	1	*135*	48273	42289	88192	46592
	2			61583	454775	
	3			63939	No Growth	
	4			35136	401300	
	5			52739	62544	
FH-C8-23	1	*135*	53451	43789	93839	60384
	2			61838	742900	
	3			64586	403849	
	4			85837	58977	
	5			86990	No Growth	
	6			80799	334538	
	7			48398	552800	
FH-C8-24	1	*135*	68753	90496	48735	98689
	2			96084	71647	
	3			90896	62936	
	4			139698	128538	
FH-C8-25	1	*135*	39419	39399	24139	47793
	2			50440	28182	
	3			66490	112573	
	4			125800	No Growth	
	5			75692	No Growth	
	6			91535	No Growth	
	7			72285	No Growth	
	8			27636	760600	
	9			55697	No Growth	
	10			44738	No Growth	
FH-C8-26	1	*135*	50369	90985	363949	72383
	2			96338	89742	
	3			73235	151294	
	4			76939	438139	
	5			52538	425037	
FH-C8-27	1	*135*	49132	27737	99494	48999
	2			67936	712222	
	3			58540	No Growth	
	4			90939	No Growth	
	5			97598	No Growth	
	6			98497	No Growth	
FH-C8-28	1	*135*	61979	67635	74536	55999
	2			36892	20237	
	3			82389	648787	
	4			70383	141850	
	5			60892	39245	
	6			69187	35243	
	7			58484	36574	
	8			62135	57276	
FH-C8-29	1	*135*	80358	46292	24185	64639
	2			79496	44547	
	3			91186	83880	
	4			68586	62081	
	5			76340	55394	
FH-C8-30	1	*135*	45329	57438	30645	52539
	2			38599	24446	
	3			109587	91145	

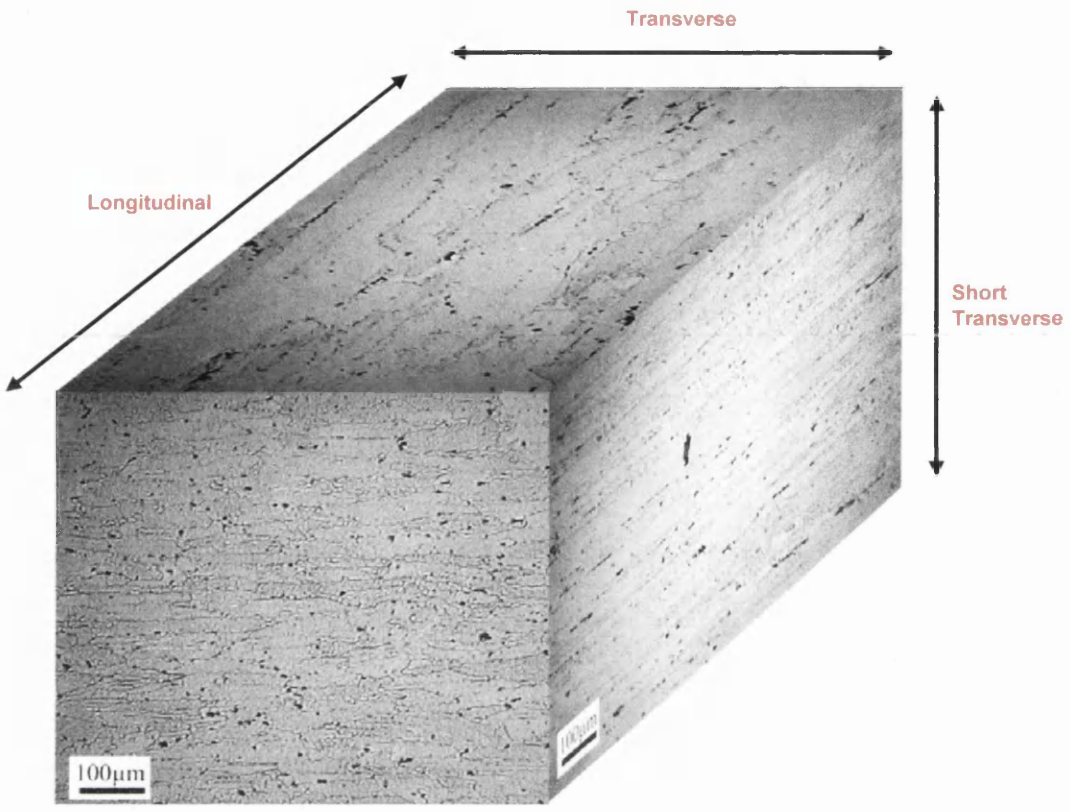

Figure 5.1 Microstructure of the AA 7010-T7651 stock plate material in the three principal planes.

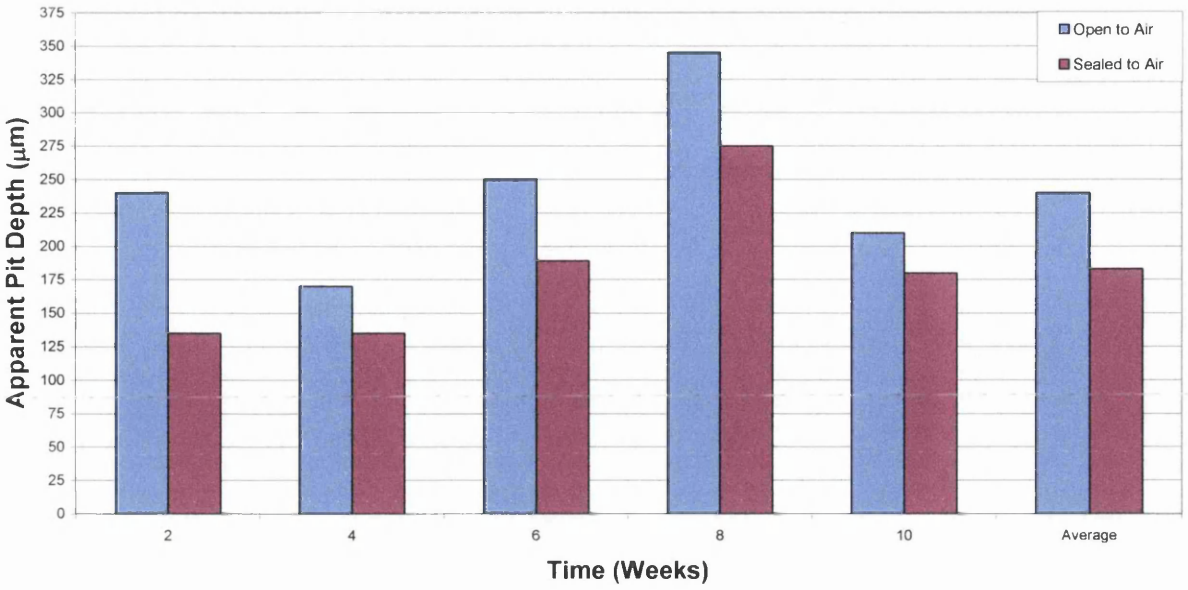

Figure 5.2 Apparent pit depth, wet/dry corrosion technique as a function of time in weeks.

Figure 5.3 Macroscopic images of typical corrosion pits produced on anodised AA 7010-T7651material.

Figure 5.4 Example of a single corrosion pit.

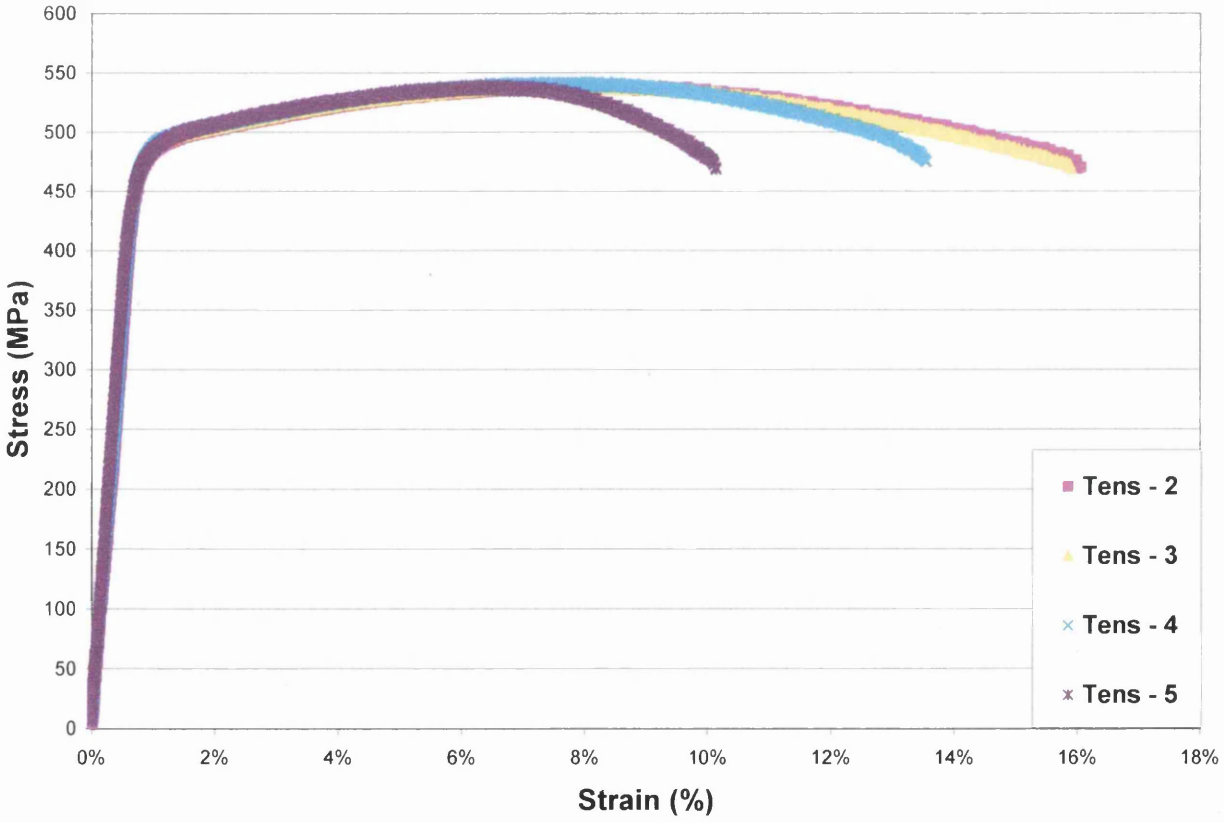

Figure 5.5 Stress vs. Strain curves for AA 7010-T7651, 20°C, extension rate of 1mm/min.

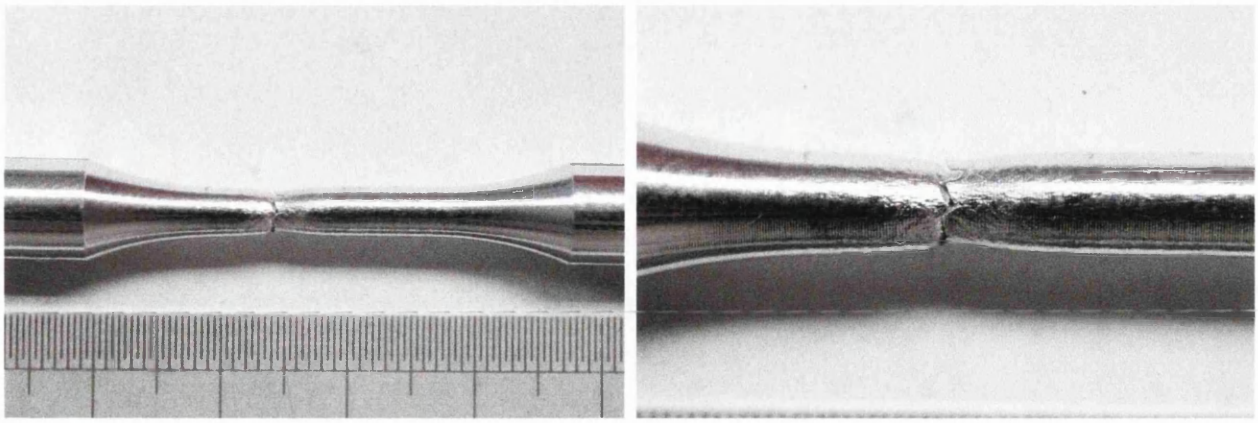

Figure 5.6 Fractured tensile specimen showing signs of a small degree of necking.

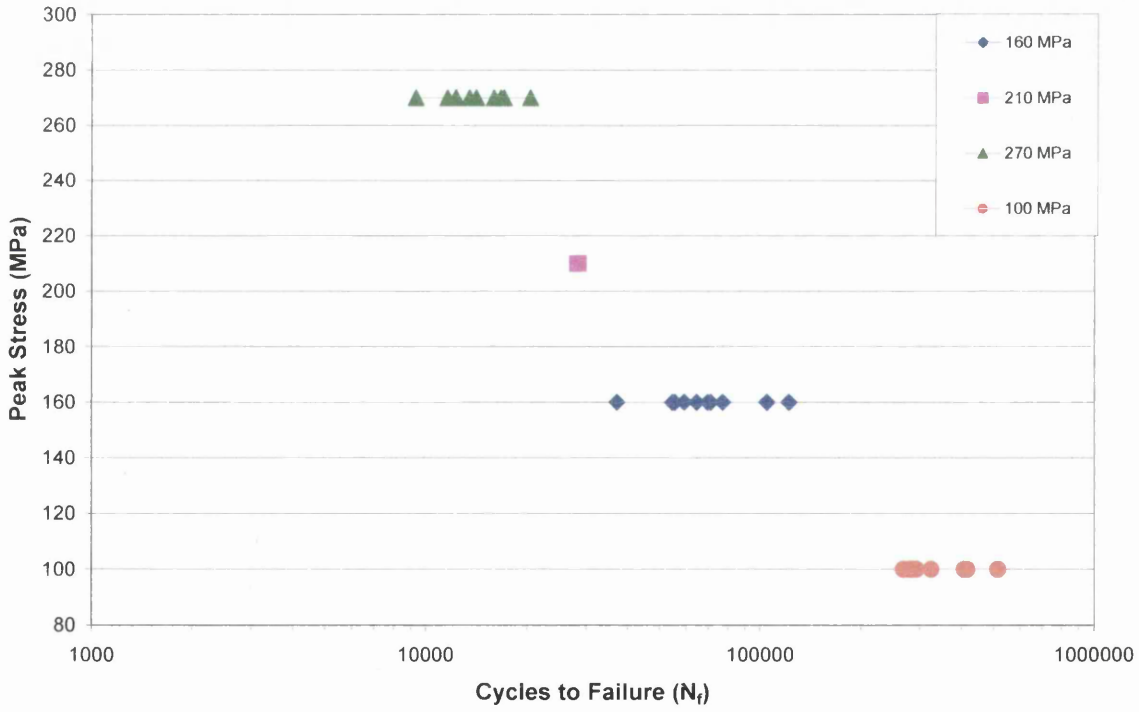

Figure 5.7 S-N response of AA 7010-T7651 flat plate specimens subjected to 8 weeks wet / dry corrosion.

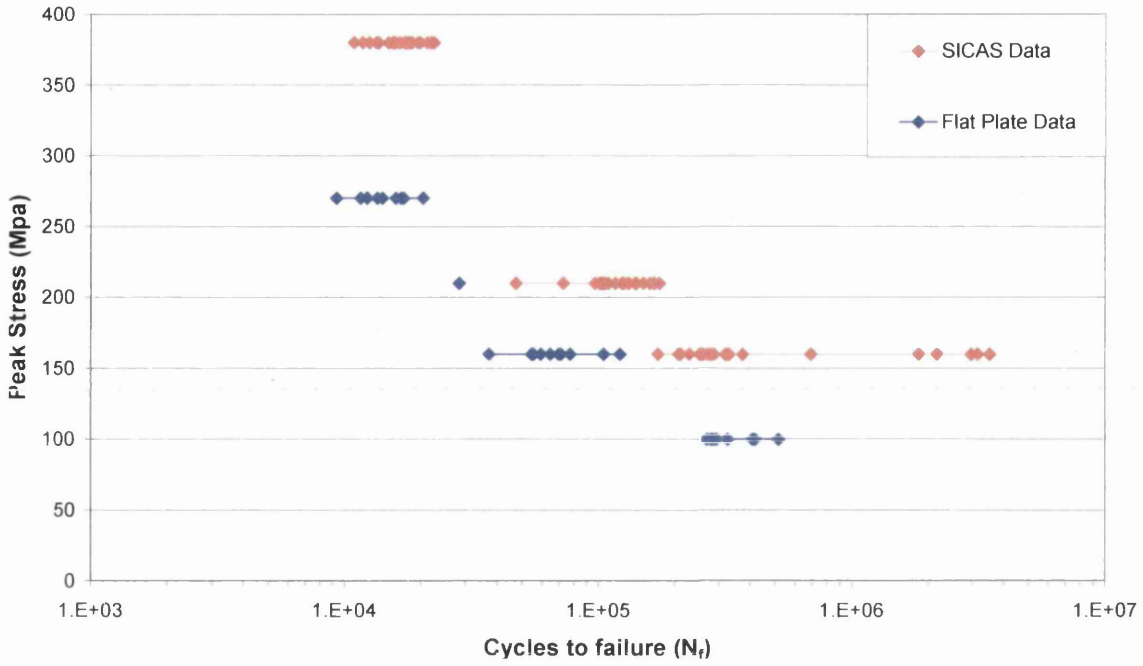

Figure 5.8 Comparison of the flat plate specimens to previously generated SICAS data.

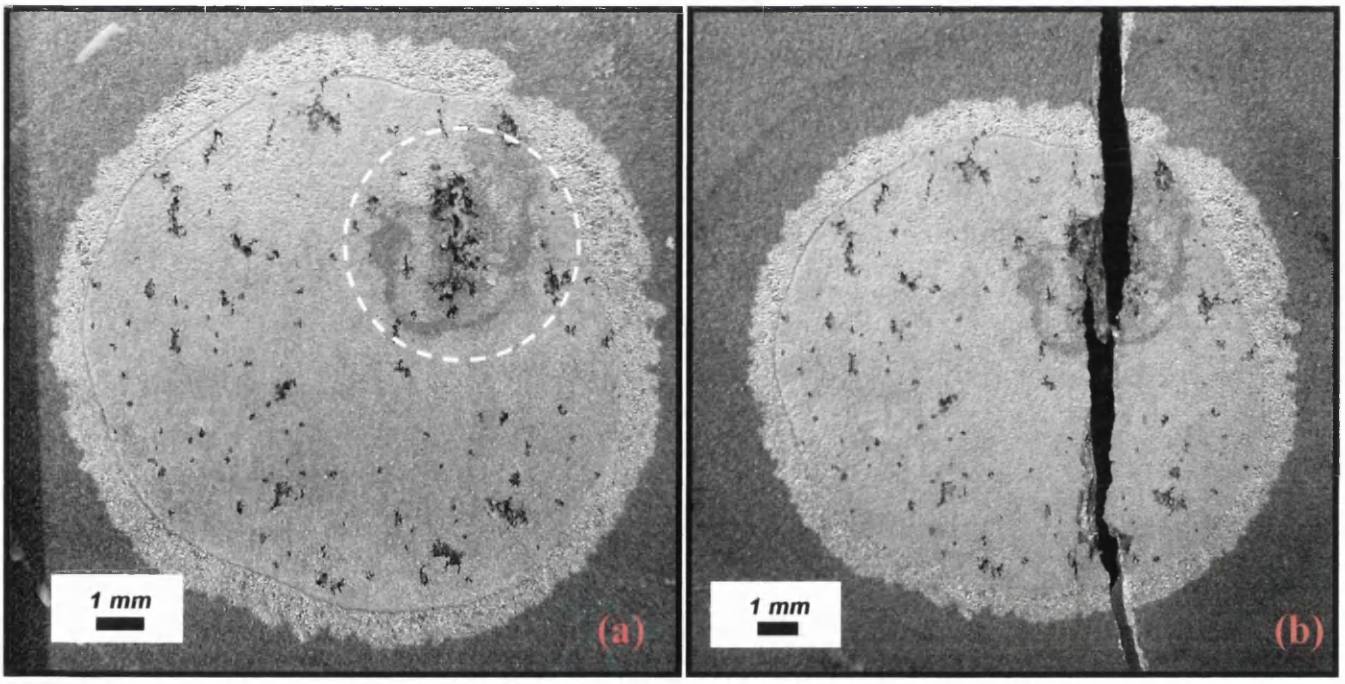

Figure 5.9 Specimen PC-4 (a) Pre and (b) Post fatigue testing at 270 MPa.

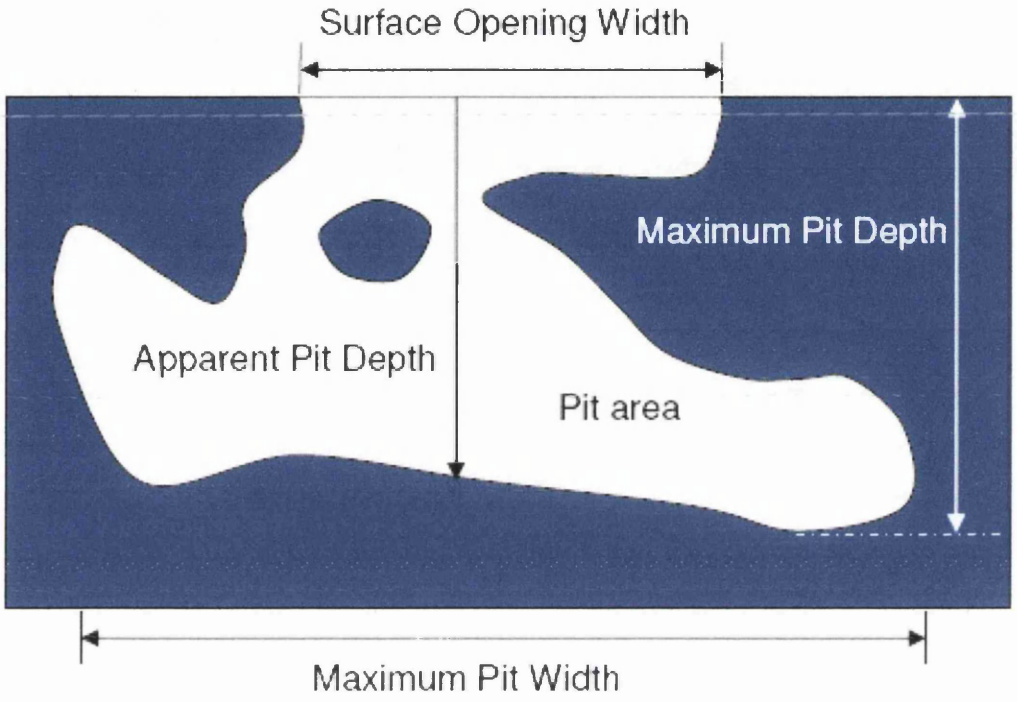

Figure 5.10 Schematic representation of corrosion pit metrics as viewed on the fracture surface of tested specimens.

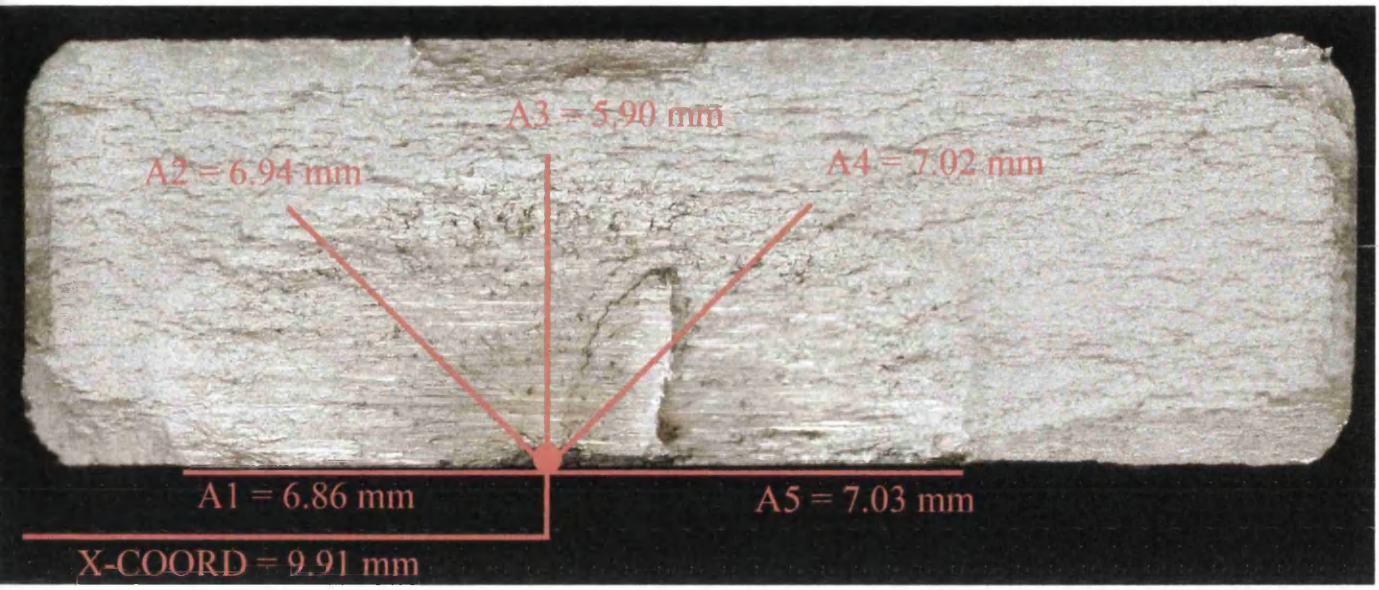

Figure 5.11 Fracture surface from specimen PC-4, used to define final crack profile measurements A1 – A5.

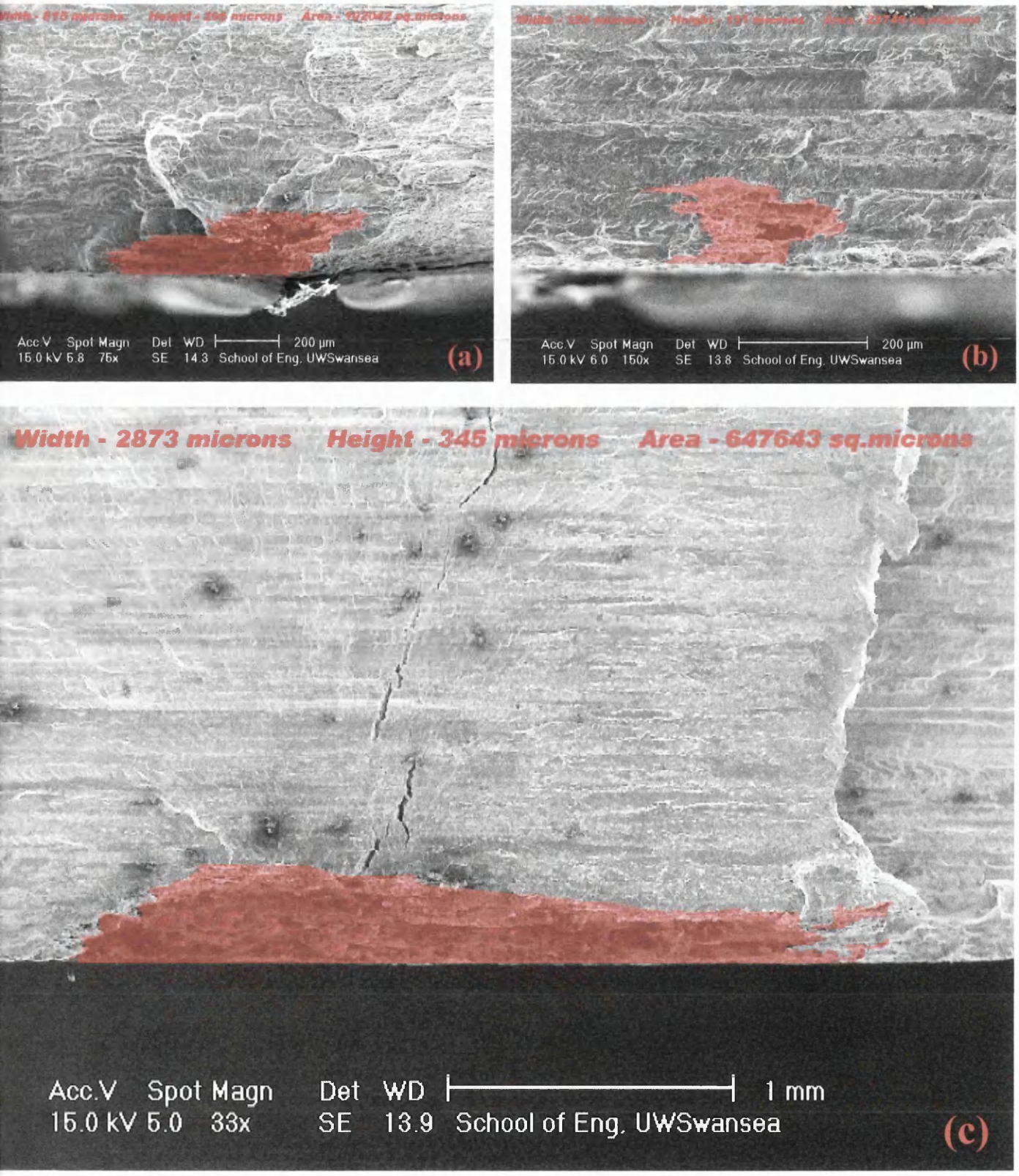

Figure 5.12 Corrosion pits on the fracture surface of PC-4. Pit shape and area is highlighted in red, dimensions clearly stated on each image. (a)Corrosion pit causing small crack growth, (b) Corrosion pit non crack initiating and (c) Main fatigue crack initiating corrosion pit.

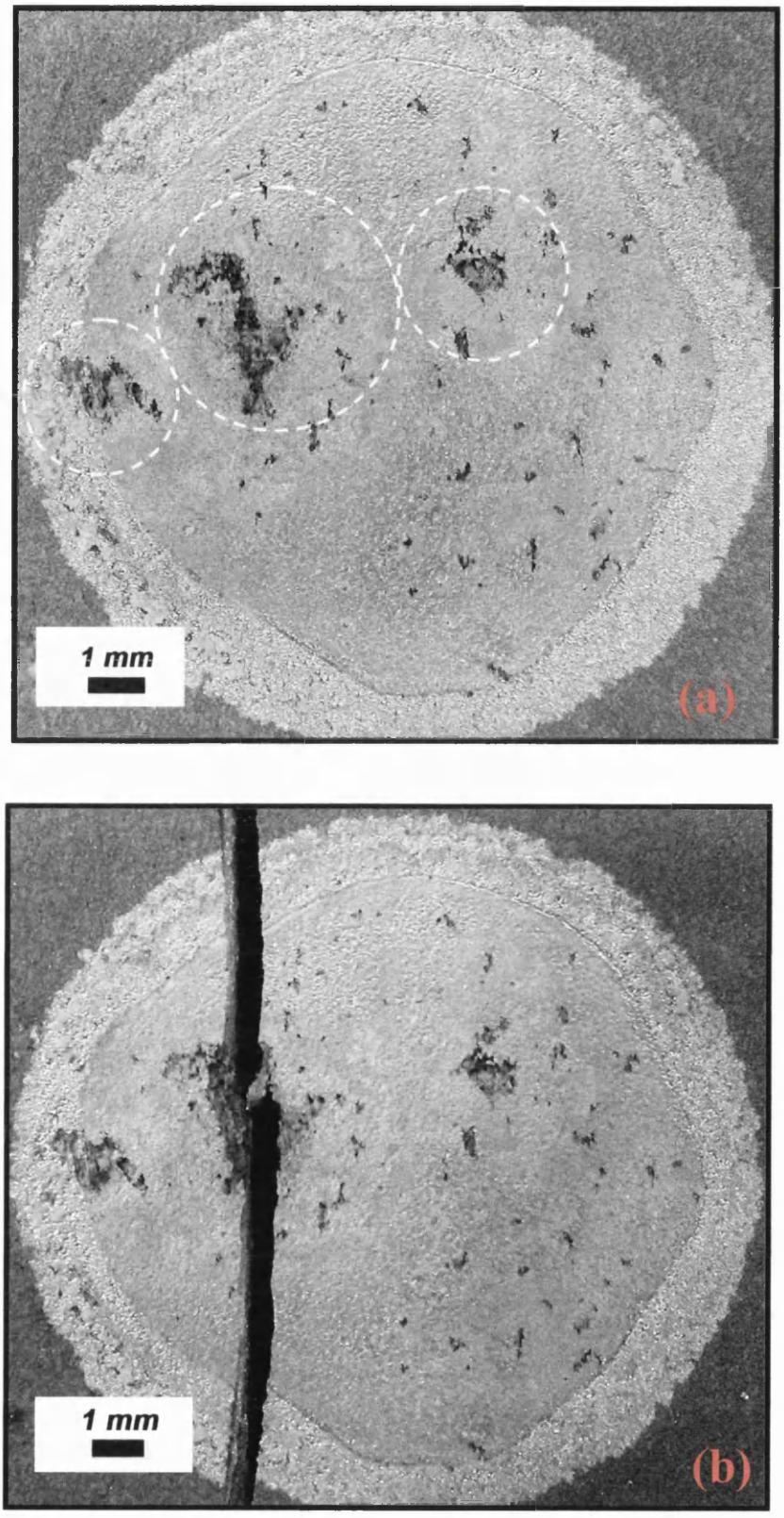

Figure 5.13 Specimen PC-21 (a) Pre and (b) Post fatigue testing at 160 MPa.

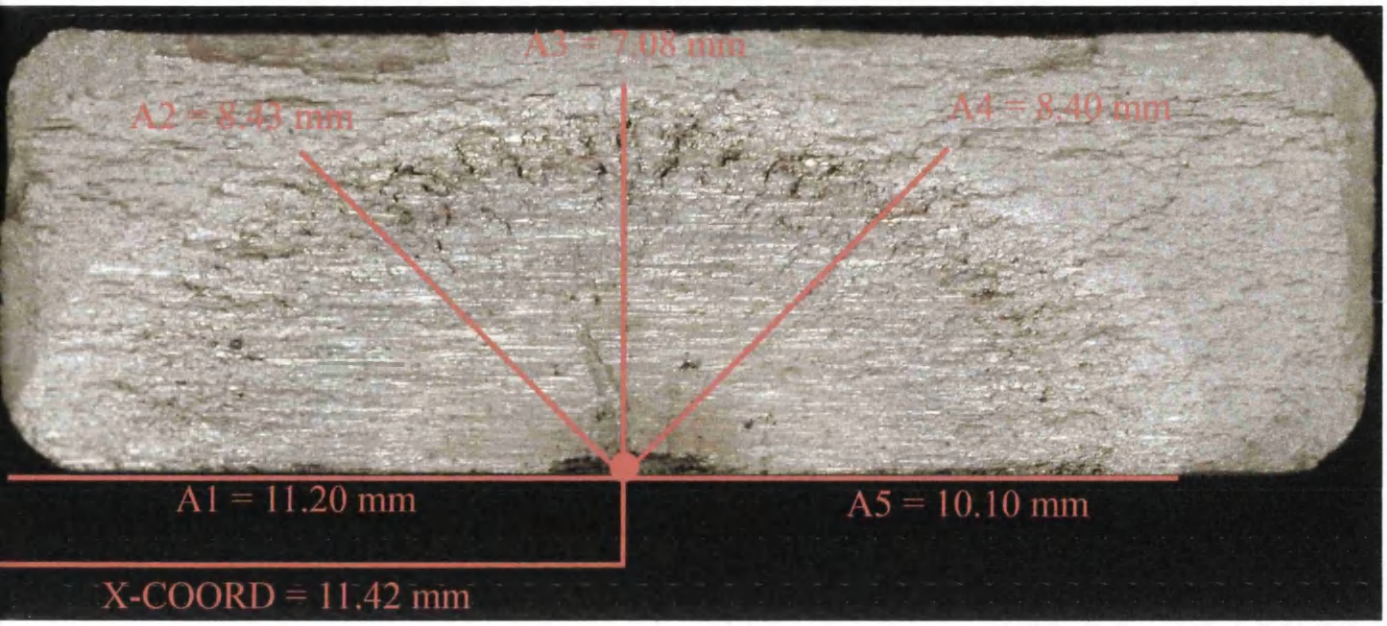

Figure 5.14 Fracture surface of specimen PC-21, including crack profile dimensions.

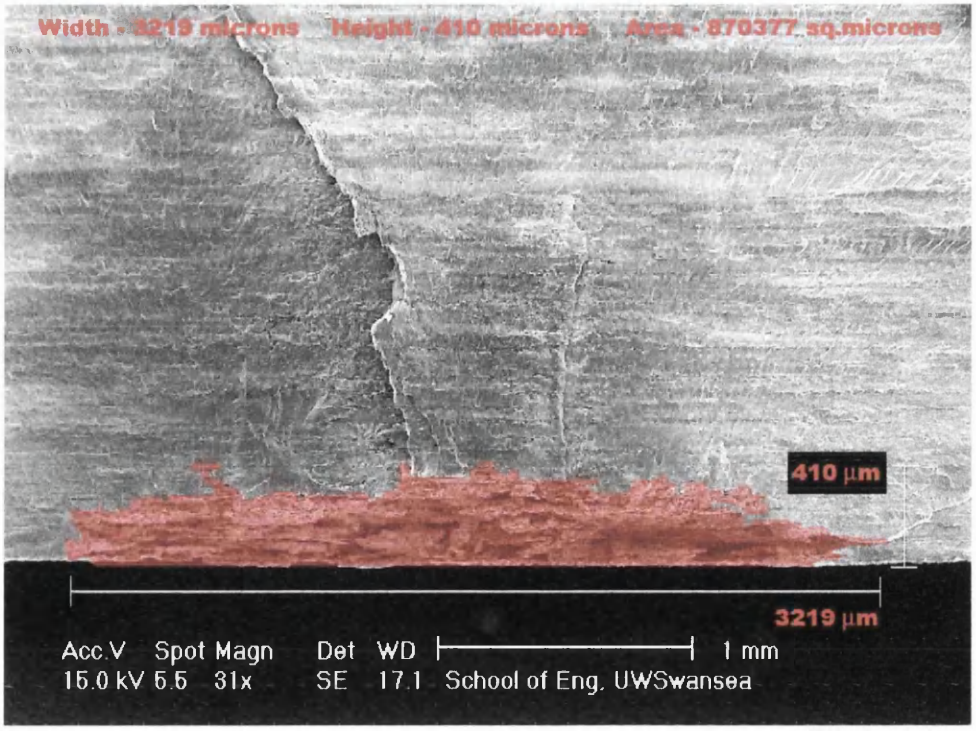

Figure 5.15 Corrosion pit initiating a fatigue crack on specimen PC-21. Pit profile is illustrated in red.

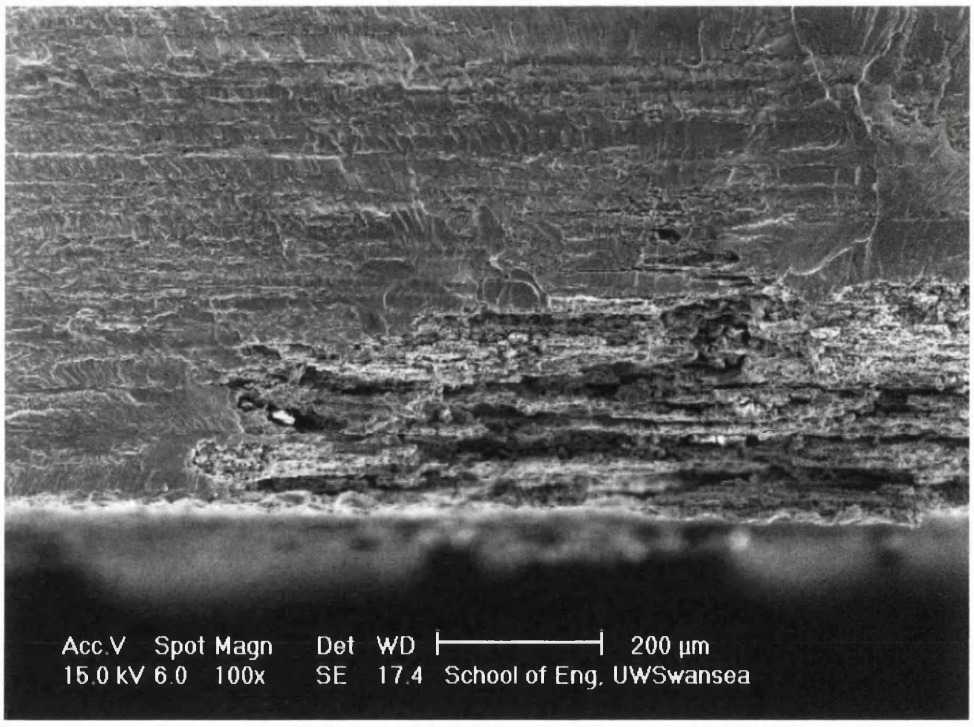

Figure 5.16 Corrosion pit on PC-21 illustrating complexity of corrosion/microstructure interaction and multiple initiation sites.

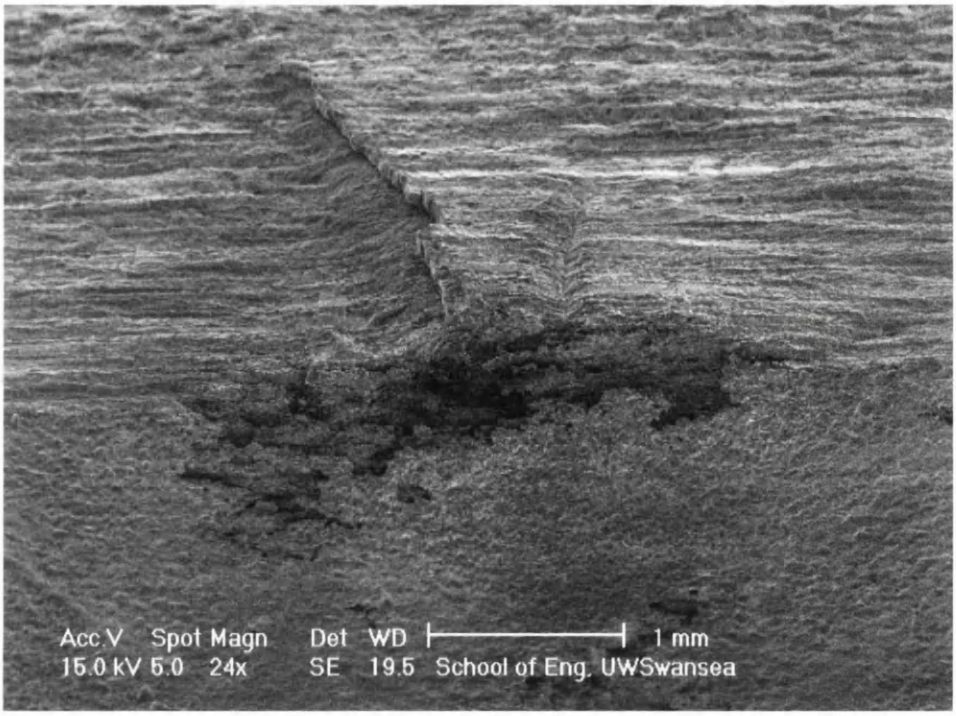

Figure 5.17 Specimen PC-21, illustrating corrosion pit, initiation and growth on neighbouring planes.

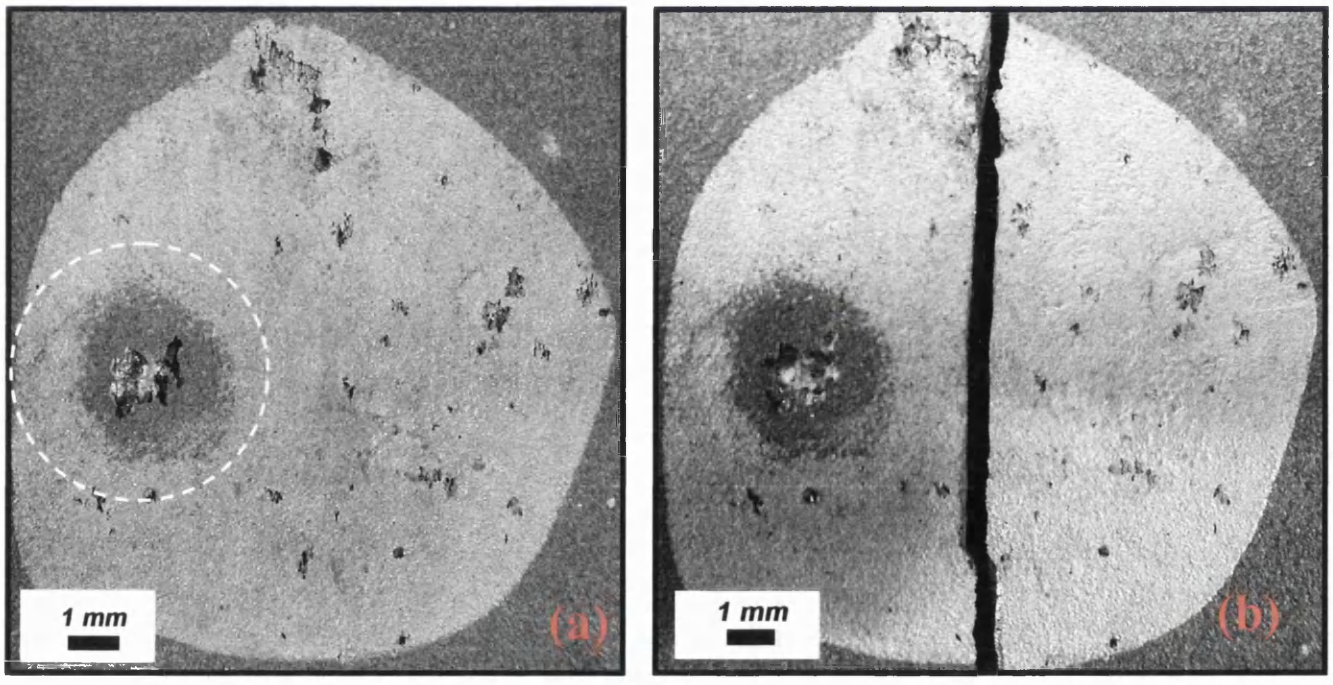

Figure 5.18 Specimen PC-17 (a) Pre and (b) Post fatigue testing at 100 MPa.

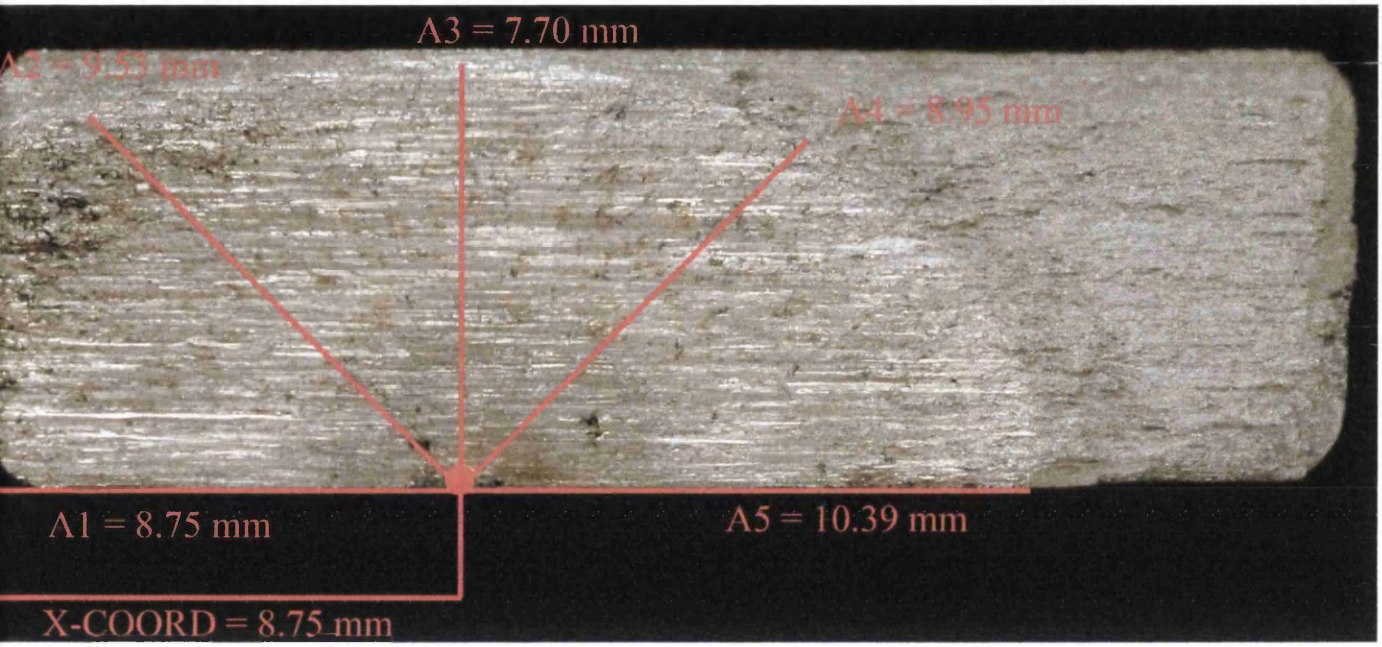

Figure 5.19 Fracture surface of specimen PC-17, including crack profile dimensions.

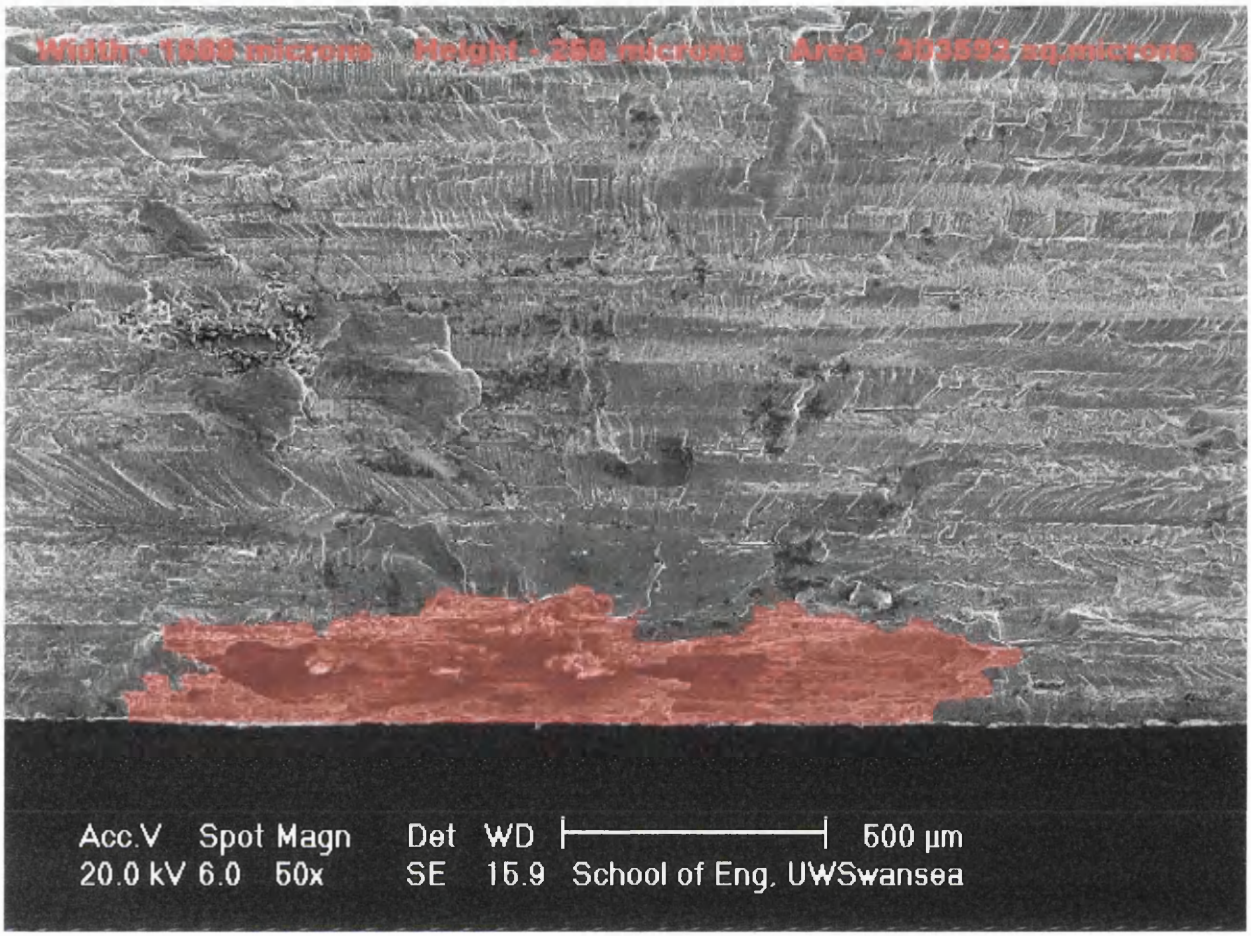

Figure 5.20 Corrosion pit causing fatigue crack initiating on specimen PC-17.

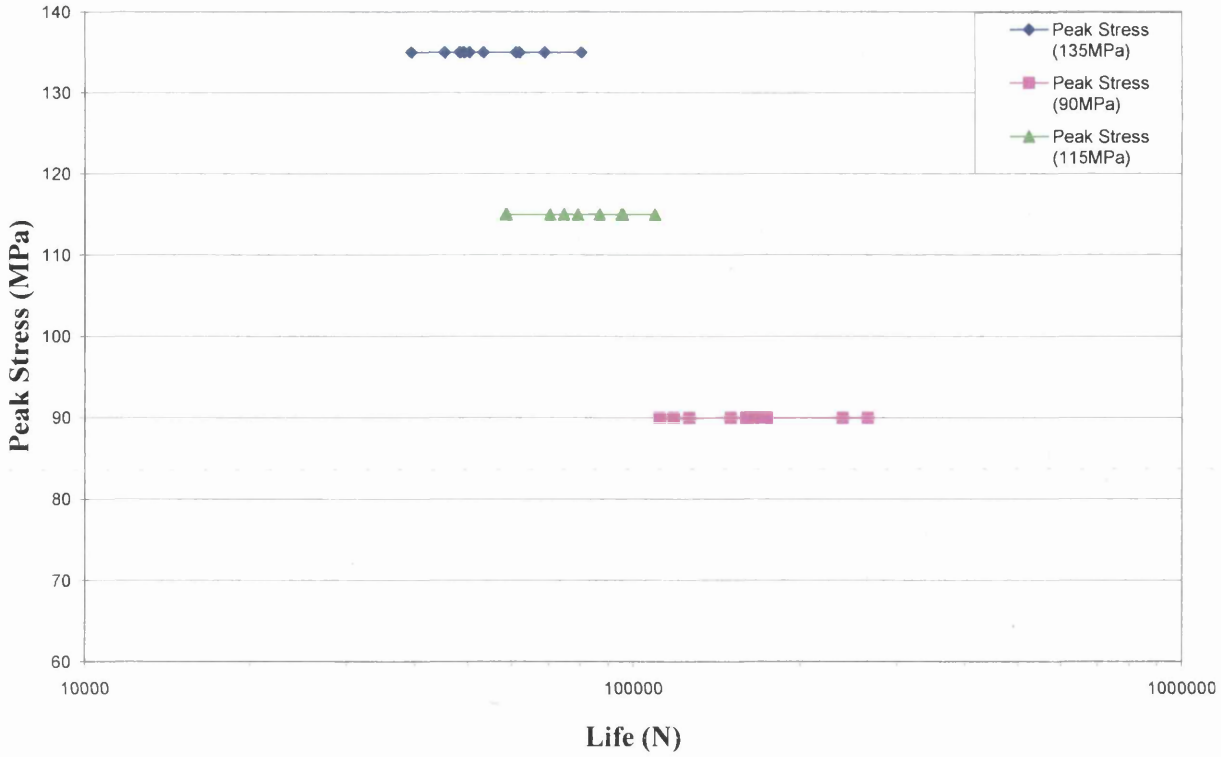

Figure 5.21 S-N response of centre hole plate specimens subjected to 8 weeks wet/dry corrosion.

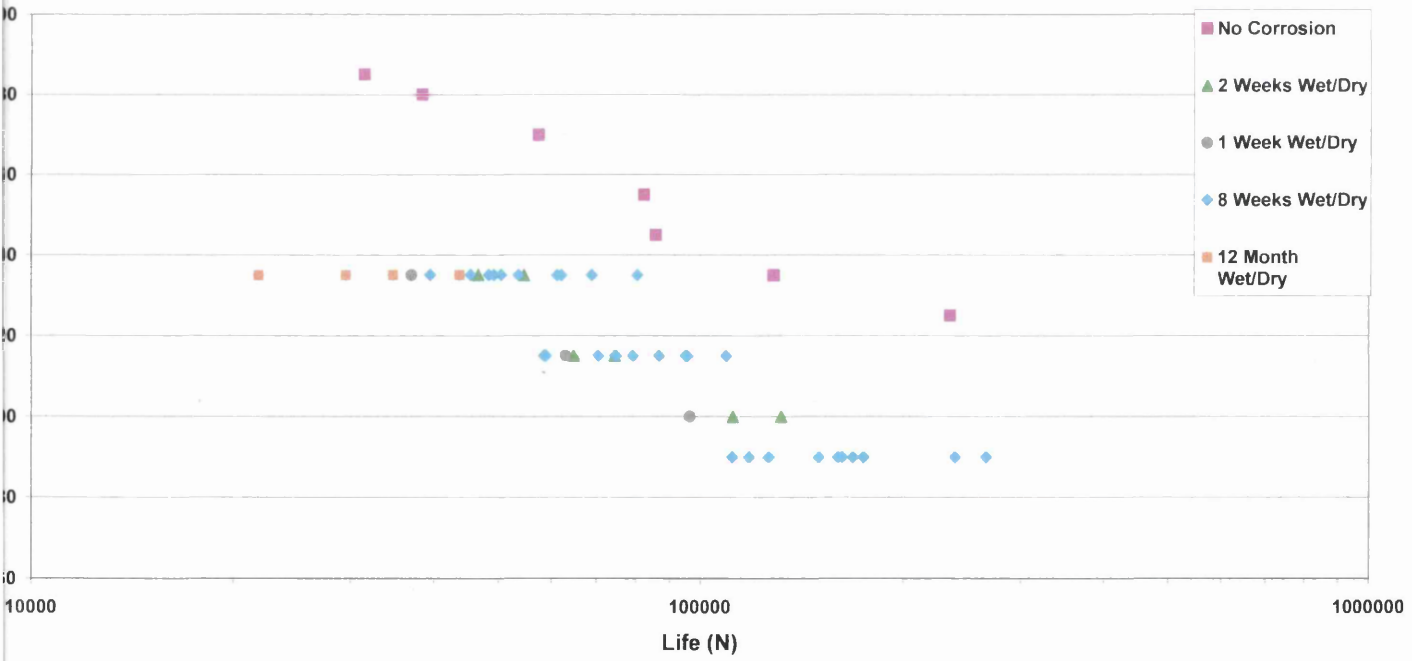

Figure 5.22 S-N data comparing corroded and corrosion free centre hole specimens.

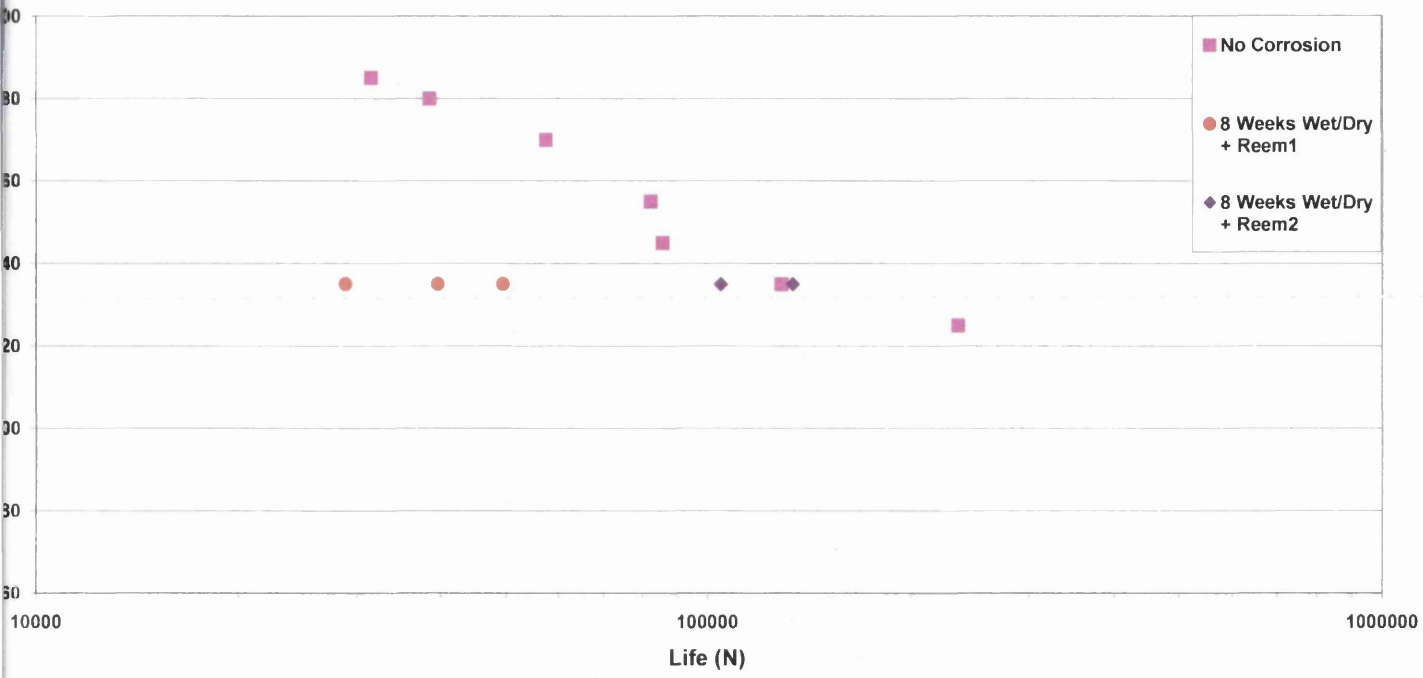

Figure 5.23 S-N data illustrating the effects of reaming corroded specimens.

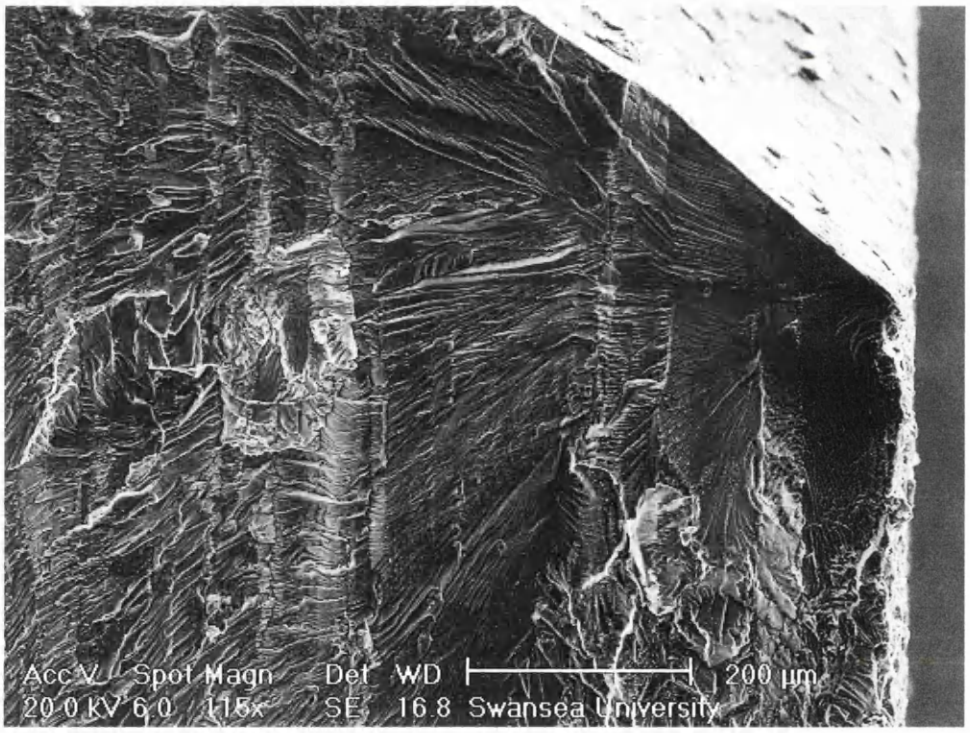

Figure 5.24 Corner edge crack initiation in as-machined centre hole specimen.

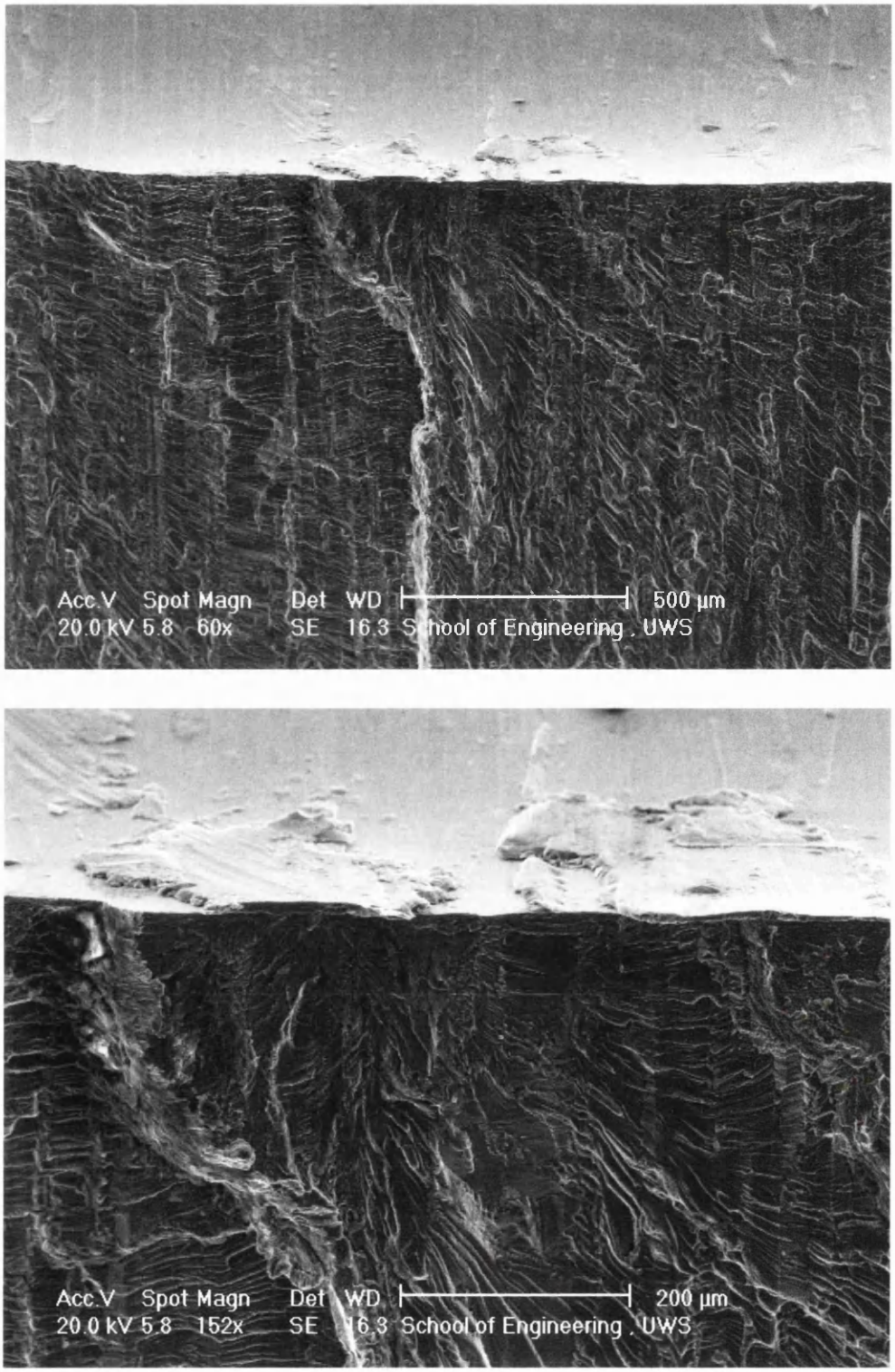

Figure 5.25 Machining features causing fatigue crack initiation along the bore of the hole in specimen FH-NC-6.

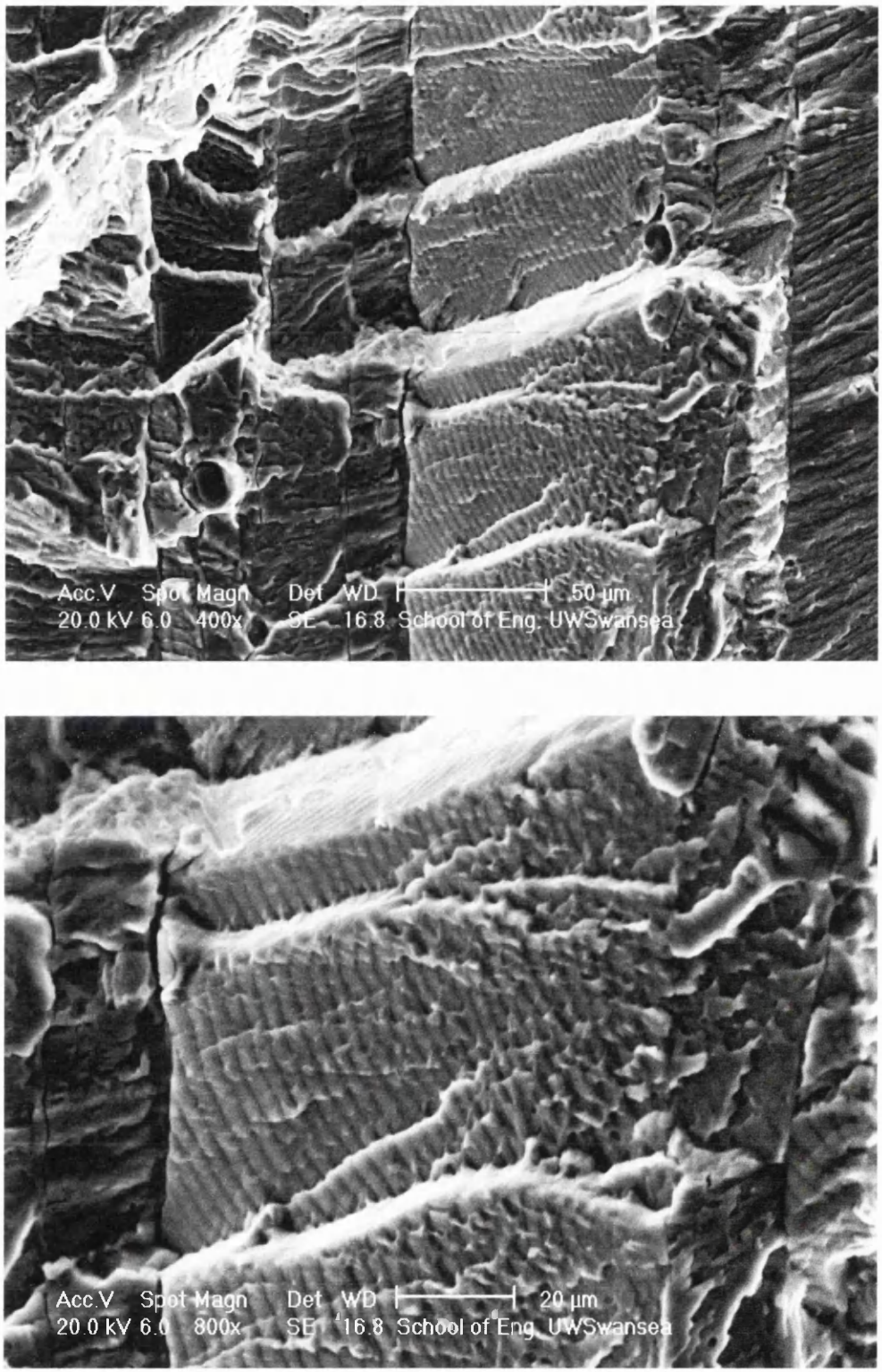

Figure 5.26 Fatigue striations and crystallographic control of crack growth observed on non corroded centre hole specimen FH-NC-4.

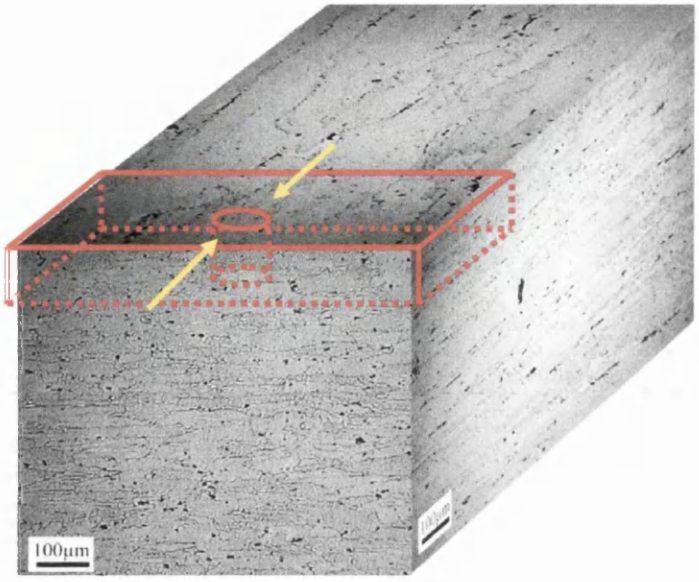

Figure 5.27 Grain structure around the centre hole specimens (arrows indicate "end-grain" locations)

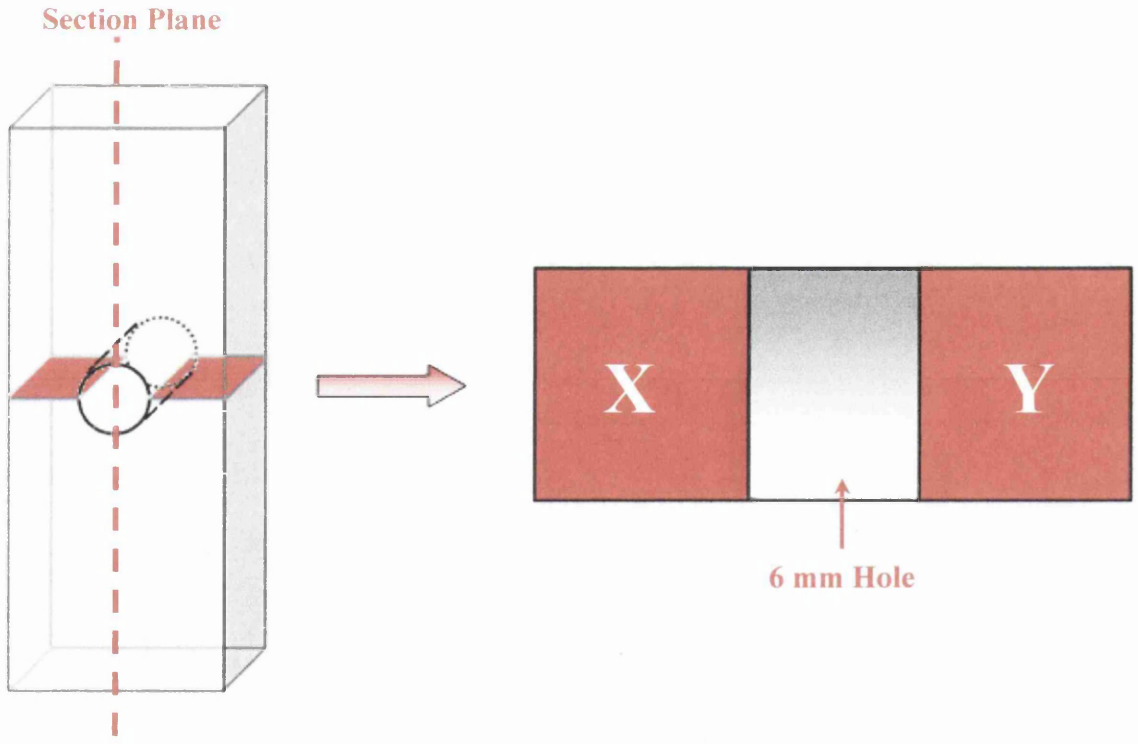

Figure 5.28 Schematic illustrating the nomenclature used to describe fracture in the centre hole specimens.

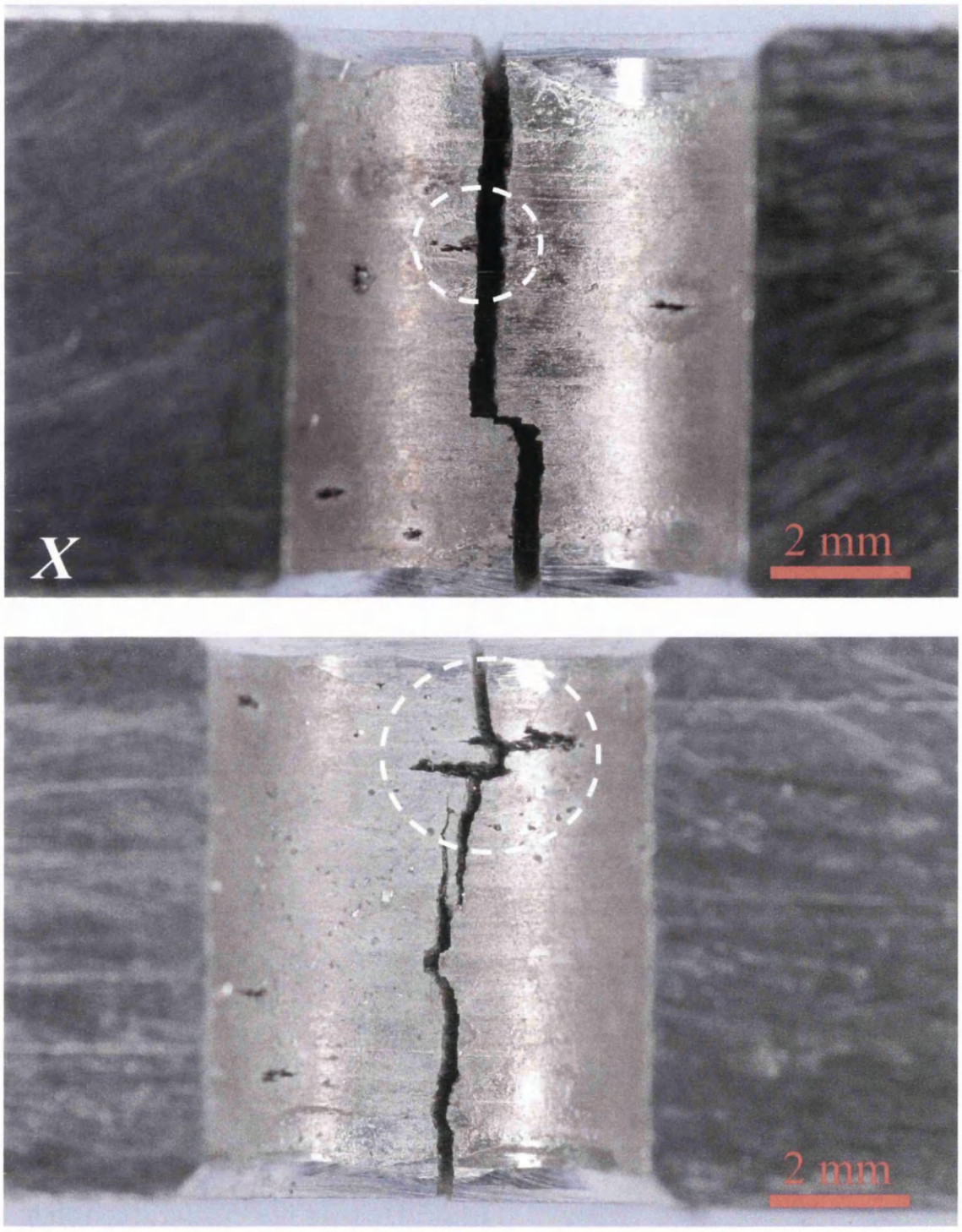

Figure 5.29 Fractured centre hole specimen FH-C8-20 showing crack initiation on opposing sides (X & Y).

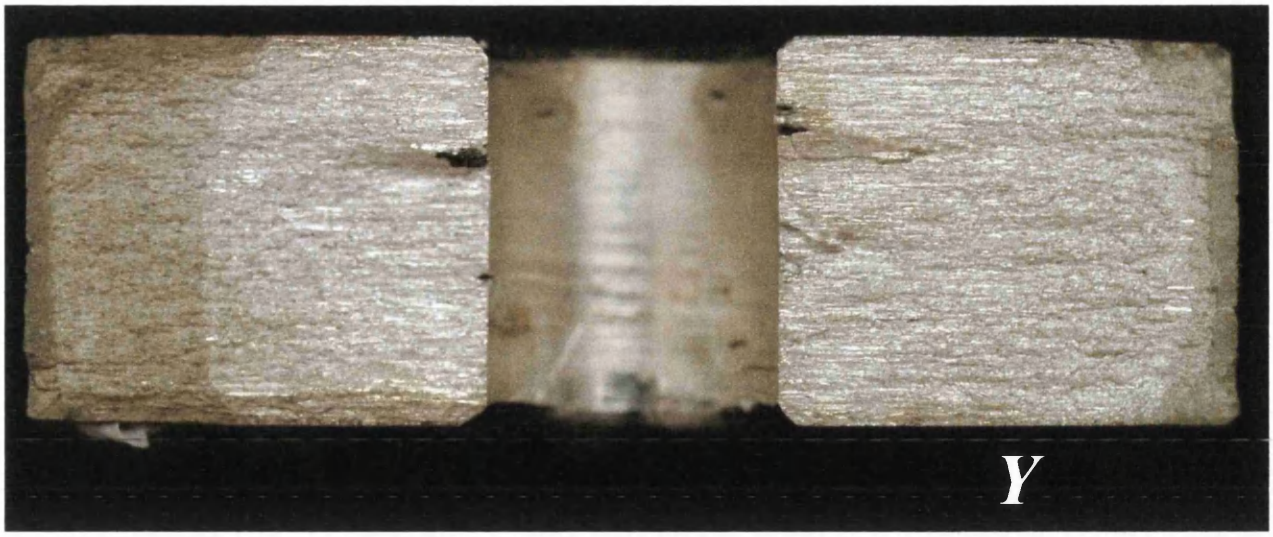

Figure 5.30 Fracture surface of specimen FH-C8-20 showing dominant growth on side *Y*.

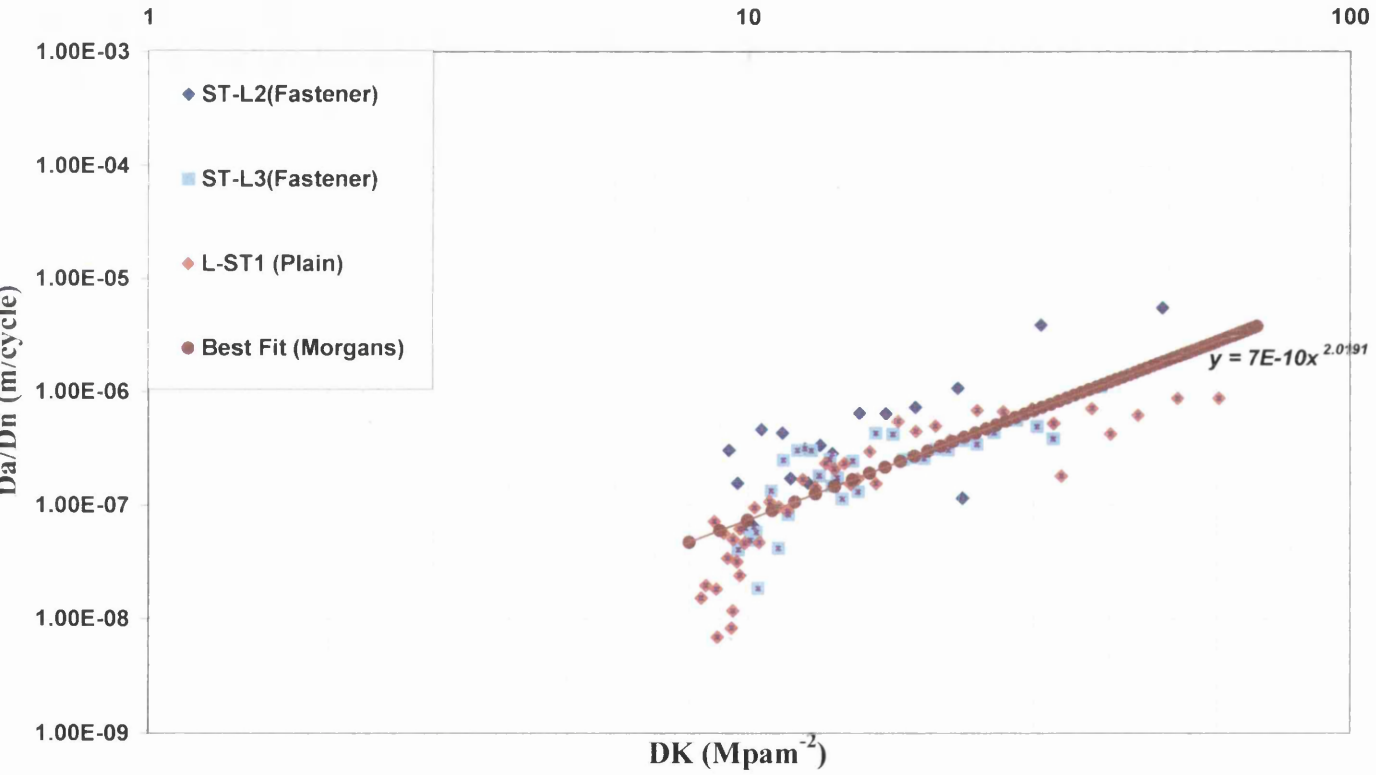

Figure 5.31 Fatigue crack propagation data measured in the ST-L and L-ST orientations.

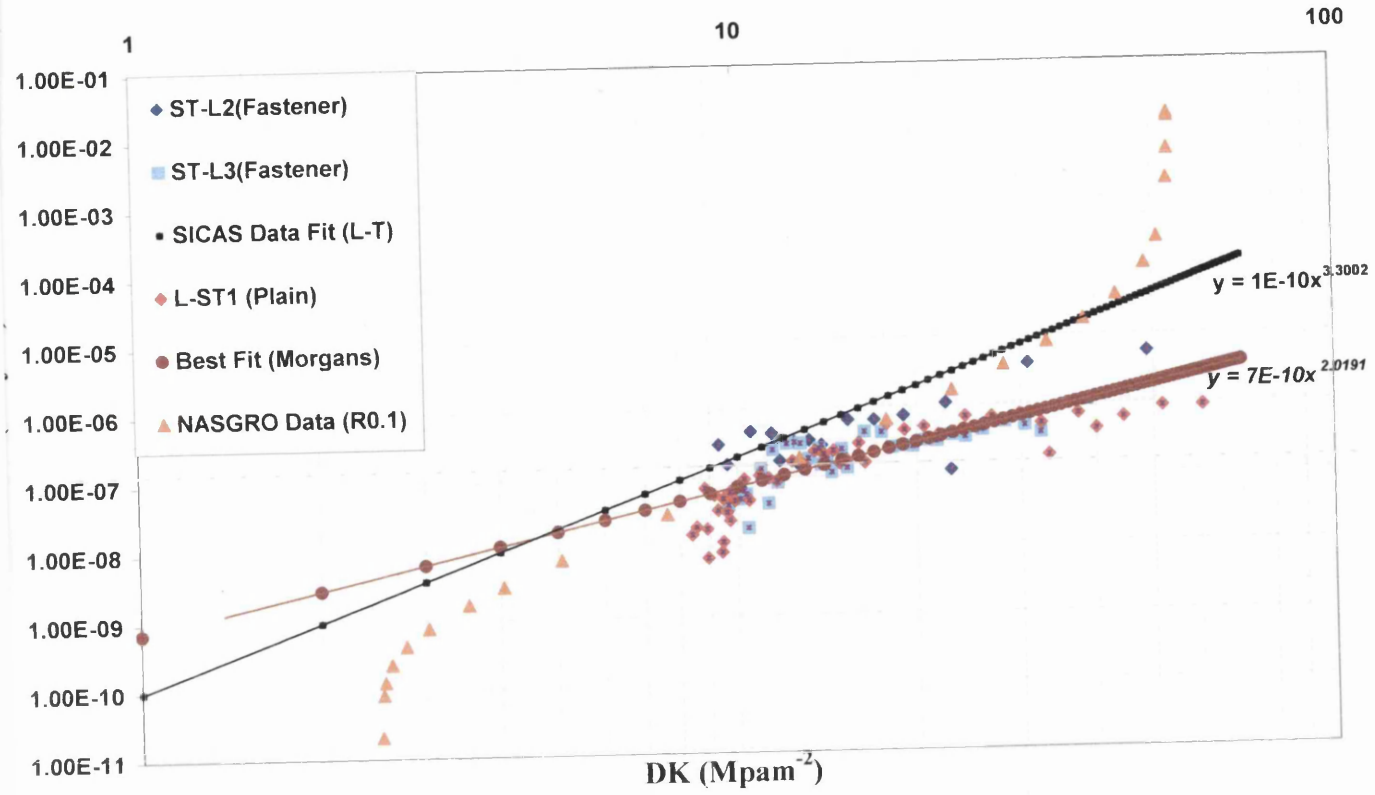

Figure 5.32 Fatigue crack propagation data compared to previously reported data from SICAS [80] and AFGROW NASGRO database.

Figure 5.33 Early stages of cracking from an SEN specimen showing bifurcation in crack path.

Figure 5.34 Surface fatigue crack in a SEN specimen illustrating crack path deviation and interaction with intermetallic particles.

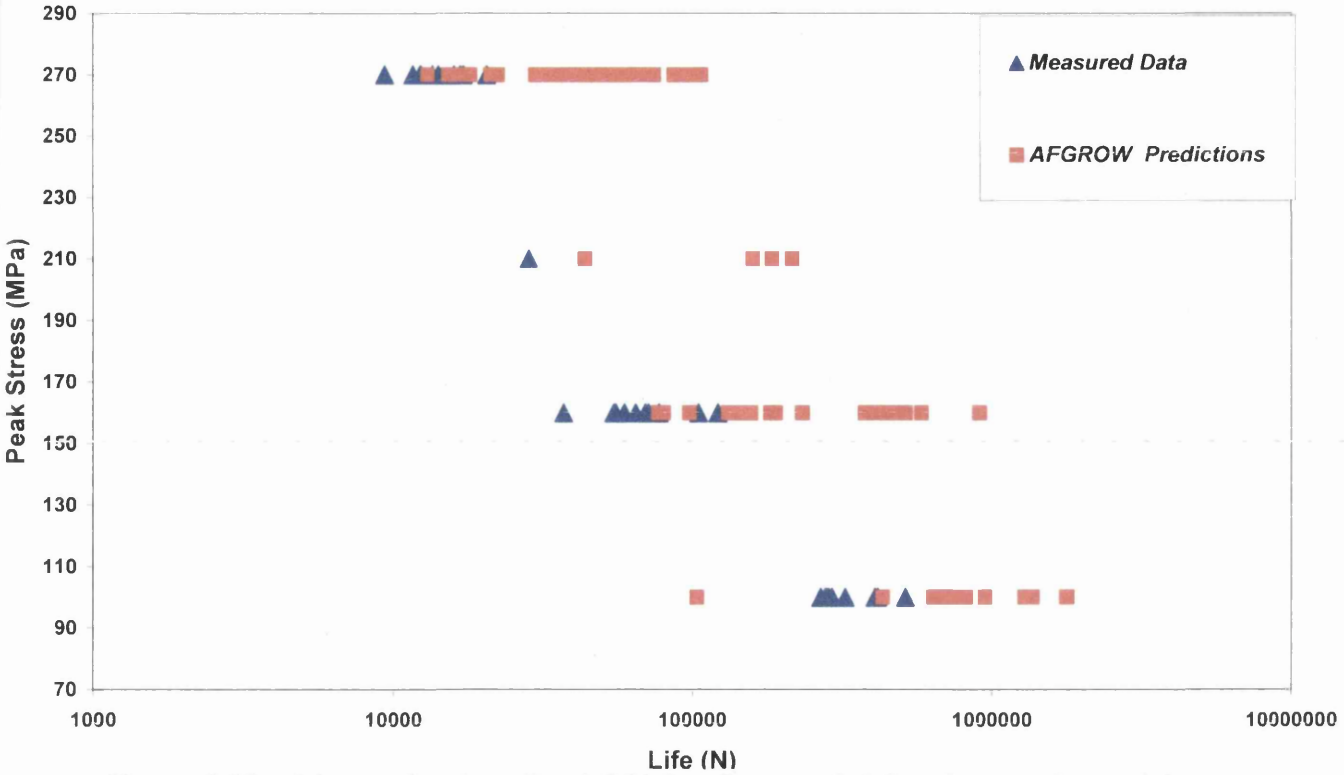

Figure 5.35 Measured and predicted S-N data for corroded flat plate specimens (a/c varied).

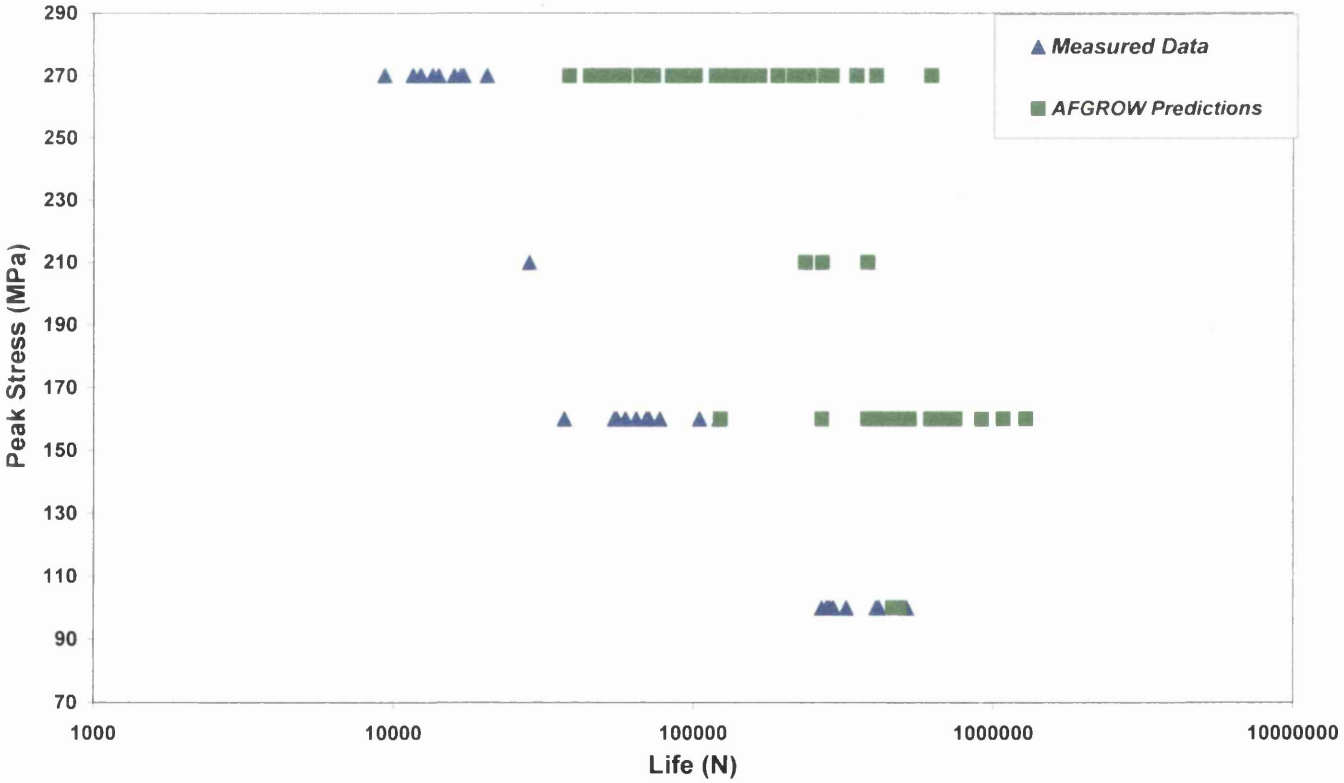

Figure 5.36 Measured and predicted S-N data for corroded flat plate specimens (a/c constant).

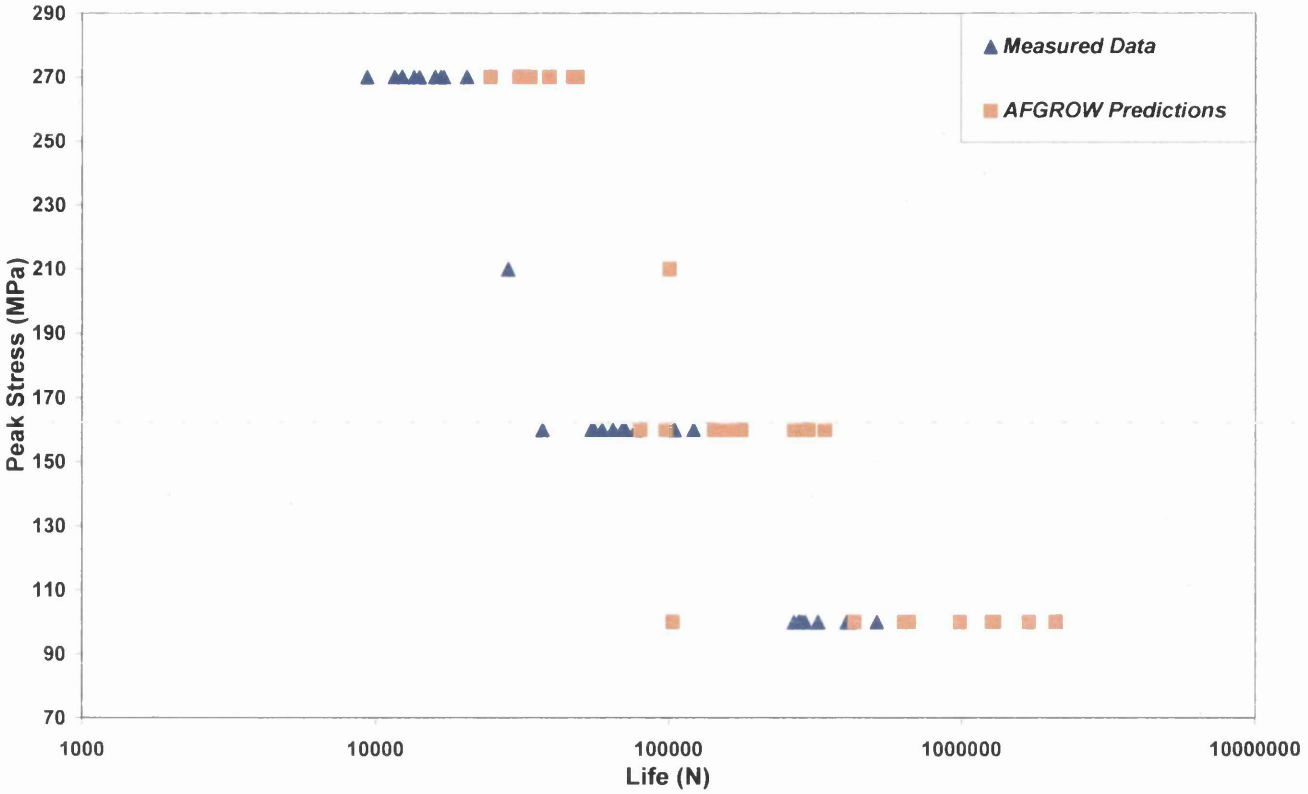

Figure 5.37 Measured and predicted S-N data for corroded flat plate specimens employing average surface opening width and average maximum pit depth.

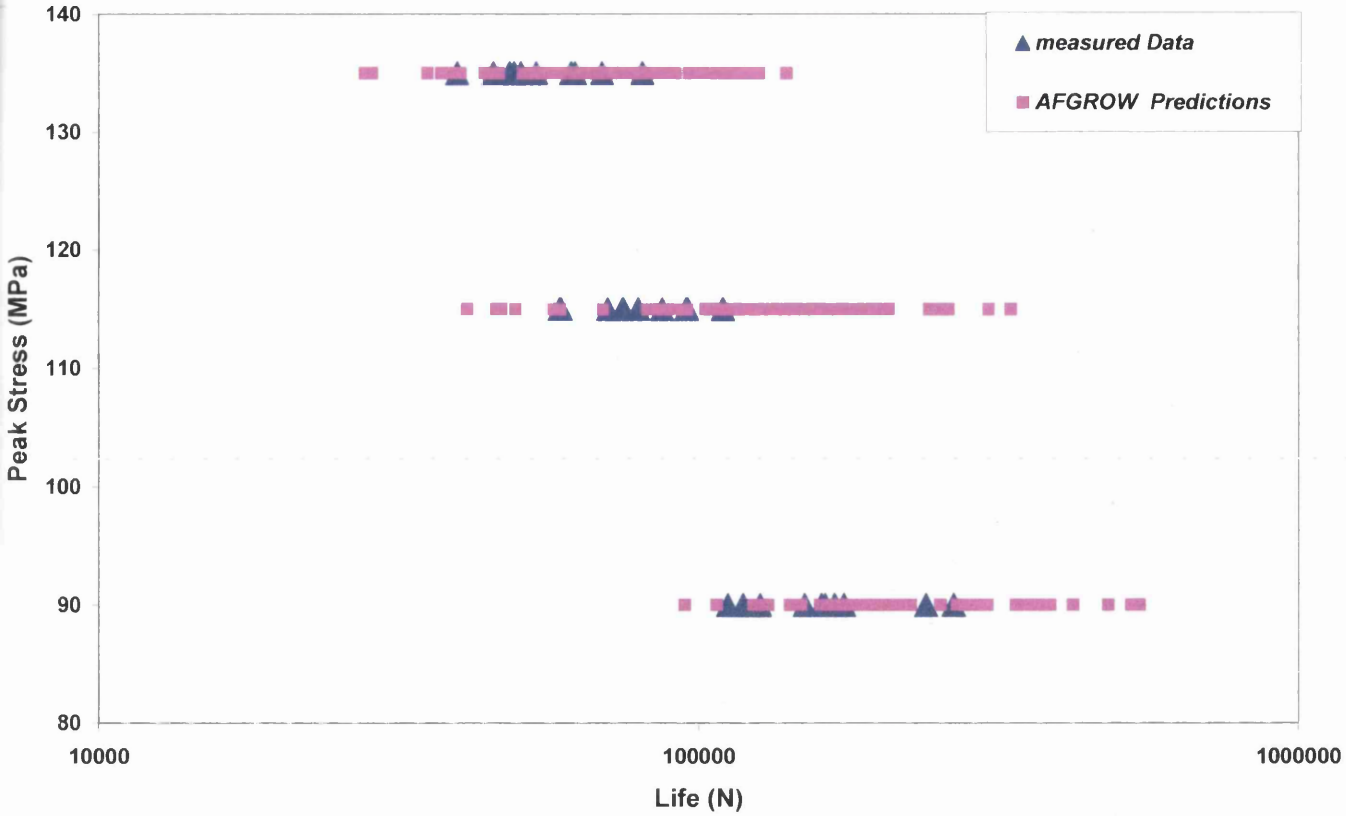

Figure 5.38 Measured and predicted S-N data for corroded centre hole specimens (a/c varied).

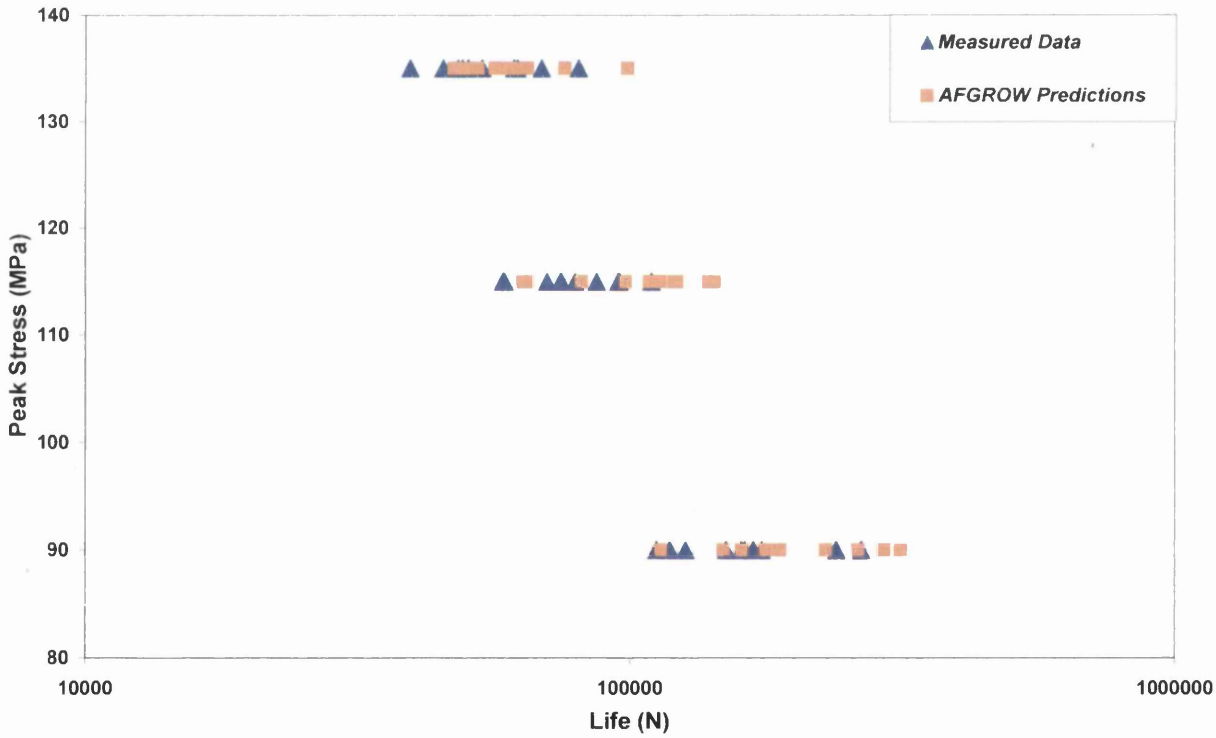

Figure 5.39 Measured and predicted S-N data for corroded centre hole specimens employing average surface opening width and average maximum pit depth.

6.0 DISCUSSION

The following chapter will consider the results from the present study and will endeavour to asses their implications in light of previous work (SICAS) carried out, and that reported openly in the scientific literature. The discussion will focus on three major topics dealing with basic alloy microstructure and mechanical properties, corrosion and fatigue assessment of the alloy in terms of flat plate and centre hole specimens and finally Linear Elastic Fracture Mechanics (LEFM) based modelling of the presented fatigue data.

The current episode will discuss the advanced research into corrosion pitting in the aerospace alloy AA 7010-T7651 and its subsequent influence on fatigue performance. The alloy is employed for numerous applications in airframe structures, most commonly as wing spars and skins. The current research programme followed the major international research project SICAS (Structural Integrity assessment of pitting Corrosion in Aircraft Structures), with both projects commissioned by BAE SYSTEMS as an attempt to minimize the costs associated with in-service corrosion damage.

6.1 BASIC ALLOY MICROSTRUCTURE & MECHANICAL PROPERTIES

The present results confirmed that the stock material consisted of an elongated grain structure parallel to the principal rolling direction, with stringers of intermetallic particles (Mg_2Si, Al_7Cu_2Fe illustrated in figure 1.1) located mainly at grain boundary areas, as shown by figure 5.1 in chapter 5. The alloys chemical composition detailed in table 6.1 also demonstrates consistent data with that published from the SICAS project [81]. The microstructure of the current alloy is seen to compare favourably with that produced in the fatigue damage study by Patton et al, i.e. the grain size and grain morphology appear very similar. The effect of the elongated grain structure alongside the presence of intermetallic particles on the mechanical properties and corrosion and fatigue resistance is now discussed in detail.

The basic monotonic properties of the AA 7010-T7651 alloy in the required orientation (fatigue loading orientation) at room temperature and humidity can be seen in figure 5.5 in the results chapter of the present study. Room temperature testing of plain test specimens resulted in ultimate tensile stresses (UTS) ranging between 540 MPa up to a maximum of 543 MPa, demonstrating consistent mechanical behaviour. The Young's moduli of the four tests are also extremely coherent, with values clustering reliably between 65 GPa and 70 GPa. Although relatively ductile for a high strength 7xxx series aluminium alloy, strain to failure values were seen to range between 10 % and 16 %, which are amongst the highest ductilities measured in this class of material.

Comparing the mechanical behaviour of the present alloy with previous published data (table 5.3 in the results chapter and figures 2.6 & 2.7 in the literature survey), in particular, the data presented by the authors Patton et al and Schra and Hart (researched the same alloy and heat treatment), it is apparent that the properties are clearly related. The first comparison to make is between the relative elongation values produced by Schra and Hart and the current data. Evidently, marginally greater strains to failures are noted for the current data (13.9% compared to 11.5%), although yield stress (480 MPa compared to 470 MPa) and tensile strength (541 MPa compared to 535 MPa) properties are similar. Patton et al also published tensile strength data regarding 7010-T7651, which again at 535 MPa is in accordance with Schra and Hart and also the current data. The other published data in table 5.3 is based on the same 7010 alloy, but with various applied heat treatments. Again, the current properties are seen to be consistent.

In addition to the mechanical property data available in the scientific literature, a limited amount of handbook data for the alloy in question used for the SICAS study is also available (table 6.2). The handbook covers a range of mechanical properties for the 7010-T7651 material in the three principal planes (Longitudinal, Transverse and Short Transverse). The orientation of highest relevance to the current research programme is transverse, in view of the fact that the test specimens (both tensile and fatigue) were examined in this orientation (see figure 5.1). Comparing the two sets of mechanical data, it is clear that the handbook properties are reasonably lower in terms of yield and tensile stress and also strain to failure, with a noticeable

30 MPa variation in strength and 9% in ductility. However Young's Modulus values of 71 GPa exceeds that of 66 GPa determined for the current research programme.

6.2 CORROSION AND FATIGUE ASSESSMENT

From the scientific literature and the mechanical property evaluation completed, it is clear that the AA 7010-T7651 exhibits favourable mechanical properties for airframe structures, although the alloy can be susceptible to in-service environmental damage, particularly through the development of various types of corrosion, mainly including the forms; pitting and intergranular. Corrosion damage has become a major cost in the maintenance of both civil and military aircraft, with customers requiring increasing service lives from their fleets. Corrosion management techniques are time consuming and expensive, and typically involve a grinding and mechanical blending procedure to remove corrosion damaged areas. However, by adopting damage tolerant fatigue lifing procedures in partnership with corrosion detection, a reduction in the cost of corrosion management and safe extensions to aircraft operational lives can be achieved.

Although an extensive fatigue database was generated by the previous SICAS investigation, further study was deemed necessary to assess the formation and subsequent mechanical effects of larger scaled corrosion pits. A new procedure of producing large scale pitting corrosion was successfully completed (see chapter 5.2) for the current research study, with pits consistently larger than observed in the SICAS study (average pit depth noted in SICAS, 95 μm). An alternate immersion technique (wet/dry) was employed for the fatigue evaluation of both flat pate and centre hole specimens. Pitting was produced on both anodised and as-machined finishes, producing variable pit size and morphology in both surfaces. From the scientific literature and through previous experience, it is known that pitting corrosion is a self nucleating and propagating process. Pits have been noted to initiate in this class of material at discontinuities in the passive layer or barrier coating. These breaks are normally introduced via mechanically induced defects, foreign bodies within the material (particles, oxides etc), intermetallic particles or even prior mechanical damage in the form of dislocations or emerging

slip steps caused by applied or residual stresses. Pitting corrosion within the current researched alloy was mainly introduced via the presence of the two types of intermetallic particles (Mg_2Si, Al_7Cu_2Fe) present at grain boundary locations within the material.

It is known that pitting corrosion in many ways is similar to crevice corrosion, as both mechanisms consume oxygen within the would-be pit and transport ions to balance the positive charge build-up, resulting in autocatalytic pit growth, as illustrated for an aluminium alloy by figure 6.1. However, pitting corrosion can propagate itself by the shrouding of the pit opening area with corrosion product/oxide build-up, often known as a "chimney". These chimneys essentially protect the pit, preventing oxygen reaching the pitting site and consequently acting as stabilisers. Examples of chimney formation observed on as-machined material are visible in figure 6.2.

Many pits initiated on the surface of the current aluminium alloy, although continued pit growth rapidly ceased, due to the protective cover (chimney) breaking down completely or incidentally providing insufficient protection. Pits of this type are commonly known as unstable and further growth is deemed improbable, figure 6.2. Pits that survived the nucleation process successfully continued to grow; these pits are known as metastable, although their continued growth is wholly dependant on the preservation of the protective chimneys. The presence of chloride ions increases the corrosion rate but is not used up in the reaction. The ions have the ability to absorb on the metal surface or the passive films and polarize the metal, initialising localised corrosion. When a pit becomes stable, the corrosive attack then becomes potentially damaging, as is subsequently illustrated in figures 6.3 & 6.4; pitting on anodised plate. The high resolution digital images reveal the severity of the corrosion pitting, together with the apparent appearance of the anodised surface surrounding the pit circumference. In light of the shrouding "chimney" behaviour of corrosion pitting, it is now possible to categorically state that the anodised surface in which pitting was produced is preferentially protected from further general corrosion by the chimneys themselves. A superlative example of this behaviour is illustrated in figure 6.4. This behaviour was noted on both as-machined and anodised surfaces as early as a single exposed week.

6.2.1 Fatigue of Flat Plate Specimens

Constant amplitude load controlled fatigue tests on the flat plate specimen focused on three distinct peak stress levels; 270 MPa, 160 MPa and 100 MPa. Multiple repeat tests were performed at high humidity conditions (>95%) at these specific conditions together with a preliminary single test at 210 MPa. These stress conditions were initially selected in order to induce fatigue lives to failure in the region of 10^4, 10^5 and $5x10^5$ cycles respectively. The stress conditions were successfully chosen to give direct comparisons to, and produce fatigue lives corresponding with those produced in SICAS. An S-N curve comparing the current data set to the previously reported SICAS database [82] is formerly illustrated in figure 5.8.

A significant reduction in fatigue strength across all evaluated stress conditions was defined for the current specimens. The considerable reduction in fatigue strength is highlighted at the intermediary stress level of 160 MPa, where a fourfold variance was observed in the shortest life. This inferior performance was attributed to the success in producing larger scale corrosion pits, introduced using the revised wet / dry corrosion protocol. The damage incurred was representative of the "worst-case" scenario observed in-service conditions. The tighter scatter band amongst the currently produced data (represented by the blue data points in figure 5.8) also confirms that consistently larger pits were present within the corroded areas of the test specimens. Pit and crack growth orientation in the present specimens almost certainly contributed a second order effect, due mainly to the fact that crack growth occurs in the L–ST direction as opposed to the T–ST direction sampled during the SICAS programme. Minor differences in crack growth rate were detected in these different orientations via a series of SEN crack propagation tests completed at Swansea, see chapter 5.4.3 [83].

It is confirmed that all the specimens failed from corrosion pits located at various positions within the corroded zone on the specimen front face. Subsequent to fatigue testing, corrosion pits causing fatigue crack initiation or consequently exposed on the plane of final fracture were measured in terms of the pre-defined metrics; maximum depth, maximum width, surface opening width and pit area. The criteria for these dimensions are previously illustrated in figure 5.10. In the majority of cases a single pit was responsible for crack initiation, as illustrated

by specimen PC-14 in figure 6.5; such images were subjected to standard image analysis techniques to obtain the relevant pit metrics. The relatively large widths of a selection of pits (maximum of 3.745 mm) encouraged multiple fatigue crack initiations along they're periphery; these are clearly highlighted within the SEM image in figure 6.6. The presence of multiple initiation sites was a regular occurrence on wide pits on flat plate specimens. Further examples of multiple initiations across pit widths can be seen in the Appendix chapter and in the pit illustrated in figure 6.7, which relates to a specimen tested at 100 MPa which achieved 293,225 cycles before failure. Multiple crack initiation sites were also detected around the periphery of this pit.

However, a few examples were noted where the main fracture exposed two or more pits each initiating individual cracks. Eventually, these cracks coalesced and advanced as a single semi-elliptical macro-crack. This type of behaviour was more common at the higher peak load conditions. Example of multiple pits causing fatigue initiation and growth are illustrated in the Appendix (specimens PC-1 – PC-10), viewed and imaged using various microscopy techniques. Another common feature noted during specimen analysis was pit clustering. This single pit on specimen PC-2, being relatively shallow but wide, developed by the localised interaction of individual, adjacent pits, as indicated by the region circled in figure 6.8. The clustering of neighbouring pits usually caused specimen failure as illustrated via the numerous examples available in the appendix, in particularly specimen PC-14.

The profiles of the final crack shape at the point of tensile overload were measured for each specimen, as defined in figure 6.9. The profile of the cracks are seen to vary with each stress condition evaluated i.e. the lower the stress, the larger the semi-elliptical macro crack. This information is tabulated for every tested specimen in table 5.5 in the results.

A degree of statistical analysis was completed on the corrosion pits found on the plane of final fracture. This was completed subsequent to fracture to yield accurate pit measurements. Figure 6.10 illustrates a set of histograms, used to define the range in metrics for pits exposed on the plain specimen fracture surfaces. Notable variations in pit size are clearly visible, for example, depth values ranged from 90 μm up to a maximum of 706 μm, while maximum widths

from 251 μm up to a massive 3.745 mm. A key feature to note from the statistical analysis is that the distribution of pit sizes for both surface opening width and maximum width appear very similar. Both are not normally distributed with the mean width values within a 100 μm. This clearly shows that in the majority of cases, the surface opening width is indeed the widest region of the corrosion pit. Of course, some of these data required a proportion of subjective judgement i.e. what constitutes a "single-pit". It is clear that some of these features have developed from the coalescence of neighbouring pits.

The fracture surfaces of the flat plate specimens tested in the current research were typical of a high strength aluminium alloy. In general, the fracture surfaces were smooth in the vicinity of the initiating corrosion pit, with increasing roughness as the distance from the pit increased. In some cases there was evidence of intergranular etching, most likely due to the high humidity environment used for testing, in the vicinity of the initiating defect. This etching took the appearance of "mud cracking" patterns. Fatigue striations were present on the surfaces of the examined specimens. Striations were not visible near the origin but became clearer as crack growth proceeded. They continued all the way to final fracture but were often hidden by the extreme roughness of the fracture surface prior to final failure.

6.2.2 Fatigue of Centre Hole Specimen

Centre hole specimens contained corrosion pits within the bore of a 6 mm diameter drilled and reamed hole. Pitting was initiated and grown on an as-machined surface, unlike the anodised finish used for the flat plate counterpart. Prior to fatigue testing, it was obvious from visual inspection that the most severe corrosion pitting was concentrated in the regions of the hole corresponding to the exposed "end grains". With respect to the loading configuration, this region provided the most significant pits at the root of the notch and coincident with the specimen net section, see figure 5.27. Pits were also distributed randomly around the surface of the hole, although these were often smaller in size and contained differing morphologies when compared to those of the "end-grain" type. The difference in pit morphology can be largely

attributed to the local microstructure surrounding the 6 mm drilled and reamed hole, in particular the grain orientation at various regions.

In total 56 centre holed specimens were tested; 7 specimens with an as machined hole (i.e. drilled and reamed with no corrosion) to generate a "baseline" SN curve, 3 specimens after a single week, 6 specimens after 2 weeks corrosion, 42 specimens with 8 weeks corrosion of which, 6 were subjected to a post corrosion over-size reaming procedure and finally 4 specimens after a prolonged 52 weeks of corrosion. Compared to the baseline response, (figure 5.22 in the results chapter) the effects of the various exposure periods can clearly be seen. An exposure period as short as one week appears to have a significant effect on fatigue performance, with the tested specimens achieving some of the shortest observed cyclic lives. Figure 6.11 illustrates typical examples of the pits observed after exposure for a single week. However, longer exposure periods ranging between two and eight weeks induce no additional reduction in fatigue lives. In addition, it may be argued that this marginally longer corrosion period slightly increased fatigue lives, as the S-N behaviour suggests.

The four specimens exposed over a twelve month period were all tested at a single stress level (135 MPa). Compared to the distribution of lives measured after eight weeks corrosion, this extreme period of exposure has now induced a significantly weaker response. Figures 6.12 and 6.13 illustrate the extent of damage caused via the prolonged corrosion period. Pits appear wider in their complexion, arguably causing the noticeable variance in the observed fatigue life.

The six specimens that were corroded for eight weeks and subsequently subjected to a post corrosion over-size reaming procedure were found to produce mixed results, in terms of their S-N behaviour. Two set reaming sizes were chosen (6.24 mm – designated ream 1, 6.5 mm – designated ream 2) in order to replicate in-service corrosion management techniques of fastener holes, figure 6.14. From the S-N curve in figure 5.22, it is apparent that the larger over-size ream (6.5 mm) procedure returns the fatigue lives of corrosion damaged specimens to similar lives noted for pristine specimens. This essentially indicates the removal of the majority of corrosion pits located within the bore of the hole.

Fractographic investigations have underlined that failures were predominantly initiated from multiple corrosion pits within the central region of the bore, although several specimens also initiated fractures from corner sites. Figure 6.15 provides typical examples of the macroscopic fractures. The extent of crack growth was normally balanced to either side of the hole, with the crack reaching through section characteristics prior to failure, figure 6.16. However, some examples were noted where fracture was dominated by growth to one side. Due to the relatively large number of pits noted on either fracture surface, it was usually impossible to identify which individual pit was responsible for the first episode of cracking. All the pits revealed on the fracture plane were analysed and measured. Figure 6.17 is a SEM image of the typical end grain pitting. Clearly the pit morphology is different to that of the flat plate specimens, with the pit being notably deeper, but with a much reduced width, presumably due to the effects of microstructural features, in particular the local orientation of grain boundaries, as previously discussed. Several crack initiation sites were visible along the flanks of these deep pits. The distribution in pit metrics for the centre hole specimens is illustrated by figure 6.18

6.3 LINEAR ELASTIC FRACTURE MECHANICS (LEFM) MODELLING

The modelling of the fatigue data was approached from a LEFM view point, since the size of the corrosion pits produced on both flat plate and centre hole specimens were often indicative of long fatigue cracks i.e. spanning multiple grains. In order to complete the modelling process, a convenient software code had to be chosen, bearing in mind cost effectiveness, in view of the fact that the end user would ultimately be industry based. The software would also have to be freely available to the Engineering community and be obtainable commercially or via other sources such as the internet.

The software chosen for the modelling process ultimately was AFGROW, given that the interface met all the above criteria and was freely available worldwide. More importantly to the current research programme, the software was previously used in the SICAS project. Direct comparisons were therefore possible with fatigue life predictions made in SICAS. However, the SICAS programme utilised an Equivalent Initial Flaw Size (EIFS) concept. Fundamentally, this

approach treats corrosion pits as if they were fatigue cracks of equivalent semi-elliptical form. This technique is useful, particularly to the aviation industry as a whole, as there are well established tools for managing fatigue damage. However, the more suitable LEFM based modelling was applied to model the current fatigue behaviour of the alloy subject to large scale corrosion pitting. Similarly to the EIFS approach, corrosion pits were assumed to take the form of a pre-existing defect/crack within the specimen of semi-elliptical form. Crack growth from static defects was dependant on the stress at the crack tip exceeding threshold stress intensity (ΔK_{TH}), which AFGROW calculated from the pre-defined inputs. Failure was estimated when the crack grew to a critical size (defined in AFGROW as > K_{IC} or 'net section' yield).

In order to apply the modelling process to the end users point of view (Aerospace Industry – BAE SYSTEMS), various model input decisions were taken (inputs have been previously reviewed in some detail in chapter 4, experimental procedures). The main model input decision involved selecting material information from the AFGROW library. This decision was taken in light of the fact that the end users may not be able to generate their own unique material database resulting mainly from cost and time issues. Therefore, the NASGRO database was used, utilising the same aluminium alloy but a slightly different heat treatment (AA 7010-T73651). In order to justify this selection, a limited number of Fatigue Crack Growth (FCG) tests were performed on both specimen geometries (flat plate – L-ST & centre hole – ST-L), figure 5.31. No effect of crack orientation was noted. The in house FCG tests were also compared to the NASGRO AA 7010-T73651 FCG data, figure 5.32, to check the Paris regime coefficients. These were found to be consistent.

Predictions were completed for both corroded flat plate and centre hole specimen geometries utilising the defining pit metrics; surface opening width and maximum pit depth, figure 5.10. The pit surface opening width metric was used since it replicates the measurements possible by inspectors/NDT technicians during routine aircraft service inspections. However, the defining pit metrics measured for the current research programme may not be entirely accurate, since they were determined from the plane of final fracture, for example, a pit may contain a wider surface opening width than that seen on the fracture plane. The same principal can be applied to the pit depth measurements, although to maintain consistency, the apparent pit depth

should have been used to predict the fatigue lives. However, in practice this was found to be very difficult, since acquiring measurements using a focussing technique tend to produce inaccuracies. Measuring pits within the bore of the centre hole specimens was also found to be virtually impossible using the focussing technique. In light of this, it was decided to use the pit metrics from the plane of final fracture as previously mentioned.

The predicted lives generated using the pit surface opening width and maximum pit depth metrics for both specimen geometries can be seen in figures 5.35 – 5.39. The S-N graphs illustrate that the fatigue life modelling of the corroded aluminium airframe material AA 7010-T7651 was relatively successful for both flat plate and centre hole specimens. The correlation between the measured and predicted lives appears to be favourable especially in the case of the centre hole specimens. Overlapping of measured and predicted scatter bands (mainly in the average pit size predictions) illustrate the validity of the modelling procedure and more importantly, the employment of the AFGROW software. Of particular success was the modelling of the average pit size metric, whereby the average surface opening width and average pit depth of any pits exposed on the eventual fracture surface were calculated. Once more, this prediction technique may be applied by service inspectors carrying out routine component/structure examinations. The predicted lives based on the average pit size metric, essentially mirrors those of the measured data, highlighting the effectiveness of this technique, figure 5.37 flat plate & figure 5.39 centre hole. From a comparison point of view, predictions were also generated using the pit maximum surface widths as an alternative to the surface opening width. The results can be seen in figures 6.19 and 6.20 representing flat plate and centre hole specimens respectively. Trendlines representing the measured data (blue), maximum pit width (orange) and surface opening width (dotted blue) have been added to the S-N graphs to illustrate the variation between the predicted and measured data sets. An interesting feature noted from both figure 6.19 and 6.20 is the minor difference between both width metrics evaluated, illustrating that in most cases, the opening width is often the widest region of the pit. This is further highlighted in tables 5.6 and 5.8

As previously indicated, the methodology behind the current research modelling of predicting the fatigue life of the material subject to corrosion pitting is compatible to that of

possible inspections made in the field. For example, when a region of corrosion pitting is identified within a component or structure, the surface pits are then characterised to define the maximum pit surface opening widths and apparent pit depths. This information can then be fed directly into AFGROW (or an equivalent LEFM based model), to predict the remaining life of that component/structure. The results have indicated that the fatigue life modelling of the alloy subject to large scale corrosion pitting via a LEFM path was successful in terms of producing relatively accurate predictions. The advantages of modelling via a LEFM route in this case far outweigh that of using an EFIS approach. LEFM theories are well understood, applicable to field engineers (ultimately the end users) and require less expertise.

Table 6.1 Specified chemical composition ranges for the 7010-T7651 material used in the SICAS investigation (remainder Al).

Alloy	Composition (wt%) (remainder Al)						
	Mg	Si	Cu	Zn	Mn	Zr	Cr
7010-T7651	2.1 - 2.6	-	1.5 -2.0	5.7 - 6.7	-	0.10 - 0.16	-

Table 6.2 Handbook mechanical properties for the 7010-T7651 material used in the SICAS study. L= Longitudinal, T= Transverse, S = Short transverse, B = B Allowable = Values achieved by 90% of population at a 95% confidence interval

Alloy	Orientation	Young's Modulus E (GPa)	Proof Stress $\sigma_{0.2}$ (MPa)	Tensile Strength σ_{TS} (MPa)	Strain to Failure ε_f (%)	Plane-Strain Fracture Toughness K_{1C}
7010-T7651	L	71	453 (B)	510 (B)	6	-
	T	71	448 (B)	515 (B)	5	-
	S	71	402 (B)	484 (B)	2	-
	L-T	-	-	-	-	24
	T-L	-	-	-	-	22

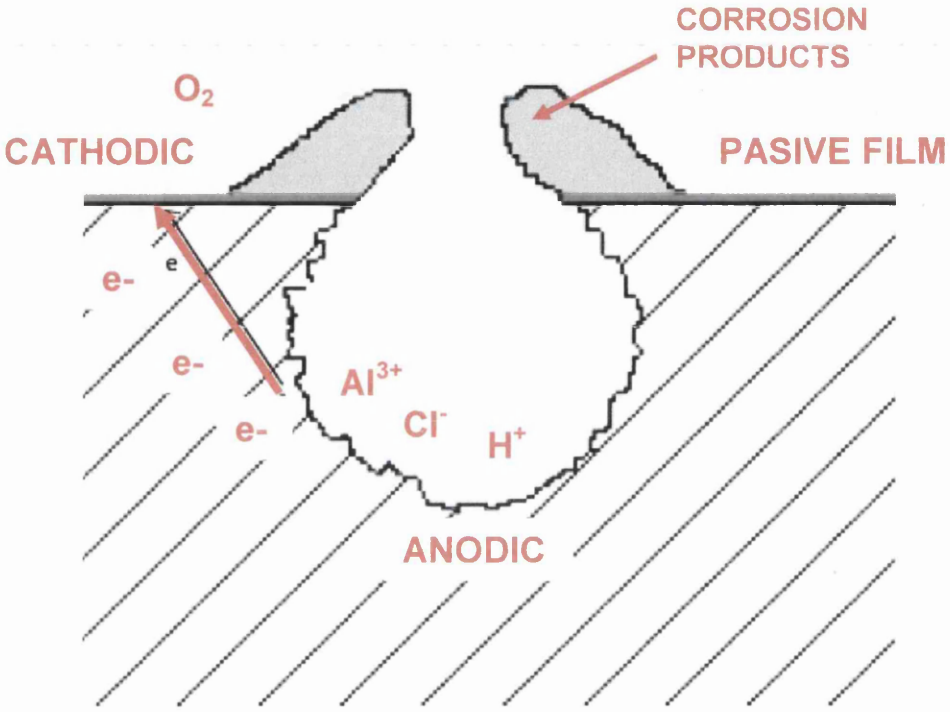

Figure 6.1 Schematic of an actively growing pit in an aluminium surface.

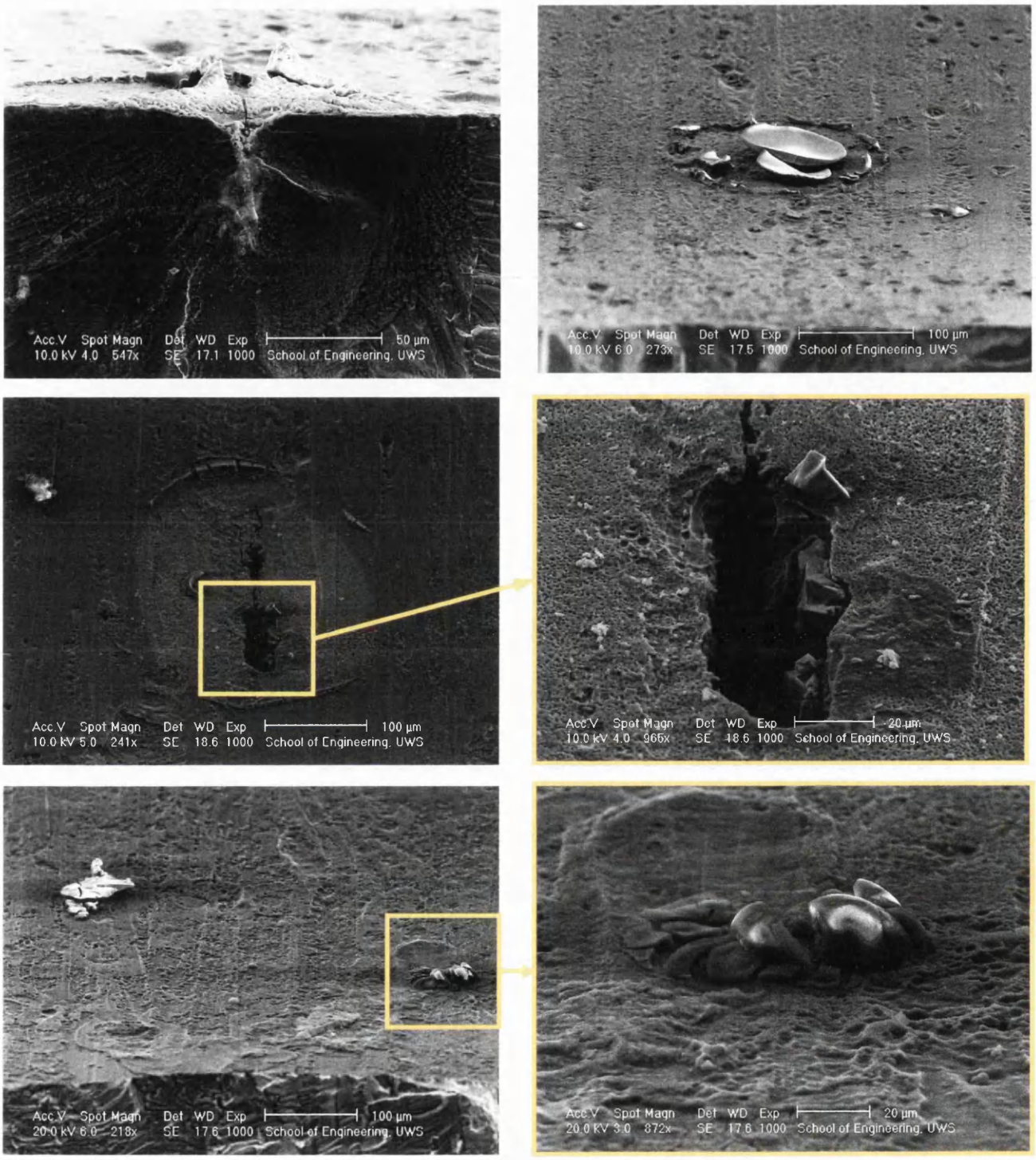

Figure 6.2 SEM images illustrating the corrosion product/oxide build-up (chimney) protecting corrosion pits. Note, pits with damaged/broken chimneys would no longer grow.

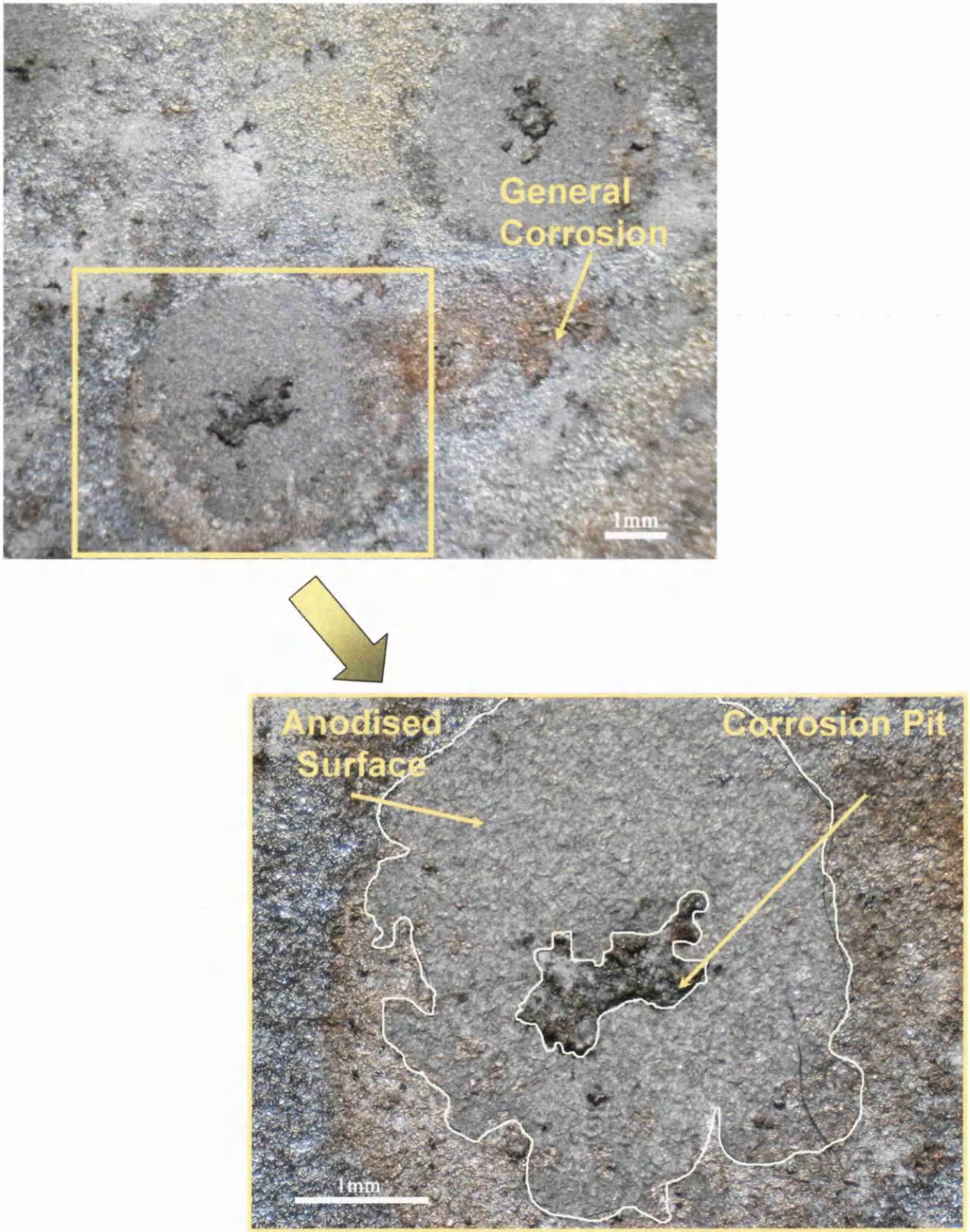

Figure 6.3 Corrosion pitting with the anodised surface surrounding the pit circumference.

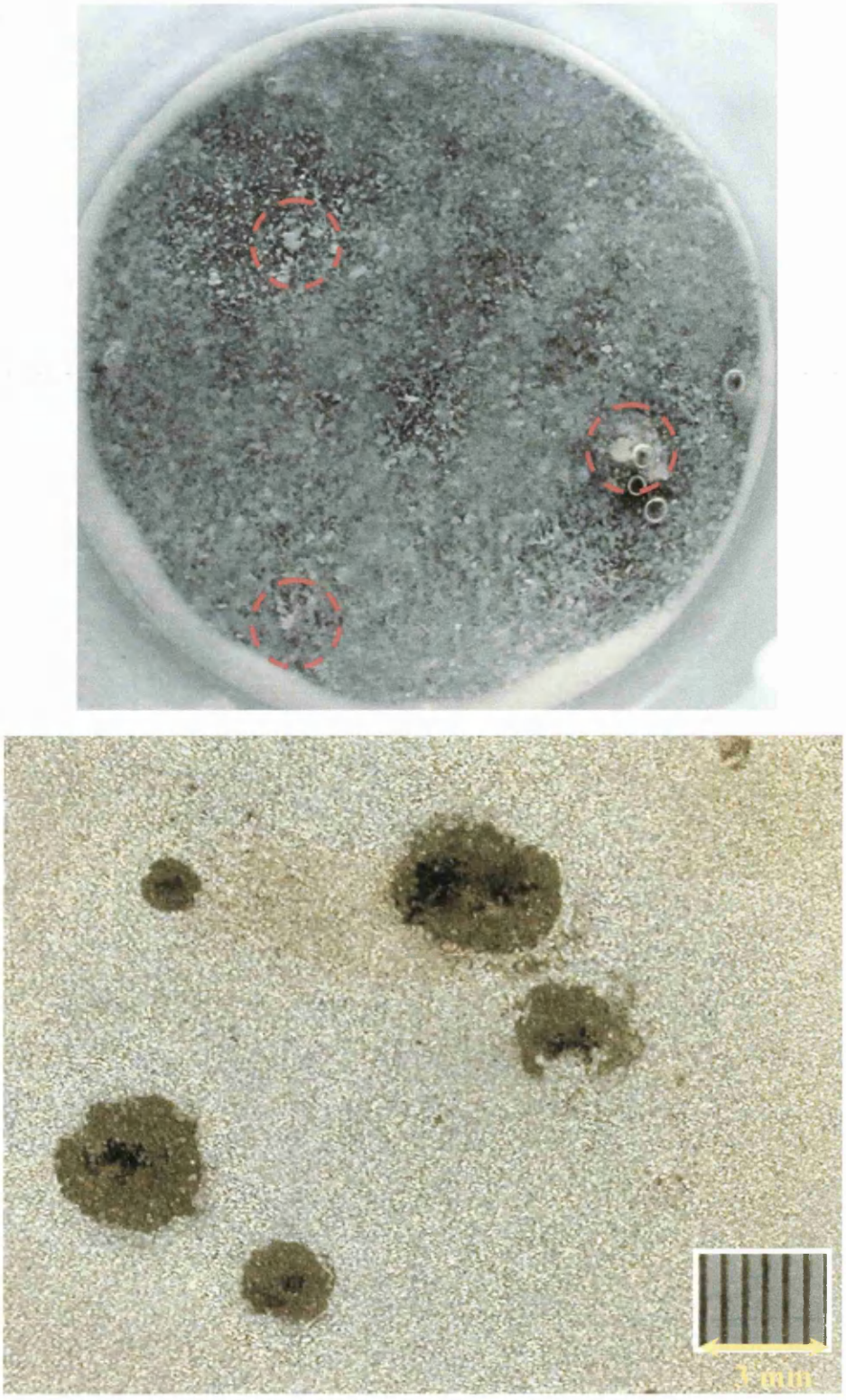

Figure 6.4 Examples of pits grown on anodised surface with the surrounding ring preferentially protected by the corrosion product/oxide build up produced as a result of the growing pit.

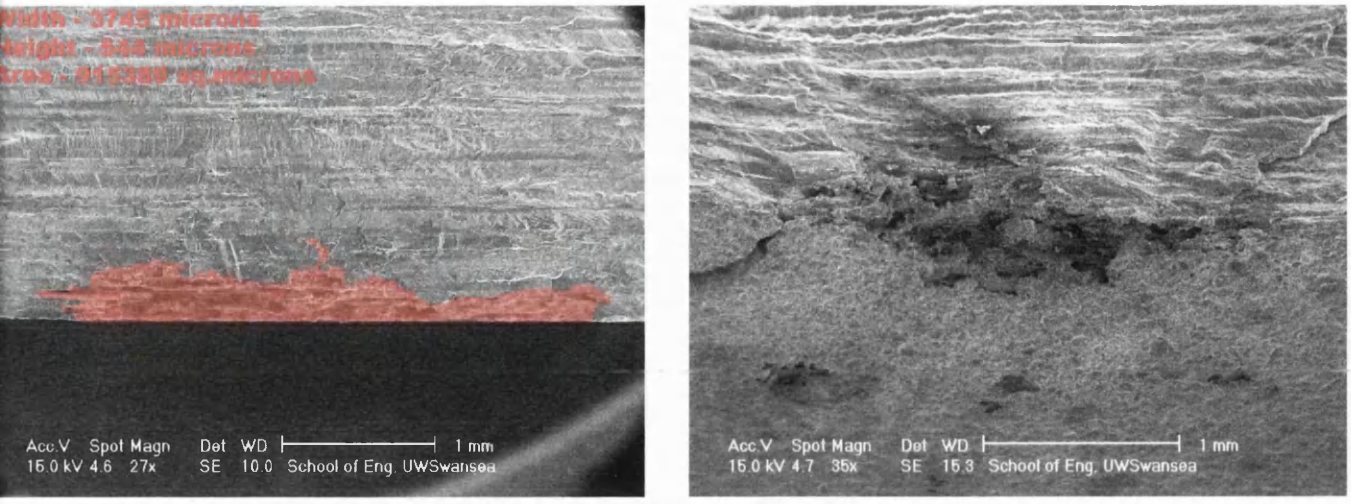

Figure 6.5 SEM image of a single pit causing considerable fatigue cracking on specimen PC-14.

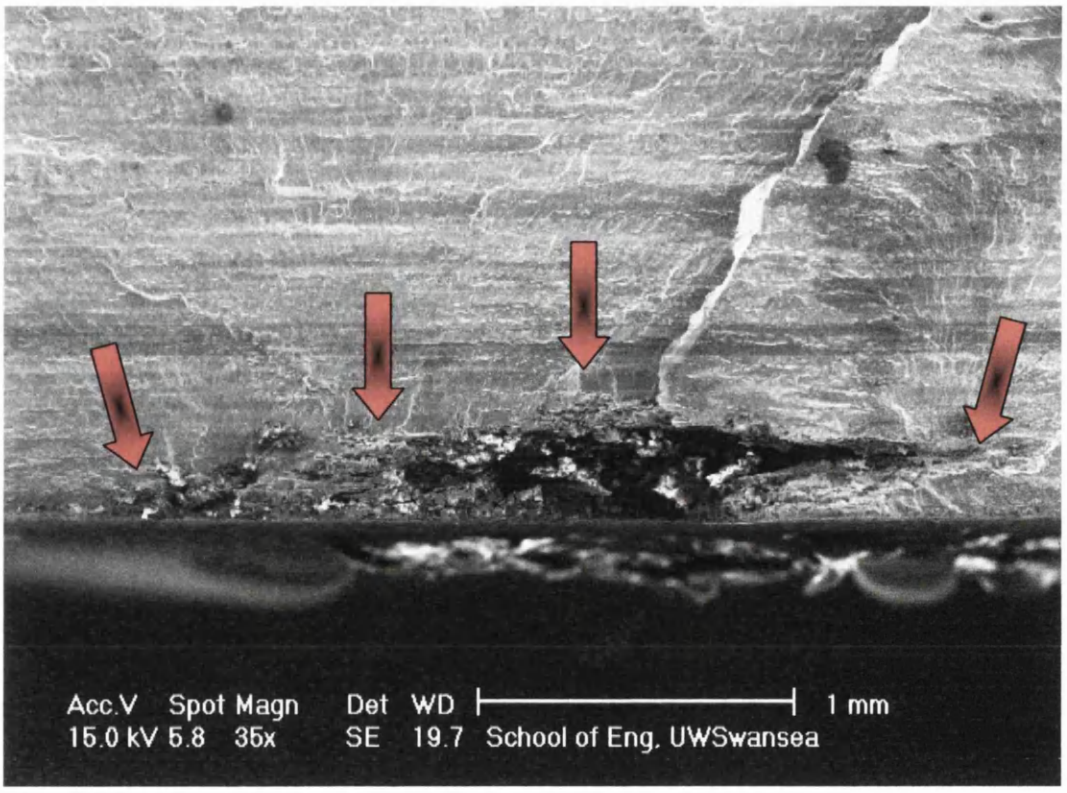

Figure 6.6 SEM image of a crack initiating corrosion pit on a specimen PC-1. Clearly multiple initiations are visible at the various locations around the large corrosion pit.

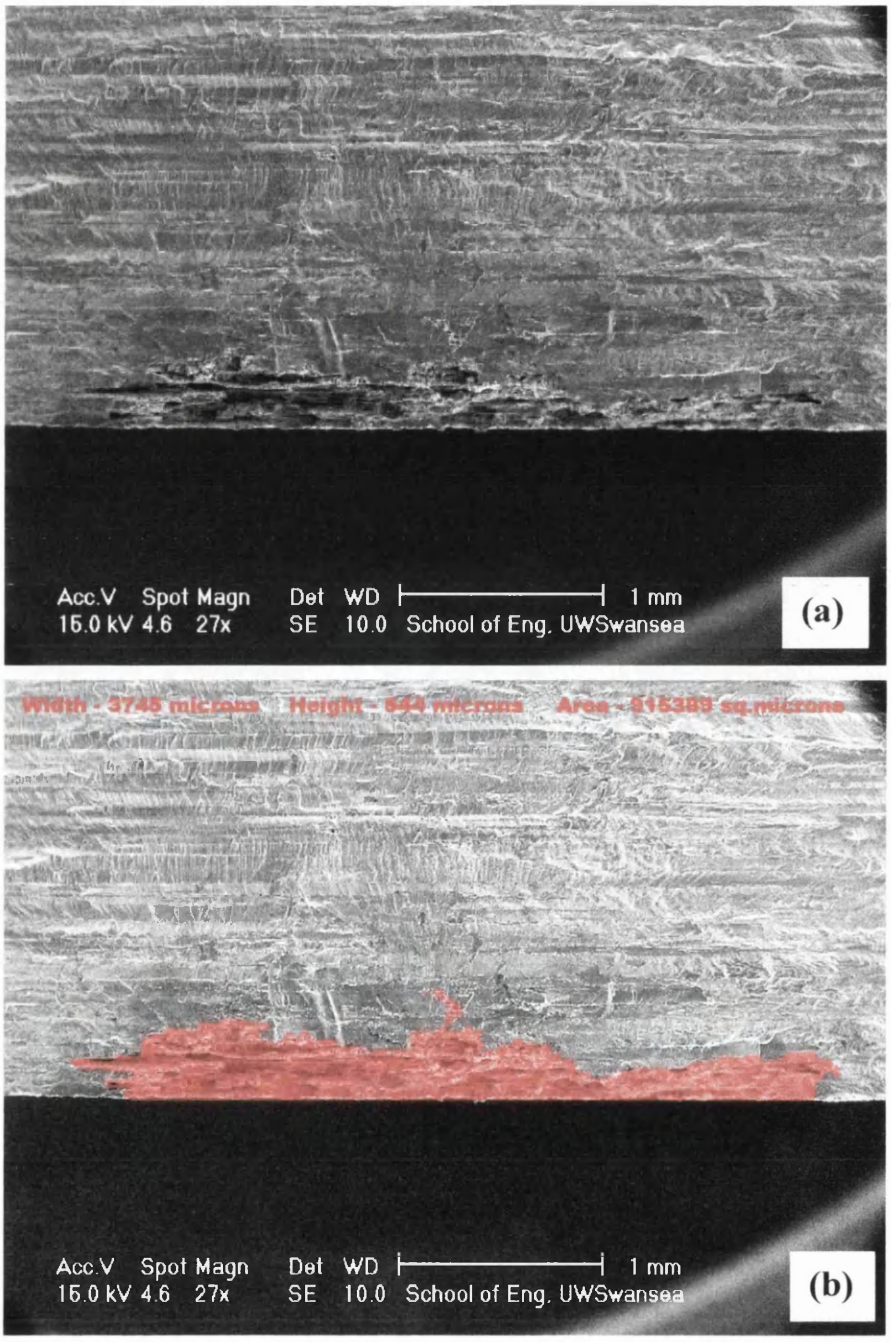

Figure 6.7 (a) SEM image of the initiating corrosion pit in a single plain specimen showing multiple initiation sites (b) post image analysis to measure pit metrics.

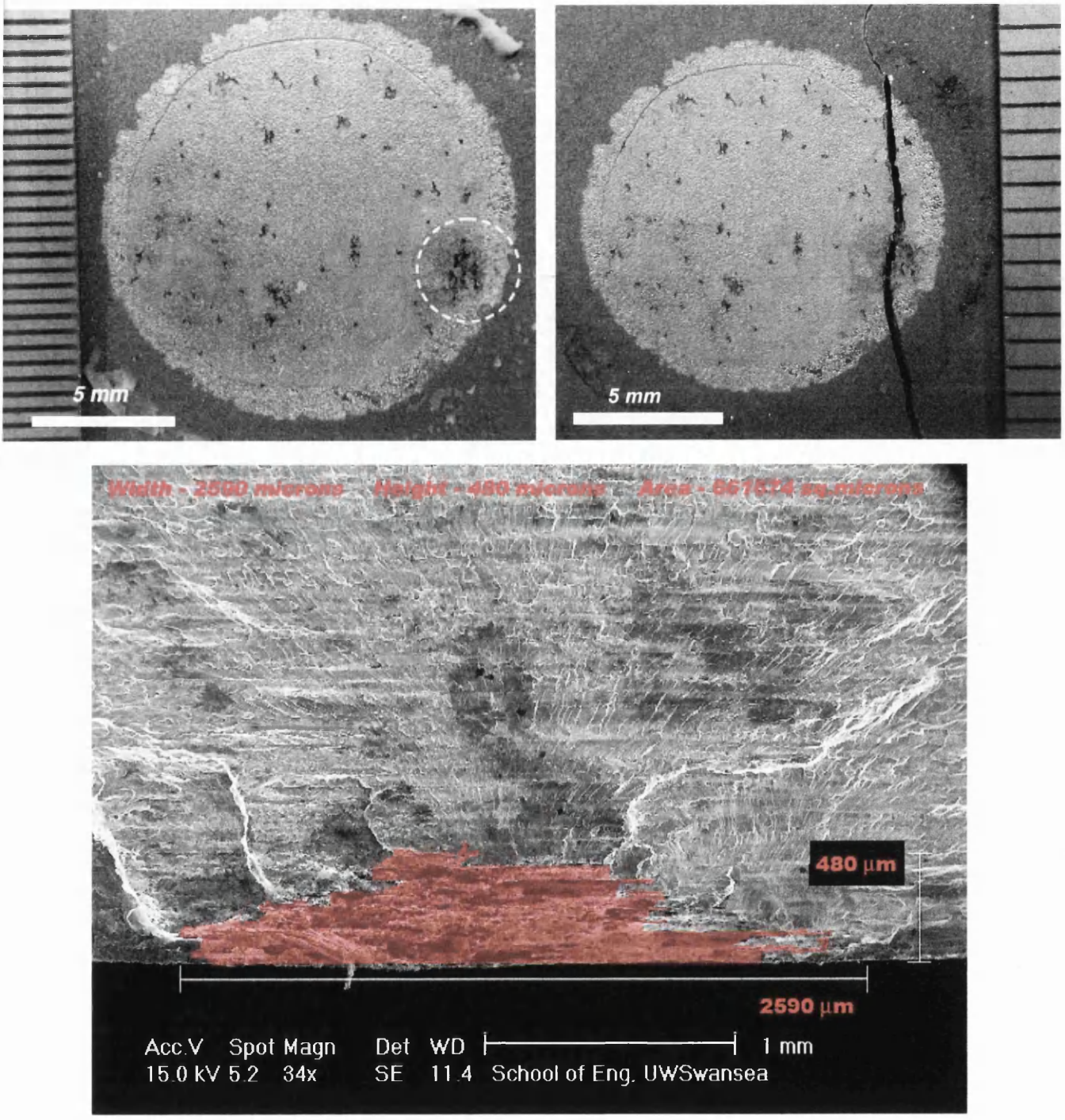

Figure 6.8 Specimen PC-2 that failed from a pit cluster area.

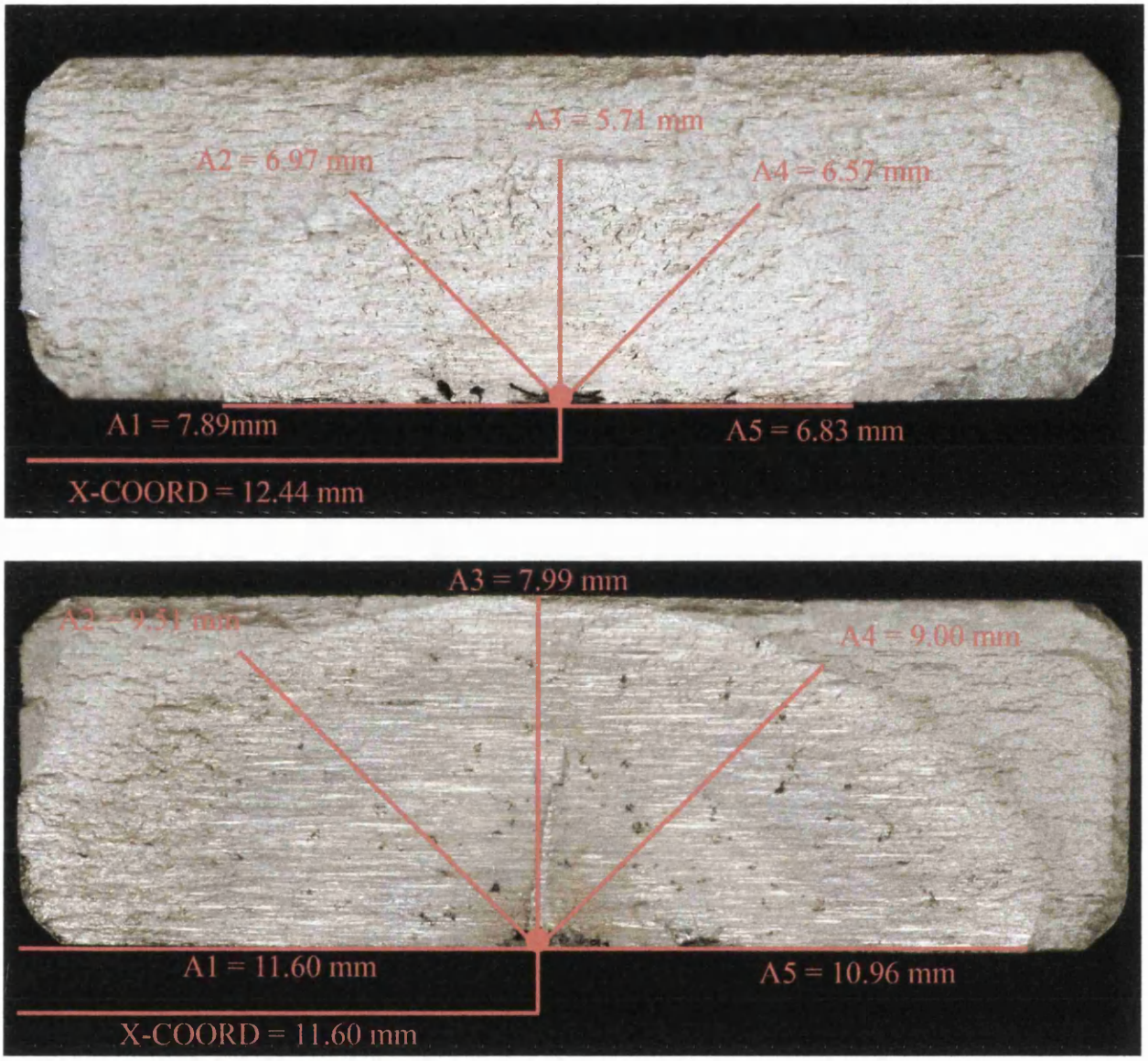

Figure 6.9 Typical plain specimen fracture surface indicating the dimensions measured to define the final fatigue crack profile. Above is an example of a high stress fracture, while below illustrates a low stress fracture.

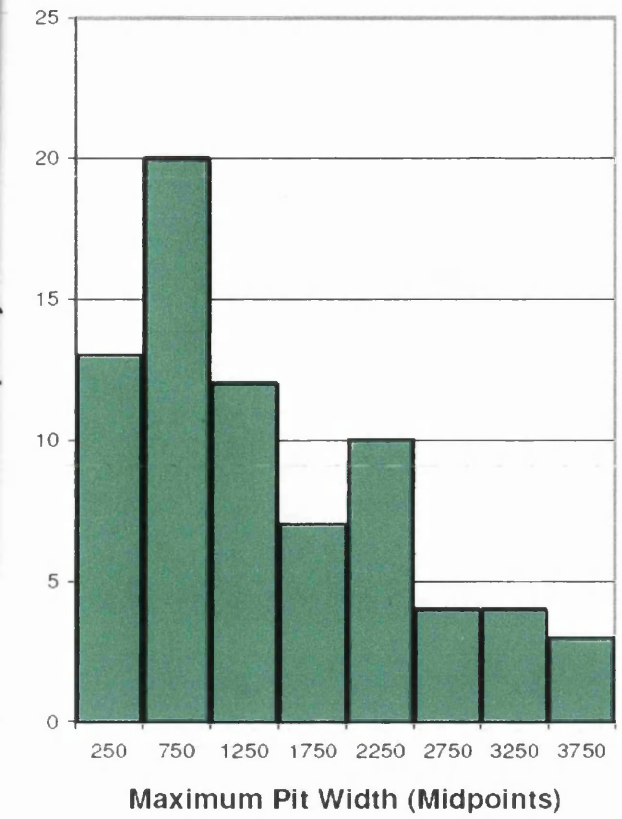

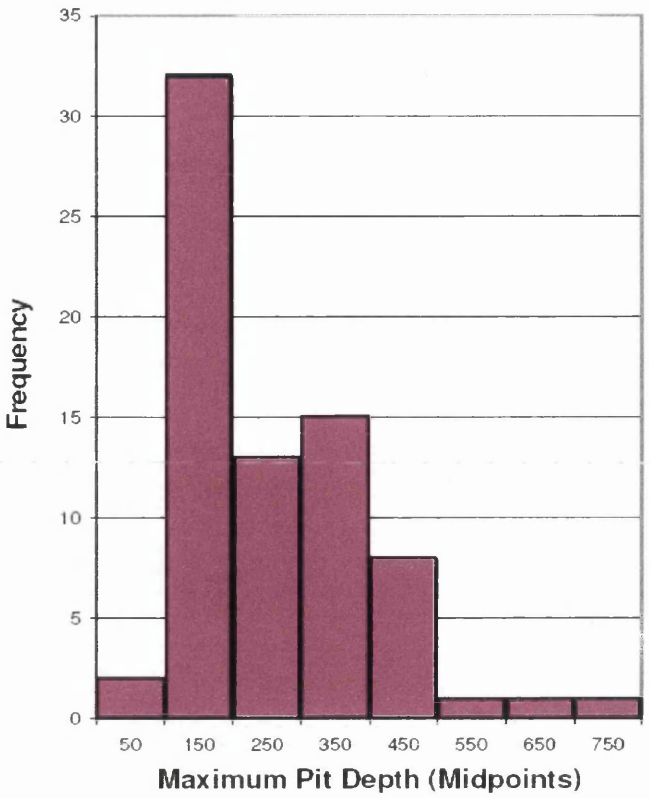

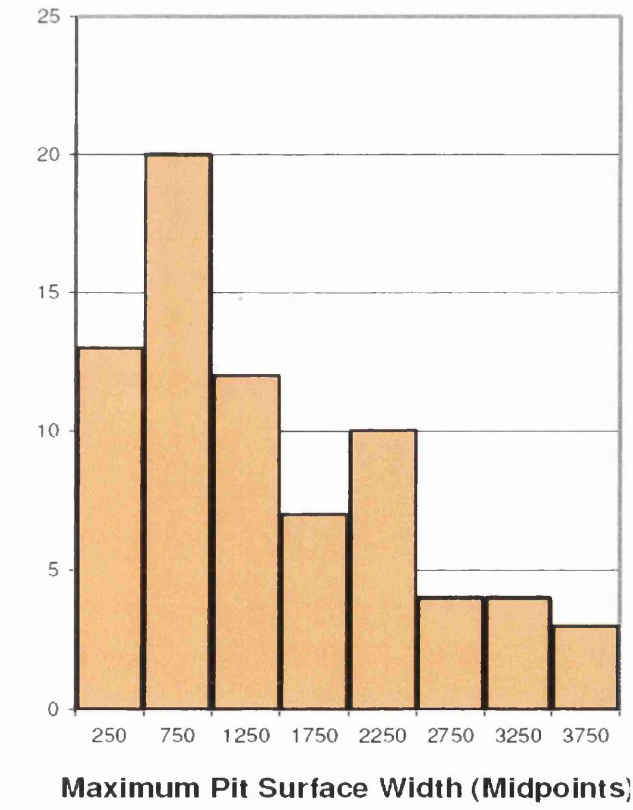

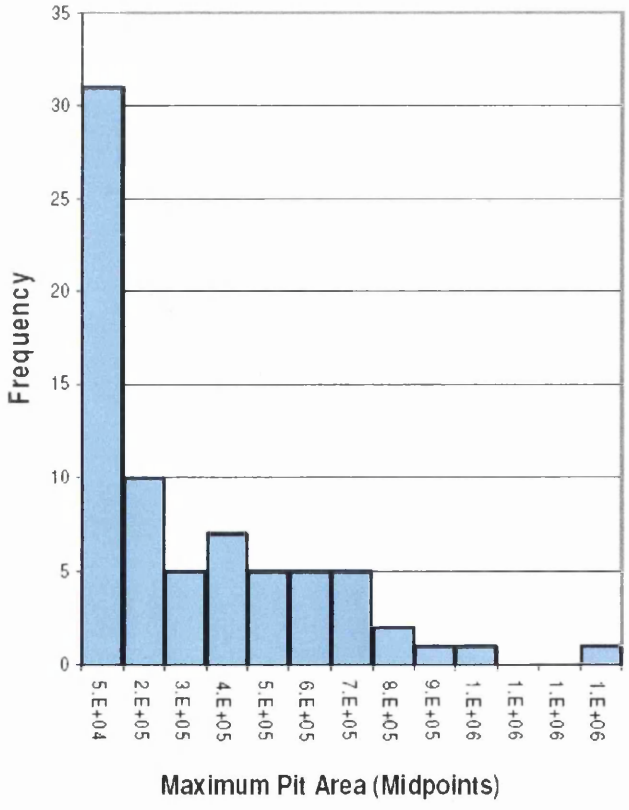

Figure 6.10 Metrics for pits exposed during fracture of plain specimens (width units μm, area units μm^2).

Figure 6.11 Typical examples of the size and morphology of corrosion pitting on AA7010-T7651 after one corroding week.

Figure 6.12 Corrosion pitting observed on 52 week specimens.

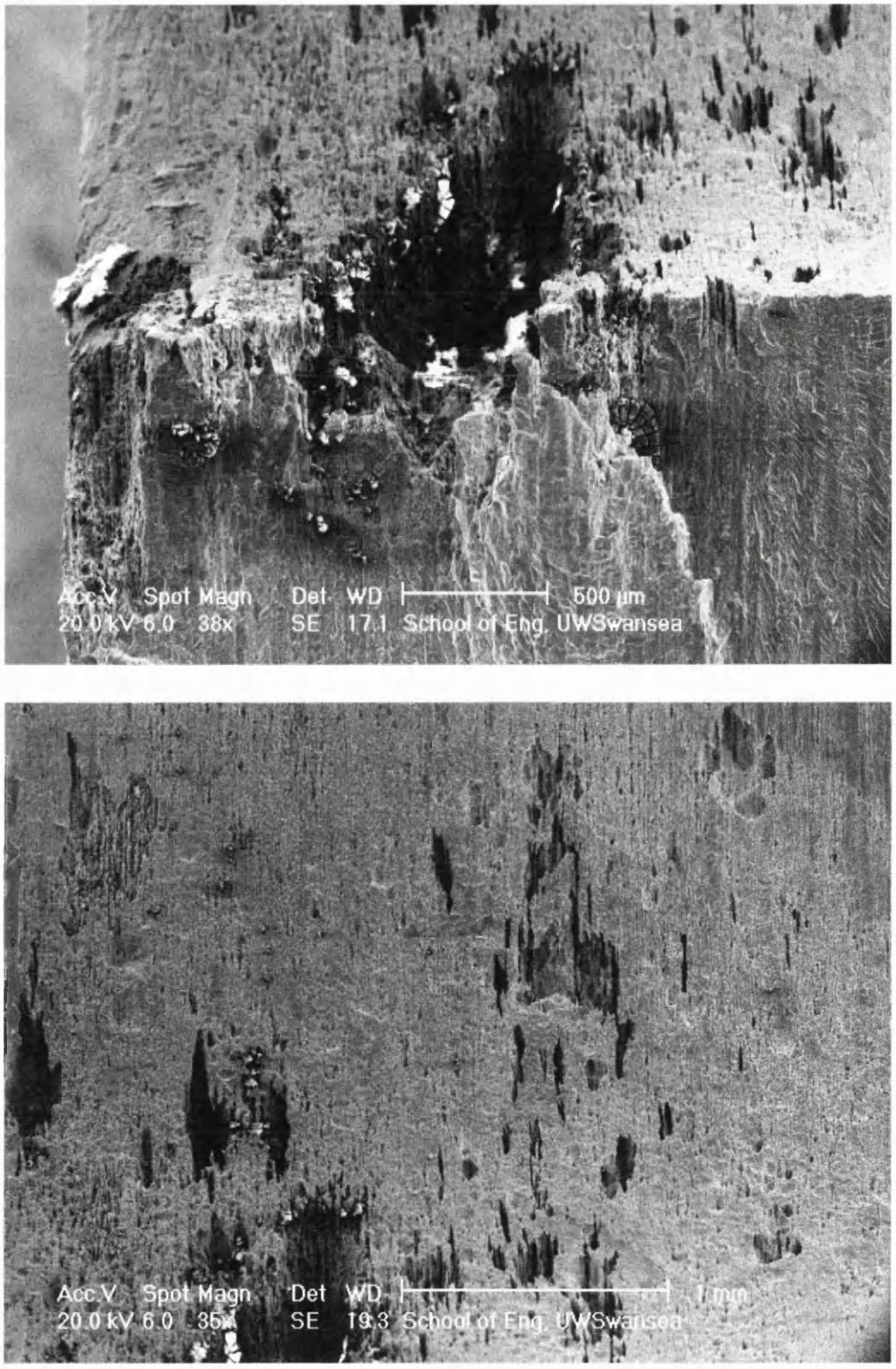

Figure 6.13 Appearance of the bore region of the 6 mm drilled and reamed hole subsequent to 52 weeks exposure.

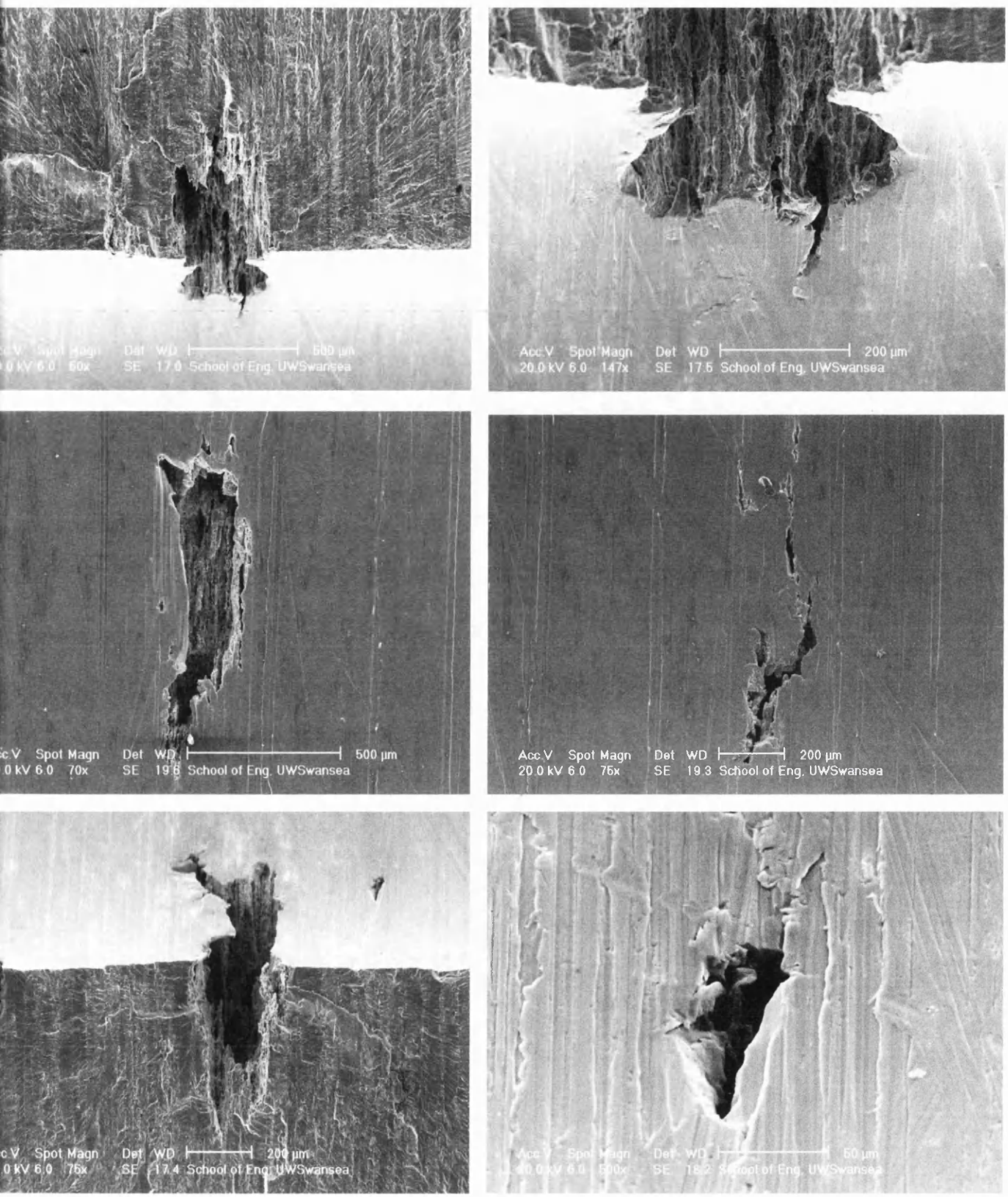

Figure 6.14 Examples of pits exposed in the bore of hole subsequent to reaming.

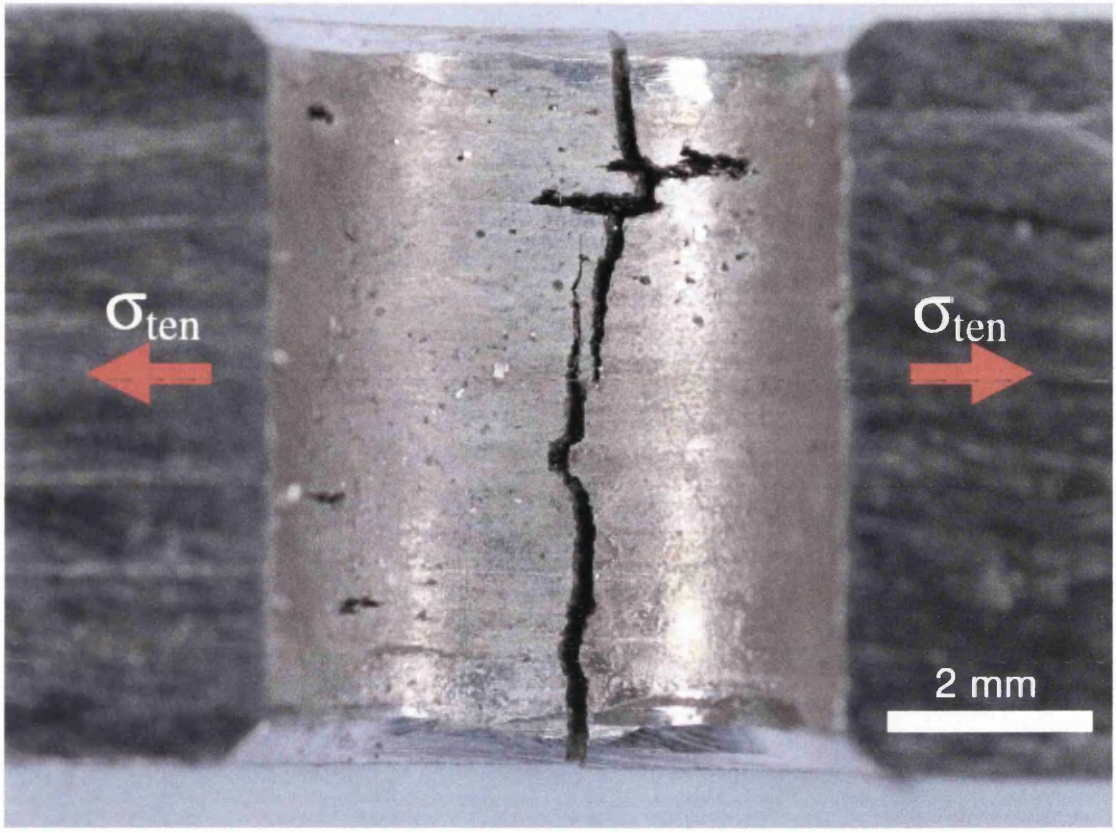

Figure 6.15 Longitudinal section prepared through a typical fractured centre hole specimen revealing severe end grain corrosion pits at the root of the hole (close to the net section plane) and the cause of subsequent cracking. Associated smaller scale pits are noted around the hole.

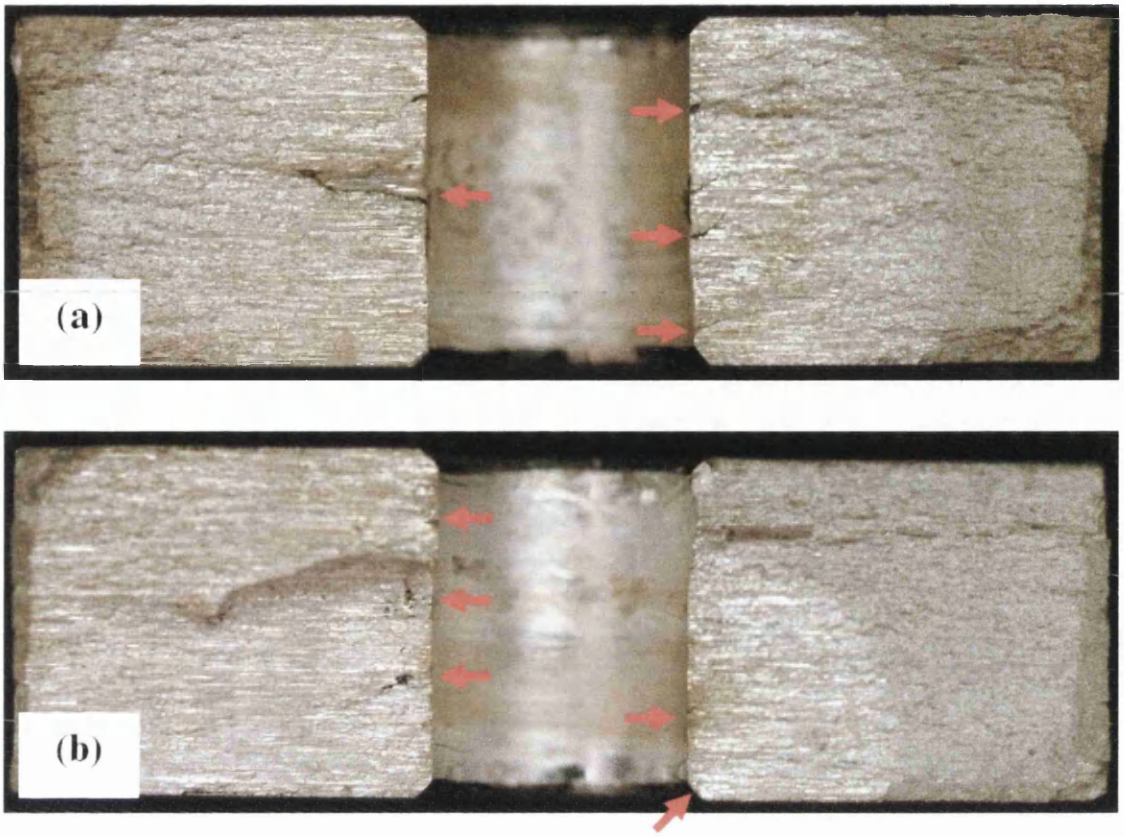

Figure 6.16 Typical fracture surfaces of centre hole plate specimens. Arrows indicate locations of dominant crack initiating pits. (a) relatively even through section crack growth to either side of the hole, (b) dominant growth to one side, with corner crack characteristics on the opposite half.

Figure 6.17 (a) SEM image of typical end grain corrosion pitting located in the bore of a centre hole specimen, (b) post image analysis to identify the pit periphery and pit metrics.

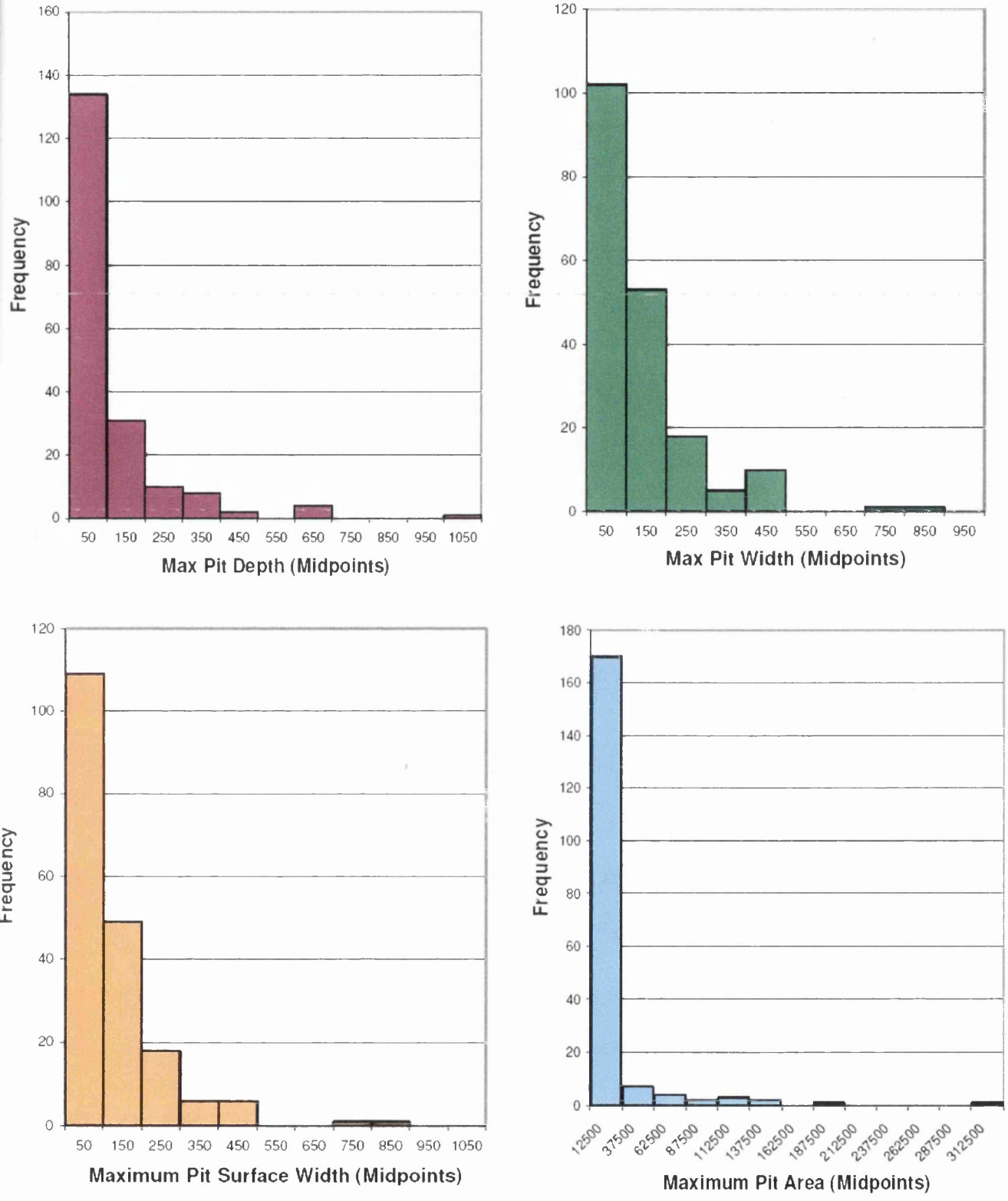

Figure 6.18 Metrics for pits exposed during fracture of centre hole specimens (width units μm, area units μm²)

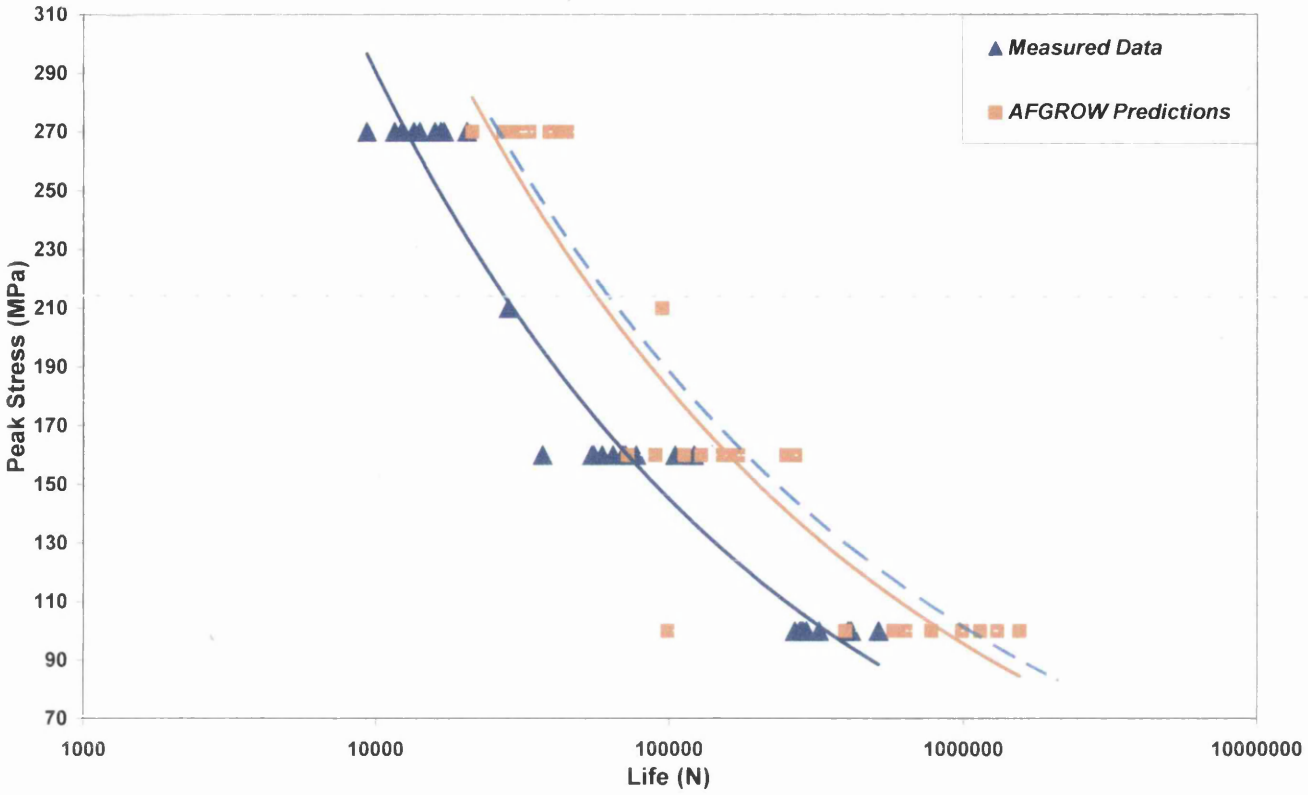

Figure 6.19 Measured and predicted S-N data for corroded flat plate specimens employing average maximum width and average maximum pit depth. Interrupted blue trendline represents the pit surface opening width.

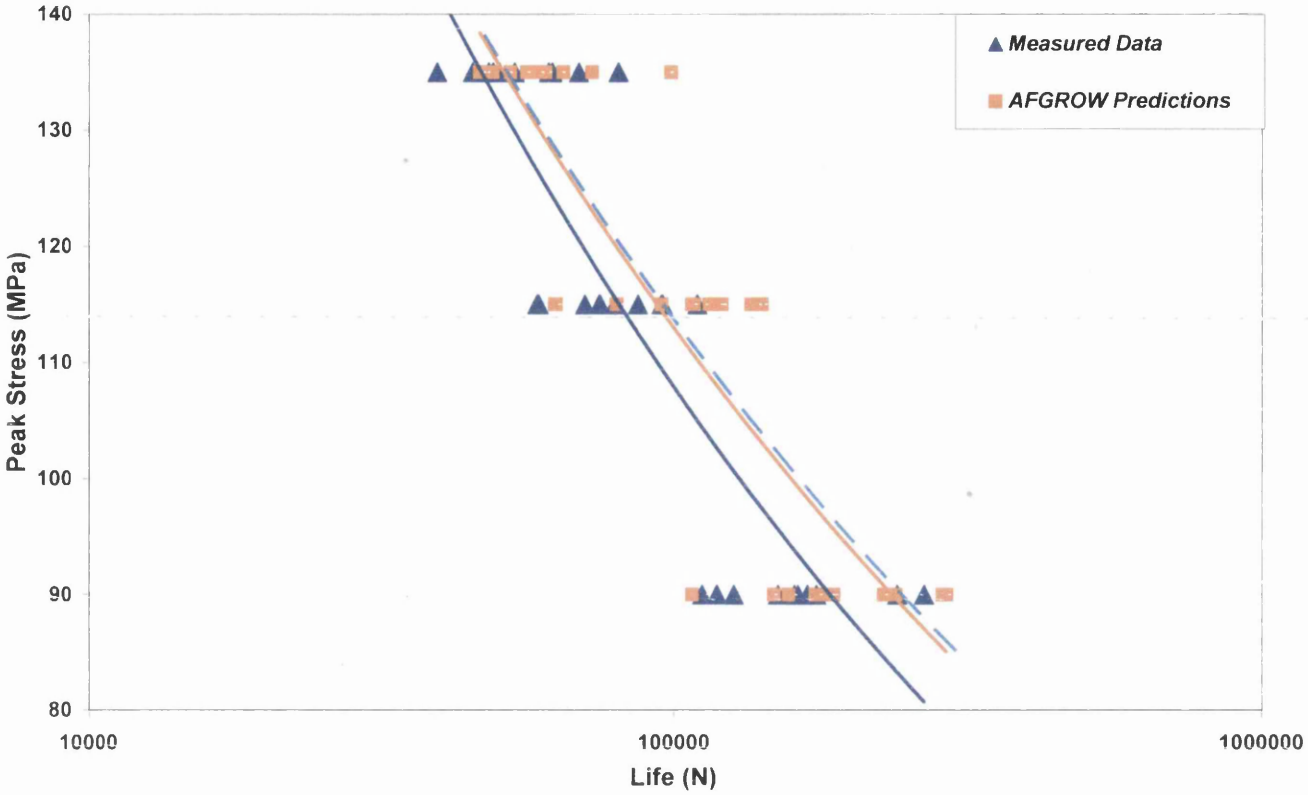

Figure 6.20 Measured and predicted S-N data for corroded centre hole specimens employing average maximum width and average maximum pit depth. Interrupted blue trendline represents the pit surface opening width.

7.0 CONCLUSIONS

Relatively severe corrosion pitting has been assessed in the aluminium alloy AA 7010-T7651 and the subsequent effects on fatigue evaluated. A number of key conclusions can be drawn:-

- A periodic wet/dry corrosion protocol has been successfully defined for the production of pits in this specific alloy. The scale of these pits was notably greater than those introduced into the same alloy over similar exposure times during the preceding SICAS study, which employed a continuous immersion technique.

- Compared to continuous immersion, the alternating wet/dry technique provides a closer representation of actual in-service conditions. However, it is emphasised that the rate of corrosion introduced into the present laboratory specimens far exceeds that found in the field.

- The microstructure of the AA 7010-T7651 alloy plays a dominant role on pit size and morphology:-

  - Flat plate specimens exposed to the environment on the L-T plane produced wide and shallow pit profiles due the coalescence of neighbouring pits. The relatively large scale of these pits led to a significantly weaker fatigue response, when compared to corrosion free specimens and to specimens with a similar orientation tested during the SICAS programme but containing relatively smaller pits.

  - In contrast, extremely narrow but deep pit profiles were noted for the end grain corrosion, found within the bore of the centre hole specimens (i.e. examined in the T-ST plane). This form of damage may be envisaged within fastener holes of riveted structures. In the simulated laboratory environments, exposure for a single week provided a reduction in fatigue performance. This was not affected by further exposure up to a period of eight weeks, however the extreme case of twelve month

corrosion did provide an additional reduction in fatigue life at specific selected stress conditions.

- Fractographic inspections have revealed that it is often difficult to identify the corrosion pit(s) that cause the first episode of cracking and subsequent failure.

- The "find it – fix it" approach to corrosion management was duplicated in the laboratory through fatigue testing of pre-corroded and reamed centre hole specimens. For a 6 mm corroded hole, reaming to 6.24 mm diameter failed to completely remove corrosion damage and consequently fatigue response remained compromised. Over-size reaming to 6.5 mm diameter was required to remove all corrosion damage and resurrect the "as machined" fatigue performance.

- Crack propagation rates, as measured from a "long crack" specimen design in the L-ST and ST-L planes, were not sensitive to microstructural orientation. A small degree of variance was noted between the current FCG measurements and those produced from the previous SICAS project on the same batch of material, however, SICAS measurements were taken in a different orientation (L-T). The NASGRO database within the commercially available AFGROW LEFM prediction package also correlates well with either of these data sets over the range of ΔK between 8 and 50 MPa$\sqrt{m}$.

- LEFM based modelling of corroded AA 7010-T7651 specimens was relatively successful in predicting fatigue lives of both flat plate and centre hole test geometries.

- Fatigue life predictions utilising the average pit size (as exposed on each specimen after fracture) produced the most favourable results. A relatively small degree of scatter was observed, with the range of lives indicated by the actual and predicted data sets overlapping.

- Due to the relatively large scale of the current corrosion pits, an effective initial flaw size (EIFS) technique previously employed by the SICAS programme was deemed un-necessary.

- The basic LEFM approach for remnant lifing of corroded AA7010 is more compatible with service inspections for corrosion damage, since the only pit metric that can be identified in the field in a non-destructive manner would be the surface pit opening width. (EIFS relies on more detailed post failure metrics such as actual maximum depth and maximum width).

APPENDIX 1

PC–1

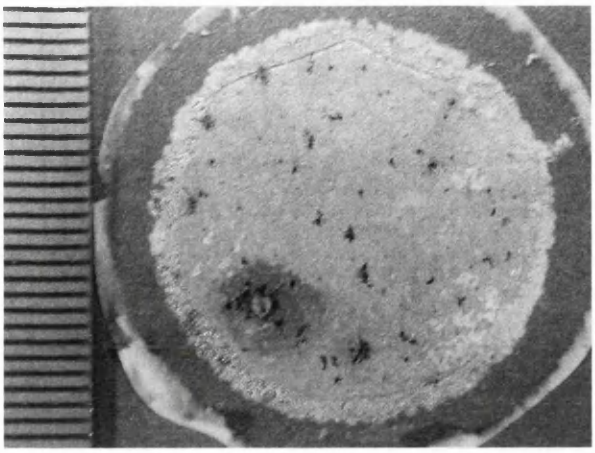

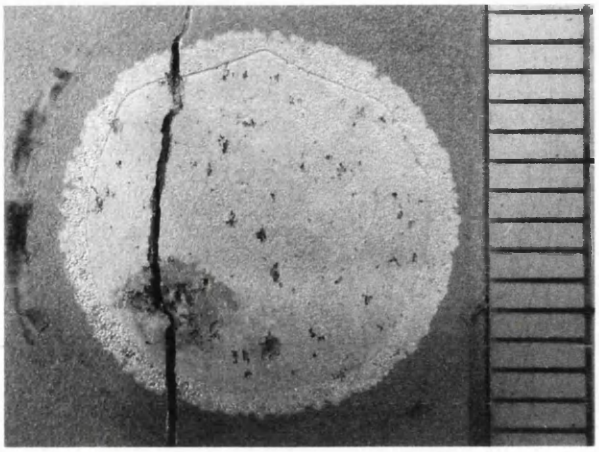

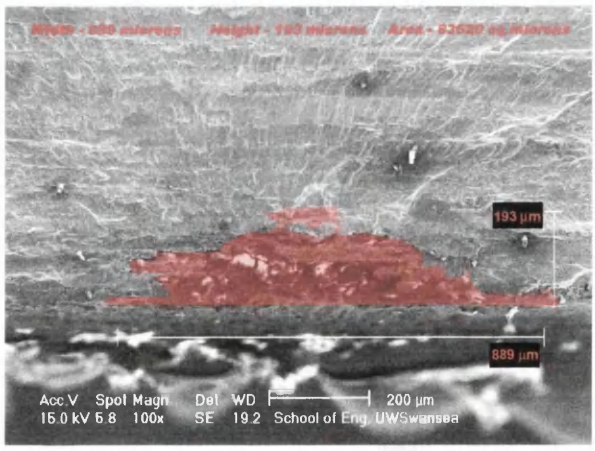
193 µm
889 µm
Acc.V Spot Magn Det WD 200 µm
15.0 kV 5.8 100x SE 19.2 School of Eng, UWSwansea

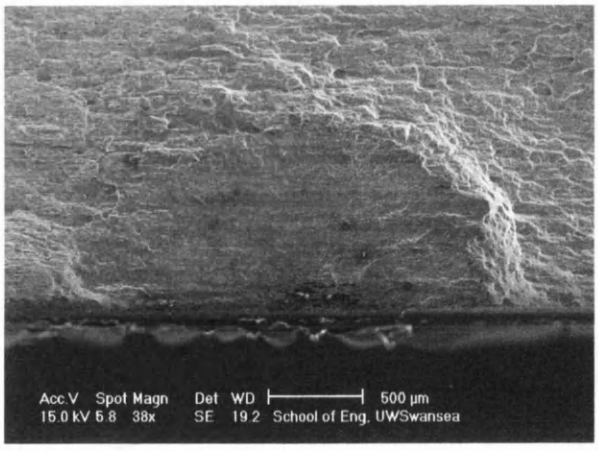
Acc.V Spot Magn Det WD 500 µm
15.0 kV 5.8 38x SE 19.2 School of Eng, UWSwansea

PC-2

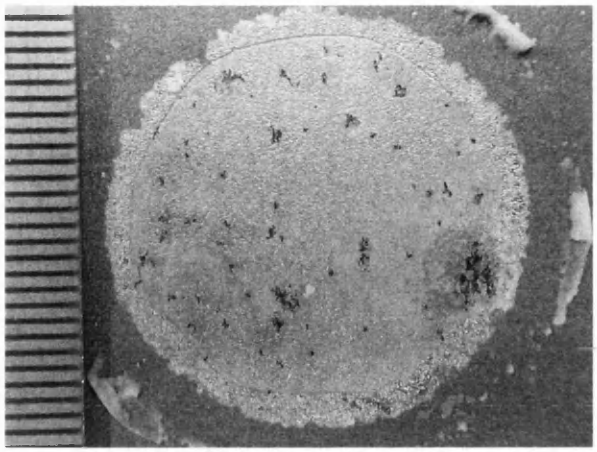

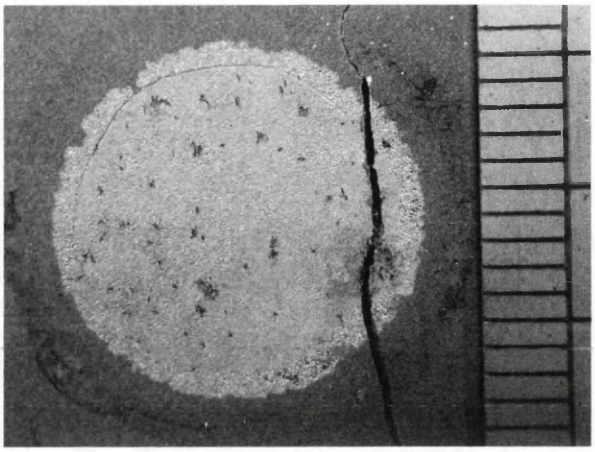

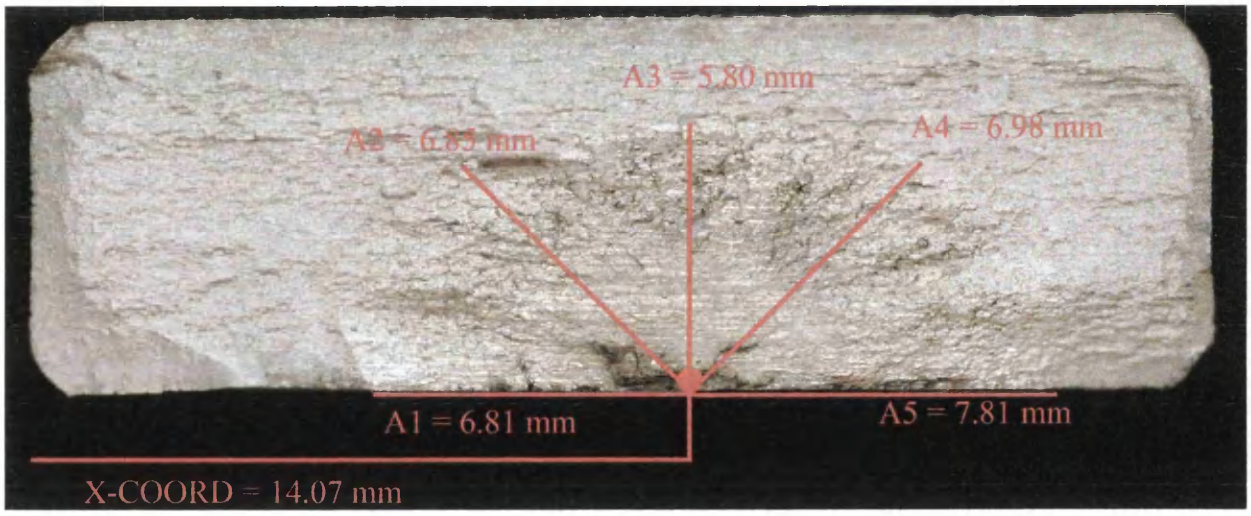
A3 = 5.80 mm
A4 = 6.98 mm
A1 = 6.81 mm
A5 = 7.81 mm
X-COORD = 14.07 mm

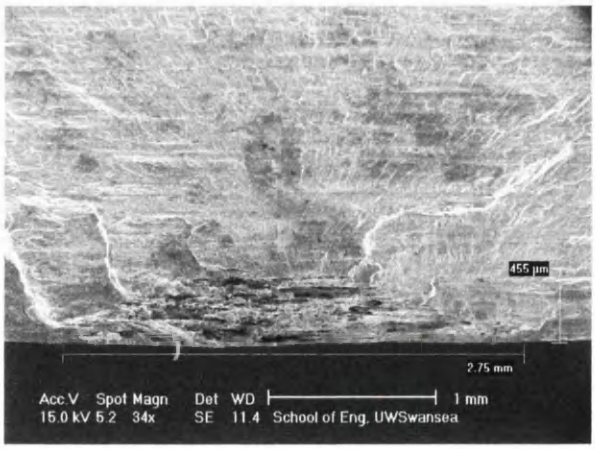
455 µm
2.75 mm
Acc.V Spot Magn Det WD 1 mm
15.0 kV 5.2 34x SE 11.4 School of Eng, UWSwansea

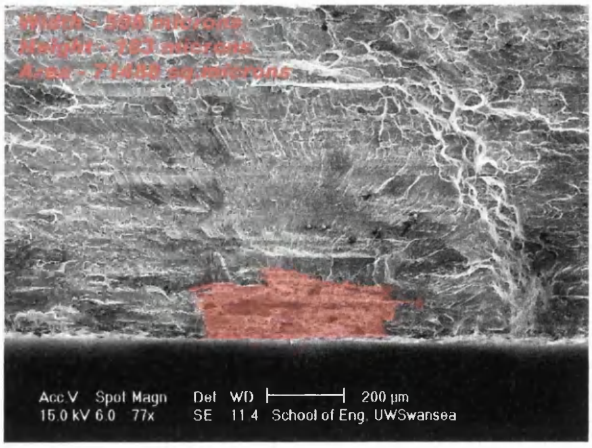
Acc.V Spot Magn Det WD 200 µm
15.0 kV 6.0 77x SE 11.4 School of Eng, UWSwansea

PC-3

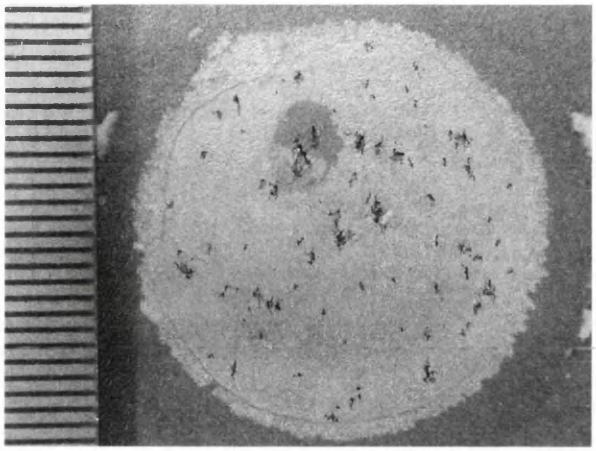

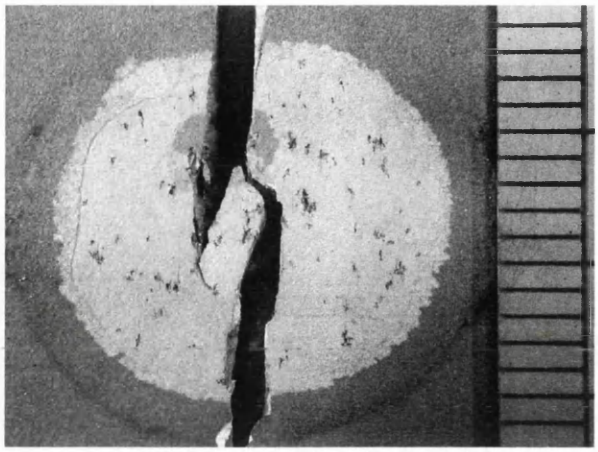

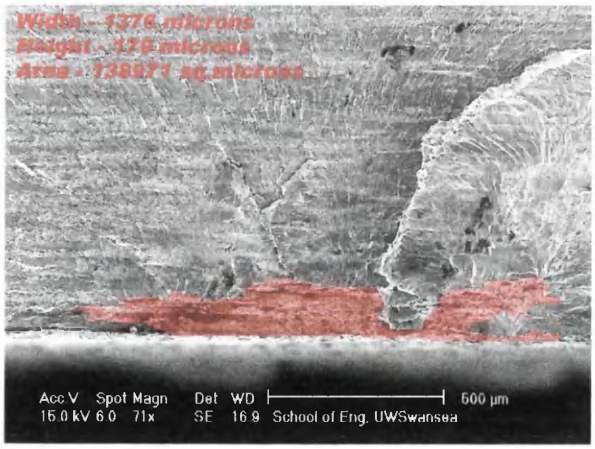
Width - 1376 microns
Height - 179 microns
Area - 139871 sq.microns
Acc.V Spot Magn Det WD 500 µm
15.0 kV 6.0 71x SE 16.9 School of Eng. UWSwansea

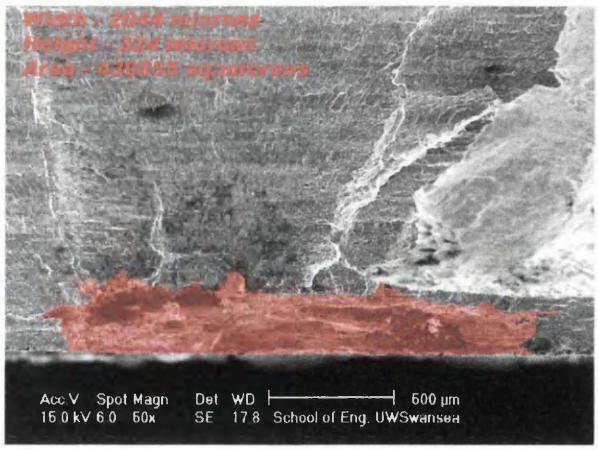
Width - 2044 microns
Height - 324 microns
Area - 439855 sq.microns
Acc.V Spot Magn Det WD 500 µm
15.0 kV 6.0 60x SE 17.8 School of Eng. UWSwansea

PC-4

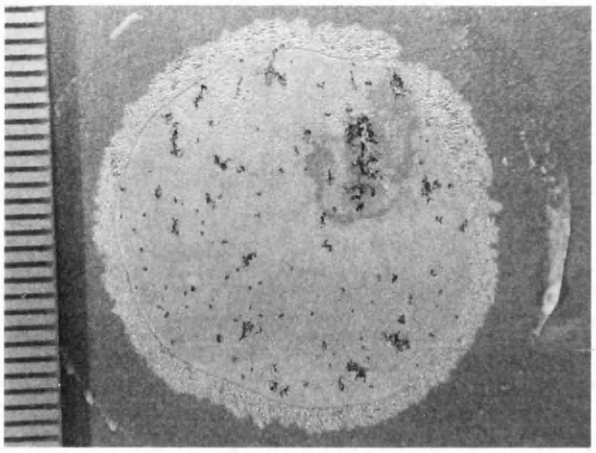

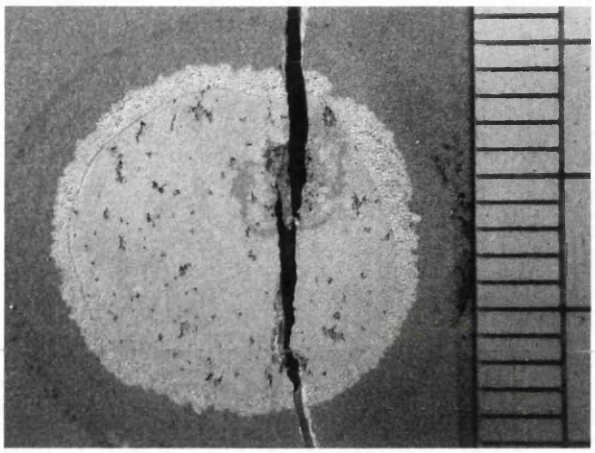

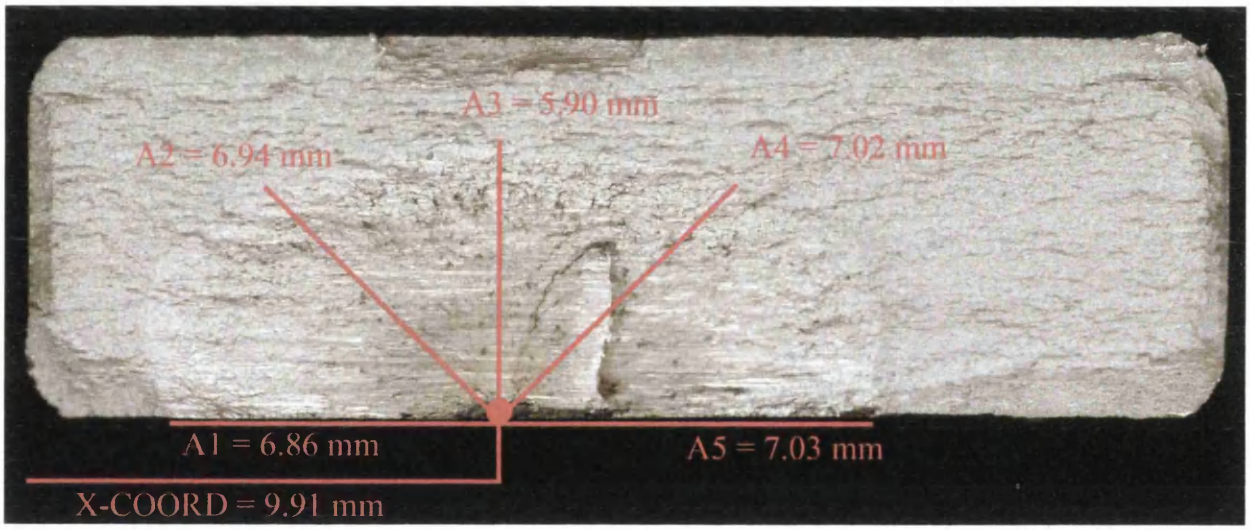
A3 = 5.90 mm
A2 = 6.94 mm
A4 = 7.02 mm
A1 = 6.86 mm
A5 = 7.03 mm
X-COORD = 9.91 mm

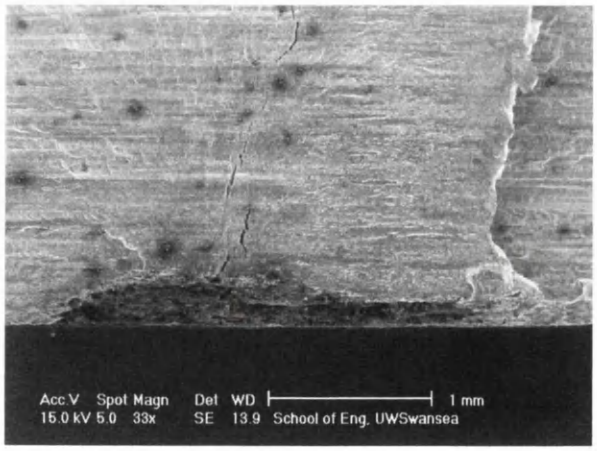
Acc.V Spot Magn Det WD 1 mm
15.0 kV 5.0 33x SE 13.9 School of Eng, UWSwansea

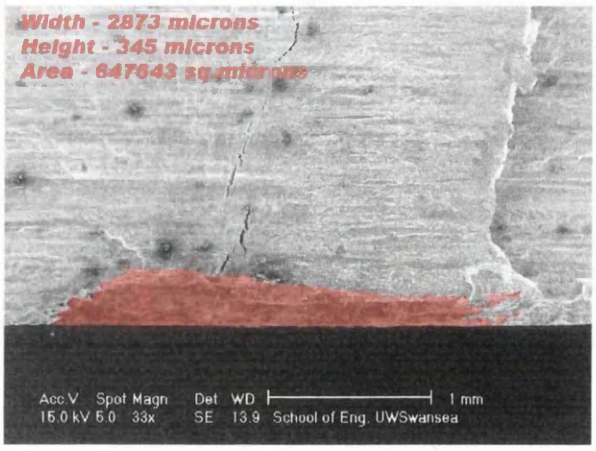
Width - 2873 microns
Height - 345 microns
Area - 647643 sq.microns
Acc.V Spot Magn Det WD 1 mm
15.0 kV 5.0 33x SE 13.9 School of Eng, UWSwansea

PC-5

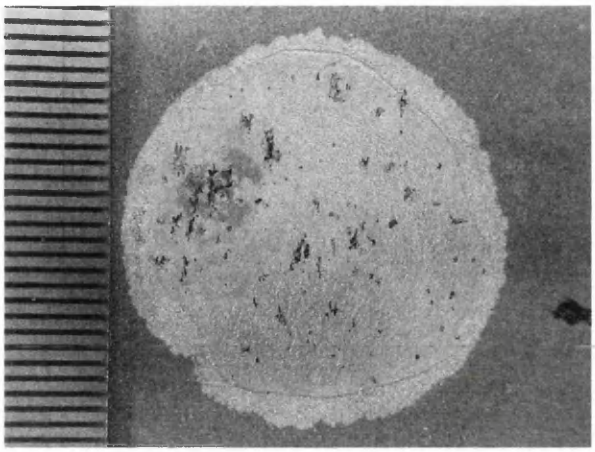

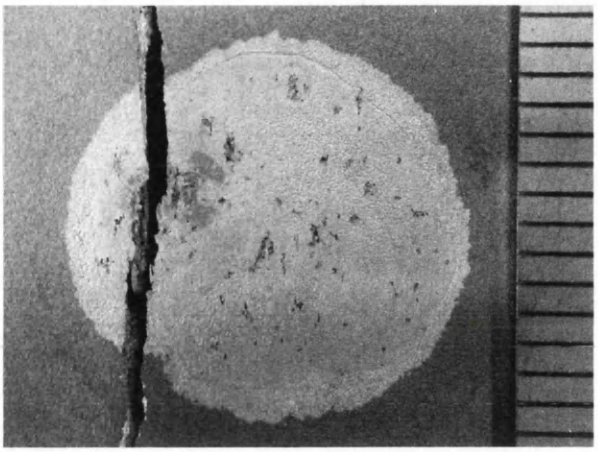

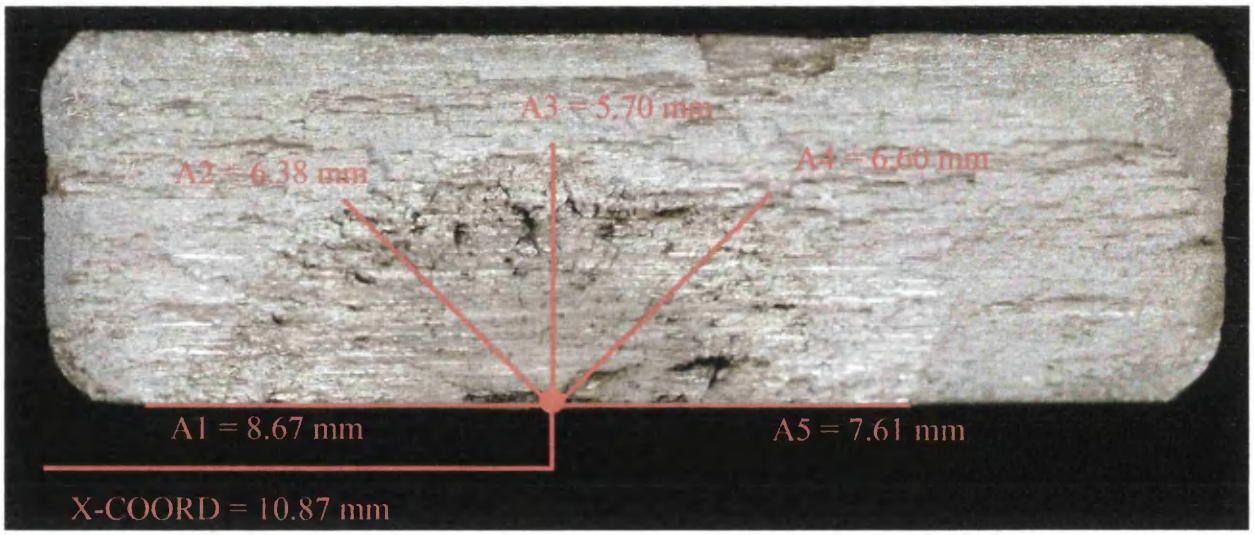
A3 = 5.70 mm
A2 = 6.38 mm
A4 = 6.60 mm
A1 = 8.67 mm
A5 = 7.61 mm
X-COORD = 10.87 mm

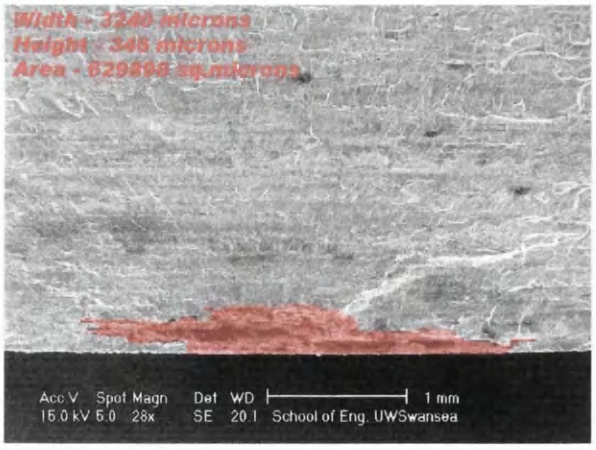
Width = 3240 microns
Height = 348 microns
Area = 629896 sq.microns
Acc.V Spot Magn Det WD 1 mm
15.0 kV 5.0 28x SE 20.1 School of Eng. UWSwansea

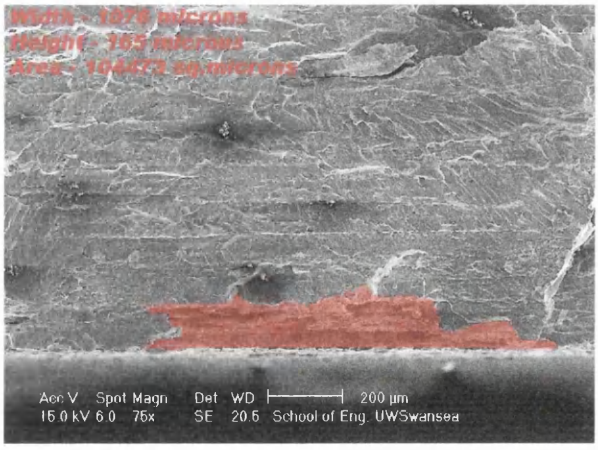
Width = 1278 microns
Height = 165 microns
Area = 104472 sq.microns
Acc.V Spot Magn Det WD 200 µm
15.0 kV 6.0 75x SE 20.6 School of Eng. UWSwansea

PC-6

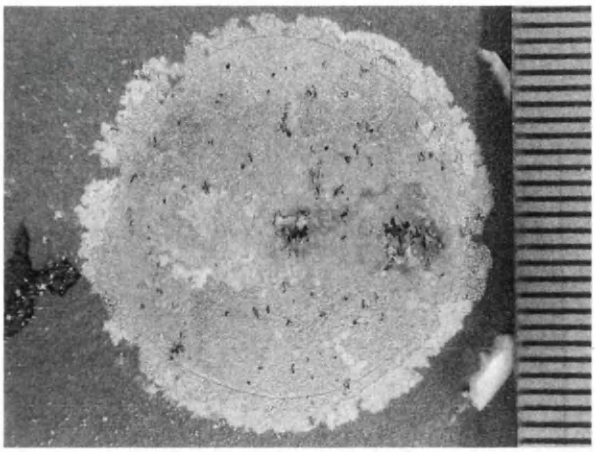

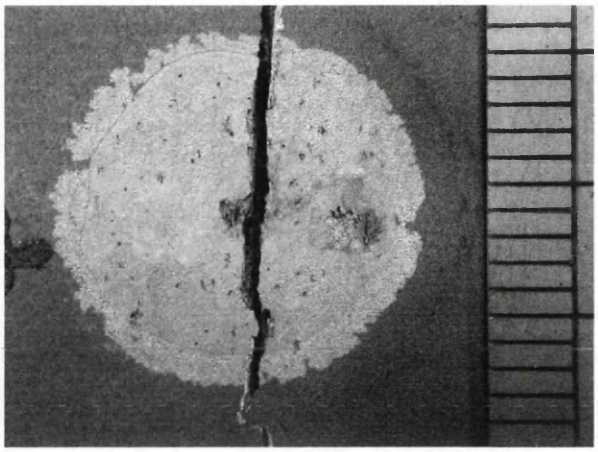

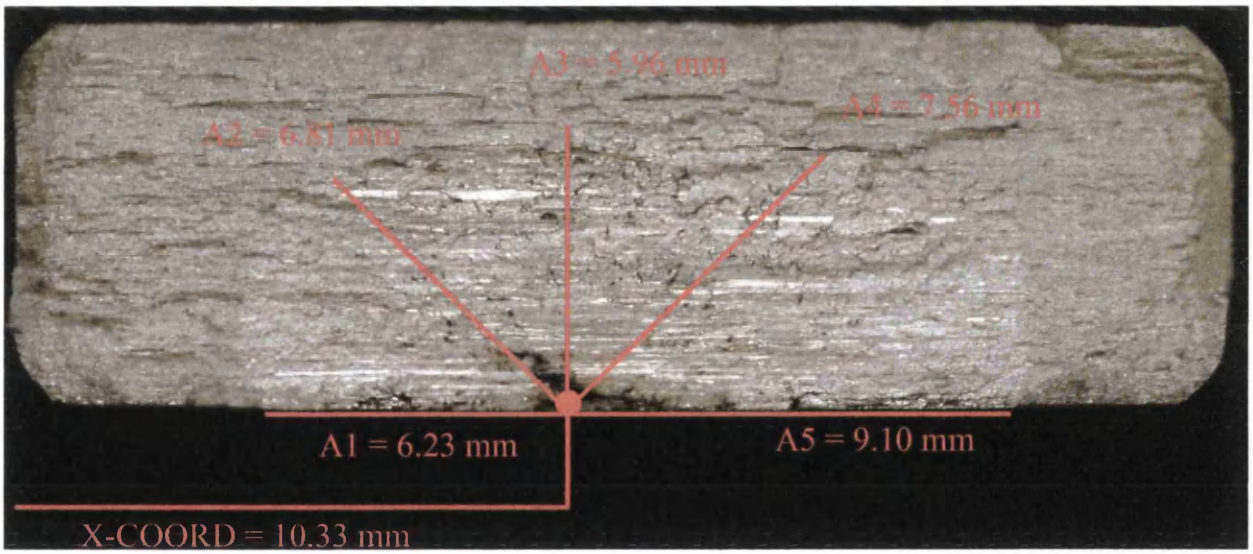
A3 = 5.96 mm
A4 = 7.56 mm
A2 = 6.81 mm
A1 = 6.23 mm
A5 = 9.10 mm
X-COORD = 10.33 mm

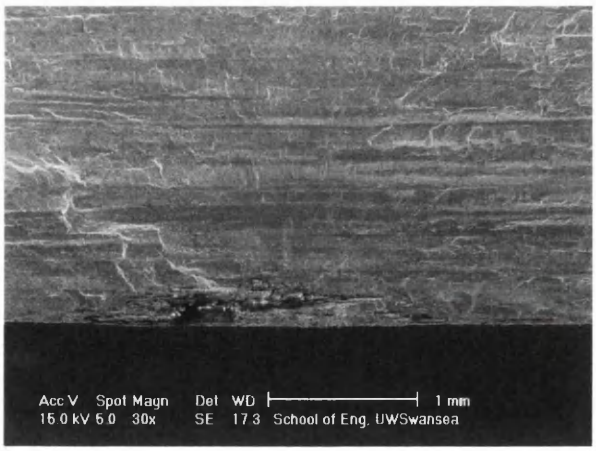
Acc.V Spot Magn Det WD 1 mm
15.0 kV 6.0 30x SE 17.3 School of Eng, UWSwansea

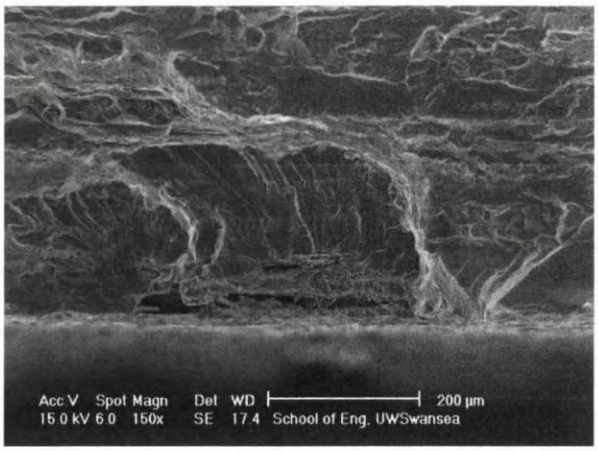
Acc.V Spot Magn Det WD 200 µm
15.0 kV 6.0 150x SE 17.4 School of Eng, UWSwansea

PC-7

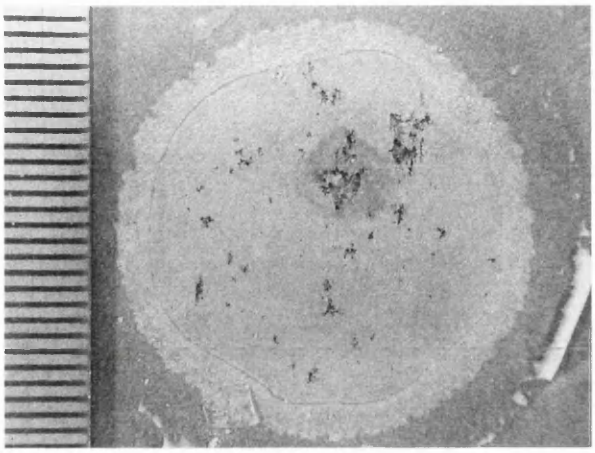

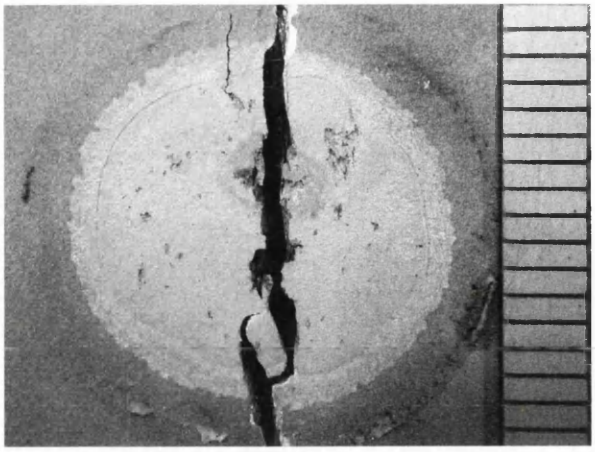

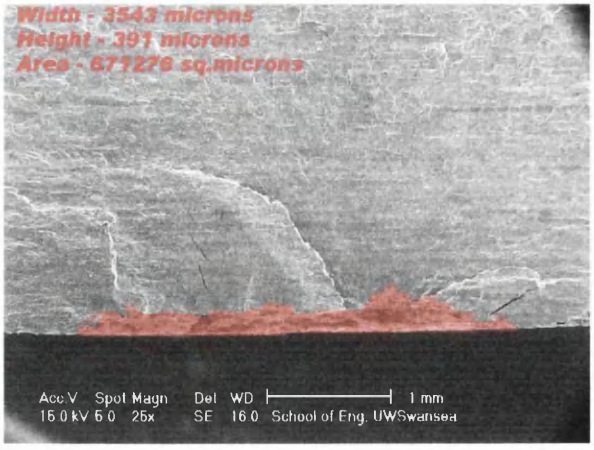
Width - 3543 microns
Height - 391 microns
Area - 671276 sq.microns
Acc.V Spot Magn Det WD 1 mm
15.0 kV 6.0 26x SE 16.0 School of Eng. UWSwansea

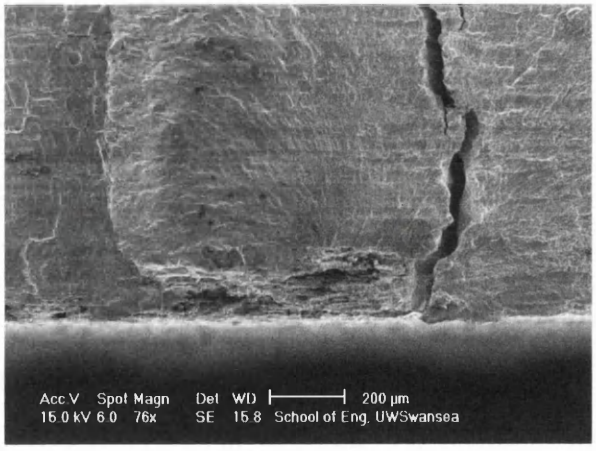
Acc.V Spot Magn Det WD 200 µm
15.0 kV 6.0 76x SE 15.8 School of Eng. UWSwansea

PC-8

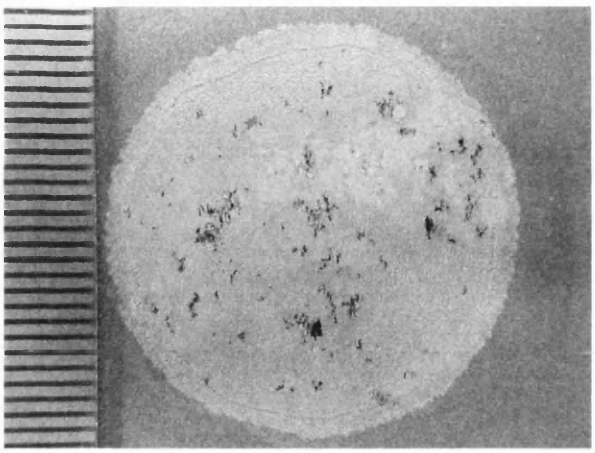

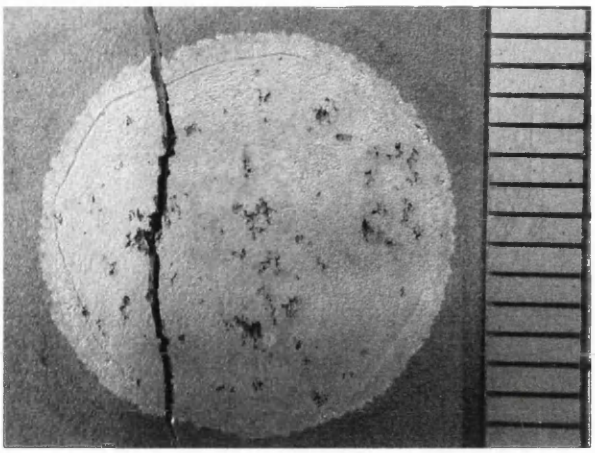

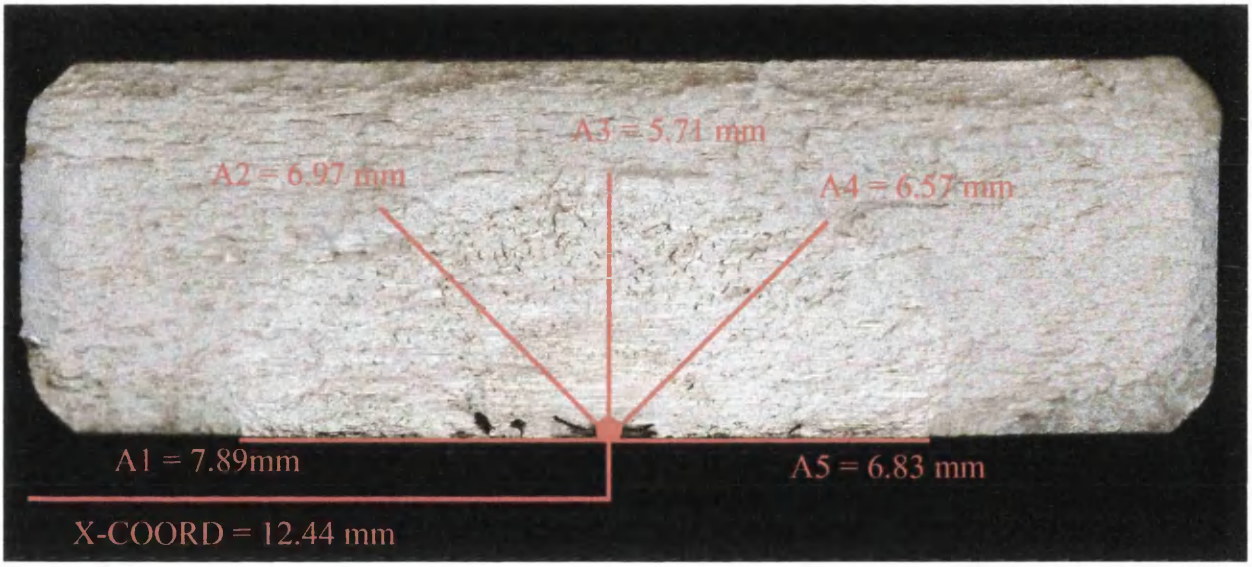
A3 = 5.71 mm
A2 = 6.97 mm
A4 = 6.57 mm
A1 = 7.89mm
A5 = 6.83 mm
X-COORD = 12.44 mm

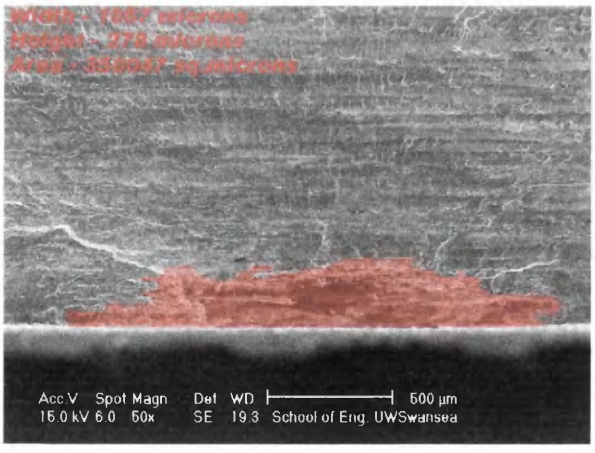
Acc.V Spot Magn Det WD 500 µm
15.0 kV 6.0 50x SE 19.3 School of Eng. UWSwansea

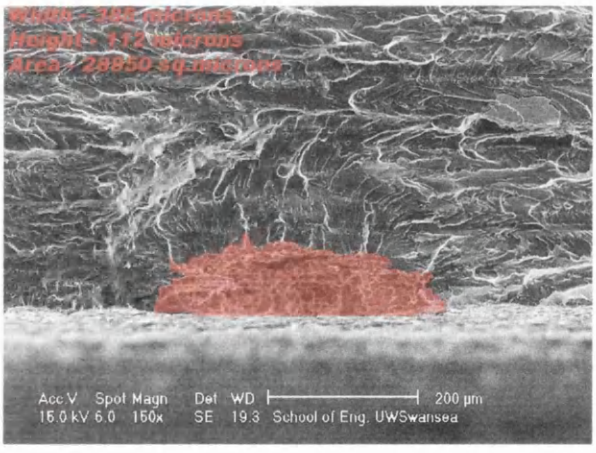
Acc.V Spot Magn Det WD 200 µm
15.0 kV 6.0 150x SE 19.3 School of Eng. UWSwansea

PC-9

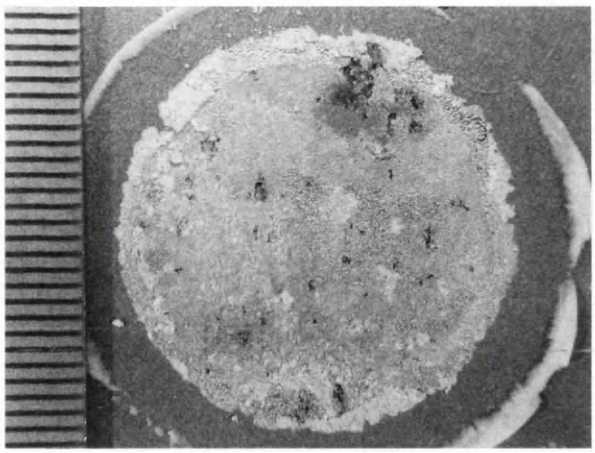

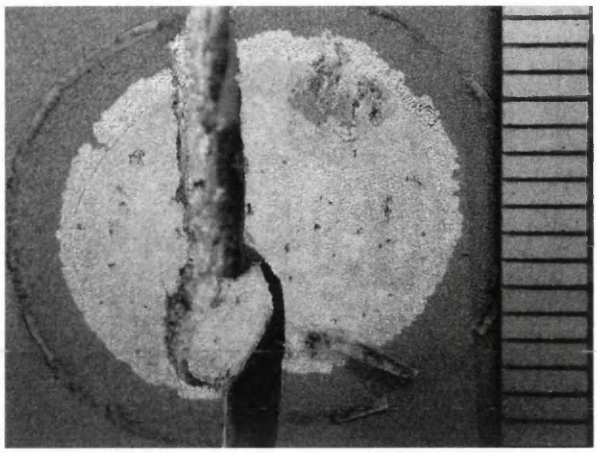

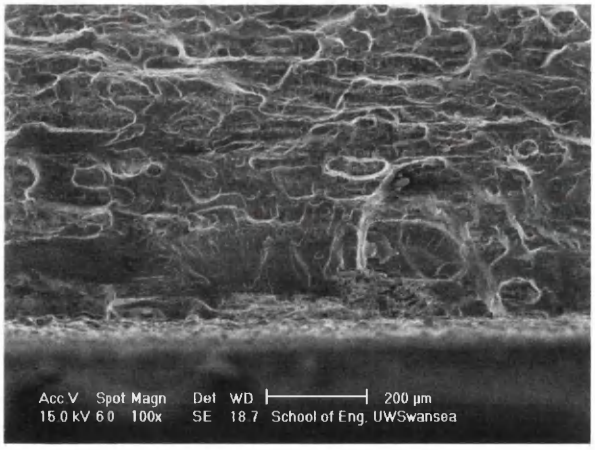
Acc.V Spot Magn Det WD 200 µm
15.0 kV 6.0 100x SE 18.7 School of Eng. UWSwansea

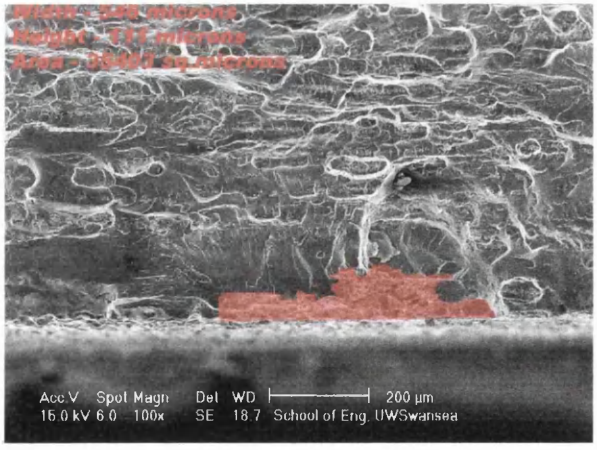
Acc.V Spot Magn Det WD 200 µm
15.0 kV 6.0 100x SE 18.7 School of Eng. UWSwansea

PC-10

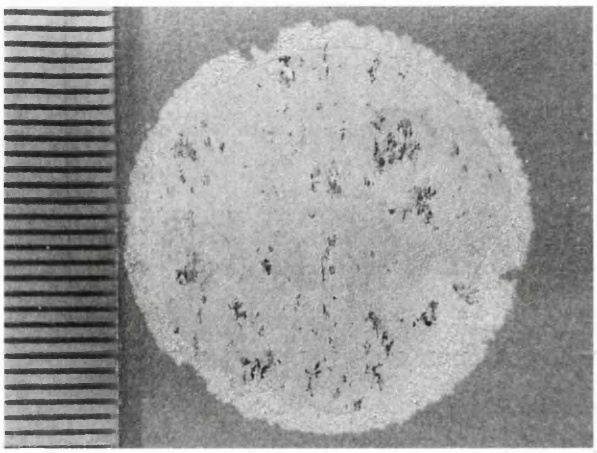

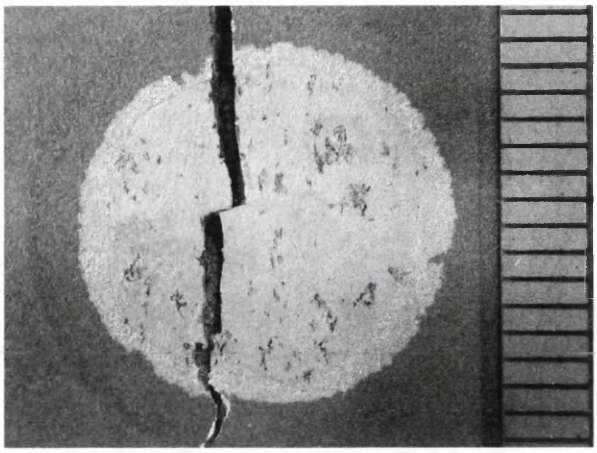

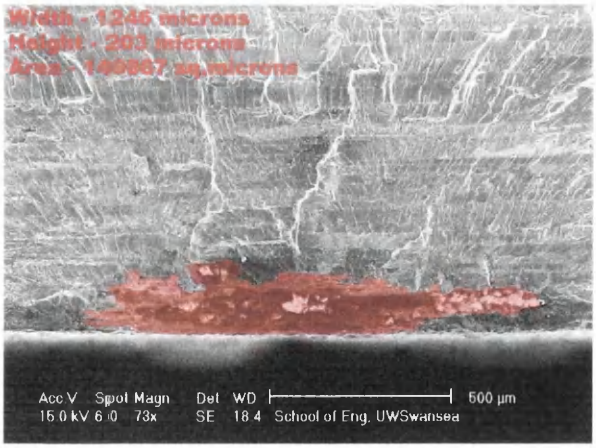
Width - 1246 microns
Height - 203 microns
Area - 140867 sq.microns
Acc.V Spot Magn Det WD 500 µm
15.0 kV 6.0 73x SE 18.4 School of Eng, UWSwansea

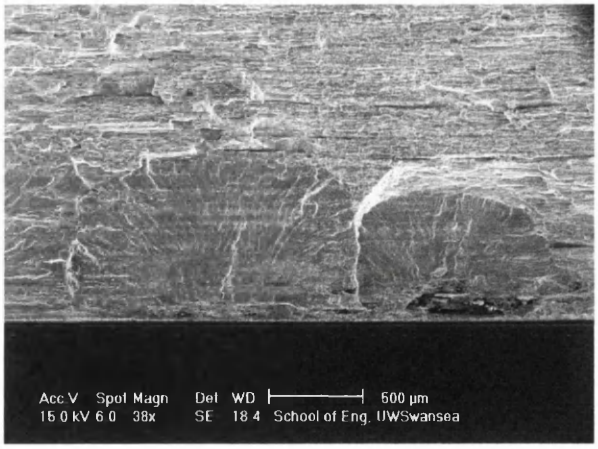
Acc.V Spot Magn Det WD 500 µm
15.0 kV 6.0 38x SE 18.4 School of Eng, UWSwansea

PC-11

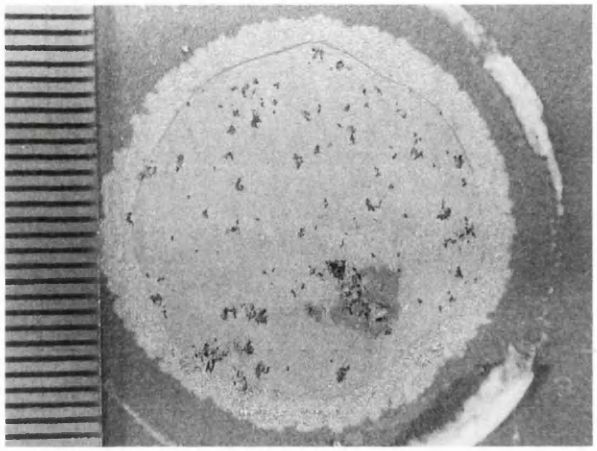

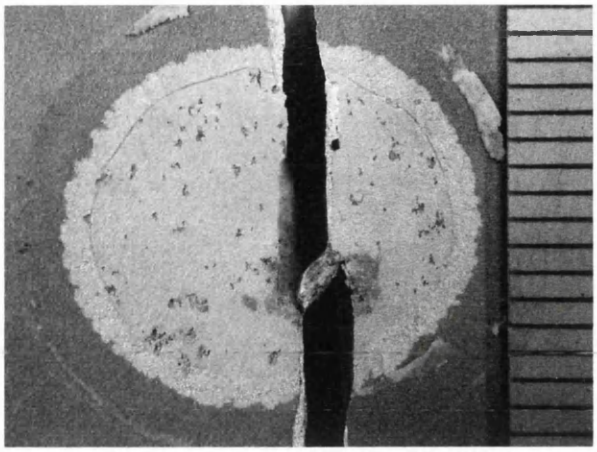

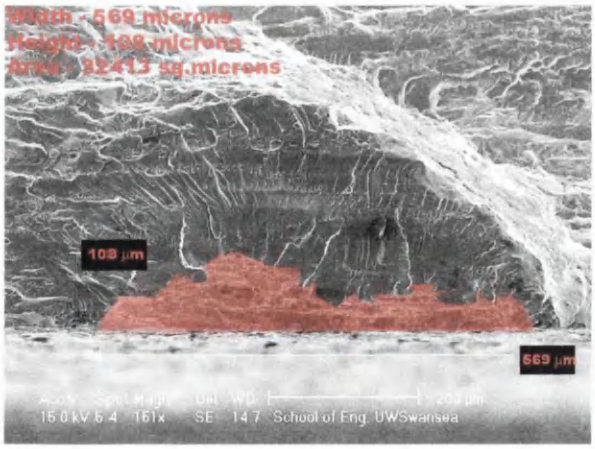
Width - 569 microns
Height - 108 microns
Area - 22413 sq.microns
108 µm
569 µm
15.0 kV 6.4 161x SE 14.7 School of Eng. UWSwansea

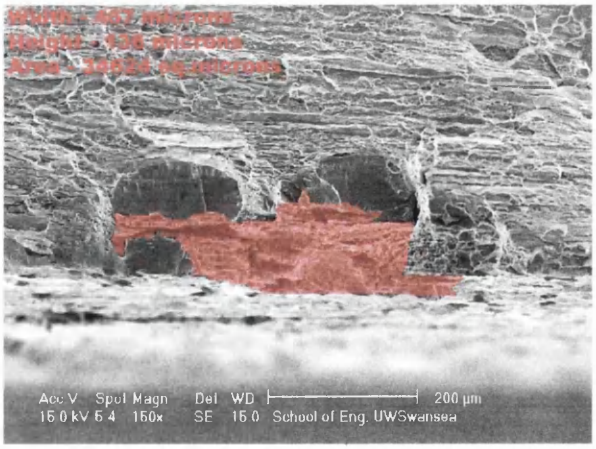
Width - 487 microns
Height - 136 microns
Area - 34824 sq.microns
Acc.V Spot Magn Det WD 200 µm
15.0 kV 6.4 160x SE 15.0 School of Eng. UWSwansea

PC-12

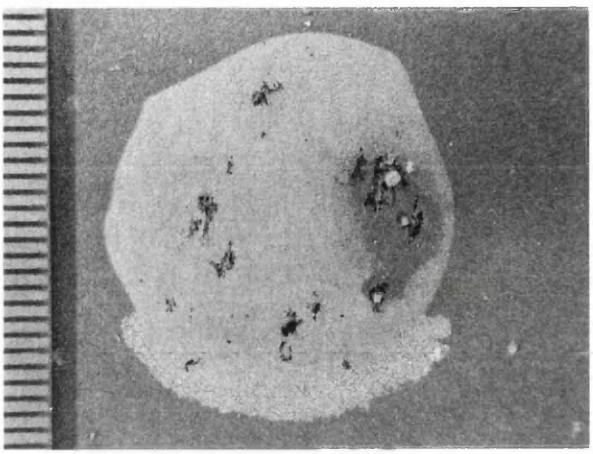

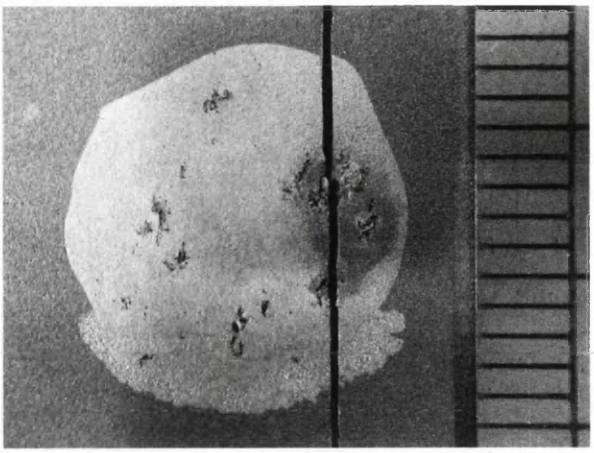

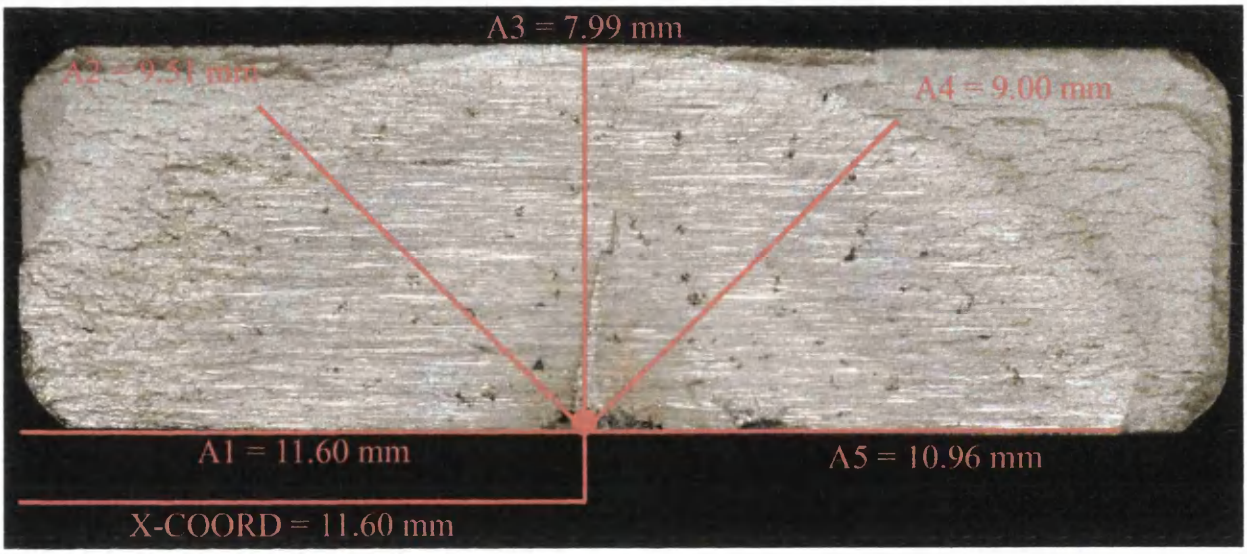
A3 = 7.99 mm
A2 = 9.51 mm
A4 = 9.00 mm
A1 = 11.60 mm
A5 = 10.96 mm
X-COORD = 11.60 mm

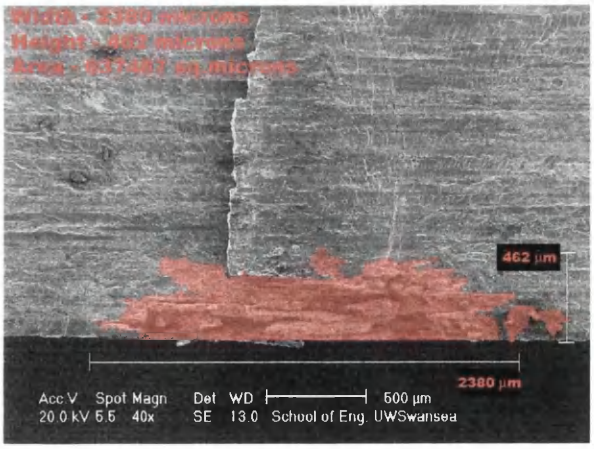
462 µm
2380 µm
Acc.V Spot Magn Det WD 500 µm
20.0 kV 5.5 40x SE 13.0 School of Eng. UWSwansea

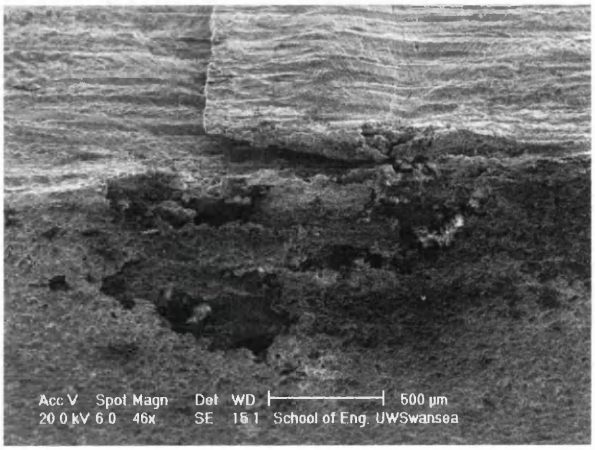
Acc.V Spot Magn Det WD 500 µm
20.0 kV 6.0 46x SE 15.1 School of Eng. UWSwansea

PC-13

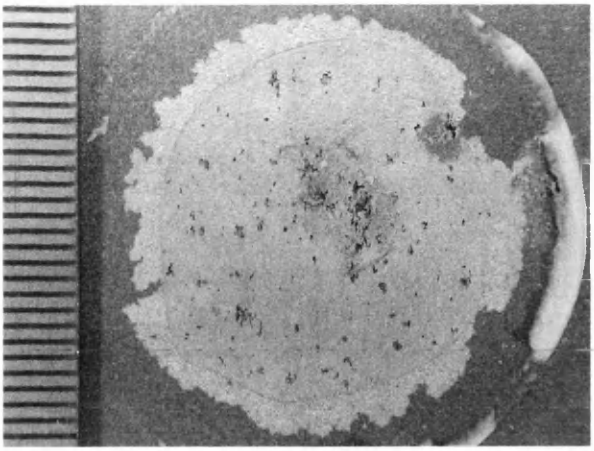

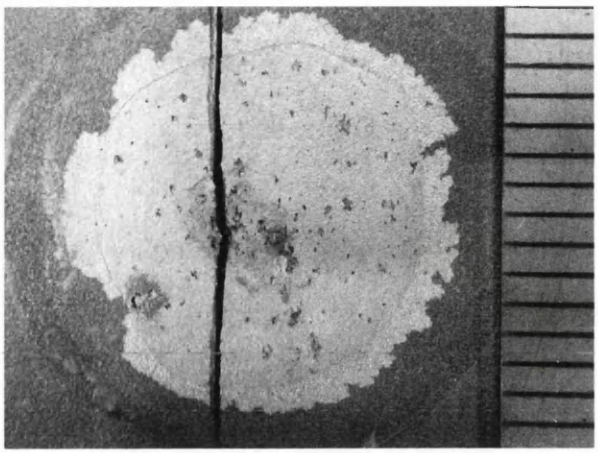

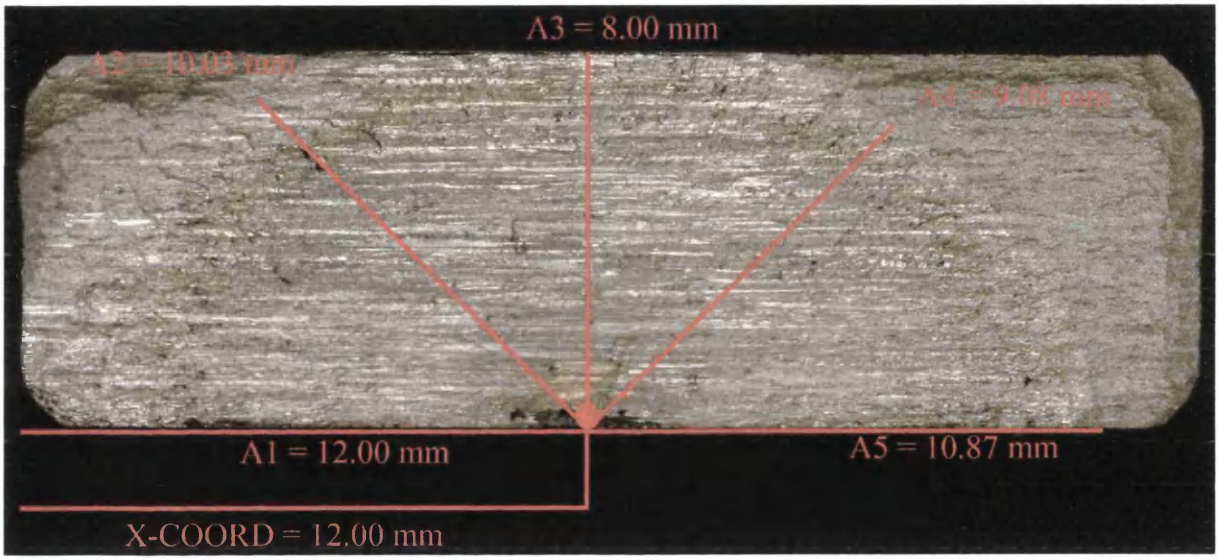
A3 = 8.00 mm
A2 = 10.03 mm
A4 = 9.08 mm
A1 = 12.00 mm
A5 = 10.87 mm
X-COORD = 12.00 mm

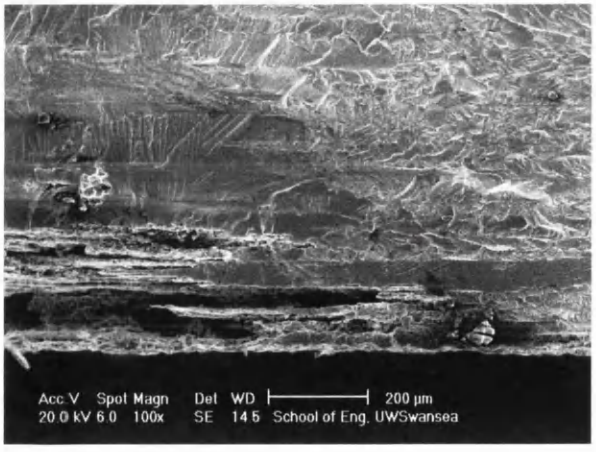
Acc.V Spot Magn Det WD 200 µm
20.0 kV 6.0 100x SE 14.5 School of Eng. UWSwansea

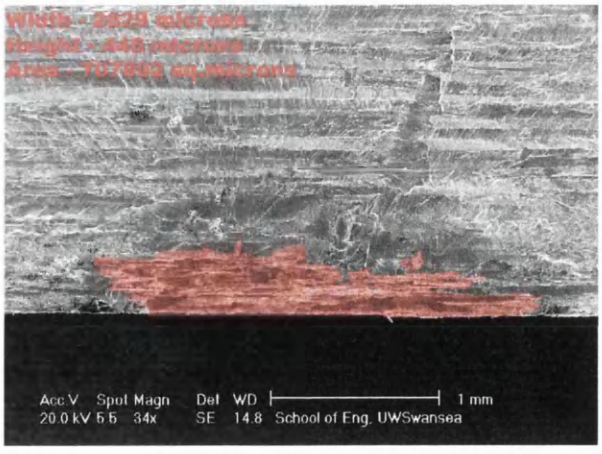
Width = 2829 microns
Height = 445 microns
Area = 707602 sq.microns
Acc.V Spot Magn Det WD 1 mm
20.0 kV 5.5 34x SE 14.8 School of Eng. UWSwansea

PC-14

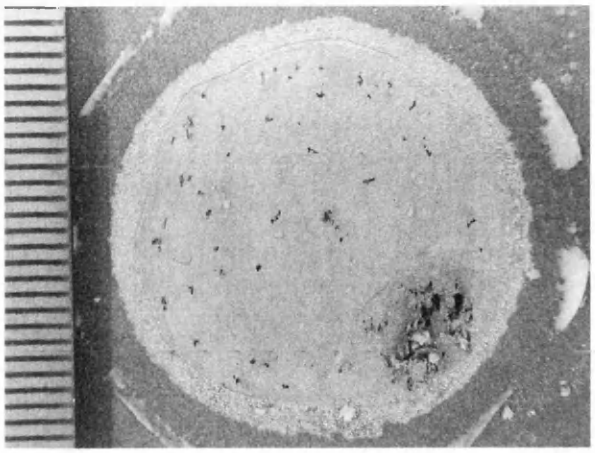

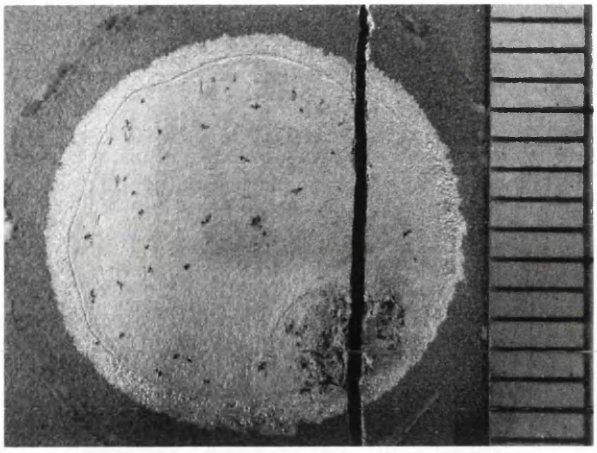

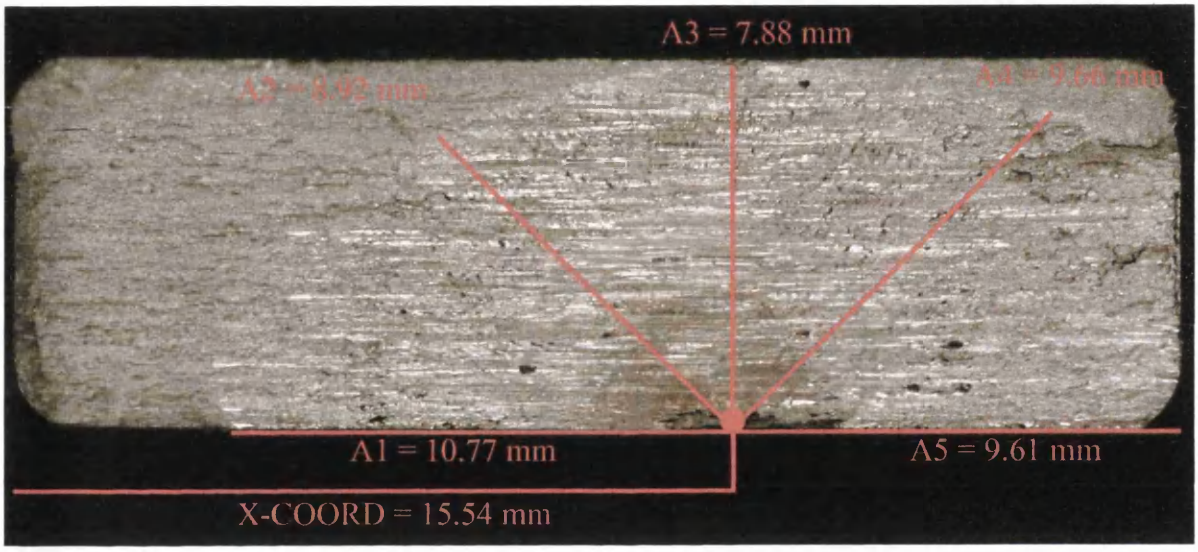
A3 = 7.88 mm
A2 = 8.92 mm
A4 = 9.66 mm
A1 = 10.77 mm
A5 = 9.61 mm
X-COORD = 15.54 mm

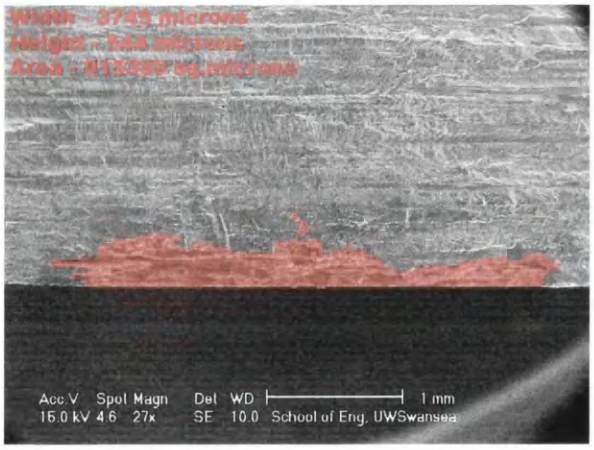
Width = 3745 microns
Height = 845 microns
Area = 813289 sq.microns
Acc.V Spot Magn Det WD 1 mm
15.0 kV 4.6 27x SE 10.0 School of Eng. UWSwansea

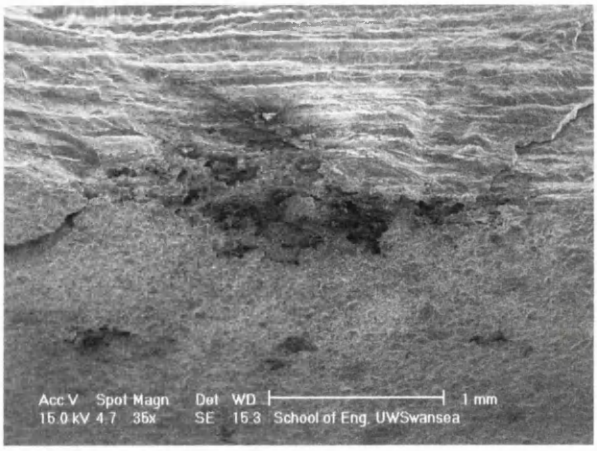
Acc.V Spot Magn Det WD 1 mm
15.0 kV 4.7 35x SE 15.3 School of Eng. UWSwansea

PC-15

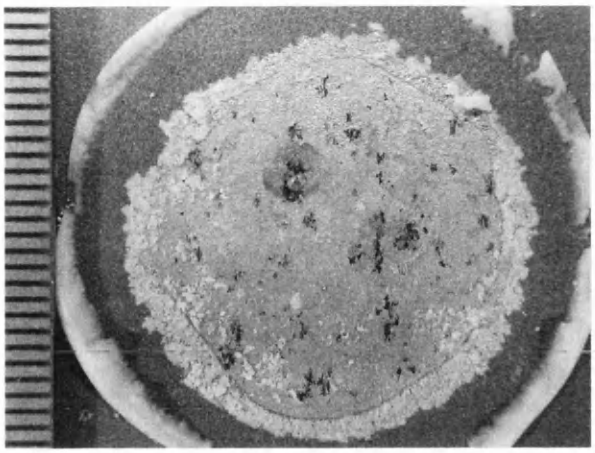

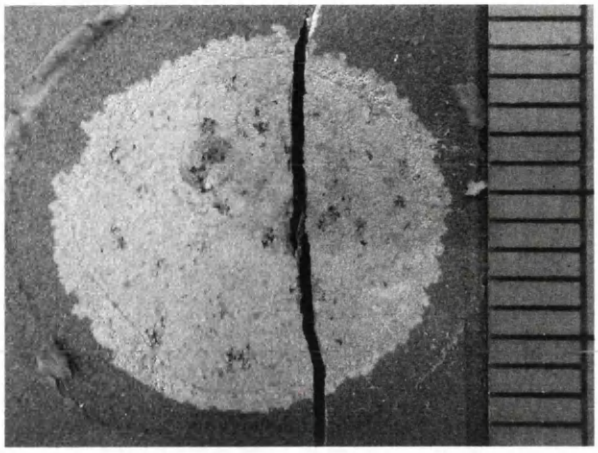

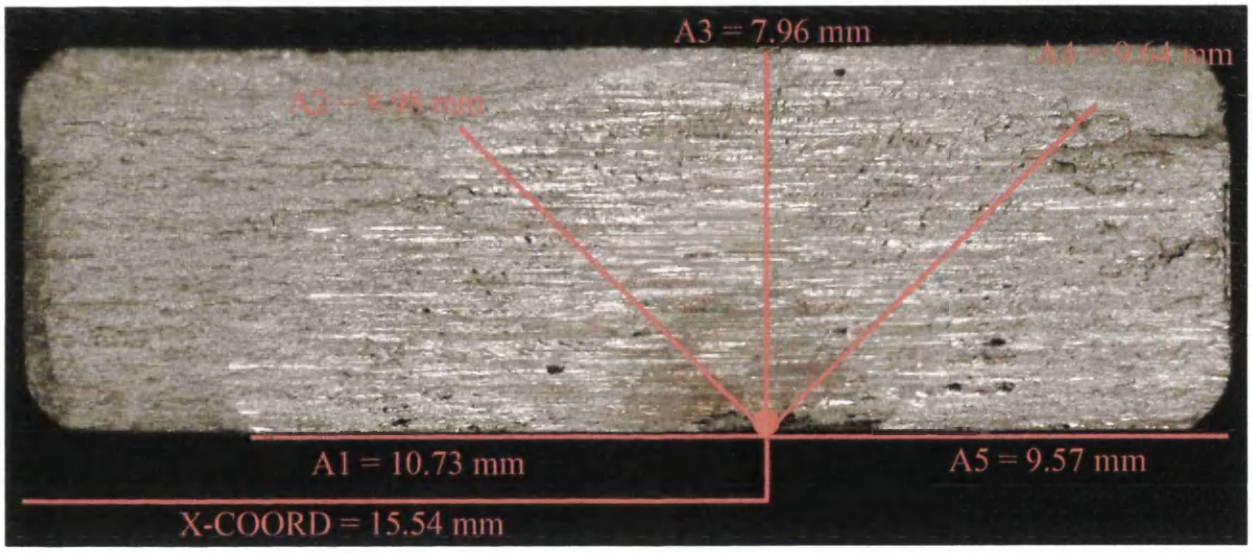
A3 = 7.96 mm
A4 = 9.64 mm
A2 = 8.98 mm
A1 = 10.73 mm
A5 = 9.57 mm
X-COORD = 15.54 mm

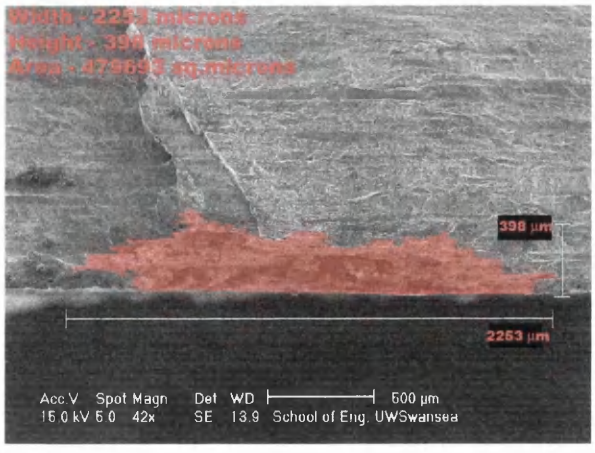
Width - 2253 microns
Height - 398 microns
Area - 479693 sq.microns
398 µm
2253 µm
Acc.V Spot Magn Det WD 500 µm
15.0 kV 5.0 42x SE 13.9 School of Eng, UWSwansea

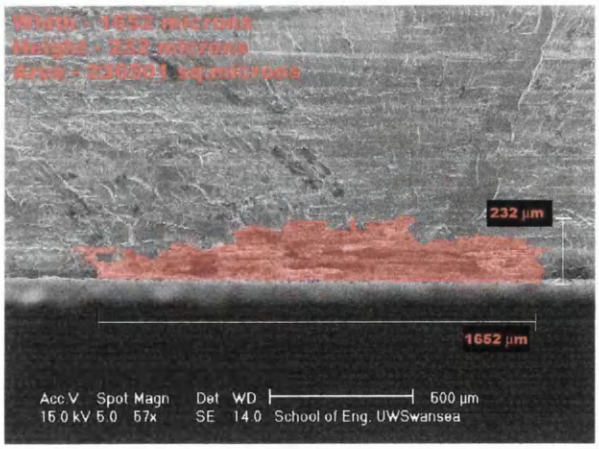
Width - 1652 microns
Height - 232 microns
Area - 236503 sq.microns
232 µm
1652 µm
Acc.V Spot Magn Det WD 500 µm
15.0 kV 5.0 57x SE 14.0 School of Eng, UWSwansea

PC-16

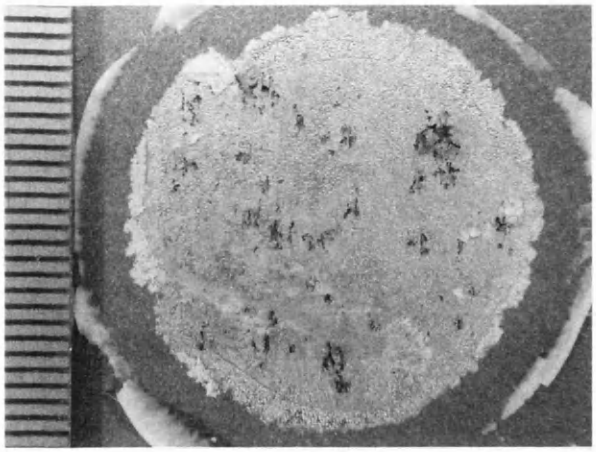

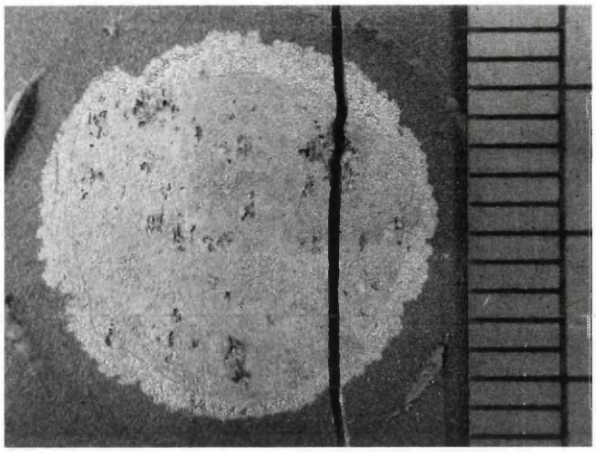

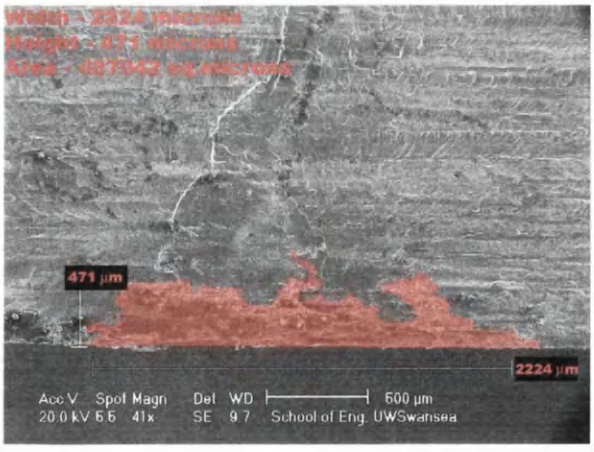
Width - 2224 microns
Height - 471 microns
Area - 407042 sq.microns
471 µm
2224 µm
Acc.V Spot Magn Det WD 500 µm
20.0 kV 5.5 41x SE 9.7 School of Eng. UWSwansea

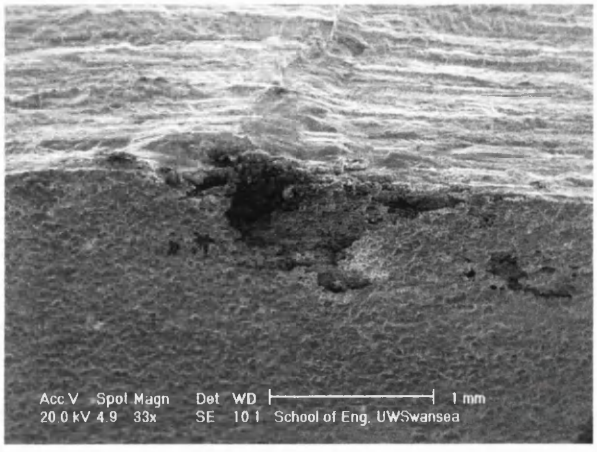
Acc.V Spot Magn Det WD 1 mm
20.0 kV 4.9 33x SE 10.1 School of Eng. UWSwansea

PC-17

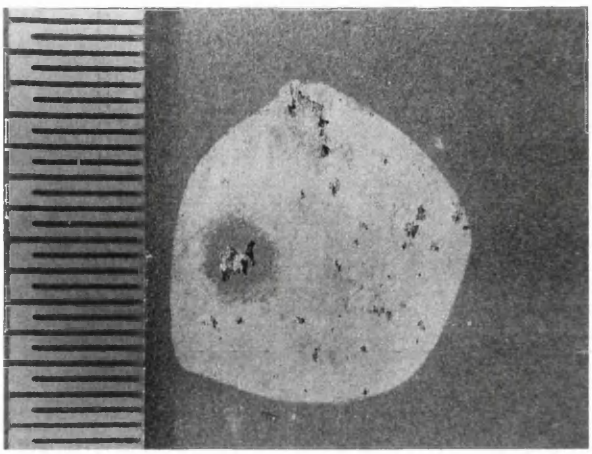

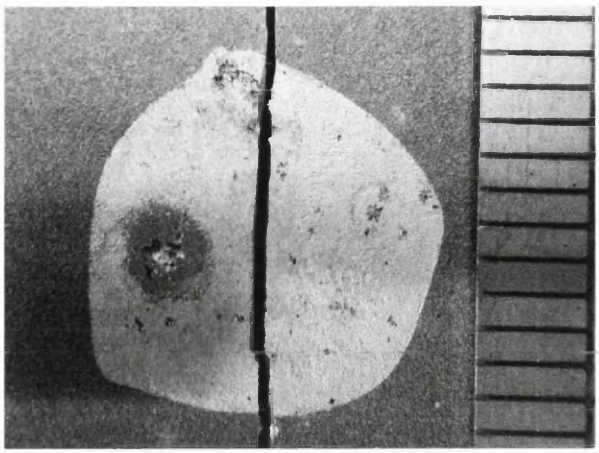

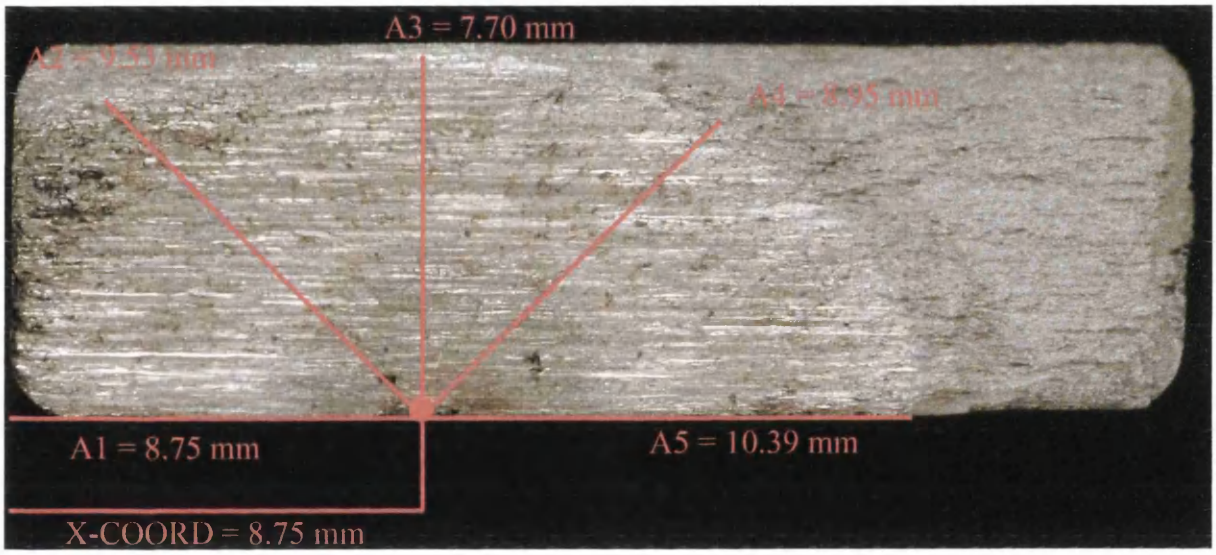
A3 = 7.70 mm
A4 = 8.95 mm
A1 = 8.75 mm
A5 = 10.39 mm
X-COORD = 8.75 mm

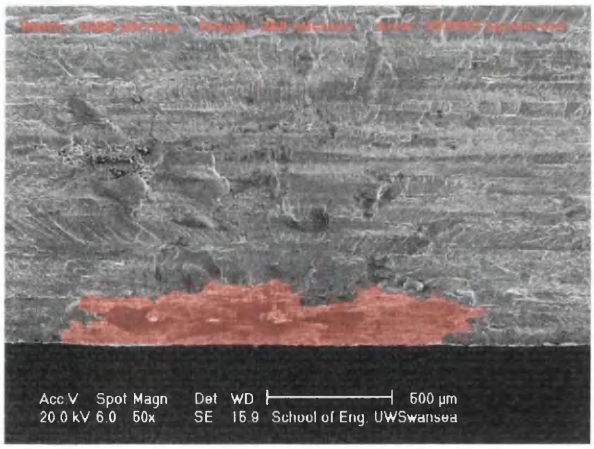
Acc.V Spot Magn Det WD 500 µm
20.0 kV 6.0 50x SE 15.9 School of Eng. UWSwansea

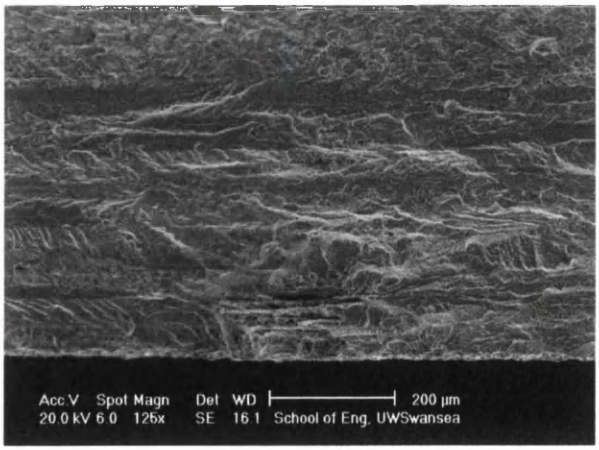
Acc.V Spot Magn Det WD 200 µm
20.0 kV 6.0 125x SE 16.1 School of Eng. UWSwansea

PC-18

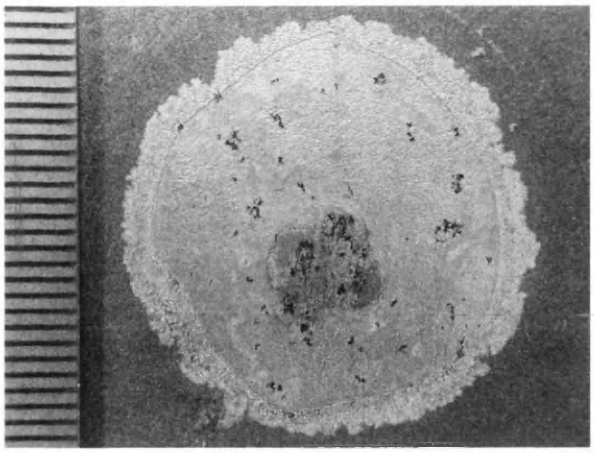

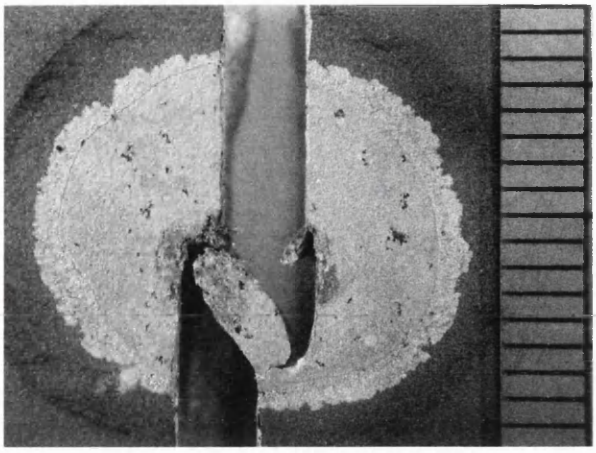

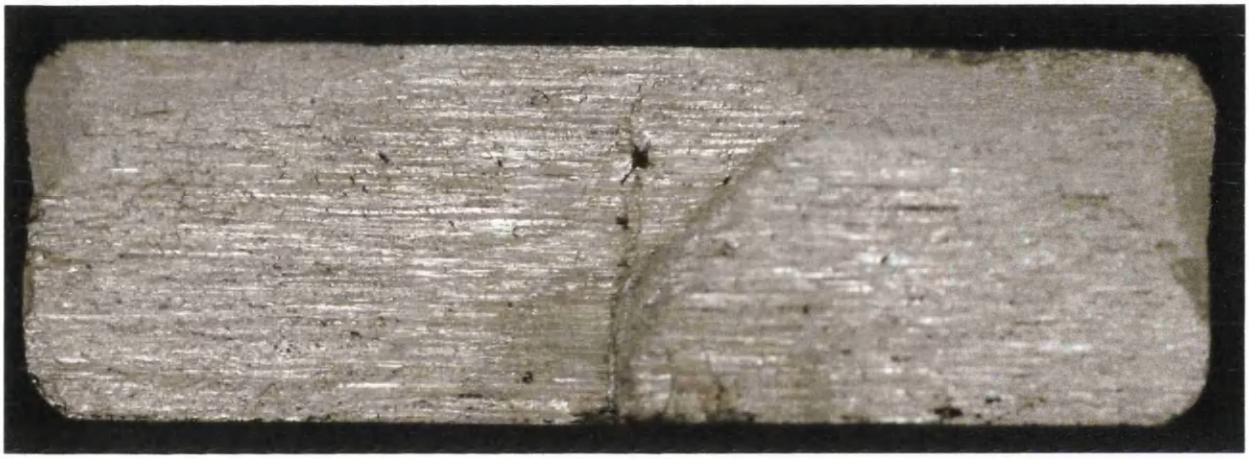

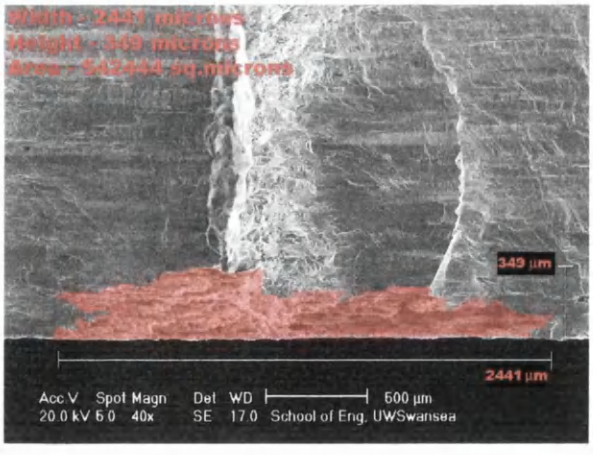
Width = 2441 microns
Height = 349 microns
Area = 542444 sq.microns
349 µm
2441 µm
Acc.V Spot Magn Det WD 500 µm
20.0 kV 6.0 40x SE 17.0 School of Eng. UWSwansea

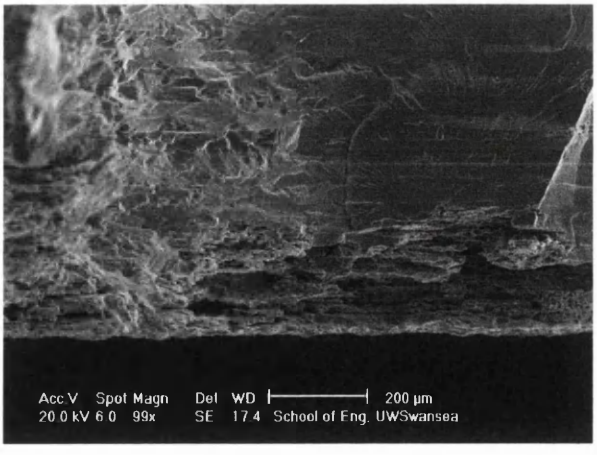
Acc.V Spot Magn Det WD 200 µm
20.0 kV 6.0 99x SE 17.4 School of Eng. UWSwansea

PC-19

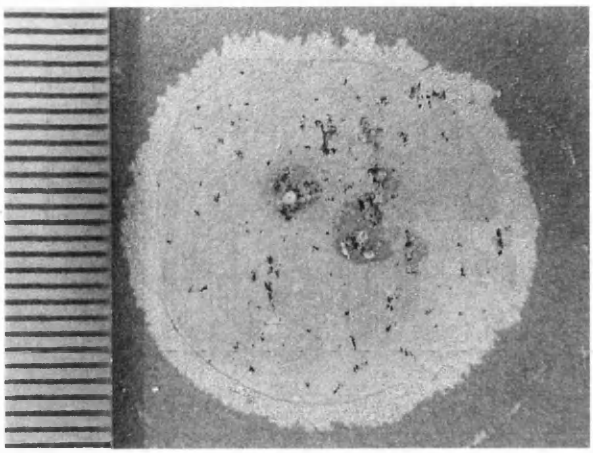

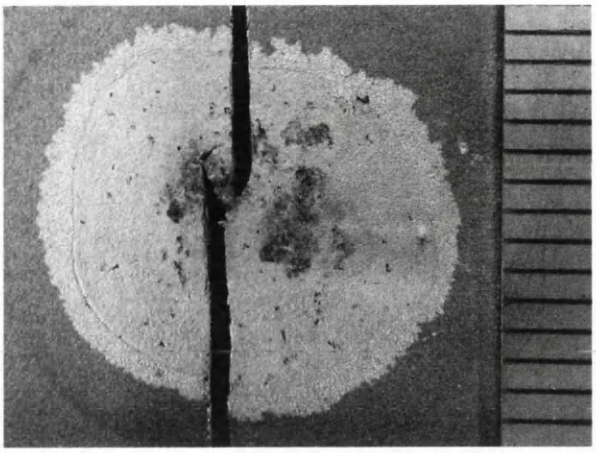

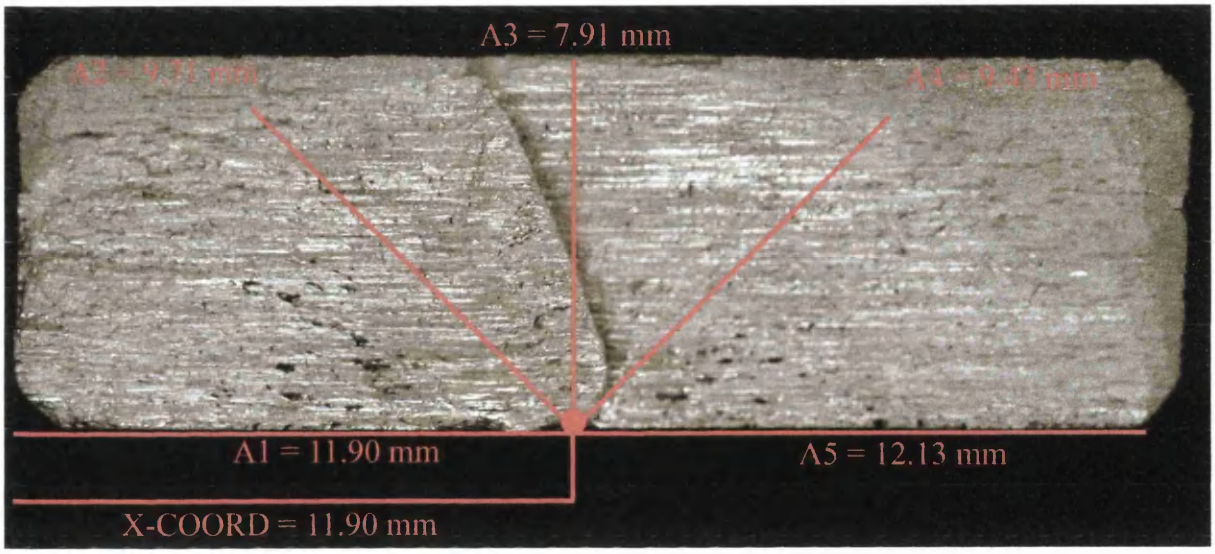
A3 = 7.91 mm
A2 = 9.31 mm
A4 = 9.43 mm
A1 = 11.90 mm
A5 = 12.13 mm
X-COORD = 11.90 mm

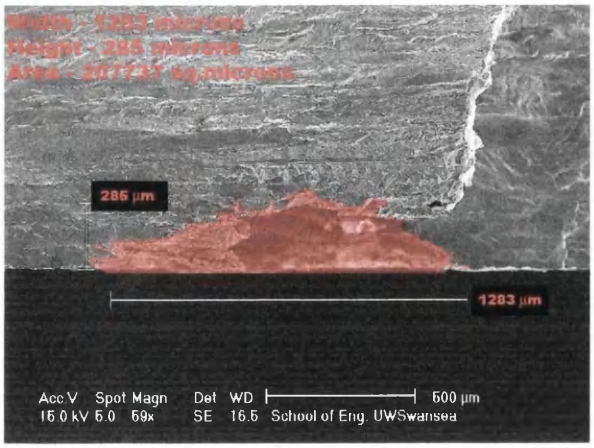
Width = 1283 microns
Height = 285 microns
Area = 207737 sq.microns
286 µm
1283 µm
Acc.V Spot Magn Det WD 500 µm
15.0 kV 5.0 69x SE 16.5 School of Eng. UWSwansea

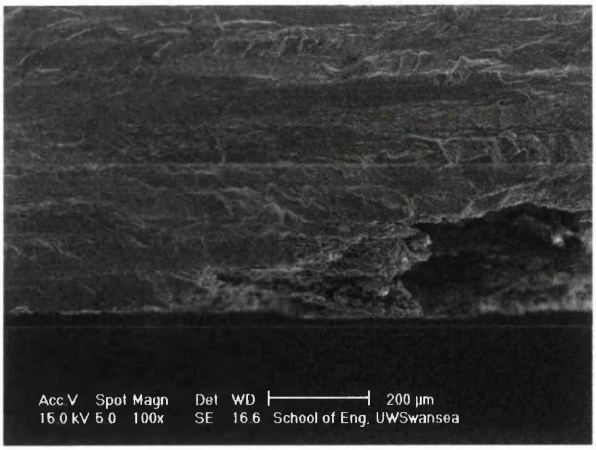
Acc.V Spot Magn Det WD 200 µm
15.0 kV 5.0 100x SE 16.6 School of Eng. UWSwansea

PC-20

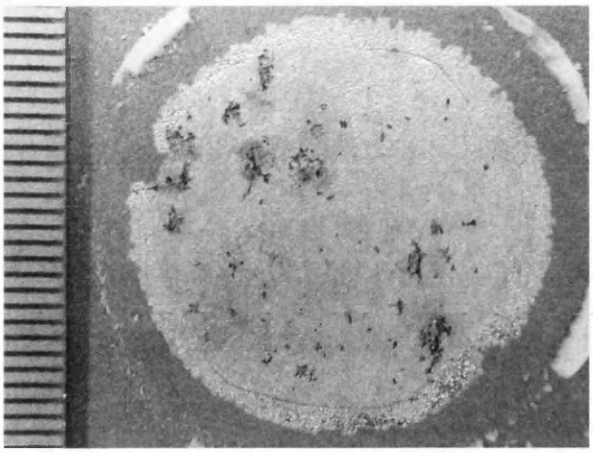

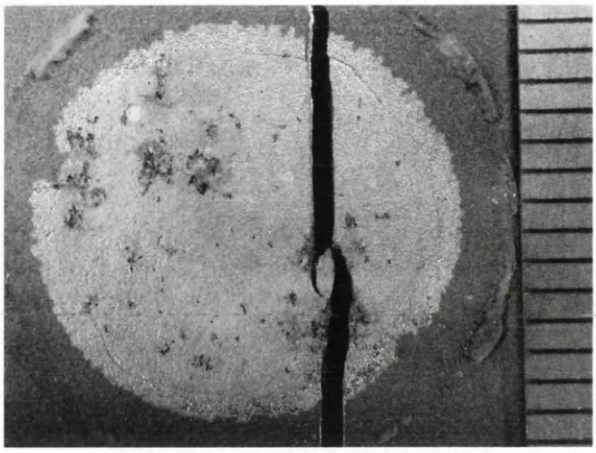

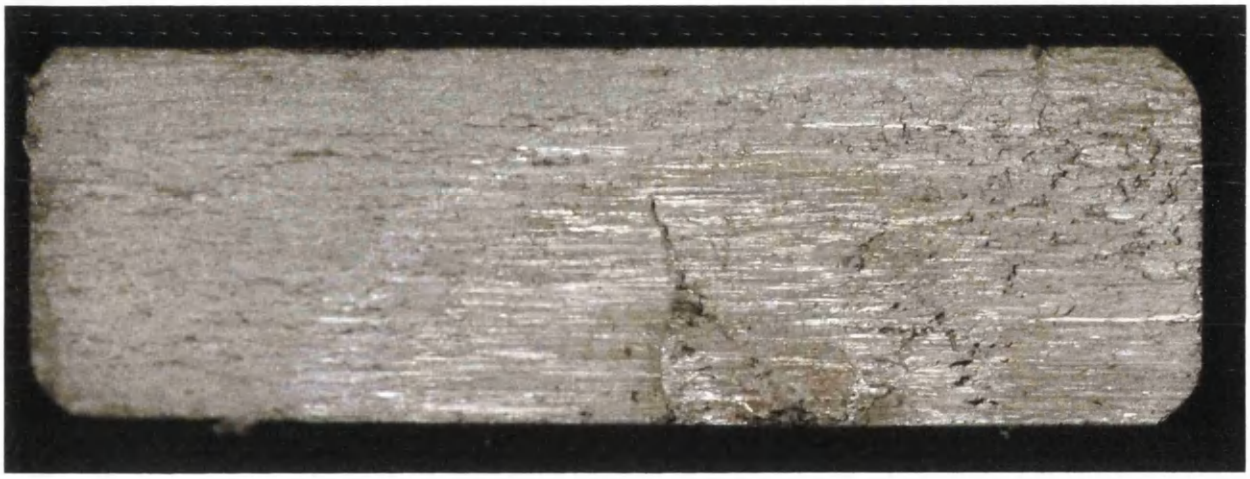

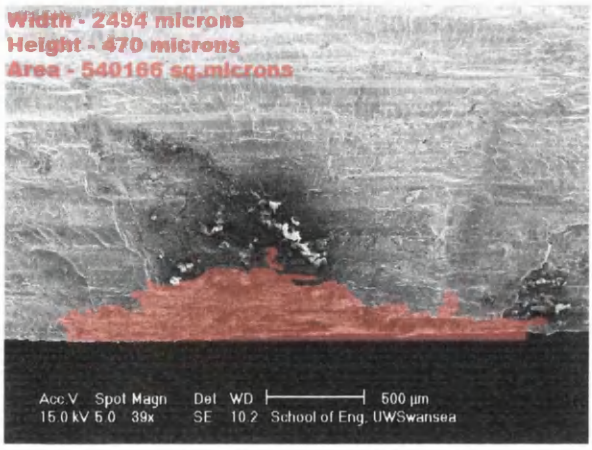
Width - 2494 microns
Height - 470 microns
Area - 540166 sq.microns
Acc.V Spot Magn Det WD 500 µm
15.0 kV 5.0 39x SE 10.2 School of Eng, UWSwansea

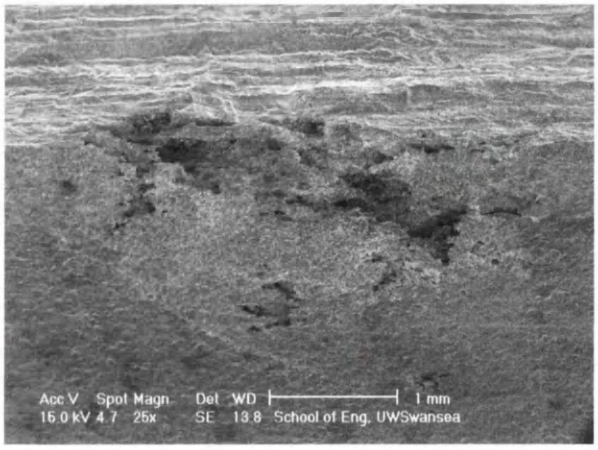
Acc.V Spot Magn Det WD 1 mm
15.0 kV 4.7 25x SE 13.8 School of Eng, UWSwansea

PC-21

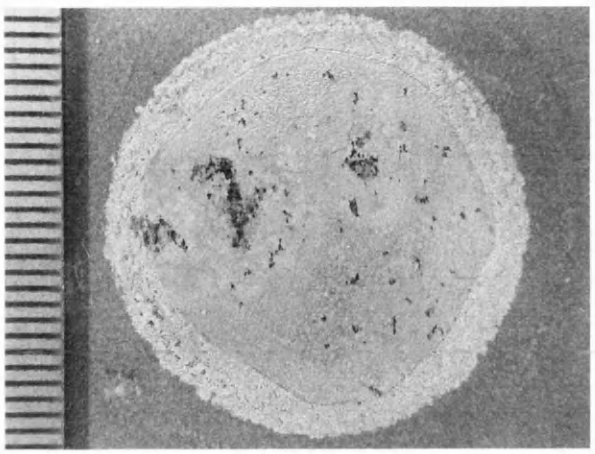

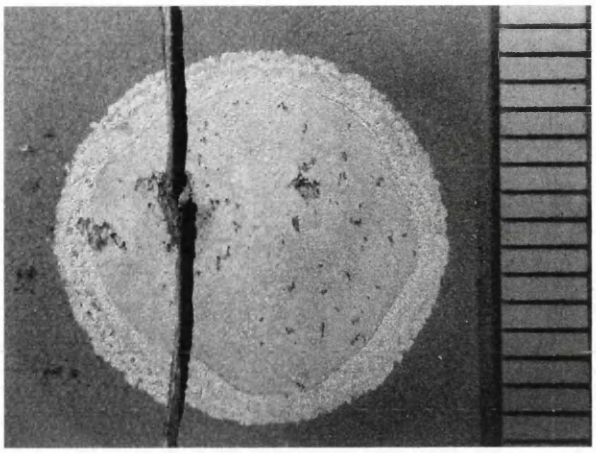

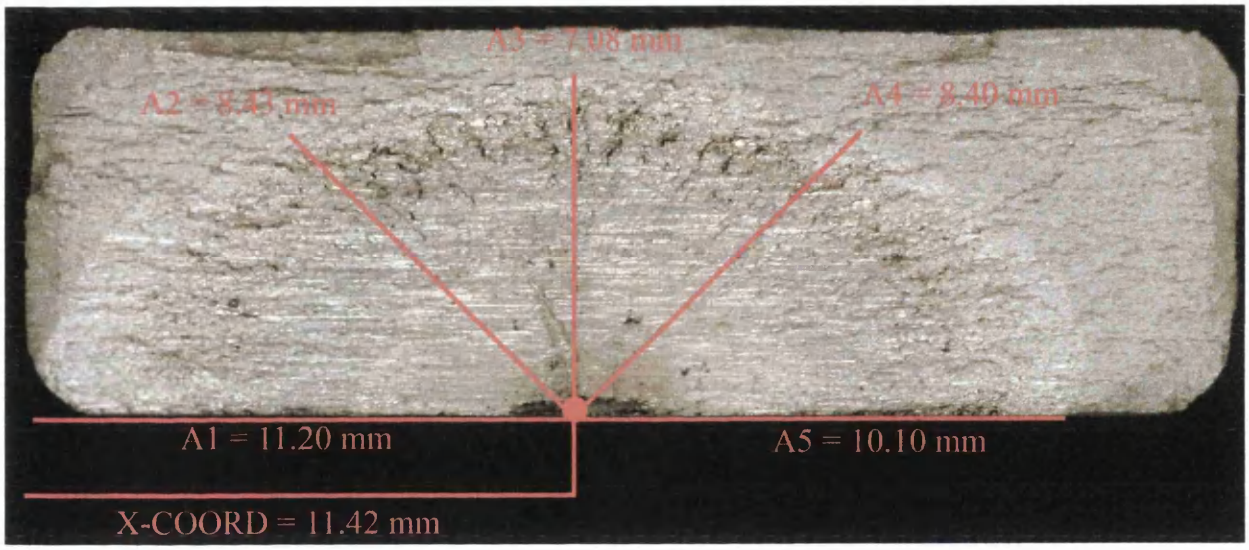
A3 = 7.08 mm
A2 = 8.43 mm
A4 = 8.40 mm
A1 = 11.20 mm
A5 = 10.10 mm
X-COORD = 11.42 mm

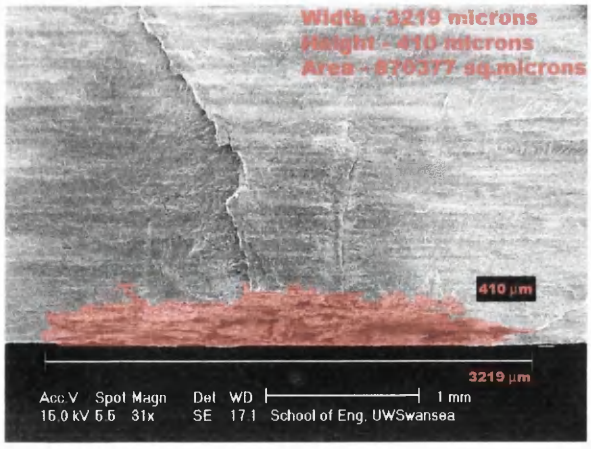
Width - 3219 microns
Height - 410 microns
Area - 870377 sq.microns
410 µm
3219 µm
Acc.V Spot Magn Det WD 1 mm
15.0 kV 5.5 31x SE 17.1 School of Eng. UWSwansea

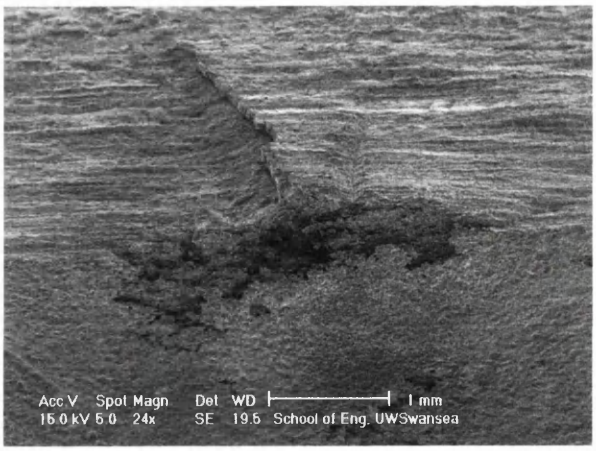
Acc.V Spot Magn Det WD 1 mm
15.0 kV 5.0 24x SE 19.5 School of Eng. UWSwansea

PC-22

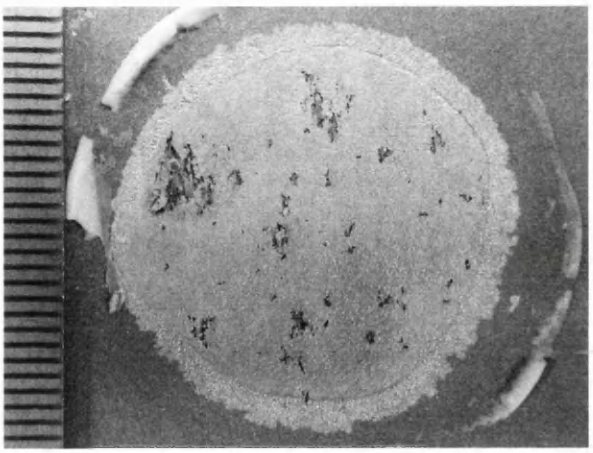

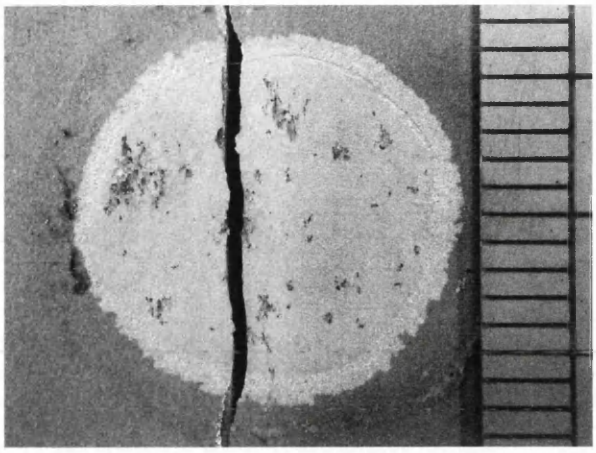

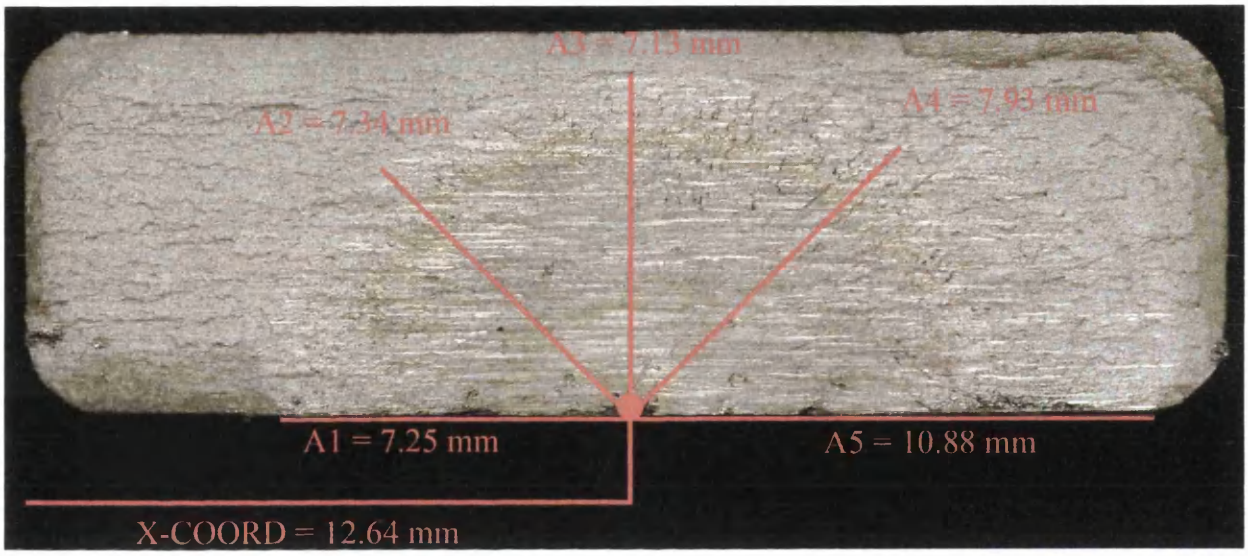
A3 = 7.13 mm
A2 = 7.34 mm
A4 = 7.93 mm
A1 = 7.25 mm
A5 = 10.88 mm
X-COORD = 12.64 mm

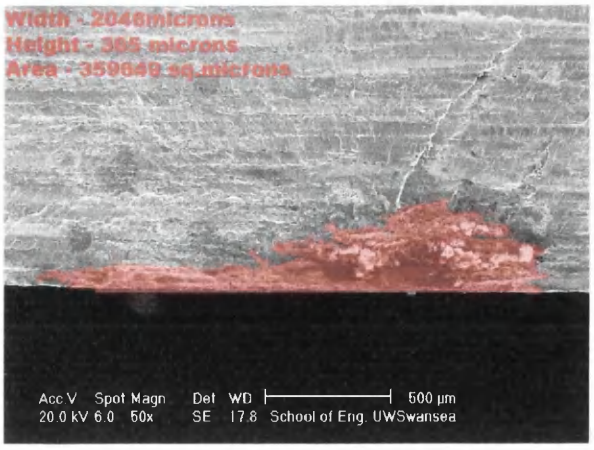
Width - 2046microns
Height - 365 microns
Area - 359649 sq.microns
Acc.V Spot Magn Det WD 500 µm
20.0 kV 6.0 60x SE 17.8 School of Eng. UWSwansea

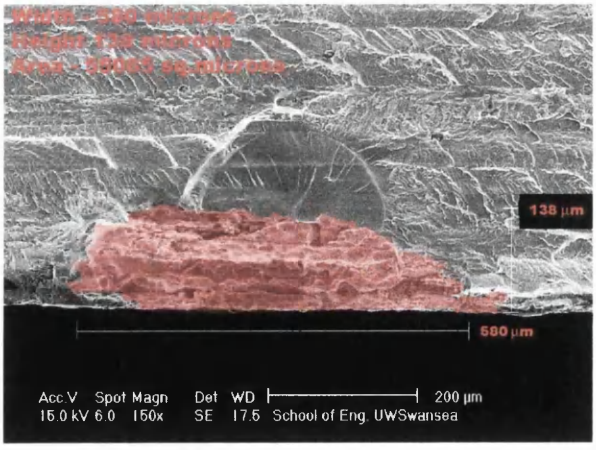
138 µm
500 µm
Acc.V Spot Magn Det WD 200 µm
15.0 kV 6.0 150x SE 17.5 School of Eng. UWSwansea

PC-23

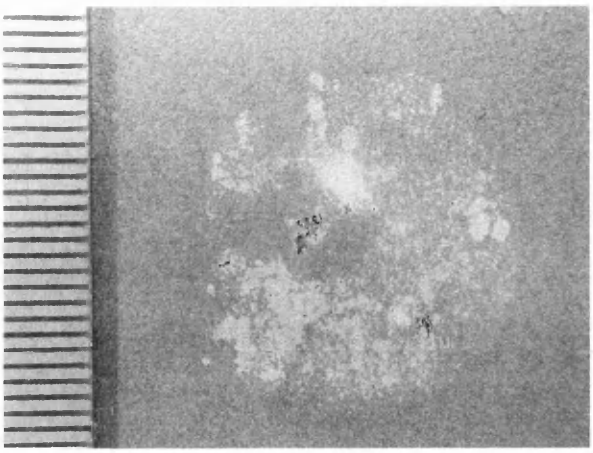

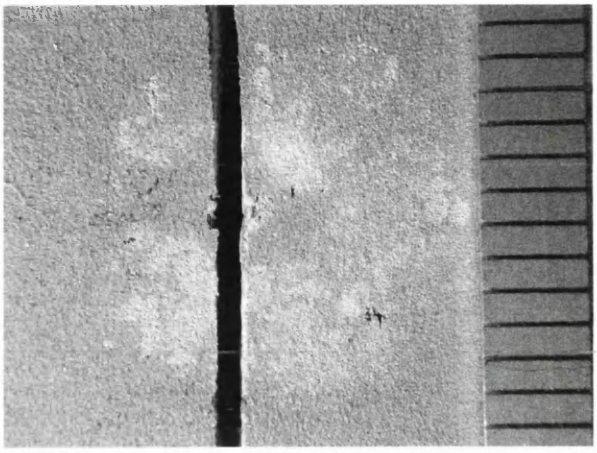

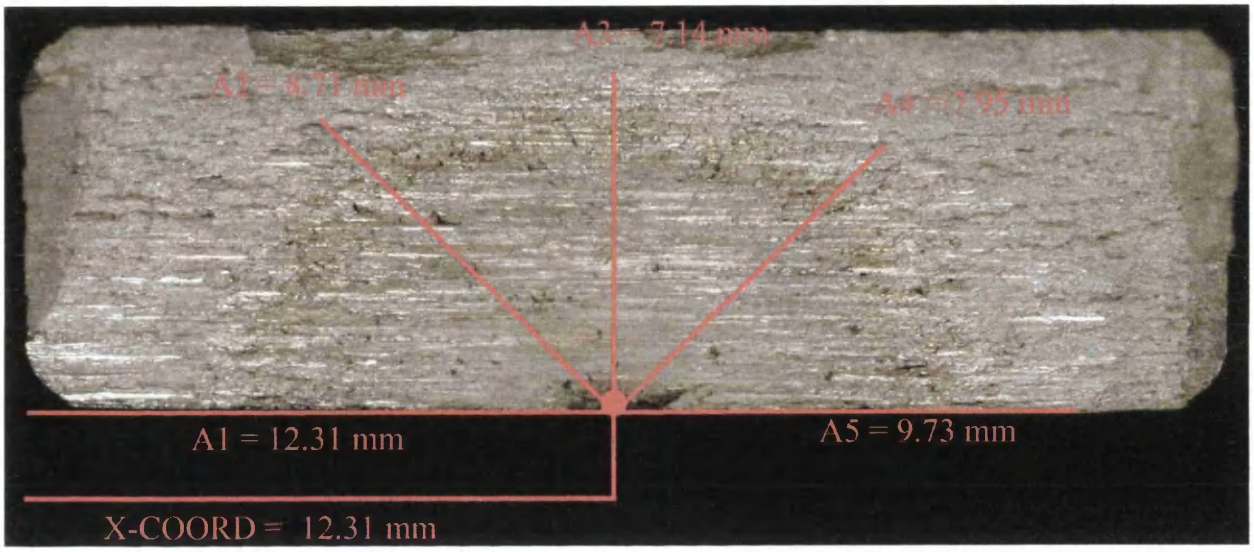
A3 = 7.14 mm
A2 = 8.71 mm
A4 = 7.95 mm
A1 = 12.31 mm
A5 = 9.73 mm
X-COORD = 12.31 mm

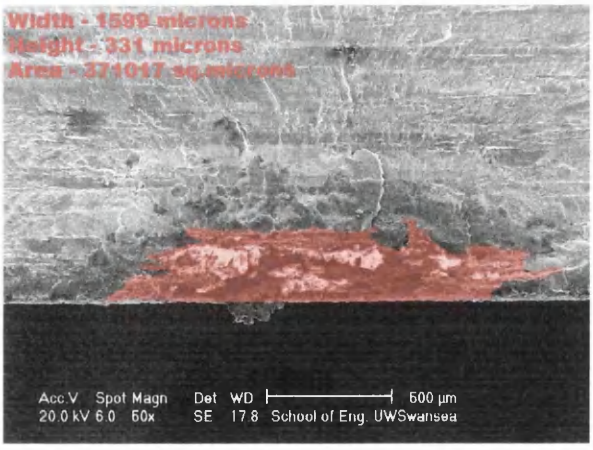
Width - 1599 microns
Height - 331 microns
Area - 371017 sq.microns
Acc.V Spot Magn Det WD 500 µm
20.0 kV 6.0 60x SE 17.8 School of Eng. UWSwansea

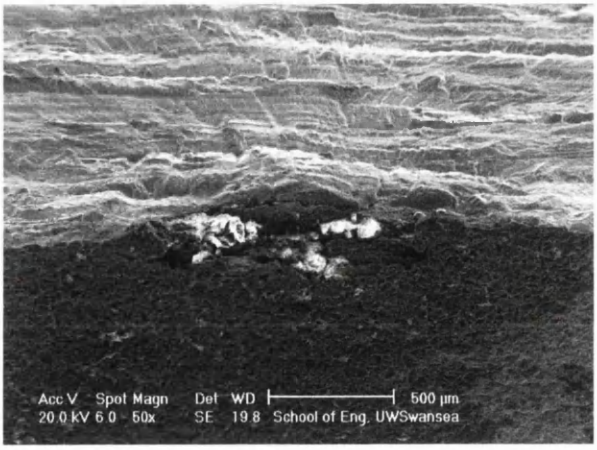
Acc.V Spot Magn Det WD 500 µm
20.0 kV 6.0 60x SE 19.8 School of Eng. UWSwansea

PC-24

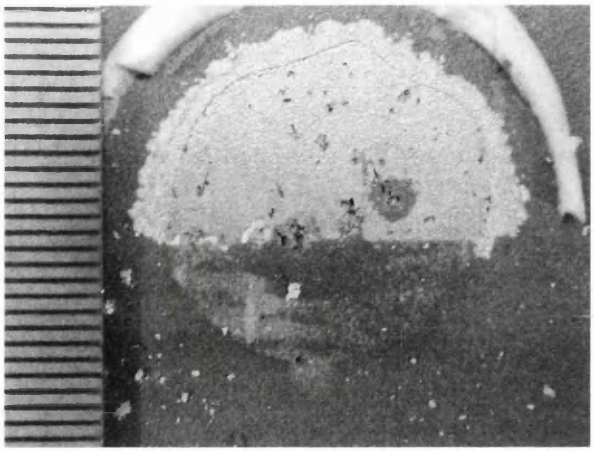

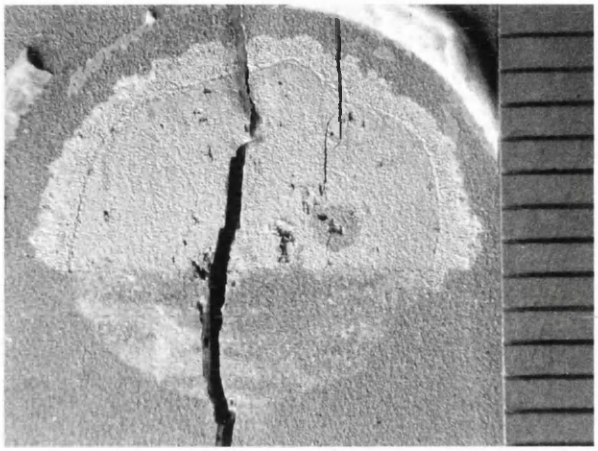

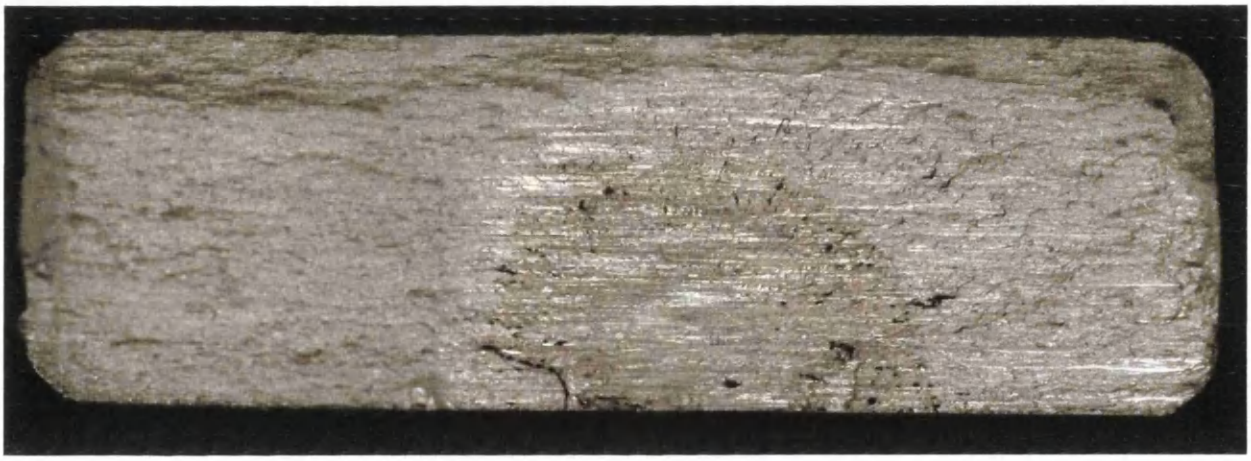

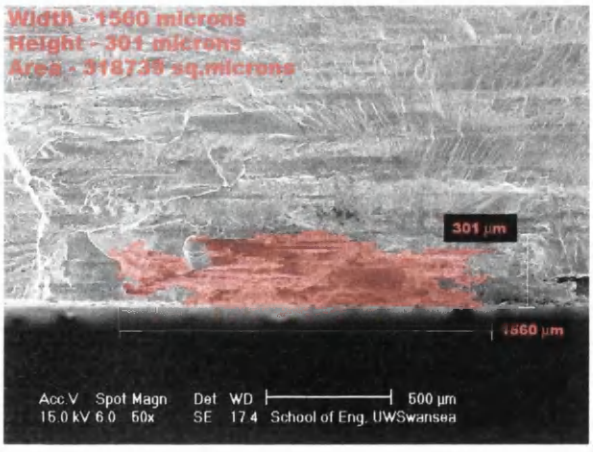
Width - 1560 microns
Height - 301 microns
Area - 318735 sq.microns
301 µm
1560 µm
Acc.V Spot Magn Det WD 500 µm
15.0 kV 6.0 60x SE 17.4 School of Eng. UWSwansea

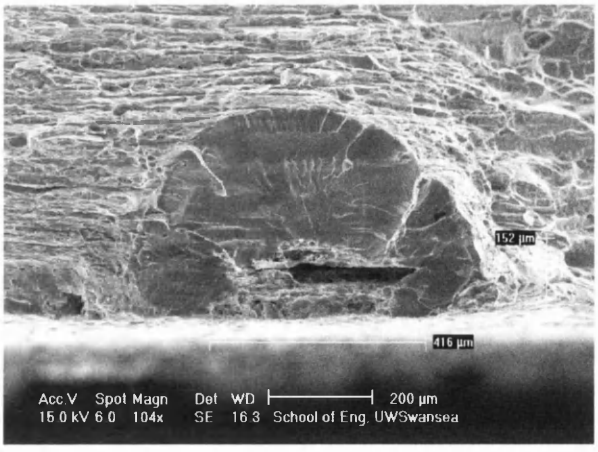
152 µm
416 µm
Acc.V Spot Magn Det WD 200 µm
15.0 kV 6.0 104x SE 16.3 School of Eng. UWSwansea

PC-25

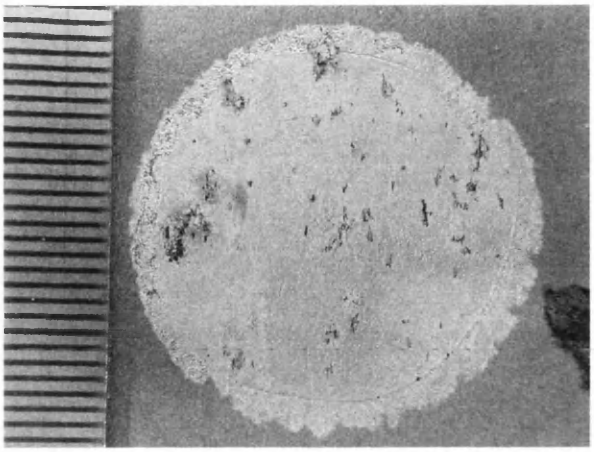

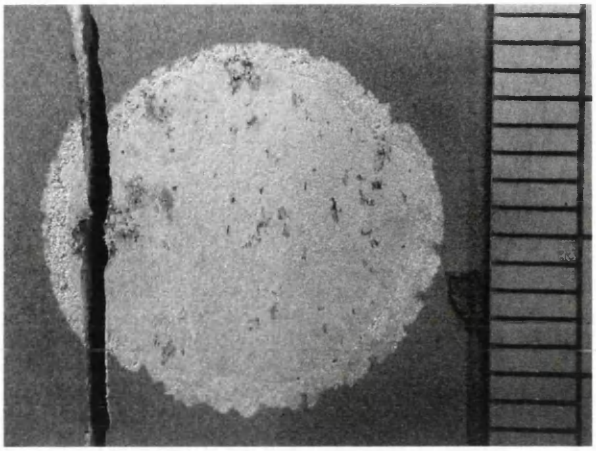

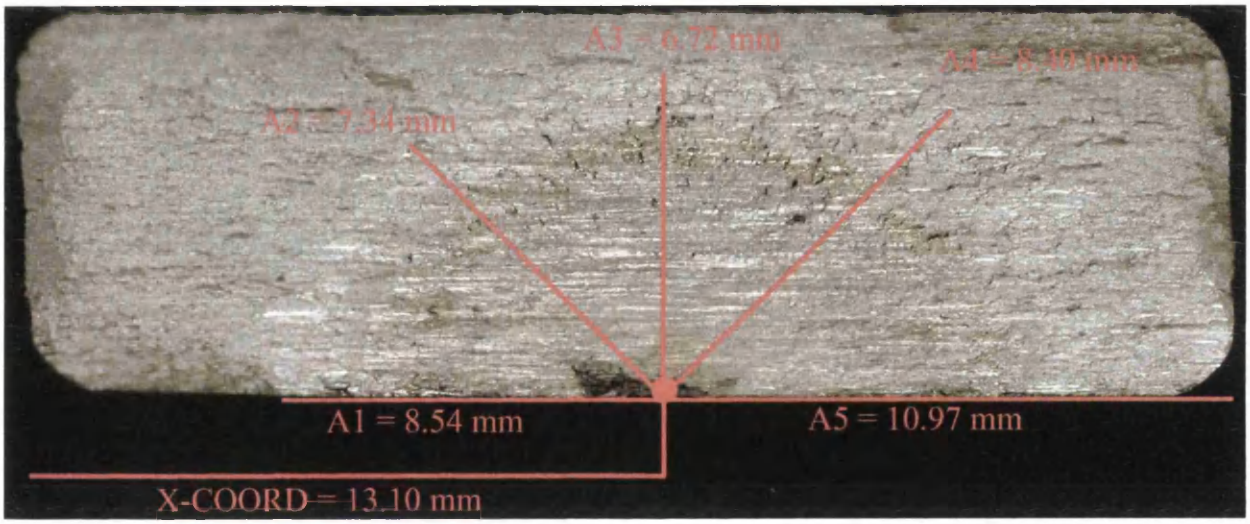
A3 = 6.72 mm
A4 = 8.40 mm
A2 = 7.34 mm
A1 = 8.54 mm
A5 = 10.97 mm
X-COORD = 13.10 mm

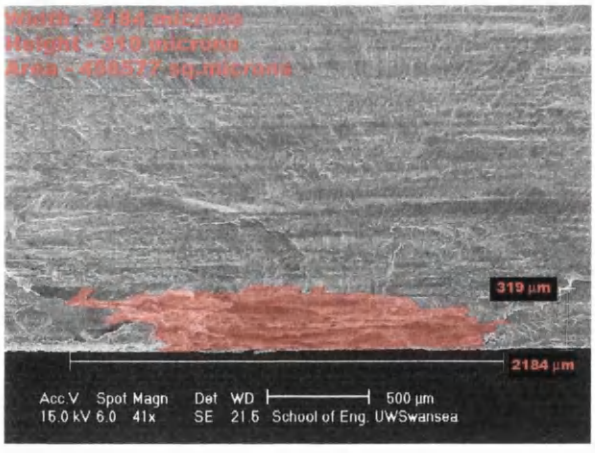
Width - 2184 microns
Height - 319 microns
Area - 458577 sq.microns
319 µm
2184 µm
Acc.V Spot Magn Det WD 500 µm
15.0 kV 6.0 41x SE 21.5 School of Eng. UWSwansea

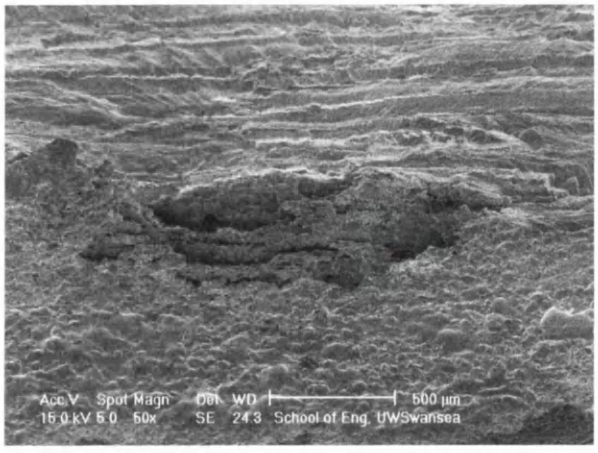
Acc.V Spot Magn Det WD 500 µm
15.0 kV 5.0 50x SE 24.3 School of Eng. UWSwansea

PC-26

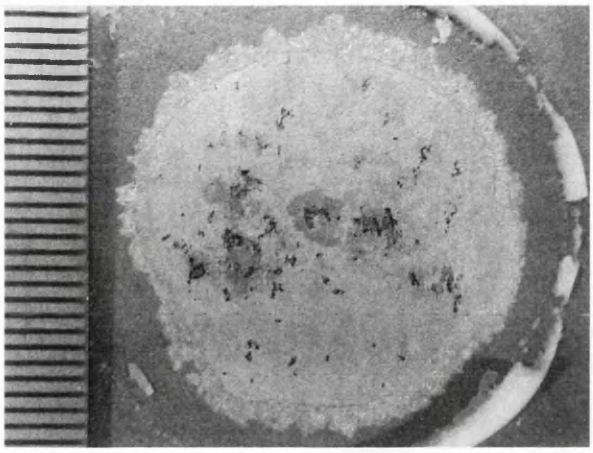

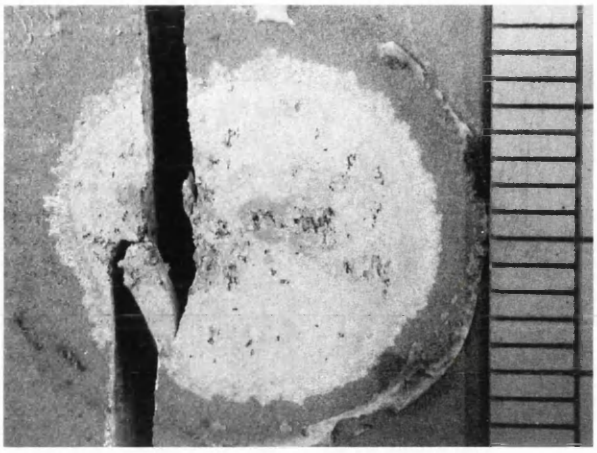

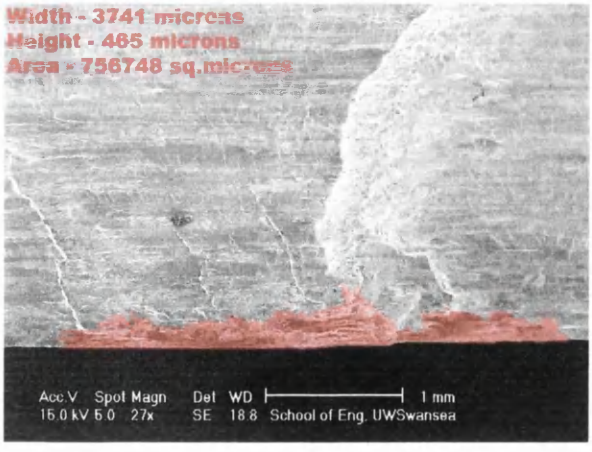
Width - 3741 microns
Height - 465 microns
Area - 756748 sq.microns
Acc.V Spot Magn Det WD 1 mm
15.0 kV 6.0 27x SE 18.8 School of Eng. UWSwansea

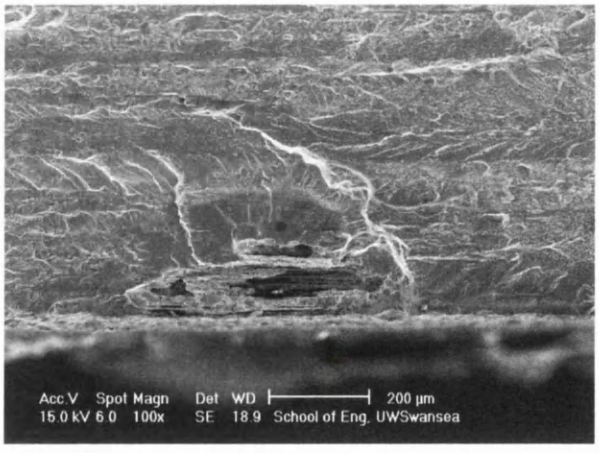
Acc.V Spot Magn Det WD 200 µm
15.0 kV 6.0 100x SE 18.9 School of Eng. UWSwansea

PC-27

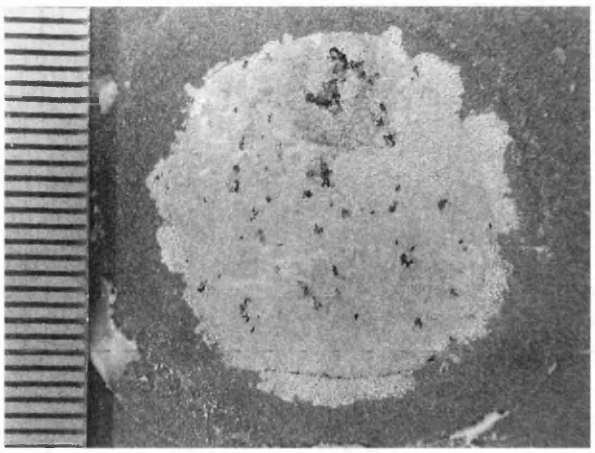

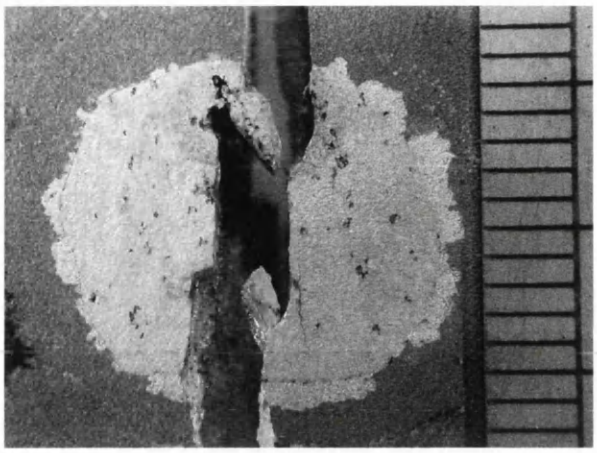

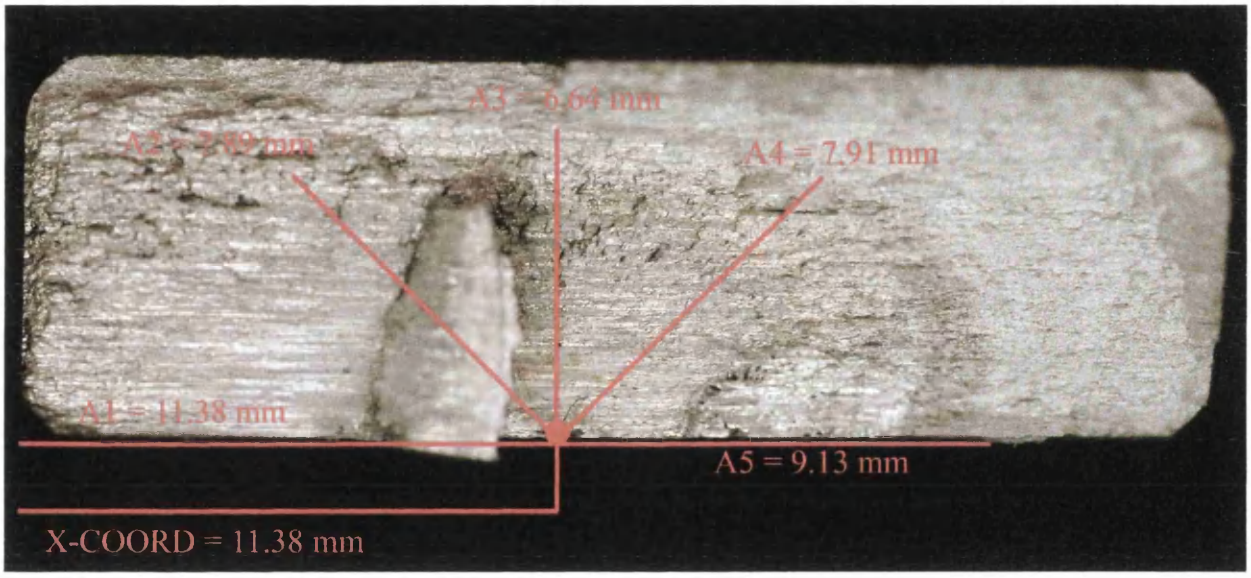
A3 = 6.64 mm
A2 = 2.89 mm
A4 = 7.91 mm
A1 = 11.38 mm
A5 = 9.13 mm
X-COORD = 11.38 mm

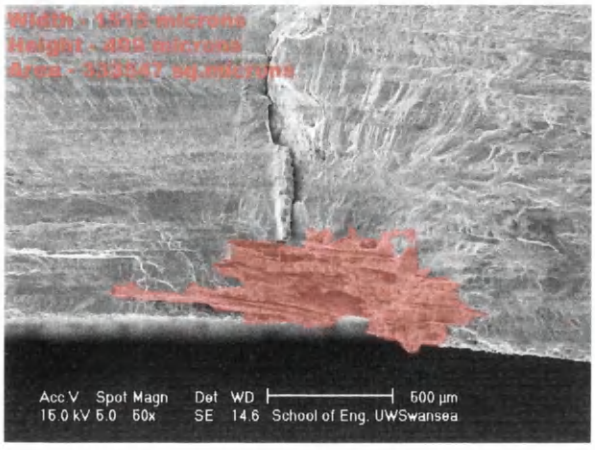
Width - 4815 microns
Height - 885 microns
Area - 532547 sq.microns
Acc.V Spot Magn Det WD 500 µm
15.0 kV 5.0 60x SE 14.6 School of Eng. UWSwansea

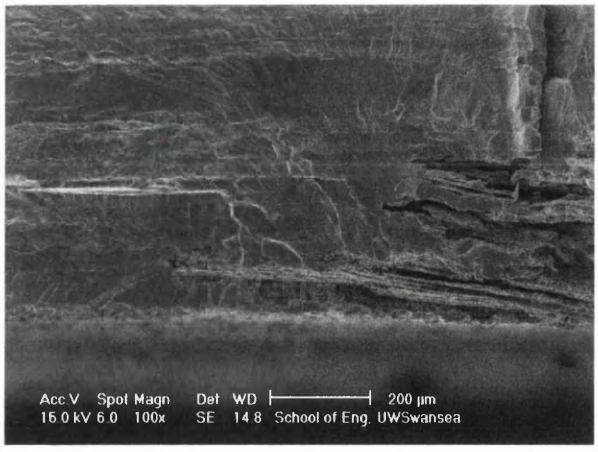
Acc.V Spot Magn Det WD 200 µm
15.0 kV 6.0 100x SE 14.8 School of Eng. UWSwansea

PC-28

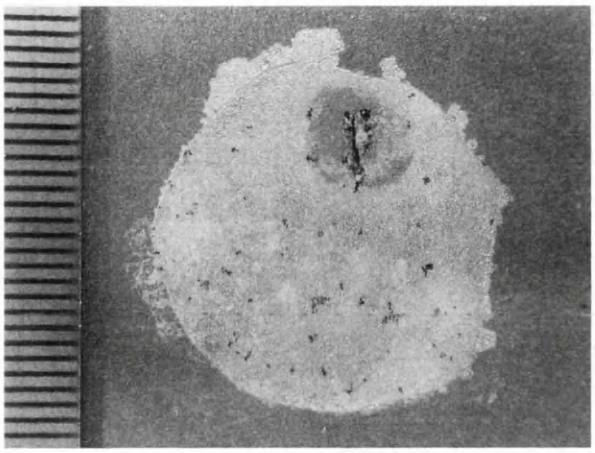

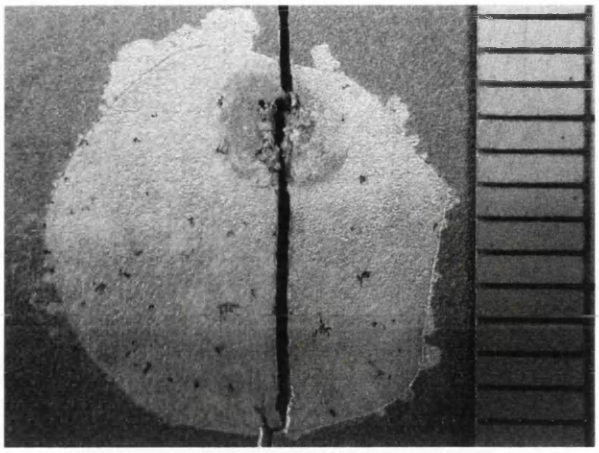

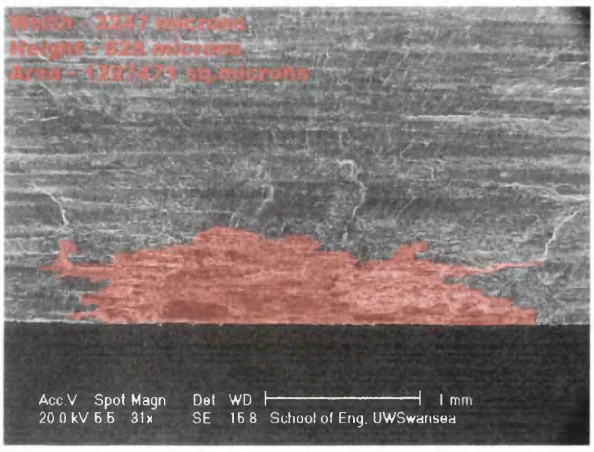
Width = 3287 microns
Height = 528 microns
Area = 1297473 sq.microns
Acc.V Spot Magn Det WD 1 mm
20.0 kV 5.5 31x SE 15.8 School of Eng. UWSwansea

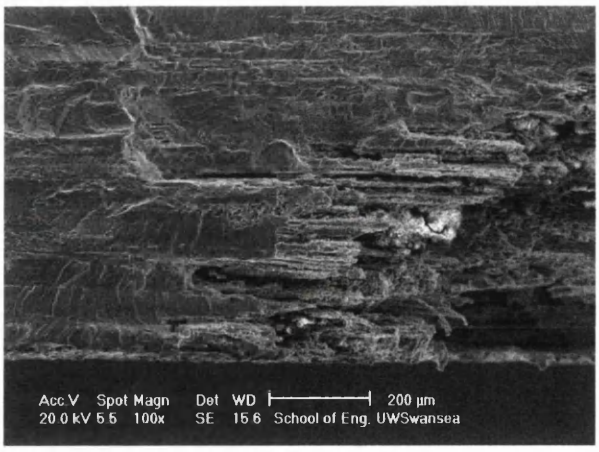
Acc.V Spot Magn Det WD 200 µm
20.0 kV 5.5 100x SE 15.6 School of Eng. UWSwansea

PC-29

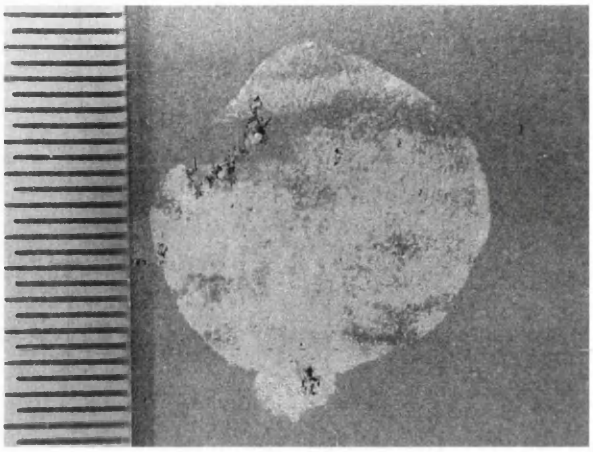

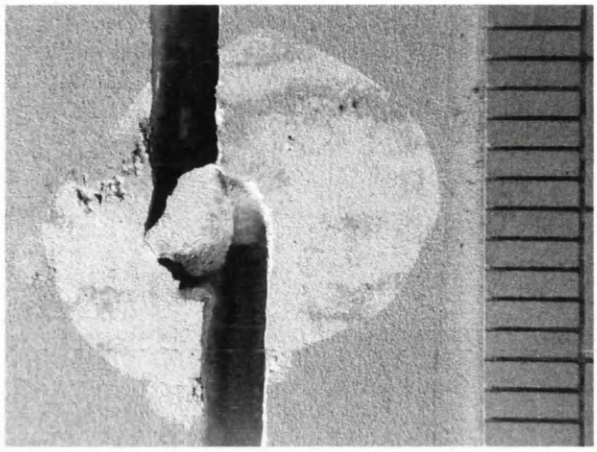

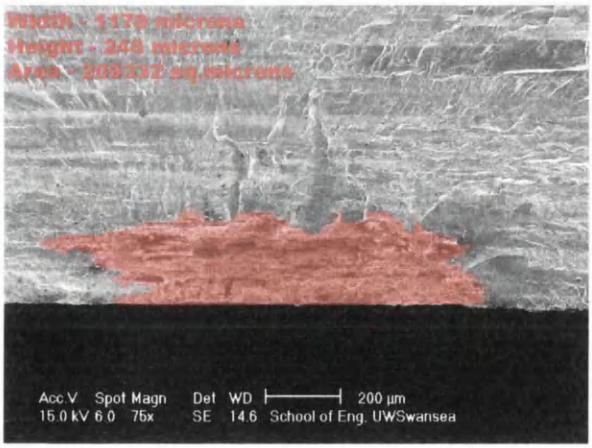
Width - 1179 microns
Height - 248 microns
Area - 209332 sq.microns
Acc.V Spot Magn Det WD 200 µm
15.0 kV 6.0 75x SE 14.6 School of Eng, UWSwansea

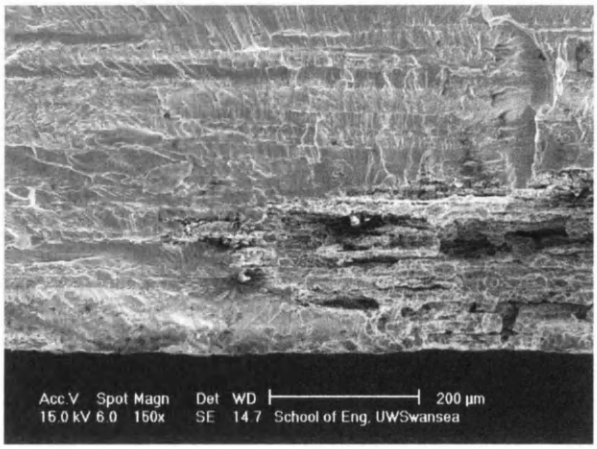
Acc.V Spot Magn Det WD 200 µm
15.0 kV 6.0 150x SE 14.7 School of Eng, UWSwansea

PC-30

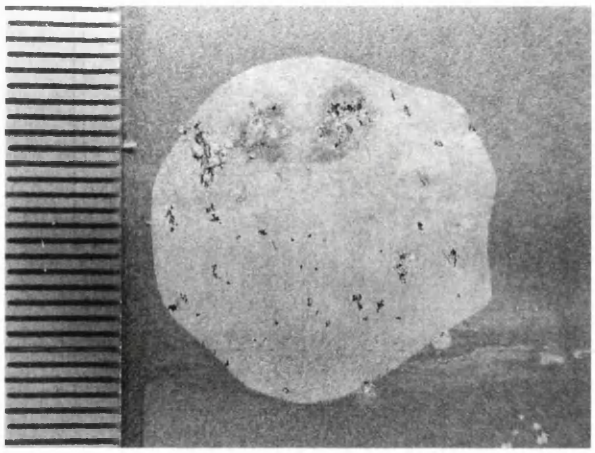

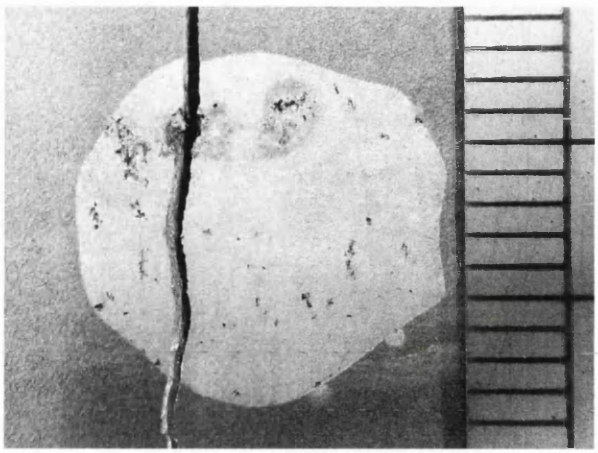

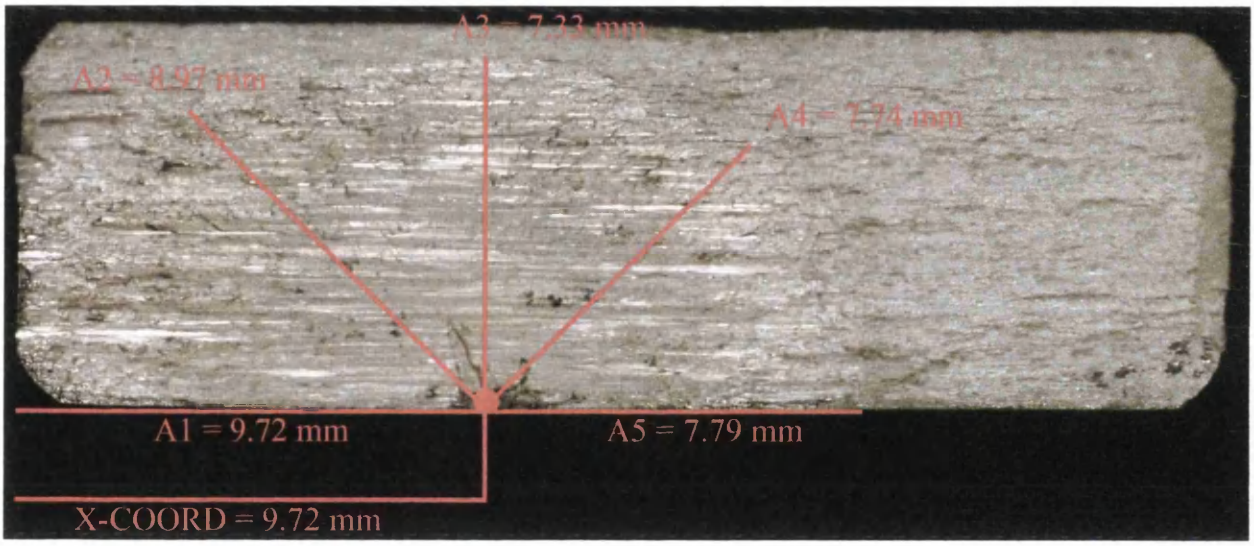
A3 = 7.33 mm
A2 = 8.97 mm
A4 = 7.74 mm
A1 = 9.72 mm
A5 = 7.79 mm
X-COORD = 9.72 mm

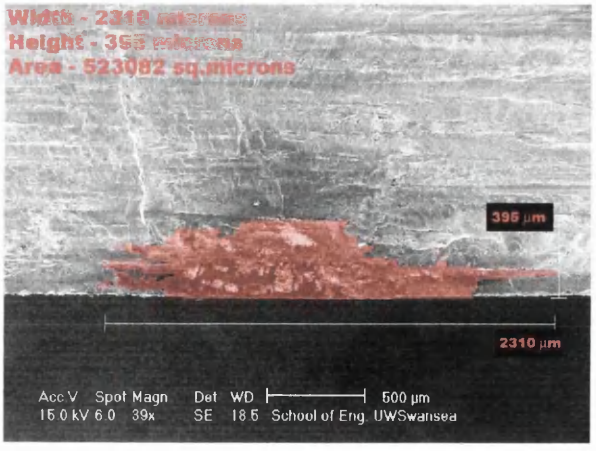
Width - 2310 microns
Height - 395 microns
Area - 523082 sq.microns
395 µm
2310 µm
Acc.V Spot Magn Det WD 500 µm
15.0 kV 6.0 39x SE 18.5 School of Eng. UWSwansea

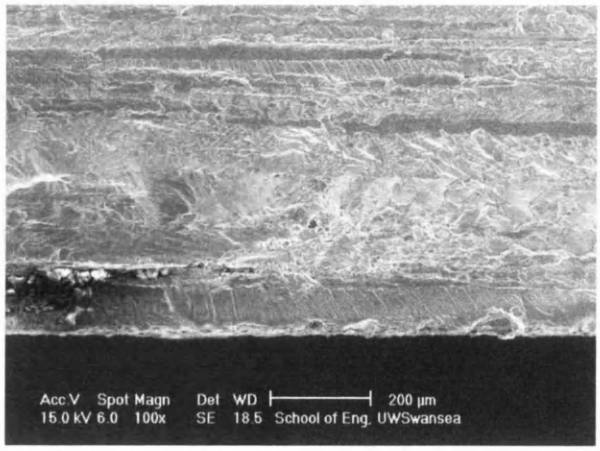
Acc.V Spot Magn Det WD 200 µm
15.0 kV 6.0 100x SE 18.5 School of Eng. UWSwansea

APPENDIX 2

FH-C8-1

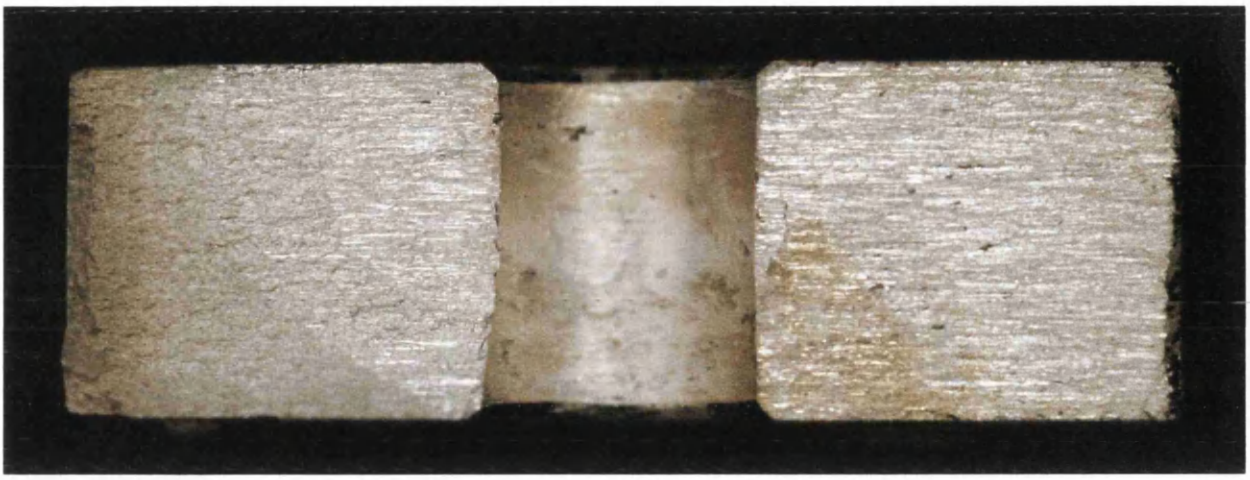

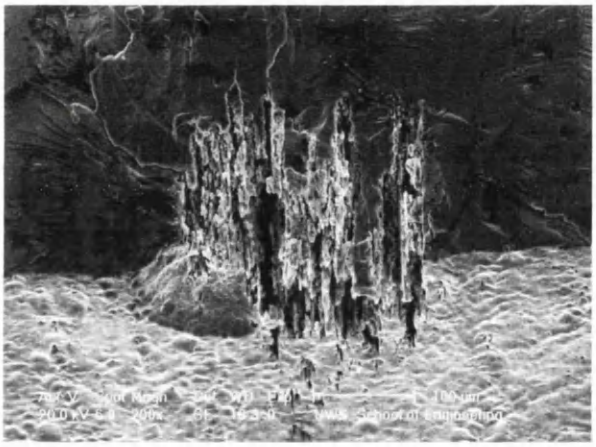

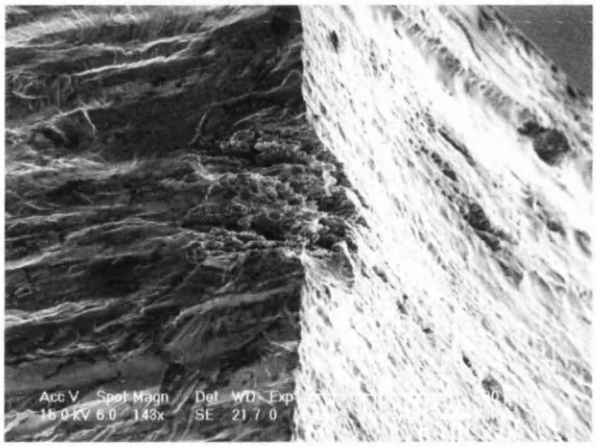
Acc.V Spot Magn Det WD Exp
15.0 kV 6.0 143x SE 21.7 0

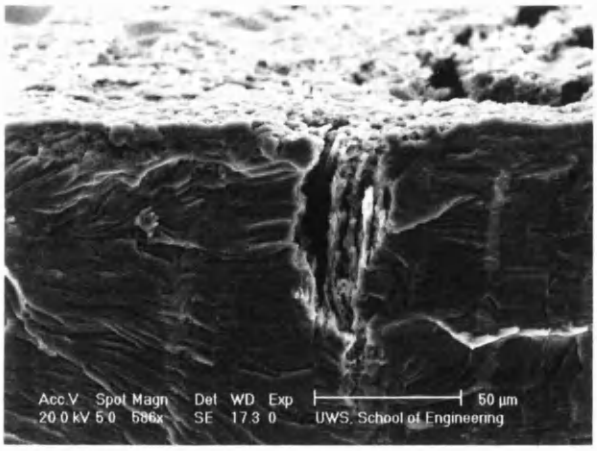
Acc.V Spot Magn Det WD Exp 50 µm
20.0 kV 5.0 686x SE 17.3 0 UWS, School of Engineering

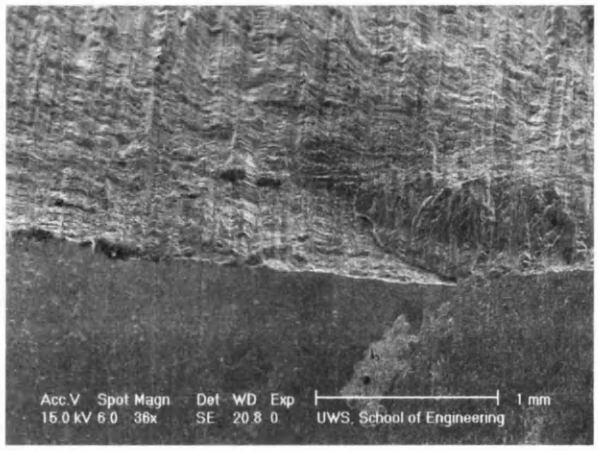
Acc.V Spot Magn Det WD Exp 1 mm
15.0 kV 6.0 36x SE 20.8 0 UWS, School of Engineering

FH-C8-2

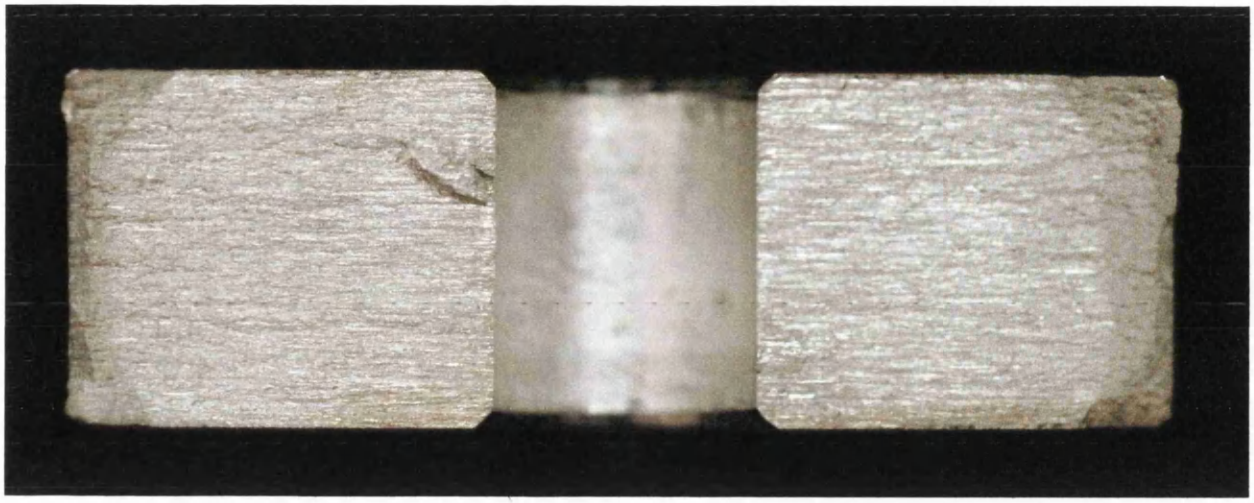

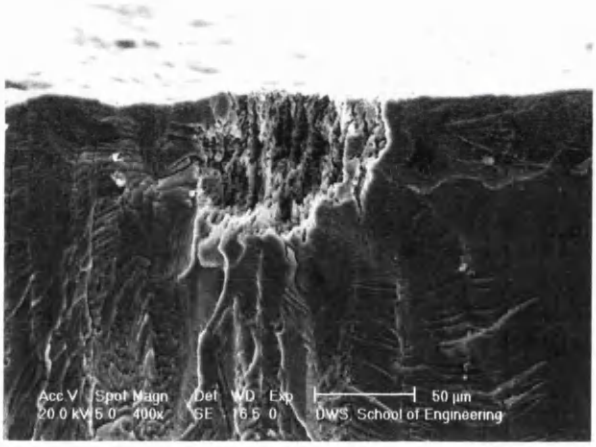
Acc.V Spot Magn Det WD Exp
20.0 kV 6.0 400x SE 16.5 0
50 µm
UWS, School of Engineering

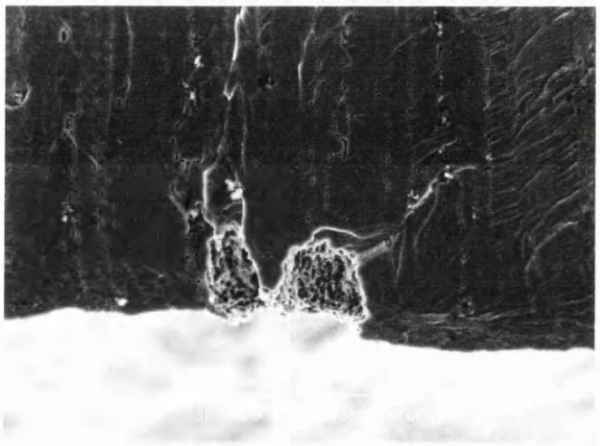

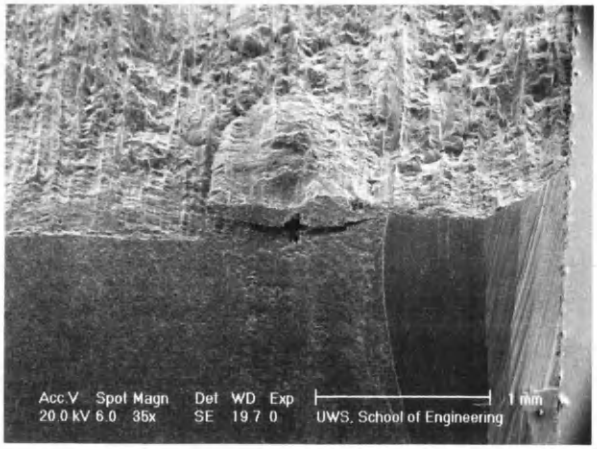
Acc.V Spot Magn Det WD Exp
20.0 kV 6.0 35x SE 19.7 0
1 mm
UWS, School of Engineering

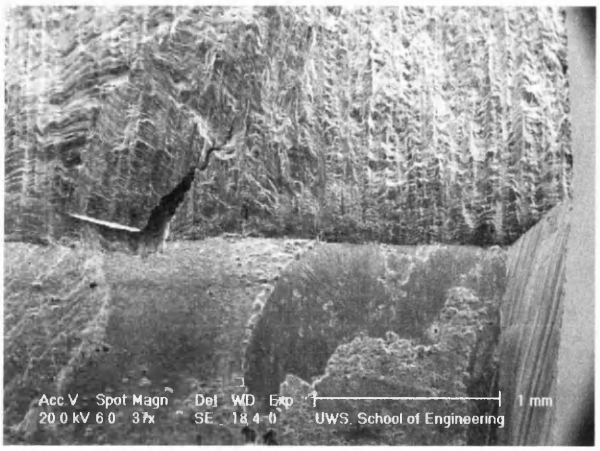
Acc.V Spot Magn Det WD Exp
20.0 kV 6.0 37x SE 18.4 0
1 mm
UWS, School of Engineering

FH-C8-3

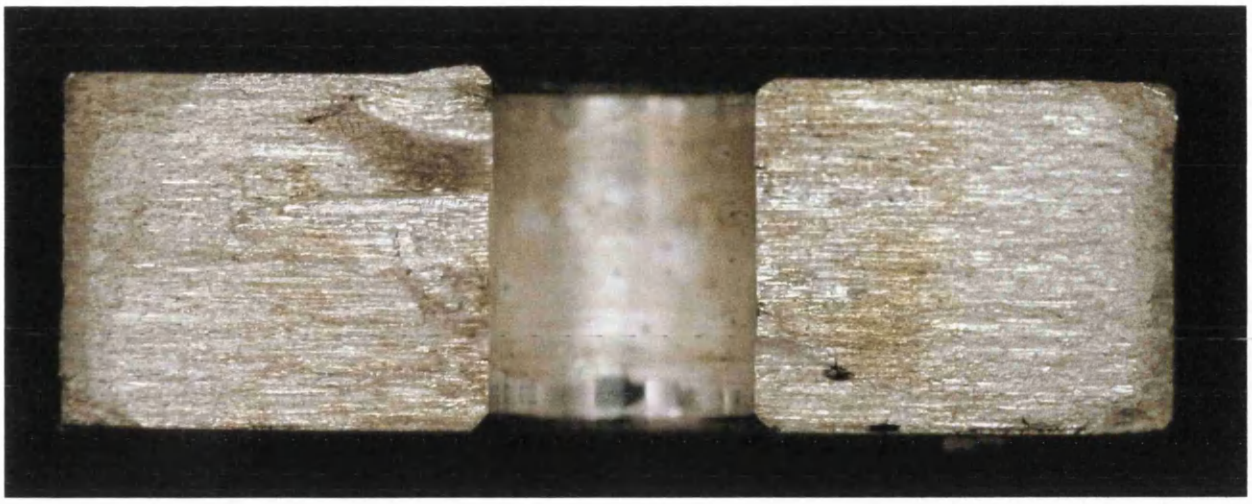

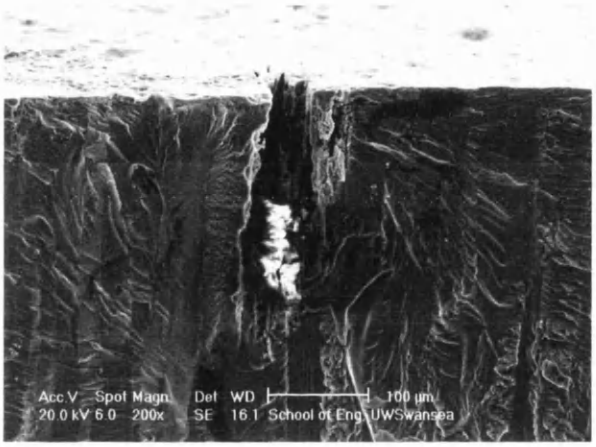
Acc.V Spot Magn Det WD 100 µm
20.0 kV 6.0 200x SE 16.1 School of Eng. UWSwansea

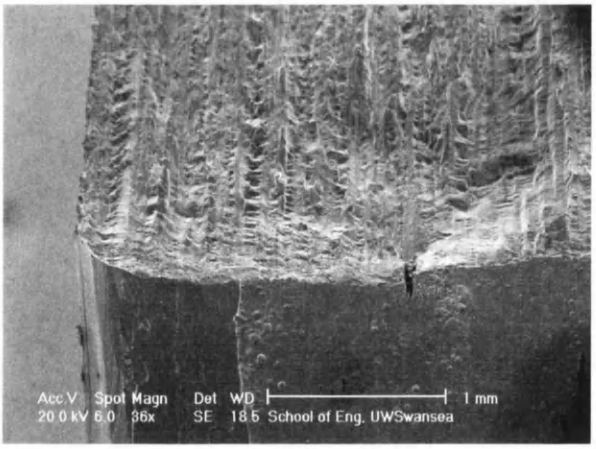
Acc.V Spot Magn Det WD 1 mm
20.0 kV 6.0 36x SE 18.6 School of Eng. UWSwansea

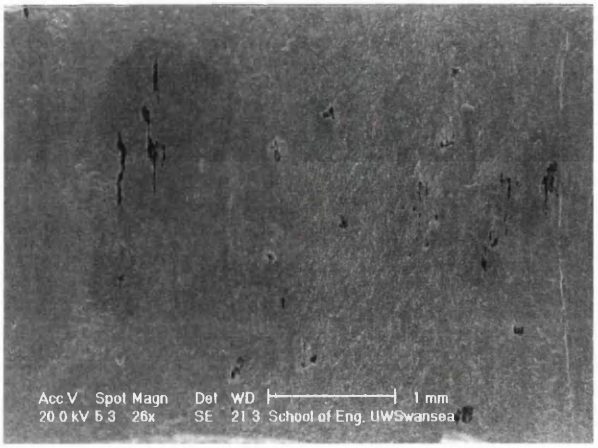
Acc.V Spot Magn Det WD 1 mm
20.0 kV 5.3 26x SE 21.3 School of Eng. UWSwansea

FH-C8-4

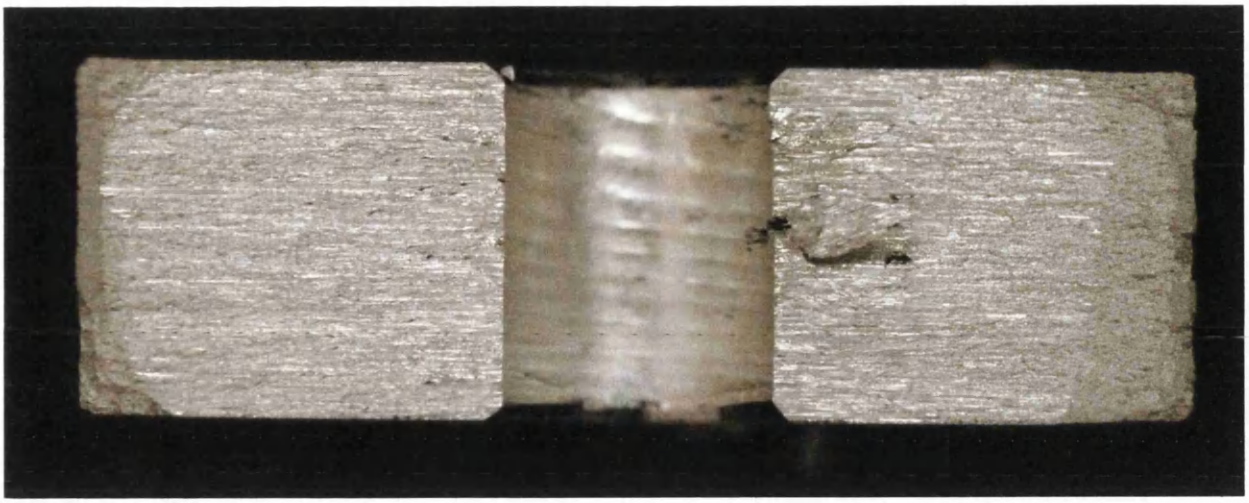


Acc.V Spot Magn Det WD 500 µm
20.0 kV 6.0 50x SE 17.7 School of Eng, UWSwansea

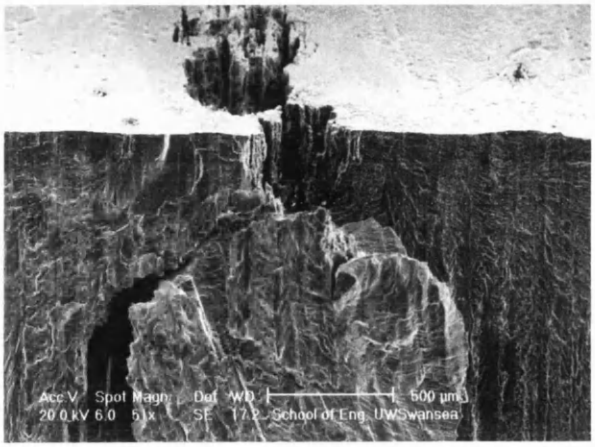
Acc.V Spot Magn Det WD 500 µm
20.0 kV 6.0 51x SE 17.2 School of Eng, UWSwansea

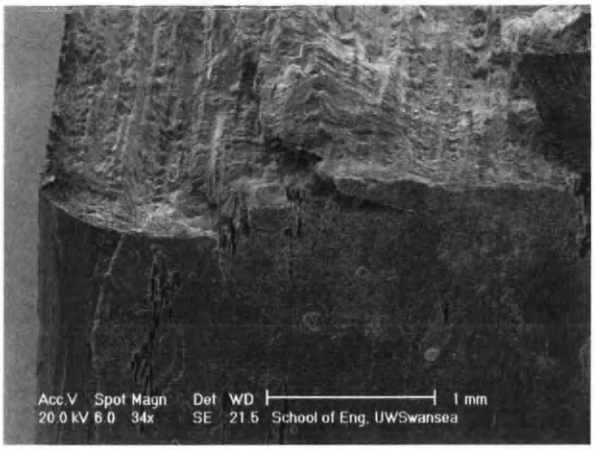
Acc.V Spot Magn Det WD 1 mm
20.0 kV 6.0 34x SE 21.5 School of Eng, UWSwansea

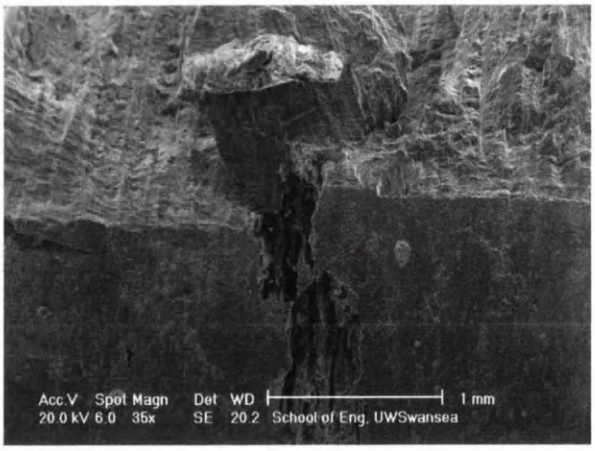
Acc.V Spot Magn Det WD 1 mm
20.0 kV 6.0 35x SE 20.2 School of Eng, UWSwansea

FH-C8-5

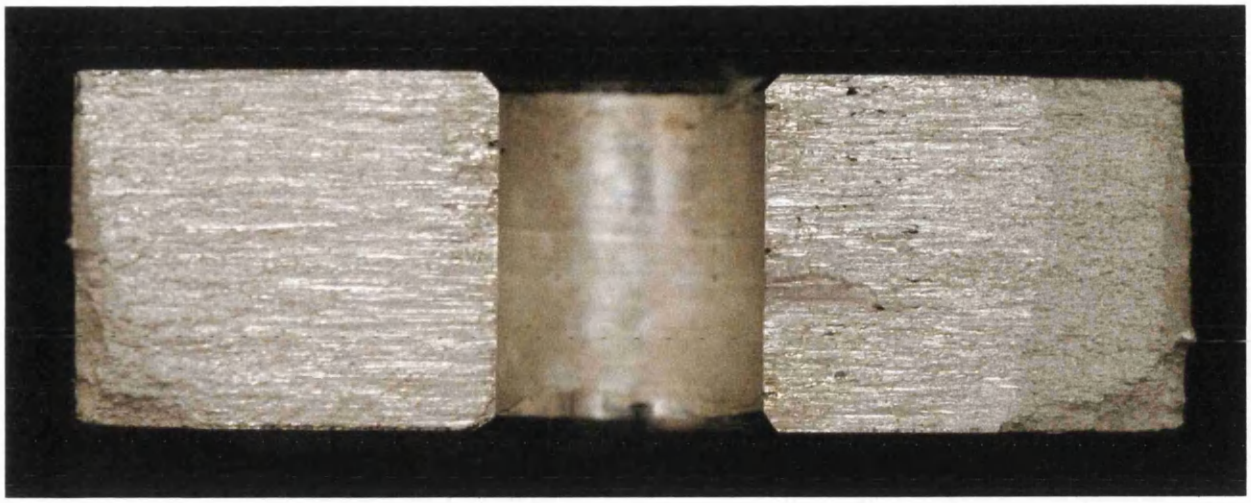

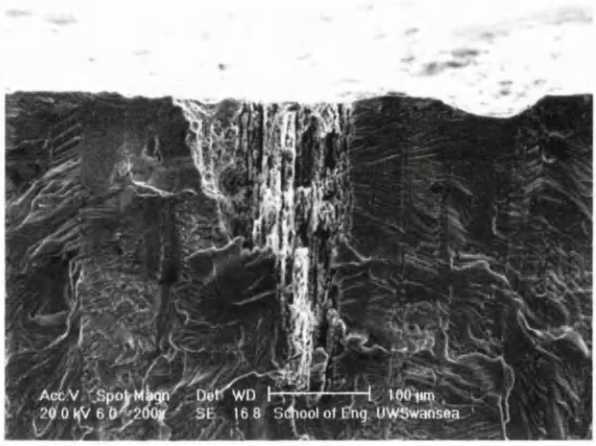
Acc.V Spot Magn Det WD 100 µm
20.0 kV 6.0 200x SE 16.8 School of Eng. UWSwansea

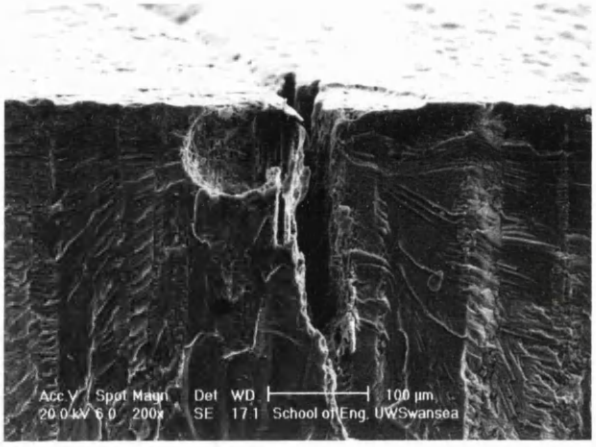
Acc.V Spot Magn Det WD 100 µm
20.0 kV 6.0 200x SE 17.1 School of Eng. UWSwansea

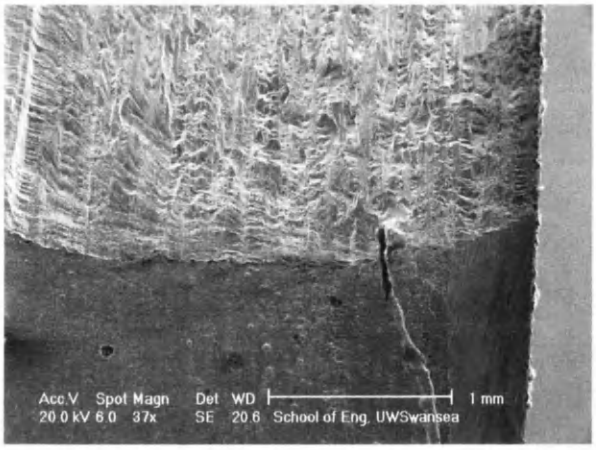
Acc.V Spot Magn Det WD 1 mm
20.0 kV 6.0 37x SE 20.6 School of Eng. UWSwansea

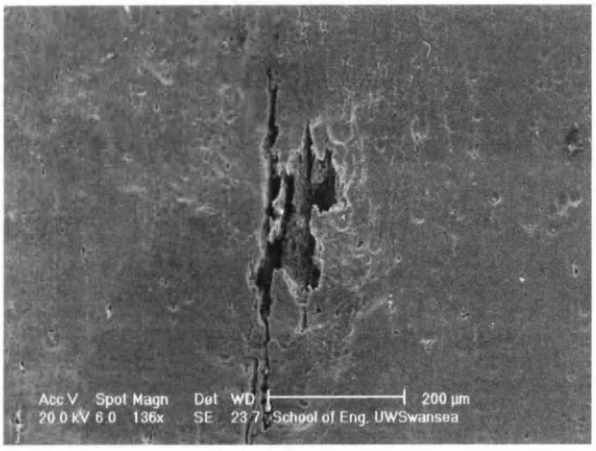
Acc.V Spot Magn Det WD 200 µm
20.0 kV 6.0 136x SE 23.7 School of Eng. UWSwansea

FH-C8-6

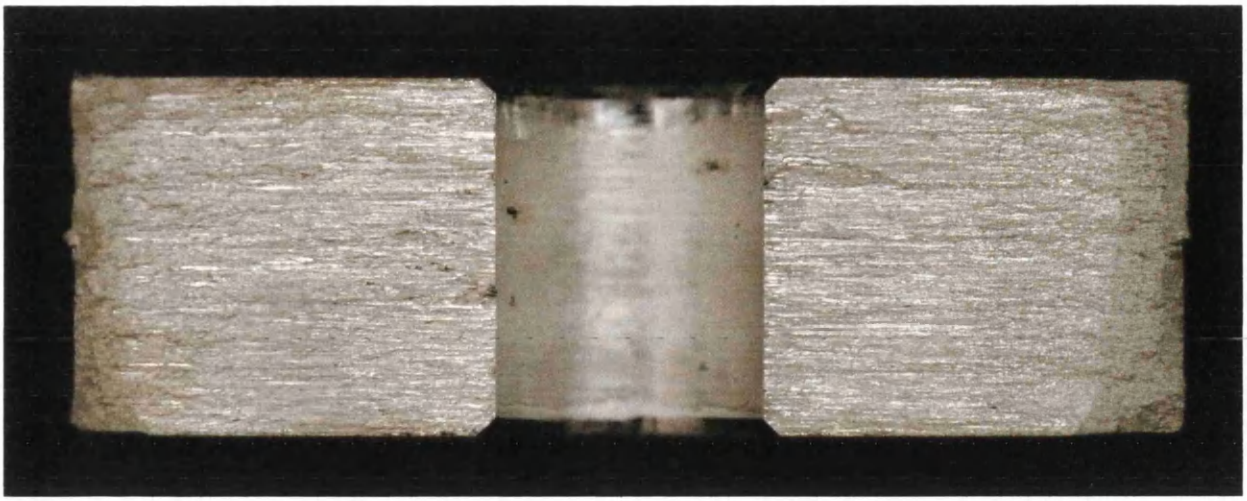

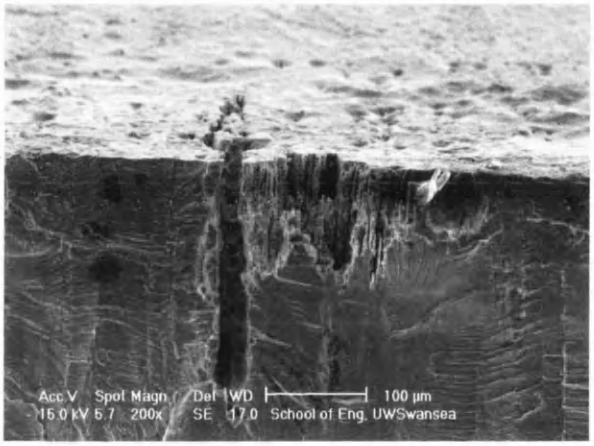
Acc.V Spot Magn Det WD 100 µm
15.0 kV 5.7 200x SE 17.0 School of Eng. UWSwansea

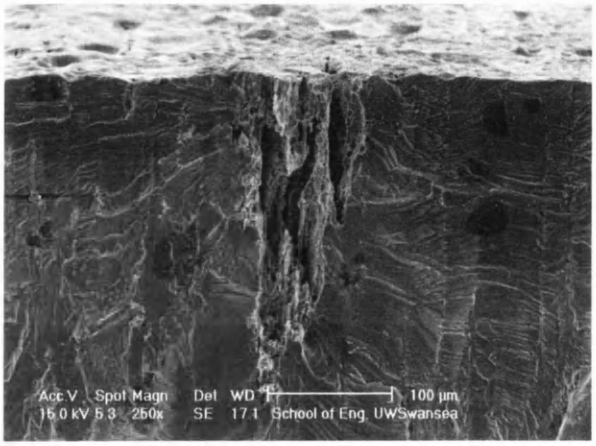
Acc.V Spot Magn Det WD 100 µm
15.0 kV 5.3 250x SE 17.1 School of Eng. UWSwansea

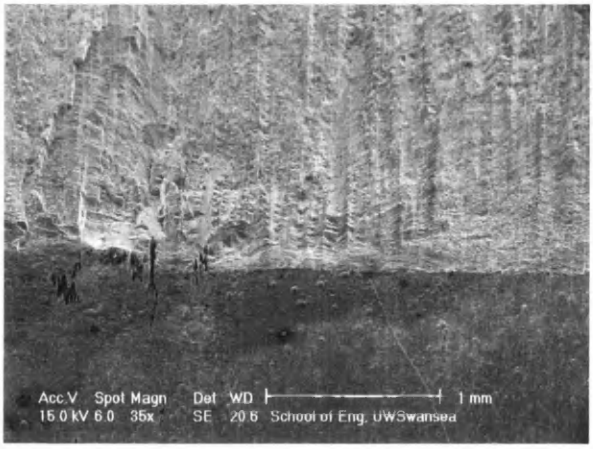
Acc.V Spot Magn Det WD 1 mm
15.0 kV 6.0 35x SE 20.6 School of Eng. UWSwansea

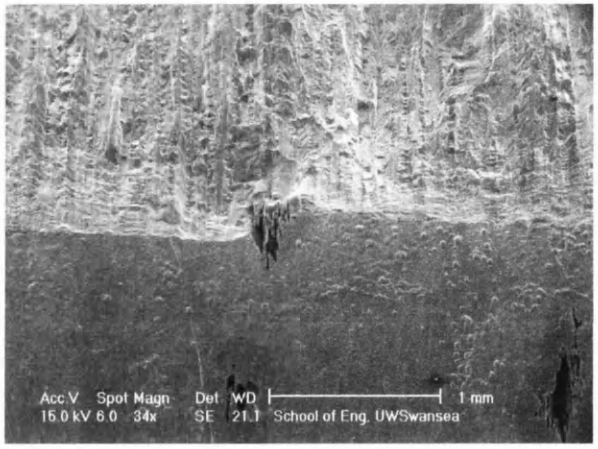
Acc.V Spot Magn Det WD 1 mm
15.0 kV 6.0 34x SE 21.1 School of Eng. UWSwansea

FH-C8-7

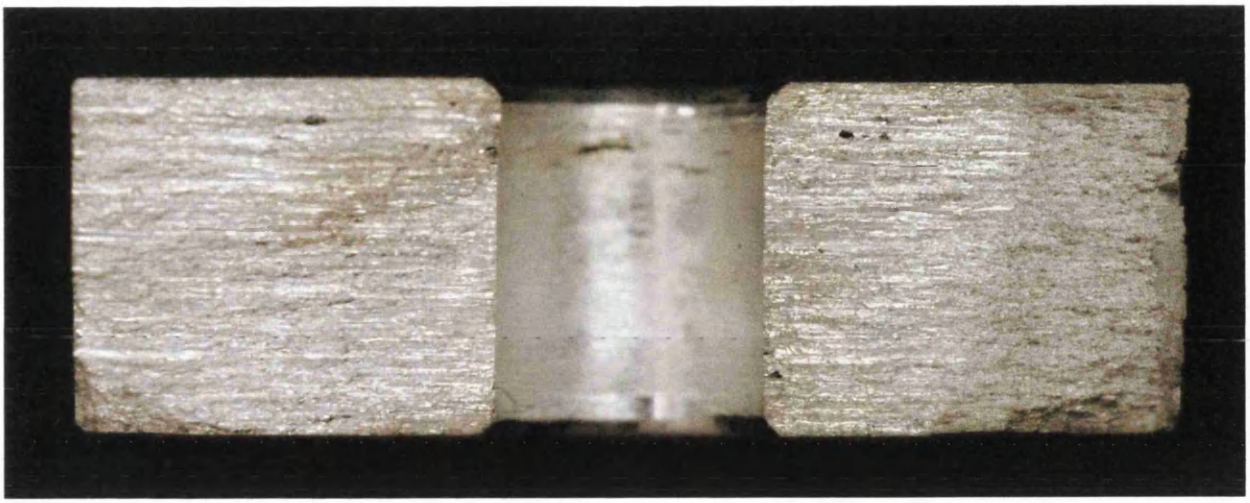

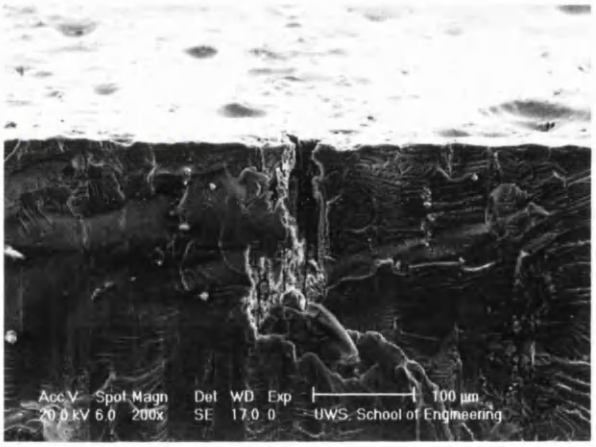
Acc.V Spot Magn Det WD Exp 100 µm
20.0 kV 6.0 200x SE 17.0 0 UWS, School of Engineering

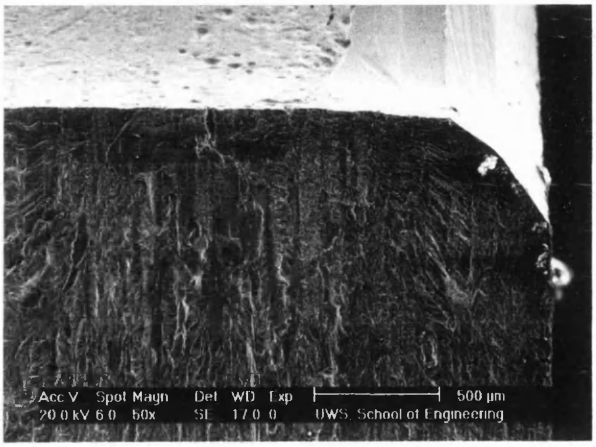
Acc.V Spot Magn Det WD Exp 500 µm
20.0 kV 6.0 50x SE 17.0 0 UWS, School of Engineering


Acc.V Spot Magn Det WD Exp 200 µm
20.0 kV 6.0 100x SE 15.9 0 UWS, School of Engineering

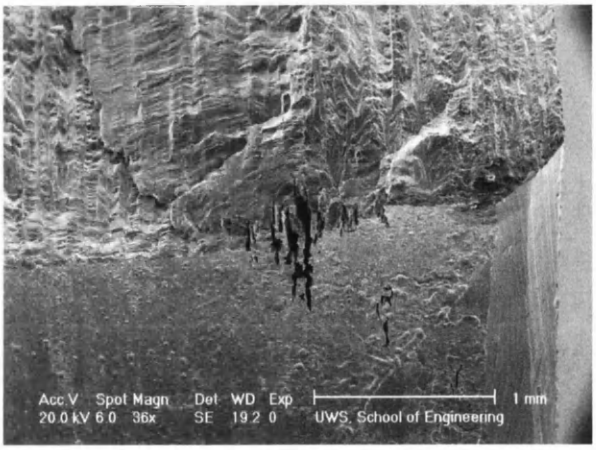
Acc.V Spot Magn Det WD Exp 1 mm
20.0 kV 6.0 36x SE 19.2 0 UWS, School of Engineering

FH-C8-8

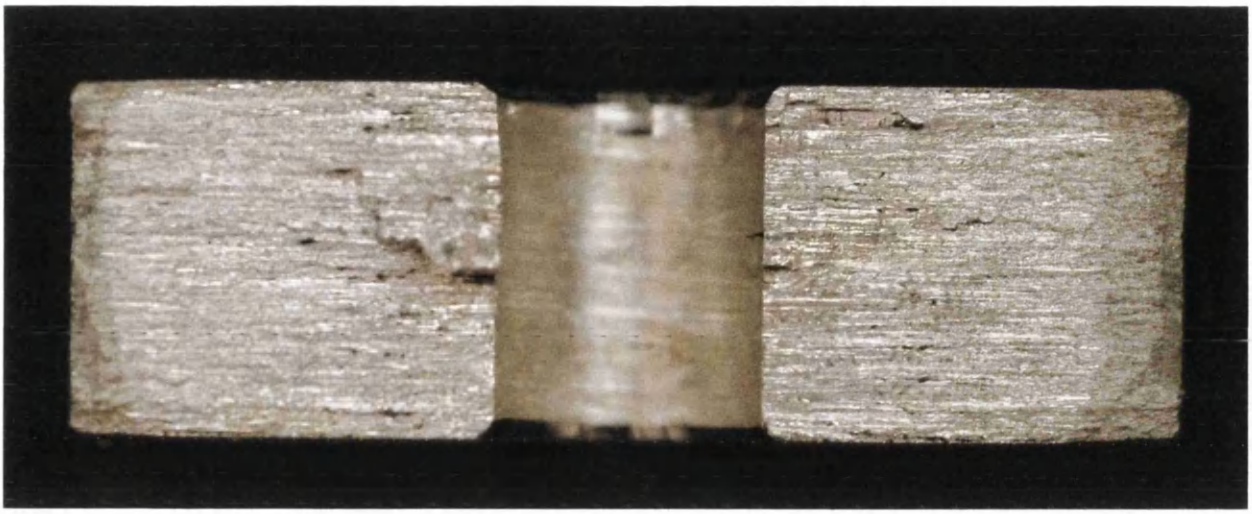

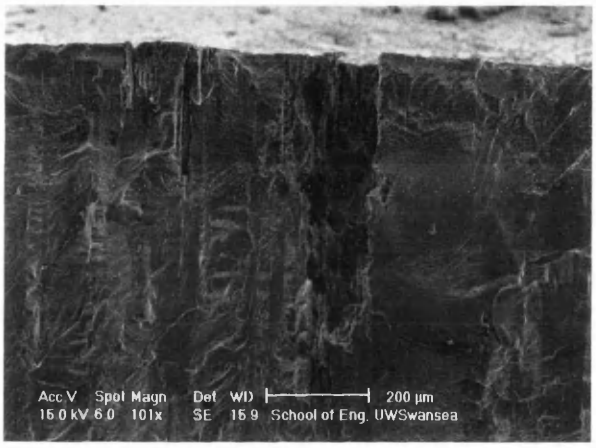
Acc.V Spot Magn Det WD 200 µm
15.0 kV 6.0 101x SE 15.9 School of Eng. UWSwansea

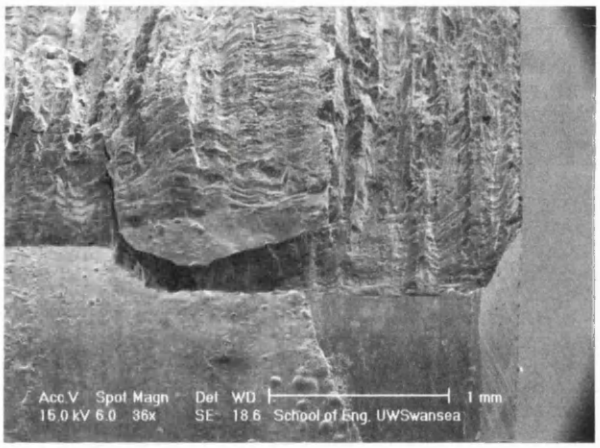
Acc.V Spot Magn Det WD 1 mm
15.0 kV 6.0 36x SE 18.6 School of Eng. UWSwansea

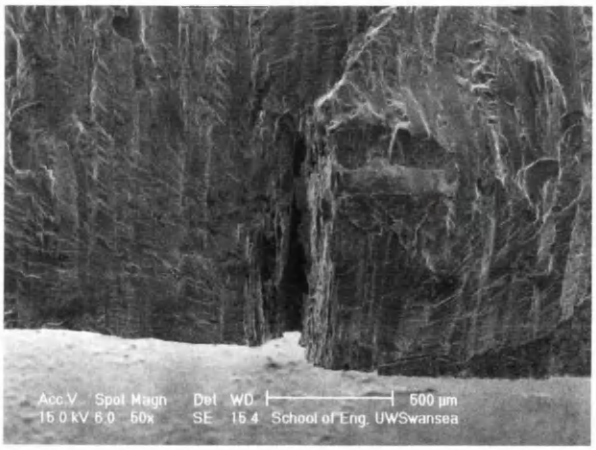
Acc.V Spot Magn Det WD 500 µm
15.0 kV 6.0 50x SE 15.4 School of Eng. UWSwansea

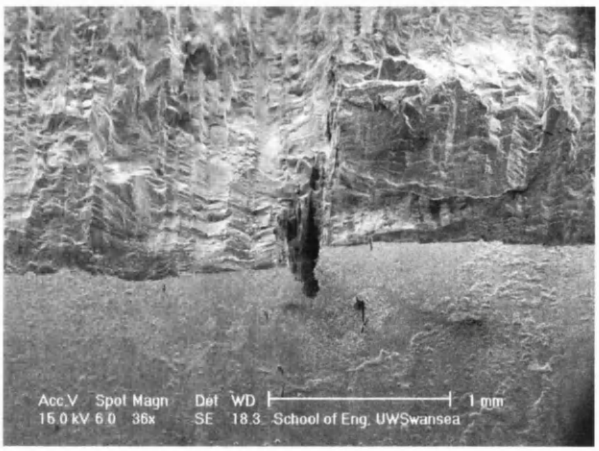
Acc.V Spot Magn Det WD 1 mm
15.0 kV 6.0 36x SE 18.3 School of Eng. UWSwansea

FH-C8-9

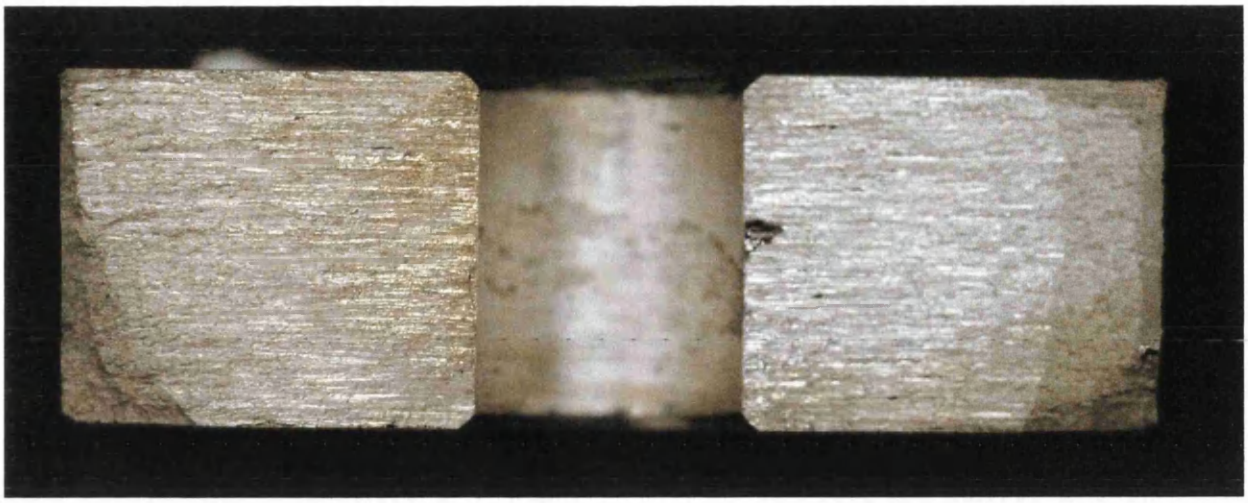

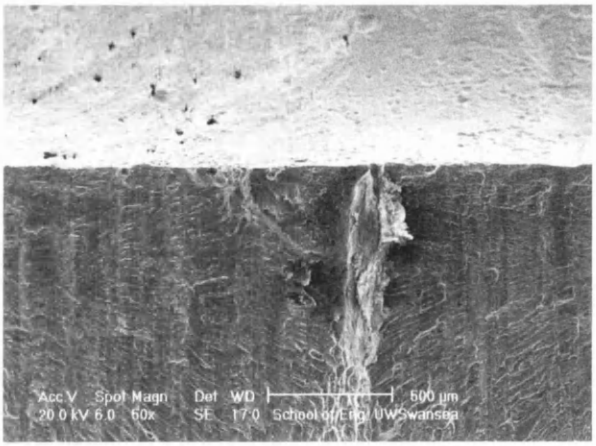
Acc.V Spot Magn Det WD 500 µm
20.0 kV 6.0 60x SE 17.0 School of Eng. UWSwansea

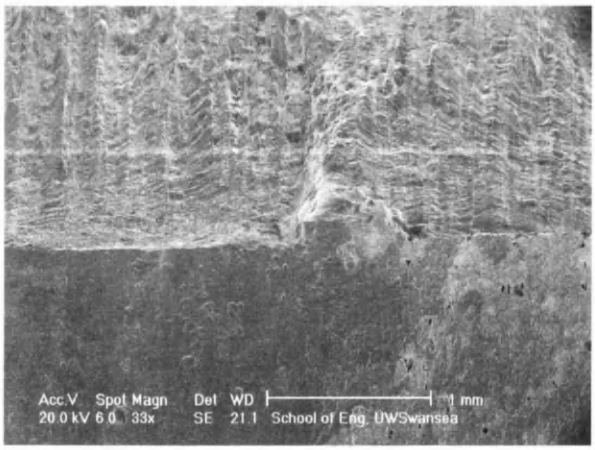
Acc.V Spot Magn Det WD 1 mm
20.0 kV 6.0 33x SE 21.1 School of Eng. UWSwansea

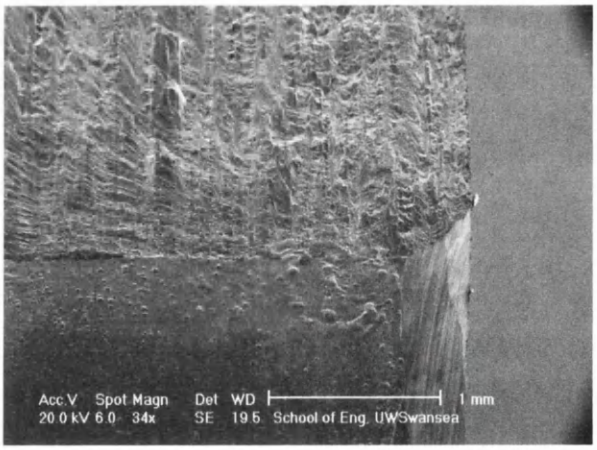
Acc.V Spot Magn Det WD 1 mm
20.0 kV 6.0 34x SE 19.5 School of Eng. UWSwansea

FH-C8-10

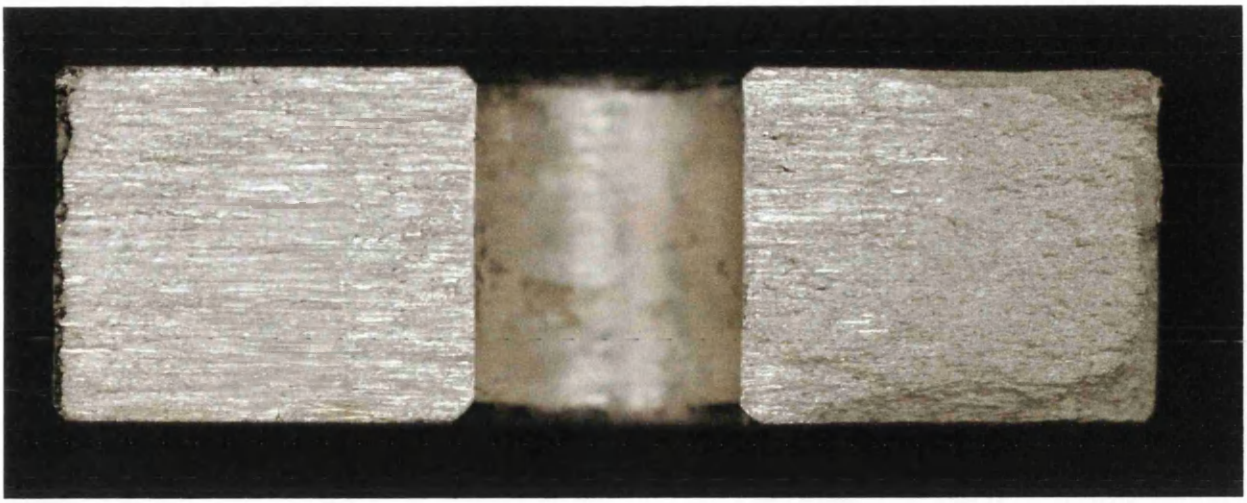

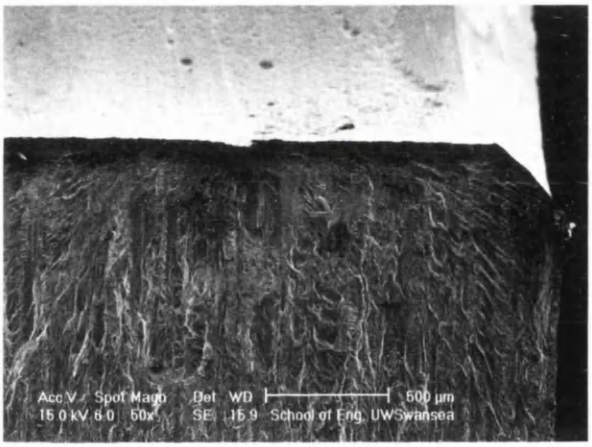
Acc.V Spot Magn Det WD 500 µm
15.0 kV 6.0 50x SE 15.9 School of Eng, UWSwansea

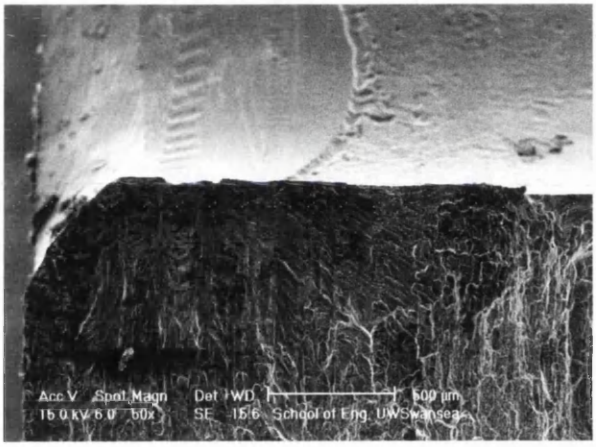
Acc.V Spot Magn Det WD 500 µm
15.0 kV 6.0 50x SE 15.6 School of Eng, UWSwansea

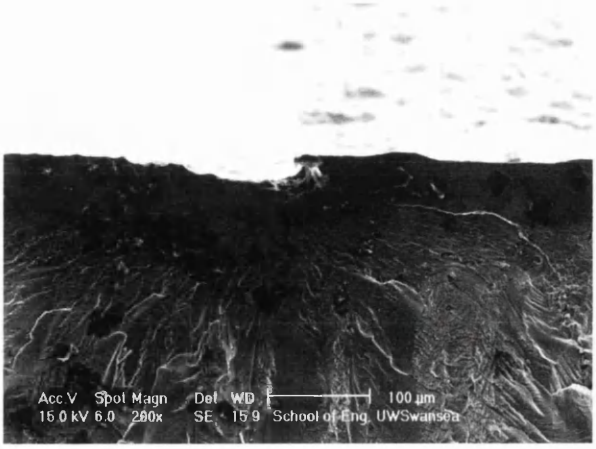
Acc.V Spot Magn Det WD 100 µm
15.0 kV 6.0 200x SE 15.9 School of Eng, UWSwansea

FH-C8-11

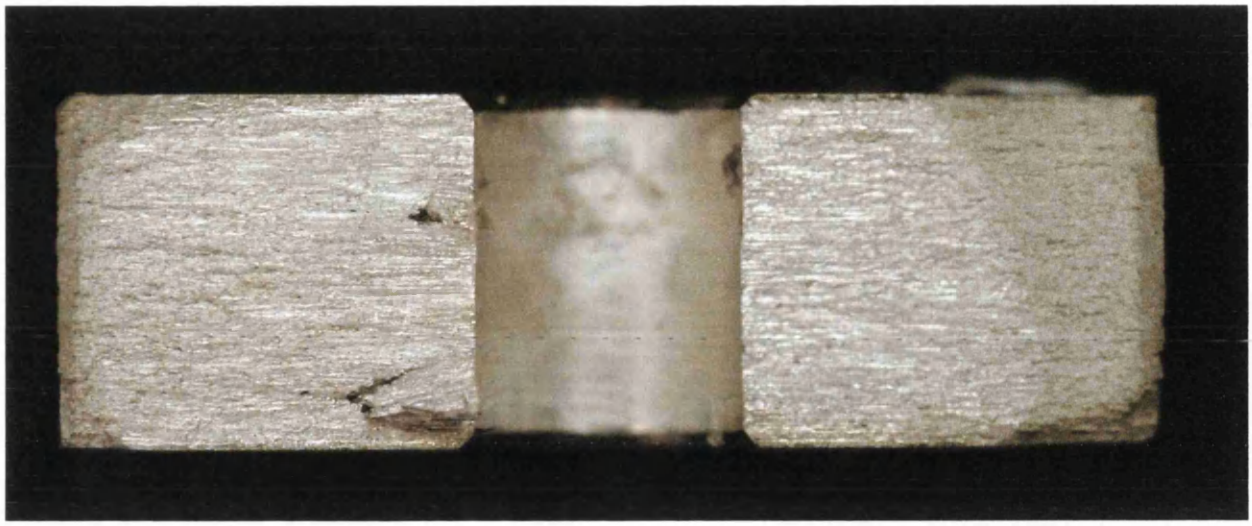

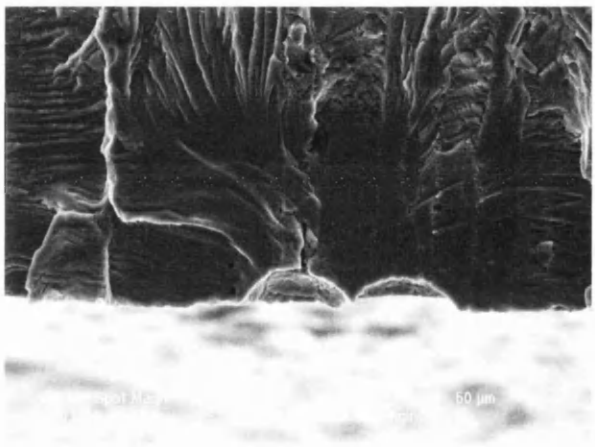

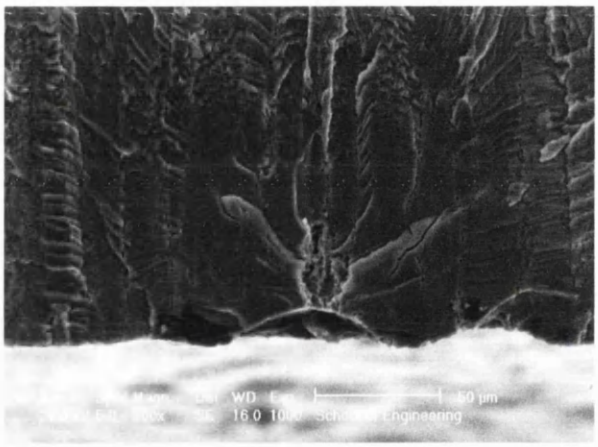

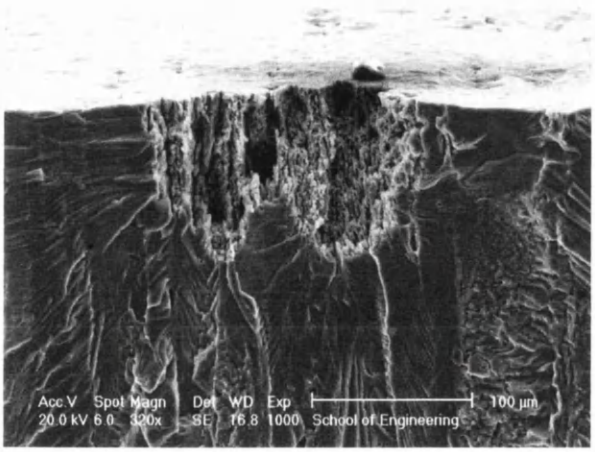
Acc.V Spot Magn Det WD Exp 100 µm
20.0 kV 6.0 320x SE 16.8 1000 School of Engineering

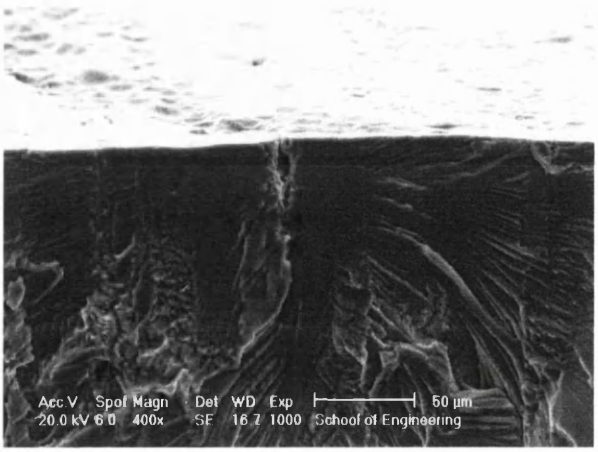
Acc.V Spot Magn Det WD Exp 50 µm
20.0 kV 6.0 400x SE 16.7 1000 School of Engineering

FH-C8-12

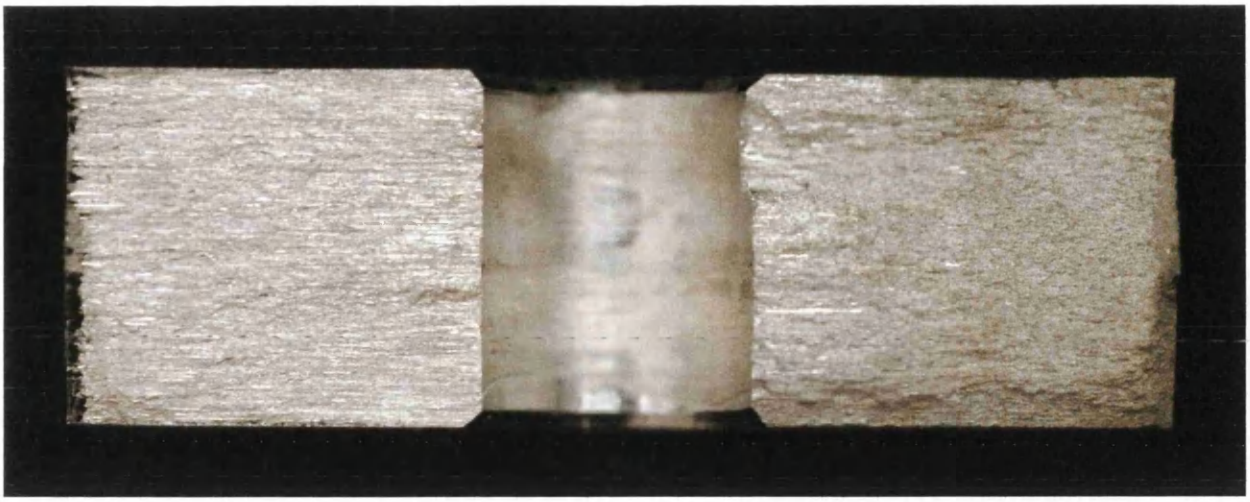


Acc.V Spot Magn Det WD Exp 500 µm
20.0 kV 6.0 48x SE 16.6 1000 School of Engineering

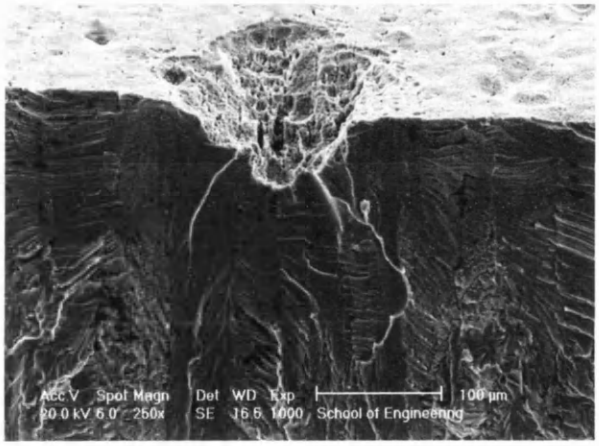
Acc.V Spot Magn Det WD Exp 100 µm
20.0 kV 6.0 250x SE 16.6 1000 School of Engineering

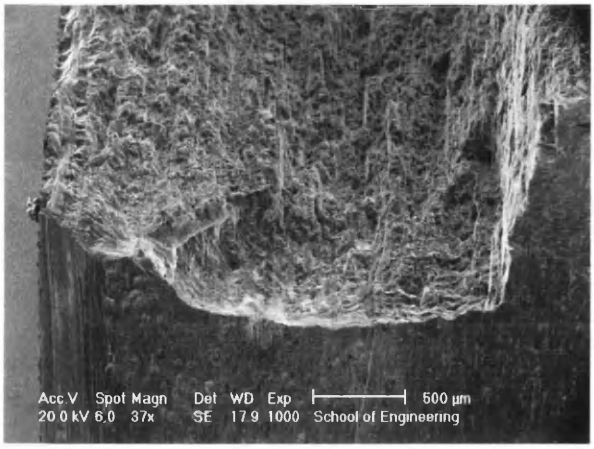
Acc.V Spot Magn Det WD Exp 500 µm
20.0 kV 6.0 37x SE 17.9 1000 School of Engineering

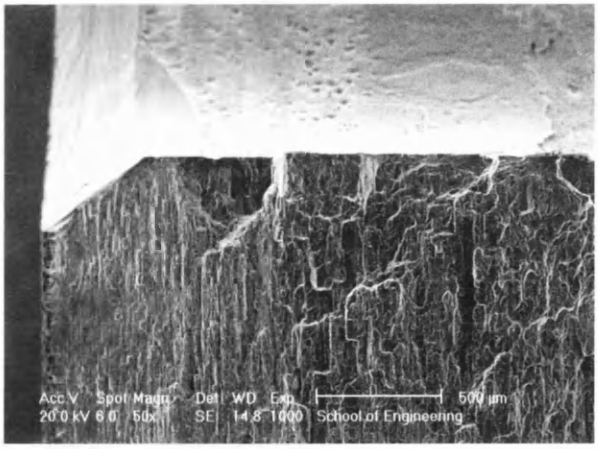
Acc.V Spot Magn Det WD Exp 500 µm
20.0 kV 6.0 50x SE 14.8 1000 School of Engineering

FH-C8-13

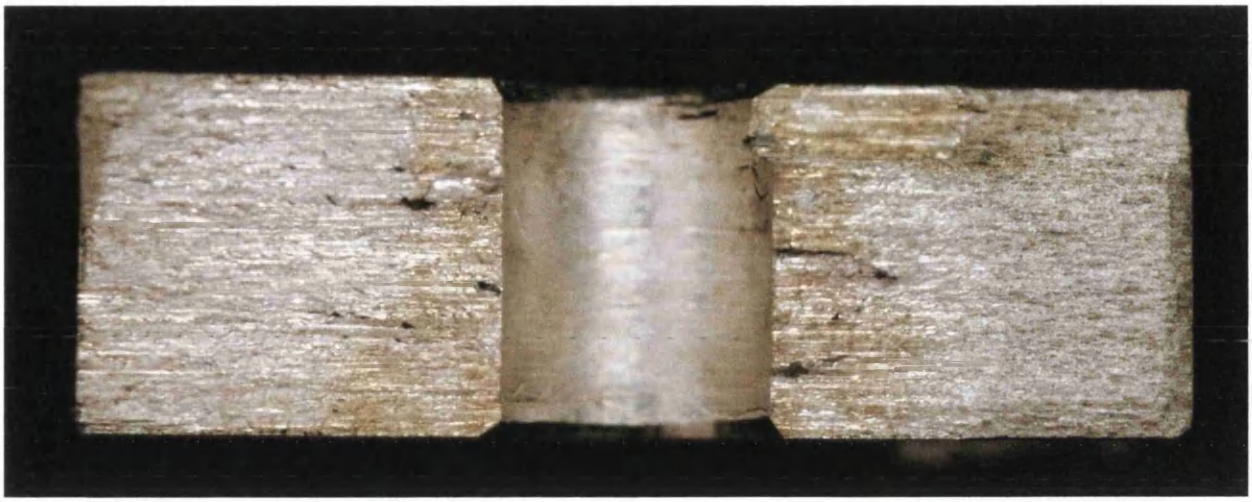

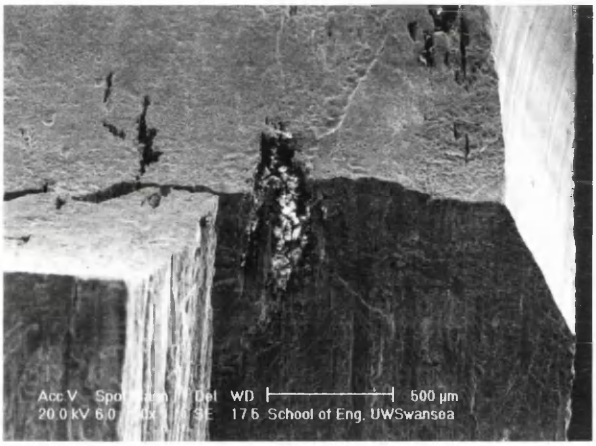
Acc.V Spot Magn Det WD 500 µm
20.0 kV 6.0 SE 17.6 School of Eng. UWSwansea

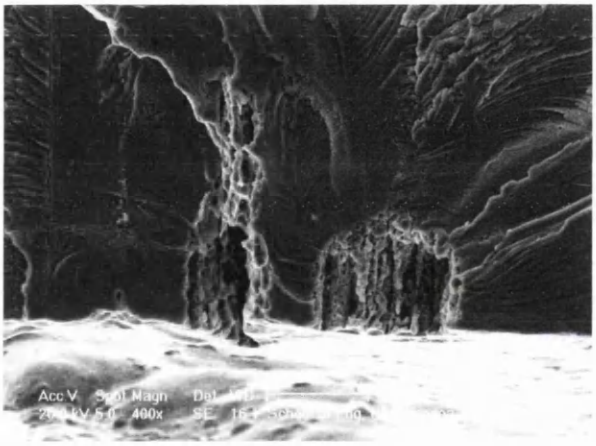
Acc.V Spot Magn Det WD

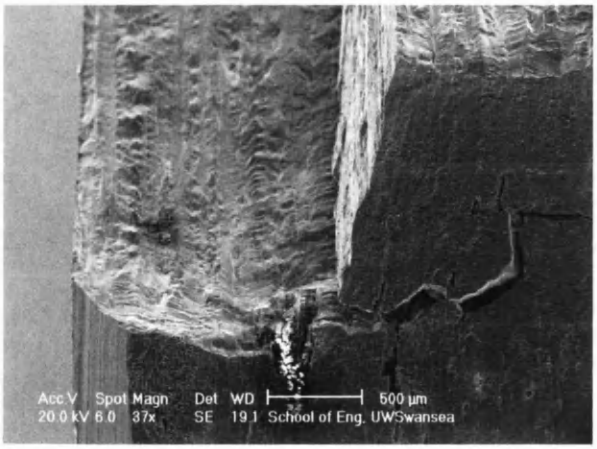
Acc.V Spot Magn Det WD 500 µm
20.0 kV 6.0 37x SE 19.1 School of Eng. UWSwansea

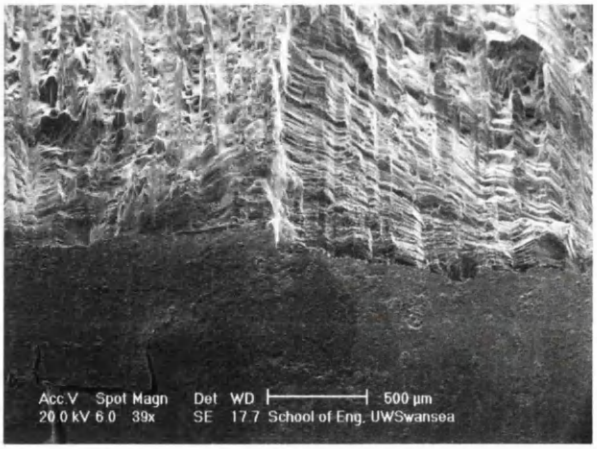
Acc.V Spot Magn Det WD 500 µm
20.0 kV 6.0 39x SE 17.7 School of Eng. UWSwansea

FH-C8-14

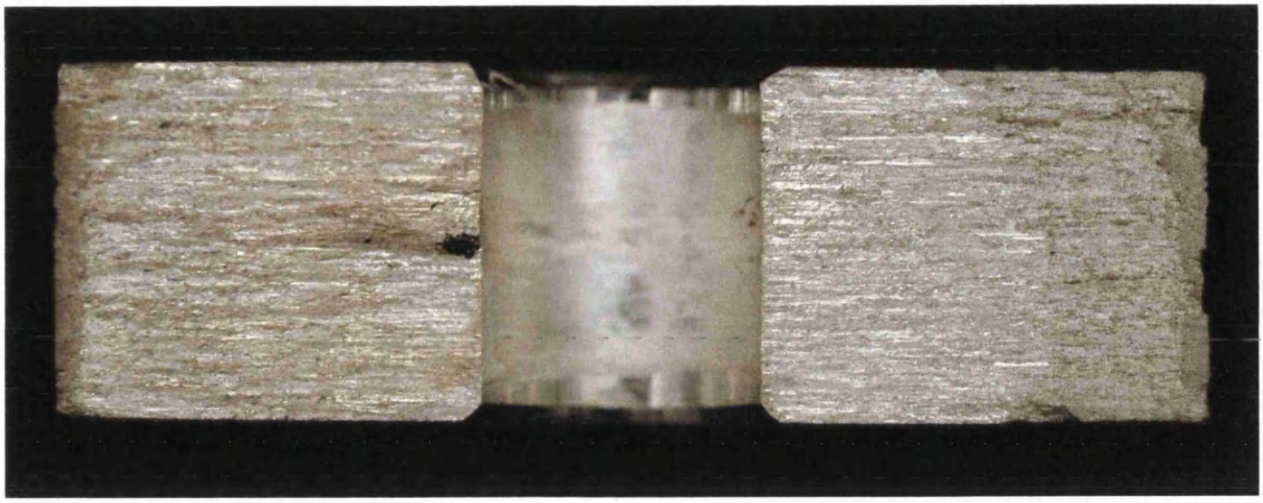

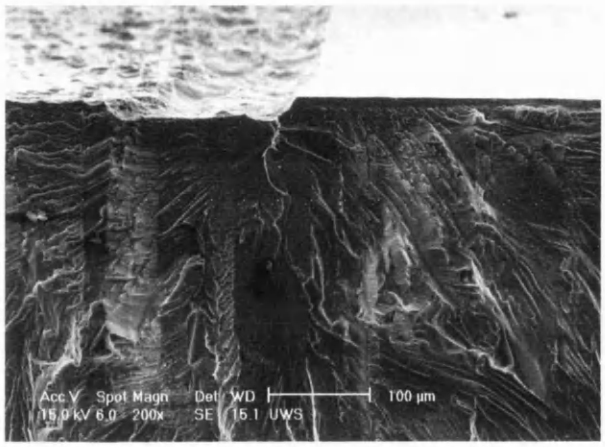
Acc.V Spot Magn Det WD 100 µm
15.0 kV 6.0 200x SE 15.1 UWS

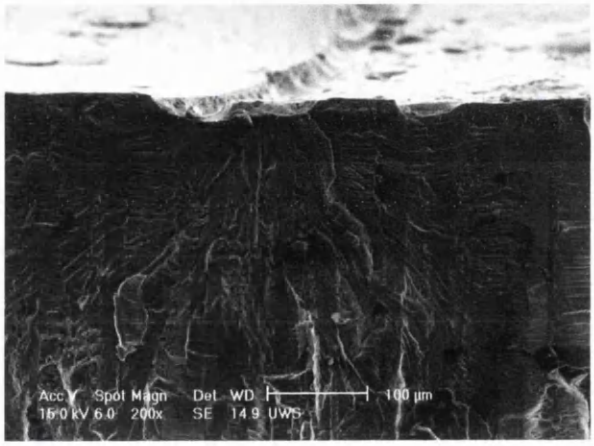
Acc.V Spot Magn Det WD 100 µm
15.0 kV 6.0 200x SE 14.9 UWS

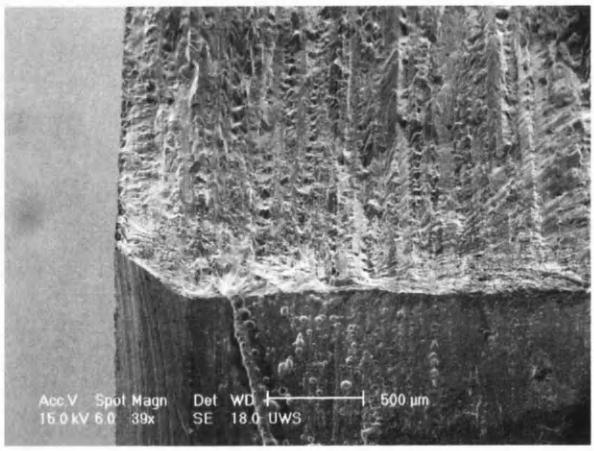
Acc.V Spot Magn Det WD 500 µm
15.0 kV 6.0 39x SE 18.0 UWS

FH-C8-15

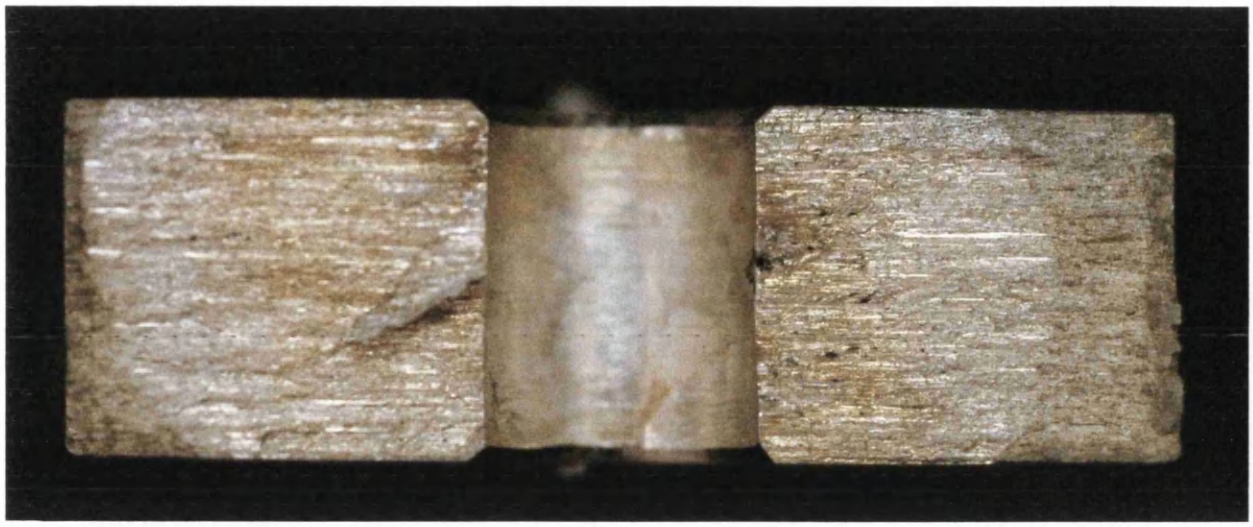

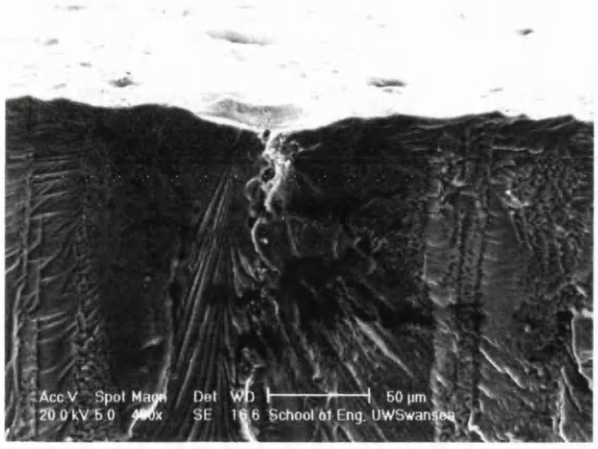
Acc.V Spot Magn Det WD 50 µm
20.0 kV 5.0 400x SE 16.6 School of Eng. UWSwansea

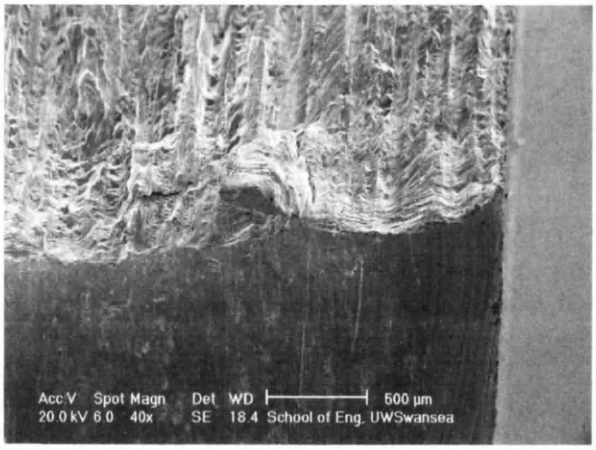
Acc.V Spot Magn Det WD 500 µm
20.0 kV 6.0 40x SE 18.4 School of Eng. UWSwansea

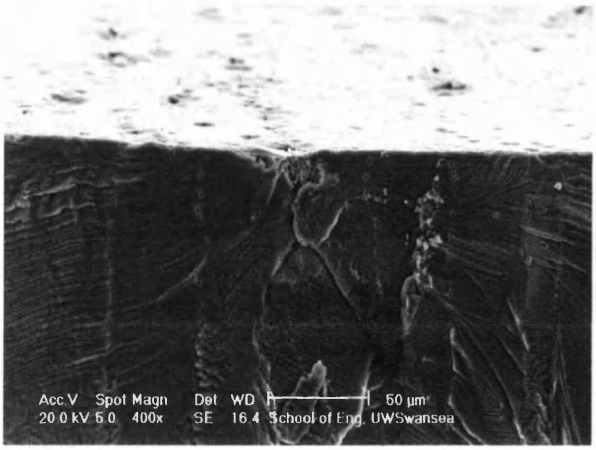
Acc.V Spot Magn Det WD 50 µm
20.0 kV 5.0 400x SE 16.4 School of Eng. UWSwansea

FH-C8-16

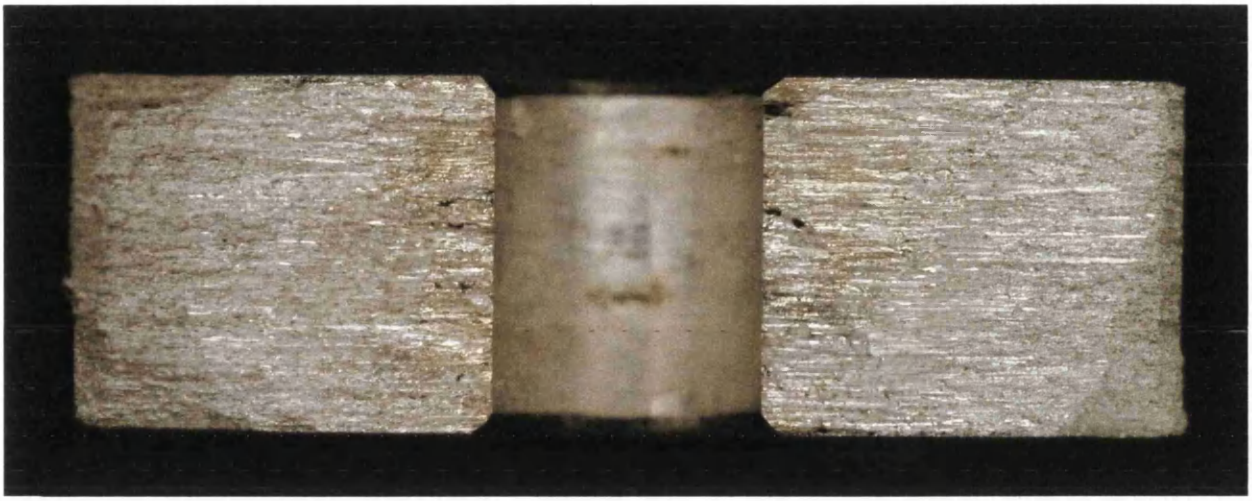

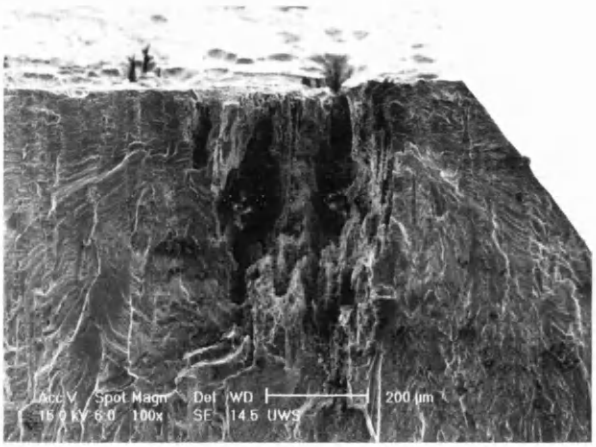
Acc.V Spot Magn Det WD 200 µm
15.0 kV 6.0 100x SE 14.5 UWS

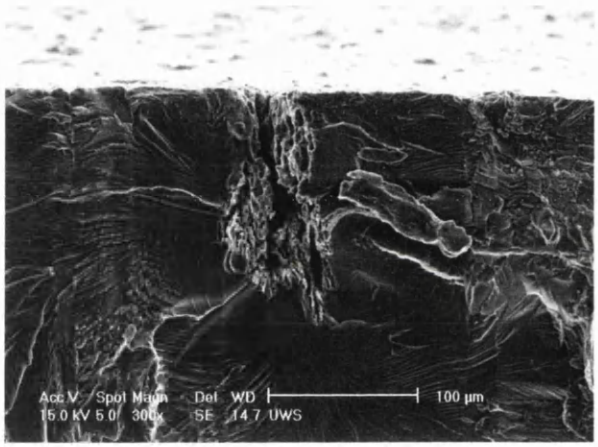
Acc.V Spot Magn Det WD 100 µm
15.0 kV 6.0 300x SE 14.7 UWS

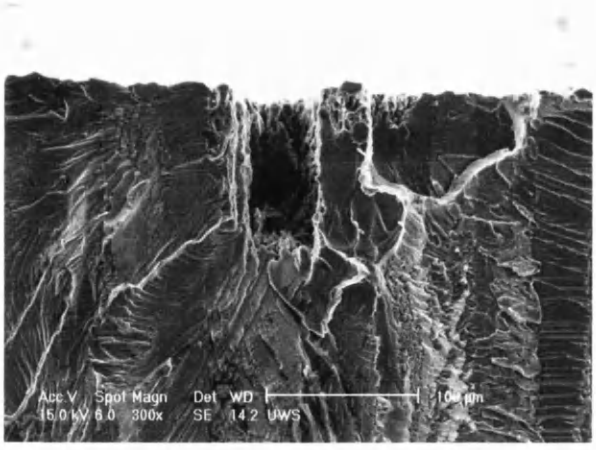
Acc.V Spot Magn Det WD 100 µm
15.0 kV 6.0 300x SE 14.2 UWS

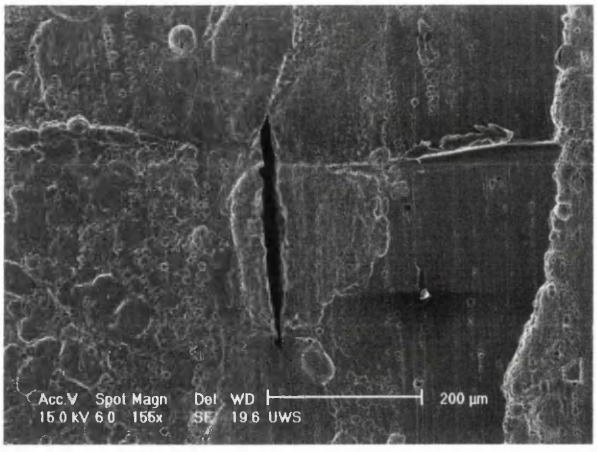
Acc.V Spot Magn Det WD 200 µm
15.0 kV 6.0 155x SE 19.6 UWS

FH-C8-17

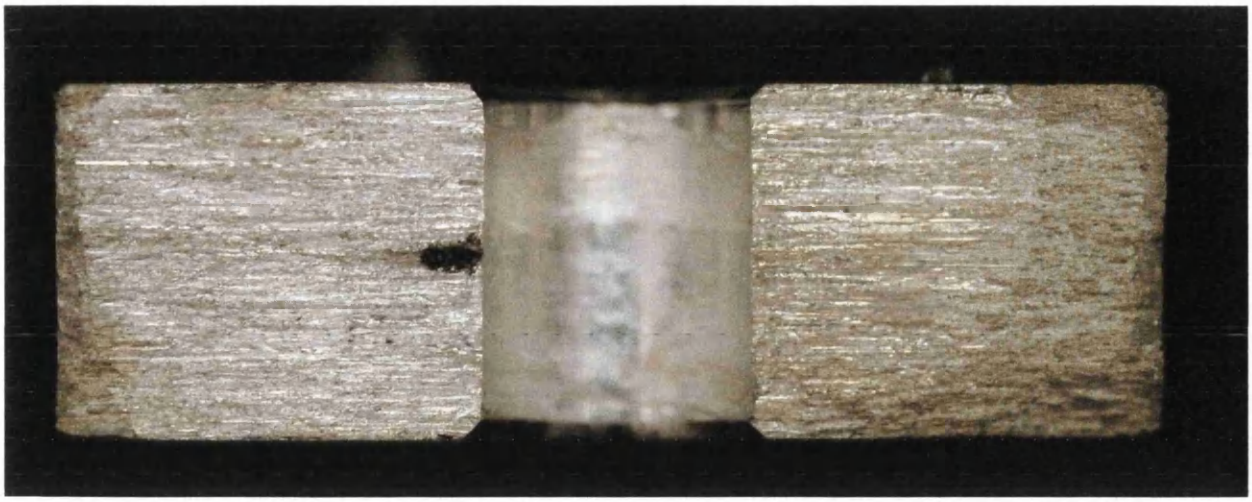

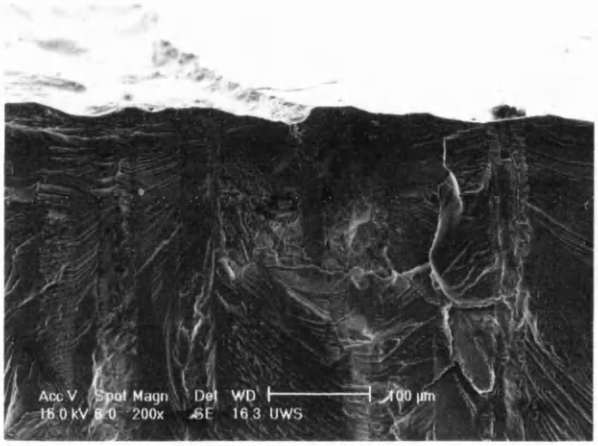
Acc.V Spot Magn Det WD 100 µm
15.0 kV 6.0 200x SE 16.3 UWS

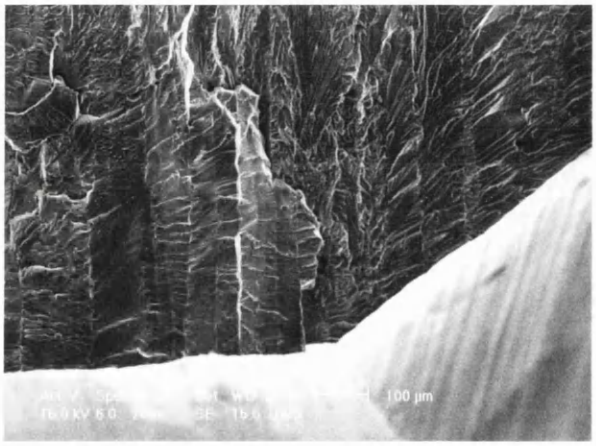
100 µm

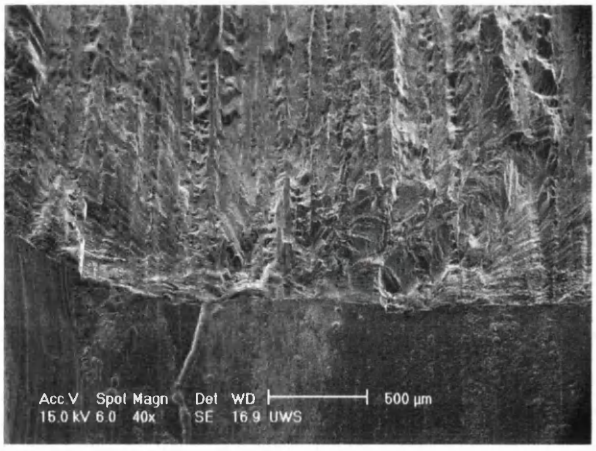
Acc.V Spot Magn Det WD 500 µm
15.0 kV 6.0 40x SE 16.9 UWS

FH-C8-18

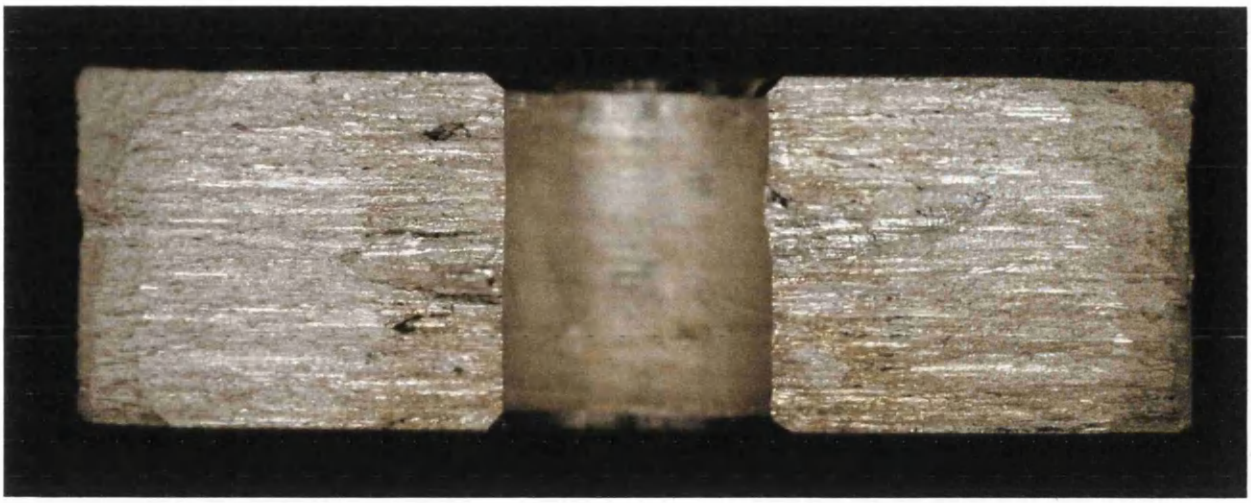

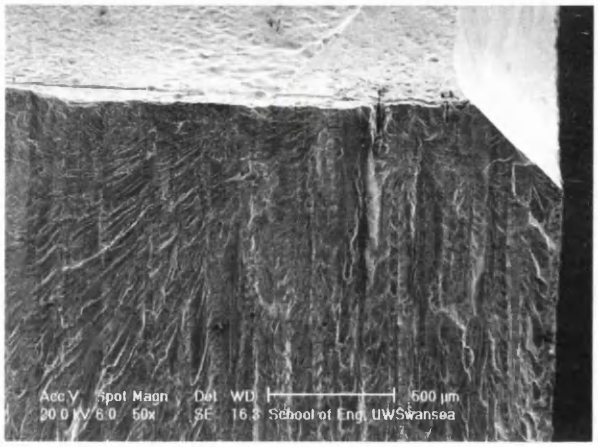
Acc.V Spot Magn Det WD 500 µm
20.0 kV 6.0 50x SE 16.3 School of Eng, UWSwansea

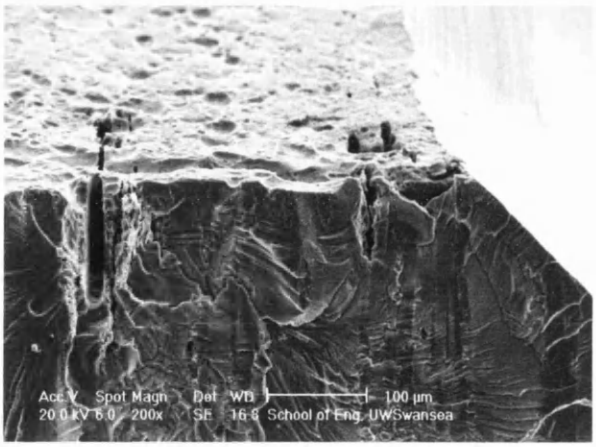
Acc.V Spot Magn Det WD 100 µm
20.0 kV 6.0 200x SE 16.8 School of Eng, UWSwansea

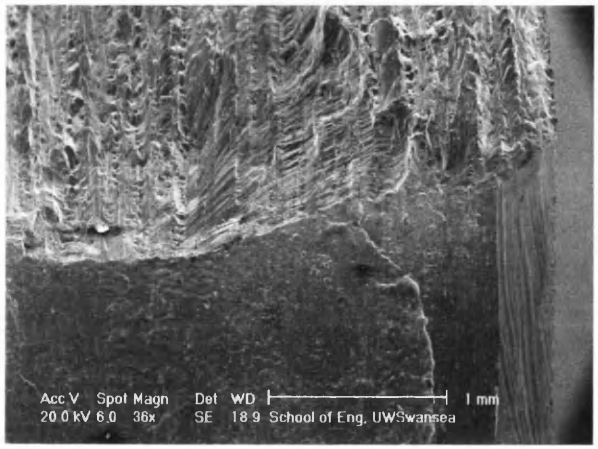
Acc.V Spot Magn Det WD 1 mm
20.0 kV 6.0 36x SE 18.9 School of Eng, UWSwansea

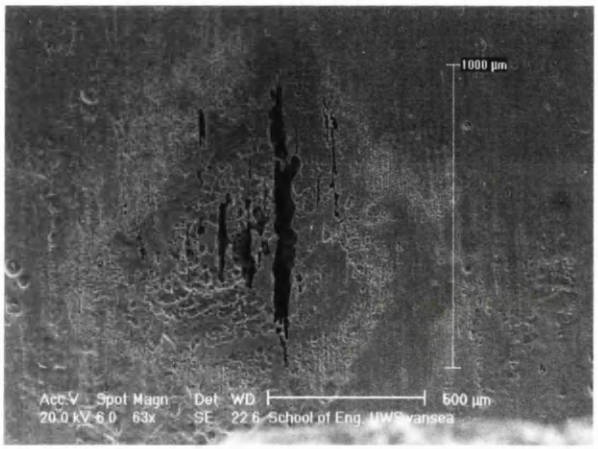
1000 µm
Acc.V Spot Magn Det WD 500 µm
20.0 kV 6.0 63x SE 22.6 School of Eng, UWSwansea

FH-C8-19

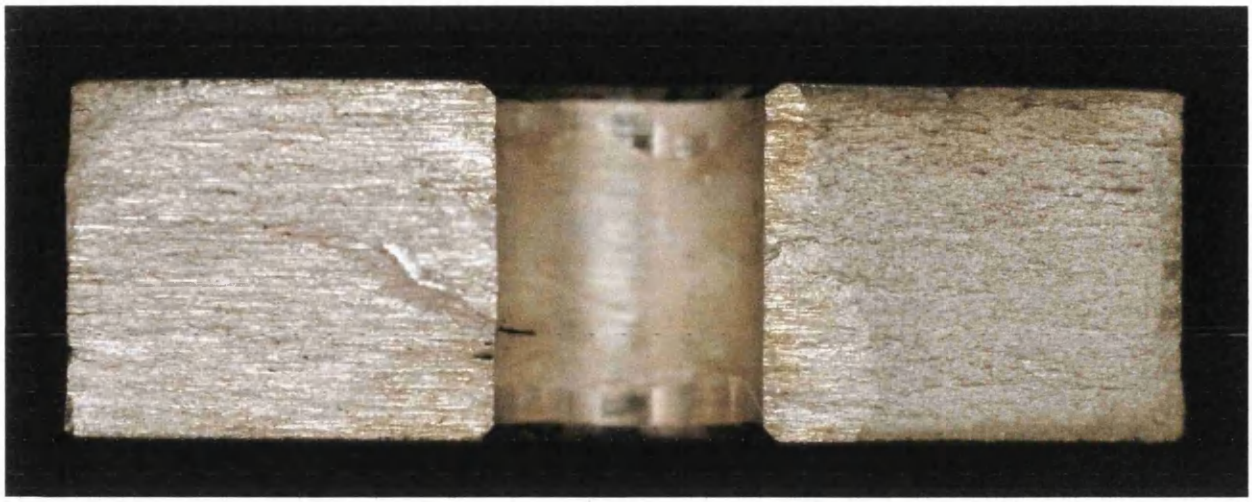

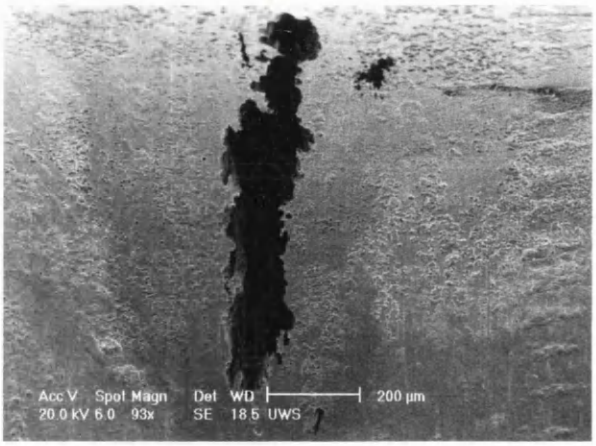
Acc.V Spot Magn Det WD 200 µm
20.0 kV 6.0 93x SE 18.5 UWS

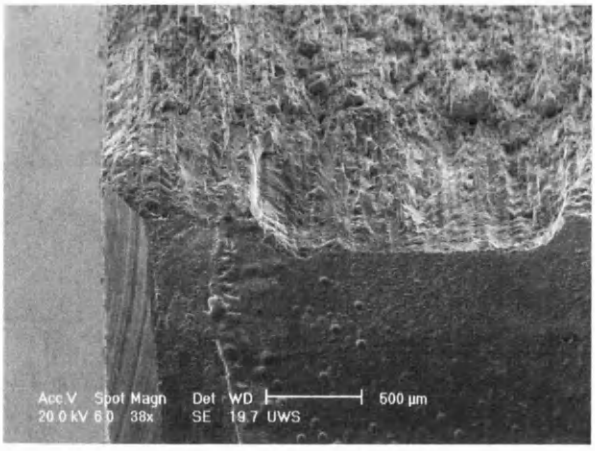
Acc.V Spot Magn Det WD 500 µm
20.0 kV 6.0 38x SE 19.7 UWS

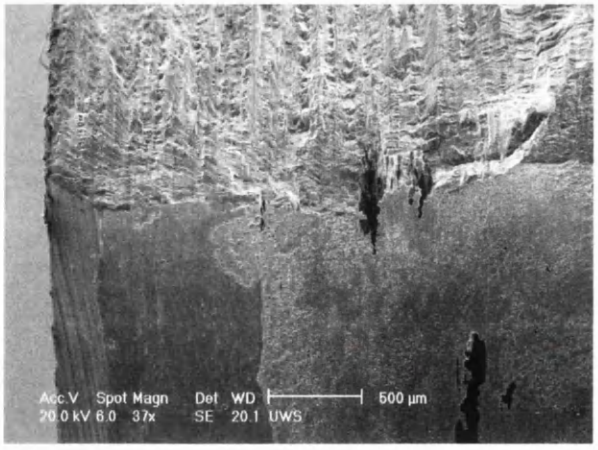
Acc.V Spot Magn Det WD 500 µm
20.0 kV 6.0 37x SE 20.1 UWS

FH-C8-20

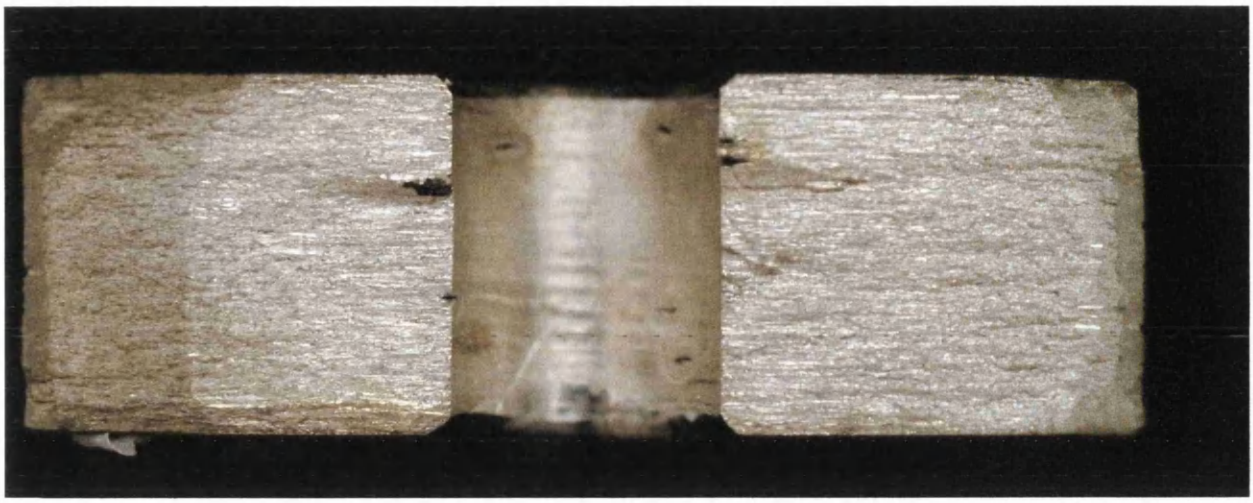

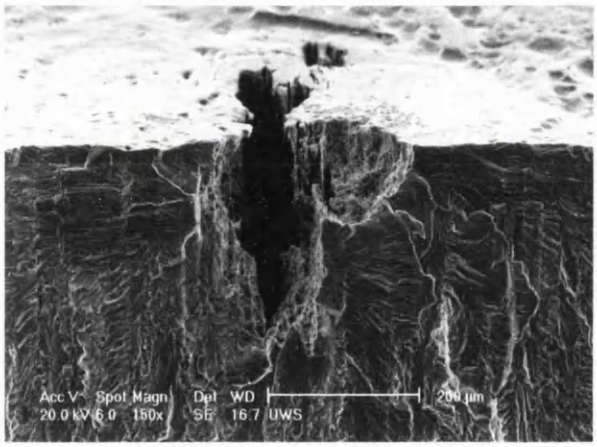
Acc.V Spot Magn Det WD 200 µm
20.0 kV 6.0 150x SE 16.7 UWS

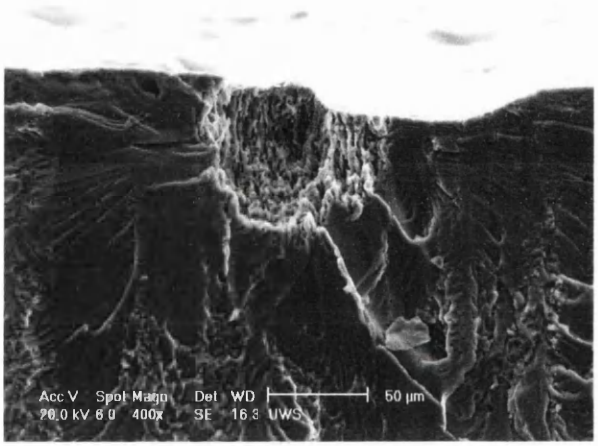
Acc.V Spot Magn Det WD 50 µm
20.0 kV 6.0 400x SE 16.3 UWS

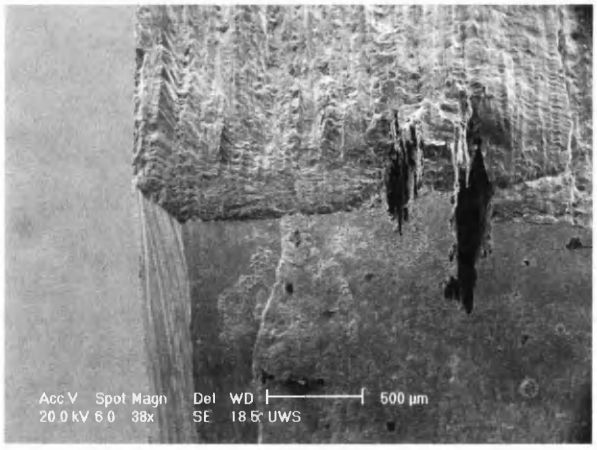
Acc.V Spot Magn Det WD 500 µm
20.0 kV 6.0 38x SE 18.5 UWS

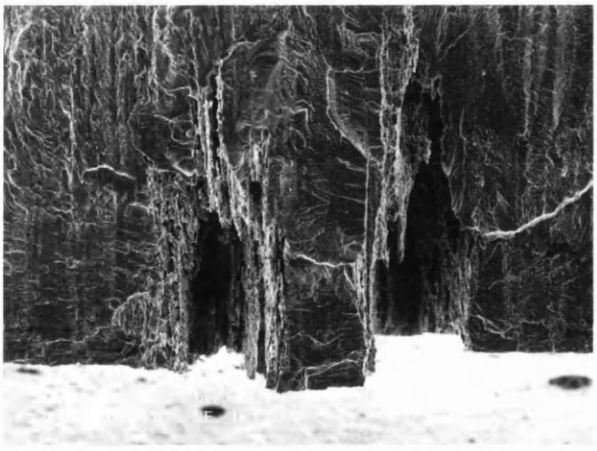

FH-C8-21

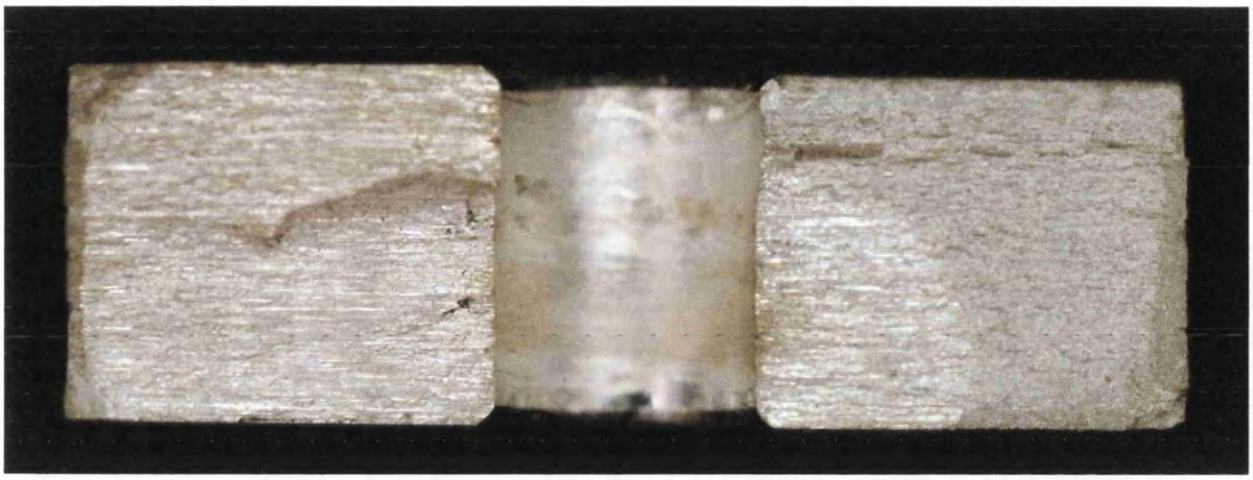


Acc.V Spot Magn Det WD 500 µm
20.0 kV 6.0 50x SE 16.3 School of Engineering, UWSwansea

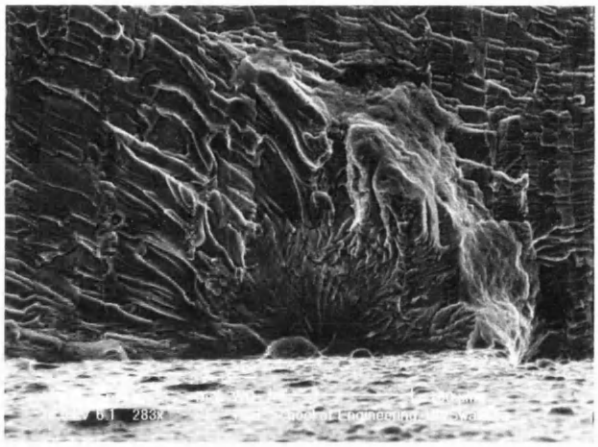

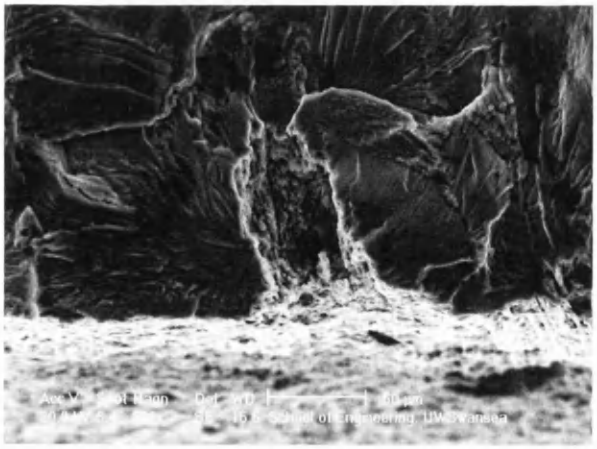

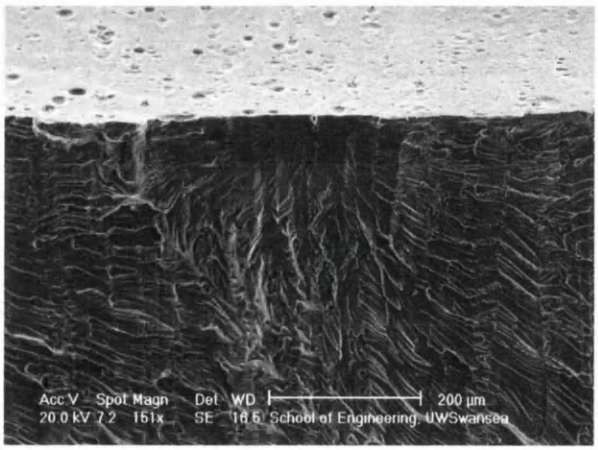
Acc.V Spot Magn Det WD 200 µm
20.0 kV 7.2 151x SE 16.5 School of Engineering, UWSwansea

FH-C8-22

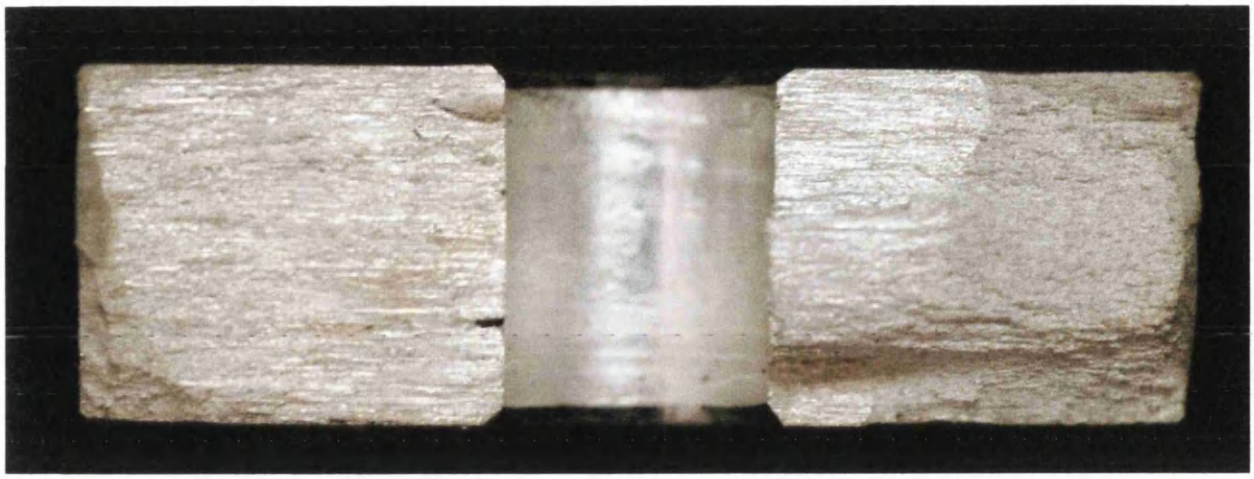

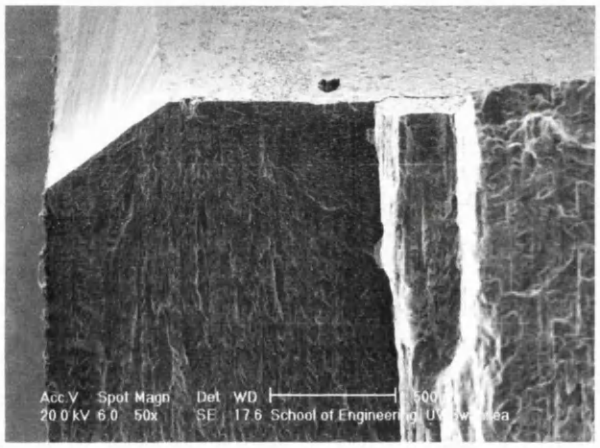
Acc.V Spot Magn Det WD
20.0 kV 6.0 50x SE 17.6 School of Engineering, UWSwansea

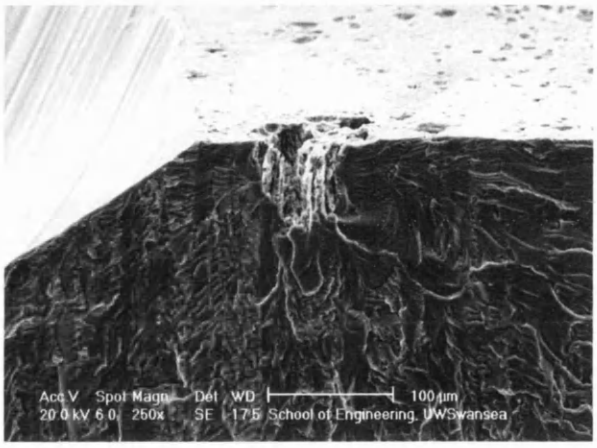
Acc.V Spot Magn Det WD 100 µm
20.0 kV 6.0 250x SE 17.5 School of Engineering, UWSwansea

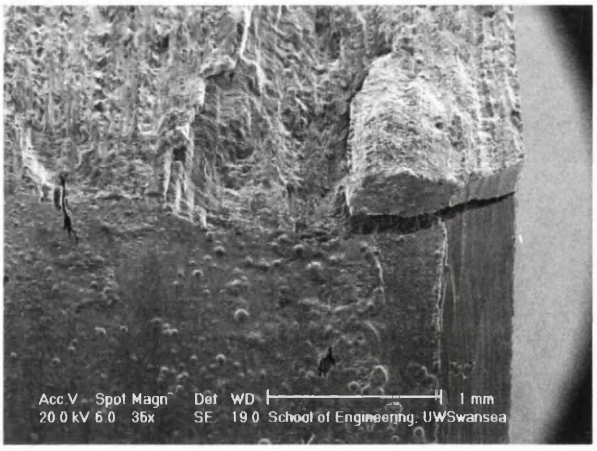
Acc.V Spot Magn Det WD 1 mm
20.0 kV 6.0 35x SE 19.0 School of Engineering, UWSwansea

FH-C8-23

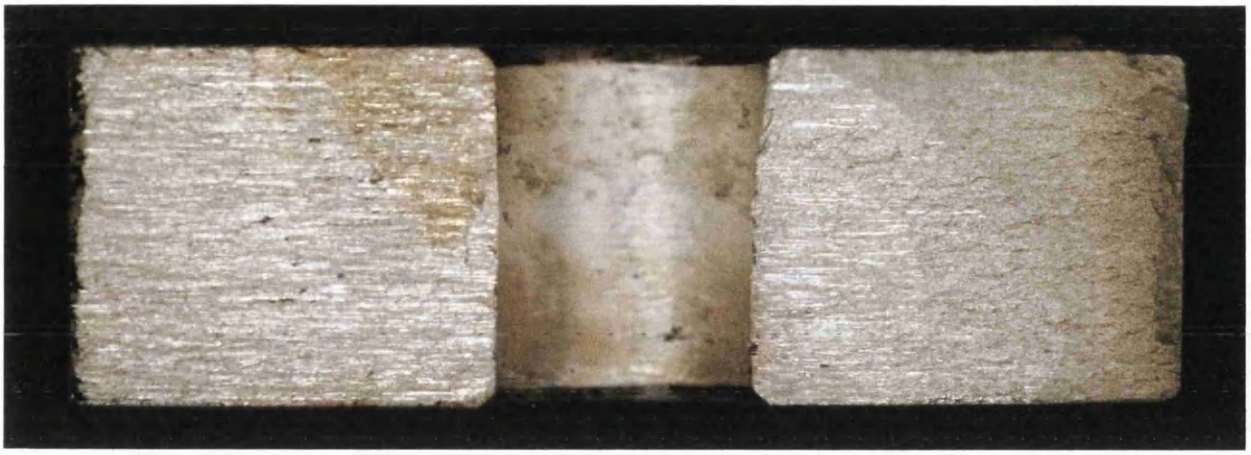

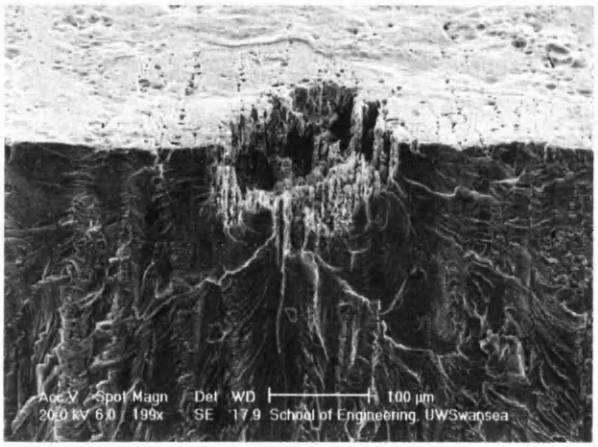
Acc.V Spot Magn Det WD 100 µm
20.0 kV 6.0 199x SE 17.9 School of Engineering, UWSwansea

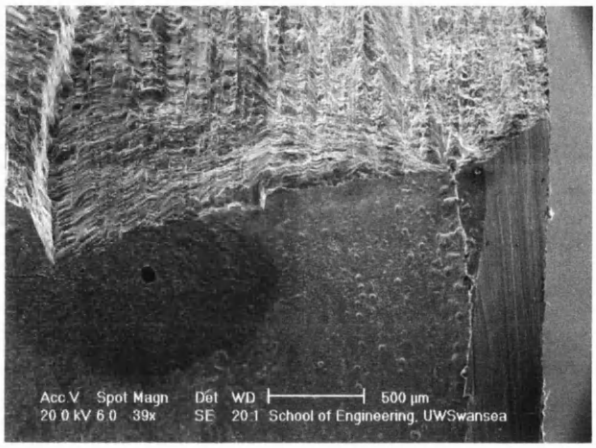
Acc.V Spot Magn Det WD 500 µm
20.0 kV 6.0 39x SE 20.1 School of Engineering, UWSwansea

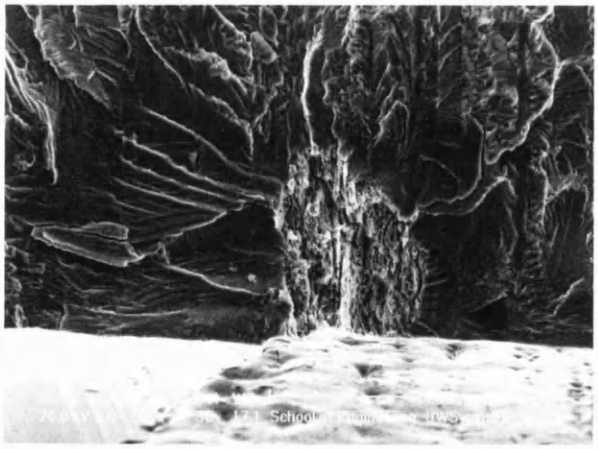

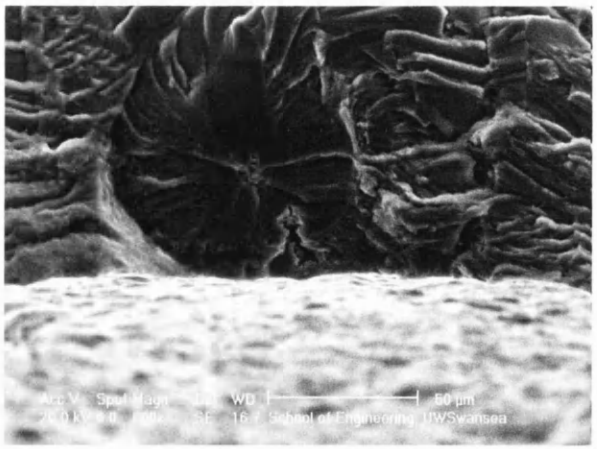
50 µm

FH-C8-24

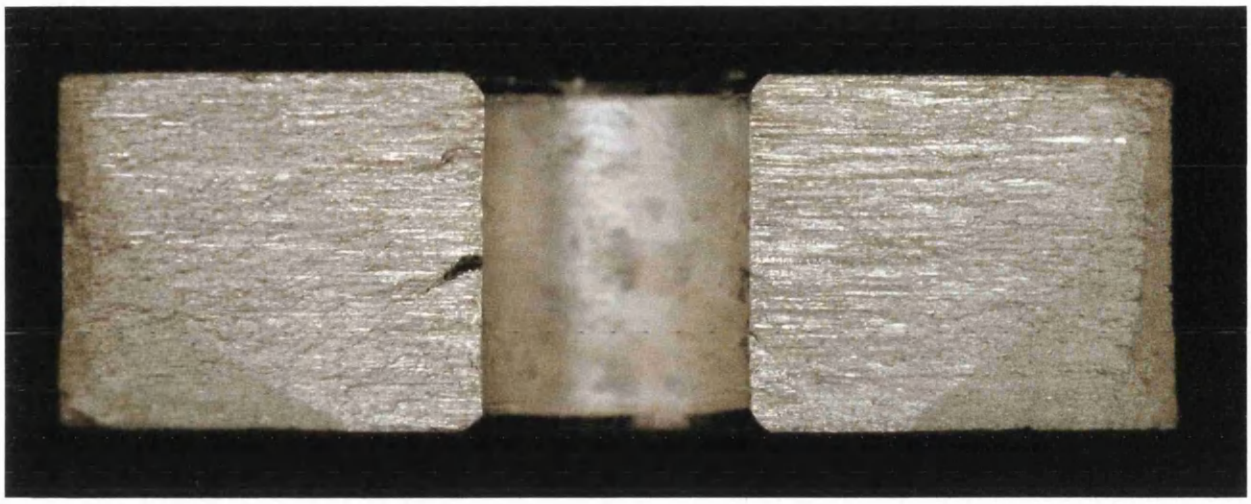

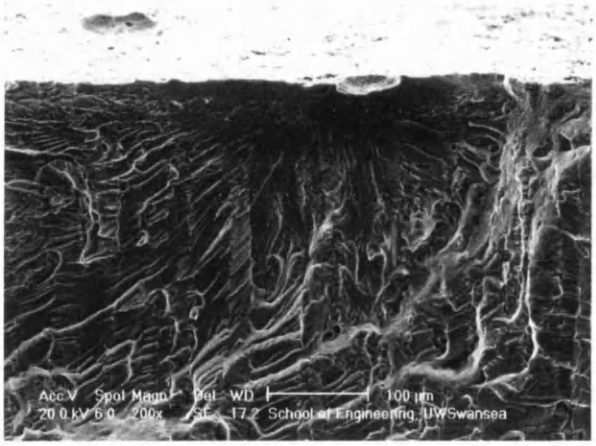
Acc.V Spot Magn Det WD 100 µm
20.0 kV 6.0 200x SE 17.2 School of Engineering, UWSwansea

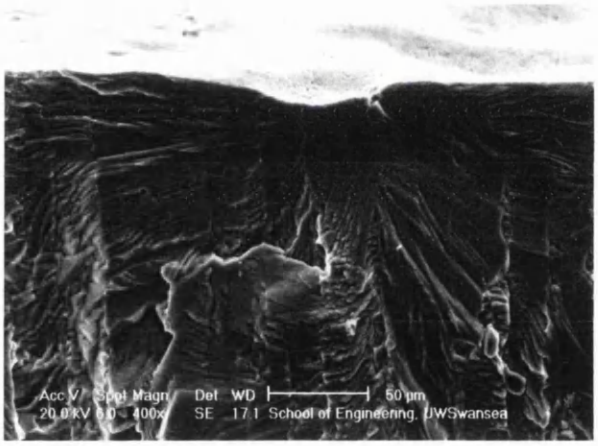
Acc.V Spot Magn Det WD 50 µm
20.0 kV 6.0 400x SE 17.1 School of Engineering, UWSwansea

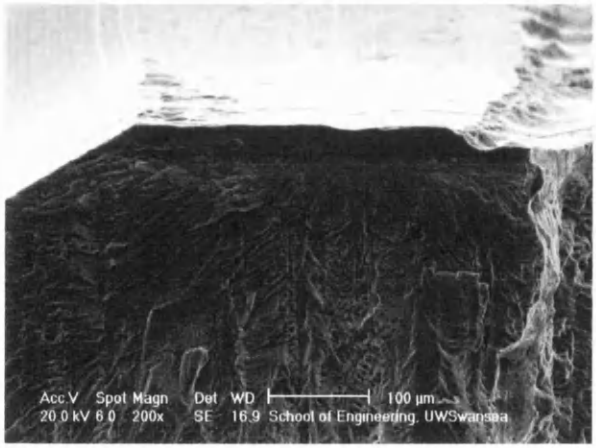
Acc.V Spot Magn Det WD 100 µm
20.0 kV 6.0 200x SE 16.9 School of Engineering, UWSwansea

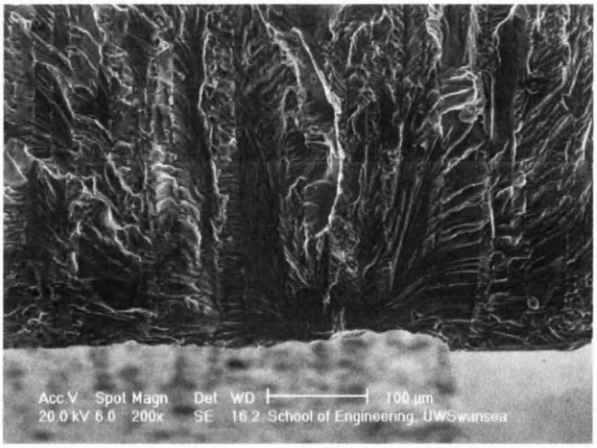
Acc.V Spot Magn Det WD 100 µm
20.0 kV 6.0 200x SE 16.2 School of Engineering, UWSwansea

FH-C8-25

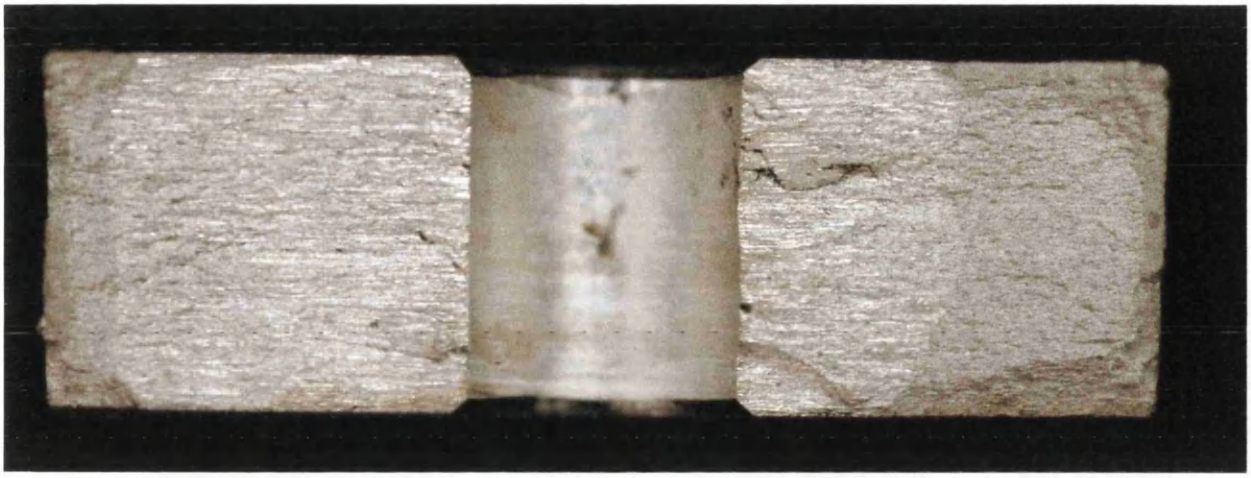

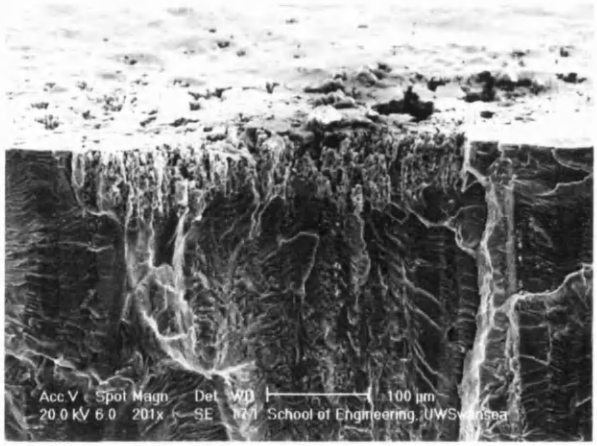
Acc.V Spot Magn Det WD 100 µm
20.0 kV 6.0 201x SE 14.1 School of Engineering, UWSwansea

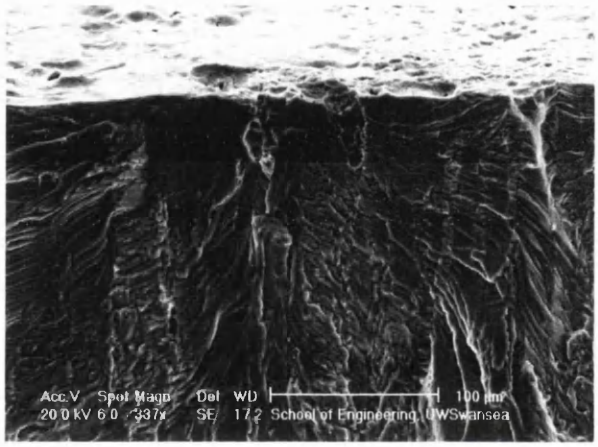
Acc.V Spot Magn Det WD 100 µm
20.0 kV 6.0 337x SE 17.2 School of Engineering, UWSwansea

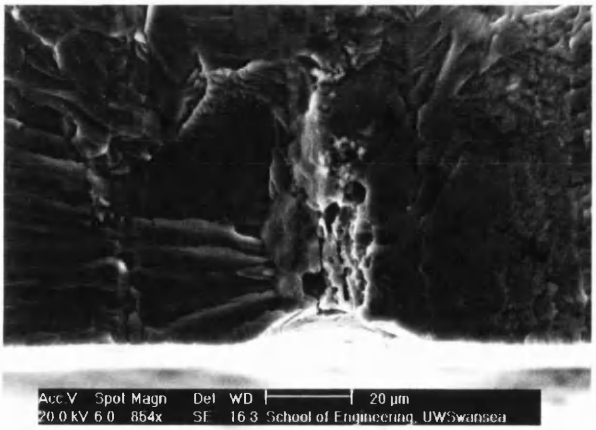
Acc.V Spot Magn Det WD 20 µm
20.0 kV 6.0 854x SE 16.3 School of Engineering, UWSwansea

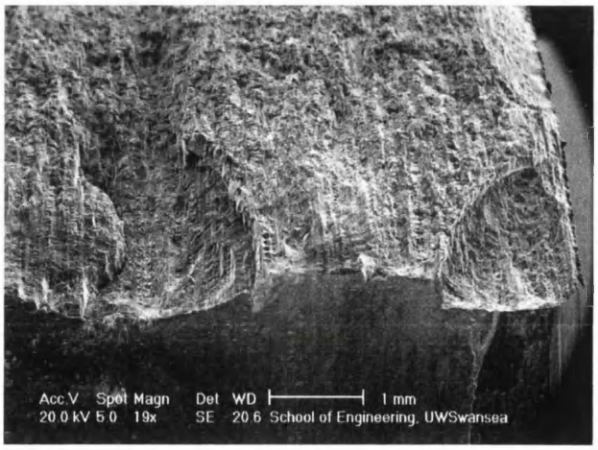
Acc.V Spot Magn Det WD 1 mm
20.0 kV 5.0 19x SE 20.6 School of Engineering, UWSwansea

FH-C8-26

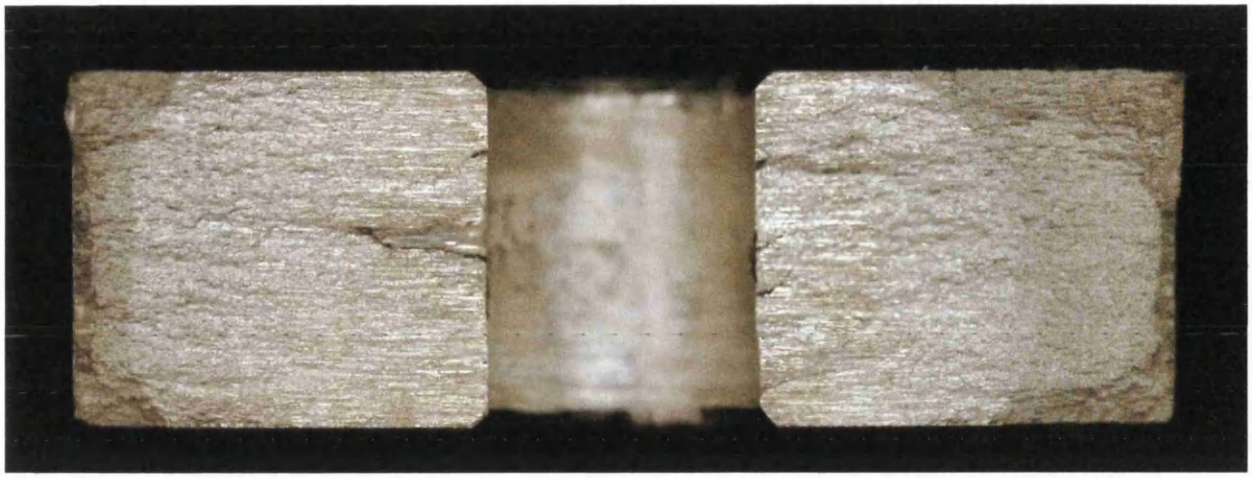

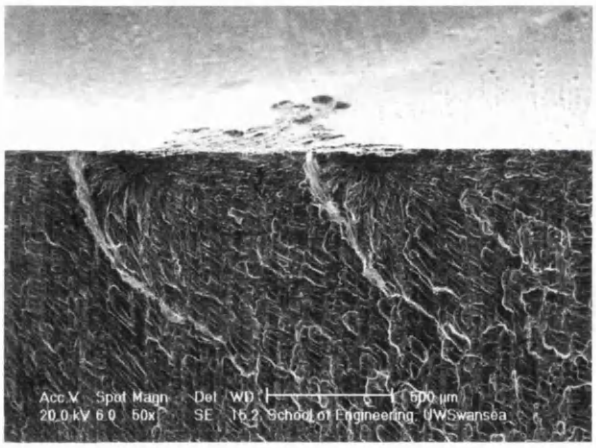
Acc.V Spot Magn Det WD 500 µm
20.0 kV 6.0 50x SE 16.2 School of Engineering, UWSwansea

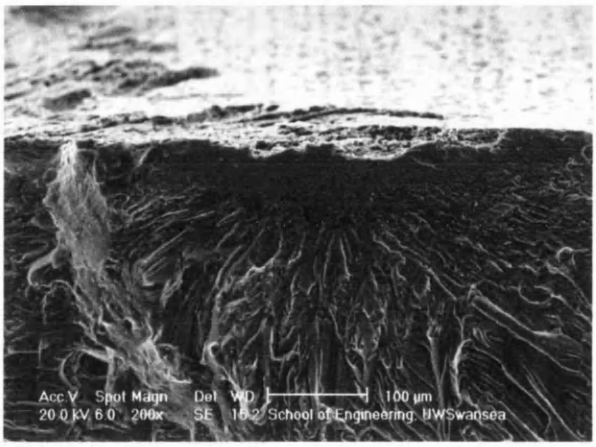
Acc.V Spot Magn Det WD 100 µm
20.0 kV 6.0 200x SE 16.2 School of Engineering, UWSwansea

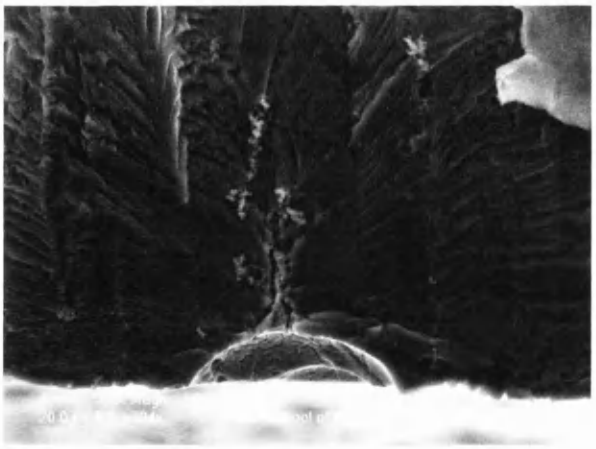

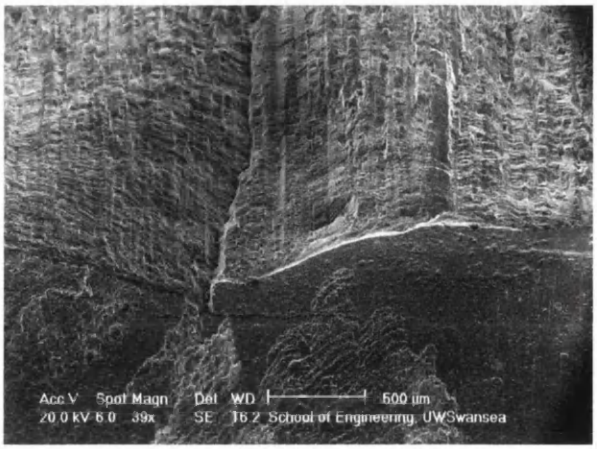
Acc.V Spot Magn Det WD 500 µm
20.0 kV 6.0 39x SE 16.2 School of Engineering, UWSwansea

FH-C8-27

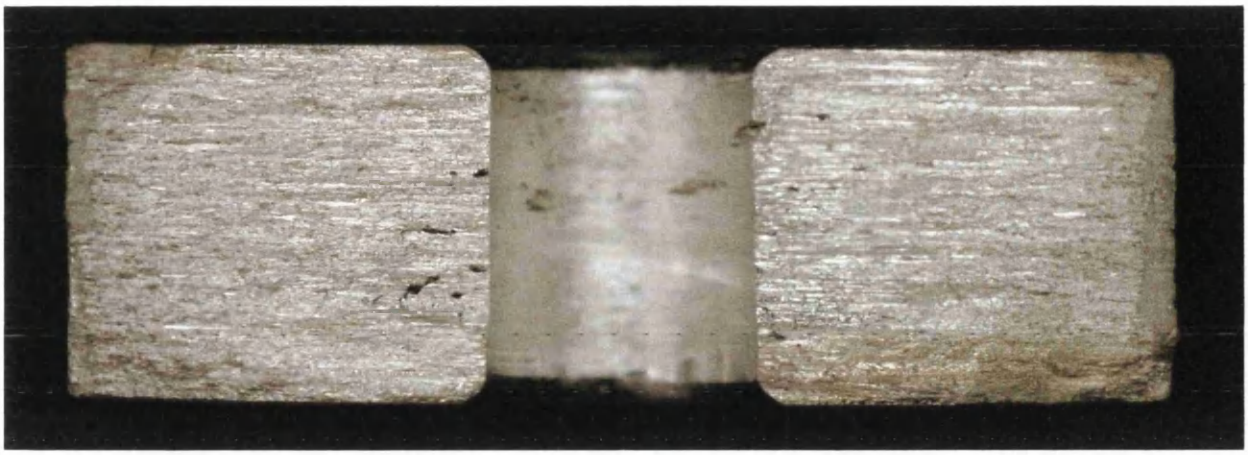

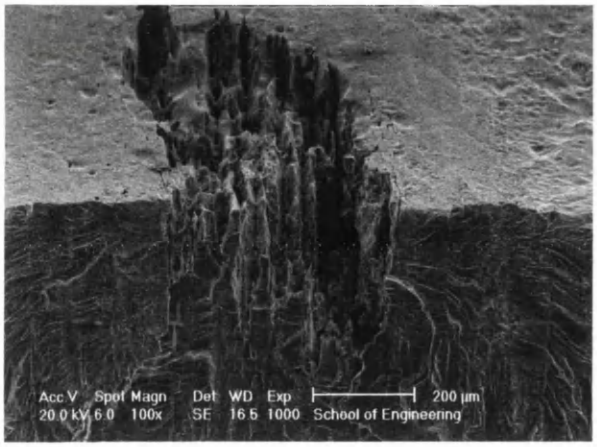
Acc.V Spot Magn Det WD Exp 200 µm
20.0 kV 6.0 100x SE 16.5 1000 School of Engineering

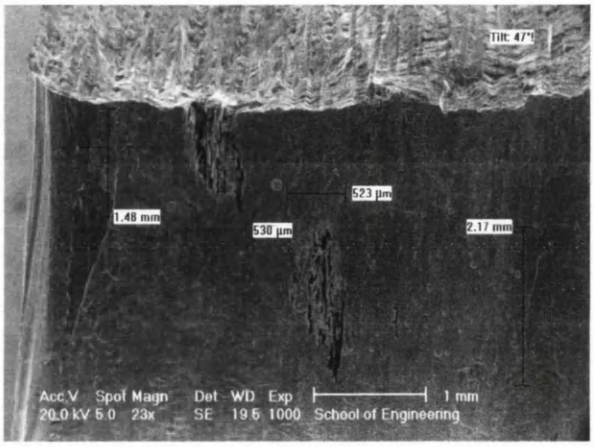
Tilt: 47°
523 µm
1.48 mm
530 µm
2.17 mm
Acc.V Spot Magn Det WD Exp 1 mm
20.0 kV 5.0 23x SE 19.5 1000 School of Engineering

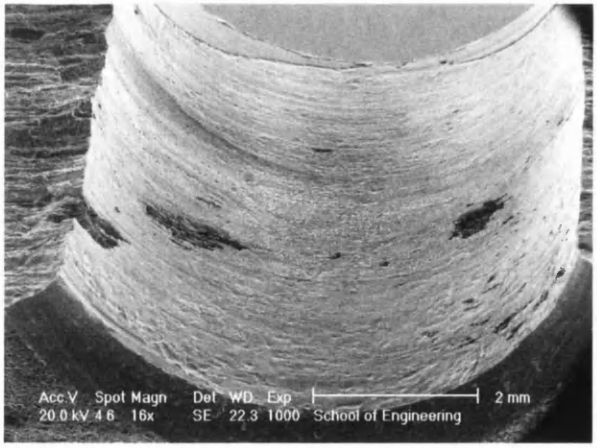
Acc.V Spot Magn Det WD Exp 2 mm
20.0 kV 4.6 16x SE 22.3 1000 School of Engineering

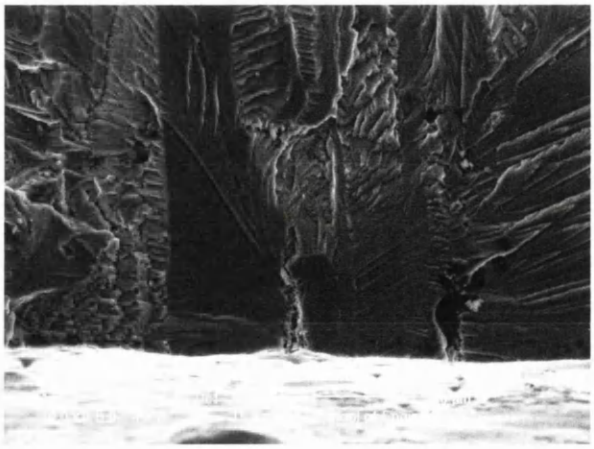

FH-C8-28

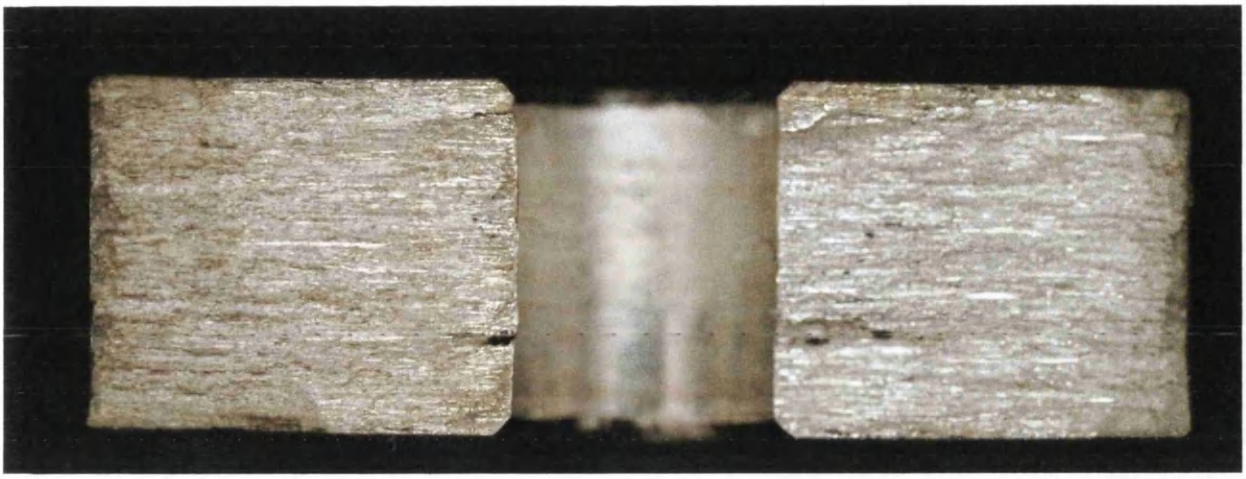

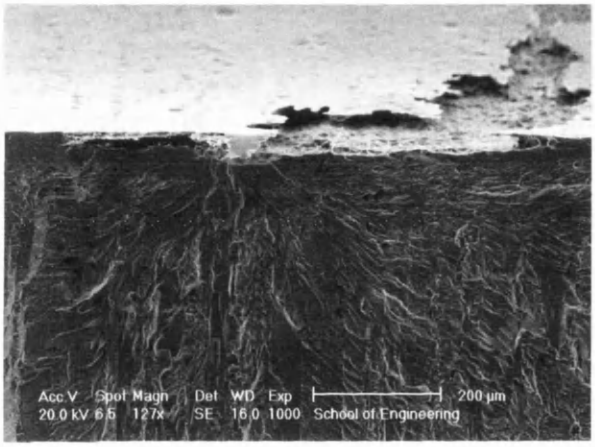
Acc.V Spot Magn Det WD Exp 200 µm
20.0 kV 6.5 127x SE 16.0 1000 School of Engineering

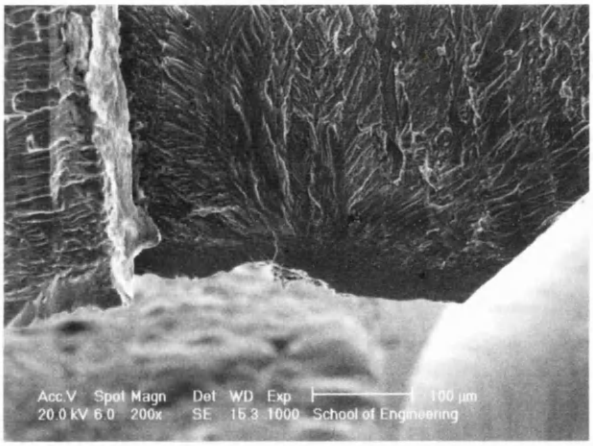
Acc.V Spot Magn Det WD Exp 100 µm
20.0 kV 6.0 200x SE 15.3 1000 School of Engineering

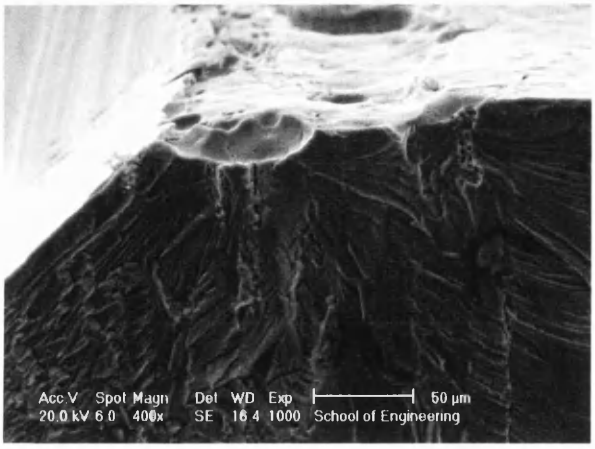
Acc.V Spot Magn Det WD Exp 50 µm
20.0 kV 6.0 400x SE 16.4 1000 School of Engineering

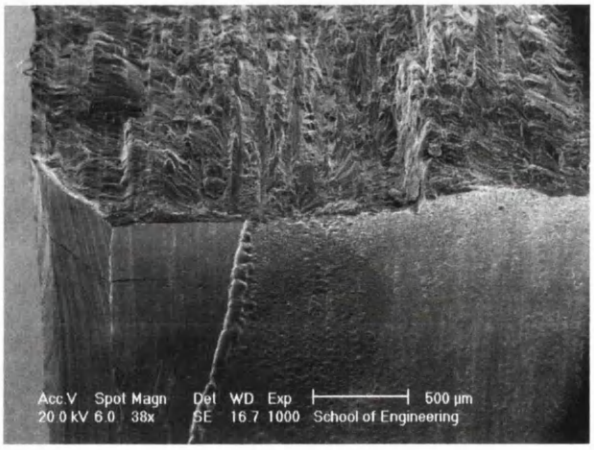
Acc.V Spot Magn Det WD Exp 500 µm
20.0 kV 6.0 38x SE 16.7 1000 School of Engineering

FH-C8-29

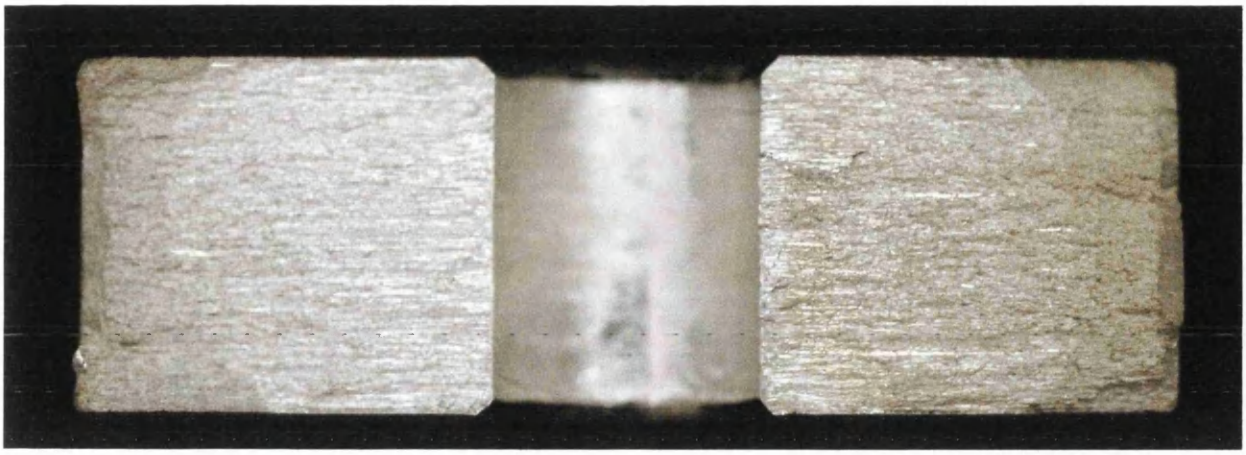

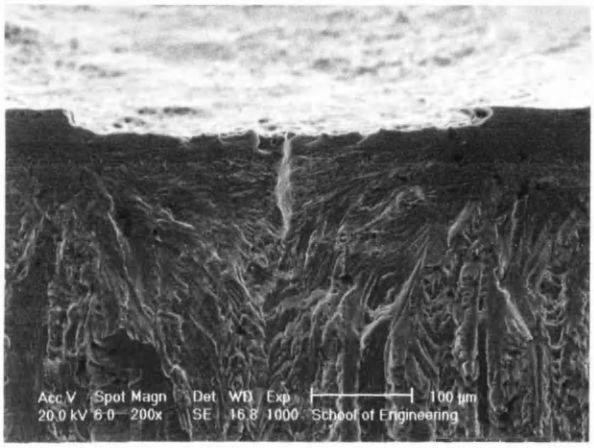
Acc.V Spot Magn Det WD Exp 100 µm
20.0 kV 6.0 200x SE 16.8 1000 School of Engineering

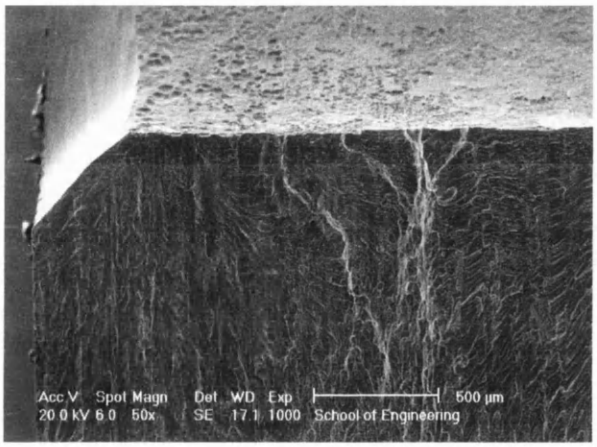
Acc.V Spot Magn Det WD Exp 500 µm
20.0 kV 6.0 50x SE 17.1 1000 School of Engineering

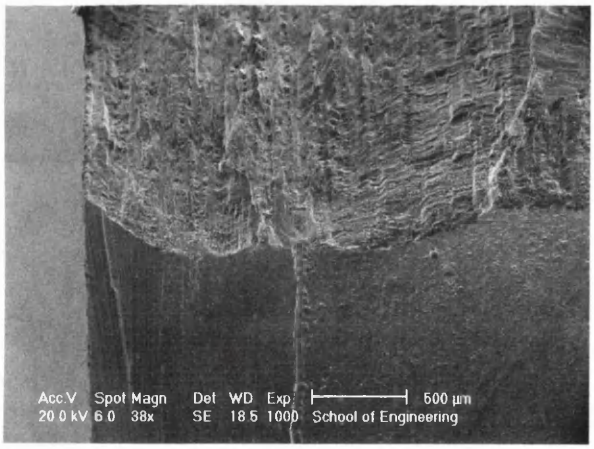
Acc.V Spot Magn Det WD Exp 500 µm
20.0 kV 6.0 38x SE 18.5 1000 School of Engineering

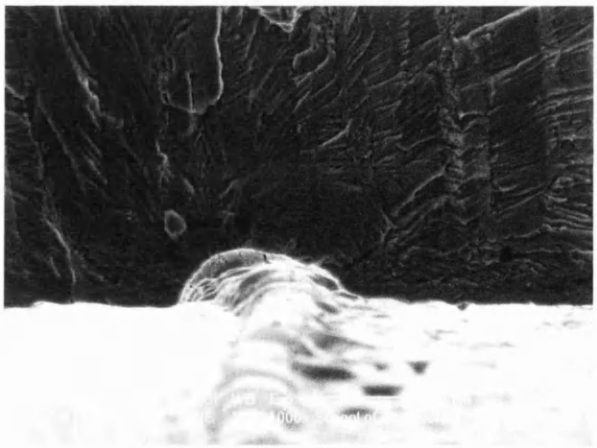

FH-C8-30

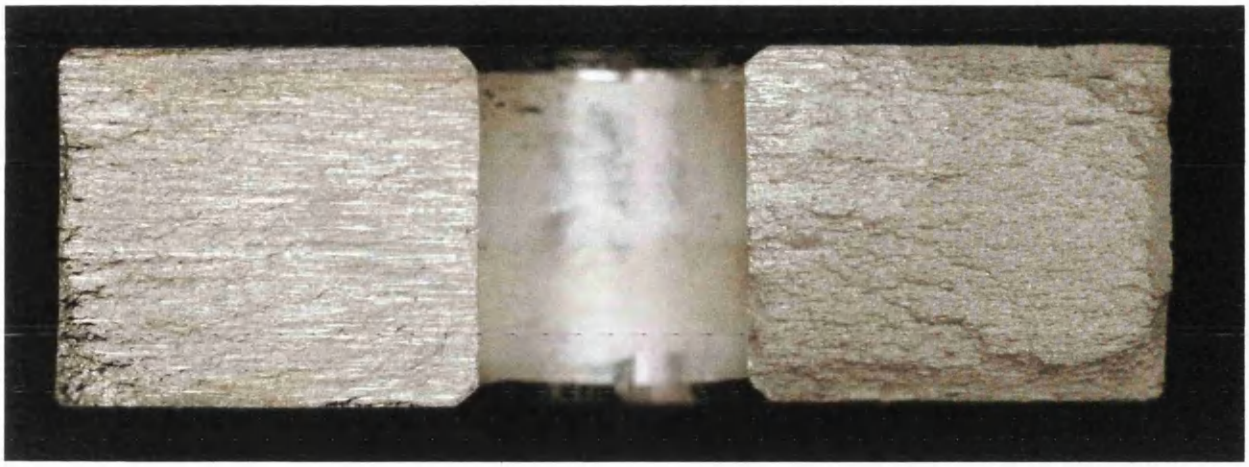

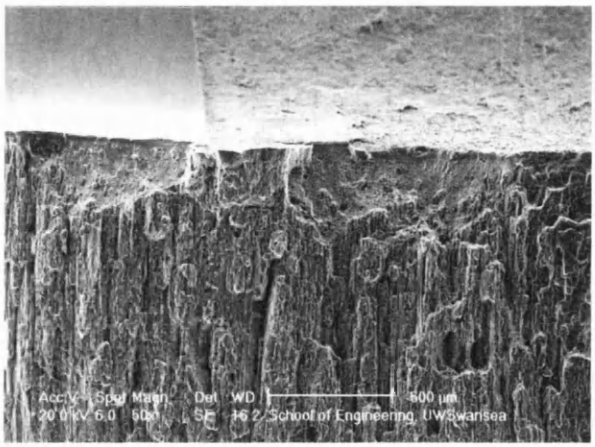
Acc.V Spot Magn Det WD 800 µm
20.0 kV 6.0 60x SE 16.2 School of Engineering, UWSwansea

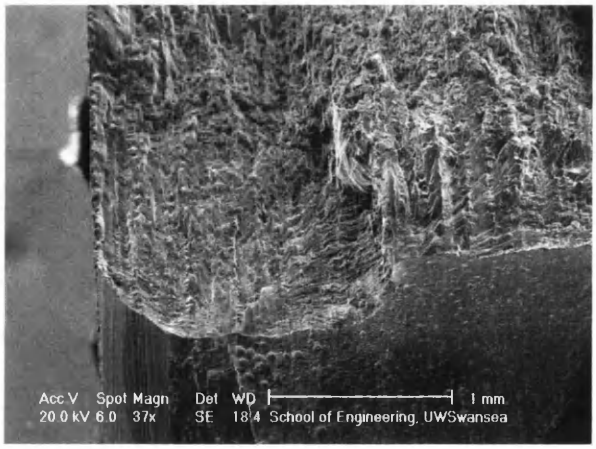
Acc.V Spot Magn Det WD 1 mm
20.0 kV 6.0 37x SE 18.4 School of Engineering, UWSwansea

REFERENCES

[1] G. Patton, C. Rinaldi, Y. Bréchet, G Lormand, R Fougères *'Study of Fatigue Damage in 7010 Aluminium Alloy'*, in **Mat.Sci.Eng A254 (1998) pp 207 – 218.**

[2] P. J. E. Forsyth *' The Influence of Tensile Stress on the Distribution of Etch Figures That are Formed by Corrosion on Metallographically Polished Surfaces of an Aluminium Alloy'* **in Materials Letters 41 (1999) pp 173 – 180.**

[3] L. Schra, W.G. J. Hart *'Engineering Property Comparisons of 7050-T73651, 7010-T7651 and 7010-T73651 Aluminium Alloy Plate'* **in Eng.Frac.Mech Vol.17 No.6 (1983) pp 493 – 507.**

[4] H. Lajain *'Corrosion protection schemes for aircraft structures: some examples for the corrosion behaviour of aluminium alloys'* **in Aircraft corrosion, AGARD conference proceedings No. 315, Papers presented at the 52nd meeting of the AGARD structures and materials panel. Meeting held in Cesme, Turkey, 5 – 10 April 1981, NATO-AGARD, 64 Rue De Varenne, Paris, France, 1981.**

[5] I. M. Scolaris *'Corrosion prevention methods developed from direct experience with aerospace structures'* **Aircraft corrosion, AGARD conference proceedings No. 315, Papers presented at the 52nd meeting of the AGARD structures and materials panel. Meeting held in Cesme, Turkey, 5 – 10 April 1981, NATO-AGARD, 64 Rue De Varenne, Paris, France, 1981.**

[6] M. Doruk *'Some observations on the corrosion of aircraft at the force base in Bandirma, Turkey'* **Aircraft corrosion, AGARD conference proceedings No. 315, Papers presented at the 52nd meeting of the AGARD structures and materials panel. Meeting held in Cesme, Turkey, 5 – 10 April 1981, NATO-AGARD, 64 Rue De Varenne, Paris, France, 1981.**

[7] C. R. Pye *'Detection and prevention of corrosion in royal airforce aircraft'* **Aircraft corrosion, AGARD conference proceedings No. 315, Papers presented at the 52nd meeting of the AGARD structures and materials panel. Meeting held in Cesme, Turkey, 5 – 10 April 1981, NATO-AGARD, 64 Rue De Varenne, Paris, France, 1981.**

[8] G. T. Browne *'US Naval fleet aircraft corrosion'* **Aircraft corrosion, AGARD conference proceedings No. 315, Papers presented at the 52nd meeting of the AGARD structures and materials panel. Meeting held in Cesme, Turkey, 5 – 10 April 1981, NATO-AGARD, 64 Rue De Varenne, Paris, France, 1981.**

[9] McLoughlin *'Control measures for military aircraft'* **Aircraft corrosion, AGARD conference proceedings No. 315, Papers presented at the 52nd meeting of the AGARD structures and materials panel. Meeting held in Cesme, Turkey, 5 – 10 April 1981, NATO-AGARD, 64 Rue De Varenne, Paris, France, 1981.**

[10] H. Cordier *'Laboratory aspects of aluminium alloy'* **Stress corrosion cracking in aircraft structural materials, AGARD Conference proceedings series 18, Report of a two day symposium held by the structures and materials panel of AGARD in Turin, Italy, 18 – 19 April, 1967, NATO-AGARD, 64 Rue De Varenne, Paris, France.**

[11] J. J. Waller *'Some engineering aspects of stress corrosion cracking in high strength aluminium alloys'* **Stress corrosion cracking in aircraft structural materials, AGARD Conference proceedings series 18, Report of a two day symposium held by the structures and materials panel of AGARD in Turin, Italy, 18 – 19 April, 1967, NATO-AGARD, 64 Rue De Varenne, Paris, France.**

[12] R. J. H. Warnhill **Aircraft corrosion, AGARD conference proceedings No. 315, Papers presented at the 52nd meeting of the AGARD structures and materials panel. Meeting held in Cesme, Turkey, 5 – 10 April 1981, NATO-AGARD, 64 Rue De Varenne, Paris, France, 1981.**

[13] R. G. Mitchell *'An airline view of the corrosion problem'* **Aircraft corrosion, AGARD conference proceedings No. 315, Papers presented at the 52nd meeting of the AGARD structures and materials panel. Meeting held in Cesme, Turkey, 5 – 10 April 1981, NATO- AGARD, 64 Rue De Varenne, Paris, France, 1981.**

[14] D. O. Sprowls, R. H. Brown *'Stress corrosion mechanisms for aluminium alloys'* **in Fundamental aspects of stress corrosion cracking, Proceedings of a conference held at Ohio state university, 11 – 15 Sept, 1967, NACE-1, National association of corrosion engineers, Houston, Texas, 1969.**

[15] G. Deshais, S. B. Newcomb *'The influence of microstructure on the formation of stress corrosion cracks in 7xxx series aluminium alloys'* **in Mat.Sci.For Aluminium Alloys: Their Physical and Mechanical Properties Part 3 Proceeding of the 7th International Conference ICAA7, Virginia, April 9 – 14, 2000. Vols 331 – 337, pp 1635 – 1640.**

[16] M. Puiggali, A. Zielinski, J. M. Olive, E. Renauld, D. Desjardins, M. Cid *'Effect of microstructure on stress corrosion cracking of an Al-Zn-Mg-Cu alloy'* **in Corrosion Science, Vol 40, No 4/5 (1998), pp 805 – 819.**

[17] L. Schra, W. G. J.'t Hart *'Engineering property comparisons of 7050-T73651, 7010-T7651 and 7010-T73651 aluminium alloy plate'* **in Engineering Fracture Mechanics, Vol 17, No 6, (1983), pp 493 – 507.**

[18] P. J. E. Forsyth *'The influence of tensile stress on the distribution of etch figures that are formed by corrosion on metallographically polished surfaces of an aluminium alloy'* **in Materials Letters, Vol. 41, (1999), pp 173 – 180.**

[19] D. Tanguy, B. Bayle, R. Dif, Th. Magnin *'Hydrogen effects during IGSCC of pure Al–5Mg alloy in NaCl media'* **in Materials Science Forum. Aluminium Alloys: Their Physical and Mechanical Properties Part 3 Proceeding of the 7th International Conference ICAA7, Virginia, April 9 – 14, 2000. Vols 331 – 337, pp 1659 – 1664.**

[20] J. S. Robinson *'Influence of retrogression and re-aging on the stress corrosion cracking resistance of 7010'* **in Materials Science Forum. Aluminium Alloys: Their Physical and Mechanical Properties Part 3 Proceeding of the 7th International Conference ICAA7, Virginia, April 9 – 14, 2000. Vols 331 – 337, pp 1653 – 1658.**

[21] K. Nisancioglu *'Corrosion of aluminium alloys'* **in Proceedings of ICAA3, Vol. 3, 239 – 259, Trondheim, (1992), NTH and SINTEF.**

[22] G. M. Scamans, J. A. Hunter, N. J. H. Holroyd *'Corrosion of aluminium alloys – a new approach'* **in Proceedings of the 8th International Light Metals Congress, pp 699 – 705, Leoben-Wien, (1987).**

[23] G. Svenningsen *'Corrosion of aluminium alloys'* **Department of materials technology, 7491 Trondheim, Norway.**

[24] Z. Szklararska-Smialowska *'Pitting corrosion of aluminium'* **in Corrosion Science, Vol. 41, (1999), pp 1743 – 1767.**

[25] J. Augustynski, R. P. Frankenthal, J. Kruger (Eds.), **Proceedings of the Fourth International Symposium on Passivity, The Electrochem. Soc., Pennington, NJ, 1978, p. 997.**

[26] J.R. Galvele, **in Journal of Electrochem. Soc, 123, (1976), 464.**

[27] H.P. Godard, **Canada, in Journal of Chemistry, Eng 21, (1960), 167 104.**

[28] F. Hunkeler, H. Boehni, **in Corrosion, vol. 37, (1981) 645.**

[29] A.K. Vijh, **in Corrosion Science vol.13, (1973), 805.**

[30] T. Hagyar, J. Williams, **in Trans. Faraday, Soc 57, (1961), 2288.**

[31] H. Lajain '*Corrosion protection schemes for aircraft structures: some examples for the corrosion behaviour of aluminium alloys*' **in Aircraft corrosion, AGARD conference proceedings No. 315, Papers presented at the 52nd meeting of the AGARD structures and materials panel. Meeting held in Cesme, Turkey, 5 – 10 April 1981, NATO- AGARD, 64 Rue De Varenne, Paris, France, 1981.**

[32] C. Blanc, G. Mankowski '*Susceptibility to pitting corrosion of 6056 aluminium alloy*' **in Corrosion Science, Vol.39, No. 5, (1997), pp. 949 – 959.**

[33] G. N. Frantziskonis, L. B. Simon, J. Woo, T. E. Matikas '*Multiscale characterisation of pitting corrosion and application to an aluminium alloy*' **in Eur.J.mech. A/Solids, Vol. 19, (2000), pp. 309 – 318.**

[34] L. Balázs, J. F. Gouyet '*Two-dimensional pitting corrosion of aluminium thin layers*' **in Physica A, 217, (1995), pp 319 – 338.**

[35] M. Shao, Y. Fu, R. Hu, C. Lin '*A study on pitting corrosion of aluminum alloy 2024-T3 by scanning microreference electrode technique*' **in Materials Science and Engineering, A344, (2003), pp 323 – 327.**

[36] W. H. Hartt, J. S. Tennant, W. C. Hooper '*Solution chemistry modification within corrosion-fatigue cracks*' **in Corrosion Fatigue Technology, ASTM STP 642, Proceedings of a symposium held in Denver, Colorado, 14 – 19 November (1978).**

[37] P. M. Scott '*Chemistry effects in corrosion fatigue*' **in ASTM STP 801, Proceedings of the symposium on corrosion fatigue: Mechanics, metallurgy, electrochemistry, and engineering held in St.Louis, MO21 – 22 October 1981, Edited by T. W. Crooker, B. N. Leis, ASTM, Philadelphia.**

[38] W. H. Bamford '*Implementing corrosion-fatigue crack growth rate data for engineering applications*' **in Corrosion Fatigue, ASTM 801, Proceedings of the symposium on corrosion fatigue: Mechanics, metallurgy, electrochemistry, and engineering held in St.Louis, MO21 – 22 October 1981, Edited by T. W. Crooker, B. N. Leis, ASTM, Philadelphia.**

[39] D. J. Duquette '*Mechanisms of corrosion fatigue of aluminium alloys*' **in Corrosion Fatigue, AGARD conference proceedings No. 316, Papers presented at the 52nd meeting of the AGARD structures and materials panel. Meeting held in Cesme, Turkey, 5 – 10 April 1981, NATO-AGARD, 64 Rue De Varenne, Paris, France, 1981.**

[40] D. Aliaga, E. Budillon '*Corrosion fatigue behaviour of some aluminium alloys*' in **Corrosion Fatigue, AGARD conference proceedings No. 316, Papers presented at the 52nd meeting of the AGARD structures and materials panel. Meeting held in Cesme, Turkey, 5 – 10 April 1981, NATO-AGARD, 64 Rue De Varenne, Paris, France, 1981.**

[41] J. S. Santner, M. Kumar '*Corrosion-fatigue crack propagation rates in commercial 7075 and P/M X7091 aluminium alloys*' **in Corrosion Fatigue, ASTM 801, Proceedings of the symposium on corrosion fatigue: Mechanics, metallurgy, electrochemistry, and engineering held in St.Louis, MO21 – 22 October 1981, Edited by T. W. Crooker, B. N. Leis, ASTM, Philadelphia.**

[42] R. P. Gangloff '*Corrosion fatigue crack propagation in metals*' **in Environment induced cracking of metals, Proceedings of the conference held in Kohler, WI, 2 – 7 October, 1988, NACE – 10, National association of corrosion engineers.**

[43] http://www.cs.iupui.edu/~msdnsf/nnayani/htmlPgs/Papers.html#PAPER1

[44] http://www.twi.co.uk/j32k/protected/band_3/ksndt004.html

[45] http://www.rmc.ca/academic/gradrech/transportation4_e.html

[46] V. R. Crispim, J. J. G. Da Silva '*Detection of corrosion in aircraft aluminium alloys*' **in Appl. Radiat. Lsot, Vol. 49, No. 7, (1998), pp. 779 – 782.**

[47] K. K. Sankaran, R. Perez, K. V. Jata '*Effects of pitting corrosion on the fatigue behaviour of aluminium alloy 7075-T6: modelling and experimental studies*' **in Materials Science and Engineering, A297, (2001), pp. 223 – 229.**

[48] L. V. Corsetti, D. J. Duquette '*The effect of mean stress and environment on corrosion fatigue behaviour of 7075-T6 aluminium*' **in Metallurgical transactions, Vol. 5, (1974), pp. 1087 – 1093.**

[49] D. L. DuQuesnay, P. R. Underhill, H. J. Britt '*Fatigue crack growth from corrosion damage in 7075-T6511 aluminium alloy under aircraft loading*' **in International Journal of Fatigue 25, (2003), pp. 371 – 377.**

[50] J. J. Medved, M. Breton, P. E. Irving '*Corrosion pit size distributions and fatigue lives—a study of the EIFS technique for fatigue design in the presence of corrosion*' **in International Journal of Fatigue 26, (2004), pp. 71 – 80.**

[51] Q. Y. Wang, N. Kawagoishi, Q. Chen '*Effect of pitting corrosion on very high cycle fatigue behaviour*' **in Scripta Materialia 49, (2003), pp. 711 – 716.**

[52] S. W. Smith, J. A. Newman, R. S. Piascik '*Simulation of Fatigue Crack Initiation at Corrosion Pits with EDM Notches*' **in NASA report - NASA/TM-2003-212166 ARL-TR-2927.**

[53] J. A. Newman, R. S. Piascik, R. A. Lindenberg '*Failure Analysis of a Helicopter External Fuel-Tank Pylon*' **in NASA report - NASA/TM-2002-211645 ARL-TR-2711.**

[54] G. S. Chen, K. –C. Wan, M. Gao, R. P. Wei, T. H. Flournoy '*Transition from pitting to fatigue crack growth – modelling of corrosion fatigue nucleation in a 2024-T3 aluminium alloy*' **in Materials Science and Engineering, Vol. A219, (1996), pp. 126 – 132.**

[55] S. I. Rokhlin, J. -Y. Kim, H. Nagy, B. Zoofan '*Effect of pitting corrosion on fatigue crack initiation and fatigue life*' **in Engineering Fracture Mechanics 62, (1999), pp. 425 – 444.**

[56] E. J. Dolley, B. Lee, R. P. Wei '*The effect of pitting corrosion on fatigue life*' **in Fatigue and fracture of engineering materials and structures, Vol. 23, (2000), pp. 555 – 560.**

[57] J. Ruiz, M. Elices '*Environmental fatigue in a 7000 series aluminium alloy*' **in Corrosion Science, Vol. 38, (1996), pp. 1815 – 1837.**

[58] D.A.Lados, D.Apelian '*Fatigue crack growth characteristics in cast Al–Si–Mg alloys Part II. Life predictions using fatigue crack growth data*' **in Materials Science and Engineering A, Vol. 385, (2004), pp. 187–199.**

[59] J. A. Harter '*Comparison of contemporary FCG life prediction tools*' **in International Journal of Fatigue, Vol. 21, (1999), pp. 181 – 185.**

[60] E. J. Dolley, B. Lee, R. P. Wei '*The effect of pitting corrosion on fatigue life*' **in Fatigue Fracture Engineering Material Structures Vol. 23, (2000), pp. 555–560.**

[61] D.L. DuQuesnay, P.R. Underhill, H.J. Britt '*Fatigue crack growth from corrosion damage in 7075-T6511 aluminium alloy under aircraft loading*' **in International Journal of Fatigue, Vol.25, (2003), pp. 371–377.**

[62] J.J. Medved, M. Breton, P.E. Irving '*Corrosion pit size distributions and fatigue lives – a study of the EIFS technique for fatigue design in the presence of corrosion*' **in International Journal of Fatigue, Vol.26, (2004), pp. 71 – 80.**

[63] J.C. Newman Jr a, E.P. Phillips, M.H. Swain '*Fatigue-life prediction methodology using small-crack theory*' **in International Journal of Fatigue, Vol.21, (1999), pp. 109–119.**

[64] D.W. Hoeppner, V. Chandrasekaran, A.M.H. Taylor '*Review of pitting corrosion fatigue models*' **in Proceedings of the Twentieth ICAF (International Committee on Aeronautical Fatigue) Symposium Hawaii, USA.**

[65] D.W. Hoeppner, D. Mann, J. Weekes 'Fracture mechanics based modelling of the corrosion fatigue process' **in AGARD conference proceedings No. 316, Papers presented at the 52nd meeting of the AGARD structures and materials panel. Meeting held in Cesme, Turkey, 5 – 10 April 1981, NATO-AGARD, 64 Rue De Varenne, Paris, France, 1981.**

[66] T.C. Lindley, P. McIntyre, P.J. Trant '*Fatigue crack initiation at corrosion pits*' **in Metals Technology, Vol. 9, (1982), pp. 135 – 142.**

[67] G.S. Chen, K-C. Wan, M. Gao, R.P. Wei, T.H. Flournoy '*Transition from pitting to fatigue crack growth – modelling of corrosion fatigue crack nucleation in a 2024-T3 aluminium alloy*' **in Materials Science and Engineering A, Vol. 219, (1996), pp. 126 – 132.**

[68] Y. Kondo '*Prediction of fatigue crack initiation life based on pit growth*' **in Corrosion, Vol. 45, (1989), No.1. pp.7 – 11.**

[69] S. Kawai, K. Kasai '*Consideration of allowable stress of corrosion fatigue (focused on the influence of pitting)*' **in Fatigue and Fracture of Engineering Materials and Structures, Vol. 45, (1985), No.1, pp. 7 – 11.**

[70] M. Müller '*Theoretical considerations on corrosion fatigue crack initiation*' **in Metallurgical Transactions A, Vol.13A, (1982), pp. 649 – 665.**

[71] http://www.richard-seaman.com

[72] SICAS unpublished data- Report No's 1312/034 & 1312/048

[73] P.K. Sharp, T. Mills, G. Clark '*Aircraft Structural Integrity: The Impact of Corrosion*'

[74] http://www.history.navy.mil/planes/fa-18e.jpg

[75] SICAS unpublished data- Report No 1312/008

[76] SICAS unpublished data.

[77] BSEN 10002-1: 1990 Tensile testing of metallic materials pt 1 – Method of testing at ambient temperature. BSI.

[78] BS3518: 1993 Methods of Fatigue Testing. BSI.

[79] D.P.Rooke, D.J Cartrwight '*Stress Intensity Factors*' Published in 1976.

[80] SICAS unpublished data- Report No 1312/033

[81] SICAS unpublished data

[82] B.R. Crawford, C. Loader, A.R. Ward, C. Urbani, M.R. Bache, S.H. Spence, D.G. Hay, W.J. Evans, G. Clark and A.J. Stonham, '*The EIFS distribution for anodised and corroded 7010-T7651 under constant amplitude loading*', Fatigue and Fracture of Engineering Materials and Structures, 28(9), 795-808, 2005.

[83] Swansea University, unpublished data.